Theoretical and experimental studies of electromagnetic resonances in the ionospheric cavities of planets and satellites; instrument and mission perspectives

Fernando dos Santos Simoes

THESE DE DOCTORAT DE L'UNIVERSITE PIERRE ET MARIE CURIE

Spécialité

Physique, ED 389

Présentée par

M. Fernando António DOS SANTOS SIMÕES

Pour obtenir le grade de

DOCTEUR de L'UNIVERSITÉ PIERRE ET MARIE CURIE

Résonances des cavités ionosphériques des planètes et de leurs satellites: progrès et perspectives instrumentales

Soutenue le 7 de Décembre de 2007

devant le jury composé de:

Mme. Laurence REZEAU	(Présidente)
M. François LEFEUVRE	(Rapporteur)
M. Christian MAZELLE	(Rapporteur)
M. Michel HAMELIN	(Directeur de thèse)
M. Christian BÉGHIN	(Examinateur)
M. Jean-Jacques BERTHELIER	(Examinateur)
M. Réjean GRARD	(Examinateur)
M. Jean-Pierre LEBRETON	(Examinateur)

Este trabalho é dedicado a todos os homens e mulheres que têm dentro de si uma vontade insaciável de conhecer, de olhar o infinito e tentar transpô-lo. Esta tese é um tributo a todos os que procuram, sabiamente, chegar sempre mais alto e promovem o conhecimento científico como um extraordinário legado da humanidade.

Acknowledgments

This thesis covers several topics of research and, consequently, many people from various disciplines have made it possible, sometimes anonymously.

I express first my thanks to all men and women who have worked for the Cassini-Huygens programme during the last three decades and have contributed to the success of this remarkable mission, which will remain a major legacy to planetary scientists for many years to come.

I am grateful to the members of the HASI-PWA-Team for inviting me to participate in the PWA data analysis and to contribute to unveiling the mysteries of Titan.

I thank CETP-IPSL (Saint Maur, France) and RSSD/ESA-ESTEC (Noordwijk, The Netherlands) that provided outstanding environments to conduct my research.

I thank my supervisor, Michel Hamelin, for his wise coordination and for creating excellent research conditions. A have appreciated very much his friendship and support, especially when my numerical models were not converging.

I thank all my CETP colleagues; with a special mention for two of them. I am particularly indebted to Alain Péan for his hardware and software expertise, when additional memory or faster computers were required. I have also appreciated having fruitful discussions with Jean-Jacques Berthelier who had always a clever suggestion every time I was faced with a problem.

I thank Christian Béghin of LPCE for his sagacity and his friendly cooperation, and for showing me how analytical and numerical models can be complementary.

The subsurface permittivity probe was initially developed at RSSD, ESA-ESTEC, and I want to show my gratitude to those who have contributed to such an achievement. I thank Gerhard Schwehm, head of Planetary Missions Division, for hosting my activities; Jean-Pierre Lebreton for his continuous encouragements and for helping me to obtain the funds required for my research; Agustin Chicarro and Roland Trautner for their efficient supervision; Jo Heida and Bart Butler for their help regarding electronics design and assembling; and Lambert Schipperheijn for mechanical parts manufacturing. I thank Bernd Lehmann and César Gómez Fernández of the Mechanical Systems Laboratory, at ESA-ESTEC, for helping me with instrument calibration and testing. I must emphasize that several of my objectives have been achieved only because they believed that such accomplishments were possible. Several ideas were extensively discussed with these people, in particular Roland Trautner; hence the subsurface permittivity probe is also theirs.

Last, but not least, I thank Réjean Grard, who has been involved in several aspects of this thesis, from its inception at ESTEC, until its completion at CETP.

Finally, I wish to thank my family and friends for their unconditional support, mainly when they felt that I was living on another planet than Earth.

This research was sponsored by the following institutions: *Fundação para a Ciência e a Tecnologia* and *Agência de Inovação*, (Portugal); *European Space Agency, European Space Research and Technology Centre,* (The Netherlands); *Centre National d'Études Spatiales* (France). I also thank the *International Space Science Institute* (Switzerland) for hosting and supporting several team meetings.

Résume

L'étude des ondes d'extrêmement basses fréquences dans les cavités ionosphériques des planètes et satellites dotés d'atmosphère suit une approche similaire à celle suivie pour la Terre. Elle contribue à la caractérisation du circuit électrique atmosphérique, des sources d'énergie associées et des limites interne et externe des cavités. Un modèle numérique à éléments finis a été développé et appliqué à ces corps planétaires en vue d'étudier en particulier les résonances de Schumann. Les paramètres du modèle sont : (a) la géométrie de la cavité, (b) les caractéristiques de l'ionosphère, (c) la réfractivité de l'atmosphère neutre et (d) la permittivité complexe de la proche sub-surface. La simulation donne la fréquence propre et le facteur Q de la résonance ainsi que la distribution spatiale du champ électrique dans la cavité. Les cavités de Vénus et Titan sont étudiées dans le détail. La première est très asymétrique et un dédoublement de la fréquence de résonance est prédit. La seconde a été explorée par la sonde Huygens et, additionnellement la faible conductivité du sol de Titan ouvre la porte à l'étude de la sub-surface. La pertinence d'un modèle de la cavité de Titan a été testée par rapport aux mesures *in situ* de l'instrument Permittivity, Waves and Altimetry (PWA) à bord de la sonde Huygens. L'instrument PWA a mesuré les profils de conductivité électronique et ioniques grâce aux techniques d'impédance mutuelle (MI) et de relaxation, et a identifié une couche conductrice à une altitude d'environ 60 km. Après atterrissage, la constante diélectrique et la conductivité locales du sol mesurées par la sonde MI sont respectivement ~2 et ~ 10^{-10}-10^{-9} Sm^{-1}. Aucune évidence d'éclair ou de coup de tonnerre n'a été enregistrée, mais un fort signal à 36 Hz a été reçu pendant toute la descente. Cette émission à bande étroite n'est probablement pas un artefact. On a montré par modélisation avec des paramètres appropriés que le signal peut être une résonance naturelle. L'expérience acquise est appliquée à la conception de nouveaux instruments, ARES et SP2, pour étudier l'atmosphère et le sol de la planète Mars dans le cadre du projet ExoMars et pour d'autres corps lors de futurs projets spatiaux. On propose de tirer profit des caractéristiques polaires de l'eau et d'appliquer la technique MI à la détection de la glace dans le régolithe martien.

Mots clés

Sciences planétaires; mission Cassini-Huygens; ondes électromagnétiques; résonance de Schumann; électricité atmosphérique; instrumentation spatiale

Theoretical and experimental studies of electromagnetic resonances in the ionospheric cavities of planets and satellites; instrument and mission perspectives

Abstract

The study of extremely low frequency electromagnetic wave propagation in the ionospheric cavities of celestial bodies in the Solar System follows an approach similar to that developed for Earth. It contributes to the characterization of the atmospheric electric circuit and associated energy sources, and to the identification of the inner and outer cavity boundaries. A wave propagation finite element model is developed and applied to all planets and satellites surrounded by an atmosphere, with the aim of studying, in particular, the Schumann resonance phenomenon. The input parameters of the model are: (a) the geometry of the cavity, (b) the ionized atmosphere characteristics, (c) the neutral atmosphere refractivity and (d) the top subsurface complex permittivity. The simulation yields the eigenfrequency and Q-factors of the resonance and the distribution of the electric field in the cavity. The cavities of Venus and Titan are studied in more detail. The former is highly asymmetric and a significant splitting of the eigenfrequency is predicted. The latter has been explored by the Huygens Probe and, additionally, the low conductivity of Titan's soil opens the door to subsurface investigations. The validity of a model of Titan's cavity is scrutinized against the *in situ* measurements performed by the Permittivity, Waves and Altimetry (PWA) analyzer, onboard the Huygens Probe. The PWA instrument measured the ion and electron conductivity profiles using the Mutual Impedance (MI) and relaxation technique, and identified a conductive layer at an altitude of about 60 km; the relative permittivity and conductivity of the surface measured by the MI probe at the landing site are ~2 and ~10^{-10}-10^{-9} Sm^{-1}, respectively. No evidence of any lightning event or thunder clapping was found; but strong electric signal at around 36 Hz was observed throughout the descent. This narrow band emission is probably not an artefact. Modelling the cavity with an appropriate set of input parameters indicates that this signal is possibly a natural resonance of the cavity. The acquired experience is then applied to the design of novel electrical probes, ARES and SP2, to study the atmosphere and the ground of the planet Mars, in the forthcoming ExoMars mission, and of other celestial bodies in future space missions. It is proposed to take advantage of the polar characteristics of the water molecule and to apply the MI technique to the detection of subsurface ice in the Martian regolith.

Keywords

Planetary sciences; Cassini-Huygens mission; electromagnetic waves; Schumann resonance; atmospheric electricity; space instrumentation

Contents

List of Tables

List of Figures

1. Introduction

The propagation of electromagnetic waves in the atmosphere of Earth has been extensively studied, in a wide spectral range, for scientific and technological purposes. This work is devoted to phenomena that fall within the Extremely Low Frequency (ELF, range 3 Hz - 3 kHz) and Very Low Frequency (VLF, 3-30 kHz) ranges, where the wavelengths are commensurate with planetary sizes. The propagation of ELF waves within the cavity formed by two highly conductive, concentric, spherical shells, such as the boundaries formed by the surface and the ionosphere of Earth, was first studied by Schumann (1952); the associated resonance phenomena were subsequently observed by Balser and Wagner (1960). Resonances in the Earth cavity are closely related with lightning activity and contain information about the global electric circuit of the cavity; their characterization contributes not only to our understanding of wave propagation but also to the study of the physical and chemical processes that take place in the atmosphere and lower ionosphere. Atmospheric ion chemistry processes are closely linked with the distribution of the energy sources, the interactions with the solar wind, the conditions for wave propagation, and the global dynamics of the gaseous envelope. Lightning plays a peculiar role because it is the major source of electromagnetic energy in the Earth cavity. In this thesis, we develop a generalized approach to the resonances of planetary cavities that involves the characteristics of the ionosphere, the atmosphere, the surface, and the interior of the planets and their moons.

Schumann resonance studies are currently, conducted in three major fields of research, specifically climate change, high altitude atmospheric electricity, and space weather. The connection between Schumann resonances, lightning, and thunderstorm activity at global scale presents a reliable method to monitoring climate variability and space weather (Williams, 1992; Williams and Sátori, 2007). Correlation between Schumann resonance measurements onboard stratospheric balloons and Earth observations from satellites, namely TARANIS (Blanc et al., 2007), reveals a promising approach for the investigation of high altitude discharging events, such as sprites (Williams et al., 2007a).

An approach similar to that used for Earth can be applied to the planets, from Venus to Neptune, and their moons that are surrounded by an atmosphere. A special attention is devoted to Titan and the *in situ* measurements performed by the Huygens Probe. Titan, the largest satellite of Saturn, is a remarkable object; it is the sole moon of the Solar System with a thick atmosphere, which might resemble that of the primordial Earth, several billion years ago. Voyager flybys, in the early eighties, revealed an atmosphere composed of nitrogen with a small amount of methane, and permeated with haze that impaired the observation of the surface. It is known that N_2-CH_4 mixtures can produce complex organic radicals when

subjected to high voltage electric discharges (e.g., Raulin and Owen, 2002). The observation of possible prebiotic conditions on Titan was therefore one of the major objectives of Cassini-Huygens, a mission dedicated to the Kronian system: Saturn, its rings and its moons (Matson et al., 2002; Lebreton et al., 2002). The spacecraft included a probe, Huygens, to perform *in situ* measurements of the composition and electrification of the atmosphere, possibly down to the surface of Titan.

The Cassini-Huygens mission is an international collaboration, where the National Aeronautics and Space Administration (NASA) provides the Cassini Orbiter, which carries a large set of remote sensing instruments, and the European Space Agency (ESA) supplies the Huygens Probe that includes several instruments entirely devoted to the *in situ* observation of Titan. The Permittivity, Waves and Altimetry (PWA) analyzer, a subsystem of the Huygens Atmospheric Structure Instrument (HASI), is part of the Huygens payload and is dedicated to atmospheric electricity and surface dielectric measurements (Grard et al., 1995; Fulchignoni et al., 2002). PWA comprises the following elements: (a) a Mutual Impedance Probe (MIP) for atmospheric and surface permittivity studies; (b) a Relaxation Probe (RP) for atmospheric ion and electron conductivity measurements; (c) a receiver to observe lighting activity, and ELF and VLF waves; (d) an acoustic transducer for thunder-clap detection; (e) a radar module to not only assist descent operations but also perform atmospheric backscatter and surface topography investigations; (f) a set of electrodes that form the electric field antenna, and the MIP and RP sensors. The PWA complex forms a comprehensive set of detectors that can significantly contribute to the characterization of the electric environment of Titan, in particular assessing the conditions for ELF wave propagation.

The mutual impedance probe technique has been introduced in geophysics at the beginning of the 20th century for measuring the ground conductivity (Wenner, 1915). The mutual impedance is the ratio of the voltage measured by a receiving dipole to the current injected into the medium through an adjacent transmitting dipole. This technique was transposed to space plasmas by Storey et al. (1969) and applied in many ionospheric and magnetospheric experiments; Grard (1990) extended the concept to study the dielectric properties of planetary surfaces. A MIP was included in the Huygens Probe to measure the dielectric properties of the atmosphere and surface of Titan; it is also part of the payload of Philae, the Rosetta Lander, *en route* to the comet Churyumov-Gerasimenko. As for future planetary missions, the instrument has been recommended for the ExoMars project, in a new configuration and with improved capabilities. The later instrument is comprehensively described in this thesis and typifies a new generation of space tools based upon the mutual impedance technique. These new developments are particularly useful for assessing the dielectric properties of a planetary surface, which is essential to ascertain the location of the inner boundary of a resonating cavity.

The understanding of wave propagation on Titan requires information about a number of cavity parameters, such as the atmospheric conductivity profile, the source of electromagnetic energy, and the boundary conditions. Prior to the Huygens Probe descent upon Titan, the cavity parameterization relied exclusively on modelling, with the exception of the upper boundary whose conductivity could be estimated from the Voyager data. Unlike the cavity of Earth, where most parameters and wave propagation conditions are known with a fair accuracy, those of other celestial bodies are mostly theoretical. Therefore, the PWA data set brings an essential improvement to the Titan cavity models and a contribution to comparative planetology.

The scientific rationale of this thesis is manifold; the work consists of: (a) a presentation of the PWA data analysis results; (b) a development of a wave propagation numerical model for the cavity of Titan; (c) a generalization of this numerical model and its application to other planetary cavities using specific parameterization; (d) a set of recommendation for the

development of instrumentation suitable for atmospheric and surface studies of planets and satellites. The data analysis of the PWA instrument is mainly focused on the electron conductivity profile of the atmosphere, the calibration of the ELF spectra, and the evaluation of surface dielectric properties. The numerical model to study wave propagation is based on several tools available in the COMSOL Multiphysics software, which uses the finite element method to solve specific equations. The algorithm is generalized and applied to other cavities, namely those of Venus, Mars, Jupiter and its moons Io and Europa, Saturn, Uranus, and Neptune. Possible instruments for measuring the electric properties of the atmosphere and surface of planets are described; a new technique to study the Martian regolith subsurface was proposed for the ExoMars mission. The instrument, known as the Subsurface Permittivity Probe (SP2), is based on the mutual impedance principle and benefits from the heritage of the Huygens and Rosetta missions.

The introduction concludes with a brief description of the publications closely related to this work. The structure of the thesis is the following:

Chapter 2 reviews the theory of wave propagation and resonance phenomena in planetary cavities. The description of the Earth cavity, energy sources and global electric circuit is followed by a presentation of the scientific purpose for studying other planetary cavities.

Chapter 3 reports a generalized numerical model that can be applied to any cavity configuration. The parameterization and numerical tools that make use of the finite element method are first described. The results, namely the lowest eigenfrequencies and Q-factors, are then presented for several planetary cavities.

Chapter 4 is dedicated to Titan. Following a recapitulation of the Cassini-Huygens mission, and a description of the Probe, we depict in more detail the PWA analyzer and the measurements performed in the atmosphere and on the surface of Titan. The experimental results are included in the model and provide new constraints for the cavity. The numerical output from the simulation consists of eigenfrequencies, ELF spectra, and electric field profiles. The results are briefly discussed in the light of our current knowledge of the electric environment of Titan. The ELF signal measured during the descent is also presented.

Chapter 5 is dedicated to prospective and future missions. The heritage and scientific objectives of the SP2 instrument proposed as a contribution to subsurface studies for the ExoMars mission are briefly presented. A full technical description of SP2 is not the aim of this work; only the most important features of the instrument are given.

Chapter 6, finally, summarizes the progress achieved about the characterization of planetary cavities, with a particular emphasis on Titan's, presents a synopsis of possible electric measurements in the atmosphere and on the surface of celestial bodies, and discusses the advances that can be expected from an instrument such as SP2.

The full articles, reports, and proceedings directly related with this thesis and including contributions of its author are added as appendices, with one exception, Simões (2004), because of its length (abstract only). A comprehensive bibliography listing all other relevant works is also included.

The appendices are sorted by topic (Titan, Planetary Cavities, Instrumentation), and are summarized hereunder.

Titan:

- **[Paper 1]** Fulchignoni et al. (2005) present the first observations made with HASI and PWA, and provide a preliminary description of the environment of Titan from the *in situ* measurements performed during the descent of Huygens. The temperature and density are both higher than expected in the upper part of the atmosphere; a lower ionospheric layer is seen between 140 km and 40 km, with a peak in electrical conductivity near 60 km; the temperature on the surface is 93.65±0.25 K, and the pressure 1467±1 hPa; the surface permittivity is about 2; a narrow line is observed in the ELF spectrum at around 36 Hz from an altitude of 140 km down to the surface. The amplitude of this line is enhanced approximately one minute after the deployment of the stabilizer parachute, at an altitude of ~110 km.

- **[Paper 2]** Simões et al. (2005) apply the finite element method to estimate the influence of the Huygens vessel upon the mutual impedance and electric field measurements. The calibration of the PWA data requires indeed an accurate determination of the effective length of the dipole antenna. The manuscript presents a simple approach, using Poisson and Laplace equations, to calibrate several of the sensors. The self and mutual capacitances of the Huygens vessel and of the electrodes, for example, are calculated as required for the calibration of the MIP data.

- **[Paper 3]** Grard et al. (2006) report the PWA measurements with further detail and provide a first overview of the electric properties and related physical characteristics of the atmosphere and surface of Titan. The electron conductivity profile shows a peak at an altitude about 60 km. The electron conductivity is measured with two independent techniques: the shapes of the profiles are similar but the conductivities differ by one order of magnitude; the ion conductivity is measured with RP, but the relaxation curves deviate from an exponential law, due to the presence of segments with constant potentials (plateaus). The RP voltage profiles show that the time constants relative to the negative and positive charges are minimal at 64 and 77 km, respectively. The narrow line at 36 Hz may not be due to a malfunction of the instrument. The surface conductivity is of the order of 4×10^{-10} Sm^{-1}. The performance of the mutual impedance during the first phase of the descent is not well understood. The ELF and VLF spectrograms show an enhancement of the signal at altitude lower than 22 km. The PWA data do not reveal any significant signal in the acoustic and lightning modes that can be assigned to natural phenomena.

- **[Paper 4]** Simões et al. (2007a) present a new numerical model of electromagnetic wave propagation in the cavity of Titan and discuss the constraints introduced by the PWA results. The analytical, semi-analytical, and numerical models of the Earth cavity are first discussed. The parameters that characterize the cavity are then introduced and the finite element model is described. The experimental and modelling results are finally compared. The major conclusions are: (a) The 36 Hz signal might be consistent with the second harmonic of the cavity resonance frequency; (b) A 90° angular separation between the electromagnetic source and the Huygens Probe might explain the predominance of the second harmonic over the fundamental resonance signal; (c) The surface of Titan cannot be considered as the inner boundary of the cavity; a subsurface ocean may instead play that role, and it is possible, in principle to

investigate the electric properties of this subsurface material because of the low surface reflectivity.

- **[Paper 5]** Béghin et al. (2007) study the ELF spectra and present several scenarios to explain the natural or artefact nature of the 36 Hz signal. Each hypothesis is then assessed with reference to the whole data set, laboratory tests on a mock-up, theoretical models, and numerical simulations. Artefacts include aerodynamic effects, boom and parachute vibrations, and instrument interferences. A natural source is more difficult to identify; several hypotheses are nevertheless offered: lightning activity, local corona discharges, atmospheric triboelectricity, and interactions with the magnetosphere of Saturn. The most likely scenario in each category is boom vibration or interaction with the magnetosphere of Saturn.

- **[Paper 6]** Hamelin et al. (2007) present an analysis of the calibrated MIP data and derive the electron conductivity and density profiles of the atmosphere of Titan. Calibrated amplitudes and phases of the signal are derived from theoretical and numerical models of PWA circuitry and Huygens vessel geometrical configuration. The effects of vertical motion and temperature are also included. The peculiar performance of the instrument in the altitude range 100-140 km is scrutinized. The major results are summarized in the following. The maximum electron conductivity is about 3×10^{-9} Sm^{-1} at 63 km, corresponding to an electron density of 650 cm^{-3}. The conductivity and electron density are significantly reduced in the altitude range from 80 up to at least 140 km. The ionized layer shows relatively steep boundaries; the scale heights are small compared with theoretical predictions. These features are probably resulting from electron attachment on aerosols.

- **[Paper 7]** Simões et al. (2007d) present an analysis of the MIP surface mode and derive constraints on surface composition. Several scenarios are discussed to explain the first measurements performed immediately after surface impact and the sudden transition observed 12 min after touchdown. The topics developed in this article are the following: the mutual impedance technique and instrument characteristics; data calibration; boom configuration after landing and Huygens attitude; surface dielectric properties for various rest positions, at five frequencies in the VLF range; comparison with radar measurements and constraints on soil composition at the landing site.

Planetary Cavities:

- **[Paper 8]** Simões and Hamelin (2006) discuss the propagation of low frequency electromagnetic waves in large cavities using the COMSOL Multiphysics tools. This work partly addresses the accuracy of the theoretical models used for Earth cavity and the generalization to other planetary environments. A special attention is devoted to Titan and to the corrections associated with the relatively large separation between the inner and outer shells. Analytical, semi-analytical, and numerical approaches are compared. The application of the time harmonic and eigenfrequency modes to the computation of eigenfrequencies, Q-factors, and electric field profiles, is discussed. The respective merits of 2D axisymmetric and 3D geometries are discussed, regarding accuracy and memory optimization.

- **[Paper 9]** Simões et al. (2007b) apply a model similar to that used for the cavity of Titan, to study the electromagnetic environment of other celestial bodies. The finite

element model is solved for the cavities of Venus, Mars, Jupiter and its moons Io and Europa, Saturn, Uranus, and Neptune. Complex eigenfrequencies and Q-factors are computed and are discussed in a preliminary comparative planetology study. It is concluded that the cavity of Venus exhibit lower losses than that of Earth and that ELF waves in the Martian atmosphere suffer higher attenuation; waves in the cavities of Io and Europa are evanescent, because a significant electron density extends down to the surface and prevents their propagation; the water content of the gaseous envelope of Uranus and Neptune can be estimated by measuring the Schumann resonances, which are strongly influenced by the conductivity profile.

- **[Paper 10]** Simões et al. (2007c) improve the existing models of the Venus cavity. They include corrections for the day-night asymmetry and atmospheric refractivity, and calculate the eigenfrequencies and field profiles. The model is validated against the VLF data collected by Venera 11 and 12. This study shows that the day-night asymmetry may split the Schumann frequency by as much as 1 Hz; and that the atmospheric refractivity introduces a maximum in the electric field, at an altitude of about 32 km. The profile predicted in the VLF range is fairly consistent with those recorded during the Venera descents, though local features, likely due to turbulence, are not reproduced.

Instrumentation:

- **[Paper 11]** Trautner and Simões (2002) describe an instrument based on the MIP technique to study the Martian regolith. The sensor consists of an array of several transmitting and receiving dipoles attached to a penetrator. Using a standard finite difference method to solve Laplace equation, they compute the potential distribution in the vicinity of the atmosphere-soil interface and in stratified media, such as those produced by water ice deposits. The spatial range and resolution are commensurate with the separation between the electrodes.

- **[Paper 12]** Hamelin et al. (2004) compare the performance of several MIP instruments proposed for the Cassini-Huygens, Rosetta, Netlander, BepiColombo, and ExoMars missions. They describe other configurations suitable for the study of the Martian regolith at shallow depths and the detection of water ice.

- **[Paper 13]** Trautner et al. (2004) present a preliminary concept for measuring the dielectric properties of planetary subsurface materials in the VLF range. They describe the technique and a specific architecture for subsurface applications, namely water ice detection and stratification characterization.

- **[Paper 14]** Simões et al. (2004a) study the dielectric properties of JSC-Mars 1, a Martian soil analogue, in the range 20 Hz-10 kHz. Laboratory measurements on Martian soil simulant JSC Mars-1 are described, which is used to support the calibration of instruments for planetary missions, namely SP2.

- **[Paper 15]** Simões et al. (2004b) study the dielectric properties of JSC-Mars 1, a Martian soil analogue, in the range 20 Hz-10 kHz. The measurements are made under controlled laboratory conditions to study the variation of the permittivity as a function of several parameters, porosity, gravimetric water content, frequency, and

temperature. It is possible to measure gravimetric ice contents of the order of 1%, due to the peculiar dielectric signature of the water molecule.

- **[Paper 16]** Simões (2004) proposes to mount a MIP on a mole, to detect water/ice in planetary regoliths at shallow depths. The report recapitulates the various stages of the study, from proof of concept to laboratory experiments and initial scientific calibration. The list of the topics covered in this work is the following: scientific rationale; water/ice dielectric properties, mechanical structure, electronics, data acquisition, control and signal processing, prototype development; hardware and software testing, instrument calibration; laboratory testing in controlled environments, instrument performance and study of Martian analogue materials. It appears possible, with less than 100 g and 1 W, to develop a MIP to measure water/ice in the Martian regolith and study the stratification at shallow depths. The gravimetric water/ice content detection threshold is ~1%, and interfaces and heterogeneities can be identified within a range of ~10 cm with a resolution of ~1 cm.

2. Wave Propagation and Resonances in Ionospheric Cavities

2.1. The Resonant Cavity

2.1.1. Basic Description

Earth can be regarded as a nearly conducting sphere, wrapped in a thin dielectric atmosphere that extends up to the ionosphere, whose conductivity is also substantial. Hence, the surface and ionosphere of Earth form a cavity where electromagnetic waves propagate. This phenomenon was first studied by Schumann (1952) and an historical perspective is presented by Besser (2007). When a cavity is excited with broadband electromagnetic sources, a resonant state can develop provided the average equatorial circumference is approximately equal to an integral number of wavelengths of the electromagnetic waves. This phenomenon is known as the Schumann resonance and was first observed by Balser and Wagner (1960); it provides information about thunderstorm and lightning activity at Earth and acts, for example, as a "global tropical thermometer" (Williams, 1992). In certain conditions, the same theory can be used to study other planetary cavities; we shall apply it to rocky planets, icy moons, and the gaseous giants.

Neglecting curvature and equating the circumference to an integer number of wavelengths, the resonant angular frequency of a thin void cavity is written

$$\omega_m = m\frac{c}{R}, \tag{01}$$

where m is an integer that identifies the eigenmode, c the velocity of light in the medium and R the average radius of the cavity. Including a 3D spherical correction yields (Schumann, 1952)

$$\omega_m = \sqrt{m(m+1)}\,\frac{c}{R}. \tag{02}$$

The first few Schumann resonances, or longitudinal modes, have frequencies that fall within the ELF range for most celestial objects, including Earth.

In addition to the longitudinal modes that are functions of the cavity radius, there exist local transverse modes along the radial direction. When the shells that form the cavity are perfect electric conductors, the transverse mode requires that the electric field be zero at the

boundaries. A resonance develops whenever the separation between the shells, generally the height of the ionosphere, h, is an integer number, p, of half-wavelengths,

$$\omega_p = p\frac{c\pi}{h}. \tag{03}$$

The value p=0 is associated with a possible electrostatic field between the ionosphere and the surface; on Earth, the lowest modes (p>0) lie in the VLF range. The longitudinal and transverse eigenfrequencies of same order (m=p) differ by more than two orders of magnitude for most bodies (h/R~0.01). However, the ratio between ionospheric height and cavity radius is relatively large on Titan (h/R~0.2) because, there, the cavity inner radius is small and the separation between the boundaries is large. Detection of the transverse resonance is more difficult than the longitudinal one due to its local nature and to the variability of the ionosphere.

These estimates give the order of magnitude of the resonances, but more accurate results require the solution of Maxwell equations with suitable boundary conditions. We shall follow the approach described by Nickolaenko and Hayakawa (2002) for the analysis of ELF wave propagation in the Earth cavity. In a first approximation, the longitudinal and transverse modes of propagation are decoupled and Equations (02-03) are obtained. A general solution, taking into account the coupling between longitudinal and transverse modes, leads to the relation (Nickolaenko and Hayakawa, 2002)

$$\omega_{mp} = \frac{c}{R}\sqrt{m(m+1)+\left(p\pi\frac{R}{h}\right)^2}. \tag{04}$$

The cavity of Earth, however, is not perfect and the models must take into account medium losses, which contribute to the dissipation of the energy supplied by the excitation sources. Wave attenuation in the cavity is generally caused by losses not only in the medium but also on the boundaries. Whereas the former is related with atmospheric conductivity, the later depends on wave reflectivity efficiency. Thus, it is useful to define two physical parameters, the skin depth and the quality factor of the cavity.
The skin depth is given by (Balanis, 1989)

$$\delta_h = \sqrt{\frac{2}{\mu_o\varepsilon_o}}\ \frac{\left(\sqrt{1+\left(\frac{\sigma}{\omega\varepsilon_o}\right)^2}-1\right)^{-1/2}}{\omega}, \tag{05}$$

where ε_o and μ_o are the permittivity and magnetic permeability of vacuum, ω the angular frequency of the propagating wave, and σ the medium conductivity. For large conductivities, $\sigma >> \omega\varepsilon_o$, Equation (05) reduces to

$$\delta_h = \sqrt{\frac{2}{\mu_o\omega\sigma}}. \tag{06}$$

The quality factor of the cavity, or Q-factor, is defined by

$$Q_m \equiv \frac{Re(\omega_m)}{2Im(\omega_m)} \approx \frac{\omega_m^{peak}}{\Delta\omega_m}, \quad (07)$$

where *Re* and *Im* are the real and imaginary parts of the complex eigenfrequency, ω_m^{peak} the peak power frequency of mode *m,* and $\Delta\omega_m$ the width of the line at half-power. Physically, the Q-factor is the ratio of the energy stored in the field over the energy lost during one oscillation period. An expedient way of estimating the quality factor consists in using the ratio of the resonator thickness over the skin depth of the electric field, $Q \propto h/\delta_h$ (Nickolaenko and Hayakawa, 2002). Increasing the ionosphere height augments the quality factor; losses are more important when the boundary is poorly conducting and the skin depth large.

The surface of Earth is generally assumed to be a perfect electric conductor (PEC) because its conductivity is of the order of 0.01 and 1 Sm^{-1} (Lide et al., 2006) on land and sea, respectively, whereas that of Titan, for example, is closer to a good dielectric and has a conductivity in the order of 10^{-10} Sm^{-1} (Grard et al., 2006) **[Paper 3]**. The skin depth on the surface of Earth is ~1 km that is two orders of magnitude lower than the height of the ionosphere. Consequently, the inner boundary of the cavity is the surface.

A contrasting situation occurs on Titan, where $\delta_h > 10^3$ km, because the surface is a poor reflector of ELF waves and cannot be considered as the inner boundary. The cavity is more intricate; ELF waves penetrate the soil and the surface is not a PEC (Simões et al., 2007a) **[Paper 4]**. In this case, the inner boundary is located below the surface.

The cavities of the giant planets present additional constraints because their surface is not well defined (Simões et al., 2007b) **[Paper 9]**. The ionosphere, though sometimes fuzzy and dynamic, represents the outer boundary for all the cavities.

In a first approximation, the cavity generally consists of two concentric spherical shells, but this is not always the case. On Earth, three peculiarities contribute to alter the spherical symmetry of the cavity, namely the day-night asymmetry, the polar non-uniformity (latitude dependence of the conductivity profile), and the geomagnetic dipole (Galejs, 1972; Bazarova and Rybachek, 1978). This asymmetry is in principle responsible for a partial or total line splitting, i.e. the eigenmode degeneracy is removed (Bliokh et al., 1968). Recent observations have shown evidences of line splitting and amplitude variation due to cavity heterogeneity, namely the day-night asymmetry (Sátori et al., 2007; Nickolaenko and Sentman, 2007).

2.1.2. General Formalism

Following a simplified formulation of the Schumann resonance frequency and the description of typical cavities in the Solar System, we shall now describe the general formalism that leads to the eigenfrequencies and eigenfunctions of the cavity. A full treatment of the Schumann resonance in a planetary cavity requires the solution of Maxwell equations,

$$\nabla \times \boldsymbol{E} = -\frac{\partial \boldsymbol{B}}{\partial t}, \quad (08)$$

$$\nabla \times \boldsymbol{H} = \sigma \boldsymbol{E} + \frac{\partial \boldsymbol{D}}{\partial t}, \quad (09)$$

$$\boldsymbol{D} = \varepsilon\varepsilon_o \boldsymbol{E}, \qquad \boldsymbol{B} = \mu_o \boldsymbol{H}, \quad (10)$$

where ***E*** and ***D*** are the electric and displacement fields, ***H*** and ***B*** the magnetic field strength and flux density, and ε the relative permittivity.

Taking into account the cavity characteristics and decoupling the electric and magnetic fields, Equations (08-10) can be solved in spherical coordinates (r, θ, φ), using the harmonic propagation approximation. One mode is characterized by H_r=0 and is called the transverse magnetic (TM) wave, the other one by E_r=0 and is known as the transverse electric (TE) wave. Neglecting the asymmetry of the cavity, and considering $h/R << 1$, the standard method of separation of variables yields (Bliokh et al., 1980)

$$\left\{\frac{d^2}{dr^2} - \frac{n(n+1)}{r^2} + \frac{\omega^2}{c^2}\varepsilon(r) - \sqrt{\varepsilon(r)}\frac{d^2}{dr^2}\left(\frac{1}{\sqrt{\varepsilon(r)}}\right)\right\}\left(r\Re(r)\right) = 0\,, \qquad (11)$$

where $\Re(r)$ is a radial function related to the electric and magnetic fields by the Debye potentials (Wait, 1962). This equation gives the eigenvalues of the longitudinal and transverse modes, assuming either $d\Re(r)/dr$=0 or $\Re(r)$=0 at both boundaries, respectively. For a thin void cavity the eigenvalues are those given by Equations (02)-(03) and $\Re(r)$ is a linear combination of Hankel functions. However, the previous approximation is no longer valid when the thickness is commensurate with the cavity radius; the separation between the TM and TE modes gives inaccurate results and Equation (11) is inappropriate. When the cavity is not spherical and is significantly thick, or when the conductivity profile deviates from an exponential law, the analytical approximations are no longer valid and Equations (08-10) must be solved numerically.

Although some approximations are accurate enough for the Earth cavity, the analytical models are generally not applicable to other environments. These simplified approaches are nevertheless useful because they give an insight into the role played by physical parameters that control wave propagation.

The model of Greifinger and Greifinger (1978) is widely used for calculating the propagation constant; it assumes an exponential law for the conductivity profile. This assumption is acceptable for Earth, less suitable for Venus, and inaccurate for Titan. The model was first used in planar geometry and its generalization to spherical coordinates was introduced by Sentman (1990). Both planar and spherical models lead to equivalent results for thin cavities. We shall therefore recapitulate the results obtained in planar geometry when the atmospheric and ionospheric conductivity profiles follow the exponential law:

$$\sigma(z) = \sigma_o \exp\left(\frac{z}{g_h}\right), \qquad (12)$$

where z is the altitude, g_h the scale height, and σ_o the conductivity at the surface. The conductivity profile is characterized by two altitudes, h_o and h_1, usually known as height of cut-off of the electric field and height of diffusion of the magnetic field, respectively. By definition, the height of cut-off for electric field is reached when $\sigma=\omega\varepsilon_o$ and is given by

$$h_o(\omega) = g_h \ln\left(\frac{\omega\varepsilon_o}{\sigma_o}\right). \qquad (13)$$

The effective altitude for the magnetic field is

$$h_1(\omega) = h_o(\omega) - 2g_h \ln\left(2g_h \frac{\omega}{c}\right). \tag{14}$$

The ELF propagation constant, ν, is a function of frequency and is written (Greifinger and Greifinger, 1978)

$$\nu(\nu+1) = \left(\frac{\omega}{c}R\right)^2 \frac{h_1(\omega) + ig_1\pi/2}{h_o(\omega) - ig_o\pi/2}. \tag{15}$$

The real and imaginary components of the propagation constant, ν_r and ν_i, can be derived from Equation (15), yielding when $g_h << g_o$ and $g_h << g_1$,

$$\nu_r(\omega) = \frac{\omega}{c}R\sqrt{\frac{h_1(\omega)}{h_0(\omega)}} \tag{16}$$

and

$$\nu_i(\omega) = R\frac{\omega\pi}{4c}\left(\frac{g_o}{h_o(\omega)} + \frac{g_1}{h_1(\omega)}\right). \tag{17}$$

As already mentioned, Equations (16-17) are strictly valid in planar geometry but are still applicable in spherical coordinates provided the radius of curvature is much larger than the skin depth (Sentman, 1990).

The limitation of the exponential approximation for the conductivity profile is extensively covered in the literature, namely dependence upon latitude, day-night asymmetry, geomagnetic field, etc. These constraints are extremely limiting in analytical studies, but are not relevant in numerical models, which consider arbitrary conductivity profiles. The analytical results, though restricted to specific conductivity models, nevertheless provide information that supports the interpretation of the numerical results.

2.2. Energy Sources and Global Circuit

The development and maintenance of resonance phenomena in planetary cavities require suitable electromagnetic sources. On Earth, lightning is the most important excitation source for Schumann resonances; it has been extensively studied in relation with atmospheric electricity, weather phenomena, and hazard prevention. Most lightning discharges on Earth are produced by precipitating clouds that contain water in solid and liquid phases. The two major requirements for lightning generation are: (i) interaction between particles of different types or between particles of the same type, but with different thermodynamic properties; (ii) significant spatial separation of the oppositely charged particles by convection or gravitational forces. In terrestrial lightning, the cloud-to-ground discharges are the most studied because they are the strongest and easiest to detect. However, it is not certain this type of lightning events occurs in other planetary atmospheres.

On Earth, lightning-like discharges produced by dust are also possible, though they release less energy per stroke. Electrical sparks, hundreds of meters long, can be produced via charge generation and separation in volcano eruptions (Rakov and Uman, 2003). Turbulent meteorological phenomena associated with dust storms are also closely related with discharging processes. Magnetohydrodynamic waves have also been proposed as a complementary source to lightning for the Earth's Schumann resonance (Abbas, 1968).

However, unlike the unambiguous lightning contribution, the role played by other sources requires further investigations.

Though not exhaustive, Table 1 summarizes some of the most important works dealing with observations, models, and global features of the Schumann resonance. Several advances in Earth cavity characterization can be applied to other planetary environments; this is one of the objectives of this thesis (Simões et al., 2007a; Simões et al., 2007b; Simões et al., 2007c) **[Papers 4, 9, and 10]**.

Subject	Contribution	Reference
First theoretical model of Earth cavity	Prediction of ELF global resonances in the Earth cavity; lightning is suggested as the main electromagnetic source	Schumann (1952)
Diurnal variations	First observation of the phenomenon and of its daily variation	Balser and Wagner (1960)
Stratospheric nuclear explosions	Disturbances in frequency spectra - one explosion shifts the resonance downwards by ~0.5 Hz	Gendrin and Stefant (1962) Madden and Thompson (1965)
Cavity asymmetry	Influence of day-night ionospheric asymmetry on resonances – line splitting	Galejs (1970) Sátori et al. (2007)
Cavity asymmetry	Influence of polar non-uniformity on resonances – line splitting	Bazarova and Rybachek (1978)
Cavity asymmetry	Influence of geomagnetic dipole on resonances – line splitting	Nickolaenko and Hayakawa (2002)
Cavity theoretical parameterization	Cavity parameterization with exponential conductivity profile and 2 scale heights	Greifinger and Greifinger (1978)
Solar cycle	Resonances are modulated by solar cycle and respond to solar flares, magnetic storms and solar proton events	Reid (1986) Hale and Baginski (1987)
Thunderstorm activity	Lightning as a tool for weather studies	Williams (1992)
Morphological features	Application of the resonance variability to the study of global lightning	Sentman (1995); Heckman et al. (1998)
Morphological features	Application of resonance variability to the study of sprite activity	Boccippio et al. (1995)
Line splitting	Attempts to measure resonance line splitting	Sentman (1989) Bliokh et al. (1980) Labendz (1998) Nickolaenko and Sentman (2007)
Altitude	Does frequency vary with altitude?	Ogawa et al. (1979) Morente et al. (2004)
Ionospheric height upper boundary	Dependence of intensity upon height of the ionosphere	Sentman and Fraser (1999)
Solar proton events	Observation of increases in amplitude, frequency, and Q-factor	Schlegel and Fullekrug (1999)
Lightning induced by sprites	Sprite lightning observed around the world with the Schumann resonance method	Williams et al. (2007a,b)

Table 1: Contributions to the study of the Schumann resonance in the Earth cavity.

The upper atmospheres of planets and satellites are ionised, partly due to interactions with solar photons and cosmic rays. The lower atmosphere of Earth is poorly conductive and is permeated by a current system that is driven by active thunderstorm clouds which act as generators, with return currents in fair weather regions. The highly conductive ground and ionosphere form the boundaries of this global electric circuit.

The global electric circuit is the system that involves the surface, atmosphere, ionosphere, and magnetosphere of Earth, which form together, a global spherical capacitor. The global circuit is sustained by thunderstorms, which raise the potential difference between the inner and outer boundaries up to several hundred thousand volts, and drive vertical currents through the atmosphere. The electric field is larger near the Earth surface, where it reaches ~100 Vm^{-1} in fair weather conditions. Siingh et al. (2007) and Aplin (2006) present an overview of the atmospheric global electric circuit of Earth and electrification processes in the Solar System,

respectively, and discuss the various charging mechanisms that play a role in atmospheric electricity.

Table 2 lists the possible electromagnetic sources that might contribute to develop resonance states in planetary cavities. Three atmospheric phenomena lightning - corona discharge and triboelectricity – are possible candidates but only the most likely one is specified for each body. It is nevertheless important to mention that, in some cases, the given scenario is even somewhat uncertain, namely on Venus, Mars, and Titan.

Body	Electromagnetic source	Reference
Venus	Possibly lightning	Russel (1991); Strangeway (2004)
Earth	Lightning	e.g. Nickolaenko and Hayakawa (2002)
Mars	Possibly dust devils / dust storms	Farrell and Desch (2001); Aplin (2006)
Jupiter	Lightning	Gurnett et al. (1979); Lanzerotti et al. (1996)
Saturn	Lightning	Fischer et al. (2006)
Titan	Possibly lightning / haze / magnetosphere	Fischer et al. (2004); Béghin et al. (2007) **[Paper 5]**
Uranus	Likely lightning	Zarka and Pedersen (1986)
Neptune	Likely lightning	Gurnett et al. (1990)

Table 2: Major energy sources in various cavities (Simões et al., 2007b) **[Paper 9]**.

On Earth, according to Harrison and Carslaw (2003), current discharges triggered by lightning cause a weak electrification of stratified clouds and produce a vertical potential gradient in atmospheric layers near the surface. Horizontal currents flow on the highly conductive surface and in the ionosphere. Currents that flow from the ground to the clouds, and also from the top of the clouds to the ionosphere, close the circuit. Hence, several types of discharging processes are possible, high-energy cloud-to-ground strokes, intercloud and intracloud discharges, and upward currents flowing from thunderstorm clouds to the ionosphere (Wilson currents). Several types of transient luminous phenomena related to upward currents, towards the ionosphere, have been observed from Earth orbit, stratospheric balloons, airplanes, and ground observatories (Figure 1). For example, high altitude atmospheric phenomena such as blue jets, red sprites, and elves have been investigated. These intriguing atmospheric phenomena present interesting opportunities to broaden our knowledge of atmospheric electricity. It is expected that future space based instrumentation, namely TARANIS, a micro satellite project dedicated to the study of impulsive transfers of energy between the Earth atmosphere, the ionosphere, and the magnetosphere (Blanc et al., 2007), contribute to clarify the nature and working mechanisms of these interesting phenomena. Additionally, recent works have been merging Schumann resonances and sprites studied to understand their interrelation (Williams et al., 2007b). Although the number of transient luminous events detected per night by FORMOSAT2 is ~10 (F. Lefeuvre, personal communication), which is much lower than the lightning rate, several researchers suggest this type of discharges may influence the Schumann resonance spectrum (Williams et al., 2007c).

Although several discharging processes take place on Earth it is not clear whether these processes take place in other planetary environments. Varying cloud compositions or low surface conductivities change the global electric circuit properties, and any comparison between the planets must be done with caution. For example, lightning events have been detected on the giant planets but remain a controversial issue on Venus. Nevertheless, recent

Venus Express results, Russell et al. (2007) apparently solve the dispute; they have found evidences of lightning on Venus inferred from whistler-mode waves in the ionosphere.

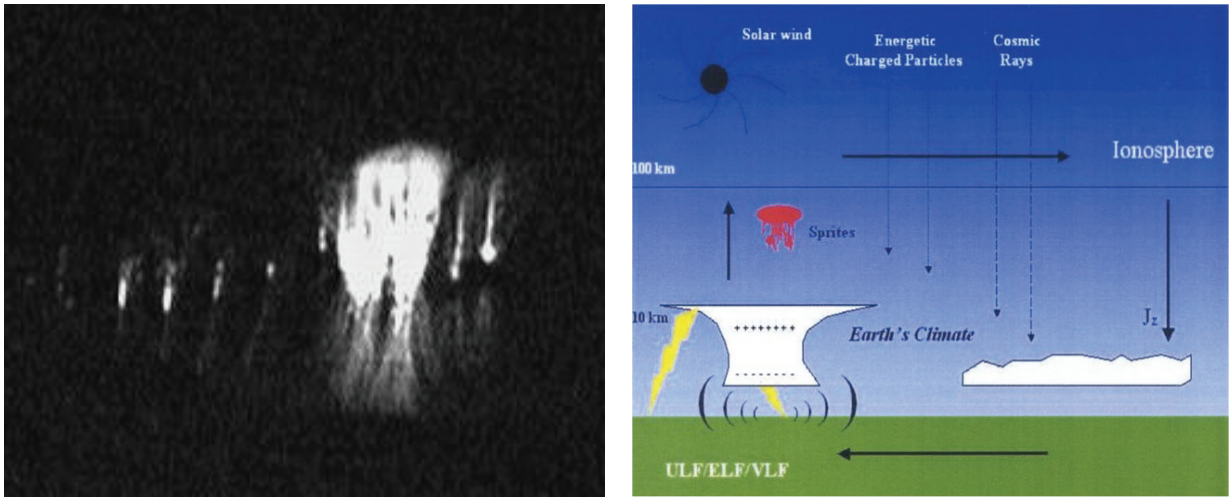

Figure 1: Image of typical transient luminous events observed at Observatoire Midi-Pyrénées, France (left, courtesy of F. Lefeuvre) and sketch of the global electric discharges mechanisms (right, Rycroft and Fullekrug, 2004).

Lightning is the major excitation source in the Earth cavity and discharges between thunderclouds and the surface produce the most powerful strokes; they radiate strong radio noise bursts which cover the ELF-VLF frequency range up to the radio band. Temporal and spatial lightning distributions are functions of many parameters but the global stroke rate is the highest over continents, mainly tropical regions (Figure 2).

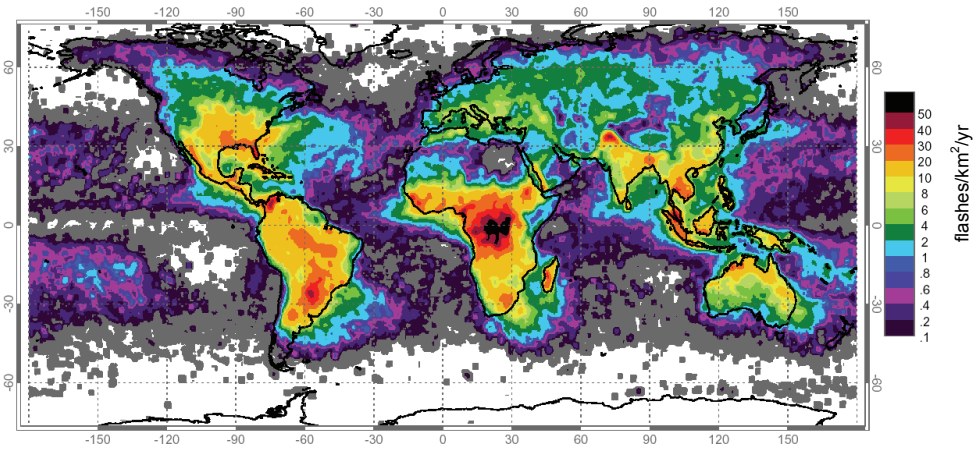

Figure 2: Satellite observation of global lightning distribution. (Credit: GSFC-NASA, National Space Science and Technology Centre Lightning Team).

Table 3 lists the most representative characteristics of lightning events and Figure 3 shows their typical profiles vs. time and frequency.

In spite of significant advances about lightning characterization, most authors consider that the excitation source is a vertical dipole with arbitrary amplitude and a flat spectrum. We shall use a similar approach, though we also consider horizontal dipoles.

Parameter	Characteristic
Energy	10^9 J
Leader duration	50 μs
Pulse duration	100 ms
Peak current	20 kA
Global rate	60 s^{-1}
Charge	10 C
Spatial distribution	Tropical regions of Africa, America, Asia
Daily distribution	Maximum at about 18 h local time
Radiation frequency distribution	Broad peak centred in the kHz range

Table 3: Typical characteristics of lightning strokes, compiled from Rakow and Uman (2003).

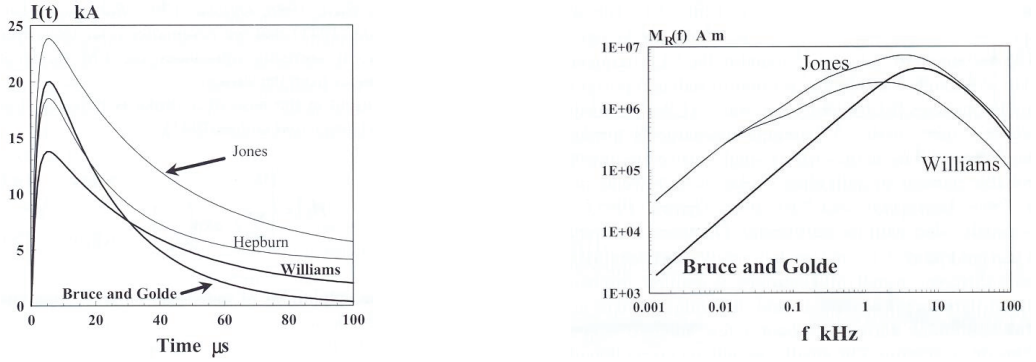

Figure 3: Characteristics of lightning strokes derived from several models: impulsive current waveforms (left; units: [kA]) and spectra (right; units: [Am]), [Nickolaenko and Hayakawa (2002)].

3. Numerical Model for Ionospheric Planetary Cavities

3.1. Numerical Tool

Calculating with accuracy the eigenfrequencies and eigenvalues of the cavity requires the utilization of numerical models, because the analytical approximations are inaccurate or not applicable at all due to the intricacy of the conductivity profiles. Thus, a numerical approach, based on the finite element method, might offer the most convenient solution to this problem. Equations (08-10) are solved in 3D geometry, or 2D axisymmetric geometry whenever applicable. Two types of algorithms are available: eigenfrequency and time-harmonic propagation analysis. Most of the numerical results presented in the thesis have been obtained with the COMSOL Multiphysics tools, which employ the finite element method with non structured meshes (Zimmerman, 2006). We shall not describe these tools in great detail, but we shall nevertheless discuss some relevant topics such as equations format, solver reliability, boundary conditions, and medium properties. The algorithms yield the complex eigenfrequencies, the electric and magnetic field profiles, and the ELF-VLF spectra. More specific tasks concern parametric studies as functions of frequency and medium properties. The medium properties are: (i) linear and isotropic in all cases; (ii) functions of radius for spherically symmetric cavities; (iii) functions of radius and angle for asymmetric cavities.

3.1.1. The 2D axisymmetric Approximation

A cavity consisting of concentric shells, where the medium properties are functions of radial distance only, can be solved in 2D axisymmetric configuration. This approach minimizes memory and time requirements and provides accurate solutions. There is no particular constraint regarding eigenfrequency analysis; the time-harmonic propagation studies require the utilization of a vertical dipole along the axis of symmetry (Simões and Hamelin, 2006) **[Paper 8]**. The eigenfrequency analysis does not require a very fine mesh, and the cavity is composed of about 5×10^4 elements, which also provides a reasonable accuracy in the time harmonic propagation mode. Figure 4 shows a typical 2D axisymmetric geometry with a vertical dipole aligned with the axis of symmetry. Equations (08-10) can be simplified in 2D axisymmetric geometry (r, φ, z) when there is no variation with the angle φ. Considering $\boldsymbol{E}(r,z)=E_r(r,z)\hat{\boldsymbol{e}}_r+E_\varphi(r,z)\hat{\boldsymbol{e}}_\varphi+E_z(r,z)\hat{\boldsymbol{e}}_z$ and $\boldsymbol{H}(r,z)=H_r(r,z)\hat{\boldsymbol{e}}_r+H_\varphi(r,z)\hat{\boldsymbol{e}}_\varphi+H_z(r,z)\hat{\boldsymbol{e}}_z$, where ($\hat{\boldsymbol{e}}_r$, $\hat{\boldsymbol{e}}_\varphi$, $\hat{\boldsymbol{e}}_z$) represent the unit vectors, Equations (08-10) can be written

$$\nabla \times \left(\frac{1}{\mu} \nabla \times \boldsymbol{E}(r,z) \right) - \left(\varepsilon - \frac{i\sigma}{\omega \varepsilon_o} \right) \left(\frac{\omega}{c} \right)^2 \boldsymbol{E}(r,z) = 0 \tag{18}$$

and

$$\nabla \times \left(\left(\varepsilon - \frac{i\sigma}{\omega \varepsilon_o} \right)^{-1} \nabla \times \boldsymbol{H}(r,z) \right) - \left(\frac{\omega}{c} \right)^2 \mu \boldsymbol{H}(r,z) = 0, \tag{19}$$

where μ is the relative magnetic permeability. The eigenmode analysis uses Equations (08-10) written in the form

$$\nabla \times \left(\frac{1}{\mu} \nabla \times \boldsymbol{E}(r,z) \right) - \Lambda_S \, \varepsilon \boldsymbol{E}(r,z) = 0 \tag{20}$$

and

$$\nabla \times \left(\frac{1}{\varepsilon} \nabla \times \boldsymbol{H}(r,z) \right) - \Lambda_S \, \mu \boldsymbol{H}(r,z) = 0, \tag{21}$$

where Λ_S denotes the eigenvalues, which are generally complex. In the case of TE and TM waves, the electric and magnetic field vectors can be simplified because TE $\Rightarrow E_r=E_z=H_\varphi=0$ and TM $\Rightarrow H_r=H_z=E_\varphi=0$.

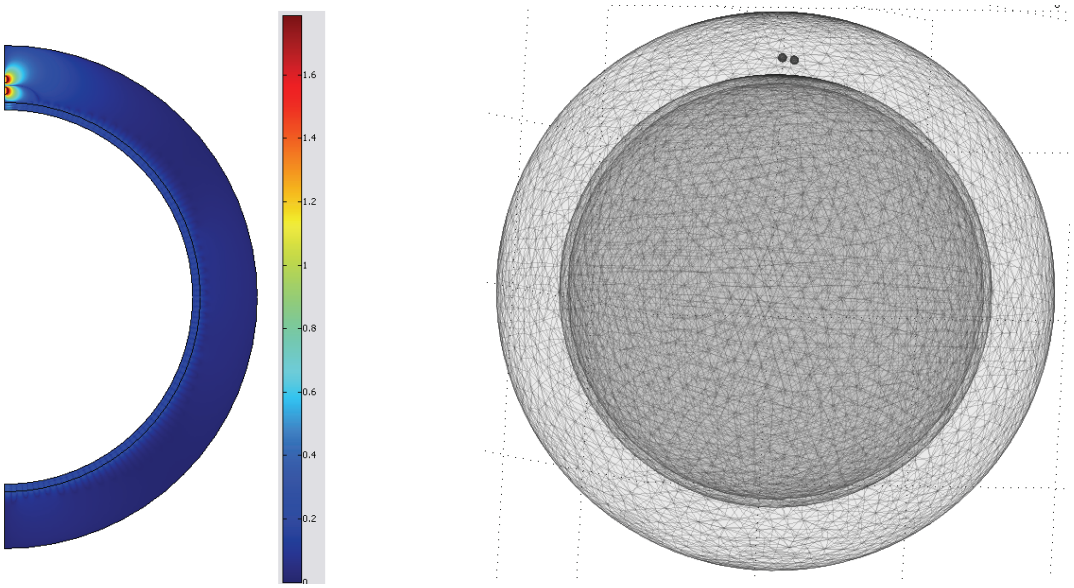

Figure 4: Spherical cavity models used in the simulations: 2D axisymmetric cavity with vertical dipole along the axis of symmetry (left); 3D mesh with horizontal dipole (right).

3.1.2. The 3D Model

When the problem cannot be reduced to a 2D axisymmetric geometry, a 3D model is necessary. Cavity geometries cannot be reduced to 2D approximations, when (i) the day-night asymmetry entails that the conductivity profiles are functions of height and angle, (ii) one horizontal or several non-aligned vertical dipolar sources are present, (iii) a planetary intrinsic magnetic dipoles must be taken into account, etc. Whereas the implementation of a 2D problem is rather straightforward because of reasonable memory and time requirements, the

utilization of 3D numerical models usually implies severe memory and time constraints. Therefore, developments of 3D simulations rely in more sophisticated algorithms. Figure 4 illustrates a 3D geometry mesh with one horizontal dipole.

Equations (08-10) are replaced by two equations, where the electric and magnetic fields are decoupled:

$$\nabla\times\left(\frac{1}{\mu}\nabla\times\boldsymbol{E}(r,\theta,\varphi)\right)-\left(\varepsilon-\frac{i\sigma}{\omega\varepsilon_o}\right)\left(\frac{\omega}{c}\right)^2\boldsymbol{E}(r,\theta,\varphi)=0 \tag{22}$$

and

$$\nabla\times\left(\left(\varepsilon-\frac{i\sigma}{\omega\varepsilon_o}\right)^{-1}\nabla\times\boldsymbol{H}(r,\theta,\varphi)\right)-\left(\frac{\omega}{c}\right)^2\mu\boldsymbol{H}(r,\theta,\varphi)=0\,. \tag{23}$$

For the eigenmode analysis, Equations (08-10) are written

$$\nabla\times\left(\frac{1}{\mu}\nabla\times\boldsymbol{E}(r,\theta,\varphi)\right)-\Lambda_S\,\varepsilon\,\boldsymbol{E}(r,\theta,\varphi)=0 \tag{24}$$

and

$$\nabla\times\left(\frac{1}{\varepsilon}\nabla\times\boldsymbol{H}(r,\theta,\varphi)\right)-\Lambda_S\,\mu\,\boldsymbol{H}(r,\theta,\varphi)=0\,. \tag{25}$$

3.1.3. Boundary and Continuity Conditions

The complete definition of the problem requires boundary and, whenever applicable, continuity conditions. The four continuity conditions between two media (subscripts 1 and 2) are given by

$$\hat{\boldsymbol{n}}_2\times\left(\boldsymbol{E}_1-\boldsymbol{E}_2\right)=0\,, \tag{26}$$

$$\hat{\boldsymbol{n}}_2\cdot\left(\boldsymbol{D}_1-\boldsymbol{D}_2\right)=\rho_s\,, \tag{27}$$

$$\hat{\boldsymbol{n}}_2\times\left(\boldsymbol{H}_1-\boldsymbol{H}_2\right)=\boldsymbol{J}_s\,, \tag{28}$$

$$\hat{\boldsymbol{n}}_2\cdot\left(\boldsymbol{B}_1-\boldsymbol{B}_2\right)=0\,, \tag{29}$$

where ρ_s and $\boldsymbol{J_s}$ denote the surface charge and current densities, and $\hat{\boldsymbol{n}}$ is the outward unit vector. Of these four conditions, Equations (26-29), only two are independent; a set of independent equations is formed by either Equation (26) or (29), together with either Equation (27) or (28). We select Equations (26) and (28), which are suitable for boundary and continuity conditions. Whereas a 3D cavity model requires information about all the components of the vectorial relations (26) and (28), the 2D axisymmetric approximation uses the φ component only. The vector $\boldsymbol{J_s}$ is either related to the dipole strength or equal to zero when continuity applies. The PEC conditions, $\hat{\boldsymbol{n}}\times\boldsymbol{E}$=0, define the inner and outer boundaries of the model domain. In 3D electromagnetic waves applications, either of the two time-harmonic Equations (22-23) can be solved. The same principle is applied to the eigenmode applications by selecting one of Equations (24-25), which minimizes the memory requirement.

In 3D, the Lagrange elements which play a role in the standard application of the finite element method, cannot be used for electromagnetic wave modelling because they force the fields to be continuous everywhere. This implies that the interface conditions cannot be fulfilled. To overcome the problem, the 3D electromagnetic wave model uses vector elements that do not carry this limitation. Though not strictly required, verifying the electric and magnetic fields divergence equations (Gauss law) improves the model accuracy.

3.1.4. Eigenfrequency Analysis

The eigenmode solver uses the ARPACK package that is based on a variant of the Arnoldi algorithm and is usually called the implicitly restarted Arnoldi method (Zimmerman, 2006). Additional information can be found in the COMSOL Multiphysics user guide and model library documentation. For some combinations of the model and medium parameters, the eigenfrequency problem may not be linear, which means that the eigenvalue appears in the equations in a different way than the expected second-order polynomial form. Equation (25) with finite conductivity is a typical problem with a nonlinear solution. In this case, the equation is solved in several steps: an initial guess is made for the eigenvalue; the equation is solved and a new eigenvalue is found; the eigenvalue is updated and the new equation is solved; the cycle is repeated until eigenvalues converge. In general, this procedure converges rapidly unless the wave attenuation is significant. Whenever the medium is lossy, i.e. $\sigma \neq 0$, the eigenvalues are complex; the real and imaginary parts characterize the wave propagation and attenuation, respectively.

3.1.5. Time harmonic Propagation Analysis

The propagation mode solves stationary problems with the tools supplied by the UMFPACK package. The harmonic propagation code computes the frequency spectra, identifies the propagating eigenmodes, calculates the electric field over a wide altitude range and evaluates the influence of the source distribution on the propagation modes. The solver employs the unsymmetrical-pattern multifrontal method and the direct LU-factorization of the sparse matrix obtained by discretizing Equations (18-19) or (22-23).

The harmonic propagation approach is especially suited to the analysis of global features and to the study of the electromagnetic field distribution generated by sparse sources. For the sake of simplicity, we shall assume a localized electromagnetic stimulus. The source is a pulsating Hertz dipole approximated by two spheres, on the surface of which a uniform surface current density is imposed. The intensity of the current is not important provided its density is uniform and its frequency spectrum flat. The dipole size is small compared to the wavelength and the cavity size. The algorithm calculates the frequency response of the cavity, in the specified frequency range. It is also possible to use a monopole, with a specified field distribution, that minimizes meshing requirements.

3.1.6. Accuracy and Numerical Solvers

Meshing is an important step in the finite element method towards the solution of the numerical model. The selection of appropriate meshes minimizes memory needs, optimizes accuracy and, in the case of intricate geometries, may improve convergence efficiency. A free

mesh consisting of triangular elements is chosen for the 2D axisymmetric geometry. A swept mesh structured over the angular direction is used for the eigenmode problem. The 3D geometry is meshed with tetrahedral elements with a resolution compatible with the hardware and software capabilities, i.e. nearly 10^6 elements and $\sim 8\times10^6$ degrees of freedom. The models are run in a dual core, dual processor, 16 Gbytes RAM station. A comparison between the 2D and 3D results, when axial symmetry applies validates the model accuracy. Continuity conditions are imposed at the surface of the body unless the latter coincides with the inner boundary of the cavity.

The numerical algorithms have been validated by comparing the eigenfrequencies computed with the finite element model and those derived from Equation (11), taking Earth and Titan as examples. In the case of a thin lossless cavity, the same results are obtained with Equations (02), Equation (11), and the finite element method (Table 4, Test A). The analytical and numerical results are similar, as long as the medium is lossless and homogeneous, and the PEC boundary conditions apply (Table 4, Test B). However, the two approaches give different results when the medium is heterogeneous (Table 4, Test C), which illustrates the limited validity of the analytical approximation.

		Spherical Approximation (Eq. 11)		Finite Element Model	
Cavity	Test	Longitudinal [Hz]	Transverse [Hz]	Longitudinal [Hz]	Transverse [Hz]
Earth	A	10.6	-	10.6	-
	B	10.5	1998	10.6	2008
	C	10.3	1670	8.86	1635
Titan	A	26.2	-	26.2	-
	B	22.9	201.2	23.1	201.2
	C	14.3	168.1	19.1	163.5

Table 4: Comparison between the eigenfrequencies derived from the analytical and numerical models. Inner shell radii R_T=2575 km and R_E= 6370 km. (A): $h\rightarrow0$, σ_{atm}=0, and ε_{atm}=1; (B): height of ionospheric boundaries h_T=750 km and h_E=75 km, σ_{atm}=0, and ε_{atm}=1; (C): Same as in (B), but the permittivity profile is represented by a sigmoid-type function, in the range 1-2. Perfect electric conductor boundaries are considered in all cases. The dimensions of Titan and Earth are identified by the subscripts T and E, respectively.

The differences are more important, in the case of the longitudinal mode, for larger ratios of the ionosphere height over shell radius, especially when the medium is heterogeneous. Inclusion of medium losses constrains the application of Equation (11) further. The numerical algorithms have also been validated against the set of parameters applicable to the Earth ionospheric cavity; the eigenfrequencies and Q-factors thus obtained are in fair agreement with expectations (Sentman, 1990; Nickolaenko and Hayakawa, 2002).

3.2. Cavity Parameterization

The various environments encountered in the Solar System can be grouped in two major classes: (i) partly rocky/icy and (ii) entirely gaseous cavities. By definition, the radius of the gaseous planets is determined by the 1-bar reference surface that is of little interest for our modelling purposes. The cavity models of Venus, Earth, Mars, Jupiter, Io, Europa, Saturn, Titan, Uranus, and Neptune are described in the following.

3.2.1. Parameter Description

The resonant cavity problem is solved in 2D axisymmetric and 3D configurations, either in the eigenfrequency or time-harmonic propagation mode. The model uses the finite element method to solve Equations (18-25) with boundary and continuity conditions (26-29) depending on geometry and mode selection. Figure 5 shows the most important cavity parameters: body surface radius; height of the ionosphere, cavity upper boundary; depth of the subsurface boundary, cavity lower boundary; conductivity profile of the atmosphere and lower ionosphere; permittivity profile of the atmosphere; conductivity profile of the interior; permittivity profile of the interior.

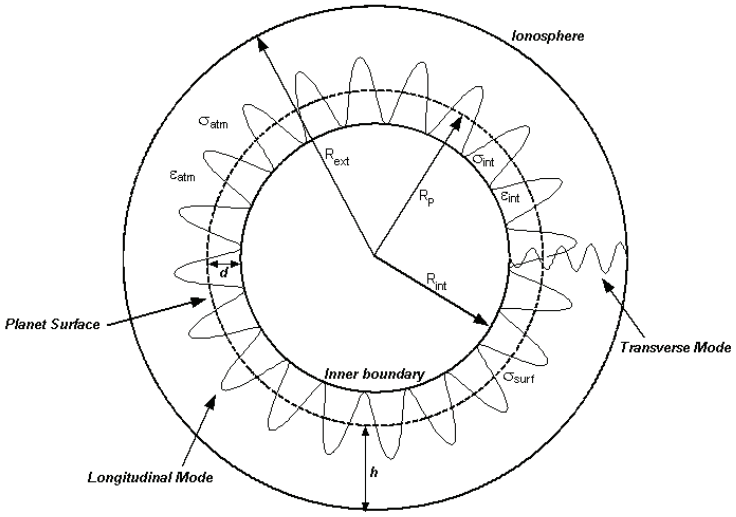

Figure 5: Sketch of the model used for calculating the Schumann resonance. R_P: Planet radius; R_{int}: lower boundary radius; R_{ext}: ionosphere radius; h: altitude of the ionosphere; d: depth of the lower boundary; σ_{surf}: surface conductivity; ε_{int} , ε_{atm} , σ_{int} , σ_{atm}: permittivities and conductivities of the interior and atmosphere, respectively.

Let us first expose how the electric properties of a cavity are estimated. The electron conductivity profile is derived from electron density and thermodynamics parameters such as temperature and pressure; the permittivity profile is derived from gas density and refractivity equations.

The electron density, n_e, is related to the conductivity by the equation

$$\sigma = \frac{n_e e^2}{m_e \nu_m}, \tag{30}$$

where e and m_e are electron charge and mass, respectively, and ν_m is the collision frequency for momentum transfer. The later can be written

$$\nu_m = \alpha_{cs}\, n_n T\,, \tag{31}$$

where T and n_n are the temperature and density of the neutrals, and α_{cs} is a parameter related to the neutrals cross section. In the case of Earth, considering a pure nitrogen atmosphere, we find $\alpha_{cs}=2.33\times10^{-17}$ $m^3K^{-1}s^{-1}$ (Banks and Kockarts, 1973, p. 194). Significant uncertainties subsist about pressure and temperature, and weighted means are used to calculate diffusion coefficients. In a first approximation, the neutral density is derived from the perfect gas law. However, elaborated profiles are used for the gas density in the case of Venus and the giant planets.

The refractivity of a neutral gas is a linear function of density at low pressure. For lack of a better estimate, it is assumed that permittivity is proportional to the square root of the gas density, a fair approximation at least for an atmosphere. The permittivity of hydrogen is interpolated between those of the low-pressure gas and of the liquid phase (~1.25). Therefore, following density increasing with depth, the permittivity of the interior of the gaseous giants varies from ~1 in the atmosphere to ~1.25 at the phase transition depth. The Schumann resonances are nevertheless more sensitive to the conductivity of the interior than to its permittivity.

Unlike the permittivity of the giant planet interiors, which can only be crudely estimated, that of Venus atmosphere is better known for several reasons: (i) the density profile is derived from *in situ* measurements rather than modelling; (ii) the deviation of the relationship between refractivity and gas density from a linear law is negligible compared to other uncertainties; (iii) the simulation code output can be checked against the electric field profiles measured with Venera 11 and Venera 12, though in a different frequency range.

In Venus cavity, the refractivity, N, is proportional to the gas density and is related to the index of refraction, n, by the relation

$$N \equiv \left(n-1\right)\times10^6 . \tag{32}$$

An atmosphere is a weak dispersive medium, in particular for large wavelengths. The dispersion in a neutral gas is a function of composition and density, i.e. molecular structure, temperature, and pressure (e.g. Bean and Dutton, 1968). We deal first with Earth and then turn towards Venus. Air refractivity is a function of pressure, temperature, and water vapour and is written

$$N_{air} = \frac{273.15}{101325}\frac{N_{g,ph}}{T}p - \frac{11.27\,p_w}{T}, \tag{33}$$

where T [K] is the temperature, and p and p_w [Pa] are the air and partial water vapour pressures. The dispersive term, $N_{g,ph}$, where the indices g and ph refer to group and phase velocities, is given by the empirical relation:

$$\boldsymbol{N_{g,ph}} = \boldsymbol{K} + \frac{\boldsymbol{A}}{\lambda^2} + \frac{\boldsymbol{B}}{\lambda^4}, \tag{34}$$

where K=287.6155 is the large wavelength limit, A=4.88600 or 1.62887 and B=0.06800 or 0.01360, for group and phase refractivity, respectively, and λ is the wavelength in μm (e.g., Ciddor, 1996; Ciddor and Hill, 1999). These values are valid for standard dry air, i.e. 0°C, 101325 Pa, and 0.0375% of CO_2. The following simplifications are possible for ELF waves in the cavity of Venus: (i) The medium is not dispersive, hence A=B=0; (ii) the weighted mean composition is assumed in the evaluation of the medium refractivity; (iii) the refractivity is proportional to gas density and Equation (33) is strictly valid; (iii) the water partial pressure is

negligible and no additional term is due to the presence of SO_2 clouds. Table 5 shows the refractivities of selected gases at radio frequencies.

Gas	Refractivity
H_2	132
He	35
N_2	294
O_2	266
CO_2	494
H_2O vapour	61 [1)]
SO_2	686 [2)]
Earth dry air 78% N_2 + 21% O_2	288
Venus atmosphere (96.5% CO_2 + 3.5% N_2)	487

Table 5: Refractivities measured and/or evaluated at radio frequencies, 0°C and 1 atm, except [1)] 20°C, 1.333 kPa and [2)] 589.3 nm, after Lide et al. (2006).

The characteristic parameters of the cavity are the following:

a) *Surface radius* (R). Most radii are estimated from osculating orbital data (Woan, 1999) and spherical shapes are assumed. By definition, the surface of the gaseous giants corresponds to the 1-bar reference level.
b) *Height of the ionosphere (h) and cavity upper boundary* (R_{ext}). The upper boundary of the cavity is located where the skin depth of propagating waves is much smaller than the separation between the shells. For example, the upper boundary is placed at h~100 km for Earth and h~750 km for Titan, where the skin depth is ~1 km for ELF waves. All cavities, but that of Venus, are defined by concentric shells. The Venus cavity is highly deformed by the day-night asymmetry. We shall tentatively assume that the effective height of Venus's ionosphere varies between h and $2h$, where h~130 km.
c) *Depth of the subsurface interface* (d) *and cavity lower boundary* (R_{int}). The surface of the body does not always coincide with the inner boundary of the cavity. Earth represents an exception because a surface conductivity of $\sim 10^{-1}$ Sm^{-1} implies a skin depth much smaller than the cavity size. In general, the surface is not a suitable PEC boundary and the inner shell is located lower down where the skin depth is less than 1 km. The inner boundaries of the giant planets are solid or liquid surfaces that are found in the planet interior, well below the 1-bar pressure level. The skin depth is calculated from theoretical models of the conductivity profile.
d) *Conductivity profile of the atmosphere and lower ionosphere* (σ_{atm}). The ionospheric conductivity profile of most planets has only been measured down to the electron density peak of what is generally known as the Chapman layer; the outer boundary of the cavity always lies beneath. The conductivity profile is known with a good accuracy only on Earth; other conductivity profiles rely partially on modelling. Titan's conductivity profile is known in the lower part of the cavity, from an altitude of 140 km down to the surface. Other conductivity profiles rely exclusively on theoretical models.
e) *Permittivity profile of the atmosphere* (ε_{atm}). The permittivity of vacuum, ε=1, is generally assumed for the atmosphere of most planets, but this is a crude approximation for Venus, because the atmospheric pressure is high. Thus, a permittivity function that takes into account the variation of refractivity with altitude is

needed for Venus. The permittivity is calculated using temperature and pressure profiles, composition, and gas refractivity in the low frequency range. It is assumed that refractivity is a linear function of density.

f) *Conductivity profile of the interior* (σ_{int}). The simplest case is that of Earth because its surface acts as a PEC inner boundary. The surfaces of rocky/icy celestial bodies are not, in general, good conductors and, consequently, do not play the role of inner boundary. In a first approximation and in the absence of better information, we consider that the conductivity is constant with depth, unless better estimations are available. This assumption does not hold in the case of the giant planets, because the density increases with depth and the model must take the theoretical conductivity profile into account.

g) *Permittivity profile of the interior* (ε_{int}). The approach applied to the subsurface conductivity profile is also valid for the permittivity. The subsurface permittivity of Venus is irrelevant because the conductivity contribution dominates. For Mars and Titan, the permittivity is considered constant and independent of frequency, temperature, and depth; typical materials, namely silicates and ices, are considered. The subsurface permittivity profile of the gaseous giants is treated like the atmosphere of Venus; and information about composition and density is required.

A detailed description of the cavity parameters can be found in Simões et al. (2007a) **[Paper 4]** for the cavity of Titan, Simões et al. (2007b) **[Paper 9]** for several other celestial bodies of the Solar System, and Simões et al. (2007c) **[Paper 10]** for Venus. These articles contain numerous references related to this subject that are not included in this Section.

3.2.2. Cavity Description

3.2.2.1. Venus

Our knowledge of Venus has been gathered from ground-based observations, and orbiter, flyby, balloon, and lander space missions. The properties of the upper ionosphere are measured with propagation techniques during radio occultation, but the electron density in the lower ionosphere and atmosphere is not known. Therefore, theoretical models are used to evaluate the conductivity profile. Surface conductivity is unknown but there are a few permittivity estimations derived from Pioneer Venus and Magellan radar data. However, the surface conductivity plays a more important role than permittivity regarding the cavity parameterization. The conductivity is based on the values observed on Earth for the same composition and temperature range; its variation with depth in the range 0-150 km is a function of temperature.

Thick sulphuric acid clouds shroud Venus but lightning activity continues to be a controversial issue. Therefore, ELF wave propagation studies provide an alternative approach to study atmospheric electricity. The results from the wave propagation model in the cavity can be compared, in the VLF range, with the data collected by the Venera 11 and Venera 12 landers.

The atmosphere is denser than on Earth – about 54 times at the surface - and enhances peculiar features. Permittivity is a function of medium density and, mainly, density gradient that cause refractivity phenomena. For example, the refractivity is strong enough to balance the curvature and enables electromagnetic waves to circle the planet. The density profile requires information about temperature, pressure and atmospheric composition, and low

frequency refractivity standard tables. The profiles in Figure 6 show the dielectric properties of the atmosphere.

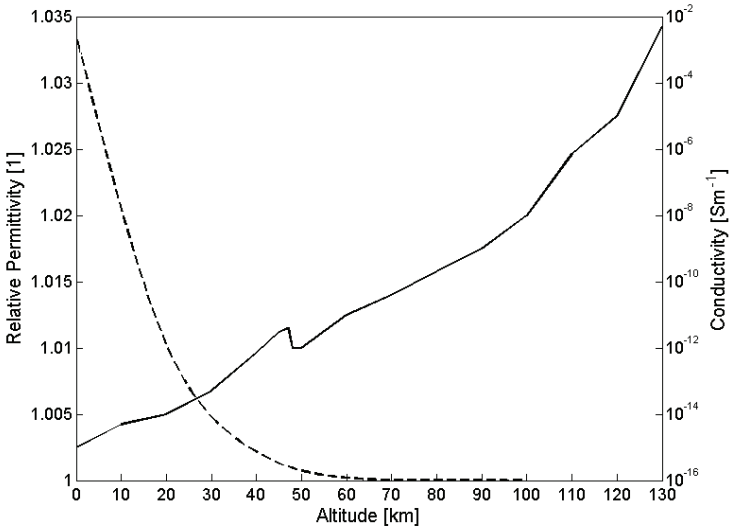

Figure 6: Conductivity (solid) and permittivity (dashed) profiles of the atmosphere of Venus.

3.2.2.2. Earth

Schumann studied the propagation of ELF electromagnetic waves in the cavity of Earth and predicted its resonance frequencies. Subsequent research on the topic lead to the identification of lightning activity as the major source of energy, and revealed the role played by many geophysical factors: day-night asymmetry of the ionosphere, climate variability, influence of the solar wind on the upper boundary, intrinsic geomagnetic dipole, etc. The work of Nickolaenko and Hayakawa (2002), and hundreds of references therein, testify to the importance of this subject. With the exception of the phenomenon recorded during the descent of the Huygens Probe through the atmosphere of Titan, which is still under investigation, the Schumann resonance has never been identified so far on any celestial body but Earth.

Earth is used for the validation of the finite element model because the relevant parameters, permittivity, conductivity, and boundary conditions, are known with a fair accuracy, and the Schumann resonance has been extensively studied experimentally (e.g., Sentman, 1995). The average Schumann frequencies and Q-factors are 7.9, 14, and 20 Hz and 4, 4.5, and 5, respectively, for the three lowest eigenmodes.

3.2.2.3. Mars

Although many missions have been flown to Mars, electron density measurements are available in the upper ionosphere only. Theoretical models are therefore used to extend the conductivity profile down to the surface.

Observations made with Mars Global Surveyor have shown that the atmosphere and ionosphere are highly variable. The presence of multiple magnetic “cusps” that connect the crustal magnetic sources to the Martian tail and shocked solar wind plasma (Acuña et al., 2001) probably introduces significant heterogeneities in the conductivity profile. Additionally,

Mitchell et al. (2001) have found that the ionopause can extend from 180 km up to 800 km, which suggests significant ionospheric asymmetries. The former phenomenon seems to imply a highly heterogeneous cavity and would imply specific atmospheric conductivity profiles. Whether the latter is important or not depends upon the altitude at which the upper boundary of the cavity is located. However, the current electron conductivity models of the atmosphere do not take into account these contributions.

Using propagation techniques, the radio science instrument onboard Mars Express measured the electron density down to ~ 70 km, where a sporadic layer is observed (Pätzold et al., 2005), though the conductivity profile is unknown at lower altitudes.

Different profiles are found in the literature and, in some instances, ELF wave propagation is questionable due to strong cavity losses. The atmosphere consists mostly of CO_2 and the density at the surface is about 70 times lower than on Earth.

The Martian environment has been explored using Earth-based, remote sensing, and in situ observation, but the electrical properties of the surface are still poorly known. Theoretical models yield conflicting results for surface conductivity and permittivity. According to several estimations, the relative permittivity of the regolith lies in the range 2.4-12.5, but no figure is given for that of the subsurface. The conductivity of the surface is also poorly defined and estimates vary between 10^{-7} and 10^{-12} Sm^{-1} in the literature. Furthermore, contrasting compositions are seen at low and high latitudes, due to the presence of ice deposits in the polar regions. The subsurface dielectric properties of the regolith should vary with depth and composition, especially if water/ice/brines are embedded in the medium.

There is no evidence of lightning activity on Mars but it is generally accepted that, due to triboelectricity effects, massive dust storms might enhance atmospheric electrification, particularly in dust devils, as simulated on Earth. The spectral features of these emissions should however considerably differ from those observed in the Earth cavity.

3.2.2.4. Jupiter

The atmosphere of Jupiter is mainly composed of hydrogen (82%) and helium (18%) with much lower mole fractions of other components, such as methane, ammonia and water vapour.

Lightning has been undoubtedly identified by several spacecrafts and the Schumann resonance frequencies were first estimated by Sentman (1990).

The atmospheric density increases significantly with depth and the vacuum approximation is no longer valid for the permittivity. Deep in the molecular hydrogen envelope, the density increases beyond the gaseous phase threshold and a liquid environment is expected. The permittivity, which is derived from gas density such as for Venus, increases with depth until it reaches the value of liquid hydrogen, which is ~1.25. The normalized radius of the solid-liquid interface is ~0.76. The conductivity profile of the interior is adopted from a theoretical model developed by Liu (2006). The conductivity of the ionosphere is derived from the electron density, pressure, temperature, and composition data collected by several spacecraft. The conductivity of the lower atmosphere is interpolated between those of the lower ionosphere and of the upper interior.

3.2.2.5. Io and Europa

This thesis deals not only with planetary cavities but also with those of a few moons. Titan, Europa, and Io environments are all different but unique. Therefore, studying the

propagation of ELF waves and the resonance that may develop in their cavities is an interesting exercise. Titan's cavity is approached in more detail in Chapter 4 and, therefore, we shall deal with Io and Europa only. The scientific rationale for studying these two moons is threefold: (i) The possible existence of Schumann resonances on Io has been predicted and their frequencies have been estimated (Nickolaenko and Rabinovich, 1982); (ii) Volcanoes on Io might modify the environment, control the propagation conditions and be an ELF-VLF source of electromagnetic energy; (iii) The subsurface exploration of several moons, mainly Europa, is of paramount importance. As on Titan, models predict the existence of a subsurface ocean on Europa, the moon that displays the smoothest surface in the Solar System.

The existence of an ionospheric layer and, therefore, of a cavity does not necessarily imply that Schumann resonances can develop. Io and Europa possess an ionosphere (Kliore et al., 1974; Kliore et al., 1997), but the electron density in the thin atmosphere of Europa is such that resonant states cannot be sustained; and the subsurface cannot be explored with ELF waves. In fact, the conductivity is high and ELF waves are evanescent. The subsurface of this Galilean satellite can however be accessed in another way. The electrical conductivity of the ionosphere and interior prevents the penetration of the time varying fraction of the external magnetic field, a phenomenon that should in principle reflect the presence of an ocean beneath the surface (Russell, 2000). Volcanic activity on Io is a likely source of energy though, like on Europa, only evanescent waves can be produced, due to the high atmospheric conductivity.

3.2.2.6. Saturn

Like that of Jupiter, the atmosphere of Saturn is mainly composed of hydrogen (94%) and helium (6%). The approach used for Jupiter cavity is also valid for Saturn, and the solid-liquid interface is expected at a normalized radius of ~0.48. Lightning has been detected with the multiple instruments onboard Cassini, which confirms previous observations.

The conductivity of the ionosphere is derived from the electron density, pressure, temperature, and composition data collected by several spacecraft. The conductivity of the atmosphere is interpolated between those of the lower ionosphere and of the upper interior.

3.2.2.7. Uranus

The cavities of the Uranian planets are quite different from those of Jupiter and Saturn. The atmosphere of Uranus is mainly composed of hydrogen (74%) and helium (26%), with molar fractions different from those of the Jovian planets. Voyager 2 measured the electron density (Lindal et al., 1987) with some discrepancy between ingress and egress. Two conductivity profiles are derived for Uranus from the Voyager data sets, based on analogy with Earth and on modelling.

The interior of Uranus significantly differs from that of the Jovian planets. A solid mantle of ices is substituted for the liquid hydrogen metallic mantle of Jupiter and Saturn. Discontinuities in the permittivity profile and in the derivative of the conductivity profile are expected at the solid-gaseous interface (Liu, 2006). The water content of the Uranus environment is unknown and a concentration of only a few percent could increase the conductivity by orders of magnitude. Voyager 2 measurements also suggest that lightning activity is the major source of electromagnetic energy in this cavity.

3.2.2.8. Neptune

Like the other gaseous giants, Neptune is wrapped in an envelope composed of hydrogen (68%) and helium (32%). This molar fraction is closer to solar abundances than those of the other planets. Contrary to Uranus, a single conductivity profile is available (Capone et al. 1977; Chandler and Waite, 1986). There are evidences of lightning on Neptune, though less convincing than on the other outer planets.
The structure of the interior of Neptune is similar to that of Uranus, where an icy solid mantle is expected. The water content in the gaseous envelope is uncertain, but should induce a significant variability of the conductivity profile.

3.3. Results

The simulation of electromagnetic wave propagation in various planetary cavities of the Solar System provides an interesting method for analysing or predicting the global electric and atmospheric phenomena that possibly develop in their atmospheres. The accuracy achieved with this model may be limited because the cavity parameterization is approximate, but wave propagation in planetary cavities reveals itself as an extremely interesting tool for assessing the properties of the atmosphere and subsurface. Global characteristics can be computed and used in comparative planetology studies.

Whereas the atmospheric refractivity does not particularly affect the frequency of the Schumann resonance, it does influence the shape of the electric field profile (Figure 7).

The model electric field maximum is reached at about 32 km on Venus, which is roughly the altitude at which refractivity makes a ray circle the planet. The Venera landers measurements show similar electric field profiles (Simões et al., 2007c) **[Paper 10]**; local features, not reproduced by the model, are probably generated by turbulences. In fact, the temperature and pressure model profiles are smooth and convection is neglected.

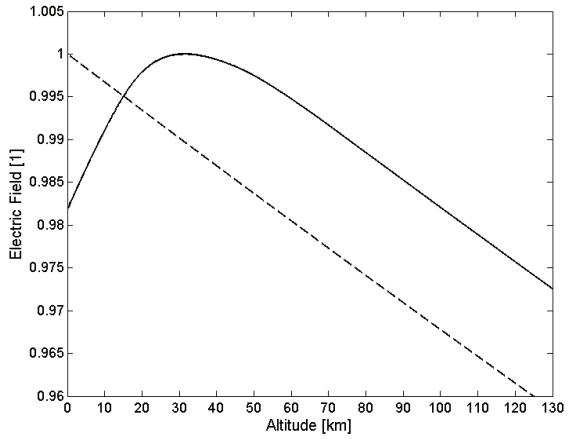

Figure 7: Electric field amplitude as a function of altitude in a lossless Venus cavity with PEC boundaries, where $R_{int}=R_v$, $R_{ext}=R_v+h$, and h=130 km, for R_v=6052 km. The permittivity is given by a specific profile (solid line) or is assumed to be that of vacuum (dashed line). The field magnitude is normalized to that of the vertical component on the surface in vacuum. See Figure 6 for details about the permittivity profile.

Table 6 shows the complex eigenfrequencies of the three lowest eigenmodes of various cavities but Titan. The major results are the following:

- Venus – The eigenfrequencies are similar to those of Earth; the Q-factor are higher than on Earth and subsurface losses cannot be neglected; like on Earth, the Q-factor increases with the eigenmode order; contrary to expectation, a lower subsurface conductivity does not necessarily imply higher losses.

- Mars – Although the lower cavity radius suggests higher eigenfrequencies, significant atmospheric electron conductivity decreases the Schumann resonance frequencies; high atmospheric conductivity also implies low Q-factors; the subsurface contribution is not significant because the planetary surface and the inner boundary are nearly coincident.
- Jupiter – The eigenfrequencies are one order of magnitude lower than on Earth, which is strictly related to the cavity radius; the Q-factor is twice that of Earth cavity and is similar for the three first eigenmodes.
- Io and Europa – The electron density is high enough to prevent wave propagation; hence a high attenuation produces evanescent waves.
- Saturn – The eigenfrequencies are similar to those of Jupiter, though slightly higher because of the difference between the radii.
- Uranus – High and low interior conductivity profiles produce significant changes in the cavity; the Q-factor is in the order of 20 and 2, for low and high conductivity profiles, respectively. Since high and low electron conductivity profiles are related to water content in the gaseous envelope, it is possible, in principle, to estimate the water concentration in the cavity from the Schumann resonance.
- Neptune – The global characteristics are similar to those of Uranus, especially those related with the high and low conductivity profiles; Q-factors are smaller than those of Uranus and propagation conditions are less favourable when the water content is high.

The results are discussed in more detail by Simões et al. (2007b) **[Paper 9]**.

Planetary body	**Parameters**				**Computed Resonance Frequencies**			**Alternative Value and Reference**	
	Atmosphere	ε_{soil}-[1]	σ_{soil}-[Sm^{-1}]	d-[km]	n=1	n=2	n=3	n=1	
Venus		-	-	0	9.01+0.56i	15.81+0.97i	22.74+1.42i	11.2	Guglielmi and Pokhotelov (1996)
	profile	[5, 10]	high profile	150	8.80+0.91i	15.77+1.38i	22.67+1.76i	9	Nickolaenko and Hayakawa (2002)
		[5, 10]	low profile	150	7.95+0.74i	14.17+1.20i	20.37+1.60i	10	Pechony and Price (2004)
Earth	measured values				7.85+0.79i	13.95+1.33i	20.05+1.79i		Nickolaenko and Hayakawa (2002)
Mars		-	-	0	8.31+2.19i	15.64+4.27i	23.51+6.59i	13	Sukhorukov (1991)
		[5, 10]	10^{-7}	5	8.28+2.10i	15.49+3.66i	22.82+5.53i	8.6	Pechony and Price (2004)
		5	10^{-10}	5	8.55+2.07i	15.93+3.62i	23.44+5.49i	11-12	Molina-Cuberos et al. (2006)
	profile	[5, 10]	10^{-7}	10	7.93+2.06i	14.93+3.94i	22.41+6.04i		
		5	10^{-10}	10	8.47+2.03i	15.85+3.89i	23.68+5.97i		
Jupiter								0.76	Sentman (1990)
	profile	profile			0.68+0.04i	1.21+0.07i	1.74+0.10i	0.95	Guglielmi and Pokhotelov (1996)
								1	Nickolaenko and Hayakawa (2002)
Io	negligible	-			evanescent wave			-	Nickolaenko and Rabinovich (1982)
Europa	negligible	-			evanescent wave			-	-
Saturn	profile	profile			0.93+0.06i	1.63+0.12i	2.34+0.18i	-	-
Uranus	ingress – low water content				2.44+0.06i	4.24+0.11i	6.00+0.15i	-	-
	ingress – high water content				1.02+0.25i	1.99+0.49i	3.03+0.67i		
	egress – low water content				2.47+0.06i	4.27+0.11i	6.04+0.16i		
	egress – high water content				1.12+0.33i	2.17+0.58i	3.26+0.82i		
Neptune	high water content				1.10+0.54i	2.03+0.96i	2.96+1.69i	-	-
	low water content				2.33+0.12i	4.12+0.22i	5.90+0.31i		

Table 6: The complex frequencies of the three lowest Schumann resonances calculated with the finite element model. For the sake of comparison, results found in the literature, but obtained with different approaches, are also given.

4. Titan Electromagnetic Environment Characterization

4.1. The Cassini-Huygens Mission

The Cassini-Huygens mission, which aims at studying Saturn, and its rings and moons, results from an international cooperation. The Cassini-Huygens mission is a joint undertaking by NASA and ESA. NASA builds the Orbiter, named Cassini after the astronomer that studied Saturn and discovered several of its satellites and ring features. ESA provides the Probe, named Huygens after the astronomer who discovered Titan. The entire mission spans three decades, from the initial proposal and planning phase until the end of the likely extension of the Orbiter mission.

The Cassini Orbiter studies Saturn, its thin system of rings, and several of its satellites (Matson et al., 2002). Cassini carries also the Huygens Probe (Figure 8) and assists the data relay during the descent of Huygens through the atmosphere of Titan. The Huygens Probe performs *in situ* measurements during its descent upon Titan (Lebreton and Matson, 2002).

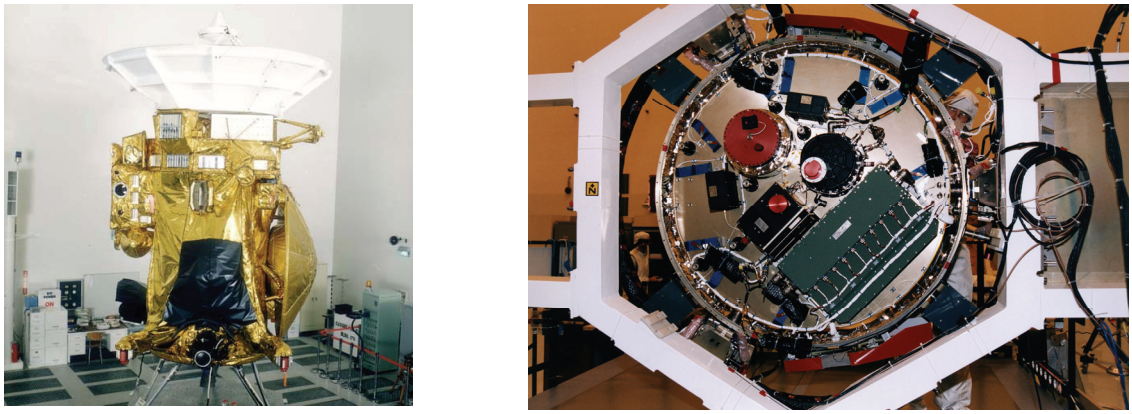

Figure 8: The Cassini Orbiter during qualification tests with the Huygens Probe attached on the right-hand-side (left; credit NASA) and top view of the instrument platform of the Huygens Probe (left; credit ESA).

Saturn has continuously proved a dazzling world since ancient times, particularly after the discovery of Titan and the system of rings. Voyager observations of the Saturnian system stimulated our imagination further, by revealing the ring structures with an unprecedented accuracy and showing Titan shrouded by a thick haze that prevents the observation of its

surface. The possible existence of prebiotic conditions on Titan similar to those that might have occurred on Earth about four billion years ago gave an additional boost to the planetary science community.

The uniqueness of Titan among the celestial bodies of the Solar System justified a dedicated mission to investigate its interaction with the Saturn environment and, mostly, to explore what lies beneath its hazy envelope. The combined Cassini flybys and Huygens *in situ* measurements revealed themselves to be a promising strategy for expanding our knowledge of this peculiar moon.

The Huygens Probe comprises six instruments dedicated to *in situ* studies (Lebreton and Matson, 2002). The major contributions of the instruments to the characterization of the atmosphere and surface of Titan are listed below:

- The Aerosol Collector Pyrolyser (ACP) is dedicated to aerosol collection and analysis (Israel et al., 2002);
- The Descent Imager and Spectral Radiometer (DISR) is a remote-sensing optical instrument mainly devoted to imaging and spectroscopy measurements (Tomasko et al., 2002);
- The Doppler Wind Experiment (DWE) uses the radio relay signal to determine the direction and strength of the Titan zonal winds (Bird et al., 2002);
- The Gas Chromatograph and Mass Spectrometer (GCMS) is designed to measure the chemical composition and determine the isotope ratios of various atmospheric constituents (Niemann et al., 2002);
- The Huygens Atmospheric Structure Instrument (HASI), which includes the Permittivity Waves and Altimetry analyzer (PWA), is a multi-sensor package used for atmospheric physical properties measurements (Fulchignoni et al., 2002);
- The Surface Science Package (SSP) comprises a suite of sensors for determining the physical properties of the surface at the impact and constraining surface composition (Zarnecki et al., 2002).

Together, this variety of instruments covers the following objectives:

- determine the abundances of the atmospheric constituents;
- measure the temperature and pressure profiles;
- establish the isotope ratios of the most abundant elements;
- search for complex organic molecules;
- investigate the energy sources and their relation with atmospheric chemistry;
- measure the wind profiles;
- determine the surface composition;
- study the aerosol distribution and properties, including size and composition;
- image the landing site, record the descent panoramas, and assess the surface morphological features;
- investigate the ionization and reaction dynamics of the upper atmosphere;
- search for lightning, transient and standing waves;
- characterize haze and clouds;
- identify local meteorological phenomena, e.g. methane rain drops.

After years of planning, development, and testing, the spacecraft was launched on October 15, 1997 and inserted in orbit around Saturn on July 1, 2004. To reach Saturn, the spacecraft required a seven-year journey through the Solar System with gravity assistances of

Venus, Earth, and Jupiter. Huygens was released from Cassini on December 25, 2004 and inserted in a free fall trajectory towards Titan. The descent through the atmosphere of Titan occurred on January 14, 2005; the descent sequence started at T0≡9:10:21 UT and followed the predetermined sequence of events sketched in Figure 9.

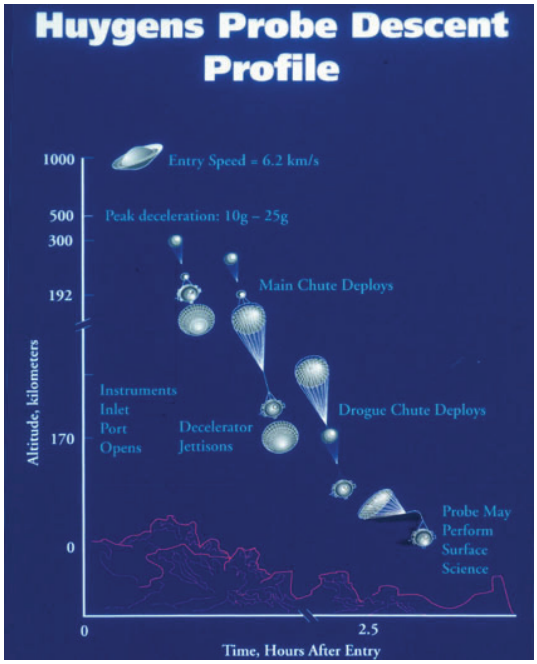

Figure 9: Sketch of the descent sequence of the Huygens Probe upon Titan.

The successful descent of Huygens upon Titan provided an unprecedented wealth of information that will remain unique for a long time. Huygens sent data during not only the 2 ½ h of the descent but also during about 1 h after landing on the surface. Various scientific teams are presently analyzing the data and improving our knowledge of Titan. This thesis is partly dedicated to the analysis of the Huygens Probe data, mainly the calibration and analysis of the PWA analyzer measurements, and to the modelling of the Titan electric environment. Special attention is devoted to the propagation of electromagnetic waves in Titan's cavity and to the related PWA observations.

4.2. The Permittivity, Waves and Altimetry Analyzer

4.2.1. Instrument Configuration

The PWA instrument was designed for the investigation of the electric properties and other related physical characteristics of the atmosphere of Titan, from an altitude of around 140 km down to the surface (Grard et al., 1995). The major objective of PWA is to investigate atmospheric electricity in the cavity of Titan; electricity plays a primordial role in the production of aerosols and soots that contain traces of complex organic, possibly pre-biotic, constituents. The strength of vertical quasi-static electric fields, the conductivity of the atmosphere and of the surface may tell us whether a global circulation current similar to that observed on Earth is conceivable on Titan. Searching for the electromagnetic and acoustic signatures of electrical discharges may provide direct evidences for such a mechanism. PWA

carried sensors to measure the atmospheric conductivity and record electromagnetic and acoustic waves up to frequencies of 11.5 and 6.7 kHz. The PWA analyzer also intended to measure the relief roughness during the descent and the permittivity of the surface after touchdown.

PWA was operated during 2 hours 25 minutes from an altitude of 141 km down to the surface, and during 32 minutes after landing. The first measurements were performed at 09:12:57 UT and an overall data volume of 551 Kbytes was collected. An equivalent amount of information was lost, due to the failure of one of the Huygens recorders onboard Cassini, which relayed the telemetry down to Earth. This data loss reduces the time or frequency resolution of most measurements by a factor of 2. For PWA records, this penalty is acceptable sometimes, and extremely detrimental in other instances, depending on the data products.

PWA consists essentially of a data processing unit that samples, digitises, and processes the signals collected with several sensors (Falkner, 2004). Two deployable booms carry six electrodes dedicated to an investigation of the electric characteristics of Titan's environment (Figure 10). The main functions of PWA are as follows: (1) the atmospheric conductivity is measured with two relaxation probes, RP1 and RP2; (2) the complex permittivity of the environment is measured during the descent, and after landing, with a MIP made of four ring electrodes, Tx1, Tx2, Rx1, Rx2; (3) electric fields in the ELF and VLF ranges, and lightning events are monitored with the dipole antenna made by Rx1 and Rx2; (4) DC and quasi-static electric fields can be evaluated from the potential difference between the Huygens Probe structure and either RP1 or RP2; (5) a pressure sensor mounted on a fixed boom monitors the acoustic noise generated by natural atmospheric phenomena; (6) the return signals of the radars (RAU) are down-converted in the radar altimeter extension (RAE) and analysed to yield information about atmospheric backscatter and surface topography.

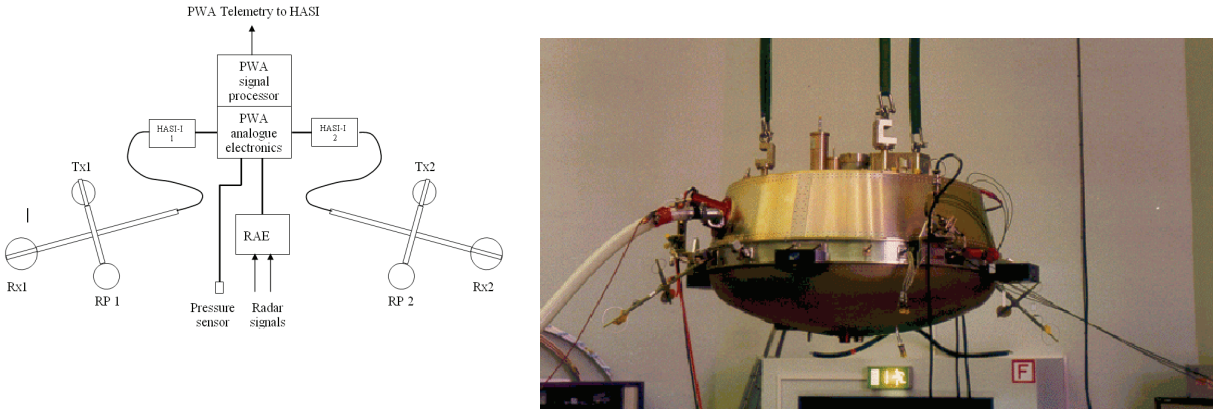

Figure 10: Sketch of PWA sensors and electronics (left) and the Huygens Probe flight model showing the booms in deployed configuration (right). Credit: HASI-PWA team.

All signals are first processed in the PWA-A analogue section. The data are then acquired by the PWA-D digital section, via a 16-bit analogue to digital converter (ADC), and submitted to a specific processing for each operation mode. The architecture of PWA, including the HASI-1 and HASI-2 preamplifiers, and the interfaces with HASI and RAU are illustrated in Figure 10. The formatted information is finally distributed between channels, which are transmitted towards Cassini on two independent radio links.

The PWA analyzer is operated in 6 different modes, which are successively selected depending upon time or altitude (Table 7). The various types of measurements are labelled as follows: VLF electric fields, AC; ELF electric fields, SH; relaxation probes, RP; mutual impedance probe, MI; acoustic pressure, AU; radar, RAE.

PWA mode	HASI status	Time T	Altitude a	Measurements
Entry	Descent 1	T_0-10 min	A ≥ 160 km	None
A	Descent 2	T_0+2.5 min	60 km ≤ a < 160 km	AC, SH, MI, RP
C	Descent 3	T_0+32 min	7 km ≤ a < 60 km	AC, SH, AU, MI, RAE, RP
D	Descent 4	-	1 km ≤ a < 7 km	AC, SH, AU, MI, RAE, RP
D	Impact	-	200 m ≤ a < 1 km 0 ≤ a < 200 m	AC, SH, AU, MI, RAE, RP
G	Surface	-	a = 0	AC, SH, AU, MI

Table 7: PWA operation mode as a function of time and altitude. Information on altitude and time is delivered to each instrument by the Huygens command and data management unit.

4.2.2. Relaxation Probe

The atmospheric polar conductivity is due to the presence of electrons and ions, and can be measured with the relaxation, or transient response, technique (Bragin et al., 1973; Ogawa, 1985). This subsection follows almost *ipsis verbis* the description made by Grard et al. (2006) **[Paper 3]**. The sensor is a thin disk, with a diameter of 70 mm and a capacitance C=2.5 pF, mounted on a boom, at a distance of (20±1) cm from the Huygens Probe body (Grard et al., 1997). When the electrode is biased at a positive, or negative, potential with respect to the Probe, it collects electric charges with the opposite polarity from the environment. When the voltage source is disconnected, the electrode potential asymptotically returns to its equilibrium level. The time constant that characterizes the response is a function of the ambient conductivity. This instrument has been tested in the Earth atmosphere during several balloon campaigns with a Huygens mock-up.

The potential of the source with respect to the vehicle structure is measured once, for reference, before the start of each relaxation sequence. The following 40 samples are taken at a rate of 50 s^{-1}; the last ones are all collected in pairs every 2 s, each pair consisting of nearly redundant measurements taken 1 ms apart. The signal is sampled at different rates during the initial and final phases of the relaxation, in order to acquire both rapid and slow responses with acceptable time resolutions. The basic sequence of measurements consists of four relaxation cycles of 56 s, where the source potential is successively given the values: +5, 0, -5, and 0 V, and is repeated during the whole descent, until touchdown.

The source is disconnected at t=0. We assume that the potential of the Huygens Probe body is in equilibrium with its environment and does not influence that of the electrode. Then the potential of the latter with respect to the vehicle follows, in a first approximation, the exponential law

$$V = (V_o - V_\infty)\, e^{-t/\tau} + V_\infty , \tag{35}$$

where V_o is the source potential and V_∞ the floating potential of the electrode, both measured with respect to the Huygens body; τ is the time constant of the discharge. When Equation (35) applies, the quantity

$$\sigma = \frac{\varepsilon_o}{\tau} \tag{36}$$

yields the medium conductivity. When V_o-V_∞ is negative, the electrode attracts positive charges and V increases; conversely, when V_o-V_∞ is positive, the electrode attracts negative charges and V decreases. In other words, σ gives the polar conductivity of the positive, or

negative charge carriers, according as $dV/dt>0$ or $dV/dt<0$, respectively. Equation (35) is a first order approximation for the relaxation profile, because descent velocity space charge effects and quasi-static electric fields distort the exponential response.

Information about the possible existence of a global atmospheric current can also be gleaned, if we make the assumption that the asymptotic potential V_∞ is induced by a vertical quasi-static electric field E_z. Then

$$\boldsymbol{E}_z = \frac{\boldsymbol{V}_\infty}{\boldsymbol{L}} \,, \tag{37}$$

where L~12 cm is the vertical effective length of the antenna made by the relaxation probe and the Huygens Probe body (Cadène, 1995).

PWA carries two relaxation probes. One sensor, RP1, yields directly the time constant τ that appears in Equation (35). The input of the amplifier which measures the potential of the other sensor, RP2, is shunted by a capacitor γ=352 pF, so that the time constant of the discharge is artificially increased by the factor $(\gamma+C)/C$=142. This feature was introduced to facilitate the observation of fast and slow relaxations with commensurate time resolutions.

4.2.3. Mutual Impedance Probe

There are several techniques for measuring the conductivity and dielectric constant of a medium. MIP measures both the real and imaginary parts of the permittivity not only in the atmosphere but also on the surface of Titan. RP is more suitable for measuring low ion conductivities. In this Section, we describe the configuration and report the performance of the MIP flown onboard Huygens; in Chapter 5, we present variations of this instrument for specific applications.

The mutual impedance probe measured the complex permittivity of the atmosphere during the descent upon Titan (Grard et al., 1995). A sinusoidal current of constant amplitude, I~10^{-9} A, with a frequency f=45 Hz, and a wavelength much larger than the size of the instrument, is injected between two transmitting electrodes, Tx1 and Tx2, and induces a voltage, V, between two receiving electrodes, Rx1 and Rx2. The complex ratio V/I is the mutual impedance of the array. If the amplitude and phase of the voltage are A_o and φ_o in a vacuum and A and φ in a given homogeneous environment, the electron conductivity and relative permittivity of the medium are:

$$\sigma = \frac{\boldsymbol{A_o}}{\boldsymbol{A}} \omega\varepsilon_o \sin(\varphi - \varphi_o) \tag{38}$$

$$\varepsilon = \frac{A_o}{A}\cos(\varphi - \varphi_o) \,, \tag{39}$$

where ω is the angular frequency of the working signal. Equations (38) and (39) are valid under the assumption that the current source and the voltage detector are perfect.
In Titan atmosphere, where ε is nearly equal to unity, Equations (38) and (39) reduce to

$$\sigma = \omega\varepsilon_o \tan(\varphi - \varphi_o) \,. \tag{40}$$

The measurement is independent of the sizes and shapes of the electrodes and of the array configuration and presents a significant advantage over the self impedance probe technique.

The instrument was calibrated on the ground, in dry air and with the booms in deployed configuration, in each mode of operation. The accurate knowledge of every discrete and stray circuit component is essential for the evaluation of systematic amplitude and phase errors that cannot be calibrated on the ground. Some elements reflect the effect, of the environment upon the load of the current source and the input impedance of the preamplifiers. Accuracies of a few percents in amplitude and less than one degree in phase are achieved with the most favourable combinations of stimulus and gain levels. MIP's calibration in the lowest frequency range is not possible in the laboratory, due to 50 Hz power line noise and must rely on circuit modelling and reference flight measurements performed in an environment with a negligible conductivity and a relative permittivity close to unity, such as the lower atmosphere of Titan. The direct application of Equations (38-40) is valid when the following conditions are fulfilled: (i) the separation between the electrodes is much larger than their size; (ii) the wavelength of the injected signal is much larger than size of the array; (iii) the medium is homogeneous; (iv) the impedances of the current generator and preamplifiers are infinite; (v) the calibrations have been performed in a vacuum (or in a controlled environment). More detail about the MIP instrument calibration and performance, is given by Hamelin et al. (2007) **[Paper 6]**, who also discuss the effects of the Huygens Probe body and of the atmospheric flow velocity. The calibration revealed more challenging than anticipated and required post-flight additional efforts, using the instrument mock-up and spare models. The calibration procedure of the atmospheric mode can be extended, within certain assumptions, to the surface mode.

PWA-MIP is not only operated during the descent through the atmosphere, at f=45 Hz, but also after touchdown at five frequencies: 45, 90, 360, 1440, and 5760 Hz. It is assumed that the impact does not change the array configuration. The interpretation of the measurements are less straightforward on the surface than in the atmosphere, because the environment is composite (gas-solid interface) and information about the attitude of the Huygens vessel is required. A preliminary analysis of the surface data is given by Grard et al. (2006) **[Paper 3]**, but Simões et al. (2005) **[Paper 2]** test the sensitivity of the measured surface dielectric properties to the vessel attitude, using a 3D finite element model to solve Poisson and Laplace equations

4.2.4. Dipole Antenna

MIP is also used in the passive mode to detect natural waves. The stimulus is switched off and the dipole made by the receiving electrodes Rx1 and Rx2 records mainly the horizontal electric component of electromagnetic and electrostatic waves. The PWA analyzer is operated in different modes that are listed in Table 8. The SH and AC modes cover the ELF and VLF ranges, respectively; one of two amplifier gains can be selected in the later mode but the best measurements are performed with the high gain. All sampling frequencies are submultiples of 46.08 kHz. More information can be found in Falkner and Jernej (2000) and Falkner (2004). The Huygens data are transmitted through two telemetry channels (A and B); the PWA spectra are split into *odd* and *even* lines, but only the *even* spectral lines are available because of the failure of the channel A receiver onboard Cassini. All spectra and RP data are split between the two telemetry channels. Only the MIP amplitude and phase are telemetered on both channels and are not affected by the loss of channel A.

Operation Mode	Sampling rate [kHz]	Spectral range [Hz]	Resolution [Hz]

SH [61.5-140 km]	3.072	3-99	3
SH [0-61.5 km]			6
AC [61.5-140 km]	23.04	0-11520	180
AC [0-61.5 km]			360

Table 8: Characteristics of the ELF and VLF spectra in the different operation modes.

The dipole antenna consists of two electrodes distant of 2.1 m, but the presence of the Huygens vessel reduces the effective length to 1.6 m; the dipole is aligned with the Y_p axis of the Probe (Figure 11).

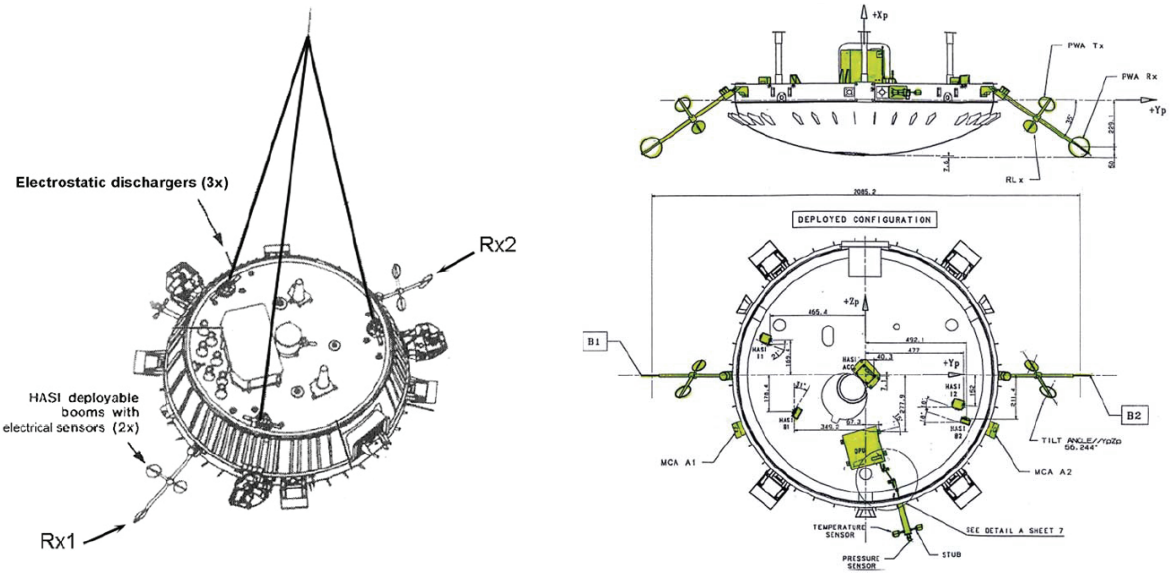

Figure 11: Overall view of the Huygens Probe attached to the parachute bridle (left, Lebreton and Matson, 2002); Accommodation of the HASI instrument on the Huygens Probe platform, top and side views (right, Fulchignoni et al., 2002).

4.2.5. Acoustic Sensor

The PWA analyzer includes a light and robust acoustic sensor mounted on a stub attached to the Huygens ring and exposed to the environment. The sensor detects the noise generated by the vessel and the parachutes, and the sounds of atmospheric events and turbulences. The acoustic transducer is a Kulite CT-190M low temperature pressure sensor and is specially suited for dynamic pressure measurements under extreme conditions. The transducer accuracy is about 5% and the pressure sensitivity is ~10 mPa, which is sufficient for detecting thunder-claps and strong winds. The sensor is operated during the descent, from an altitude of 61.5 km down to the surface. The sampling rate is 15.36 kHz; the spectra cover the range 240 Hz - 6.72 kHz with a resolution of 240 Hz, corresponding to 28 lines with an 8-bit resolution. In the burst mode, the signal waveform is recorded during short time periods for complementary analyses. More detailed descriptions are given by Falkner (2004) and Hofe (2006).

4.2.6. Radar

Huygens carries two Frequency Modulation Continuous Wave (FMCW) radars working at 15.4 and 15.6 GHz (Lebreton and Matson, 2002). Their primary function is to support the payload operation, which depends upon altitude. The radar data is also used for scientific purposes, cloud backscattering and surface roughness studies. The frequency of the FMCW radar is modulated by a triangular waveform of peak to peak amplitude Δf, whose period T_R is automatically adjusted so that a constant intermediate frequency f_o=200 kHz is produced by mixing the transmitted and returned signals. The radar altimeter, a unit dedicated to analogue processing and conditioning, converts the frequency band from (200±7.5) kHz down to the base-band (10±7.5) kHz, in the VLF range. The RAE delivers to PWA: (1) a VLF waveform which contains information about the atmosphere and the surface topography and (2) a flag, called blanking signal, which indicates the periods of validity of the base-band signal. PWA insures the acquisition, numerical processing, and formatting of the data. When the echo is too weak, the altitude range 150 m - 60 km is scanned by continuously modifying the period T_R. A detailed description can be found in Fulchignoni et al. (2002) and Falkner (2004).

4.3. Experimental Results

In preparation for the Cassini-Huygens mission, the performance of the instrument was validated during the Comas Sola and Trapani balloon campaigns. The first campaign took place, in Léon (Spain), on December 1, 1995 (López-Moreno et al., 2002) and the latter in Trapani (Italy), in 1997 and 2003. The measurements performed in the Earth atmosphere supported the instrument calibration and they provide a reference for the data collected in the atmosphere of Titan.

In this Section, we present the main results collected by the PWA sensor, and emphasize their respective contributions to the characterization of Titan's environment.

4.3.1. Data Synopsis

The PWA data synopsis is plotted in Figure 12 (Fulchignoni et al., 2005) **[Paper 1]**; it includes relaxation, mutual impedance, acoustic, electromagnetic waves, and radar data. The approximate extent of the ionized layer due to the interaction of cosmic rays with the atmosphere is indicated by a thick black line along the top axis. **a)**, **b)** Relaxation carpets for V_o= +5 V and -5V, respectively. The relaxation probe, initially biased at a potential V_o with respect to the vehicle body, subsequently returns to its equilibrium potential, V_1, with a time constant that yields the DC conductivity of the charges with polarity opposite to that of V_o-V_∞. The measurements taken during each relaxation cycle form a string of pixels aligned with the ordinate axis; the voltages are given by the colour scales shown on the right-hand side. The electrode potential is measured every 20 ms during the first second, then every 2 s for the remainder of each 1 min cycle. These panels give a visual impression of the speed at which the potential of a conductive body (colour coded) returns from ±5 V to zero ('relaxes'), owing to the collection of ambient charges with opposite polarities. In the lower altitude range, for example, the colour of the carpet is uniform (brown for +5 V and blue for -5 V), which shows that the ambient charge densities are low. Above 40 km, on the contrary, the distinctive carpet patterns tell us that the probe voltage is strongly affected by the ionized environment. **c)** Mutual impedance phase shift, $\Delta\varphi=\varphi_o-\varphi$ (non-calibrated). The AC conductivity is measured with the quadrupolar probe. A current I with frequency 45 Hz and amplitude ~10^{-10} A, is injected between two transmitting electrodes, and the voltage V induced between two receiving electrodes is measured. If the phase of V/I at 45 Hz is φ_o in a

vacuum and φ in a collisional medium, then the conductivity of the medium is proportional to tan (φ_o-φ). **d)** Dynamic spectrum of the voltage V measured between two electrodes 2.1 m apart, in the bandwidth 0–9.22 kHz, when a current stimulus I is injected between two transmitting electrodes. The spectrum of the signal provides information about its energy distribution as a function of frequency, at a given time. Successive spectra are represented by adjacent strings of pixels aligned with the ordinate axis, where spectral amplitude is coded in colour according to the logarithmic scale shown on the right-hand side. **e)** Dynamic spectrum of the voltage V measured with two electrodes ~2m apart, in the bandwidth 0–11.5 kHz, without current stimulus. **f)** Same as e), but in 0–100 Hz bandwidth. **g)** Dynamic spectrum of acoustic differential pressure in the bandwidth 0–6.7 kHz. A sound pressure level (SPL) of 0 dB corresponds to 20 mPa. The variability of the acoustic noise is caused by changes in the atmospheric density and wind velocity. **h)** The altitude represented by the red dots is measured whenever the radar altimeter is locked on the surface; permanent lock is maintained from 34 km down to 150 m. At higher altitudes, the green dots indicate the distances at which the signal is returned by the atmosphere. Several events are identified with triangles along the top axis: (1) stabilizer parachute opening, (2) mode change, (3) impulsive event in e), (4) surface touch down. Discontinuities in time or frequency are artefacts due to mode change. The following Subsections present a detailed description of each data subset. The measurements of PWA are also compared with those collected during field campaigns or returned by other Huygens instruments.

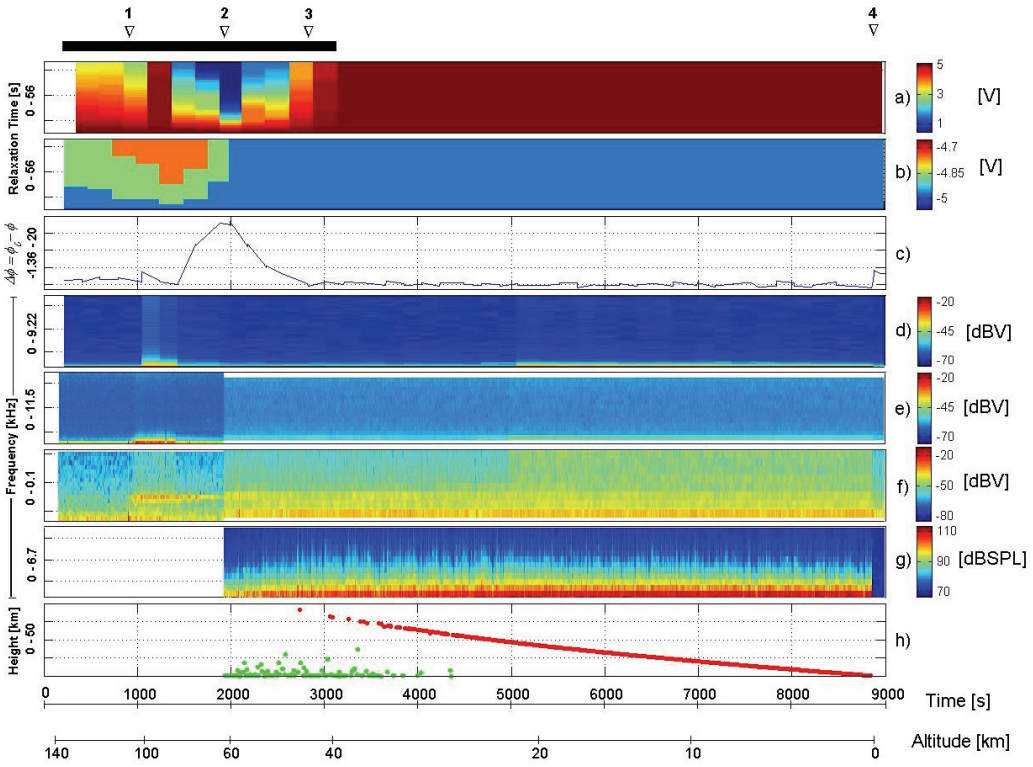

Figure 12: The synopsis of PWA data - a) relaxation probe biased to +5 V; b) relaxation probe biased to -5 V; c) mutual impedance phase shift; d) mutual impedance spectra; e) VLF data; f) ELF spectra; g) acoustic spectra; h) radar data. See text for details.

4.3.2. Relaxation Data

Although the short-relaxation probe data sent in channel A was lost, the available measurements still contribute to our investigation of the electrical properties of Titan's atmosphere. Figure 13 shows the relaxation carpets at +5, 0, and -5V, where the relaxation time is plotted against the descent time. The panels give a visual impression of the speed at which the potential of a conductive body returns from ±5 V to zero, owing to the collection of ambient charges with opposite polarities. In the lower altitude range, the conductivity is below probe sensitivity; above 40 km and 70 km, on the contrary, the distinctive carpet patterns allow us to estimate the conductivities of negative and positive charges, respectively. When the initial potential of the RP2 electrode is that of the vehicle, the relaxation shows a very small variation (Figure 13, middle panel). Nevertheless, after jettisoning the parachute, the potential increases up to about 0.3V during the relaxation, which suggests that charging processes might play a role.

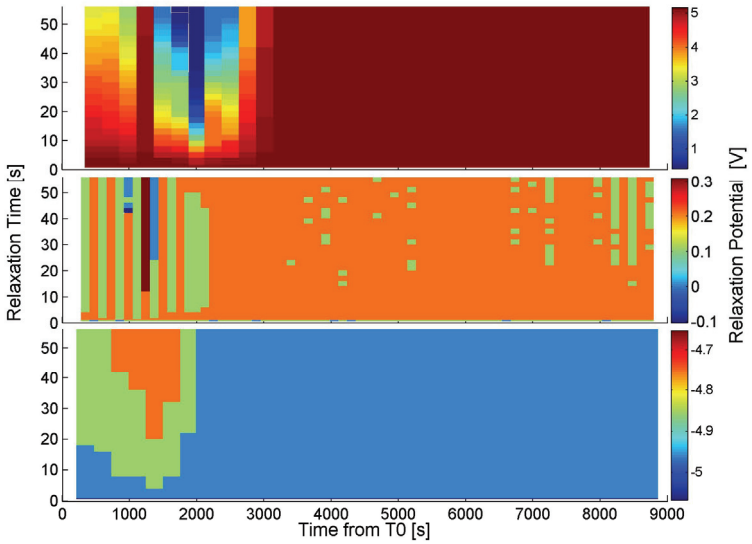

Figure 13: Relaxation carpets when the RP2 electrode is biased to +5 (top), 0 (middle), and -5V (bottom).

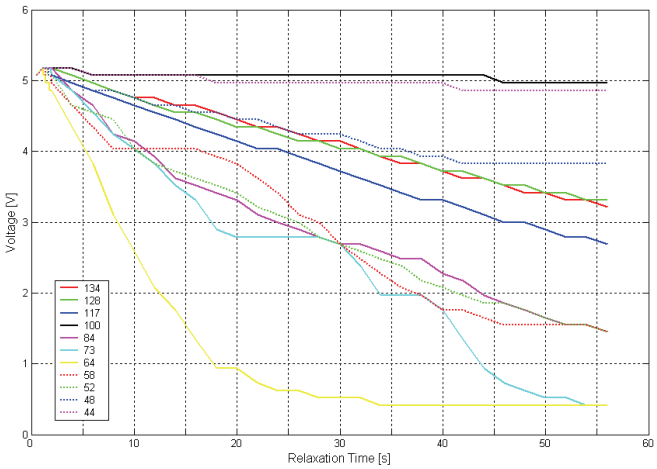

Figure 14: Relaxation curves of RP2 due to the collections of negative charge carriers (V_o=+5 V). The labels indicate the average altitude, in km, at which the measurements are taken.

Figure 14 shows the relaxation curves due to the collection of negative carriers in the altitude range 40-140 km. A few profiles present segments where the voltage is constant ("plateaus"), hence no measurable relaxation takes place during those time intervals. The altitude ranges where these plateaus occur are listed in Table 9. The nature of the plateaus has not been identified yet, but two interpretations are possible: a) a hardware or a software artefact; b) a significant reduction of the electron concentration. A careful analysis of the hardware and software did not reveal any artefact so far. The performance of RP during the descent on Titan has been simulated in the Earth atmosphere, and in the laboratory using the engineering model, but no similar feature could be reproduced. Qualitative experiments show that spraying 1,1-difluorethane ($C_2H_4F_2$) on the electrodes decreases the relaxation time. It has also been shown that ice cirrus clouds change the electric conductivity profile and it might be assumed that thin haze layers in Titan's atmosphere might produce a similar effect. At about 95 km, the largest plateau of the relaxation curve n°4 (Table 9) coincides with the velocity increase that follows the parachute release, which suggests that velocity effects must be taken into account when the thermal velocity of the ion clusters is comparable to the descent velocity of the Probe. Although the origin of the plateaus is still under investigation, a natural origin is likely. If so, the plateaus could reflect the presence of aerosol clouds in the atmosphere of Titan.

Relaxation Curve	Time [s]	Altitude [km]
4	1111-1166	92.9-96.2
6	1644-1652 1658-1662	69.9-70.2 69.6-69.7
7	1910-1914	62.1-62.2
8	2124-2132 2162-2170	57.0-57.2 54.2-54.4
10	2454-2458 2670-2684	56.5-56.6 50.8-50.9

Table 9: Time and altitude of the plateaus identified in the relaxation curves.

4.3.3. Radar Data

The return signal of the radar not only supports the sequence of the descent operations that depends upon altitude, but also provides information about surface roughness and atmospheric structure, namely rain drops and clouds.

Figure 15 shows the radar signal reflected by the surface (red dots) and backscattered by the atmosphere (green dots). The scattered green dots deviate from the altitude profile and are likely due to atmospheric structures. The backscattered signal is under investigation and its strength imposes constraints on aerosol concentration in clouds. When the radar is locked, PWA records the altitude profile represented by the red dots.

The surface roughness is characterized by spectra such as that illustrated by Figure 16. The shape of the spectra is highly variable and depends upon the topography of the terrain that reflects the radar signal.

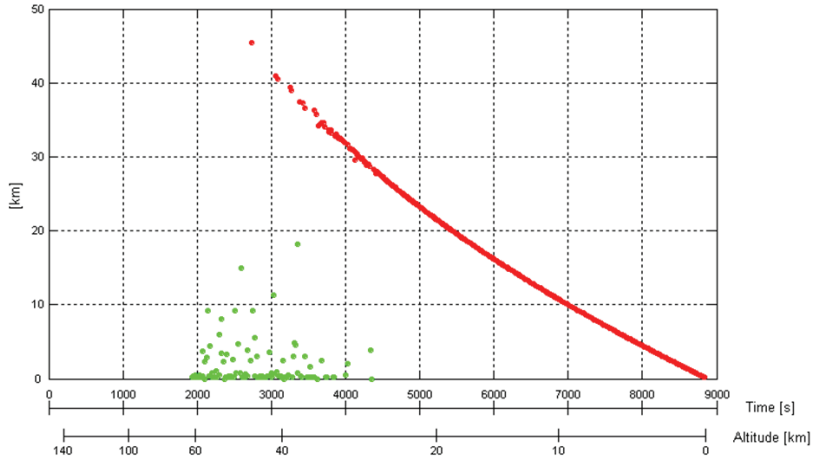

Figure 15: Atmospheric backscatter distance (green) and Huygens Probe altitude (red) measured by PWA.

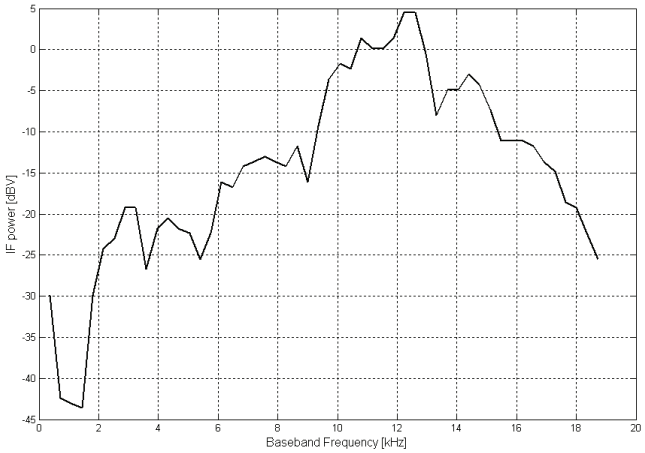

Figure 16: Spectral representation of the surface roughness observed from an altitude of 23.9 km.

4.3.4. Extremely Low Frequency Spectra

The ELF dynamic spectra recorded with the PWA analyzer are shown in Figure 17. The potential difference measured by the electric antenna, in the frequency range 0-100 Hz and between 60 and 140 km, is shown in the upper panel; the white stripes represent the channel-A data loss; the strength of the electric field at around 36 Hz is shown below, considering an effective length of 1.6 m for the dipole antenna. A similar representation at altitudes below 60 km is shown in the two lower panels of Figure 17, though the width of the spectral lines is doubled due to an operation mode change. The narrow spikes in the 36 Hz signal at 900 and 8870 s correspond to the stabilizer parachute deployment and touchdown, respectively. Four other spikes at 1996, 2094, 2190, and 2288 s are almost equally spaced and seem to be artefacts but their origin has not been identified so far.

Figure 18 shows average spectra in the range 0-100 Hz, which reveals a peak at 36 Hz during the descent but not on the surface. The ELF spectra are averaged in the following altitude ranges: (1) 60-140 km, (2) 60-110 km and (3) 115-140 km, before the mode change; (4) 0-60 km, (5) 22-60 km, (6) 0-22 km, and (7) surface, after the mode change; the dashed

lines represent the signal level measured during the cruise with the booms in a folded position.

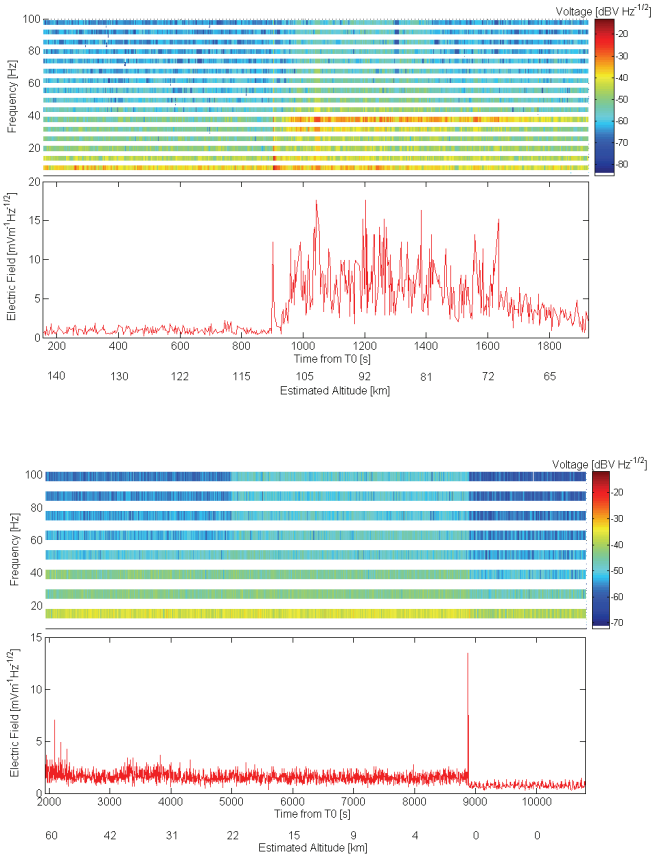

Figure 17: Electric signal measured with the PWA receivers in the ELF range before (upper two panels: 1 and 2), and after (lower two panels: 3 and 4), the operation mode change. *Panels 1 and 3*: Dynamic spectra with frequency resolutions 3 and 6 Hz, respectively. Spectral levels are given by the colour scales shown on the right-hand side. White stripes correspond to the data loss in channel A. *Panels 2 and 4*: Electric field of the spectral line around 36 Hz against time. The peaks at ~900 and ~8870 s are due to the deployment of the third parachute and touchdown, respectively.

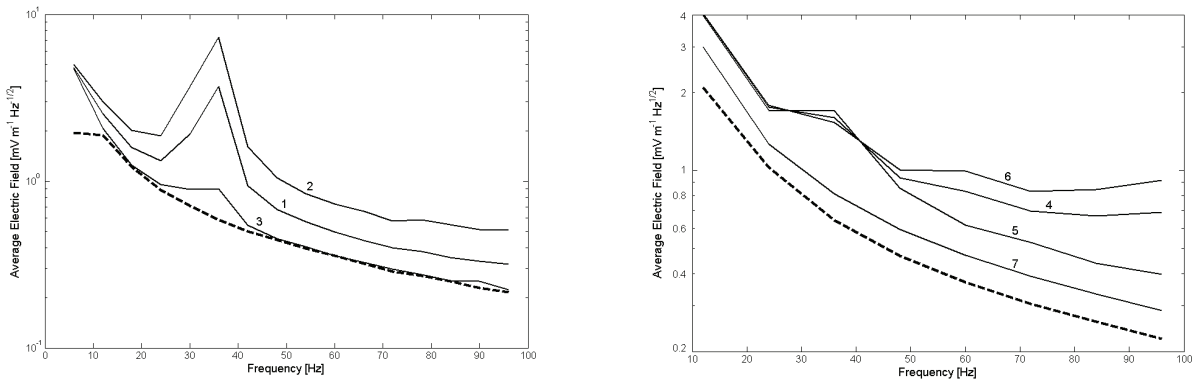

Figure 18: Average electric field spectra measured by PWA in the ELF range before (left; profiles 1, 2, and 3) and after (right; profiles 4, 5, 6, and 7) the mode change, in several altitude ranges: (1) 60-140 km; (2) 60-110 km; (3) 115-140 km; (4) 0-60 km; (5) 20-60 km; (6) 0-20 km; (7) surface. The dashed lines represent the signal level during the cruise.

The data sets recorded before and after the operation mode change are split in bins of 50 and 100 spectra, respectively, and the weighted arithmetic mean frequency of the emission, i.e. the average value of the 36 Hz and adjacent lines, is evaluated within each bin. The output of this crude analysis is reported in Figure 19 and indicates that the peak frequency increases by about 1.5 Hz throughout the descent.

The most significant features of the ELF spectra that deserve a further analysis are listed below:

A) A narrow-band emission is observed at 36 Hz during the descent but not on the surface (Figures 17 and 18);
B) An electric field spike at 900 s coincides with the stabilizer parachute deployment (Figure 17, top);
C) Another spike at 8870 s is due to the touchdown (Figure 17, bottom);
D) An increase in the amplitude of the 36 Hz signal is seen at about 30 s after the deployment of the parachute; the signal reaches a steady low level at about 2350 s (Figure 17);
E) The signal in the upper frequency range increase between 950 and 1400 s (Figure 17, top);
F) The noise at high frequency (f>60 Hz) increases after 4975 s, corresponding to an altitude of 22.5 km (Figure 17, bottom);
G) Four narrow lines at 1996, 2094, 2190, and 2288 s are almost equally spaced (Figure 17, bottom);
H) The electric field maximum and mean amplitudes are 17.5 and 2 $mVm^{-1}Hz^{-1/2}$ (Figures 17 and 18);
I) The mean electric field at 80-100 km is ~7 $mVm^{-1}Hz^{-1/2}$ (Figures 17 and 18);
J) The frequency of the narrow-band emission, at around 36 Hz, increases by about 1.5 Hz throughout the descent (Figure 19);
K) The electric field amplitudes at 36 Hz are 0.65 and 0.8 $mVm^{-1}Hz^{-1/2}$, during the cruise and after touchdown, respectively (Figure 18);
L) The ELF background spectrum in the altitude range 115-140 km is similar to that of the cruise level (Figure 18, left);
M) A small increase of the electric field amplitude is observed at 36 Hz in the interval 3200-4000 s (Figure 17, bottom);
N) Noise increases at 48 Hz between 4600 and 5600 s.

The interpretation of the 36 Hz signal must comply with the observations described above. The Huygens Probe mock-ups were not fully representative of the flight model but no similar signal has ever been observed during balloon campaigns. At this stage, the nature of the source that might explain the 36 Hz signal and the associated features has not been determined (Simões et al., 2007a **[Paper 4]**; Béghin et al., 2007 **[Paper 5]**). Nevertheless, the morphological transition observed at ~22 km in the higher frequency range seems to be related with a thin haze layer detected by the onboard camera.

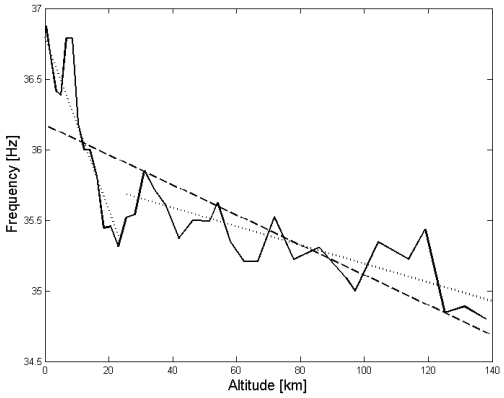

Figure 19: Variation of the peak signal frequency during the descent (solid line), and linear fits to the data sets collected during the entire descent (dashed line) and at altitudes above and below 21 km (dotted lines).

4.3.5. Very Low Frequency Spectra

The VLF dynamic spectra recorded with the PWA analyzer are shown in Figures 20 and 21, before and after the operation mode change. The PWA analyzer acquired 2204 and 301 spectra during descent and on the surface, respectively. Although loss of channel A also doubles the VLF spectrum resolution, like in the ELF range, white stripes are not shown in these plots. The top panels show the raw VLF spectra in Least Significant Bit (LSB) units. The lower panels present the plots of the spectral lines below 2.7 kHz, to ease the comparison between the major morphological features visible at these frequencies. Alike the ELF data, the width of the VLF spectral lines doubles at about 60 km, due to an operation mode change.
The most significant features observed in the VLF spectra include:

O) A spike at 256 s in the 180 Hz line (Figure 20);
P) A peak at about 400 s in the 540 Hz line (Figure 20);
Q) The peak present at 900 s in the ELF data is also observed in the VLF spectra (Figure 20);
R) The signal increases after the stabilizer parachute deployment at frequencies up to 2 kHz; the effect vanishes at higher frequencies (Figure 20);
S) The noise in the frequency range 500-2000 Hz ceases at 1408 s (Figure 20);
T) The signal in the lowest frequency lines decreases between 1290 and 1310 s down to the instrument noise level (Figure 20);
U) An impulsive event is seen in the whole frequency range at 2798 s, corresponding to an altitude of~46 km (Figure 21);
V) Three wide peaks at 2945, 3590, and 4675 s occur at 720 Hz (Figure 21);
W) The first VLF line (720 Hz) shows a transition at 4975 s that is similar to those observed in the ELF range (F) (Figure 21);
X) The background noise level of the first line after touchdown is similar to that at altitudes above 25 km (Figure 21);
Y) A narrow spike at 8872 s coincides with the touchdown (Figure 21).

Some of the features observed in the ELF and VLF ranges can be compared with the sequence of events that took place during the descent; for example, several artefacts match the ACP pump operation sequence.

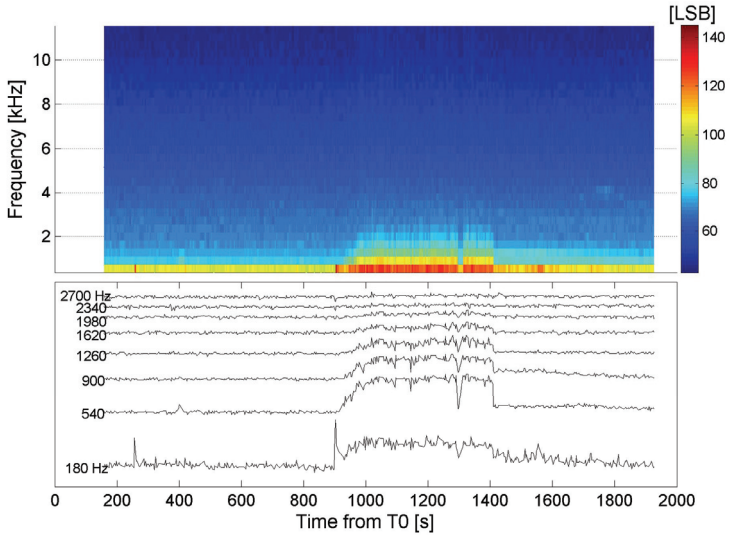

Figure 20: Electric signal measured with the PWA receivers in the VLF range between 140 and 60 km. *Top*: Dynamic spectrum with frequency resolution of 180 Hz. Spectral levels are given by the colour scales shown on the right hand side in LSB units. *Bottom*: Spectral lines below 2.7 kHz shown in arbitrary units and shifted for better visualization. The spike at 900 s coincides with the deployment of the stabilizer parachute; a sudden noise reduction is observed at 1408 s, between 0.5 and 1.5 kHz.

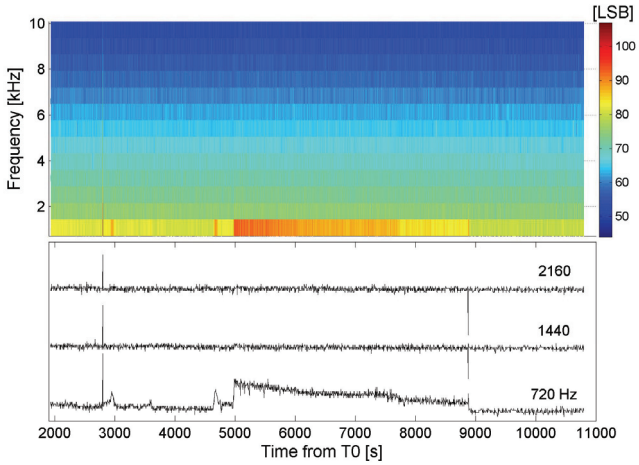

Figure 21: Electric signal measured with the PWA receivers in the VLF range below 60 km and on the surface. *Top*: Dynamic spectrum with frequency resolution of 360 Hz. The spectral levels are given by the colour scales shown on the right hand side in LSB units. *Bottom*: Spectral lines below 2.2 kHz shown in arbitrary units and shifted for better visualization. A significant amplitude increase is observed at about 5000 s and the spike at 8870 s corresponds to touchdown.

4.3.6. Mutual Impedance Data

The PWA analyzer performed 88 mutual impedance measurements at 45 Hz during the descent and 300 on the surface (60 at 5 different frequencies). Figure 22 shows the spectra and mutual impedance amplitude and phase at 45 Hz during the descent and on the surface. The amplitude and phase measured in the digital processor unit are shown in the top and middle panels. The even spectral lines are shown in the bottom panel with a resolution of 45 Hz. The transition observed at 8870 s is due to touchdown and a noise increase is observed between 1000 and 1400 s and below 22 km until touchdown. A peculiar amplitude variation is

seen before 1400 s, i.e. above 80 km; a prominent phase shift corresponding to an ionized layer is visible between 1450 and 2850 s, which corresponds to the altitude range 80-45 km.

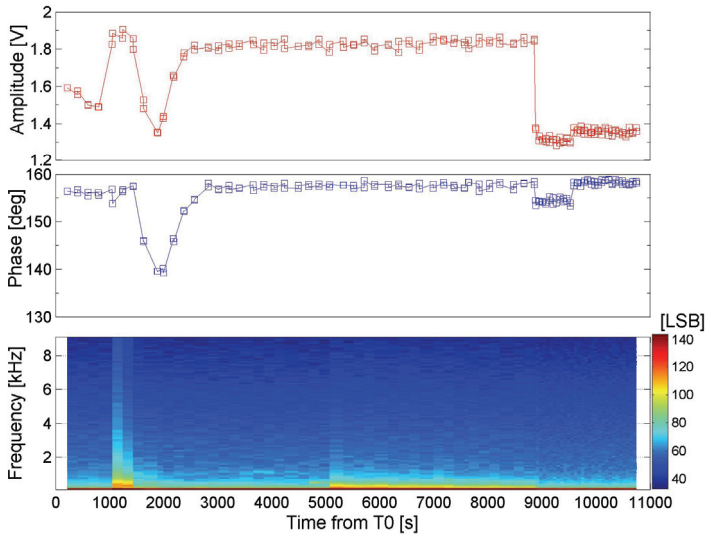

Figure 22: Mutual impedance amplitude (top) and phase (middle) measured during the descent and on the surface. Dynamic spectra (bottom) with frequency resolution of 45 Hz. Spectral levels are given by the colour scale on the right hand side in LSB units.

After touchdown, the mutual impedance of the medium is measured at 5 frequencies (Figure 23). The last measurements performed at 45 Hz before touchdown are also included for comparison. A monotonic variation is observed during the first minute followed by a sudden transition at ~9539 s (about 11 min after landing). The transition is more pronounced on the phase and at lower frequencies.

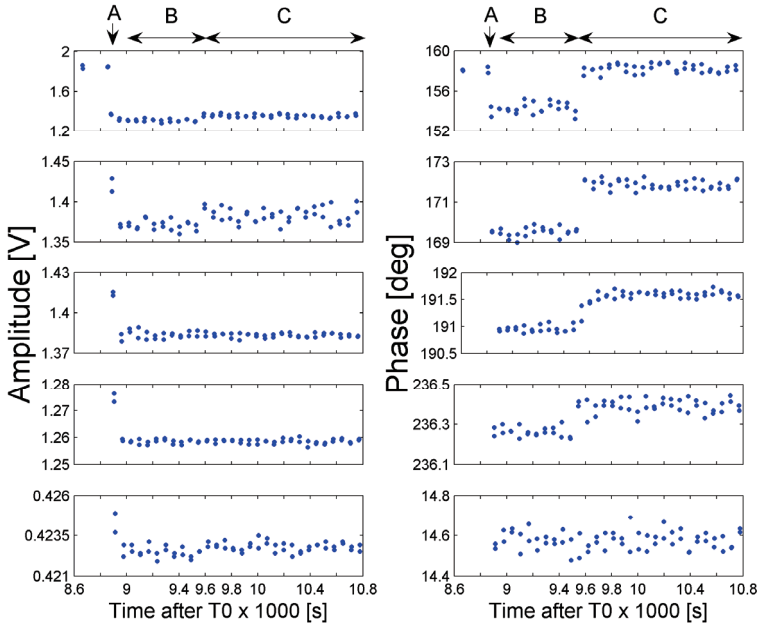

Figure 23: Mutual impedance amplitude (left) and phase (right) measured at low altitude and on the surface. The stimulus frequency is from top to bottom: 45, 90, 360, 1440, and 5760 Hz. About 11 min after landing (B-C transition), one observes a discontinuity that is more visible on the phase and at lower frequencies. The amplitude shows also a decrease immediately after landing (group-A data).

4.3.7. Lightning Data

The PWA measurements acquired in the lightning mode do not disclose any obvious activity. It is possible however to predict the maximum stroke rate that might have been observed during the descent of the Huygens Probe and several events still are under investigation. A comparison between balloon campaign data and PWA measurements reveals that, if present, the stroke rate is much less common on Titan than on Earth, at least 100 times lower.

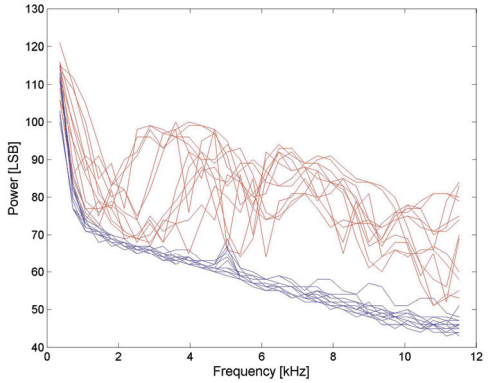

Figure 24: Selected electric field amplitude in LSB units as a function of frequency, measured during the Trapani balloon campaign. *Blue*: background noise; *Red*: impulsive events associated with lightning.

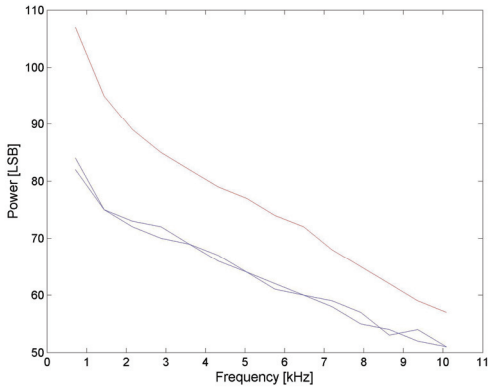

Figure 25: Impulsive events (red) and background noise level (blue) measured in the VLF range on Titan at 2798 s (~46 km).

Figure 24 illustrates typical measurements performed during balloon campaigns and interpreted as lightning strokes, where the blue and red curves represent, respectively, the background level and the impulsive events related to lightning activity. Figure 25 shows the spectra of the impulsive event, and of the background noise, recorded on Titan at 2798 s (~46 km) and previously reported in the VLF data. Other weaker events have also been detected but their meaning is even more dubious because data evaluation is extremely difficult. Electrostatic and corona discharge phenomena are under investigation as the possible sources of the impulsive events.

4.3.8. Acoustic Spectra

The acoustic sensor was operated below 61.5 km after the operation mode change. The PWA analyzer performed 2168 measurements during the descent and 420 on the surface. Figure 26 shows the dynamic acoustic spectrum in the range 0-6.7 kHz, where the signal amplitude is measured in LSB. The top and bottom panels show, respectively, the Trapani balloon measurements and the Titan acoustic data. The acoustic noise recorded during the descent on Titan is 15 LSB higher than that observed during Earth balloon campaigns, and is drastically reduced after touchdown. The acoustic data is still under investigation, but no thunder-clap has been clearly identified.

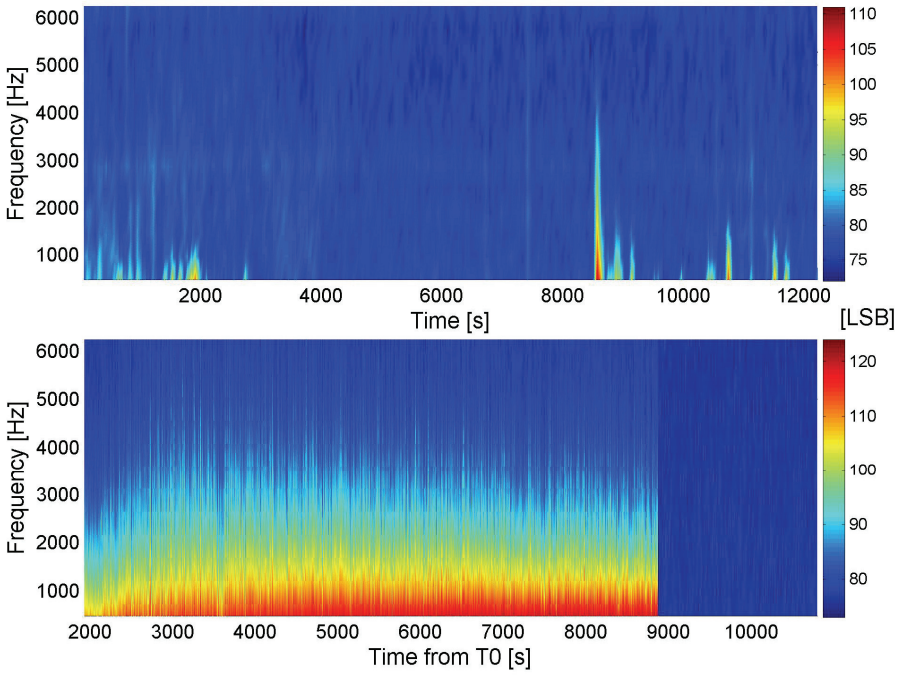

Figure 26: Dynamic spectra measured with the acoustic transducer. *Top*: Trapani balloon campaign. *Bottom*: Titan measurements performed in the lower atmosphere and on the surface. The touchdown drastically reduces the acoustic noise.

4.4. PWA Data Analysis

The wealth of information provided by PWA is unprecedented and will remain unique for a long time. The data set therefore deserves a careful analysis, supported by, theoretical models, and comparisons with the results obtained with other instruments.

It is clear, at a first glance, that RP and MIP observe a peak in conductivity during the descent. However, the magnitudes of the peak measured by the two instruments do not match. For example, Equations (36) and (38) are not accurate enough and an elaborated model is required that takes into account the descent velocity. Hamelin et al. (2007) **[Paper 6]** have analyzed the MIP data, including circuit calibration, vehicle and descent velocity effects. The pre-flight calibrations revealed insufficient, which required post-flight calibrations and modelling. The amplitude and phase shift recorded during the descent are split into several sets: the amplitude and phase below 40 km can be used as a reference because the conductivity lies below the instrument sensitivity ($\sim 5\times10^{-11}$ Sm^{-1}), thus providing an *in situ* calibration as in a vacuum; above 80 km, the anomalous behaviour of the mutual impedance can be explained either by an aerosol deposit on the booms or an incomplete boom deployment, though the issue remains open; between 40 and 80 km an ionized layer is observed with a conductivity peak of 3 nSm^{-1} at 63 km (Figure 27). The layer shows relatively steep boundaries not predicted by existing models. In fact, although the theoretical profiles (Borucki et al., 1987; Molina-Cuberos et al., 1999) yield a maximum in electron density at about 90 km, the conductivity peak at 63 km was not foreseen at all. Figure 28 shows the derived electron density profile between 40 and 100 km with a maximum density of 650 cm^{-3}. The profile structure is probably caused by electron attachment in aerosols layers. The differences between measurements and model predictions must therefore be explained in terms of aerosols physics and atmospheric chemistry.

Analysis of the ELF spectra above 115 km suggests that incomplete boom deployment during the first part of the descent is the most probable explanation for the anomalous mutual impedance amplitude. Numerical modelling and laboratory tests with partially deployed booms are consistent with the measurements. Though less probable, condensation or aerosol deposit on the booms might also be compatible with the results. The ELF average signal strength recorded during the first part of the descent is similar to the noise level during the cruise (Figure 18). The booms are folded during the cruise and the ELF integrated signal, excluding the 36 Hz peak, is similar to that observed in the first part of the descent, until the stabilizer parachute deploys (Figure 18, left). Furthermore, the noise is significantly higher on the surface than during the cruise (Figure 18, right), suggesting a partial deployment as the likely explanation for the anomalous measurements at high altitude. Similar conclusions can be drawn from the VLF spectra, namely analyzing the 540 Hz spectral line. Pre-flight calibrations show that the situation that matches best the amplitude observed during the first part of the descent on Titan is the configuration where one boom is fully deployed and the other one partially deployed.

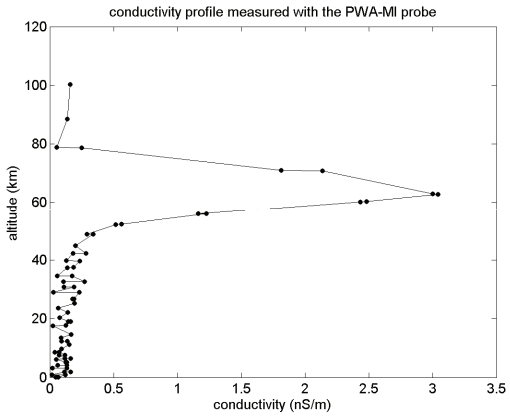

Figure 27: Electron conductivity profile below 100 km.

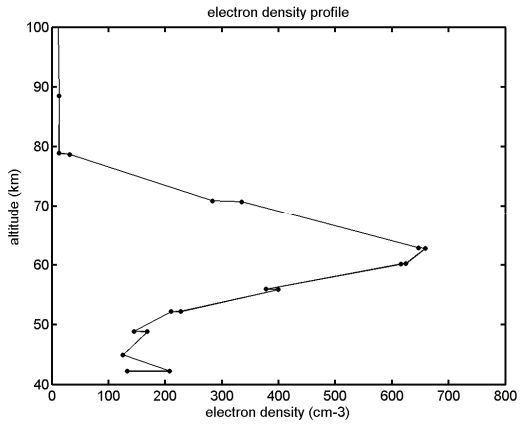

Figure 28: Electron density profile between 40 and 100 km.

As for MIP, velocity effects must be taken into account in the RP calibration. The spherical charge distribution around the RP electrode is deformed due to the velocity and the Debye sphere is transformed in an oblate spheroid. The effective Debye length is modified because the medium is not homogeneous, Equation (36) reveals inaccurate due to velocity effects, and the corrected conductivity is higher. The RP data calibration remains under scrutiny and it is not clear whether MIP and RP yield the same peak conductivity, but their ratio is not larger than two. Although uncertain in the range 100-140 km, MIP and RP measurements show that electron conductivity is less than $\sim 10^{-10}$ Sm^{-1}.

The detection of lightning activity was one of the major goals of PWA. A negative answer is so far in agreement with the Cassini observations. Several events remain under investigation, but a comparison between Earth balloon (Figure 24) and Titan (Figure 25) data, gives an estimation of the maximum lightning stroke rate; if the events under scrutiny are all natural, the ratio between these rates is less than 0.01, assuming that the phenomena are similar on Titan and on Earth. Béghin et al. (2007) **[Paper 5]** report a survey of possible electric discharge scenarios in the atmosphere. The acoustic data do not confirm the presence of thunder claps; the spectrum is extremely smooth and the noise vanishes after touchdown. The acoustic data can nonetheless be analysed for the exploration of other atmospheric features, such as wind profile.

The narrow band signal detected in the ELF spectra deserves a deep analysis. The 36 Hz signal resembles a Schumann resonance though some pieces of the puzzle do not match. The

amplitude increase after the stabilizer parachute deployment is suspicious. Simões et al. (2007a) **[Paper 4]** and Béghin et al. (2007) **[Paper 5]** assess the validity of various hypotheses, including artefacts and natural sources. A complete characterization of the cavity of Titan is not possible because the atmospheric conductivity profile in the range 140-750 km and the subsurface dielectric properties are unknown, wave propagation in the ELF range can be modelled yet. The most important results of this study are the following (Simões et al., 2007) **[Paper 4]**:

- The 36 Hz emission could correspond to the second eigenmode of a Schumann resonance;
- Though unlikely, the lowest eigenmode is not seen because its frequency could fit the 15 Hz line of the missing channel A;
- The amplitude of the electric field of the first eigenmode decreases when the angular separation between the source and the receiver is close to 90°;
- The frequency increase observed during the descent roughly fits model predictions;
- The electric field enhancement at about 100 km might be explained because the antenna measures mainly the horizontal component of the field that is more tilted at this altitude;
- After landing, the receiving dipole touches the ground and the field amplitude decreases due to the variation of the ambient dielectric properties.

However, several features do not fit the puzzle, namely the electric field amplitude. The electric field is at least one order of magnitude larger than on Earth and no evidence is found for lightning activity. Therefore, the resonance is either an artefact or is excited by another source. Béghin et al. (2007) **[Paper 5]** assess the artefact versus natural scenarios and the major conclusions include:

- The 36 Hz signal was never observed before, neither during balloon campaigns nor in the laboratory, hence hardware or software failure is unlikely; all other PWA functions are nominal;
- Booms vibration induces parasitic signals due to microphonic effect but post-flight laboratory tests do not show any resonance around 36 Hz.

Possible scenarios are still under investigation. Laboratory experiments are programmed to assess further the boom vibration hypothesis, namely measuring a possible variation of the Young modulus of the boom composite material with temperature. Natural sources that might excite cavity resonances are also being studied, namely the plasma-wave emission mechanism evoked here above, involving the Titan wake induced by the magnetosphere of Saturn (Béghin et al., 2007) **[Paper 5]**.

Several experiments have been conducted to study the effects of aerosols sprays on the booms and electrodes. These tests are preliminary and qualitative, but it is clear that aerosols and small dust particles impact on the electrodes modify the ELF spectra (Figure 29). Different hazes produce distinctive spectral features that must be quantified. For example, a water spray raises the electromagnetic noise in the lower part of the spectrum, whereas a difluoroethane spray increases the noise in the whole frequency range. Aerosols concentration, particle size and charging processes play a role in the electrification of the atmosphere. The morphological transition observed at about 22 km (F and W features) matches the altitude of a thin haze layer observed by DISR (Tomasko et al., 2005), and deserve further analysis.

Correlating the PWA measurements, e.g. the electric field amplitude in the ELF range, and the data returned by other instruments can test the validity of different hypotheses. If the attitude of the Probe during the descent was known with a fair accuracy and the published

results did not sometimes contradict each other, the correlation between the electric field amplitude at 36 Hz and the Huygens Probe tilt, for example, would provide information about the nature of the signal. In the absence of a consensus about the Probe attitude, we shall tentatively compare the tiltmeter and electric field profiles

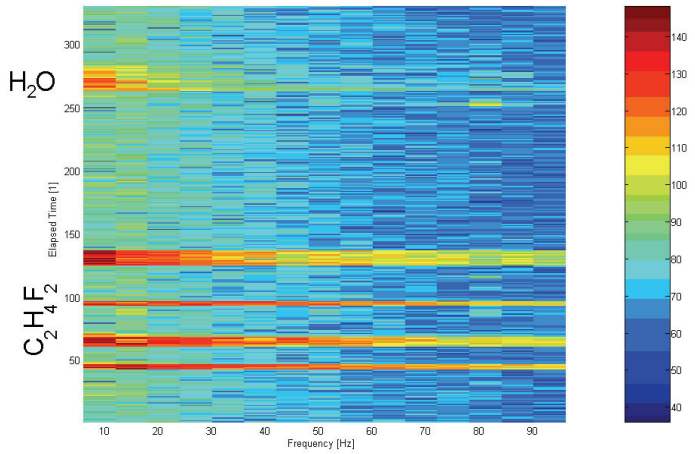

Figure 29: Dynamic spectrum, elapsed time against frequency, in the range 3-99 Hz, obtained by spraying fresh water and difluoroethane ($C_2H_4F_2$) hazes on the antenna. The colour scale, in arbitrary units, represents the potential measured with the digital processor unit.

The SSP instrument includes two tiltmeters (Til-X and TIL-Y) that are used to derive the angle between the Huygens Probe and the gravity vector; a coordinate transformation is required to convert these two angles into the X_p-Y_p system of the Probe, which is more suited for an evaluation of the PWA antenna orientation. Lorenz et al. (2007) discuss the tilt measurements and the transformation from the X-Y to Probe reference systems. The tilt and ELF electric field measurement are asynchronous, and are acquired approximately at the rates of 3 and 1 Hz respectively; consequently, only values averaged over intervals of a few seconds can be compared. The dispersion of the 36 Hz data points between 900 and 1600 s is consistent with the DISR data, which often reveals swing rates above 40°/s (Karkoschka et al., 2007). Figure 30 shows a comparison between the ELF electric field and several other panels of measurements.

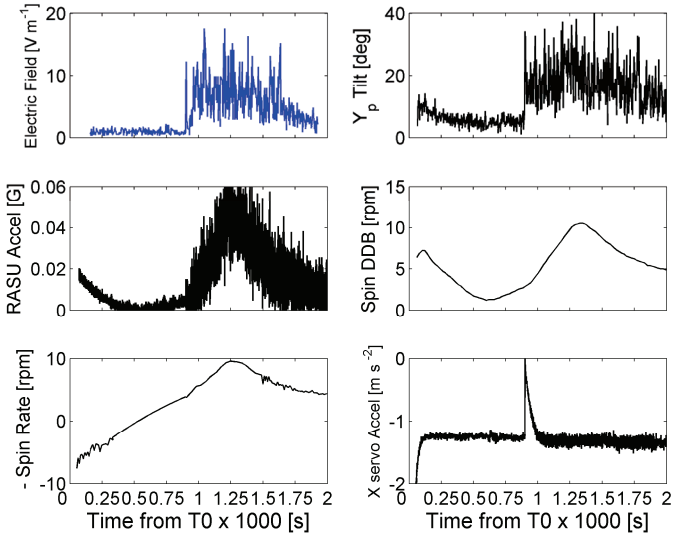

Figure 30: Profiles of various sensor outputs in the altitude range 140-60 km. *Top-left*: ELF electric field (36 Hz); *Top-right*: Tilt of the antenna with respect to the horizontal direction (Y_p-axis), derived from the TIL-X and TIL-Y SSP data; *Middle-left*: housekeeping data collected with the Radial Accelerometer Sensor Unit (RASU); *Middle-right*: spin rate inferred from Descent Data Broadcasting (DDB); *Bottom-left*: spin rate reconstructed from several other sources; *Bottom-right*: acceleration measured with the X-servo accelerometer along the Probe descent velocity (approximately vertical).

This comparison shows a similitude between the electric field amplitude at 36 Hz and the inclination of the antenna, suggesting a natural origin for the signal. However, the antenna tilt and radial acceleration (top-right and middle-left panels) are similar, which is confirmed by the spin data (middle-right and bottom-left panels). The vertical acceleration is derived from the X-servo data and shows a peak between 900 and 1000 s, during parachute release and deployment, and a rather smooth profile elsewhere. Whereas the electric field seems to be correlated with tilt, the lack of similitude with the X-servo output is less clear and suggests that the vibrations induced by the parachute cannot easily explain the enhancement of the 36 Hz signal. At present, there is no definite agreement between the tilt measurements performed by SSP, HASI, and DISR; there is a possible constant offset on the TIL-X and TIL-Y data that could modify the adopted Y_p tilt angles. After landing, for example, the tilt measured with different instruments differ by as much as ~10° (Fulchignoni et al., 2005 **[Paper 1]**; Tomasko et al., 2005; Zarnecki et al., 2005; Karkoschka et al., 2007). The transformation of the TIL-X and TIL-Y data to the X_p-Y_p axes shows that the arithmetic mean and standard deviations of the antenna tilt during the interval 900-2000 s are 17.4° and 10.5°. At low altitude, below 20 km, the arithmetic mean and standard variation values of the tilt are 4.8° and 3.3°; the tilt on the surface is 2.1°; maximum inclination reaches almost 50° at about 1400 s though the SSP team is not confident about the magnitude of strongest acceleration spikes.

In addition to the 36 Hz signal, Figures 31 and 32 present the electric field derived from the Schumann resonance model (Simões et al., 2007a, Figure 10) **[Paper 4]** and taking into account the Yp tilt profile. Although matching is not perfect, two major features are clearly visible on the two panels, which support the idea that the 36 Hz signal has a natural origin. Additionally, the electric field enhancement at 30-40 km is not directly related to the parachute deployment. To definitely reject any possible artefact, we will test the boom at cryogenic conditions similar to those met on Titan. It is expected that the foreseen laboratory experiments and complementary analysis shall bring a final answer to this issue.

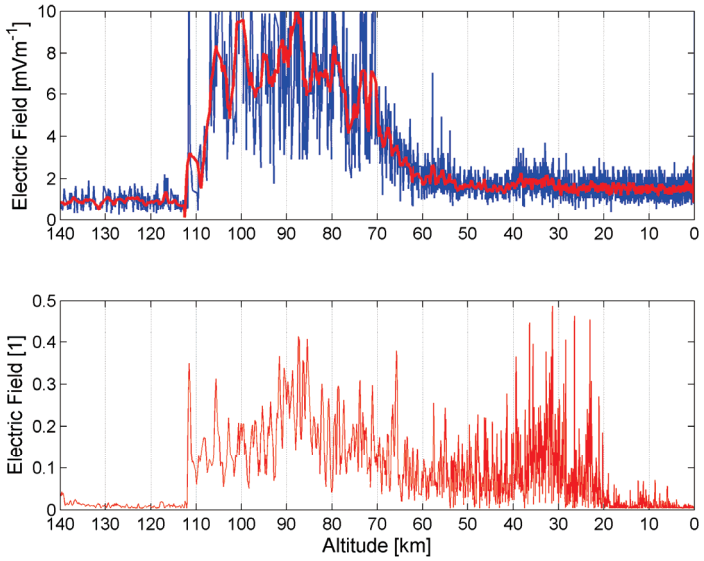

Figure 31: Comparison between the 36 Hz signal and the electric field theoretical profile derived from the Schumann model in the range 0-140 km. *Top*: Electric field profile measured at 36 Hz. *Bottom*: Electric field theoretical profile taking into account the antenna tilt.

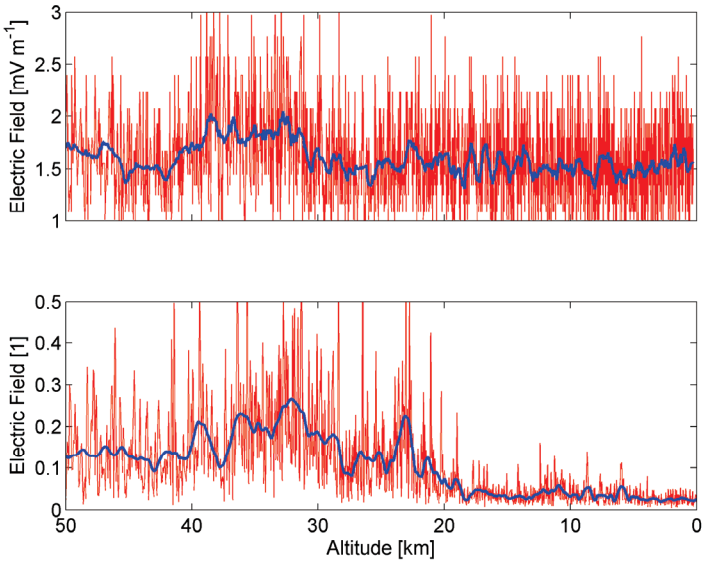

Figure 32: Same caption as Figure 31 but in the range 0-60 km.

Comparing the VLF and ACP data reveals a similitude that cannot be easily explained. Figures 33 and 34 show the lowest VLF spectral lines and the current supplied to the ACP pump. There is a clear match of the ACP current with some of the VLF discontinuities, but there is none with the ELF, and lowest VLF line fluctuations. It was known that switching-on and-off the ACP pump generated a transient at about 400 Hz, and it is observed that switching-on ACP at 1411 s decreases the VLF signal not only in the second spectral line but also at higher frequencies. No correlated event is identified in the ELF range (compare, for example, Figures 31 and 33). Below 60 km, there are 3 major events in the ACP pump status: switch-off at 3600 and 5310 s, and switch-on at 4643 s. The first switch-off is visible in the lowest VLF spectral line, but not the second event that is detected in a single line at around 400 Hz, in the MIP spectrum. When the pump is switched-on at 4643 s, a broad peak is observed in the VLF data. A similar peak at about 2950 s visible in the VLF spectrum has no corresponding event in the ACP pump. A further study of the effect of the ACP pump on the ELF and VLF spectra is required, but interference in the VLF spectra is obvious. However, the amplitude transition at about 5000 s is not an artefact linked with the ACP pump operation. Vibrations probably induce the noise observed in the VLF data between 900 and 1410 s, because they coincide with the parachute deployment and the first switch-on of the ACP pump. A possible explanation, that requires confirmation, is that the acceleration triggers the vibrations of the Probe platform or entire structure and that the ACP motor rotation damps these vibrations. An alternative explanation is that turning-on the pump switches-off other elements, e.g. valves. These explanations require clarification. Figures 35-38 show profiles of several sensors obtained during the descent, where results from PWA and other instruments are presented in blue and black, respectively.

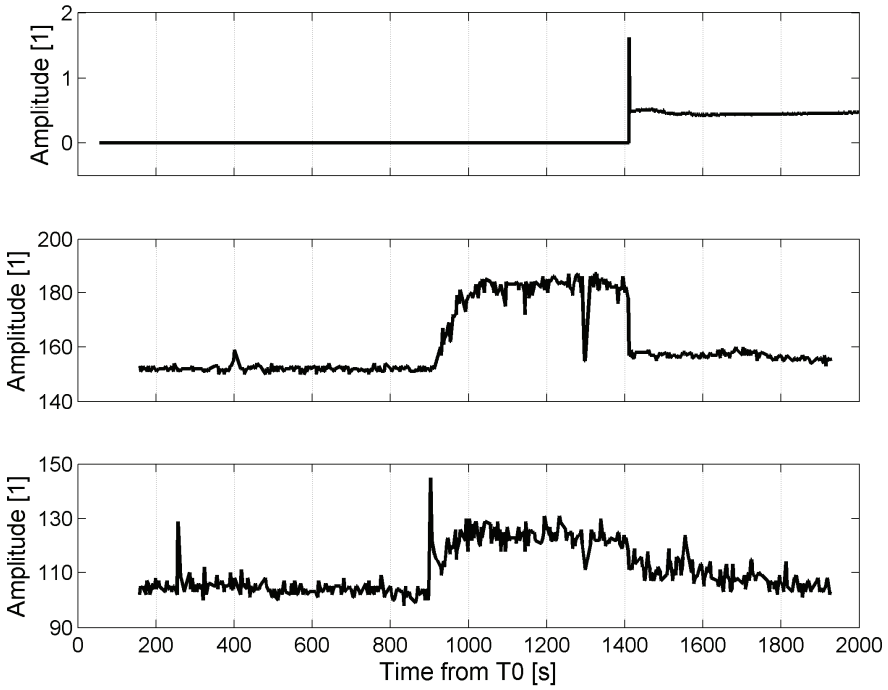

Figure 33: Profiles of the ACP pump current (*top*), and 540 Hz (*middle*) and 180 Hz (*bottom*) VLF spectral lines, between 60 and 140 km.

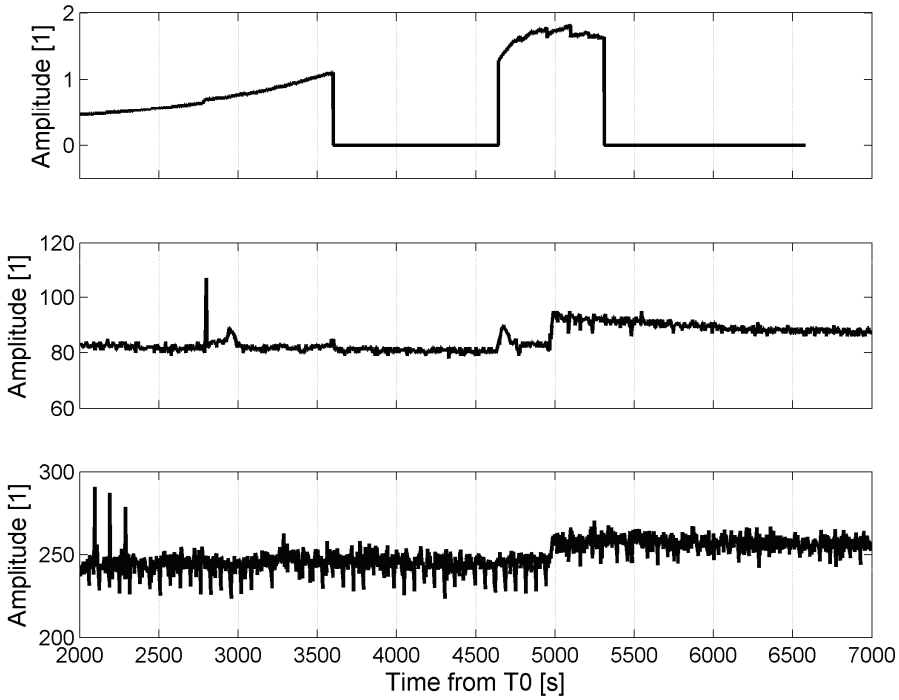

Figure 34: Profiles of the ACP pump current (*top*), 720 Hz spectral line (*middle*), and ELF integrated spectrum in the range 0-96 Hz (*bottom*), between 10 and 60 km.

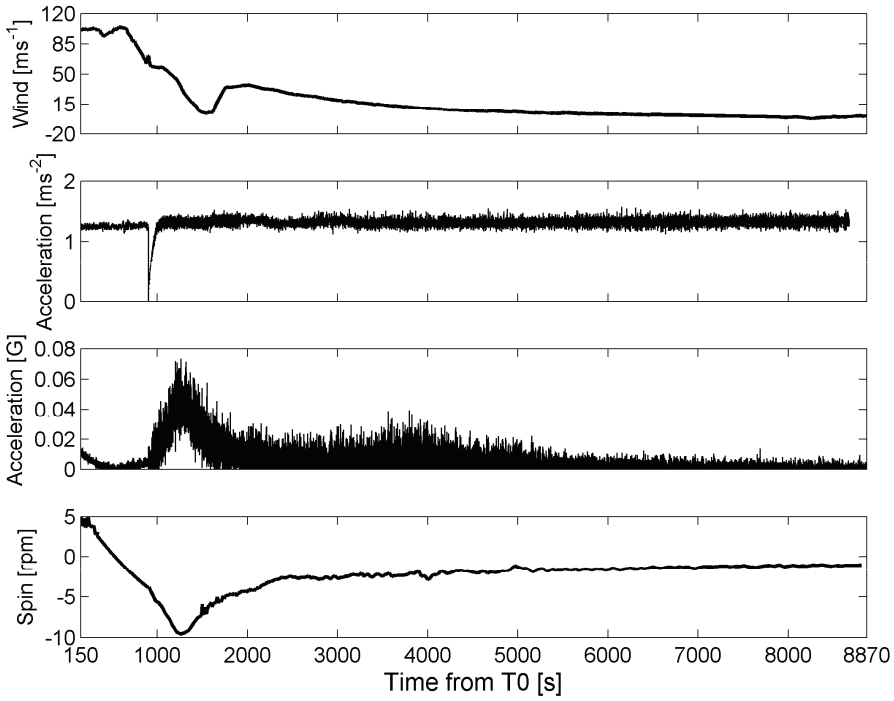

Figure 35: Data measurements collected during the descent of the Huygens Probe. From top to bottom: i) zonal wind velocity; ii) vertical acceleration; iii) RASU (Radial Accelerometer Sensor Unit) acceleration; iv) spin.

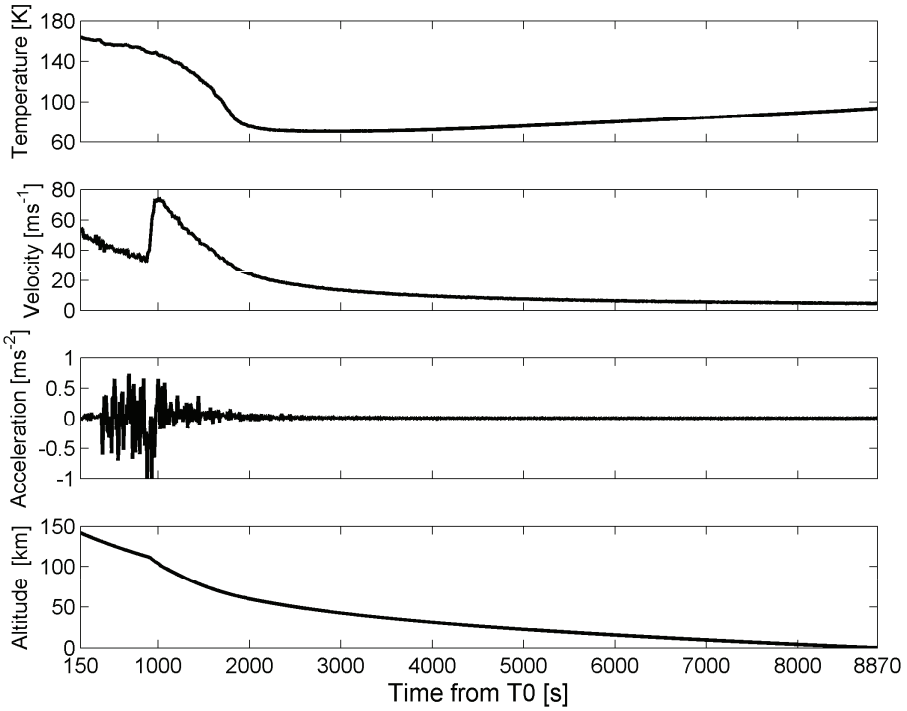

Figure 36: Data measurements collected during the descent of the Huygens Probe. From top to bottom: i) atmospheric temperature; ii) vertical velocity; iii) vertical acceleration derived from ii); iv) altitude.

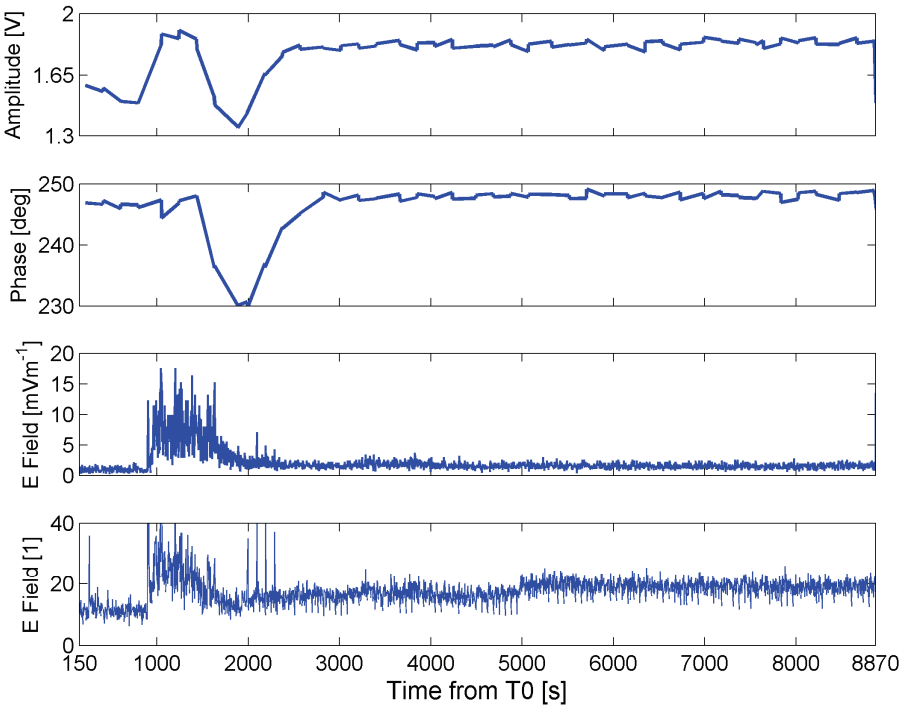

Figure 37: Data measurements collected during the descent of the Huygens Probe. From top to bottom: i) MIP amplitude; ii) MIP phase; iii) electric field at 36 Hz; iv) electric field integrated in the range 3-99 Hz.

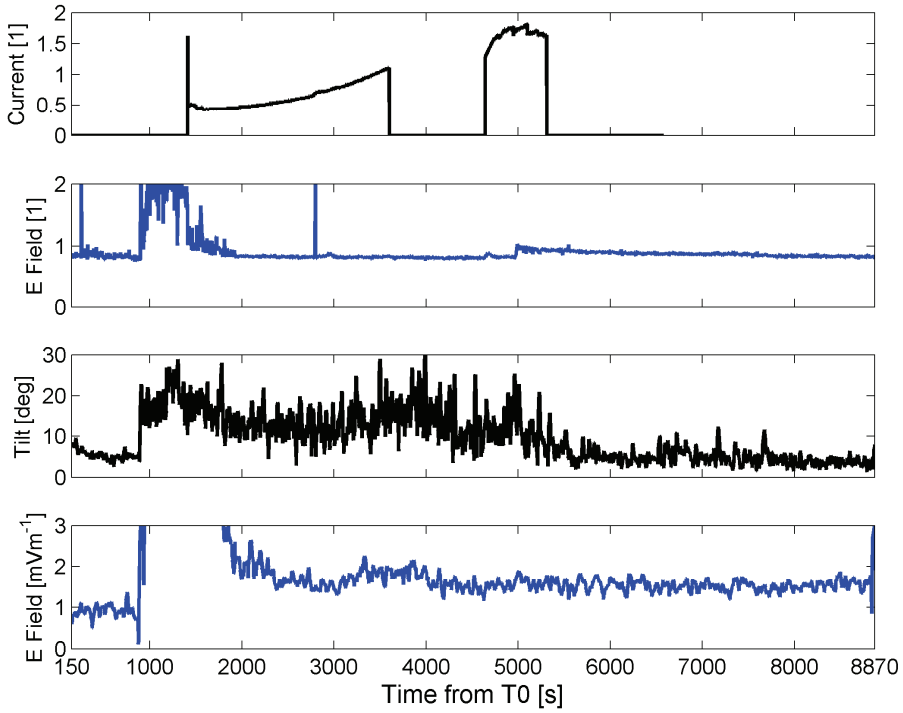

Figure 38: Data measurements collected during the descent of the Huygens Probe. From top to bottom: i) ACP current; ii) electric field at ~500 Hz; iii) antenna tilt; iv) electric field at 36 Hz.

Although the Huygens Probe data requires more investigation involving multidisciplinary teams of various instruments, the most important results obtained from the PWA data can nevertheless be summarized as follows:

- The electron conductivity profile shows a peak at about 60 km that is likely related to cosmic ray activity and aerosol distribution;
- The conductivity of the surface is extremely low and enables ELF wave propagation below the surface;
- The 36 Hz signal observed during the descent resembles a Schumann resonance though possible artefacts are not entirely ruled out;
- Cassini and Huygens did not find any strong evidence of lightning activity.

5. Prospective Space Instrumentation and Missions

This Chapter describes the development, modelling, assembling, and calibration of a MIP instrument that benefits from the experience gathered from previous space missions, namely Rosetta and Cassini-Huygens.

The major objective is to apply suitable technologies to the development of a mature permittivity probe that can be used to study the surface and subsurface of celestial bodies in the Solar System. Although intended for the evaluation of the water and ice contents in Martian soils and subsurface materials, the instrument can also be adapted to other environments, like the Moon and Titan.

5.1. Planetary Surfaces Dielectric Properties Measurement

In the previous chapters we have presented the ground truth measurements performed by a MIP that probed the dielectric properties of Titan and the electrification of its atmosphere. Characterizing the surface and ionospheric cavity of Mars is even more difficult due to a poor understanding of the atmosphere and cavity inner boundary. Hence, surface dielectric measurements would provide useful information for wave propagation modelling, water/ice content evaluation, and mitigation of electrostatic discharges and triboelectricity hazards.

Many missions have been flown to Mars, but only ionospheric electron density profiles are available (e.g. Fjeldbo et al., 1977; Pätzold et al., 2005). Theoretical models are therefore used to extend the conductivity profile down to the surface (Cummer and Farrell, 1999; Pechony and Price, 2004; Molina-Cuberos et al., 2006). Different profiles are found in the literature, but ELF wave propagation is sometimes questioned due to possible strong cavity losses. Despite numerous observations from Earth-based instruments, remote sensing from orbiting spacecraft, and *in situ* lander measurements, the electrical properties of the surface remain largely unknown. Theoretical models yield conflicting results for surface conductivity and permittivity. According to Christensen and Moore (1992), the relative permittivity of the regolith lies in the range 2.4-12.5, but no figure is given for that of the subsurface. The conductivity of the surface is unknown and estimations vary between 10^{-12} and 10^{-7} Sm^{-1}. Berthelier et al. (2000) tentatively restrict the range down to 10^{-12}-10^{-10} Sm^{-1}. Contrasting compositions are seen at low and high latitudes due to the presence of ice deposits in the polar regions. The subsurface dielectric properties of the regolith should vary with depth and composition, especially if water/ice/brines are embedded in the medium. There is no evidence of lightning activity on Mars but it is generally accepted that, due to triboelectricity effects,

massive dust storms might enhance atmospheric electrification, in particular in dust devils, as simulated on Earth (Krauss et al., 2003; Farrell and Desch, 2001). Therefore, the surface electric properties provide useful inputs for several fields, namely wave propagation, surface-atmosphere interaction, soil composition characterization, and electrostatic discharge hazards mitigation for unmanned and human exploration of the Red Planet.

The abundance and distribution of water in the atmosphere and under the surface of Mars have fundamental significance for the geological, hydrological, and climate history of the planet. Furthermore, water is a fundamental ingredient of life and represents an important potential resource for future manned missions. On the Polar Regions, water is in the solid phase and mixed in the regolith with dry ice (CO_2). Liquid water may be present in the subsurface in a variety of forms and current thermal models suggest that major reservoirs of liquid water that survive on the planet today are probably restricted to depths of 1 to 3 km at the equator and much deeper at higher polar latitudes (Clifford, 1993), with the depth of the 0°C isotherm being possibly reduced by both pressure and solute effects. Since the Martian landscape provides persuasive evidence of the possible existence of groundwater, the next generation of orbiters and landers will essentially track the water under the surface. For example, the Mars Advanced Radar for Subsurface and Ionosphere Sounding (MARSIS) onboard Mars Express analyses subsurface echoes in order to identify water deposits; future missions will pursue the same objective.

Water possesses several peculiar properties, but the most relevant parameters are the dielectric properties that can be measured using the mutual impedance technique. Water possesses a particular electrical signature that allows the identification of its presence among other materials, even at very low concentrations. Not only the permittivity, but also the conductivity of permafrost and water-bearing rocks depends upon the presence of water. The knowledge of these two electrical parameters motivates the development of new water detection techniques.

5.2. Dielectric Properties of Water, Ice, and Soils

5.2.1. Polarization Mechanisms and Effects

5.2.1.1. Polarization Theory

The relative permittivity characterizes the ability of a material to store charge. Since the polarization mechanisms that occur in most materials vary with frequency, temperature, and composition, so does the dielectric constant. This behaviour is valid not only for pure media, like water, but also for mixtures such as soils. Many textbooks deal with this phenomenon and we shall not go into all the details. Nevertheless, it is useful to present the most significant polarization mechanisms to define a suitable scientific rationale for the MIP that is under discussion.

Several polarization mechanisms can take place in dielectric bulk materials, namely electronic, atomic, orientation, and interfacial polarizations. Electronic and atomic polarizations occur at atomic level; they are referred to as instantaneous polarizations and are effective in the visible and adjacent bands. Electronic polarization is due to a shift of the centre of mass of the electronic cloud that surrounds the nucleus. Atomic polarization results from charge displacements in bound atoms with different electro negativities. Atomic polarization differs from electronic polarization because it is due to the relative motion of the atoms instead of a shift of the charge cloud surrounding the atoms. Orientation polarization mechanisms are generated by molecules with permanent dipole moments, and occur in the

infrared spectrum, and at lower frequencies. The interfacial polarization mechanisms are important at very low frequencies, and appear when multiple phase materials or interfaces are involved, such as in soils. Figure 39 illustrates the various polarization mechanisms.

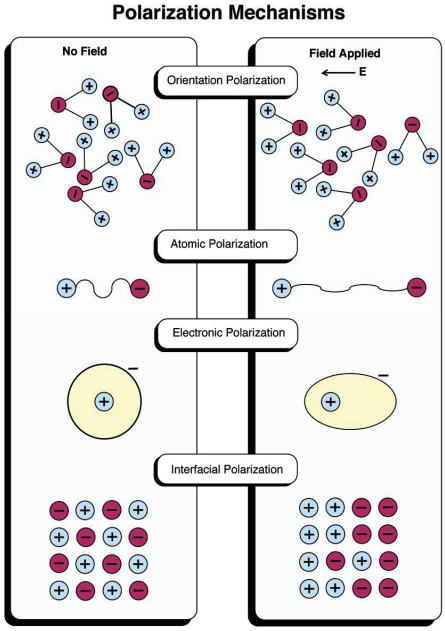

Figure 39: Schematic representation of the different polarization mechanisms (Kingery *et al.*, 1976).

Electronic polarization is found in all materials. When an external electric field is applied, the electronic cloud is displaced to balance the electric field. The same approach is valid to explain atomic polarization; in this case the atoms are displaced from each other. Atomic and electronic polarization response times are very small and referred to as instantaneous dipoles; the result is a temporary dipole that vanishes when the external electric field is removed. However, molecules like water possess permanent dipoles that give them specific properties concerning orientation polarization. In the case of water, the permanent dipole facilitates an interaction between molecules that involves the hydrogen bonds, which enhances the ability of water molecules to respond to external electric fields, i.e. increase the polarization capabilities. This effect plays a key role in the identification of water and ice signatures because water is a polar molecule. Finally, interfacial polarization that occurs at low frequencies also contributes to increasing the dielectric constant. Electrically heterogeneous materials may experience interfacial polarization; the motion of charge carriers in these materials can for each phase and, consequently, charging mechanisms develop. Polarization mechanisms exist in homogeneous pure materials; with the exception is interfacial polarization that requires either multiple phases or mixtures of pure materials to be effective.

5.2.1.2. Frequency Effects

The polarization presents a behaviour that is a function of frequency. Therefore, the relative permittivity is driven by specific mechanisms when the frequency changes. Figure 40 shows the contribution of each polarization mechanism as a function of frequency. The

relaxation mechanism in simple single phase media is described for the higher frequencies by the Debye equation (Debye, 1929)

$$\varepsilon(\omega) = \varepsilon_\infty + \frac{\varepsilon_s - \varepsilon_\infty}{1 + i\omega\tau}, \tag{41}$$

where ε_s and ε_∞ are the static and 'infinite' frequency limits of the dielectric constant and τ is the relaxation time of the process. The indices (s, ∞) in Equation (41) represent the high and low frequency limits. In fact, several relaxations can be present and Equation (41) should be written as a sum of several contributions in different frequency ranges. Often, heterogeneous materials that include several phases exhibit multiple relaxation times. Materials that have an interfacial polarization mechanism may also undergo an anomalous dispersion with some similarities with the dipolar relaxation. Thus, models of interfacial polarization often rely on the Debye equations, though with time constants larger than a few milliseconds.

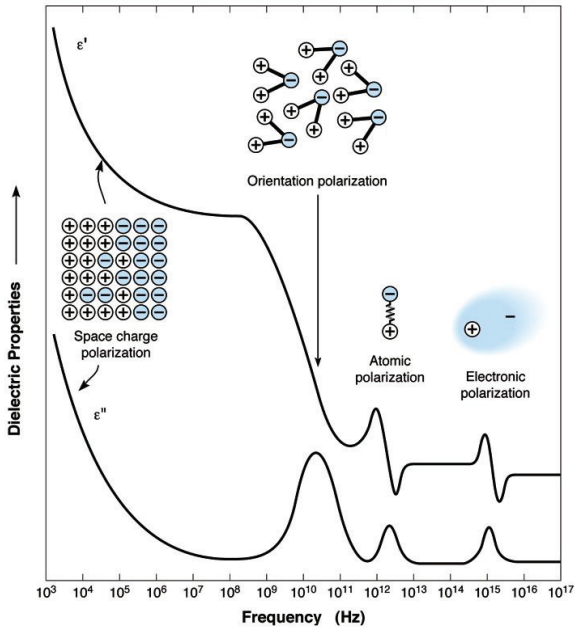

Figure 40: Contribution of the different polarization mechanisms to the frequency dependence of the relative permittivity (Kingery *et al.*, 1976).

As discussed above, the frequency response is caused by several mechanisms. Electronic polarization takes place in the higher frequency range, around the visible band, and is irrelevant for mutual impedance applications. The same argument can generally be invoked for atomic polarization. Instruments that make use of the mutual impedance technique work below 100 MHz and, therefore, only orientation and space charge polarizations play a role. The contribution of each polarization mechanism is strictly related to medium phase, temperature, and homogeneity. Orientation polarization is more important in liquids and space charge polarization dominates in solids and heterogeneous media. Water is a particular case because orientation polarization is somewhat relevant both in solid and liquid phases. It is interesting to note that medium losses reach a maximum when the stimulus matches internal resonances because energy transfer is easier and thermal losses maximized.

5.2.1.3. Temperature Effects

The dielectric properties of a material are temperature dependent because molecular vibrations and polarization are related. Atomic polarization, for example, varies with temperature because bonding forces between ions or atoms are thermally sensitive. The ability of a dipole to rotate in an applied field is also temperature dependent and, therefore, affects orientation polarization. Finally, the charge mobility varies with temperature and the interfacial mechanism is also temperature dependent. The standard models describing these variations were developed by Debye (1929) and Kirkwood (Kirkwood, 1939) for the static dielectric constant of materials, when molecular orientation polarization is important.

Kirkwood developed a general equation that considers the interaction between dipoles and is approximately valid in condensed phases:

$$\frac{(\varepsilon-1)(2\varepsilon+1)}{3\varepsilon}=\frac{\rho}{\varepsilon_o}\left(\alpha_e+g\frac{\mu_o^2}{3kT}\right), \tag{42}$$

where ρ is the number of molecules per unit volume, T the temperature, α_e the deformation polarizability, μ_o the dipole moment of a molecule, k the Boltzmann constant, and g the Kirkwood correlation function relative to dipole interaction. More general relations have been formulated, namely the Onsager-Kirkwood and Kirkwood–Fröhlich equations, which are variations of Equation (42). Our objective is simply to show that the dielectric properties are functions of temperature, not to present a detailed theory, because the associated corrections lie well below the measurement accuracy.

5.2.1.4. Composition Effects

Polarization mechanisms in heterogeneous materials, mostly solid, are more complex than in single phase media because several relaxation mechanisms can be involved simultaneously. A typical material is water ice with lattice defects due to either the presence of two protons (D-defect) or absence of protons (L-defect) in ice bonds, a phenomenon also known as Bjerrum defects (Bjerrum, 1951). The phenomenon is more complex when the water ice lattice contains impurities. The presence of several solid phases in the medium induces more intricate polarization mechanisms.

Simple mixtures (two phases) of ideal dielectrics can be can be represented by layers of different materials arranged in a parallel direction or perpendicularly to the applied field. Each layer has the ability to store charges and therefore acts as a capacitive element when an electric field is applied to the plate capacitor. Although very simple, this model provides an upper and a lower bound for the equivalent dielectric constant. The upper limit may be written

$$\varepsilon=\boldsymbol{v}_1\varepsilon_1+\boldsymbol{v}_2\varepsilon_2, \tag{43}$$

and the lower limit

$$\frac{1}{\varepsilon}=\frac{\boldsymbol{v}_1}{\varepsilon_1}+\frac{\boldsymbol{v}_2}{\varepsilon_2}, \tag{44}$$

with ε_i and ν_i representing the permittivity and volume fraction of both phases, respectively. For more complex mixtures, the permittivity value is given by

$$\varepsilon = \left(\sum_i \nu_i \sqrt[3]{\varepsilon_i} \right)^3 \tag{45}$$

for an arbitrary number of phases with homogeneous distribution (Landau and Lifschitz, 1984). As expected, heterogeneous media require more sophisticated analysis. For example, the Looyenga equation (Looyenga, 1965) is applied to spherical particles dispersed in a dielectric medium and is given by

$$v_2 = \frac{\varepsilon^{1/3} - \varepsilon_1^{1/3}}{\varepsilon_2^{1/3} - \varepsilon_1^{1/3}}, \tag{46}$$

and the equation suggested by Bruggeman (1935) for oblate spheroids suspended in a dielectric medium can be written

$$\varepsilon = \varepsilon_2 \frac{3\varepsilon_1 + 2v_2(\varepsilon_2 - \varepsilon_1)}{3\varepsilon_2 - v_2(\varepsilon_2 - \varepsilon_1)}. \tag{47}$$

A detailed discussion about the derivation of the previous equations is presented by Van Beek (1969), where more elaborated models can also be found.

The polarization effects in heterogeneous media are functions of, not only composition and temperature, but also frequency. In addition to composition and geometrical arrangement, the dielectric properties of mixed materials often exhibit strong frequency dependence that cannot be attributed to any intrinsic properties of either of the pure phases. These effects are usually attributed to polarization mechanisms resulting from component mixtures. One example of such dependence is the interfacial polarization mechanism, responsible for a strong increase of the dielectric constant in the ELF-VLF range. This mechanism is caused by charging processes on interfaces between two phases of different conductivities and permittivities, a phenomenon usually known as the Maxwell-Wagner effect (Polk and Postow, 1986). A second mechanism is related to the presence of an electrical double layer, which can easily polarize in an applied field, and is known as the counter-ion effect (Polk and Postow, 1986). A schematic representation of both effects for spherical particles suspended in a dielectric medium is shown in Figure 41.

The Maxwell-Wagner effect is related to interface charging that occurs in electrically heterogeneous materials. These effects lead to a significant increase of the dielectric properties of soils; high dielectric constants are often reported at frequencies below 1 MHz (e.g., Perrier and Bergeret, 1995; Rusiniak, 2000).

For several mixtures, electrical double layers exist on the surface of one component. A double-layer results from the attraction of oppositely charged ions by a charged surface. The surface of particles in solution can contain a net charge, which attracts oppositely charged ions and polar molecules (Reed, 1988). The result is a difference in the electrical potential between surface and bulk. The ions may be present in solid or liquid phases and the layers consist essentially of free charges that are easily displaced by an applied field. These effects are strongest at low frequencies, where the double layer has time to fully polarize because their relaxation time is high. Dielectric dispersion at low frequencies is often observed in colloidal particles suspended in electrolytes and water ice mixtures. This effect clearly differs

from Maxwell-Wagner mechanisms in such a way they are related to the nature of the interface instead of bulk properties.

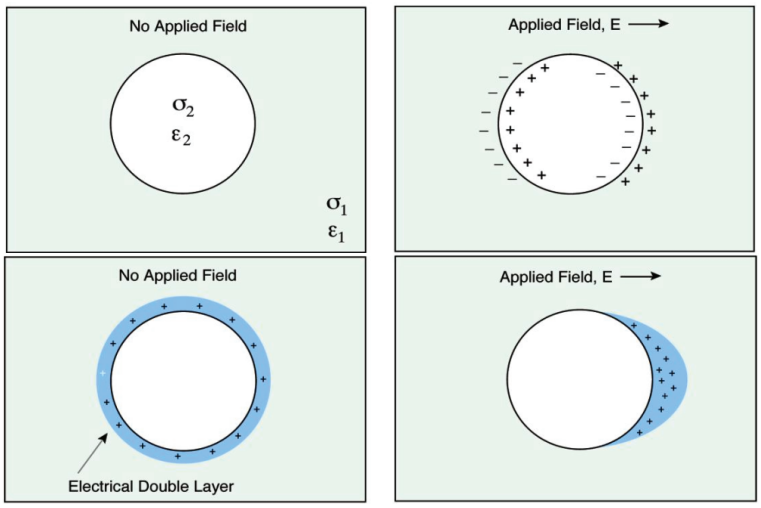

Figure 41: Schematic representations of the Maxwell-Wagner (top) and Counter-ion (bottom) polarization effects with (right) and without (left) applied electric field (Kingery *et al.*, 1976).

The electrical double layer is often modelled as charged particles with an immobile absorbed layer of counter-ions and a concentration gradient of ions in a diffuse layer (Figure 42). A model of the potential gradient may be derived using Fick law.

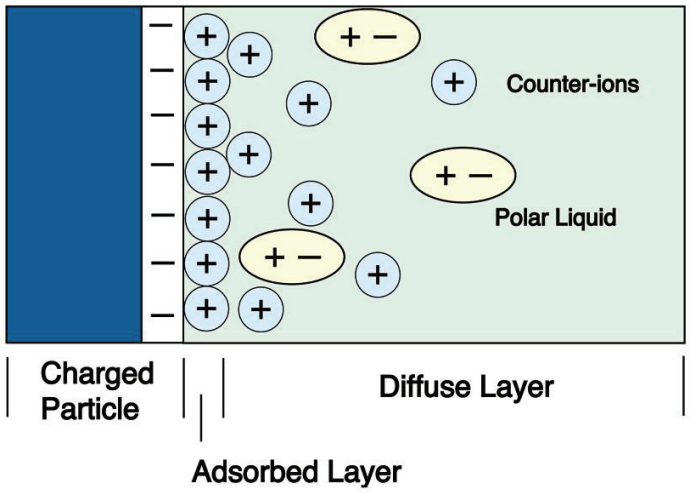

Figure 42: The diffuse electrical double-layer model for particle charging (Reed, 1988).

Several models have been developed in order to determine the equivalent permittivity for soil mixtures with n-phase. At frequencies higher than 10 MHz, the dielectric properties of water-bearing rocks are explained by the Maxwell-Wagner-Bruggeman-Hanai (MWBH) theory of composite dielectrics (e.g., Bruggeman, 1935; Hanai, 1968). However, this model is not valid at lower frequencies.

5.2.2. Water Dielectric Properties

Despite molecular simplicity, water molecule is unique and complex, which makes it one of the most remarkable substances in solid, liquid or gas phases. Though a simple molecule, just consisting of two hydrogen atoms attached to one oxygen atom, water complexity is due to its intermolecular interactions, mainly the hydrogen bond. Owing to this interaction, water has an unusually high melting point; water ice exists in a wide variety of stable and metastable crystal and amorphous configurations, and the critical point is unusually high, compared to that of other liquids.

Like other water properties, the electrical permittivity is different from that of most other substances. This particularity feature facilitates the identification of water, for example in the subsurface of Mars.

Polar molecules, like water, whose positive and negative charge centres are separated, possess a dipole moment, and tend to align themselves with an applied electric field. Although water is a polar molecule, its hydrogen-bonded network tends to oppose this alignment. The degree to which a substance possesses this property is its dielectric constant and, because water is exceptionally cohesive, it has a high dielectric constant. This allows it to act as a solvent for ionic compounds, where the attractive electric field between the oppositely charged ions is reduced by about 80-fold, allowing thermal motion to separate the ions into solution. On heating, the dielectric constant drops, and liquid water becomes far less polar. The dielectric constant similarly reduces if the hydrogen bonding is broken by other means, such as strong electric fields. Few other liquids have such high permittivities and a good example is HCN with a dielectric constant the order of 150. The conductivity of pure water is listed in Table 10 as a function of temperature and pressure (Marshall, 1987).

Temperature [^{o}C]	Saturated vapour	50MPa	100Mpa	200MPa	400MPa	600MPa
0	0.0115	0.0150	0.0189	0.0275	0.0458	0.0667
25	0.0550	0.0686	0.0836	0.117	0.194	0.291
100	0.765	0.942	1.13	1.53	2.45	3.51
200	2.99	4.08	5.22	7.65	13.1	19.5
300	2.41	4.87	7.80	14.1	28.6	46.5
400	-	1.17	4.91	14.3	39.2	71.3
600	-	-	0.134	4.65	33.8	85.7

Table 10: Conductivity [$\mu S\ cm^{-1}$] of pure water as a function of temperature and pressure.

The static, i.e. $\omega \rightarrow 0$, dielectric constant of pure water is listed in Table 11 as a function of temperature (Archer and Wang, 1990).

Temperature [^{o}C]	Relative Dielectric Constant
0	87.90
10	83.96
20	80.20
30	76.60
40	73.17
50	69.88
60	66.73
70	63.73
80	60.86
90	58.12
100	55.51

Table 11: Static dielectric constant of pure water as a function of temperature.

The complex dielectric constant of pure water, real and imaginary components, is listed in Table 12 as a function of temperature and frequency (Archer and Wang, 1983).

	0 °C		25 °C		50 °C	
Frequency	ε_r	ε_i	ε_r	ε_i	ε_r	ε_i
0	87.90	0.00	78.36	0.00	69.88	0.00
1 kHz	87.90	0.00	78.36	0.00	69.88	0.00
1 MHz	87.90	0.01	78.36	0.00	69.88	0.00
10 MHz	87.90	0.09	78.36	0.04	69.88	0.02
100 MHz	87.89	0.91	78.36	0.38	69.88	0.20
200 MHz	87.86	1.82	78.35	0.76	69.88	0.39
500 MHz	87.65	4.55	78.31	1.90	69.87	0.98
1 GHz	86.90	9.01	78.16	3.79	69.82	1.96
2 GHz	84.04	17.39	77.58	7.52	69.65	3.92
3 GHz	79.69	24.64	76.62	11.13	69.36	5.85
4 GHz	74.36	30.49	75.33	14.58	68.95	7.75
5 GHz	68.54	34.88	73.73	17.81	68.45	9.62
10 GHz	42.52	40.88	62.81	29.93	64.49	18.05
20 GHz	19.56	30.78	40.37	36.55	52.57	28.99
30 GHz	12.50	22.64	26.53	33.25	40.57	32.74
40 GHz	09.67	17.62	18.95	28.58	31.17	32.43
50 GHz	08.26	14.34	14.64	24.53	24.42	30.47

Table 12: Real and imaginary components of the dielectric constant of pure water as functions of frequency and temperature.

5.2.3. Ice Dielectric Properties

The dielectric properties of water ice are usually discussed in the light of the theory developed by Debye (1929). In a perfect single crystal of pure ice it is believed that the number of free electrons is negligible, so that, if a DC field is applied, the only mechanism available for conduction is the proton-jump process (Pounder, 1965), which means that only ionic conduction is acting. If the sample contains impurities the conductivity is increased. Polarization effects at the surface and internal anisotropies such as cracks, gas bubbles and inter-crystalline boundaries mask the true conductivity of ice. Ice conductivity is extremely low $\sigma \sim 10^{-7}$-10^{-6} Sm^{-1}, approximately 10 times lower than that of pure water at room temperature.

When an AC field is applied, additional phenomena appear. Unlike liquid water, ice has no permanent electric dipole moment but is readily polarized due to ionic conduction and electronic polarization. When the induced dipole moment is reversed as the field reverses, some of the electrical energy is dissipated as heat in the lattice. This dissipative effect, called dielectric absorption, gives rise to an effective electrical conductivity, which is much larger than in the static field.

Since charge distortion distribution requires time, the permittivity depends on the frequency of the alternating field, which leads to the introduction of a relaxation time. In an ideal system, the polarization occurs instantaneously in response to the applied electric field. However, most materials require a finite time for polarization to occur. This time dependence involves inertia and charge, and is characterized by a relaxation time for charge transport or dipole rearrangement.

In the case of water ice, we define

$$\alpha = \frac{\tau}{2\pi} \frac{\varepsilon_s + 2}{\varepsilon_\infty + 2}, \tag{48}$$

and use the Debye theory, to derive the Drude-Debye relations for real, ε_r, and imaginary, ε_i, permittivity:

$$\varepsilon_r = \frac{\varepsilon_s + \varepsilon_\infty \alpha^2 \omega^2}{1 + \alpha^2 \omega^2}, \tag{49}$$

and

$$\varepsilon_i = \frac{(\varepsilon_s - \varepsilon_\infty)\alpha^2 \omega^2}{1 + \alpha^2 \omega^2}. \tag{50}$$

As already defined, the ε_s and ε_∞ represent the static and high frequency limits of the permittivity. The parameter α does not depend on frequency but on temperature, and is defined by the empirical relation:

$$\alpha = \alpha_o e^{-\beta T}. \tag{51}$$

The best fit is obtained with ε_s=75, ε_∞=3, α_o=1.9×10^{-5} s, and β=0.1°C^{-1} in the ranges 0-10 GHz and 0-70^{o}C, in the absence of impurities (Pounder, 1965). Improved models exist, but Equations (49-51) provide a fair estimation of the dielectric constant and losses of pure water ice as functions of temperature and frequency. At very low frequencies, impurities strongly affect the validity of this fitting because ion mobility increases. Table 13 gives the static dielectric constant of water ice as a function of temperature (Auty and Cole, 1952) and provides a first insight on the variation of the permittivity with temperature. The static dielectric constant of different crystalline ices is listed in Table 14 at a temperature of -30^{o}C (Lide et al., 2006).

Temperature [^{o}C]	Dielectric Constant
0	91.6
-10	94.4
-20	97.5
-30	99.7
-40	101.9
-50	106.9
-60	119.5

Table 13: Static dielectric constant of pure ice I as function of temperature.

Ice structure	Dielectric Constant
Ice I (0 kbar)	99
Ice III (3 kbar)	117
Ice V (5 kbar)	114
Ice VI (8 kbar)	193

Table 14: Static dielectric constant of pure ice with different crystal lattices.

5.2.4. Water and Ice Dielectric Signature in Soils

The dielectric constants of water ($\varepsilon \approx 80$ at 300 K,), and water ice ($\varepsilon \approx 120$ at 210 K,) are relatively high at extremely low frequencies, but most substances have relative permittivities lower than 10. This large discrepancy is crucial for the recognition of water signature. Several studies conclude that the dielectric constants of the major components of the desiccated

Martian regolith are less than 12, and a simple estimate gives a mean value smaller than 5 for the soil composite, which is one order of magnitude smaller than the dielectric constant of water ice. Then, if a significant permittivity is measured on Mars, the straightforward conclusion is that, in the absence of any other substance with such a high dielectric constant, this signature necessarily reveals the presence water.

There is a significant quantity of CO_2 ice on the surface of Mars, at high latitude, but the permittivity of CO_2 solid phases, including snow, and powder, is very low. At 1 kHz and 200 K, CO_2 has a relative dielectric constant lower than 2 (Pettinelli *et al.*, 2001).
The conductivities of rocks and soils are listed in Table 15, at room temperature and in normal weather conditions, i.e. rocks with high water contents. These values are rough estimations because conductivity is function of not only water content but also macroscopic and mineralogical compositions.

Material	**Conductivity [Sm^{-1}]**
Granite	10^{-5}-10^{-7}
Lava	10^{-4}-10^{-5}
Quartz vein	$<10^{-4}$
Marble	10^{-8}-10^{-7}
Limestone	10^{-2}-10^{-3}
Sandstone	10^{-2}-10^{-3}
Clay	10^{-2}
Sand	10^{-3}-10^{-4}

Table 15: Conductivity of Earth rocks and soils.

5.3. Subsurface Permittivity Probe

5.3.1. General Description

The measurement of dielectric properties using the mutual impedance technique is particularly useful for assessing the water/ice content in a medium. In fact, water possesses a particular unique electrical signature that reveals its presence in other materials, even at low concentrations. The distinctive variations of the dielectric properties of liquid water with frequency, below ~1 MHz, and with temperature, are controlled by the moisture content in the soil. Moreover, these particular dielectric features are enhanced in water ice, increasing the ability to detect ice among other materials. The water/ice threshold detection is a function of not only soil characteristics but also frequency and temperature. Sweeping the frequency in a suitable range and measuring the thermal inertia, such as day/night temperature variations, provide a method for evaluating the dielectric properties of the Martian regolith.

The scientific and technical knowledge gathered with the instruments onboard the Cassini-Huygens and Rosetta missions have significantly contributed to the definition of the scientific and technical requirements of a new instrument, the Subsurface Permittivity Probe (SP2), presented in this Section. The SP2 instrument (Figure 43) was proposed for the ExoMars mission, the next ESA mission to the Red Planet, typifies a new configuration and improved measurement capabilities, and complies with the specific scientific rationale and technical constraints of the mission. The instrument is included in the *Mole* (self-locomotion cylindrical device) that is part of the Geophysical and Environmental Package (GEP), the static station of the ExoMars project, which also includes a rover. In order to adjust to the expected characteristics of the Martian soil, the working frequency should lie in the range 10 Hz -10 kHz. The measurement accuracies which comply with the scientific goals have been estimated using numerical simulations, and can be achieved. The space heritage of this

technique (Grard et al. 1995; Fulchignoni et al. 2002) allows us to set the accuracies to about 0.1 for the relative permittivity, and 10^{-12} Sm^{-1} for the conductivity, which corresponds to a water content threshold not higher than a few percents (Simões, 2004) **[Paper 16]**. Table 16 presents a list of the most significant instrument characteristics and measurement accuracies.

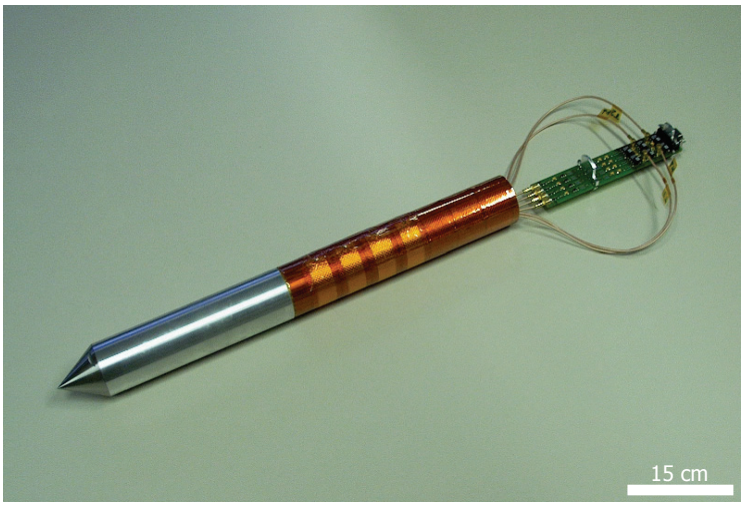

Figure 43: The SP2 prototype attached to a mole-type carrier. The golden rings are the transmitting and receiving electrodes.

Measured parameters - range, - accuracy, resolution	PERMITTIVITY 1-120 in 0-5 m depth better than 2.5%, ~0.5% CONDUCTIVITY 10^{-12}-10^{-6} Sm^{-1}, in 0-5m depth better than 2.5%, ~0.5%
MASS - analogue electronics - digital electronics - electrodes and cabling	 20g 35g 50g
FREQUENCY RANGE	10 Hz – 10 kHz
POWER	<0.25 W
TELEMETRY	5 bytes per measurement
Measurement technique Space heritage	PWA/Huygens PP/ Philae-Rosetta

Table 16: The main characteristics of the SP2 instrument.

5.3.2. Electrodes

The *Mole* is a cylindrical tube with a hammering device that provides self locomotion and enables the system to penetrate the soil. The transmitting and receiving electrodes of SP2 are attached outside the payload compartment that contains the electronics. The electrodes must be thin, lightweight, and protected from soil abrasion.

Several configurations are possible for the array, with different sensor separations, to explore the subsurface at various spatial resolutions. The system consists of at least 4 rings mounted on a cylindrical rod. An insulating support is preferable though a metallic one can be accommodated with appropriate electric guarding and insulation. An external insulating layer

is also added to avoid a direct contact between the electrodes and the medium. The outer layer material must be an insulator resistant to abrasion; several polymeric materials are under test.

Each electrode is a sandwich made of a thin kapton layer between two copper foils that forms a capacitance and filters out any DC component from the signals. Figures 44 and 45 show the cross-sections of the prototype electrodes (Simões, 2004, chapter 6) **[Paper 16]**. Each ring is further split in two angular sectors of ~270° and ~90°, in order to test the response when the instrument is rotated around its axis. The areas of each 90° and 270° sectors are 3 and 12 cm^2, respectively. The prototype therefore includes 4 transmitting and 4 receiving sensors that can be combined in many ways to form various quadrupolar configurations, two transmitting electrodes (Tx1 and Tx2) and two receiving electrodes (Rx1 and Rx2), in order to test their ability to detect interfaces and heterogeneities in the medium.

A simpler configuration is foreseen for the flight model. The experience gained with the HASI-PWA package onboard Huygens Probe, confirms that stray capacitances should be minimized and that electrode assembling is an important issue.

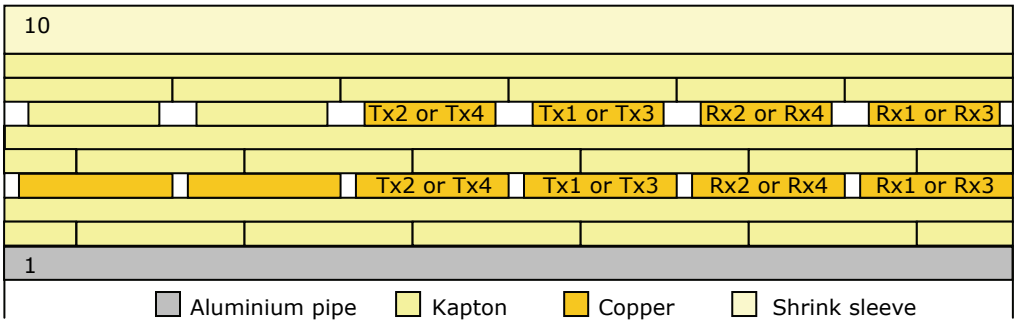

Figure 44: Cross section of the multilayer electrodes. Layer 10 is a protective material that resists abrasion.

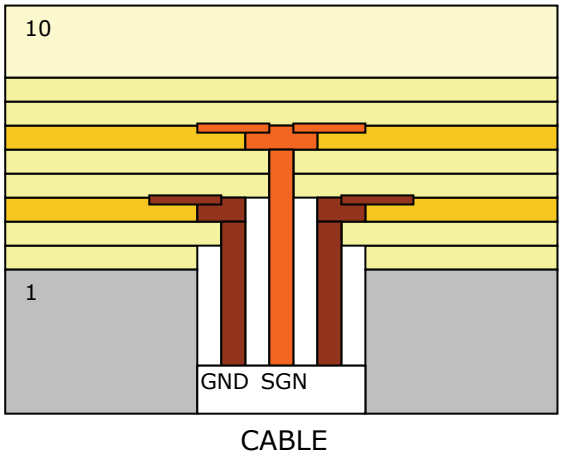

Figure 45: Wiring cross section of the multilayer electrodes.

Figure 46 illustrates the layout of the SP2 electrodes though other arrangements are possible.

Figure 46: The SP2 electrode prototype.

5.3.3. Electronics

The electronics block-diagram (Figure 47) shows a configuration with 4 transmitters and 3 receivers, though a simplest version includes 2 transmitters and 2 receivers only. Signal generation and acquisition are controlled via the FPGA (Field-Programmable Gate Array) accommodated in the *Mole*. Both transmitting currents and receiving voltages are sampled. The pairs of transmitting and receiving electrodes are selected with two multiplexers. A sinusoidal waveform is generated and sent to an amplifier with a differential output. Electric guards minimize losses in the cables. The receiving electrodes are connected to the inner wire of triaxial cables with grounded shields. The inner shields are bootstrapped to reduce the cable stray capacitance to ground, which is a much larger than the electrode capacitance. The properties of the Martian regolith are unknown, and the system includes an amplifier with two gains (high and low) to increase the dynamic range of the permittivity and conductivity measurements.

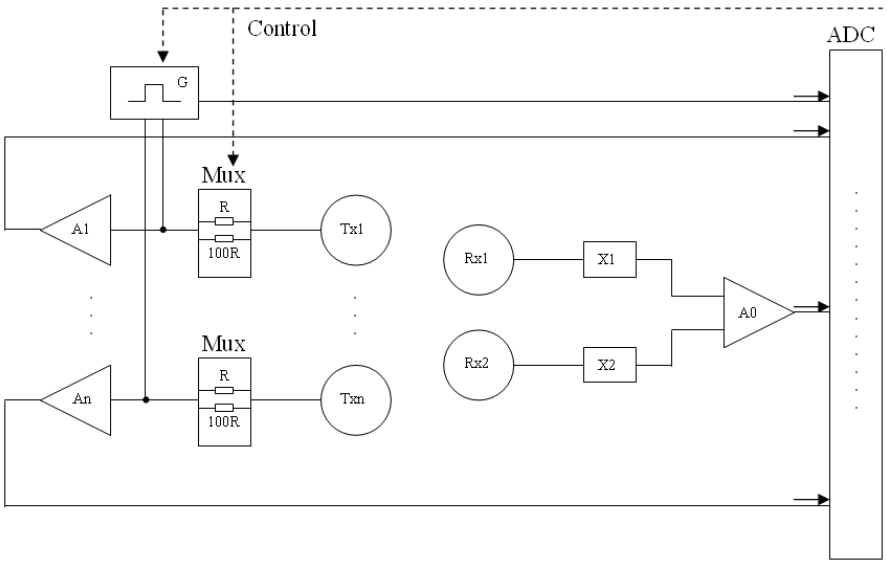

Figure 47: The SP2 electronics block-diagram. The simpler configuration includes only two transmitters and two receivers.

The prototype does not include digital electronics because it uses an ADC (Analogue to Digital Converter) card directly connected to a computer, which simplifies control, and data acquisition and processing. Little space is available within the mole, which imposes severe constraints on the electronic circuitry. Furthermore, the effects of the shocks and vibrations induced by the self-locomotion system on cables and connectors require a systematic test programme.

5.3.4. Signal Processing

Signal processing plays a key role in the quality of the results. An AC signal is injected in the medium and both its amplitude and phase are measured. The received signal is similarly handled by the data acquisition converter, processed, and stored for subsequent telemetry to Earth. The signals can be handled in two ways: either the waveforms are sampled and sent as time sequences, or processed in the frequency domain before telemetry. The both solutions present advantages and inconveniences; the former approach requires transmission of large amounts of data but the later involves additional onboard data processing and extra resources. Handling time domain sequences on the ground facilitates data analysis but is not always possible, due to data rate and communications constraints. Therefore, the signals are usually transformed in the frequency domain and processed, to reduce the data volume. In general, onboard data processing with Fast Fourier Transform (FFT) and averaging provides the amplitudes and phases of the signals. Sometimes, the complete waveform spectra are transmitted. These algorithms have been extensively used in space, namely in the PWA analyzer, because of their robustness and reliability. In the case of SP2, several signal frequencies are used with a maximum sampling rate of 20 kS/s per channel. Other signal analysis techniques are envisaged for future applications though they require extra processing time. In fact, onboard dedicated time-domain techniques can be more accurate than FFT because they do not entail spectral leakage. These techniques take advantage of the fact that the injected signal is known.

For specific applications of the SP2 instrument, several methods such as the sine-fitting algorithm produce more accurate results than the standard FFT method though they require more computational time. This algorithm is a time domain analysis of the acquired sample sequence that yields the parameters of sinusoidal signals (frequency, amplitude, phase, and DC bias). These algorithms are extremely powerful because they measure the medium impedance at several frequencies simultaneously using a multi-harmonic sine-fitting. The selected frequencies can be injected simultaneously in the medium and no sweep is required; this technique is known as the multi-harmonic stimulation.

The SP2 signal processing system must comply with several constraints: (i) mission telemetry limitation; (ii) maximum data transfer rate between the mother station and the *Mole*; (iii) overall *Mole* processing capabilities; (iv) number of SP2 receiving electrodes and maximum signal sampling rate. Whatever the final solution may be, onboard signal processing seems unavoidable.

5.3.5. Operation

The main objective of the *Mole* is to perform thermal and electrical measurements of the Martian regolith at the landing site. The *Mole* is attached to a 5 m long tether that powers the sensors and the data bus. The knowledge of temperature provides extra information about the presence of water ice in the soil. Dielectric measurements are conducted during the

penetration phase of the *Mole* in the regolith, every ~5 cm. This resolution is required to identify successive layers of different materials and study stratigraphy. Four working frequencies have been selected: 10, 10^2, 10^3 and 10^4 Hz. The MIP also works in the passive mode (no transmitted signal) and records the ambient electromagnetic noise. Synergy can also be expected from the comparison of these data with those collected by the atmospheric electricity and meteorological instruments, for example. A coordinated operation with components of the rover payload, specifically the ground penetrating radar, will provide ground truth for the soil permittivity, though at frequencies several orders of magnitude smaller.

Once the *Mole* has reached its rest location below the surface, a few daily measurements will open the door to the study of the diurnal and seasonal phenomena induced by variations of the soil temperature and composition.

5.4. Laboratory Experiments

5.4.1. Experimental Setup and Instrument Calibration

The tests are conducted in a thermal chamber with Martian soil analogues. The measurements are performed with the SP2 prototype and, for comparison, a plate capacitor with a guard. The capacitor consists of two parallel disks with a diameter of 10 cm and a separation that can be adjusted between 1 mm and 1 cm and, which corresponds to a capacitance between 10 and 100 pF.

Figure 48 shows the sketches of the two experimental test setups. The SP2 prototype is connected to a wave generator that produces sinusoidal and square waves with amplitudes between 0.1 and 5 V, in the frequency range 10 Hz – 10 kHz. The analogue electronics is connected to a laptop through an analogue to digital converter card with 16 channels, 16-bit resolution, and a sampling rate of 20 kS/s per channel. The software controls the wave generator, data acquisition, and signal processing. The second setup shows the plate capacitor connected to a signal analyzer that works in the same frequency range. A resistor is connected in series with the plate capacitor and an initial calibration is made in air to take into account phase corrections, due to the stray capacitances of the cables and connectors. The amplitude and phase shift of the signal in the resistor yields the complex dielectric constant of the material that fills in the space between the capacitor plates.

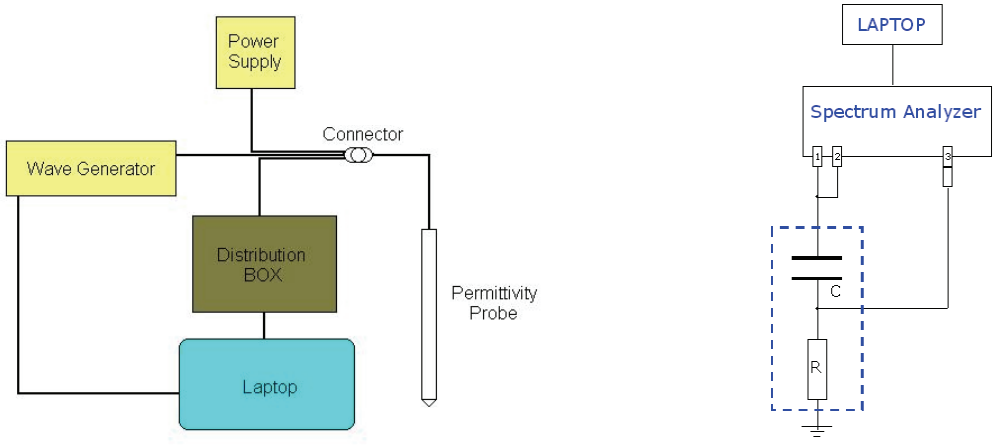

Figure 48: Sketches of the SP2 prototype (left) and plate capacitor (right) experimental setups.

Figures 49 and 50 show the experimental apparatus: the test equipment, the capacitor cell inside the thermal chamber and the SP2 prototype that are used to measure the soil stimulant properties. Because of hardware constraints, the SP2 prototype was operated at temperatures above -50°C.

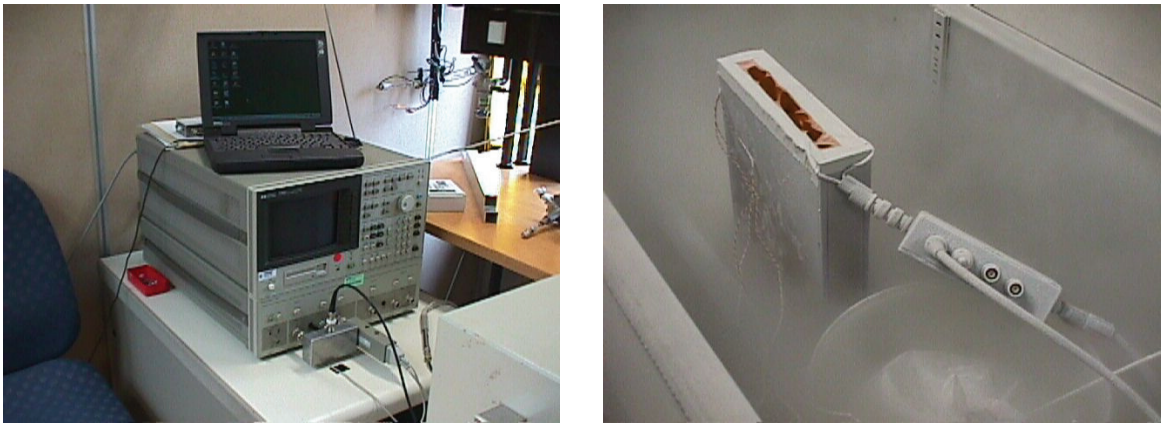

Figure 49: Test equipment for the plate capacitor technique (left) and measurement cell in the thermal chamber (right).

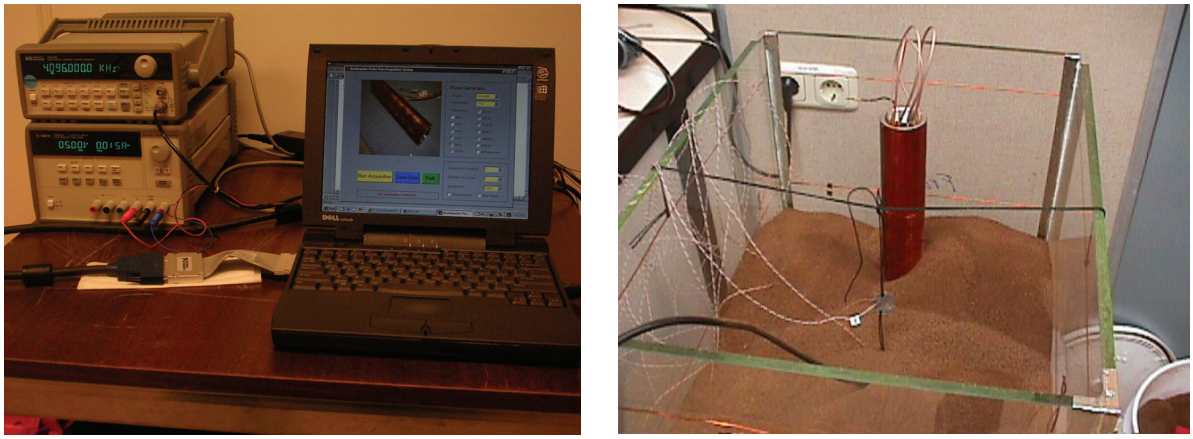

Figure 50: Test equipment for the SP2 prototype (left) partially buried in the JSC Mars-1 soil stimulant (right).

The conductivity measurements are validated against those of three different reference media, namely dielectric oil, pure water, and a standard KCl 0.01 mol dm^{-3} solution, which offer conductivities from ~10^{-12} Sm^{-1} for oil to ~10^{-1} Sm^{-1} for the KCl solution in the frequency range 10 Hz-10 kHz. The experimental results fit the nominal values within an error of 0.1% both for oil and the KCl solution. The error associated with pure water is about 12%, which might be due to the presence of dissolved CO_2; the conductivity of CO_2 saturated water is indeed much higher (~10^{-4} Sm^{-1}) than that of pure water (5.5 × 10^{-6} Sm^{-1}, at 25°C). The permittivity measurements are calibrated with pure acetone, pure water and the dielectric oil already used for conductivity. The relative errors are 0.1% and 0.8% for oil and acetone, respectively. Permittivity was measured in acetone, at 10 kHz only.

The permittivity result for pure water does not match the theoretical value because an increase in permittivity is observed in the ELF range. Thus, experimental results were

confirmed at 1 kHz with a RLC meter, using the same plate capacitor technique, and a difference below 0.25% was obtained between the two approaches.

For water ice, the experiment was conducted in a stationary nitrogen flow, in a thermal chamber at temperatures between –55°C and 0°C, in step of 5°C. The difference between the measured permittivity and the theoretical value is ~2%.

The SP2 prototype was calibrated not only in air but also in a solid medium, namely polyethylene; the probe was inserted in a hole which had been bored in a large block of this material.

After performing the calibration measurements, we used the JSC Mars-1 analogue (Allen et al., 1998) as a substitute for the Martian regolith. We also used glass beads of various sizes (50 μm and 1 mm ranges) and a simulated stratified and heterogeneous soil. The experiments have been conducted for various combinations of environmental parameters, such as gravimetric water content, porosity, frequency, and temperature.

5.4.2. Soil Analogues Testing

A limited knowledge about the mineralogical and chemical composition of the Martian regolith is a prerequisite to the development of earth-made soil analogues, or simulants. Palagonitic tephra from the Pu'u Nene cinder cone, located in the saddle between Mauna Loa and Mauna Kea volcanoes, in Hawaii, has been often cited as a close spectral analogue to the bright regions of Mars. It is commonly known as the JSC Mars-1 simulant (Allen et al., 1997). Another Earth material claimed to be a good Mars analogue, mainly for exobiology experiments, is found in the desert of Atacama, Chile.

The JSC Mars-1 simulant was selected for this experimental investigation. This analogue has already been studied by other experimenters (Cooper and Mustard, 2002). Allen et al. (1998) described the properties of JSC Mars-1, namely mineralogy, chemical composition, magnetic properties, and other physical parameters. The water content of JSC Mars-1 has been modified for the purpose of this work, but its chemical composition has not been altered otherwise. Although there necessarily remains some doubt about the suitability of JSC Mars-1 as a Martian analogue, instrument calibration and testing must nevertheless rely, not only on standard and well known media, but also on soils that more or less effectively reproduce the properties of the Martian regolith.

The JSC Mars-1 is highly hygroscopic, and the gravimetric water content at the saturation point is about 0.6 for a porosity of 0.54. Thermal gravimetry was utilized to measure the water content of the samples used in the experiments. Since the Mars soil simulant includes other volatiles, the precise measurement of the water content is difficult. Hydroxides are fully removed above 700°C, but free water is eliminated below 200°C (Yen et al., 1998). The sample has been heated at 180°C; interlayer water is fully removed, but some bond water may remain. In order to prevent the absorption of atmospheric humidity, the dried soil container remains sealed during the experiments.

5.4.3. Results

5.4.3.1. Gravimetric Water Content

The measurements with JSC Mars-1 (Table 17), glass beads, rocks, gauge materials, and other media that play the role of heterogeneities, were made with the plate capacitor technique and the SP2 prototype. The purpose of these experiments is not only to study the dielectric

properties of the materials under testing but also assess the performance of the SP2 prototype (Simões et al., 2004a, b) **[Papers 14-15]**.

The measurements are performed using JSC Mars-1 simulants with different porosity and gravimetric water contents. Soil samples are dried at 180°C for several hours. The water content is modified by spraying distilled water over the desiccated simulant and subsequent mixing. The different porosity values are obtained by vibration and compaction of the soil.

Oxide	Weight percent	Permittivity
SiO_2	43.5	4.48 (*)
Al_2O_3	23.3	10.1 (*)
TiO_2	3.8	114 (*)
Fe_2O_3	15.6	4.5
MnO	0.3	12.8
CaO	6.2	11.8
MgO	3.4	9.65
K_2O	0.6	5 (?)
Na_2O	2.4	7 (?)
P_2O_5	0.9	10 (?)

Table 17: Chemical composition of the JSC Mars-1 simulant and associated permittivities. (*) Average permittivity of anisotropic oxides; (?) Representative value. (*Allen et al*., 1998; *Lide et al.*, 2006).

Figures 51 to 55 show how the dielectric properties of JSC Mars-1 simulant (conductivity, relative permittivity, and loss tangent) vary in the frequency range from 10 Hz up to 10 kHz, for different combinations of temperature (T), porosity (ϕ), and gravimetric water content (θ). The measurements are performed with a plate capacitor and the SP2 prototype. The gravimetric water content refers to free water content, because traces of bond water may have remained in the soil. For the sake of clarity, data points severely contaminated by electromagnetic noise, at 50 Hz and harmonics, or by ambient noise, at low frequencies, have been eliminated.

Several sources of error have been identified, namely the circuit wiring, the spectrum analyzer, the external environment, and the bulk material heterogeneity. The effects of spurious resistance and capacitance in the circuit are minimized by the calibration procedure. The error associated with the spectrum analyzer is negligible. The external interferences are reduced with a Faraday cage, but cannot be completely eliminated when the temperatures or water contents are low. The dispersion associated with particle distribution, porosity, temperature gradients, and water/soil heterogeneity is reduced by averaging several acquisition cycles. An error summary is presented in Table 18 but, for the sake of clarity, no error bars are included in the plots. An increase in the relative error of the measurements is observed, if frequency, temperature, or water content is decreased. Although less pronounced, a similar effect is observed when porosity decreases. One explanation for this behaviour is that, for high impedances of the material under test, the circuit is more susceptible to interferences from external sources. Another explanation is the lower accuracy of the phase

shift measurement at low frequencies (Chelidze et al., 1999), but it does not account for the role of temperature and water content.

Frequency	T=-55°C	T=20°C
10 Hz	30	20
100 Hz	2	1.5
1 kHz	1	0.5
10 kHz	0.5	0.5
100 kHz	0.5	0.5

Table 18: Relative error percentages for permittivity and conductivity at given frequencies and temperatures, for the highest porosity (ϕ=0.58) and the lowest water content (θ<0.005), which represents the worst case.

The electric properties of the dry simulant are illustrated in Figure 51 for different porosities. At a given frequency, both conductivity and permittivity show a quasi-linear increase with density. At 10 Hz the conductivity is in the order of $(5\pm1)\times10^{-10}$ Sm^{-1}, a value close to that expected for dry rocks without metallic components. For the sake of comparison the conductivity in a JSC Mars-1 saturated solution is ~ 5×10^{-4} Sm^{-1} at 10 Hz and at room temperature.

Assuming a dry JSC Mars-1 with homogeneous particle distribution and no porosity, Equation (45) yields a permittivity of 7.5±0.4. For a porosity of 0.54±0.01, the measured permittivity is 2.49±0.05 at 100 Hz and 2.09±0.01 at 10 kHz. The effective permittivity derived from Equations (43-44) lies within a few percent from the later value assuming the composition given in Table 17 and a porosity of 0.54.

Leuschen (1999) used a coaxial transmission line to measure the electric and magnetic properties of the JSC Mars-1 simulant between 10 MHz and 1 GHz. The derived permittivities were ε_s=3.57 for DC and ε_∞=3.12 for infinite frequency. The differences between these results and the static theoretical predictions are significant, which may be due to the extrapolation of the static value from the MHz frequency range and variation in the particle or bulk properties.

The temperature has been raised from -55°C to 20°C in steps of 15°C, with different gravimetric water contents. The results obtained at -55°C and -25°C are reported in Figures 52 and 53. The results are seen from another perspective in Figure 54, where the dielectric constant is plotted against frequency, with temperature as a parameter, for two selected values of the gravimetric water content.

Both water content and temperature increase the conductivity and permittivity of the soil simulant. This effect is mostly conspicuous when the gravimetric water content is larger than 0.05; below this threshold, the electric properties of JSC Mars-1 are not very sensitive to moisture and temperature.

Plotting the loss tangent reveals new signatures whose complexities deserve further analyses. Two features, at least, are readily visible. The loss tangent increases with the water content and temperature. Note, however, that the general ordering of the curves is different for θ=0.05. The study of these features may help clarifying the processes at work in this frequency range.

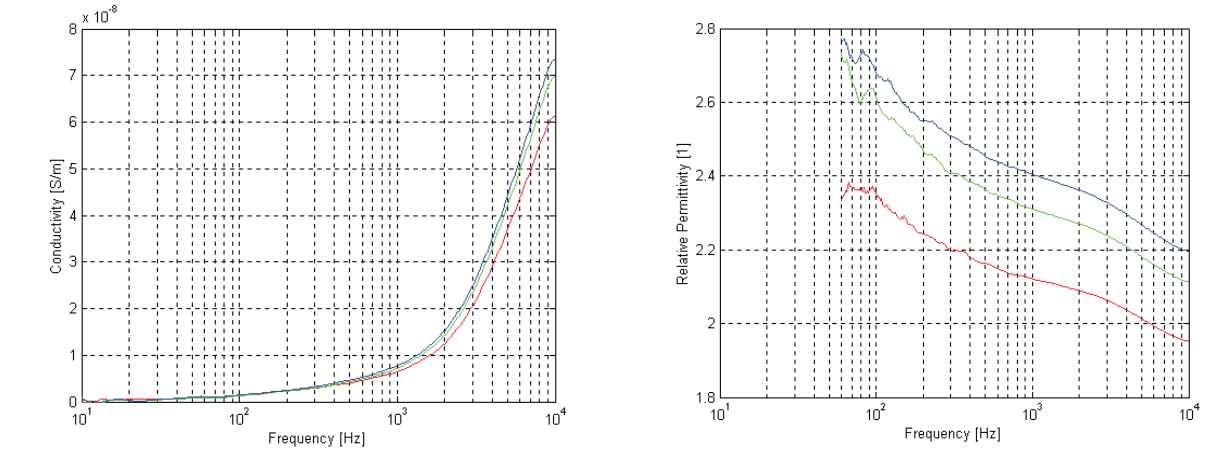

Figure 51: Conductivity (left) and relative dielectric constant (right) of the dry *JSC Mars-1* simulant (θ<0.005), as functions of frequency, at a temperature T=+20°C, for different porosities: ϕ=0.58 (red), ϕ=0.54 (green), and ϕ=0.52 (blue).

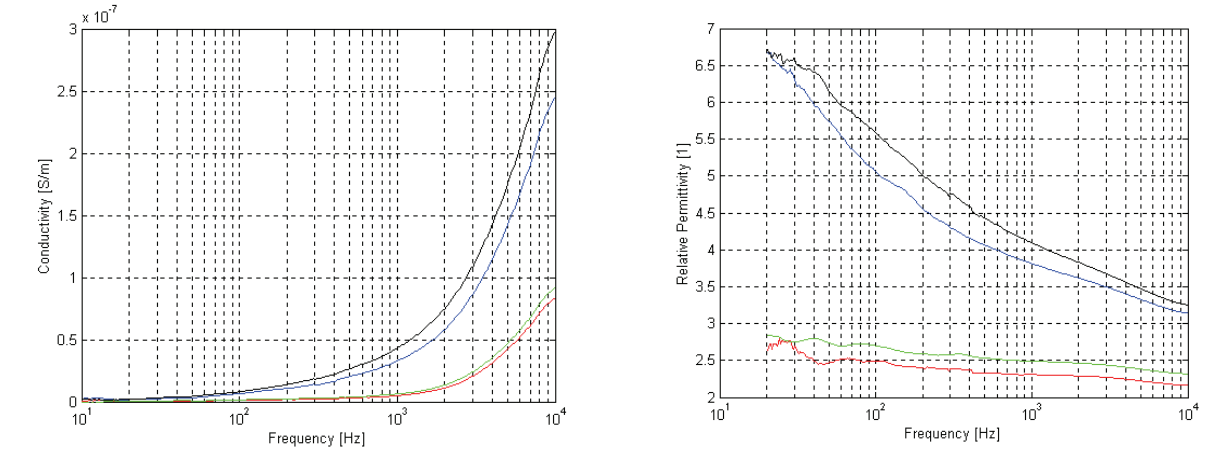

Figure 52: Conductivity (left) and relative dielectric constant (right) of the *JSC Mars-1* simulant as functions of frequency, at ϕ=0.54 and T=-55°C, with different gravimetric water contents: θ<0.005 (red), θ=0.01 (green), θ=0.05 (blue), and θ=0.1 (black).

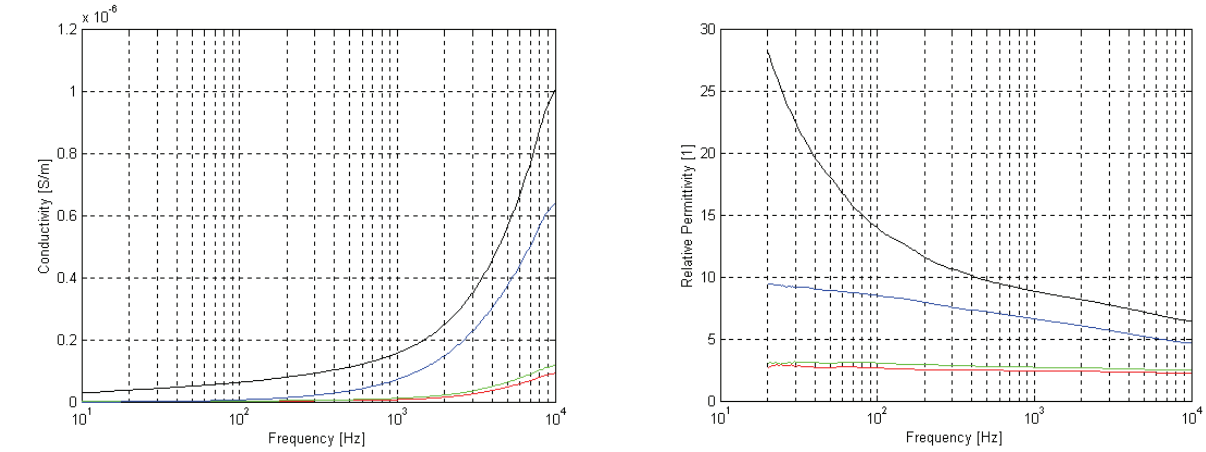

Figure 53: Same caption as for Figure 52, but at a temperature T =-25°C.

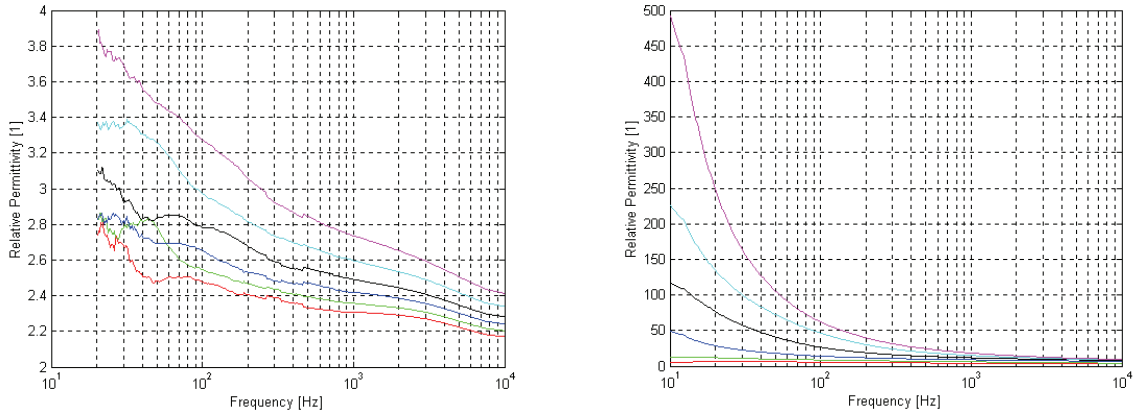

Figure 54: Relative dielectric constant of the *JSC Mars-1* simulant with gravimetric water contents θ<0.005 (left) and θ=0.1 (right), as functions of frequency, for ϕ=0.54 and at different temperatures: T=-55°C (red), -40°C (green), -25°C (blue), -10°C (black), +5°C (cyan), and +20°C (magenta).

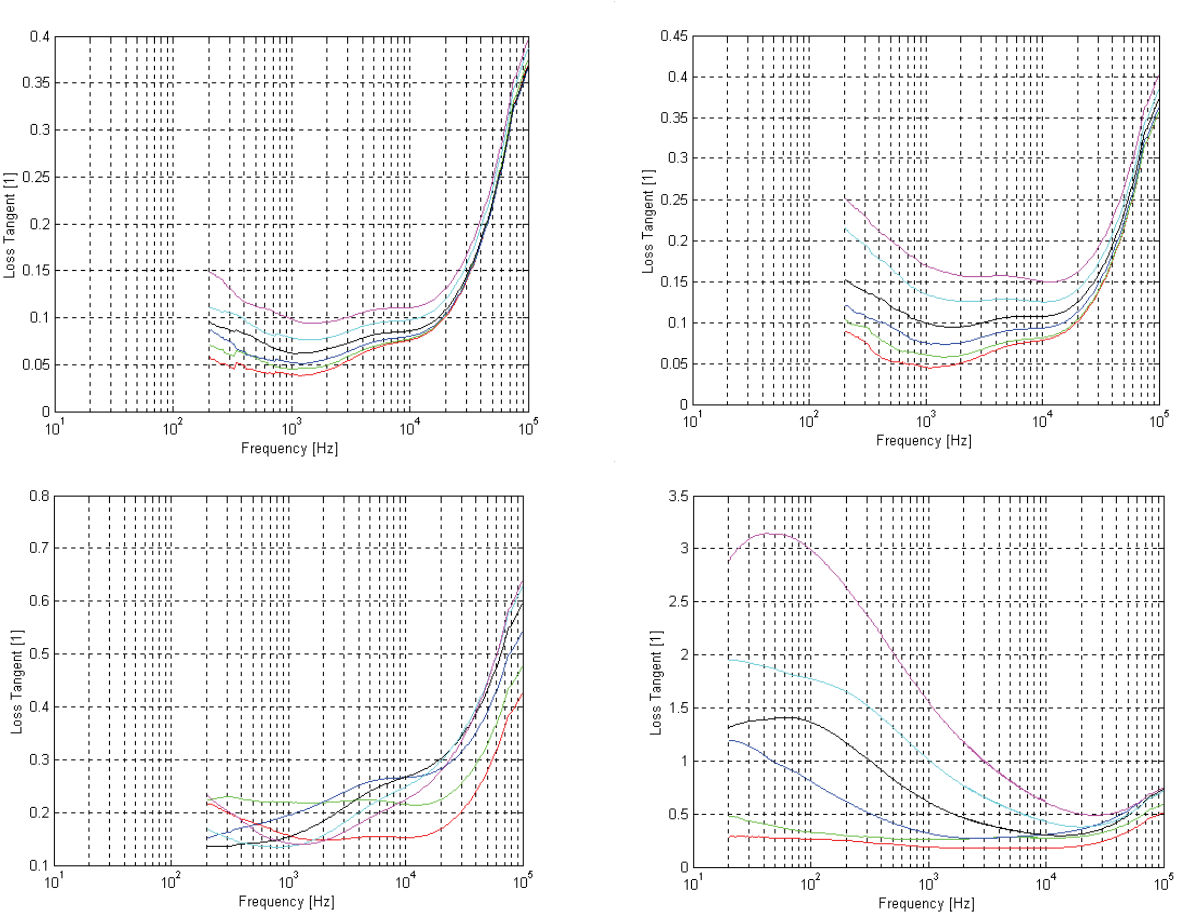

Figure 55: Loss tangent of the *JSC Mars-1*simulant, with gravimetric water content θ<0.005 (top left)), θ=0.01 (top right), θ=0.05 (bottom left), and θ=0.1 (bottom right), as function of frequency, for ϕ=0.54 and at different temperatures: T=-55°C (red), -40°C (green), -25°C (blue), -10°C (black), +5°C (cyan), and +20°C (magenta).

5.4.3.2 Stratigraphic Measurements

The detection of layer interfaces and heterogeneities is one of the main objectives of SP2. A special medium test bed is prepared to study the response of the instrument to stratigraphic features, such as interfaces, thin layers, holes, local heterogeneities in permittivity and conductivity, etc. Figure 56 shows the test medium that consists of a stratified soil with differentiated composition and local features.

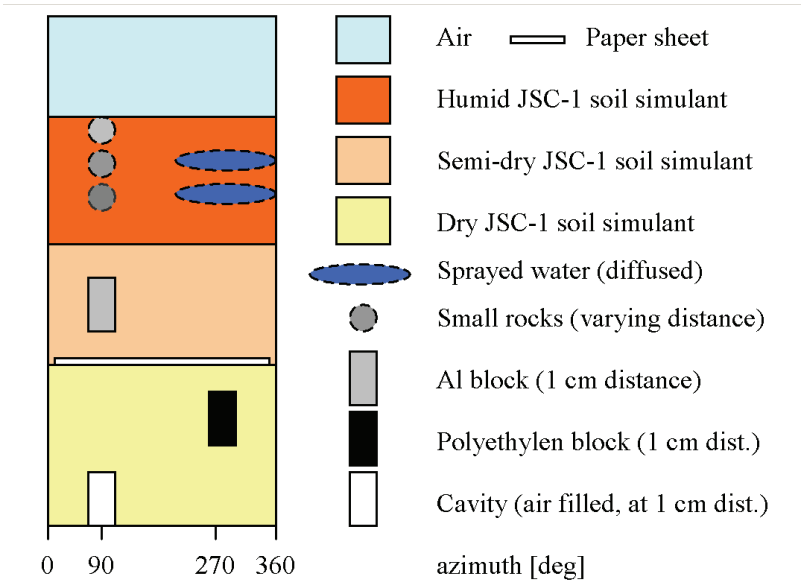

Figure 56: Sketch of the stratified medium used to produce the 2D electric maps.

The soil used for stratigraphic studies consists of three layers of JSC Mars-1 with different water contents. It also contains a layer of paper and several other items at identified positions: a polyethylene block ($\varepsilon \sim 2$), an aluminium block ($\sigma >> 1$ Sm^{-1}), an empty plastic shell ($\varepsilon < 1.05$), small pebbles, and water. The objective is to record the response of SP2 when it crosses this heterogeneous environment and when it is rotated around its axis. The probe is placed in a vertical position in the medium sketched in Figure 56. Several hundred measurements are performed during the following sequence of operations: (i) the probe is placed at the bottom of the container; (ii) the probe is rotated through 360° in steps of 30°; (iii) the probe is moved upwards over a distance of ~50 cm in steps of 2 cm until it reaches the top of the container. The Figures 57 and 58 show typical 2D electric maps that comprise more than 300 data points each. In each data set, the frequency is swept between 4 and 8192 Hz, and takes the values 2^n (Hz) where n=2, 3,..., 13.

Figures 57 and 58 show remarkable similarities with Figure 56; the following conclusions are drawn:

- Interfaces can be easily detected, mainly in the lower frequency range;
- Heterogeneities can be identified, including dielectric materials and conductors;
- The differential mode, i.e. the potential difference considering multiple receiving electrodes, is more suitable for detecting thin layers;
- The differential mode can be also used to detect local heterogeneities provided their sizes are not smaller than the separation between the receiving;
- As expected, a highly heterogeneous soil gives a more complex map.

Smaller structures seem to be more easily identified in the kHz range than at lower frequencies. A numerical model is employed in the following section to identify some of the most intricate structures.

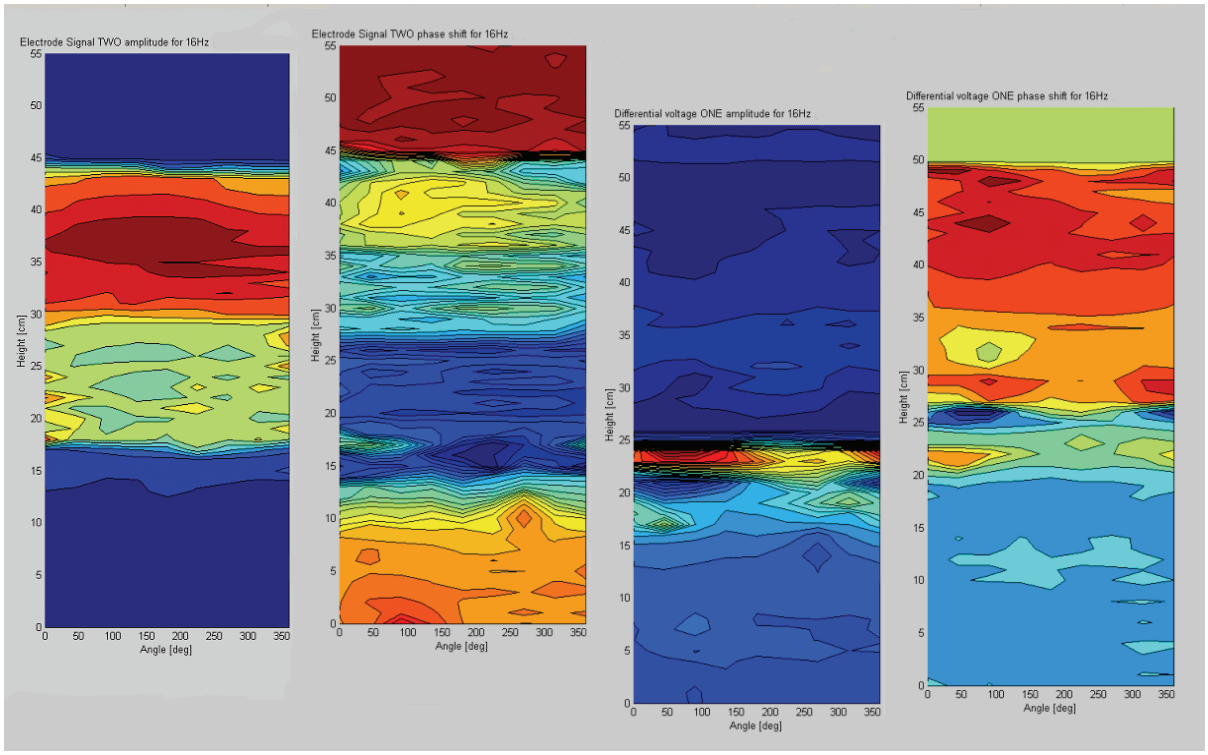

Figure 57: 2D raw electric maps of the stratified medium recorded with the electrodes of larger size (sectors of 270°), at 16 Hz. Depth is plotted against angle; the arbitrary colour code represents either amplitude or phase. From left to right: amplitude of the Tx signal; phase shift of the Tx signal; Rx amplitude; Rx phase shift.

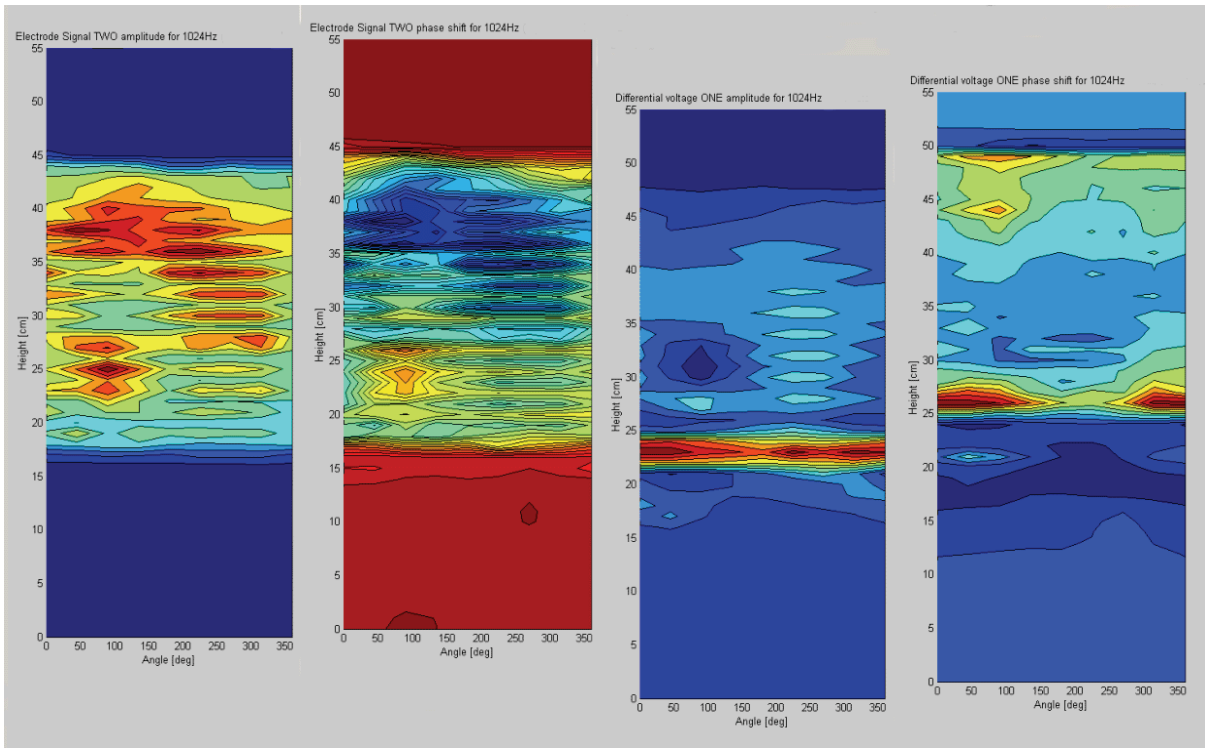

Figure 58: Caption is the same as for Figure 57, but at 1024 Hz.

Comparing Figures 56-58 shows several similar signatures in the 2D maps. The calibrated mutual impedance maps require further analysis but the simple self-impedance measurements illustrate the suitability of the instrument for stratigraphic studies. Although a complex soil structure due to several layers and embedded heterogeneities is present, a few characteristics shown in Figure 56 resemble the measurements (Figures 57-58). For example, soil layers are easily identified and the dielectric sheet is also visible. Moreover, few heterogeneities can be identified, namely the air cavity, the dielectric material, and the metallic block. However, local intricate structures are observed, mainly in humid and semi-dry layers. Experiment completion takes a few weeks, thus high soil structure was used to maximize the scientific outcome of a single trial; the disadvantage is that data is extremely intricate. Furthermore, the utilization of sprayed water produced diffusion phenomena in the soil and introduced additional interpretation difficulties.

The configuration of the flight model array configuration requires further studies, in order to optimize stratigraphic resolution. The SP2 prototype reveals nevertheless extremely promising for planetary subsurface studies and its capability seems to extend beyond than the dielectric measurements that had been initially foreseen.

5.5. Probe Modelling

The optimization of the mutual impedance probes architecture and calibration procedures require the development of appropriate theoretical and numerical tools. For simple configurations, namely linear and planar electrode arrangements in a multilayer medium, it is possible to develop analytical solutions using the method of image charges. However, numerical methods are required for arbitrary array configurations in heterogeneous media. We assume that the working frequency is low and the electrostatic approximation can be used for modelling the potential distribution in the medium. Poisson equation is written

$$\nabla \cdot \left(\varepsilon(r) \nabla \Phi(r) \right) = -\rho(r) \tag{52}$$

where r is the space variable, $\Phi(r)$ the electric potential, and $\rho(r)$ the charge density. When frequency variation is requested, Equation (52) can be generalized and the time-harmonic quasi-static approximation is obtained

$$\nabla \cdot \left((\sigma + i\omega\varepsilon_o\varepsilon) \nabla\Phi(r) - J(r) \right) = 0 , \tag{53}$$

where $\boldsymbol{J}$ is the current density due to an external source, i.e. the MIP transmitting dipole current.

A numerical model was developed to simulate the SP2 architecture (Figure 59) and the 2D map of the stratified medium experiment. The model not only provides information about the electric field distribution around the electrodes but also quantifies the effect of stratification upon the instrument response.

The numerical model solves Equation (53) by employing the finite element method to evaluate potential distribution in the medium around the probe. The model computes the potential distribution produced by a Hertz dipole and estimates its value on the receiving electrodes. The potential difference between the receivers is plotted in Figure 60. The potential 2D map is obtained by sliding and rotating the probe along the vertical and azimuthal directions, respectively. Comparison between the SP2 data and the simulation shows some similarities though some intricate structures are also present. The agreement in

the large scale structures is satisfactory because not only the three thick layers of soil but also the surface-atmosphere and dielectric sheet interfaces can be identified. However, a few localized features deserve dedicated analysis. For example, the metallic block does not show complete symmetry. Additionally, splitting structures are visible in the spherical pebbles and in the water spray layers. The structure results from the fact that the Tx-Tx-Rx-Rx electrode configuration is not symmetric along the longitudinal direction. When layers distance commensurate with receiving electrodes separation the potential distribution is more intricate and produces layer splitting. However, the SP2 measurements reveal more complex structures in the vicinity of the water spraying layers; likely, the effect is due to water diffusion processes because the medium is highly hygroscopic. Additionally, significant conductivity variations have been observed in desiccated media that were left exposed to atmospheric humidity for several hours.

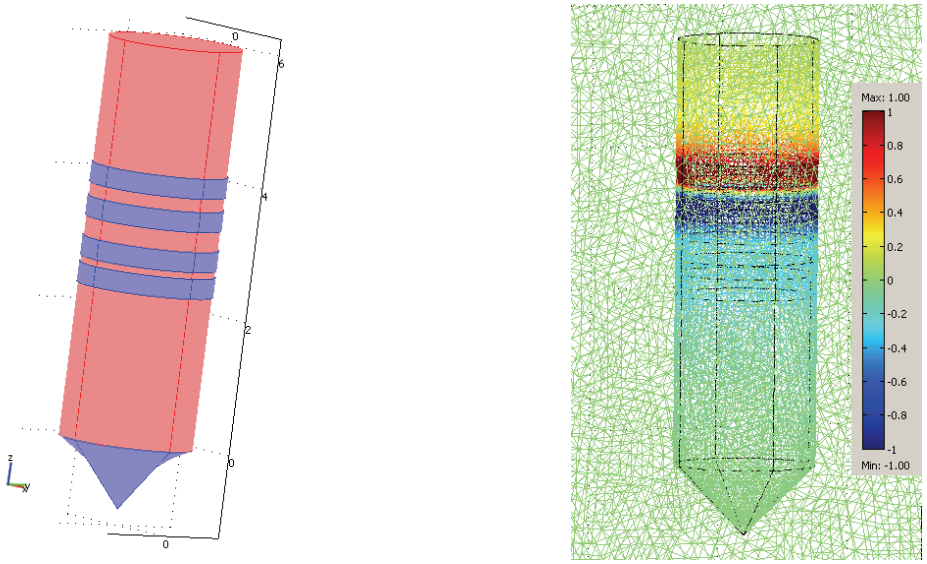

Figure 59: 3D finite element model of the SP2 architecture (left) and potential distribution around the transmitting dipole (right).

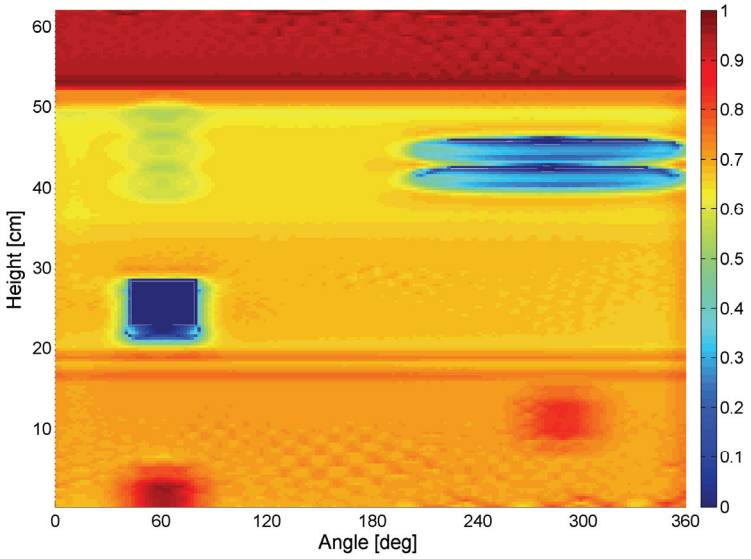

Figure 60: 2D map of potential distribution derived from a numerical model of the configuration used in Figure 56. The colour code bar represents the normalized potential difference measured between the SP2 receivers when a 16 Hz signal is injected in the medium.

Equation (52) was previously used to calculate the depth detection range of a linear electrode array that lay on the surface of a stratified medium. The deformation of the equipotential lines due to the presence of heterogeneities and interfaces are illustrated in Figures 61 and 62 for a simple dipole laying on a solid surface.

The apparent dielectric properties of the subjacent medium are derived from the amplitude and phase of the received voltage. Equations (38-39) yield the mean properties of a homogeneous medium and cannot be generalised to all arbitrary environments. The MIP onboard the Huygens Probe, for example, measured the "apparent" dielectric properties of the surface of Titan, because the electrodes lied at the interface between the soil and the atmosphere (Grard et al., 2006; Simões et al., 2007d) **[Papers 3 and 7]**. It is relatively simple, however, to derive the effective permittivity and conductivity of the ground if one assumes that the later is homogeneous and the permittivity of the atmosphere is close to that of vacuum. The situation is less straightforward in heterogeneous media, especially when the stratification is unknown. Mapping a large surface area with an adequate spatial resolution, and then deriving the dielectric properties from the recorded data set might overcome this difficulty. The inversion of Poisson equation yields the dielectric constant spatial distribution that best fits the recorded potential data set and the known boundary conditions, namely the electrode potentials and charges. One particularly efficient method is known as the Tikhonov regularization (Tikhonov and Arsenin, 1977), which provides the simplest solution with the smoothest structure. This approach is very flexible and can combine various types of constraints, e.g. potential distributions. Other techniques can reconstruct the positions and strengths of a number of point sources in a 3D potential distribution from boundary measurements (Nara and Ando, 2003). These inversion methods are particularly useful for deriving the soil dielectric properties from the measurements performed on the surface with a mobile probe, for example a linear array attached to a rover.

Contrary to a system in a homogeneous medium, where the electrode array is not subjected to any special constraint, the architecture of the probe must be optimized for a lander mission. One typical example is a planetary surface, which is either solid or liquid. When the surface is liquid or the soil very soft, the electrode system can burry itself into the medium without any significant deformation, and simplifies the derivation of the dielectric properties. In this case the electrodes array should be compact in order to minimize the contribution of the upper medium.

The more suitable configuration for a solid surface is a linear array attached to a rover (Trautner and Simões, 2002; Hamelin et al., 2004) **[Papers 11-12]**. The standard quadrupolar probe measures the dielectric properties down to a depth roughly commensurate with the electrode separation. The addition of alternative electrodes to the array provides extra information about soil stratigraphy, that is better resolved if the probe moves on the surface. A proper data analysis with inversion techniques may provide the dielectric constant spatial distribution. Noticeably, the more data points offered, for example when a 2D survey is performed, the better for refining the inversion function accuracy. However, a proper positioning of the receiver with respect to the transmitter is essential for maximizing the information retrieved from the measured potentials.

In certain conditions, parts of the structure can play the role of electrodes, such as rover wheels, lander feet, drilling tools, mole devices, etc.

Figures 61 and 62 illustrate the results obtained for stratified media with local heterogeneities. The calculations show that the interfaces are more easily identified and characterized in the following conditions: (i) a higher sensitivity to depth is achieved with larger $\overline{TxTx}$ and $\overline{TxRx}$ separations; (ii) the optimal array distance ratio is $\overline{RoRx}/\overline{RoTx} \sim 2$, for which the potential varies most (Figure 61), but also depends of the interface depth; (iii) if more receivers are available they should be placed at locations such that $1.5 < \overline{RoTx} < 3$, in order

to improve the sensitivity of the data set to stratification. Placing one of the receiving electrodes between the transmitters is not very useful for interface characterization, but it is helpful for the localisation of heterogeneities: cavities, buried rocks, and gravel. In fact, the zero potential position is a suitable location because any unbalanced potential indicates soil heterogeneity. However, the inclusion of too many receiving electrodes must be avoided to minimize possible mutual perturbations.

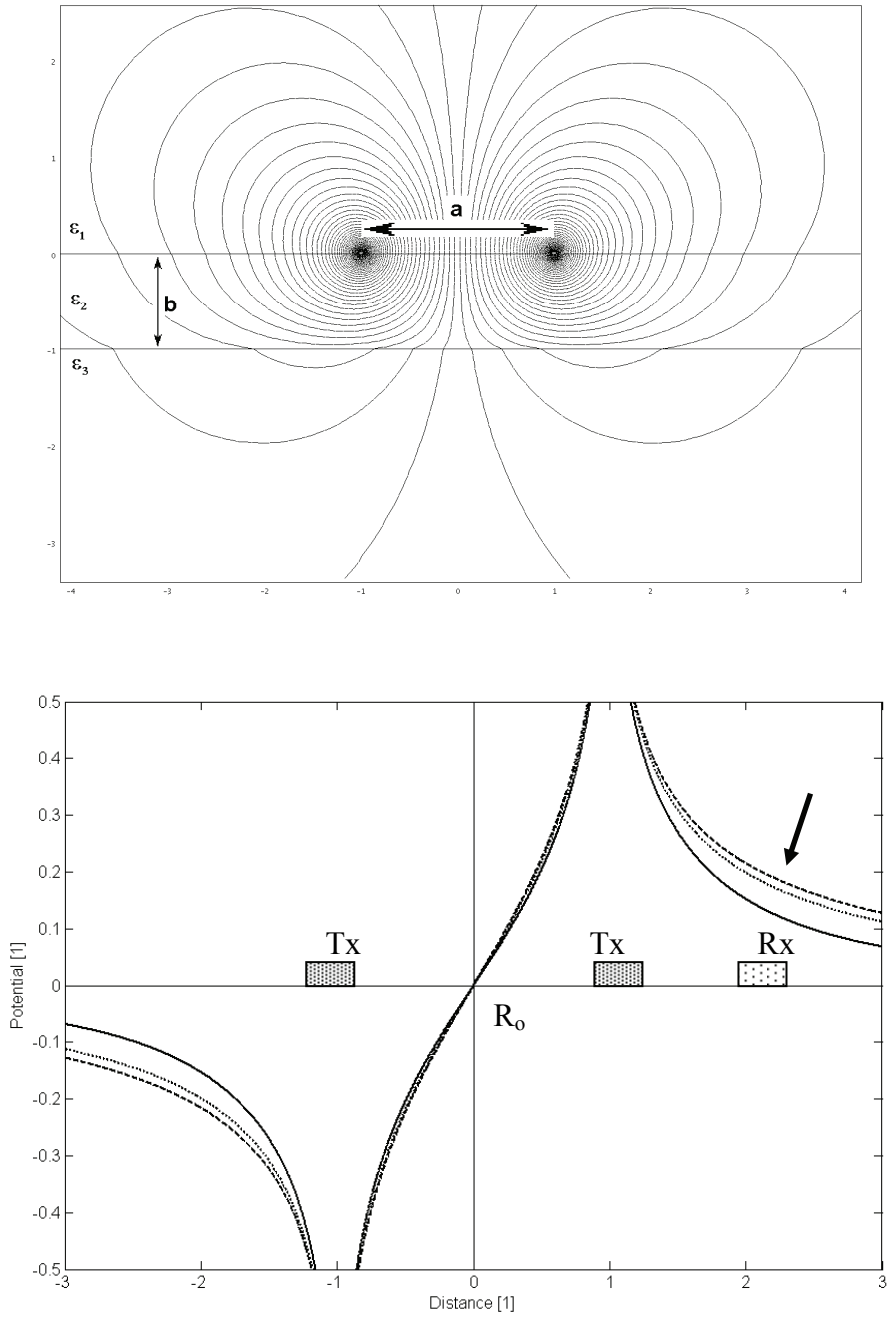

Figure 61: Potential distribution around a dipole laying on the surface of a stratified medium. Top: equipotential lines in a plane containing the dipole axis, and perpendicular to the surface, with ε_1=1, ε_2=2, and a=2. Bottom: potential profiles along the dipole axis, with ε_3=10, a=1 (solid); ε_3=3, a=1 (dashed); ε_3=3, a=3 (dotted). The arrow shows the region of maximum sensitivity that is the most suitable location for the receivers, and R_o represents the zero potential coordinate on the surface.

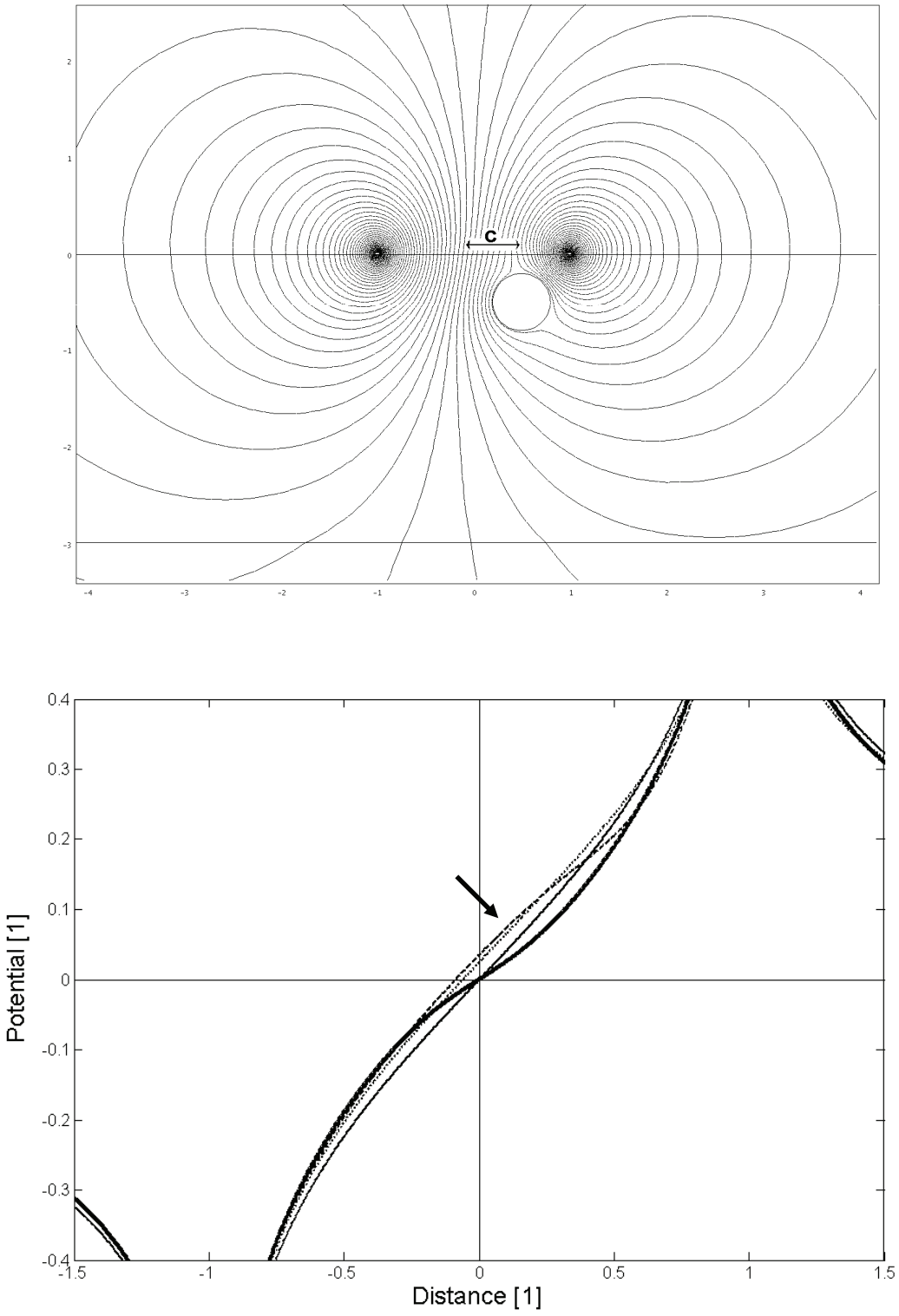

Figure 62: Potential distribution near a dipole lying on a stratified medium comprising a spherical heterogeneity. Top: equipotential lines in a plane containing the dipole axis and the heterogeneity centre, and perpendicular to the surface, with ε_1=1, ε_2=2, ε_3=3, a=2, and b=3. Bottom: potential profiles along the dipole axis, with c=0 (solid); c=0.5 (dashed); c=1 (dotted); and without heterogeneity (thick solid). The arrow shows the region of maximum sensitivity that is the most suitable location for the receivers.

The subsurface of planetary environments can be studied with surface and intrusive probes. In the latter case, the quadrupolar array is attached to -or embedded in- devices, such as penetrometers, drills, and moles. The array must cope with the geometry to the holding device that penetrates the soil. The SP2 prototype fulfils these requirements regarding not only the instrument geometry and electrode configuration, but also the electronics, data acquisition and data processing constraints (Trautner et al., 2004; Simões et al., 2004a, b) **[Papers 13-15]**. The electrode configuration lends itself not only to the evaluation of dielectric properties of the environment but also to the identification of interfaces and heterogeneities, as shown previously. The electrodes that cover several angular sectors are sensitive to local dielectric anomalies. It is therefore possible to characterize the medium along directions parallel and perpendicular to the axis of motion, using the cylindrical coordinates (ρ, θ, z), the longitudinal-moving (z-axis) and the transverse-rotating (θ-axis) directions. The sensitivity along the remaining ρ-axis is associated to the other axis: large distance between electrodes increases radial measurement range though longitudinal accuracy for interface detection is decreased. Hence, a trade-off is required for establishing a compromise between competing accuracy in the different directions. One possible solution is to include transmitting and receiving electrodes with different separations along the z-axis. This type of instruments provides a suitable potential distribution regarding inversion techniques.

5.6. Future Missions

The SP2 sensor shares the *Mole*, a component of the GEP payload, with the Heat Flow and Physical Properties Package (HP3). Integrated in the static station of the ExoMars mission, SP2 is expected to contribute to the mission objectives by measuring the dielectric properties of the soil down to a maximum depth of 5 m, performing stratigraphic studies, and evaluating the water ice content of the Martian regolith.

The space heritage of the mutual impedance technique and the results achieved with the by SP2 prototype confirm that this type of instruments can contribute usefully to planetary sciences studies. The MIP sensor array configuration can be optimized for atmospheric, surface, and subsurface dielectric measurements. The instrument is under consideration for other missions and has been proposed within the ESA Cosmic Vision program.

6. Conclusions

The Cassini-Huygens mission to Saturn, and its rings and moons has revealed itself an extremely successful endeavour. The scientific data gathered by the Cassini Orbiter and the Huygens Probe provided a wealth of data that will remain unique for a long time. The remarkable set of data returned by the Huygens Probe during the descent through the atmosphere of Titan and after landing on the surface has improved our understanding of the largest moon of Saturn.

The PWA analyzer was designed for the investigation of the electric properties and other related physical characteristics of the atmosphere of Titan, from an altitude around 140 km down to the surface. PWA measured the atmospheric conductivity with a MIP and detected an ionized layer with a maximum conductivity of ~3 nSm^{-1} and an electron density of ~650 cm^{-3}, at 63 km; the shape of the conductivity profile is confirmed by RP measurements. The conductive layer shows relatively steep boundaries and was not predicted by existing models. Most likely, these features are caused by electron attachment in aerosol layers.

The noise observed in the ELF and VLF spectra are most likely related with some sort of haze that permeates the atmosphere. The Cassini Orbiter detected haze stratification above 200-300 km, and the Huygens camera identified higher haze concentration than expected that prevented surface observation above 50 km. The PWA analyzer measured noise increase in ELF and VLF ranges between 80 and 115 km and below 22.5 km. Although the origin of the noise increase at higher altitude is questionable because it also matches the deployment of the stabilizer parachute and could be induced by vibrations; at low altitude there is clear evidence that the noise increase is related with the atmospheric environment. At the altitude where the noise transition occurs the DISR camera has identified a thin haze layer. Qualitative experiments in laboratory have shown that spraying the booms with haze also increases ELF noise. More elaborated experiments are foreseen to quantify the concentration of the aerosols and determine their nature.

The Huygens Probe descended in a region with landscapes that are common on Earth, namely hills and intricate systems of dry rivers and shorelines and landed on a dry river-bed. Methane evaporation increased after touchdown; the most likely explanation is that methane evaporation occurred due to surface warming caused by the Probe. The soil is a mixture of water ice, organic materials, and other unknown constituents; the mean relative permittivity and conductivity of the soil down to a depth of about 1 m are of the order of 2.1-2.25 and 10^{-9} Sm^{-1}. These values suggest that either the medium porosity is high if the major constituent is water ice or there is a significant fraction of hydrocarbons in the soil.

The dielectric properties of the surface remained stable until a sudden transition is observed by MIP at all working frequencies, about 11 min after landing. Although no artefact has been identified, the cause of such a transition is not definitely established yet. Possible scenarios include: (i) a galvanic contact loss between one of the receiving electrodes and the surface; (ii) medium desiccation due to methane evaporation. Local warming plays a critical role in either case but the two scenarios lead to the same conclusions and cannot be differentiated. At about the same time, a small variation of the atmospheric temperature is measured by HASI and higher dispersion in the sound velocity is detected by SSP though no obvious link has been established between these measurements. Laboratory experiments with representative media are foreseen to better understand the nature of this event.

The PWA analyzer carried an acoustic sensor and an electromagnetic wave receiver but neither lightning activity nor thunder clapping were detected. A few impulsive events are still under investigation and should confirm whether or not any lightning stroke has occurred during the descent. The PWA data nonetheless set an upper limit to the peak electric activity observed during the descent; the maximum stroke rate is less than 1 flash per second if lightning has similar properties on Titan and on Earth. This conclusion is corroborated by the Cassini Orbiter, whose instruments did not detect any lightning activity.

For lack of lightning PWA detected an electric signal at around 36 Hz throughout the descent, but it is not clear yet whether this emission is a resonance of the ionospheric cavity or an artefact. A Schumann resonance model can explain several features of the 36 Hz signal provided the angular separation between the source and the receiver is ~90º, but some doubt still remain about the electromagnetic energy source, because the field amplitude is one order of magnitude higher than on Earth. Additionally, the frequency increase observed during the descent is consistent with the model. However, the nature of the hypothetical source that pumps energy in the cavity is unknown at the present time and should differ from that at work on Earth.

Although it is indeed not possible to identify unquestionably the nature of the 36 Hz signal, several hypotheses remain under scrutiny. The most likely explanation is that PWA observes the second and possibly the fourth eigenmode of a Schumann-like resonance; the mechanism is possibly driven by the interaction of Saturn's corotating magnetosphere with Titan's ionosphere, a scenario that is at least consistent with the global power budget. The proposed mechanism involves the production of a high level of ELF ion acoustic turbulence in the ionospheric regions that load the wake currents, and a coupling between this electrostatic turbulence and whistler-mode wavelets that propagate downwards into the polar caps of the atmospheric cavity. This model accounts for a strengthening of the electric component of the Schumann even eigenmodes at the location of the landing site. A Schumann resonance triggered by lightning is therefore quite unlikely, unless a very high flash rate of weak discharges exists.

Although qualitative, laboratory tests suggest that the 36 Hz signal is not compatible with microphonic effects induced by vibrations of the Huygens vessel or of the PWA booms. Complementary laboratory experiments are scheduled in representative environments, mainly at low temperature, to ascertain that no artefact is responsible for this narrow-band emission. In addition to the interaction between Titan ionosphere and the magnetosphere of Saturn, other scenarios are also under investigation, such as electrostatic discharging induced by haze, and ionospheric plasma waves.

The low conductivity of the surface implies that ELF waves can penetrate the subsurface and, therefore, that the Schumann resonance can be used to explore the interior of Titan. Although the nature of the 36 Hz signal is not clearly established yet, the PWA measurements constrain the conditions for electromagnetic wave propagation in the cavity. For example, the

quality factor of the cavity is expected to be similar to that of Earth. The Huygens atmospheric conductivity peak detected between 40 and 80 km splits to some extent the cavity in two shells and, consequently, the propagation conditions are different from those prevailing on Earth. The subsurface ocean predicted by theoretical models can act as the cavity inner boundary and its depth can be assessed if the detected ELF signal is a natural phenomenon.

Several questions about Titan's environment have been answered by the analysis of the PWA data and by numerical modelling, but several issues remain unsolved and new intriguing questions have been raised. Making sense of the entire puzzle will require further investigation, modelling and laboratory experiments. Future missions would will, hopefully, clarify the remaining open questions and continue improving our knowledge about the Saturnian system, and its interaction with Titan.

The finite element model developed for Titan is also applied to study the environments of Venus, Mars, Jupiter, Saturn, Uranus, Neptune, Io, and Europa. Specific parameterization is used for each cavity, by introducing permittivity corrections that were not included in previous models. The cavity model is generalized by introducing permittivity and refractivity contributions whenever applicable, namely for Venus and the giant planets. A comparison between the ionospheric cavities shows that Schumann resonance of the gaseous giants is roughly one order of magnitude larger than that of the rocky planets. The cavity quality factor is highly variable and water dependent, which suggests that the Schumann resonance can be used to estimate the atmospheric water content because of its key role in atmospheric conductivity. Consequently, the Schumann resonance is a tool for investigating wave propagation on the planets and their satellites, and exploring not only their atmospheres and lower ionospheres but also their subsurface. For example, the wave propagation conditions in the atmosphere of Venus, where refractivity effects play a role, are unique among those of the rocky planets. The ELF electric field shows peculiar variations with altitude, and features similar to those observed in the VLF range by the Venera landers. This observation is corroborated by the modelling results that predict a maximum for the electric field at ~32 km for both ELF and VLF waves; the analytical derivation introduced in this thesis, considering an approximate exponential profile of the atmospheric permittivity, predicts a peak in the electric field profile at about 30 km, in fair agreement with the numerical model and the altitude of "critical refraction". The line splitting due to the day-night asymmetry of the cavity is another interesting feature of the ELF spectrum also predicted by the model. A line splitting of ~ 1Hz should be easily identified on Venus if any resonance develops in the cavity, contrary to Earth where this phenomenon is too insignificant to be observable.

The performance of the PWA analyzer, in particular the MIP that measured the dielectric properties of Titan's atmosphere and surface, the quality of the global scientific return of this experiment and the know-how gained during the development of this instrument, gave us the incentive to propose the mutual impedance technique for other future planetary missions. An instrument dedicated to the measurement of the dielectric properties of the Martian soil at shallow depths was studied, and a prototype was developed, assembled, and tested. This instrument, called SP2, can be attached to a mole or a drill, due to its robustness and reliability. The main technical requirements are: (i) power consumption less than 0.15 W in active mode and less than 0.1 W in passive mode; (ii) mass of about 100 g, including electronics and electrodes. The scientific rationale of SP2 for a Martian mission is manifold: (i) measurement of permittivity; (ii) measurement of conductivity; (iii) estimation of the water ice content in the regolith; (iv) stratification studies, namely identification of interfaces and heterogeneities; (v) measurement of ELF and VLF electromagnetic noise in the passive mode.

Because of its unique scientific capability, low mass, and low power, the SP2 instrument was selected as a possible payload element of ExoMars, the next ESA mission to Mars. The final goal of the SP2 instrument is to contribute to the characterization of the regolith and the detection of water ice. Measuring the dielectric properties of the soil provides information about the inner boundary of the Martian cavity. In the passive mode, measuring electromagnetic noise identifies the atmospheric electricity and triboelectricity phenomena that are induced by dust devils and dust storms.

The mutual impedance probe should be considered as a potential addition to the payloads of most space missions performed with balloons, descent probes, and landers. The mutual impedance technique revealed extremely useful to planetary surface studies and, consequently, the optimization proposed in this thesis deserves continuous efforts regarding its optimization, calibration, and qualification. Measuring the dielectric properties of the Martian regolith with this instrument would, for example, contribute to characterizing the inner boundary of the cavity.

This thesis presents theoretical and experimental studies of electromagnetic resonances in the ionospheric cavities of planets and satellites. In the case of Titan, the PWA analyzer provides unique measurements that constrain wave propagation in the cavity. The 3D finite element model developed for Titan can be used to investigate not only the ionosphere and the atmosphere but also the subsurface, in order to confirm the possible presence of the subsurface ocean predicted by theoretical models. The model is generalized and applied to other celestial bodies, namely Venus, Mars, Jupiter and its moons Io and Europa, Saturn, Uranus, and Neptune. The wealth of data provided by the Huygens Probe instruments, in particular the atmospheric electricity package, shows that *in situ* measurements yield an exceptional scientific outcome and must be considered in future missions to complement remote sensing techniques. *In situ* measurements performed during the descent - and on the surface - of planetary bodies can be used as ground truth for orbiter and Earth-based observations; additionally, they provide unique information that cannot be gathered by any other means, and thus broaden the scope of planetary research studies.

7. References

Abbas, M., 1968. Hydromagnetic wave propagation and excitation of Schumann resonances. *Planet. Space Sci.* **16**, 831-844.

Acuña, M.H., Connerney, J.E.P., Wasilewski, P., Lin, R.P., Mitchell, D., Anderson, K.A., Carlson, C.W., McFadden, J., Rème, H., Mazelle, C., Vignes, D., Bauer, S.J., Cloutier, P., Ness, N.F., 2001. Magnetic field of Mars: Summary of results from the aerobraking and mapping orbits. *J. Geophys. Res.* **106**, 23,403–23,417.

Allen, C.C., Morris, R.V., Lindstrom, D.J., Lindstrom, M.M., Lockwood, J.P., 1997. JSC Mars-1 - Martian regolith simulant. *Lunar Planet. Sci. Conf.* **28**, 27-28, Houston, TX, USA.

Allen, C.C., Morris, R.V., Jager, K.M., Golden, D.C., Lindstrom, D.J., Lindstrom, M.M., Lockwood, J.P., 1998. Martian regolith simulant JSC Mars-1. *Lunar Planet. Sci. Conf.* **29**, 160, Houston, TX, USA.

Aplin, K.L., 2006. Atmospheric electrification in the Solar System. *Surv. Geophy.* **27**, 63-108.

Archer, D.G., Wang, P., 1990. The dielectric constant of water and the Debye-Huckel limiting law slopes. *J. Phys. Chem. Ref. Data* **19**, 371-411.

Auty, R.P., Cole, R.H., 1952. Dielectric properties of ice and solid. *J. Chem. Phys.* **20**, 1309-1314.

Balanis, C.A., 1989. *Advanced Engineering Electromagnetics*. Wiley, New York, NY, USA.

Balser, M., Wagner, C.A., 1960. Observations of Earth-ionosphere cavity resonances. *Nature* **188**, 638–641.

Banks, P.M., Kockarts, G., 1973. *Aeronomy*. Academic Press, London, UK.

Bazarova, M.P., Rybachek, S.T., 1978. Splitting of the eigen−values of the spherical cavity with irregular boundary conditions having the axial symmetry. In *Problems of Wave Diffraction and Propagation* **16**, 176−182, Leningrad State University Press, Russia (in Russian).

Bean, B.R., Dutton, E.J., 1968. *Radio Meteorology*. Dover Publications, New York, N.Y., USA.

Béghin, C., Simões, F., Karsnoselskhikh, V., Schwingenschuh, K., Berthelier, J.J., Besser, B.P., Bettanini, C., Grard, R., Hamelin, M., López-Moreno, J.J., Molina-Cuberos, G.J., Tokano, T., 2007. A Schumann-like resonance on Titan driven by Saturn's magnetosphere possibly revealed by the Huygens Probe. *Icarus* **191**, 251-266. **[See Appendix, Paper 5]**

Berthelier, J.-J., Grard, R., Laakso, H., Parrot, M., 2000. ARES, atmospheric relaxation and electric field sensor, the electric field experiment on NETLANDER. *Planet. Space Sci.* **48**, 1193-1200.

Besser, B.P., 2007. Synopsis of the historical development of Schumann resonances. *Radio Sci.* **42**, RS2S02, doi:10.1029/2006RS003495.

Bird, M.K., Dutta-Roy, R., Heyl, M., Allison, M., Asmar, S.W., Folkner, W.M., Preston, R.A., Atkinson, D.H., Edenhofer, P., Plettemeier, D., Wohlmuth, R., Iess, L., Tyler, G.L., 2002. The Huygens Doppler Wind Experiment - Titan winds derived from probe radio frequency measurements. *Space Sci. Rev.* **104**, 613-640.

Bliokh, P.V., Nickolaenko, A.P., Filippov, Yu.F., 1968. Diurnal variations of the eigen−frequencies of the Earth−ionosphere cavity in connection with the eccentricity of the geomagnetic field. *Geomagn. Aeron.* **8**, 250–260 (in Russian).

Bliokh, P.V., Nickolaenko, A.P., Filippov, Yu.F., 1980. *Schumann Resonances in the Earth-Ionosphere Cavity*. D. L1. Jones-ed, Peter Peregrinus, Oxford, England.

Boccippio, D.J., Williams, E., Lyons, W.A., Baker, I., Boldi, R., 1995. Sprites, ELF transients and positive ground strokes. *Science* **269**, 1088–1091.

Borucki, W.J., Levin, Z., Whitten, R.C., Keesee, R.G., Capone, L.A., Summers, A.L., Toon, O.B., Dubach, J., 1987. Predictions of the electrical conductivity and charging of the aerosols in Titan's atmosphere. *Icarus* **72**, 604-622.

Bragin, Yu.A., Tulinov, V.F., Smirnykh, L.N., Yakovlev, S.G., 1973. Simultaneous measurements of the ion density and of the intensity of corpuscular streams at heights between 10 and 70 km. *Kosm. Issled.* **11**, 488-489.

Bruggemann, D.A.G., 1935. Computation of different physical constants of heterogeneous substances. *Ann. Phys., Lpz.* **22**, 636-679 (in German).

Cadène, F., 1995. *Methodology for measuring planetary atmospheric conductivities*. Thèse d'Université, Electronique, PhD thesis, Université de Paris 6, France (in French).

Capone, L.A., Whitten, R.C., Prasad, S.S., Dubach, J., 1977. The ionospheres of Saturn, Uranus, and Neptune. *Astrophys. J.* **215**, 977-983.

Chandler, M.O., Waite, J.H., 1986. The ionosphere of Uranus - A myriad of possibilities. *Geophys. Res. Lett.* **13**, 6-9.

Chelidze, T.L., Gueguen, Y., Ruffet, C., 1999. Electrical spectroscopy of porous rocks: a review-II. Experimental results and interpretation. *Geophys. J. Int.* **137**, 16-34.

Ciddor, P.E., 1996. Refractive index of air: new equations for the visible and near infrared. *Appl. Optics* **35**, 1566-1573.

Ciddor, P.E., Hill, R.J., 1999. Refractive index of air. 2. Group index. *Appl. Optics* **38**, 1663-1667.

Christensen, P.R., Moore, H.J., 1992. The Martian surface layer. In: *Mars,* (Eds.) Kieffer, H.H., Jakosky, B.M., Snyder, C.W., Matthews, M.S., pp. 686-729, Univ. of Arizona Press, Arizona, USA.

Clifford, S.M., 1993. A model for the hydrologic and climatic behavior of water on Mars. *J. Geophys. Res.* **98**, E6, 10973-11016.

Cooper, C.D., Mustard, J.F., 2002. Spectroscopy of loose and cemented sulfate-bearing soils: implications for duricrust on Mars. *Icarus* **158**, 42-55.

Cummer, S.A., Farrell, W.M., 1999. Radio atmospheric propagation on Mars and potential remote sensing applications. *J. Geophys. Res.* **104**, E6, 14149-14158.

Debye, P., 1929. *Polar Molecules*. Leipzig Press, Germany (in German).

Falkner, P., 2004. *Permittivitäts Wellen und Altimeter Analysator für das ESA/NASA Projekt Cassini-Huygens*. PhD thesis, Technical University of Graz, Graz, Austria (in German).

Falkner, P., Jernej, I., 2005. *HASI-PWA Calibration Document*, HASI-PWA-FM-DOC-41, ESA Report.

Farrell, W.M., Desch, M.D., 2001. Is there a Martian atmospheric electric circuit? *J. Geophys. Res.* **106**, 7591-7595.

Fischer, G., Tokano, T., Macher, W., Lammer, H., Rucker, H.O., 2004. Energy dissipation of possible Titan lightning strokes. *Planet. Space Sci.* **52**, 447-458.

Fischer, G., Desch, M.D., Zarka, P., Kaiser, M.L., Gurnett, D.A., Kurth, W.S., Macher, W., Rucker, H.O., Lecacheux, A., Farrell, W.M., Cecconi, B., 2006. Saturn lightning recorded by Cassini/RPWS in 2004. *Icarus* **183**, 135-152.

Fjeldbo, G., Sweetnam, D., Brenkle, J., Christensen, E., Farless, D., Mehta, J., Seidel, B., Michael Jr., W., Wallio, A., Grossi, M., 1977. Viking radio occultation measurements of the Martian atmosphere and topography - Primary mission coverage. *J. Geophys. Res.* **82**, 4317-4324.

Fulchignoni, M., Ferri, F., Angrilli, F., Bar-Nun, A., Barucci, M.A., Bianchini, G., Borucki, W., Coradini, M., Coustenis, A., Falkner, P., Flamini, E., Grard, R., Hamelin, M., Harri, A. M., Leppelmeier, G.W., López-Moreno, J.J., McDonnell, J.A.M., McKay, C.P., Neubauer, F.H., Pedersen, A., Picardi, G., Pirronello, V., Rodrigo, R., Schwingenschuh, K., Seiff, A., Svedhem, H., Vanzani, V., Zarnecki, J., 2002. The characterization of Titan's atmosphere

physical parameters by the Huygens Atmospheric Structure Instrument (HASI). *Space Sci. Rev.* **104**, 395-431.

Fulchignoni, M., Ferri, F., Angrilli, F., Ball, A. J., Bar-Nun, A., Barucci, M.A., Bettanini, C., Bianchini, G., Borucki, W., Colombatti, G., Coradini, M., Coustenis, A., Debei, S., Falkner, P., Fanti, G., Flamini, E., Gaborit, V., Grard, R., Hamelin, M., Harri, A.M., Hathi, B., Jernej, I., Leese, M.R., Lehto, A., Lion Stoppato, P.F., López-Moreno, J.J., Mäkinen, T., McDonnell, J.A.M., McKay, C.P., Molina-Cuberos, G., Neubauer, F.M., Pirronello, V., Rodrigo, R., Saggin, B., Schwingenschuh, K., Seiff, A., Simões, F., Svedhem, H., Tokano, T., Towner, M. C., Trautner, R., Withers, P., Zarnecki, J.C., 2005. In situ measurements of the physical characteristics of Titan's environment. *Nature* **438**, 785-791. **[See Appendix, Paper 1]**

Galejs, J., 1970a. F-layer reflections and ion effects in the propagation of terrestrial ELF waves. *J. Geophys. Res.* **75**, 4439-4443.

Galejs, J., 1970b. Frequency variations of Schumann resonances. *J. Geophys. Res.* **75**, 3237-3251.

Galejs, J., 1972. *Terrestrial Propagation of Long Electromagnetic Waves*. Pergamon Press, New York, USA.

Grard, R., 1990. A quadrupolar system for measuring in situ the complex permittivity of materials – Application to penetrators and landers for planetary exploration. *Measurement Science and Technology* **1**, 801-806.

Grard, R., Svedhem, H., Brown, V., Falkner, P., Hamelin, M., 1995. An experimental investigation of atmospheric electricity and lightning activity to be performed during the descent of the Huygens Probe on Titan. *J. Atmos. Terr. Phys.* **57**, 575-585.

Grard, R., Smit, A., Smit, L., Van Der Hoek, J., 1997. Development and qualification of a deployable boom system for the Huygens Probe. *Proceedings 7th European Space Mechanics and Tribology Symposium*, ESTEC, Noordwijk, The Netherlands. **ESA SP-410,** 181-183.

Grard, R., Hamelin, M., López-Moreno, J.J., Schwingenschuh, K., Jernej, I., Molina-Cuberos, G.J., Simões, F., Trautner, R., Falkner, P., Ferri, F., Fulchignoni, M., Rodrigo, R., Svedhem, H., Béghin, C., Berthelier, J.-J., Brown, V.J.G., Chabassière, M., Jeronimo, J.M., Lara, L.M., Tokano, T., 2006. Electric properties and related physical characteristics of the atmosphere and surface of Titan. *Planet. Space Sci.* **54**, 1124–1136. **[See Appendix, Paper 3]**

Greifinger, C., Greifinger, P., 1978. Approximate method for determine ELF eigen–values in the Earth–ionosphere waveguide. *Radio Sci.* **13**, 831–837.

Gendrin, R., Stefant, R., 1962. Effect of high altitude thermonuclear explosion on July 1962 on the resonance in the Earth-ionosphere cavity. Experimental results. *C.R. Acad. Sci.* **255**, 2273–2275 (in French).

Guglielmi, A.V., Pokhotelov, O.A., 1996. *Geoelectromagnetic Waves*. Institute of Physics Publishing, London, UK.

Gurnett, D.A., Shaw, R.R., Anderson, R.R., Kurth, W.S., 1979. Whistlers observed by Voyager 1 - Detection of lightning on Jupiter. *Geophys. Res. Lett.* **6**, 511-514.

Gurnett, D.A., Kurth, W.S., Cairns, I.H., Granroth, L.J., 1990. Whistlers in Neptune's magnetosphere - Evidence of atmospheric lightning. *J. Geophys. Res.* **95**, 20967-20976.

Hale, L.C., Baginski, M.E., 1987. Current to the ionosphere following a lightning stroke. *Nature* **329**, 329–333.

Hamelin, M., Grard, R., Laakso, H., Ney, R., Schmidt, W., Simões, F., Trautner, R., 2004. Conductivity and dielectric characteristics of planetary surfaces deduced by Mutual Impedance Probes: from Huygens and Rosetta Lander to Netlanders and future missions to solid planetary bodies. *Proceedings of the 37th ESLAB Symposium*, Editor: B. Battrick, Noordwijk, The Netherlands. **ESA SP-543**, 169-174. **[See Appendix, Paper 12]**

Hamelin, M., Béghin, C., Grard, R., López-Moreno, J.J., Schwingenschuh, K., Simões, F., Trautner, R., Berthelier, J.J., Brown, V.J.G., Chabassière, M., Falkner, P., Ferri, F., Fulchignoni, M., Jernej, I., Jeronimo, J.M., Molina-Cuberos, G.J., Rodrigo, R., Tokano, T., 2007. Electron conductivity and density profiles derived from the mutual impedance probe measurements performed during the descent of Huygens through the atmosphere of Titan. *Planet. Space Sci.* **55**, 1964-1977. **[See Appendix, Paper 6]**

Hanai, T., 1968. Electrical Properties of Emulsions. In *Emulsion Science*, P. Sherman (ed.), pp. 354–478, Academic Press, San Diego, CA, USA.

Harrison, R.G., Carslaw, K.S., 2003. Ion–aerosol–cloud processes in the lower atmosphere. *Rev. Geophys.* **41**, doi:10.1029/2002RG000114.

Heckman, S.J., Williams, E.R., Boldi, R., 1998. Total global lightning inferred from Schumann resonance measurements. *J. Geophys. Res.* **103**, 31775–31779.

Hofe, R., 2006. *Signal analysis of the electric and acoustic field measurements by the Huygens instrument HASI/PWA*. Diploma Thesis, Technical University of Graz, Graz, Austria.

Israel, M., Cabane, J.-F., Brun, G., Niemann, S., Way, H., Riedler, W., Steller, M., Raulin, F., Coscia, D., 2002. Huygens Probe Aerosol Collector Pyrolyser experiment. *Space Sci. Rev.* **104**, 433-468.

Karkoschka, E., Tomasko, M.G., Doose, L.R., See, C., McFarlane, E.A., Schröder, S.E., Rizk, B., 2007. DISR imaging and the geometry of the descent of the Huygens probe within Titan's atmosphere. *Planet. Space Sci.* 55, 1896-1935.

Kingery, W.D., Bowen, H.K., Uhlmann, D.R., 1976. *Introduction to Ceramics*. 2nd Edition, John Wiley and Sons, New York, NY, USA.

Kirkwood, J.G., 1939. The dielectric polarization of polar liquids. *J. Chem. Phys.* **7**, 911−919.

Kliore, A., Cain, D.L., Fjeldbo, G., Seidel, B.L., Rasool, S.I., 1974. Preliminary results on the atmospheres of Io and Jupiter from the Pioneer 10 S-Band Occultation Experiment. *Science* **183**, 323-324.

Kliore, A.J., Hinson, D.P., Flasar, F.M., Nagy, A.F., Cravens, T.E., 1997. The ionosphere of Europa from Galileo radio occultations. *Science* **277**, 355-358.

Krauss, C.E., Horányi, M., Robertson, S., 2003. Experimental evidence for electrostatic discharging of dust near the surface of Mars. *New J. Phys.* **5**, 70.1-70.9.

Labendz, D., 1998. Investigation of Schumann resonance polarization parameters. *J. Atmos. Solar-Terr. Phys.* **60**, 1779–1789.

Landau, L.D., Lifshitz., E.M., 1984. *Electrodynamics of Continuous Media*. Vol 8, 2nd Edition, Pergamon Press, Oxford, UK.

Lanzerotti, L.J., Rinnert, K., Dehmel, G., Gliem, F.O., Krider, E.P., Uman, M.A., Bach, J., 1986. Radio frequency signals in Jupiter's atmosphere. *Science* **272**, 858-860.

Lebreton, J.-P., Matson, D.L., 2002. The Huygens Probe: science, payload and mission overview. *Space Sci. Rev.* **104**, 59-100.

Leuschen, C., 1999. Analysis of the complex permittivity and permeability of a Martian soil simulant from 10 MHz to 1 GHz. *Proceedings of the 2001 International Geoscience and Remote Sensing Symposium* (IGARSS '01). Syndey, Australia, July 2001, 0-7803-5207.

Lide, D.R. et al., 2006. *CRC Handbook of Chemistry and Physics*, 86th Edition, Taylor and Francis, Boca Raton, Florida, USA.

Lindal, G.F., Lyons, J.R., Sweetnam, D.N., Eshleman, V.R., Hinson, D.P., 1987. The atmosphere of Uranus - Results of radio occultation measurements with Voyager 2. *J. Geophys. Res.* **92**, 14987-15001.

Liu, J., 2006. *Interaction of Magnetic Field and Flow in the Outer Shells of Giant Planets*. PhD Thesis, Caltech, California, USA.

Looyenga, H., 1965. Dielectric constant of heterogeneous mixtures. *Physica* **31**, 401-406.

López-Moreno, J.J., Molina-Cuberos, G.J., Hamelin, M., Brown, V.J.G., Ferri, F., Grard, R., Jernej, I., Jerónimo, J.M., Leppelmeier, G.W., Mäkinen, T., Rodrigo, R., Sabau, L., Schwingenschuh, K., Svedhem, H., Zarnecki, J., Fulchignoni, M., 2002. The Comas Sola mission to test the HUYGENS/HASI instrument on board a stratospheric balloon. *Adv. Space Res.* **30**, 1359-1364.

Lorenz, R.D., Zarnecki, J.C., Towner, M.C., Leese, M.R., Ball, A.J., Hathi, B., Hagermann, A., Ghafoor, N.A.L., 2007. Descent motions of the Huygens probe as measured by the Surface Science Package (SSP): Turbulent evidence for a cloud layer. *Planet. Space Sci.* **55**, 1936-1948.

Madden, T., Thompson, W., 1965. Low frequency electromagnetic oscillations of the earth–ionosphere cavity. *Rev. Geophys.* **3**, 211–254.

Marshall, W.L., 1987. Electrical conductance of liquid and supercritical water evaluated from 0ºC and 0.1 MPa to high temperatures and pressures: reduced-state relationships. *J. Chem. Eng. Data* **32**, 221-226.

Matson, D.L., Spilker, L.J., Lebreton, J.-P., 2002. The Cassini/Huygens mission to the Saturnian System. *Space Sci. Rev.* **104**, 1-58.

Mitchell, D.L., Lin, R.P., Mazelle, C., Rème, H., Cloutier, P.A., Connerney, J.E.P., Acuña, M.H., Ness, N.F., 2001. Probing Mars' crustal magnetic field and ionosphere with the MGS electron reflectometer. *J. Geophys. Res.* **106**, 23,417-23,427.

Molina-Cuberos, G.J., López Moreno, J.J., Lara, L.M., Rodrigo, R., O'Brien, K., 1999. Ionization by cosmic rays of the atmosphere of Titan. *Planet. Space Sci.* **47**, 1347-1354.

Molina-Cuberos, G.J., Morente, J.A., Besser, B.P., Portí, J., Lichtenegger, H., Schwingenschuh, K., Salinas, A., Margineda, J., 2006. Schumann resonances as a tool to study the lower ionospheric structure of Mars. *Radio Sci.* **41**, RS1003.

Morente, J.A., Portí, J.A., Salinas, A., Molina-Cuberos, G.J., Lichtenegger, H., Besser, B.P., Schwingenschuh, K., 2004. Do Schumann resonance frequencies depend on altitude? *J. Geophys. Res.* **109**, A05306, doi:10.1029/2003JA010305.

Nara, T., Ando, S., 2003. A projective method for an inverse source problem of the Poisson equation. *Inverse Problems* **19**, 355–369.

Niemann, H.B., Atreya, S.K., Bauer, S.J., Biemann, K., Block, B., Carignan, G.R., Donahue, T.M., Frost, R.L., Gautier, D., Haberman, J.A., Harpold, D., Hunten, D.M., Israel, G., Lunine, J.I., Mauersberger, K., Owen, T.C., Raulin, F., Richards, J.E., Way, S.H., 2002. The Gas Chromatograph Mass Spectrometer for the Huygens Probe. *Space Sci. Rev.* **104**, 553-591.

Nickolaenko, A.P., Rabinowicz, L.M., 1982. On the possibility of the global electromagnetic resonances on the planets of Solar System. *Kosm. Issled.* **20**, 82–87 (in Russian).

Nickolaenko, A.P., Hayakawa, M., 2002. *Resonances in the Earth-ionosphere cavity*. Kluwer Academic Publishers, Dordrecht, The Netherlands.

Nickolaenko, A.P., Sentman, D.D., 2007. Line splitting in the Schumann resonance oscillations, *Radio Sci.* **42**, RS2S13, 10.1029/2006RS003473.

Ogawa, T., Kozai, K., Kawamoto, H., 1979. Schumann resonances observed with a balloon in the stratosphere. *J. Atmos. Terr. Phys.* **41**, 135–142.

Pätzold, M., Tellmann, S., Häusler, B., Hinson, D., Schaa, R., Tyler, G.L., 2005. A sporadic third layer in the ionosphere of Mars. *Science* **310**, 837-839.

Pechony, O., Price, C., 2004. Schumann resonance parameters calculated with a partially uniform knee model on Earth, Venus, Mars, and Titan. *Radio Sci.* **39**, RS5007.

Perrier, G., Bergeret, A., 1995. Maxwell–Wagner–Sillars relaxations in polystyrene–glass-bead composites. *J. App. Phys.* **77**, 2651-2658.

Petrenko, V.F., Whitworth, R.W., 1999. *Physics of Ice*. Oxford University Press, Oxford, UK.

Pettinelli, E., Della Monica, G., Bella, F., Losito, G., Di Maio, R., Vannaroni, G., Storini, M., Orsini, S., Cerulli-Irelli, R., 2001. High and low frequency electrical measurements of Martian soil simulants, *Conference on the Geophysical Detection of Subsurface Water on Mars*, abstract 7019, Houston, TX, USA.

Polk, C., Postow, E., 1986. *CRC Handbook of Biological Effects of Electromagnetic Fields*. CRC Press, Boca Raton, Florida, USA.

Pounder, E. R., 1965. *Physics of Ice*. Pergamon Press, New York, NY, USA.

Rakov, V., Uman, M., 2003. *Lightning*. Cambridge Univ. Press, Cambridge, UK.

Raulin, F., Owen, T., 2002. Organic chemistry and exobiology on Titan. *Space Sci. Rev.* **104**, 379-395.

Reed, J., 1988. *Introduction to the Principles of Ceramic Processing.* John Wiley and Sons, New York, NY, USA.

Reid, G.C., 1986. Electrical structure of the middle-atmosphere. In *Study in Geophysics: the Earth's electrical environment*. Krider, E.P., Roble, R.G. (Eds.), pp. 183–194, National Academy Press, Washington, DC, USA.

Rusiniak, L., 2000. Dielectric properties and structure of water at room temperature. New experimental data in 5Hz-13MHz frequency range. *Phys. Chem. Earth* (A) **25**, 201-207.

Russell, C.T., 1991. Venus lightning. *Space Sci. Rev.* **55**, 317–356.

Russell, C.T., 2000. Some simple guidelines to the interpretation of the magnetic signatures seen at the galilean moons. *Adv. Space Res*. **26**, 1653-1664.

Rycroft, M.J., Füllekrug, M., 2004. The initiation and evolution of SPECIAL. *J. Atmos. Sol-Terr. Phy.* **66**, 1103-1113.

Sátori, G., Neska, M., Williams, E., Szendrői, J., 2007. Signatures of the day-night asymmetry of the Earth-ionosphere cavity in high time resolution Schumann resonance records. *Radio Sci.* **42**, RS2S10, 10.1029/2006RS003483.

Schlegel, K., Fullekrug, M., 1999. Schumann resonance parameter changes during high energy particle precipitation. *J. Geophys. Res.* **104**, 10111–10118.

Schumann, W.O., 1952. On the free oscillations of a conducting sphere which is surrounded by an air layer and an ionosphere shell, *Z. Naturforsch. A* **7**, 149-154 (in German).

Sentman, D.D., 1989. Detection of elliptical polarization and mode splitting in discrete Schumann resonance excitations. *J. Atmos Terr. Phys.* **51**, 507–519.

Sentman, D.D., 1990a. Approximate Schumann resonance parameters for a two−scale height ionosphere. *J. Atmos Terr. Phys.* **52**, 35.

Sentman, D.D., 1990b. Electrical conductivity of Jupiter's shallow interior and the formation of a resonant of a resonant planetary-ionospheric cavity. *Icarus* **88**, 73-86.

Sentman, D.D., 1995. Schumann Resonances. In *Handbook of Atmospheric Electrodynamics 1*, H. Volland (ed.), pp. 267−298, CRC Press, London, UK.

Sentman, D.D., Fraser, B.J., 1999. Simultaneous observations at Schumann resonance in California and Australia: Evidence for intensity modulation by the local height of the D-region. *J. Geophys. Res.* **96**, 15973−15984.

Siingh, D., Gopalakrishnan, V., Singh, R.P., Kamra, A.K., Singh, S., Vimlesh, P., Singh, R., Singh, A.K., 2007. The atmospheric global electric circuit: An overview. *Atmos. Res.* **84**, 91−110.

Simões, F., 2004. *Subsurface Permittivity Probe to Detect Water/ice in Planetary Environments*. ESA-ESTEC, Internal Report, December 2004, revised version. **[See Appendix, Paper 16]**

Simões, F., Trautner, R., Grard, R., Hamelin, M., 2004a. Laboratory measurements on Martian soil simulant JSC Mars-1: supporting the calibration of instruments for planetary missions. *Proceedings of the 37th ESLAB Symposium `Tools and Technologies for Future Planetary Exploration'*. **ESA SP-543**, 205-209. **[See Appendix, Paper 14]**

Simões, F., Trautner, R., Grard, R., Hamelin, M., 2004b. The dielectric properties of Martian soil simulant JSC Mars-1 in the frequency range from 20 Hz to 10 kHz. *Lunar Planet. Sci. Conf.* **35**, Houston, USA. **[See Appendix, Paper 15]**

Simões, F., Brown, V., Chabassière, M., Falkner, P., Ferri, F., Fulchignoni, M., Grard, R., Hamelin, M., Hofe, R., Jernej, I., Lara, L., López-Moreno, J.J., Molina-Cuberos, G., Rodrigo, R., Schwingenschuh, K., Trautner, R., 2005. Calibrating electric instruments of the Huygens Probe and modelling the dielectric properties of the atmosphere and of the surface of Titan. *Proceedings of the Comsol Multiphysics Conference* 2005, 247-250, Paris, France. **[See Appendix, Paper 2]**

Simões, F., Hamelin, M., 2006. Low frequency electromagnetic wave propagation in large cavities: a tool for investigating planetary electric environments. Study of the cavity of Titan after the Cassini-Huygens mission. *Proceedings of the Comsol Multiphysics Conference* 2006, 23-29, Paris, France. **[See Appendix, Paper 8]**

Simões, F., Grard, R., Hamelin, M., López-Moreno, J.J., Schwingenschuh, K., Béghin, C., Berthelier, J.-J., Besser, B., Brown, V.J.G., Chabassière, M., Falkner, P., Ferri, F., Fulchignoni, M., Hofe, R., Jernej, I., Jeronimo, J.M., Molina-Cuberos, G.J., Rodrigo, R., Svedhem, H., Tokano, T., Trautner, R., 2007a. A new numerical model for the simulation of ELF wave propagation and the computation of eigenmodes in the atmosphere of Titan: did Huygens observe any Schumann resonance? *Planet. Space Sci.* **55**, 1978-1989. **[See Appendix, Paper 4]**

Simões, F., Grard, R., Hamelin, M., López-Moreno, J.J., Schwingenschuh, K., Béghin, C., Berthelier, J.-J., Lebreton, J.-P., Molina-Cuberos, G.J., Tokano, T., 2007b. The Schumann resonance: a tool for exploring the atmospheric environment and the subsurface of the planets and their satellites. *Icarus* 10.1016/j.icarus.2007.09.020. **[See Appendix, Paper 9]**

Simões, F., Hamelin, M., Grard, R., Aplin, K.L., Béghin, C., Berthelier, J.-J., Besser, B., Falkner, P., Lebreton, J.-P., López-Moreno, J.J., Molina-Cuberos, G.J., Schwingenschuh, K., Sittler, E.C., Svedhem, H., Tokano, T., Trautner, R., 2007c. Electromagnetic wave propagation in the surface-ionosphere cavity of Venus. *Submitted to J. Geophys. Res*. **[See Appendix, Paper 10]**

Simões, F., Grard, R., Hamelin, M., López-Moreno, J.J., Schwingenschuh, K., Béghin, C., Berthelier, J.-J., Brown, V.J.G., Chabassière, M., Falkner, P., Ferri, F., Fulchignoni, M., Hofe, R., Jernej, I., Jeronimo, J.M., Molina-Cuberos, G.J., Rodrigo, R., Svedhem, H., Tokano, T., Trautner, R., 2007d. Huygens Probe in situ Measurements of Titan Surface Dielectric Properties. *To be submitted*. **[See Appendix, Paper 7]**

Strangeway, R.J., 2004. Plasma waves and electromagnetic radiation at Venus and Mars. *Adv. Space Res.* **33**, 1956–1967.

Storey, L.R.O., Aubry, M.P., Meyer, P., 1969. A quadrupole probe for the study of ionospheric resonances, in *Plasma Waves in Space and in the Laboratory*. Eds. J.O. Thomas and B.J. Landmark, pp. 303-332, Edinburgh University Press, UK.

Sukhorukov, A.I., 1991. On the Schumann resonances on Mars. *Planet. Space Sci.* **39**, 1673-1676.

Tikhonov, A.N., Arsenin, V.A., 1977. *Solution of Ill-posed Problems*. Winston & Sons, Washington, DC, USA.

Tomasko, M.G., Buchhauser, D., Bushroe, M., Dafoe, L.E., Doose, L.R., Eibl, A., Fellows, C., Farlane, E.M., Prout, G.M., Pringle, M.J., Rizk, B., See, C., Smith, P.H., Tsetsenekos, K., 2002. The Descent Imager/Spectral Radiometer (DISR) experiment on the Huygens Entry Probe of Titan. *Space Sci. Rev.* **104**, 469-551.

Tomasko, M.G., Archinal, B., Becker, T., Bézard, B., Bushroe, M., Combes, M., Cook, D., Coustenis, A., de Bergh, C., Dafoe, L.E., Doose, L., Douté, S., Eibl, A., Engel, S., Gliem, F., Grieger, B., Holso, K., Howington-Kraus, E., Karkoschka, E., Keller, H.U., Kirk, R., Kramm, R., Küppers, M., Lanagan, P., Lellouch, E., Lemmon, M., Lunine, J., McFarlane, E., Moores, J., Prout, G.M., Rizk, B., Rosiek, M., Rueffer, P., Schröder, S.E., Schmitt, B., See, C., Smith, P., Soderblom, L., Thomas, N., West, R., 2005. Rain, winds and haze on Titan. *Nature* **438**, 765-778.

Trautner, R., Simões, F., 2002. Detection and characterization of ice and water deposits on Mars by means of mutual impedance probes on surface and subsurface vehicles. *Proceedings of the Second European Workshop on Exo-Astrobiology,* Graz, Austria. **ESA SP-518**, 319-322. **[See Appendix, Paper 11]**

Trautner, R., Simões, F., Grard, R., Hamelin, M., 2004. A new instrument for measuring the low-frequency electrical properties of planetary subsurface materials. *Proceedings of 37th*

ESLAB Symposium. Editor: B. Battrick, Noordwijk, The Netherlands. **ESA SP-543**, 193-196. **[See Appendix, Paper 13]**

Wenner, F., 1915. A method of measuring the Earth resistivity. *U.S. Bur. Stand. Bull., Sci. Pap.* **25**, 469-478.

Williams, E., 1992. The Schumann resonance: A global tropical thermometer. *Science* **256**, 1184-1187.

Williams, E.R., Sátori, G., 2007. Solar radiation-induced changes in ionospheric height and the Schumann resonance waveguide on different timescales. *Radio Sci.* **42**, RS2S11, 10.1029/2006RS003494.

Williams, E.R., Downes, E., Boldi, R., Lyons, W., Heckman, S., 2007a. Polarity asymmetry of sprite-producing lightning: A paradox? *Radio Sci.* **42**, RS2S17, 10.1029/2006RS003488.

Williams, E.R., Mushtak, V.C., Boldi, R., Dowden, R.L., Kawasaki, Z.-I., 2007b. Sprite lightning heard round the world by Schumann resonance methods. *Radio Sci.* **42**, RS2S20, 10.1029/2006RS003498.

van Beek, L.K.H., 1967. Dielectric behavior of heterogenous systems. In: *Progress in Dielectrics*. Birks, J.B. (ed.), pp. 69-114, CRC Press, Cleveland, OH, USA.

Woan, G., 1999. *The Cambridge Handbook of Physics Formulas*. Cambridge University Press, Cambridge, UK.

Yen, A.S., Murray, B.C., Rossman, G.R., 1998. Water content of the Martian soil: laboratory simulations of reflectance spectra. *J. Geophys. Res.* **103**, E5, 11125-11134.

Zarka, P., Pedersen, B. M., 1986. Radio detection of Uranian lightning by Voyager 2. *Nature* **323**, 605-608.

Zarnecki, J.C.; Leese, M.R.; Garry, J.R.C.; Ghafoor, N.; Hathi, B., 2002. Huygens' Surface Science Package. *Space Sci. Rev.* **104**, 593-611.

Zarnecki, J.C., Leese, M.R., Hathi, B., Ball, A.J., Hagermann, A., Towner, M.C., Lorenz, R.D., McDonnell, J.A.M., Green, S.F., Patel, M.R., Ringrose, T.J., Rosenberg, P.D., Atkinson, K.R., Paton, M.D., Banaszkiewicz, M., Clark, B.C., Ferri, F., Fulchignoni, M., Ghafoor, N.A.L., Kargl, G., Svedhem, H., Delderfield, J., Grande, M., Parker, D.J., Challenor, P.G., Geake, J.E., 2005. A soft solid surface on Titan at the Huygens landing site as measured by the Surface Science Package (SSP). *Nature* **438**, 792–795.

Zimmerman, W.B.J., 2006. Multiphysics Modelling with Finite Element Methods. World Scientific, Oxon, UK.

Paper 1

In situ measurements of the physical characteristics of Titan's environment

Fulchignoni, M., Ferri, F., Angrilli, F., Ball, A. J., Bar-Nun, A., Barucci, M.A., Bettanini, C., Bianchini, G., Borucki, W., Colombatti, G., Coradini, M., Coustenis, A., Debei, S., Falkner, P., Fanti, G., Flamini, E., Gaborit, V., Grard, R., Hamelin, M., Harri, A.M., Hathi, B., Jernej, I., Leese, M.R., Lehto, A., Lion Stoppato, P.F., López-Moreno, J.J., Mäkinen, T., McDonnell, J.A.M., McKay, C.P., Molina-Cuberos, G., Neubauer, F.M., Pirronello, V., Rodrigo, R., Saggin, B., Schwingenschuh, K., Seiff, A., Simões, F., Svedhem, H., Tokano, T., Towner, M. C., Trautner, R., Withers, P., Zarnecki, J.C.

Nature **438**, 785-791 (2005)

ARTICLES

In situ measurements of the physical characteristics of Titan's environment

M. Fulchignoni[1,2], F. Ferri[3], F. Angrilli[3], A. J. Ball[4], A. Bar-Nun[5], M. A. Barucci[1], C. Bettanini[3], G. Bianchini[3], W. Borucki[6], G. Colombatti[3], M. Coradini[7], A. Coustenis[1], S. Debei[3], P. Falkner[8], G. Fanti[3], E. Flamini[9], V. Gaborit[1], R. Grard[8], M. Hamelin[10,11], A. M. Harri[12], B. Hathi[4], I. Jernej[13], M. R. Leese[4], A. Lehto[12], P. F. Lion Stoppato[3], J. J. López-Moreno[14], T. Mäkinen[12], J. A. M. McDonnell[4], C. P. McKay[6], G. Molina-Cuberos[15], F. M. Neubauer[16], V. Pirronello[17], R. Rodrigo[14], B. Saggin[18], K. Schwingenschuh[13], A. Seiff‡, F. Simões[10], H. Svedhem[8], T. Tokano[16], M. C. Towner[4], R. Trautner[8], P. Withers[4,19] & J. C. Zarnecki[4]

On the basis of previous ground-based and fly-by information, we knew that Titan's atmosphere was mainly nitrogen, with some methane, but its temperature and pressure profiles were poorly constrained because of uncertainties in the detailed composition. The extent of atmospheric electricity ('lightning') was also hitherto unknown. Here we report the temperature and density profiles, as determined by the Huygens Atmospheric Structure Instrument (HASI), from an altitude of 1,400 km down to the surface. In the upper part of the atmosphere, the temperature and density were both higher than expected. There is a lower ionospheric layer between 140 km and 40 km, with electrical conductivity peaking near 60 km. We may also have seen the signature of lightning. At the surface, the temperature was 93.65 ± 0.25 K, and the pressure was 1,467 ± 1 hPa.

Earlier Voyager fly-bys of Titan and telescopic observations indicated that Titan's atmosphere is composed of N_2 with small amounts of CH_4. The surface pressure was determined to be approximately 1,400 hPa, with a surface temperature of about 95 K decreasing to a temperature minimum of about 70 K at 40 km altitude before increasing again to about 170 K in the stratosphere[1–3]. The atmospheric structure at high elevations (1,000–1,500 km) was inferred from the solar occultation measurements by the Voyager ultraviolet spectrometer (UVS)[4]. The middle atmosphere (200–600 km) was not well determined, although telescopic observations indicated a complex vertical structure[5–10] and models have been used to predict the atmospheric structure in this region[11–13]. Very little was known about the surface of Titan because it is hidden by a thick haze and is almost undetectable, except by radar sounding[14] and a few infrared windows that have been observed from telescopes[15,16]. Initial speculation was that the surface was covered by a deep hydrocarbon ocean, but infrared and radar measurements showed definite albedo contrasts—possibly consistent with lakes, but not with a global ocean. Recently, measurements by the Cassini orbiter in the near-infrared and at radar frequencies provided new results on the nature of the surface of the satellite[17–19].

Earlier observations showed that the surface pressure on Titan was comparable to that on the Earth, and that CH_4 formed a plausible counterpart to terrestrial H_2O for cloud and rain formation. There was also speculation on the possibility of lightning occurring in Titan's atmosphere[20–22] which could affect the chemical composition of the atmosphere.

In this Article, we report results from the HASI instrument on the Huygens probe[23]. By monitoring the probe deceleration, the HASI instrument directly determined the density of the upper atmosphere and derived the temperature from the density scale height. In the lower atmosphere and on the surface of Titan, the HASI instrument directly measured the pressure and temperature. During the probe descent, electrical activity was monitored to search for evidence of lightning activity. A search for acoustic signals produced by any thunder or other shock waves was also conducted. A comprehensive description of the HASI instrument can be found in ref. 24.

In the upper atmosphere, the density profile is used to infer the temperature profile. Above 500 km, the temperature structure shows strong wave-like variations of 10–20 K about a mean of about 170 K. Below 500 km, the temperature increases to a relative maximum of 186 K and then reaches an absolute minimum of 70 K at 44 km. Below about 200 km, the temperature and pressure profile measured by HASI agrees with the results of the Voyager radio occultation data[2]. The surface temperature is determined to be 93.65 ± 0.25 K, and the surface pressure is 1,467 ± 1 hPa. The values are within the range allowed by the uncertainties in the Voyager data[13] owing to previous uncertainties in the mixing ratio of CH_4 and argon. Electrical conductivity measurements indicate the presence of charged particle

[1]LESIA, Observatoire de Paris, 5 Place Janssen, 92195 Meudon, France. [2]Université Denis Diderot – Paris 7, UFR de Physique, 2 Place Jussieu, 75006 Paris, France. [3]CISAS "G. Colombo", Università di Padova, Via Venezia 15, 35131 Padova, Italy. [4]PSSRI, The Open University, Walton Hall, Milton Keynes MK7 6AA, UK. [5]Department of Geophysics and Planetary Sciences, University of Tel Aviv, 69978 Tel Aviv, Israel. [6]NASA/AMES Research Center, MS 244-30, Moffett Field, California 94035, USA. [7]ESA Headquarters, Science Directorate, 8-10 rue Mario-Nikis, 75015 Paris, France. [8]ESA-ESTEC, European Space Agency, Keplerlaan 1, 2200 AG Noordwijk, The Netherlands. [9]Agenzia Spaziale Italiana, Viale Liegi 26, 00198 Roma, Italy. [10]CETP-IPSL, 4 Avenue de Neptune, 94107 Saint Maur, France. [11]LPCE-CNRS, 3A, Avenue de la Recherche Scientifique, 45071 Orléans cedex 2, France. [12]Finnish Meteorological Institute (FMI), Vuorikatu 15 A 00100 Helsinki, Finland. [13]Space Research Institute, Austrian Academy of Sciences (IWF), Schmiedlstrasse 6, 8042 Graz, Austria. [14]Instituto de Astrofisica de Andalucia (IAA-CSIC), PO Box 3004, 18080 Granada, Spain. [15]Applied Electromagnetic Group, Department of Physics, University of Murcia, Murcia 30100, Spain. [16]Institut für Geophysik und Meteorologie, Universität zu Köln, Albertus-Magnus-Platz, 50923 Köln, Germany. [17]DMFCI, Università di Catania, Viale A. Doria 6, 95125 Catania, Italy. [18]Politecnico di Milano, Dipartimento di Meccanica, Piazza Leonardo da Vinci 32, 20133 Milano, Italy. [19]Center for Space Physics, Boston University, 725 Commonwealth Avenue, Boston, Massachusetts 02215, USA.
‡Deceased.

species in an ionized layer, presumably induced by cosmic rays, and the detection of some electrical discharges.

Atmosphere

We inferred the atmospheric structure of Titan on the basis of measurements taken during entry phase and while the probe was descending under the parachutes. The atmosphere was first detected at an altitude of ~1,500 km, when it exceeded the sensitivity threshold of the accelerometer[25]. Broadly speaking, the temperature and density of the upper atmosphere exceeded predictions. Titan's atmosphere is apparently highly stratified. The density of the upper atmosphere was derived from the probe deceleration due to aerodynamic drag force, following a method[24,25] previously used for other planetary atmospheres such as Venus, Mars and Jupiter. The velocity as a function of time was determined by integrating the measured probe deceleration. Altitude was determined by integrating the vertical component of the velocity using the state vector of the probe provided by the Cassini navigation team. The entry altitude has a 1σ uncertainty of about 30 km; we adjusted the nominal entry altitude within this standard deviation to ensure consistency between the entry phase and descent phase measurements[26].

The derived density profile is shown in Fig. 1, with a comparison of the engineering model[13] obtained from the reanalysis[2–4,11,12] of Voyager data (radio occultations, infrared interferometry (IRIS) and UVS spectrometers). In the upper part of the atmosphere down to an altitude of about 500 km, the HASI measurements show density values systematically higher than those expected. Pressures were obtained from the density profile under the assumption of hydrostatic equilibrium and the knowledge of planetary gravity (1.354 m s^{-2} at surface level), mass (1.35×10^{23} kg) and radius (2,575 km). Temperatures were derived from the pressures, the inferred densities and the equation of state of a perfect gas using the atmospheric mean molecular weight, as a function of altitude given by the engineering model. The pressure versus temperature profile of Titan's atmosphere is shown in Fig. 2. The thermosphere is characterized by the presence of temperature variations due to inversion layers or other dynamic phenomena (such as gravity waves and gravitational tides) between 500 km and 1,020 km.

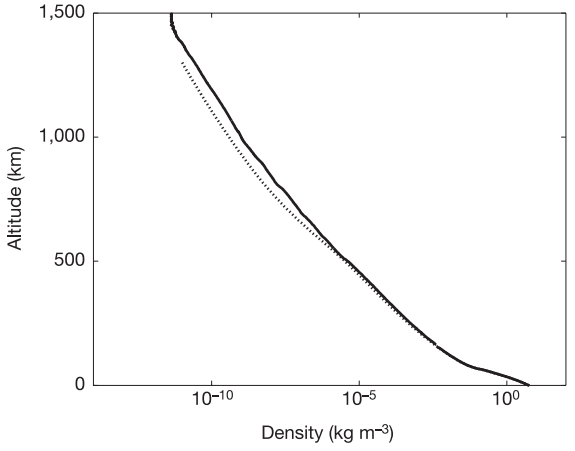

Figure 1 | The atmospheric density profile of Titan as measured by HASI. The density profile as derived from HASI measurements (solid line) is shown in comparison with the engineering model of Titan's atmosphere[13] derived from Voyager 1 data[2–4,11,12] (dashed line). Density in the upper part of the atmosphere is derived from the ACC accelerometer data. The threshold density was 5×10^{-12} kg m^{-3}. The uncertainty on the density determination[25] is of the order of 10%, mainly due to the uncertainty on the aerodynamic drag coefficient and on the probe velocity. Density values relevant to the lower atmosphere, below 160 km, have been inferred from HASI direct measurements of pressure and temperature with the assumption of hydrostatic equilibrium and real gas law[29].

Temperatures in this region are generally higher than those predicted by the engineering model, with a minimum value of 152 K at an altitude of ~490 km (2×10^{-3} hPa, which could mark the mesopause) and then increase down to the stratopause (~186 K at 250 km, 0.3 hPa). In the region between the lower part of the mesosphere and the upper part of the stratosphere, the temperatures are 5–10 K higher than those predicted by the model[12].

The temperature gradient profile, shown in Fig. 3, exhibits in general a cut-off at the dry adiabatic lapse rate, implying that fluctuations lead to marginally convective instabilities. The inversion layers in the upper atmosphere are clearly visible, with strong peaks towards positive values. The peak at 510 km corresponds to the inversion layer already observed from the ground on 14 November 2003 when Titan occulted two bright Tycho stars[10]. These lines of evidence all indicate that Titan's atmosphere is highly stratified.

After the parachute deployment and heatshield separation, the temperature sensors[27] and pressure sensors[28] were directly exposed to Titan's environment during the entire descent under parachute. The altitude and velocity are derived from these measurements, the hypothesis of hydrostatic equilibrium, and the equation of state for a real gas[29], given the atmospheric mean molecular weight measured by the Gas Chromatograph-Mass Spectrometer (GCMS)[30]. The measured pressure and temperature profiles shown in Figs 4 and 5 connect well with the profiles derived during the entry phase. From the surface up to about 150 km altitude, the HASI temperatures are in very good agreement (within 1–2 K) with the temperature measurements obtained by the Voyager 1 radio occultation assuming a pure nitrogen atmosphere[2].

The temperature minimum of 70.43 ± 0.25 K is reached at the tropopause (~44 km, 115 hPa). Figure 6 shows the temperature lapse rate in the low atmosphere. A number of inversion layers in the lower stratosphere and the strong increase in temperature with altitude between 80 km and 60 km are visible. Below 200 km, the fine

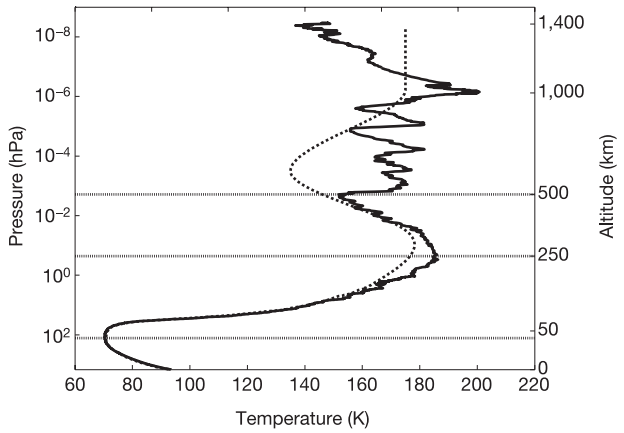

Figure 2 | The atmospheric temperature profile. The temperature profile as measured by HASI (solid line) is shown compared to Titan's atmospheric engineering model[13] (dashed line). In the upper atmosphere (above 160 km), temperature and pressure have been derived from the density using the ideal gas equation; below 160 km, temperature data are direct measurements collected by the TEM sensor. The temperature profile in the upper atmosphere (thermosphere) is characterized by several temperature variations due to inversion layers and other dynamic phenomena (for example, gravity waves and tides). Temperatures in this region are higher than those predicted by the model. The virtual absence of a mesosphere (in contrast with the theoretical models' predictions[11,12]) and the wave-like nature of the temperature profile suggest that the region in Titan's atmosphere above 250 km may not be dominated by radiative processes and may be strongly influenced by wave activity. Thus the structure that we observe may vary with time. The horizontal lines mark the mesopause (152 K at 490 km), the stratopause (186 K at 250 km) and the tropopause (70.43 K at 44 km).

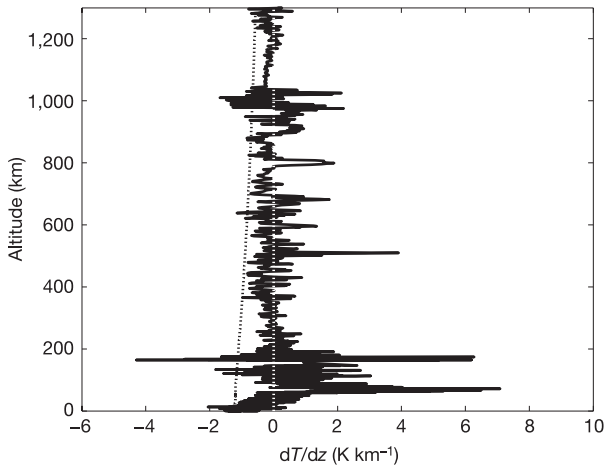

Figure 3 | The temperature lapse rate. The temperature gradient dT/dz was computed from the HASI temperature ($T(z)$) profile, and the altitude (z) was derived from the Huygens trajectory reconstruction[26]. The spatial resolution of the HASI measurements is of the order of 20 km from the top of the atmosphere down to the 400-km altitude level, decreasing down to 1 km at the 160-km level[24]. The profile shows in general a cut-off at the dry adiabatic lapse rate (dotted line), implying that fluctuations may lead to convective instabilities. The line at zero temperature variation is shown in white against the black curve. Six inversion layers in the upper atmosphere (at about 510, 600, 680, 800, 980 and 1,020 km) could be detected by strong peaks towards positive values. The strong lower inversion layer (4 K km^{-1} at ~510 km) corresponds to the feature already observed from the ground during Titan's stellar occultations[10]. The strong peaks between the 160- and 110-km levels correspond to the parachute deployment sequence.

structure seen in Fig. 5 provides evidence for a regime of gravity waves similar to those observed in the Voyager radio occultation data[31,32]. Turbulence due to shear instability (Kelvin–Helmholtz instability) is expected wherever the vertical shear of the wind speed is large. The wind shear measured by the Doppler Wind Experiment[33] is sufficiently large that the features present between 50 and 150 km are likely to be related to turbulence.

The vertical resolution of the temperature measurement was sufficient to resolve the instantaneous structure of the planetary boundary layer. On the basis of the nearly constant values of the potential temperature, the convective planetary boundary layer had a thickness of about 300 m at the place and time of landing.

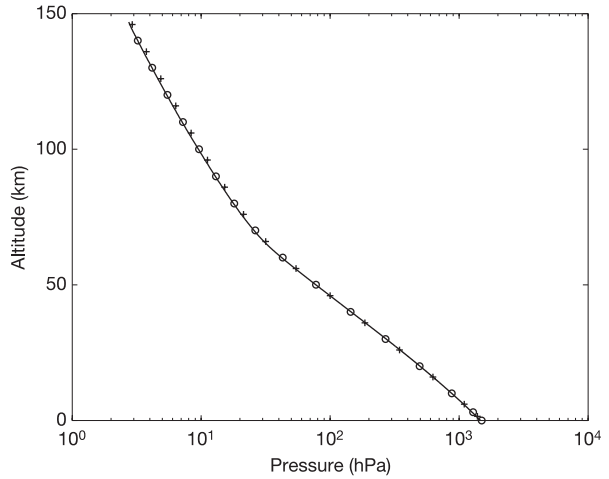

Figure 4 | Pressure profile of the lower atmosphere as measured by the Pressure Profile Instrument (PPI)[28]. Measurements (solid line) corrected for dynamic effects are shown together with values obtained by Voyager 1 radio occultation[2] (ingress, circles; egress, crosses). HASI pressure values are determined with an uncertainty of 1% along the entire descent.

Atmospheric electricity

Models of Titan's ionosphere predicted that galactic cosmic rays would produce an ionospheric layer with a maximum concentration of electrons between 70 and 90 km altitude[34–37]. The Permittivity, Wave and Altimetry package[20] (PWA) measured the electrical state of the atmosphere below 140 km. We found that the electrical conductivity peaks at ~60 km. We might have seen evidence for lightning.

Observations of the electron and ion conductivities were made with two different techniques: relaxation and mutual impedance probes. The results of the relaxation probes (shown in Fig. 7a, b) indicate peaks in the electron/negative-ion conductivities at 60 km. Figure 7c shows that the altitude of the maximum in the conductivity (60 km) is confirmed by the mutual impedance probe measurements. This instrument gives the impedance of the medium at 45 Hz and yields a phase shift, which is sensitive to the presence of electrons only. The quadrupolar probe also records the spectrum of the electric signal induced in the probe environment by the 45 Hz stimulus, in the bandwidth 0–9.22 kHz (Fig. 8a, active mode).

The electric field due to natural wave emissions was investigated during the descent, using the receiving dipole of the mutual impedance probe in two frequency ranges, 0–11.5 kHz and 0–100 Hz (Fig. 8b, c, passive mode). This provided a unique opportunity to investigate *in situ* lightning and related phenomena (for example, corona discharges) on Titan[21] that would produce electromagnetic waves[38], excite global and local resonance phenomena in the surface–ionospheric cavity[39,40] and could drive a global electric circuit[22]. Several impulsive events have been observed during the descent, for example at 2,800 s. The narrow-band wave emission seen near 36 Hz is reminiscent of a possible resonance generated by lightning activity in the spherical waveguide formed by the surface of Titan and the inner boundary of its ionosphere, but should be interpreted with caution. A comparison of the records presented in Fig. 8a and b shows that the first spectrogram (active mode) not only displays the

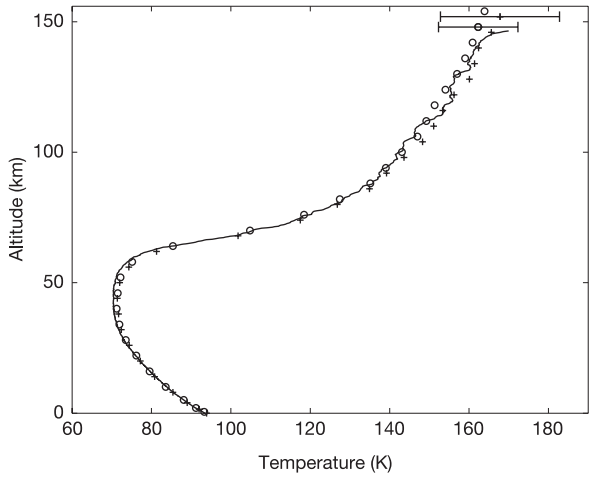

Figure 5 | Temperature profile of the lower atmosphere as measured by the temperature sensors, TEM[27] (expanded from Fig. 2). Temperature uncertainty is ±0.25 K in the range from 60 to 110 K, and ±1 K above 110 K. The temperature minimum of 70.43 K is reached at the tropopause (about 44 km; 115 ± 1 hPa). HASI temperatures are in very good agreement (within the error bars) with data obtained by Voyager radio occultation[2] (ingress, circles; egress, crosses) assuming a pure nitrogen atmosphere. The error bars for Voyager data are reported: ±15 K (egress) ±10 K (ingress) near the 200-km level, ±0.5 K at the tropopause. At the tropopause, HASI measured temperature values ~1 K colder than Voyager[2], but reanalysis of these data[3] suggested a similar temperature value (70.5 K) assuming a stratospheric composition of 98.5% N_2 plus 1.5% CH_4.

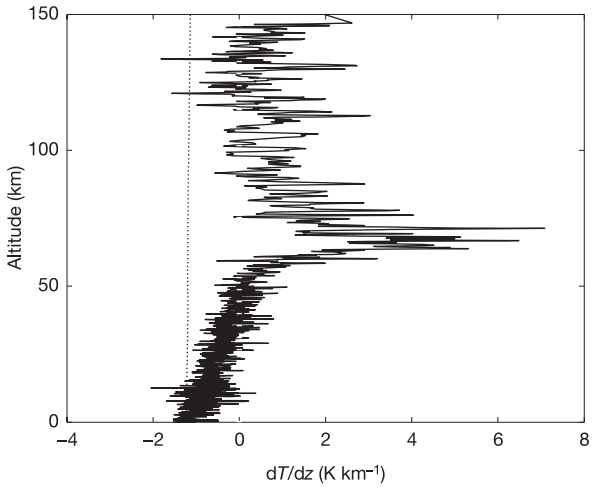

Figure 6 | The temperature lapse rate for the low atmosphere (expanded from Fig. 3). A number of inversion layers in the lower stratosphere and the strong temperature increase with altitude between 80 and 60 km are visible. Features present between 50 and 150 km could be related to turbulence due to Kelvin–Helmholtz instability induced by the large vertical shear of the wind speed, measured by the Doppler Wind Experiment[33]. The temperature gradient in this part of the atmosphere has been derived from direct temperature measurements with vertical spatial resolution of the order of 200–150 m above 60-km altitude, and decreasing from 70 m down to 11 m until the last kilometre.

signals seen in the second spectrogram (passive mode), but also includes a broadband emission in the altitude range 110–80 km, and to lesser extent at altitudes lower than 25 km. It is believed that the energy injected in the medium at 45 Hz is partly dissipated in nonlinear effects, which seems to strengthen the evidence for the presence of free charges in the upper atmosphere.

Surface

Before the probe landed, the nature of the surface was unknown. From the abundance of methane in its atmosphere, there was speculation that Titan might be covered by a methane ocean[41], but recent observations[14] have restricted the fraction of the surface covered with liquid to be just a few per cent. The probe touched down on a solid surface, which has properties something like wet sand[42]. The instruments continued to monitor the meteorological conditions for almost half an hour after impact.

The nature of Titan's surface at the landing site was investigated by spectral analysis of the Huygens radar return signal, the recording of the impact signature, *in situ* measurements of the ground electrical properties, and the surface environmental conditions.

The piezoresistive accelerometers of HASI recorded the impact instant at $T_0 + 2\,\mathrm{h}\,27\,\mathrm{min}\,49.840\,\mathrm{s}$ (where T_0 is the time of the parachute deployment device firing and corresponds to the beginning of the descent phase), when the event exceeded the threshold of $\sim 40\,\mathrm{m\,s^{-2}}$. A complete trace of the impact in the three orthogonal reference axes is shown in Fig. 9. The initial small peak in the X accelerometer data preceding the impact of the main probe may be related to a touch down on uneven topography, or the possible initial contact of a portion of the probe foredome, given the likely probe tilt at landing[42]. A sharp drop in acceleration is seen briefly in all three sensors at 8,869.86 s. The peak probe deceleration measured is $141\,\mathrm{m\,s^{-2}}$, in reasonable agreement with the value measured by the accelerometer of the Science Surface Package (SSP)[42]. Over the length of the full data set, two possible events are seen in all three axes, at impact ($\sim$8,869.86 s) and $\sim$3 s later at $\sim$8,872.2 s. These correspond respectively to the initial impact event, and then to some short-term settling that may be surface related, or probe related (parachute system dynamics or structural relaxation of foredome). Further

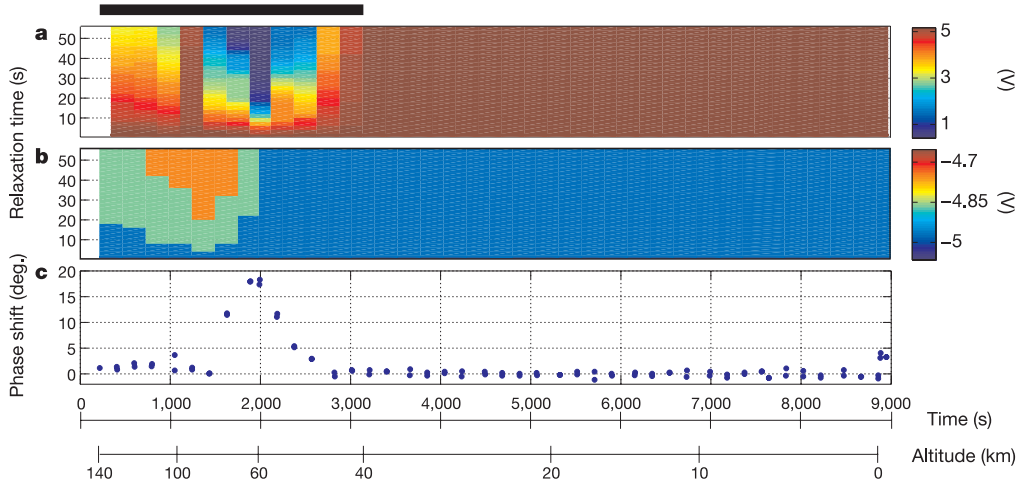

Figure 7 | A synopsis of PWA data: the signature of the ionosphere. The approximate extent of the ionized layer due to the interaction of cosmic rays with the atmosphere is indicated by a thick black line along the top axis. **a**, **b**, Relaxation carpets for $\Phi_o = +5$ V and -5 V, respectively. The relaxation probe, initially biased at a potential Φ_o with respect to the vehicle body, subsequently returns to its equilibrium potential, Φ_∞, with a time constant that yields the d.c. conductivity of the charges with polarity opposite to that of $\Phi_o - \Phi_\infty$. The measurements taken during each relaxation cycle form a string of pixels aligned with the ordinate axis; voltages are given by the colour scales shown on the right-hand side. The electrode potential is measured every 20 ms during the first second, then every 2 s for the reminder of each 1 min cycle. These panels give a visual impression of the speed at which the potential of a conductive body (colour coded) returns from ± 5 V to zero ('relaxes'), owing to the collection of ambient charges with opposite polarities. In the lower altitude range, for example, the colour of the carpet is uniform (brown for $+5$ V and blue for -5 V), which shows that the ambient charge densities are low. Above 40 km, on the contrary, the distinctive carpet patterns tell us that the probe voltage is strongly affected by the ionized environment. **c**, Mutual impedance phase shift, $\Delta\phi = \phi_o - \phi$ (non-calibrated). The a.c. conductivity is measured with a quadrupolar array. A current I with frequency 45 Hz and amplitude $\sim 10^{-10}$ A is injected between two transmitting electrodes, and the voltage V induced between two receiving electrodes 2 m apart is measured. If the phase of V/I at 45 Hz is ϕ_o in a vacuum and ϕ in a collisional medium, then the conductivity of the medium is proportional to $\tan(\phi_o - \phi)$.

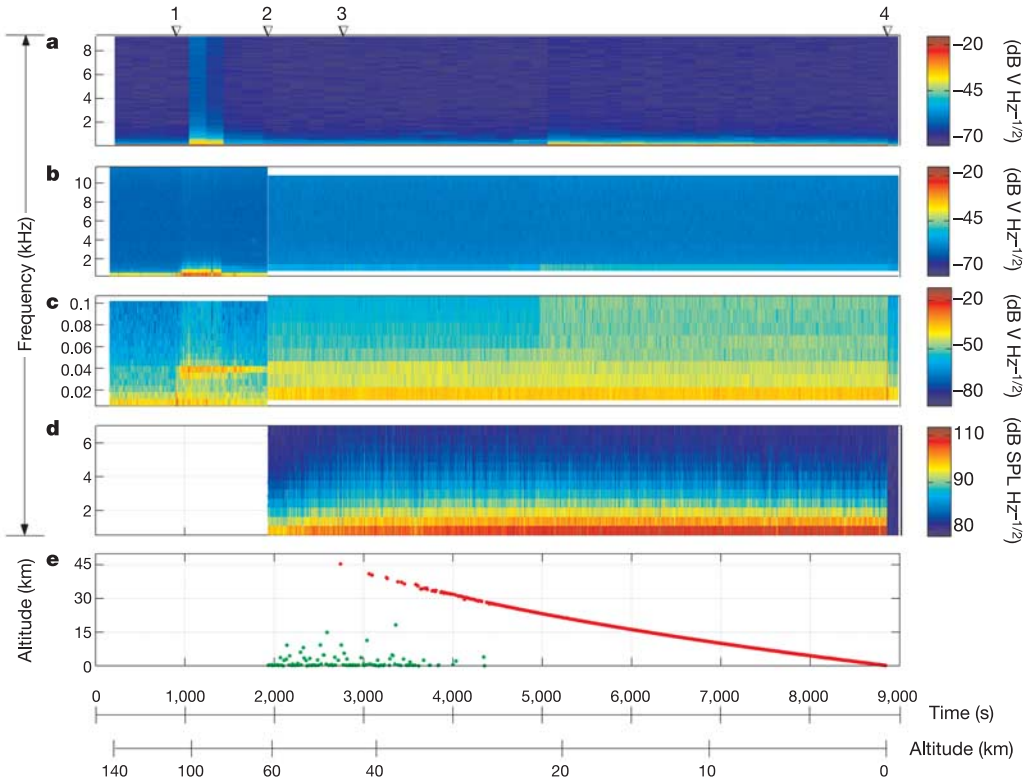

Figure 8 | A synopsis of PWA data: electric field, acoustic pressure and radar measurements. **a**, Dynamic spectrum of the voltage *V* measured between two electrodes 2 m apart, in the bandwidth 0–9.22 kHz, when a current stimulus *I* is injected between two transmitting electrodes. The spectrum of the signal provides information about its energy distribution as a function of frequency, at a given time. Successive spectra are represented by adjacent strings of pixels aligned with the ordinate axis, where spectral amplitude is coded in colour according to the logarithmic scale shown on the right-hand side. **b**, Dynamic spectrum of the voltage *V* measured with two electrodes 2 m apart, in the bandwidth 0–11.5 kHz, without current stimulus. **c**, Same as **b**, but in 0–100 Hz bandwidth. **d**, Dynamic spectrum of acoustic differential pressure in the bandwidth 0–6.7 kHz. A sound pressure level (SPL) of 0 dB corresponds to 20 μPa. The variability of the acoustic noise is caused by changes in the atmospheric density and wind velocity[50]. **e**, The altitude represented by the red dots is measured whenever the Radar Altimeter (RA) is locked on the surface; permanent lock is maintained from 34 km down to 150 m. At higher altitudes, the green dots indicate the distances at which the signal is returned by the atmosphere. Several events are identified with triangles along the top axis: (1) stabilizer parachute opening, (2) mode change, (3) impulsive event in **b**, (4) surface touch down. Discontinuities in time or frequency are artefacts due to mode change.

modelling of the probe structure behaviour is required to quantify these effects. Additionally, the area of stable data points immediately following the initial impact (8,870.1–8,870.3 s) may be due to a small bounce of the probe or to some structure vibrations. Integration of Y and Z axes after further processing, in combination with other sensors, will indicate any possible probe lateral movement. The integration of the accelerometer data gives a probe impact velocity of 4.33 m s^{-1}, in reasonable agreement with the values obtained by SSP[42] and from the velocity profile during the last kilometre of the descent as derived from pressure measurements. For the final rest position of the probe, the X servo accelerometer gives an estimate of the probe tilt of about 11°, in good agreement with SSP tilt sensors.

At the surface, the HASI temperature and pressure sensors monitored the meteorological conditions for almost half an hour after the impact, measuring a temperature of 93.65 ± 0.25 K and a pressure of 1,467 ± 1 hPa. The complex permittivity of the surface material is measured after impact with the PWA mutual impedance probe[43], at five frequencies. As a first estimation, the mean relative permittivity within the sensor range (radius 1 m, depth 2 m) is of the order of 2, in reasonable agreement with the measurements performed with the radar on board Cassini[19].

In addition to providing altitude (Fig. 8), the Radar Altimeter measures the signal backscattered within the footprint of the beam, whose diameter is 0.14 times the altitude. This signal is strong and smooth with small variations over the ground track, indicating a

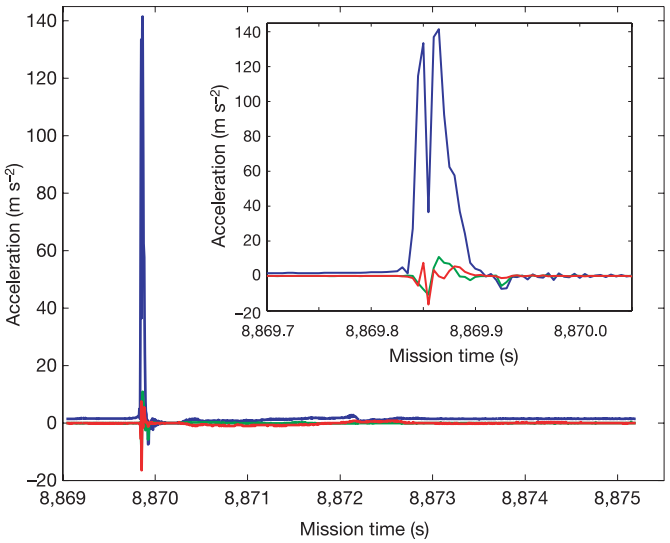

Figure 9 | The HASI signature of the impact trace, at 200 samples per second. The complete impact trace (6 s) is shown; the inset shows a magnified view of the deceleration peak. The X sensor (blue line) is aligned to the probe symmetry axis, corresponding to the descent direction. The Y (green line) and Z (red line) sensors are mounted orthogonal to the Huygens probe symmetry axis.

surface with little relief. The atmosphere was scanned and return signal from droplets was searched for, but no significant signature of rain could be found.

Discussion

Although the HASI data have now provided a great wealth of information on the conditions in the atmosphere and at the surface of Titan, many questions and challenges remain.

Atmospheric structure. The HASI temperature profile in the lower atmosphere was compared to the separate egress and ingress profiles based on the Voyager occultation experiment 25 years earlier. This comparison suggests that the atmosphere of Titan in mid-latitudes is uniform and slowly changing in accordance with model predictions. The open question is the poleward extent of this non-variability, given the latitudinal temperature gradient in the stratosphere inferred from infrared data[44,45]. One interpretation of the south polar clouds is that they are due to heating associated with polar summer warming[46,47]. If this is true, then the temperature profile in the polar summer should be different from the mid-latitude profiles sampled here, and could be revealed by Cassini infrared mapping[45] and radio science[48]. In the middle and upper atmosphere (above 300 km), the prominent wave-like structure reported here requires further modelling to unambiguously identify the causal mechanisms. The observed vertical variation would suggest that large-scale temperature gradient in this region is also time variable. Unfortunately, the necessary observations of the time and spatial evolution of these structures must await future missions.

The atmosphere was scanned by the radar altimeter (before getting in lock), but no significant signature of rain was found. The instrument sensitivity to mass loadings of methane or other hydrocarbon droplets needs to be determined so that an upper limit to droplet mass loadings can be estimated.

Atmospheric electricity. The maximum in the conductivity due to positive ions, 20 km above the peak electron conductivity at 60 km, demands the presence of sufficient aerosols or electrophilic species in order to preserve charge neutrality. The altitude of the maximum conductivity due to electrons lies below that predicted by theoretical models[35–37]. Several pulses similar to terrestrial sferics (natural electromagnetic waves) have been observed during the descent. Large convective clouds were observed near the south pole during the summer season[17] and low-frequency electromagnetic waves could easily propagate from the south pole to the Huygens location. Lightning activity would also be consistent with the observations of waves in the Schumann frequency range.

Nature of the surface. The lack of any rhythmic motion during the half hour of operation on the surface indicated that the probe had landed on a solid surface rather than a liquid, which agrees with the image taken after the landing[49]. The measured relative permittivity (of the order of 2) constrains the soil composition. No evidence for the presence of liquid phase on the surface was returned by the signal of the radar altimeter.

The HASI measurements of the atmospheric structure, electrical state and surface properties provide a unique insight into Titan's characteristics, unequalled in any planetary atmosphere except the Earth's. The many discoveries and puzzles will require synergetic analysis with the Cassini orbiter observations and years of laboratory and modelling efforts to solve.

Received 28 May; accepted 11 October 2005.
Published online 30 November 2005.

1. McKay, C. P., Pollack, J. B. & Courtin, R. The thermal structure of Titan's atmosphere. *Icarus* **80,** 23–53 (1989).
2. Lindal, G. F. *et al.* The atmosphere of Titan—an analysis of the Voyager 1 radio occultation measurements. *Icarus* **53,** 348–363 (1983).
3. Lellouch, E. *et al.* Titan's atmosphere and hypothesized ocean: a reanalysis of the Voyager 1 radio-occultation and IRIS 7.7 μm data. *Icarus* **79,** 328–349 (1989).
4. Vervack, R. J., Sandel, B. R. & Strobel, D. F. New perspectives on Titan's upper atmosphere from a reanalysis of the Voyager 1 UVS solar occultations. *Icarus* **170,** 91–112 (2004).
5. Coustenis, A. *et al.* Titan's atmosphere from ISO mid-infrared spectroscopy. *Icarus* **161,** 383–403 (2003).
6. Hubbard, W. B. *et al.* Results for Titan's atmosphere from its occultation of 28 Sagittarii. *Nature* **343,** 353–355 (1990).
7. Sicardy, B. *et al.* The structure of Titan's stratosphere from the 28 Sgr occultation. *Icarus* **142,** 357–390 (1999).
8. Tracadas, P. W., Hammel, H. B., Thomas-Osip, J. E. & Elliot, J. L. Probing Titan's atmosphere with the 1995 August stellar occultation. *Icarus* **153,** 285–294 (2001).
9. Bouchez, A. H. *et al.* Adaptive optics imaging of a double stellar occultation by Titan. *Bull. Am. Astron. Soc.* **34,** 881 (2002).
10. Sicardy, B. *et al.* The two stellar occultations of November 14, 2003: revealing Titan's stratosphere at sub-km resolution. *Bull. Am. Astron. Soc.* **36,** 1119 (2004).
11. Lellouch, E., Hunten, D., Kockarts, G. & Coustenis, A. Titan's thermosphere profile. *Icarus* **83,** 308–324 (1990).
12. Yelle, R. V. Non-LTE models of Titan's upper atmosphere. *Astrophys. J.* **383,** 380–400 (1991).
13. Yelle, R. V., Strobel, D. F., Lellouch, E. & Gautier, D. *Engineering Models for Titan's Atmosphere* 243–256 (ESA SP-1177, European Space Agency, Noordwijk, 1997).
14. Campbell, D. B., Black, G. J., Carter, L. M. & Ostro, S. J. Radar evidence for liquid surfaces on Titan. *Science* **302,** 431–434 (2003).
15. Coustenis, A. *et al.* Maps of Titan's surface from 1 to 2.5 μm. *Icarus* **177,** 89–105 (2005).
16. Meier, R., Smith, B. A., Owen, T. C. & Terrile, R. J. The surface of Titan from NICMOS observations with the Hubble Space Telescope. *Icarus* **145,** 462–473 (2000).
17. Porco, C. C. *et al.* Imaging of Titan from the Cassini spacecraft. *Nature* **434,** 159–168 (2005).
18. Brown, R. H. *et al.* Cassini Visual and Infrared Mapping Spectrometer (VIMS): Results for the SOI- and near-SOI period of the Cassini orbital tour. *Astron. Astrophys.* (submitted).
19. Elachi, C. *et al.* Cassini radar views the surface of Titan. *Science* **308,** 970–974 (2005).
20. Grard, R. *et al.* An experimental investigation of atmospheric electricity and lightning activity to be performed during the descent of the Huygens probe onto Titan. *J. Atmos. Terr. Phys.* **57,** 575–578 (1995).
21. Desch, S. J., Borucki, W. J., Russell, C. T. & Bar-Nun, A. Progress in planetary lightning. *Rep. Prog. Phys.* **65,** 955–997 (2002).
22. Tokano, T., Molina-Cuberos, G. J., Lammer, H. & Stumptner, W. Modelling of thunderclouds and lightning generation on Titan. *Planet. Space Sci.* **49,** 539–560 (2001).
23. Lebreton, J.-P. & Matson, D. L. The Huygens probe: science, payload and mission overview. *Space Sci. Rev.* **104,** 59–100 (2002).
24. Fulchignoni, M. *et al.* The characterization of Titan's atmospheric physical properties by the Huygens Atmospheric Structure Instrument (HASI). *Space Sci. Rev.* **104,** 395–431 (2002).
25. Zarnecki, J. C. *et al. In-Flight Performances of the Servo Accelerometer and Implication for Results at Titan* 71–76 (ESA SP-544, European Space Agency, Noordwijk, 2004).
26. Lebreton, J. P. *et al.* An overview of the descent and landing of the Huygens probe on Titan. *Nature* doi:10.1038/nature04347 (this issue).
27. Ruffino, G. *et al.* The temperature sensor on the Huygens probe for the Cassini mission: Design, manufacture, calibration and tests of the laboratory prototype. *Planet. Space Sci.* **44–10,** 1149–1162 (1996).
28. Harri, A.-M. *et al.* Scientific objectives and implementation of the Pressure Profile Instrument (PPI/HASI) for the Huygens spacecraft. *Planet. Space Sci.* **46,** 1383–1392 (1998).
29. Mäkinen, T. Processing the HASI measurements. *Adv. Space Res.* **17,** 217–222 (1996).
30. Niemann, H. B. *et al.* The abundances of constituents of Titan's atmosphere from the GCMS instrument on the Huygens probe. *Nature* doi:10.1038/nature04122 (this issue).
31. Hinson, D. P. & Tyler, G. L. Internal gravity waves in Titan's atmosphere observed by Voyager radio occultation. *Icarus* **54,** 337–352 (1983).
32. Friedson, A. J. Gravity waves in Titan's atmosphere. *Icarus* **109,** 40–57 (1994).
33. Bird, M. K. *et al.* The vertical profile of winds on Titan. *Nature* doi:10.1038/nature04060 (this issue).
34. Molina-Cuberos, G. J., López-Moreno, J. J., Rodrigo, R. & Lara, L. M. Chemistry of the galactic cosmic ray induced ionosphere of Titan. *J. Geophys. Res.* **104,** 21997–22024 (1999).
35. Borucki, W. J. *et al.* Predictions of the electrical conductivity and charging of the aerosols in Titan's atmosphere. *Icarus* **72,** 604–622 (1987).
36. Borucki, W. J., Whitten, R. C., Bakes, E. L. O., Barth, E. & Tripathi, S. Predictions of the electrical conductivity and charging of the aerosols in Titan's atmosphere. *Icarus* (in the press).
37. Molina-Cuberos, G. J., López-Moreno, J. J., Rodrigo, R. & Schwingenschuh, K. Capability of the Cassini/Huygens PWA-HASI to measure electrical conductivity in Titan. *Adv. Space Res.* **28,** 1511–1516 (2001).

38. Schwingenschuh, K. *et al.* Propagation of electromagnetic waves in the lower ionosphere of Titan. *Adv. Space Res.* **28,** 1505–1510 (2001).
39. Nickolaenko, A. P., Besser, B. P. & Schwingenschuh, K. Model computations of Schumann resonance on Titan. *Planet. Space Sci.* **51,** 853–862 (2003).
40. Morente, J. A., Molina-Cuberos, G. J., Portí, J. A., Schwingenschuh, K. & Besser, B. P. A study of the propagation of electromagnetic waves in Titan's atmosphere with the TLM numerical method. *Icarus* **162,** 374–384 (2003).
41. Lunine, J. I., Stevenson, D. J. & Yung, Y. L. Ethane ocean on Titan. *Science* **222,** 1229–1230 (1983).
42. Zarnecki, J. C. *et al.* A soft solid surface on Titan as revealed by the Huygens Surface Science Package. *Nature* doi:10.1038/nature04211 (this issue).
43. Hamelin, M. *et al.* Surface and sub-surface electrical measurement of Titan with the PWA-HASI experiment on Huygens. *Adv. Space Res.* **26,** 1697–1704 (2000).
44. Coustenis, A. & Bézard, B. Titan's atmosphere from Voyager infrared observations. IV. Latitudinal variations of temperature and composition. *Icarus* **115,** 126–140 (1995).
45. Flasar, F. M. *et al.* Titan's atmospheric temperatures, winds, and composition. *Science* **308,** 975–978 (2005).
46. Brown, M. E., Bouchez, A. H. & Griffith, C. A. Direct detection of variable tropospheric clouds near Titan's south pole. *Nature* **420,** 7995–7997 (2002).
47. Tokano, T. Meteorological assessment of the surface temperatures on Titan: constraints on the surface type. *Icarus* **173,** 222–242 (2005).
48. Kliore, A. J. *et al.* Cassini Radio Science. *Space Sci. Rev.* **115,** 1–70 (2004).
49. Tomasko, M. G. *et al.* Rain, winds and haze during the Huygens probe's descent to Titan's surface. *Nature* doi:10.1038/nature04126 (this issue).
50. Ksanfomaliti, L. V. *et al.* Acoustic measurements of the wind velocity at the Venera 13 and Venera 14 landing sites. *Sov. Astron. Lett* **8(**4), 227–229 (1982).

Acknowledgements We thank the following people for their contributions to the realization of the HASI experiment: A. Buccheri, R. DeVidi, and M. Cosi of Galileo Avionica, A. Aboudan, S. Bastianello and M. Fabris of CISAS, M. Chabassière of LPCE, V. Brown, J.M. Jeronimo and L.M. Lara of IAA, R. Hofe of IWF, A. Smit, L. Smit and J. Van der Hooke from RSSD-ESTEC, H. Jolly from the UK, R. Pellinen, G. Leppelmeier, T. Siili, P. Salminen from FMI, and at the Aerodynamics Laboratory of Helsinki University of Technology T. Siikonen and B. Fagerström. HASI has been realised and operated by CISAS under a contract with the Italian Space Agency (ASI), with the participation of RSSD, FMI, IAA, IWF, LPCE and PSSRI sponsored by the respective agencies: ESA, TEKES, CSIC, BM:BWK, CNES and PPARC. We also acknowledge the long years of work by some hundreds of people in the development and design of the Huygens probe. The Huygens probe is part of the Cassini-Huygens mission, a joint endeavour of the National Aeronautics and Space Administration (NASA), the European Space Agency (ESA) and the Italian Space Agency (ASI).

Author Information Reprints and permissions information is available at npg.nature.com/reprintsandpermissions. The authors declare no competing financial interests. Correspondence and requests for materials should be addressed to F.F. (francesca.ferri@unipd.it).

Paper 2

Calibrating electric instruments of the Huygens Probe and modelling the dielectric properties of the atmosphere and of the surface of Titan

Simões, F., Brown, V., Chabassière, M., Falkner, P., Ferri, F., Fulchignoni, M., Grard, R., Hamelin, M., Hofe, R., Jernej, I., Lara, L., López-Moreno, J.J., Molina-Cuberos, G., Rodrigo, R., Schwingenschuh, K., Trautner, R.

Proceedings of the Comsol Multiphysics Conference Paris-2005, 247-250 (2005)

F. Simões *et al.*

Calibrating Electric Instruments of the Huygens Probe and Modelling the Dielectric Properties of the Atmosphere and of the Surface of Titan

Abstract In 14 January, 2005, the Huygens Probe has descent through the atmosphere of Titan and has survived to touchdown, collecting data in the atmosphere and on the surface of the largest moon of Saturn. One of the instruments, the Huygens Atmospheric Structure Instrument (HASI), includes the Permittivity, Waves, and Altimetry (PWA) analyser, which is a subsystem for studying the electric activity of the atmosphere and for measuring the dielectric properties of the surface at the landing site. The PWA analyser includes several electric sensors, namely two Relaxation Probes (RP) and a Mutual Impedance Probe (MIP). The calibration of these sensors is crucial for achieving good quality measurements of the atmospheric parameters and for modelling the dielectric properties of the ground. Furthermore, the final attitude of the probe on the surface and its complex geometry require proper modelling of electrostatic equations, namely Poisson equation. In this work we briefly describe the finite element models implemented in FEMLAB, present simulations of electric parameters and discuss the implications in data analysis.

Keywords Electrostatics – Space Science FEMLAB

1 Introduction

After a journey of about seven years, the Cassini-Huygens mission, a joint project of the National Aeronautics and Space Administration (NASA) and the European Space Agency (ESA), is inserted in orbit around Saturn. In January 14, 2005, the Huygens Probe descends through the atmosphere of Titan and successfully lands on the surface.

The Permittivity, Waves, and Altimetry (PWA) analyser, which is a subsystem of the Huygens Atmospheric Structure Instrument (HASI), collects data during the descent through the atmosphere, namely using two Relaxation Probes (RP) and a Mutual Impedance Probe (MIP). Furthermore, the MIP sensor also measures the dielectric properties of the ground in the vicinity of the landing site.

The RP sensors are two thin metallic disks (ϕ=7cm, h=1mm) and are used to measure both the electron and ion conductivities of the atmosphere. These electrodes are biased at potentials +5V, 0V, or –5V, up to time t=0, and subsequently returned to their equilibrium, or floating, potential. The relaxation time of the sensor allows the calculation of the electron and ion conductivities of the medium.

The MIP sensor is made of four metallic ring electrodes, specifically two transmitters (ϕ=10cm and 1mm thick) and two receivers (ϕ=6.5cm and 1mm thick). The complex permittivity of the environment is measured with this quadrupolar array. An a.c. current is inject between the two transmitters and the voltage perturbation induced in the medium is measured by the two receivers. Furthermore, the two receivers of the array, functioning in the passive mode as an antenna, are able to measure electric fields with frequency up to 10kHz (Grard *et al.*, 1995).

2 The Numerical Models

The complexity of the Huygens Probe and the distribution of the PWA electrodes (Figure 1) prevent any useful analytical solution. Thus, a finite element method is required for solving electrostatic equations, which are essential in support of the calibration of the sensors.

The finite element models developed in FEMLAB includes the resolution of the equations

$$\nabla\cdot\left(\varepsilon(r)\nabla\Phi(r)\right)=0 \qquad (01)$$

F. Simões
Centre d'Etude des Environnements Terrestre et Planétaires (CETP), Saint Maur des Fossès, France
Tel: + 33 (0)1 45 11 42 73
Fax: + 33 (0)1 48 89 44 33
E-mail: fernando.simoes@cetp.ipsl.fr

and

$$\nabla\cdot\left(\varepsilon(r)\nabla\Phi(r)\right)=-\rho(r) \qquad (02)$$

where $\Phi(r)$ is the electric potential, $\varepsilon(r)$ is the permittivity of the medium, and $\rho(r)$ is the charge distribution.

Equations (01) and (02) are solved with many boundary conditions, namely for computing self and mutual capacitance, transverse and longitudinal electric field sensitivity, and the coupling between the Probe and an heterogeneous embedding medium.

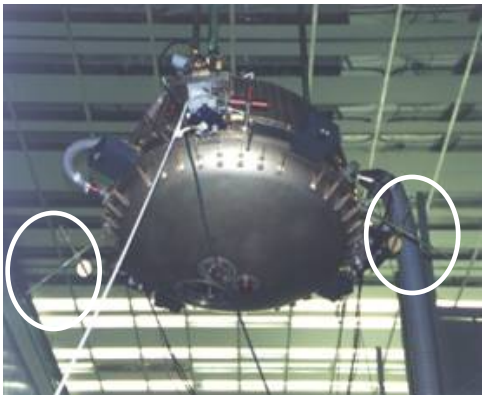

Figure 1 - The Huygens Probe and the two deployable booms (circle marks), where it is possible to observe the set of electrodes.

The complexity of the booms and significant size difference between the body of the Huygens Probe (diameter ~1.3m) and the sensors (thickness ~1mm) require highly intricate meshes (Model A). The first approximation considers electrodes as spheres with equivalent capacitances. However, in some models, such as for calculating mutual capacitances of the system vessel-electrodes, where boundary conditions at infinite are required ($\Phi_\infty=0$), one non structured mesh is not enough to solve the problem. Therefore, the domain is split in two regions and the meshes are matched in the interface. Furthermore, boundary condition values are approximated with the potential generated by a set of spheres at large distance (Durand, 1964). The analytical solution considering spherical bodies allows not only the validation of the model but also the minimization of the error due to boundary perturbations.

A more simplified model (Model B) is used for calculating the electric potential perturbation generated by the body of the probe, when the electrodes are embedded in a constant electric field. An important goal of the measurements performed during the descent of the Probe in Titan is to infer the presence of a fair weather field, which is a vertical d.c. electric field. In order to calculate the electric perturbation induced by the probe, several laboratory tests are carried out and modelled in FEMLAB. The experimental apparatus includes a large plate capacitor at potential Φ=-5V (bottom plate) and Φ=+5V (top plate), separated by a distance of d=3.8m, with length l=5.4m and width w=4.9m. The probe is held in the centre of the capacitor and the walls are either absent or at a potential varying with height ($\Phi_{wall}=2\Phi y/d$, where y is the height measured from the centre). In the second case edge effects are minimized, and all boundary conditions of this model are straightforward to implement because of a solution at infinite is not required.

For deriving the dielectric properties of the landing site, i.e. the permittivity and the conductivity of the medium, the calibration of the MIP sensor must include not only the internal electric parameters but also the final attitude of the probe (Model C). The complex geometry of the Huygens Probe, and also its electric coupling with the soil and the atmosphere, plays an important role evaluating the properties of the medium.

The model used in this problem considers the probe partially buried in a soil of unknown dielectric properties (Figure 2). The main goal is to compare the electric potential obtained in this model with reference values obtained in air, which are used for fitting the dielectric parameters of the soil.

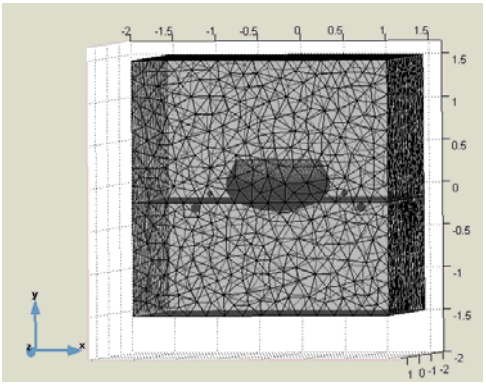

Figure 2 - Mesh model (Model C) for a probe partially buried in the soil - air (top layer) and soil (bottom layer).

3 Discussion and Conclusions

From Model A it is possible to calculate the self capacitance of the Huygens Probe by removing the electrodes, setting its surface potential to 1V and grounding the external boundary conditions. The integration of charge density on the surface of the Probe gives its self capacitance, which is (61.5 ± 0.8)pF. Then, including the relaxation probes, it is possible to compute the mutual capacitance between the body of the probe and the relaxation probes electrodes which yields (-1.8±0.1)pF. This value is computed by setting the relaxation probe potential to 1V and measure the surface charge density induced in the large vessel. The mutual capacitance value is negative, as is foreseen by the electrostatics theory.

These values are required for calibrating the relaxation constant of the probes. Although the calculation of these values is very simple, namely using post processing functions of FEMLAB, good accuracy is very difficult to achieve because of geometry constraints and boundary conditions.

The perturbation induced by the presence of the body of the Probe has several effects in the measurements (Model B). On one hand, in the region between the body of the probe and the electrodes, the field lines are compressed and the measured values lower than the real ones. The maximum difference can be the order of 15% depending on the angle between the Probe and the electric field. On the other hand, farther from the body of the large vessel, the equipotentials are expanded and the measured values are higher than the unperturbed solution (Figure 3). Furthermore, as the presence of the large vessel induces potential distortion around the relaxation probes, the charge distributions produced by electrons and ions around the electrodes lose their spherical symmetry. This influence is not fully understood so far and is under investigation. Moreover, the relative position between the relaxation probes, the body of the Huygens Probe and the hypothetical vertical electric field varies during the descent trajectory, which demands for more sophisticated models (Figure 4 and Figure 5).

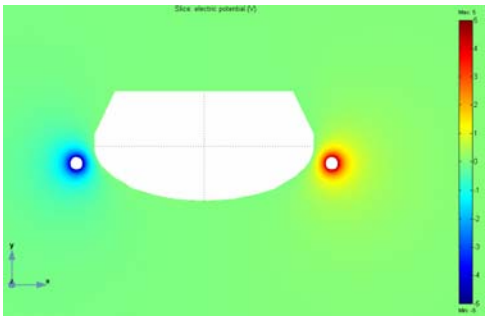

Figure 3 - Slice in the plane z=0 that shows the electric potential distribution generated by the two relaxation probes (Model A). The potential of the electrodes is symmetric (+5V and –5V) and the perturbation induced by the body of the probe is visible.

A multiphysics model including electrons, heavy ions and neutrals is being implemented. The system comprises the modelling of electrostatics, particle diffusion and incompressible flow equations for a more accurate analysis of the global dynamics and its influence in the electric measurements.

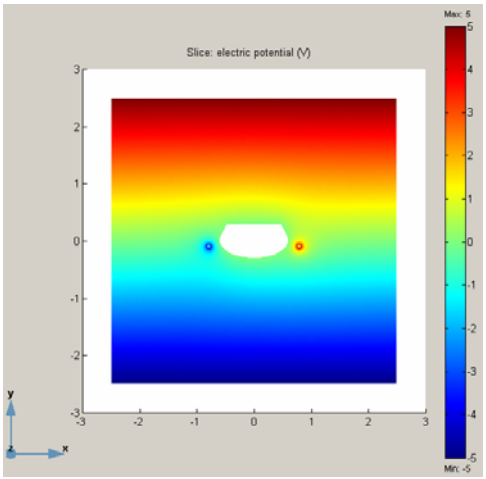

Figure 4 - Slice in the plane z=0 that shows the electric potential distribution generated by the two relaxation probes and the vertical electric field (Model B).

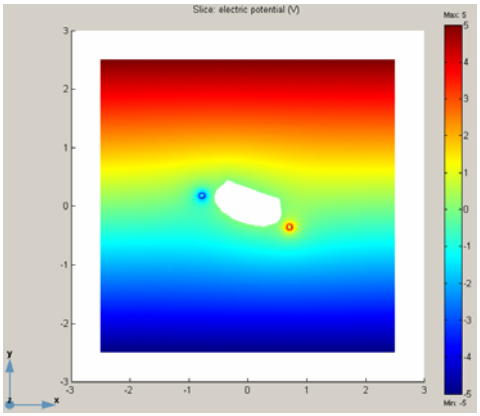

Figure 5 - Slice in the plane z=0 that shows the electric potential distribution generated by the two relaxation probes and a non perpendicular (20°) electric field (Model B).

The MIP sensor has successfully obtained measurements from the surface of Titan during 30min. Although the results are strongly dependent of the attitude of the probe on the ground (Model C), and several parameters are not fully determined yet, the order of magnitude of the permittivity value of the ground can be established (Fulchignoni *et al.*, 2005). Future improvements can be included in the model as far as the attitude of the probe on the ground is known, and improved parameters can be determined, namely the dielectric constant value. These constraints may provide some interesting information regarding the characterisation of the composition of Titan at the Huygens landing site.

These simulations were performed in FEMLAB 2.3 and FEMLAB 3.1i.

Authors
F. Simões, V. Brown, M. Chabassière, P. Falkner, F. Ferri, M. Fulchignoni, R. Grard, M. Hamelin, R. Hofe, I. Jernej, L. Lara, J. J. Lopez-Moreno, G. Molina-Cuberos, R. Rodrigo, K. Schwingenschuh and R. Trautner

---

References

1. R. Grard *et al.*, An experimental investigation of atmospheric electricity and lightning activity to be performed during the descent of the Huygens Probe on Titan, *J. Atmos. Terr. Phys.*, **57**, 575-585, (1995).
2. E. Durand, *Electrostatics*, volume 2, chap. 3, Masson et Cie Éditeurs, Paris, (in French), (1964).
3. M. Fulchignoni *et al.*, Titan's Physical Characteristics Measured by the Huygens Atmospheric Structure Instrument (HASI), submitted to *Nature*, (2005).

Paper 3

Electric properties and related physical characteristics of the atmosphere and surface of Titan

Grard, R., Hamelin, M., López-Moreno, J.J., Schwingenschuh, K., Jernej, I., Molina-Cuberos, G.J., Simões, F., Trautner, R., Falkner, P., Ferri, F., Fulchignoni, M., Rodrigo, R., Svedhem, H., Béghin, C., Berthelier, J.-J., Brown, V.J.G., Chabassière, M., Jeronimo, J.M., Lara, L.M., Tokano, T.

Planetary and Space Science **54**, 1124–1136 (2006)

Available online at www.sciencedirect.com
ScienceDirect
Planetary and Space Science 54 (2006) 1124–1136
Planetary and Space Science
www.elsevier.com/locate/pss

Electric properties and related physical characteristics of the atmosphere and surface of Titan

R. Grard[a], M. Hamelin[b], J.J. López-Moreno[c], K. Schwingenschuh[d], I. Jernej[d], G.J. Molina-Cuberos[c,e], F. Simões[b,*], R. Trautner[a], P. Falkner[a], F. Ferri[f], M. Fulchignoni[g], R. Rodrigo[c], H. Svedhem[a], C. Béghin[h], J.-J. Berthelier[b], V.J.G. Brown[c], M. Chabassière[h], J.M. Jeronimo[c], L.M. Lara[c], T. Tokano[i]

[a]*RSSD, ESA-ESTEC, European Space Agency, Keplerlaan 1, 2200 AG Noordwijk, The Netherlands*
[b]*CETP/IPSL-CNRS 4, Avenue de Neptune, 94107 Saint Maur, France*
[c]*Instituto de Astrofisica de Andalucia IAA-CSIC, Camino Bajo de Huetor, 50, 18008 Granada, Spain*
[d]*Space Research Institute, Austrian Academy of Sciences (IWF), Schmiedlstrasse 6, 8042 Graz, Austria*
[e]*Applied Electromagnetic Group, Department of Physics, University of Murcia, Murcia 30100, Spain*
[f]*CISAS "G. Colombo", Università di Padova, Via Venezia 15, 35131 Padova, Italy*
[g]*LESIA, Observatoire de Paris, 5 Place Janssen, 92195 Meudon, France*
[h]*LPCE-CNRS, 3A, Avenue de la Recherche Scientifique, 45071 Orléans cedex 2, France*
[i]*Institut für Geophysik und Meteorologie, Universität zu Köln, Albertus-Magnus-Platz, 50923 Köln, Germany*

Received 1 December 2005; received in revised form 24 February 2006; accepted 4 May 2006
Available online 4 August 2006

Abstract

The permittivity, waves and altimetry (PWA) instrument was designed for the investigation of the electric properties and other related physical characteristics of the atmosphere of Titan, from an altitude around 140 km down to the surface. PWA carried sensors to measure the atmospheric conductivity, and record electromagnetic and acoustic waves up to frequencies of 11.5 and 6.7 kHz, respectively. PWA also measured the relief roughness during the descent and the permittivity of the surface after touchdown. The measurements and the results of the preliminary analysis are presented. An ionized layer is detected at altitudes above 50 km, using two independent techniques, and the presence of free electrons in the upper atmosphere is confirmed. An electric signal at around 36 Hz is observed throughout the descent, but it is not yet confirmed that this emission is unambiguously related to a resonance of the ionospheric cavity. The relative dielectric constant of Titan's surface material is nearly 2 and the electric conductivity 4×10^{-10} S m^{-1}. The electric properties of the surface seem to evolve after touch-down, possibly due to a local warming of the landing site by the Huygens Probe body.

Keywords: Titan; Atmospheric electricity; Electric fields; Acoustic pressure; Surface properties

1. Introduction

The permittivity, waves and altimetry (PWA) analyser (Grard et al., 1995) is one element of the scientific payload carried by the Huygens Probe that landed on Titan, on 14 January 2005. PWA is one component of the Huygens Atmospheric Structure Instrument (HASI), which is dedicated to the study of the physical properties of the gaseous environment of Saturn's largest satellite (Fulchignoni et al., 2002).

Atmospheric electricity plays a primordial role in the production of aerosols and soots that contain traces of complex organic, possibly pre-biotic, constituents. The objectives of PWA are therefore to characterize in situ the electrical state of Titan's environment down to the surface,

*Corresponding author. Tel.: +33 1 4511 4273; fax: +33 1 48 89 44 33.
E-mail address: Fernando.Simoes@cetp.ipsl.fr (F. Simões).

0032-0633/$ - see front matter © 2006 Elsevier Ltd. All rights reserved.
doi:10.1016/j.pss.2006.05.036

at altitudes beneath the reach of orbiters, and to study features that cannot be resolved with remote sensing or propagation techniques (Lindal et al., 1983; Wahlund et al., 2005).

Measuring the altitude of the lower ionospheric boundary, the strength of vertical quasi-static electric fields, the conductivity of the atmosphere and that of the surface may tell us whether a global circulation current similar to that observed on Earth is conceivable on Titan. Searching for the electromagnetic and acoustic signatures of electrical discharges may provide direct evidences for such a mechanism.

PWA was operated during 2 h 25 min from an altitude of 141 km down to the surface, and during 32 min after landing. The first measurements were performed at 09:12:57 UT and an overall data volume of 551 Kbytes was collected. An equivalent amount of information was lost, due to the failure of one of the recorders onboard the Cassini Saturn Orbiter, which relayed the telemetry down to Earth. This data loss reduces the time or frequency resolution of most measurements by a factor of 2. For our observations, this penalty is acceptable sometimes, and extremely detrimental in other instances, depending on the data products.

After recapitulating the main functions and technical features of the instrument, we present the measurements collected by the different sensors: electric field antenna, mutual impedance probe (MIP), relaxation probe, acoustic pressure sensor and radar. The time of the measurements is counted from the nominal beginning of the descent, at $T_0 = 09:10:21$ UT, when the pilot parachute is deployed. The data analysis is in progress, and the interpretation of the measurements is still preliminary.

2. Experimental approach

2.1. The instrument

PWA consists essentially of a data processing unit that samples; digitises; and processes the signals collected with several sensors (Falkner, 2004). Two deployable booms carry six electrodes dedicated to an investigation of the electric characteristics of Titan's environment (Fig. 1). The main functions of PWA are as follows: (1) The atmospheric conductivity is measured with two relaxation probes, RP1 and RP2. (2) The complex permittivity of the environment is measured during the descent, and after landing, with a MIP made of four ring electrodes, TX1, TX2, RX1, RX2. (3) Electric fields in the ELF and VLF ranges, and lightning events are monitored with the dipole antenna made by RX1 and RX2. (4) DC and quasi-static electric fields can be evaluated from the potential difference between the Huygens Probe structure and either RP1 or RP2. (5) A pressure sensor mounted on a fixed boom monitors the acoustic noise generated by natural atmospheric phenomena. (6) The return signals of the radars (RAU) are down-converted in the radar altimeter extension (RAE) and analysed to yield information about atmospheric backscatter and surface topography.

All signals are first processed in the PWA-A analogue section. The data are then acquired by the PWA-D digital section, via a 16-bit analogue to digital converter (ADC), and submitted to a specific processing for each operation mode. The architecture of PWA, including the HASI-1 and HASI-2 preamplifiers, and the interfaces with HASI and RAU are illustrated in Fig. 2. The formatted information is

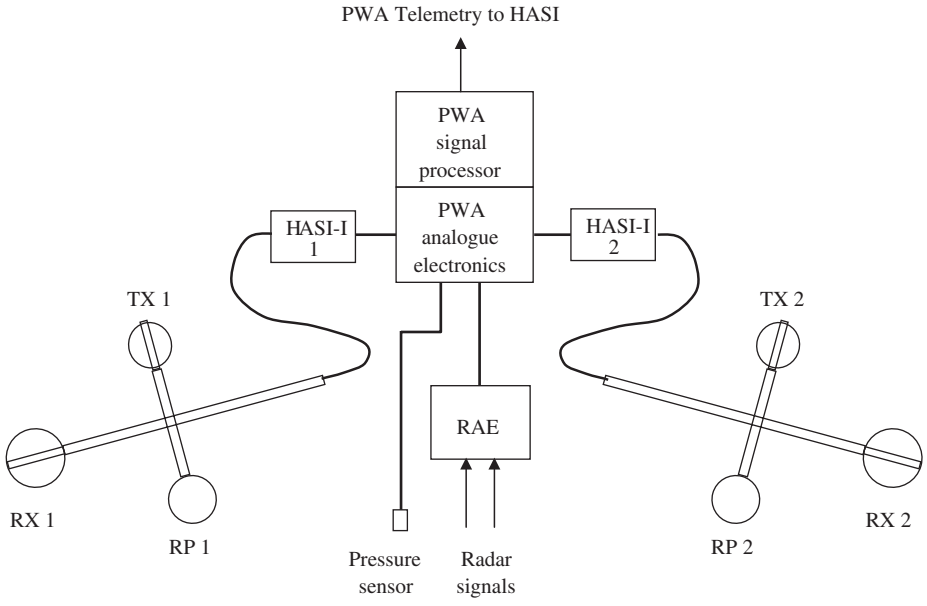

Fig. 1. PWA instrument architecture. The digital and analogue electronics, as well as the radar altimeter extension are accommodated in the HASI experiment box. The HASI-1 and HASI-2 preamplifiers are located near the deployable booms. The pressure sensor is mounted on a fixed stub.

finally distributed between channels, which are transmitted towards the Cassini Orbiter on two independent radio links.

2.2. Modes of operation

The PWA instrument is operated in six different modes, which are successively selected depending upon time or altitude (Table 1). The various type of measurements are labelled as follows: VLF electric fields, AC; ELF electric fields, SH; relaxation probes, RP; mutual impedance probe, MI; acoustic pressure, AU; radar, RAE.

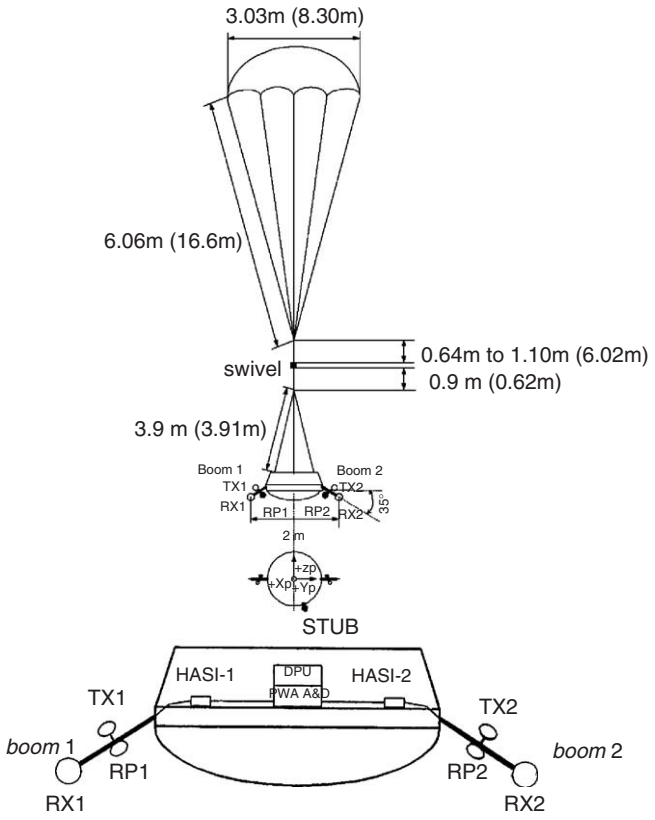

Fig. 2. Configuration of the Huygens Probe under the stabilizer parachute (top). Views of the gondola showing the locations of the PWA sensors (bottom).

3. Atmospheric conductivity

3.1. The relaxation probe (RP)

The atmospheric polar conductivity is due to the presence of electrons and ions, and can be measured with the relaxation, or transient response, technique (Bragin et al., 1973; Ogawa, 1985). The sensor is a flat disk, with a diameter of 70 mm and a capacitance $C = 2.5$ pF, mounted on a boom, at a distance of (20 ± 1) cm from the Huygens Probe body (Grard et al., 1997). When the electrode is biased at a positive, or negative, potential with respect to the Probe, it collects electric charges with the opposite polarity from the environment. When the voltage source is disconnected, the electrode potential asymptotically returns to its equilibrium level. The time constant that characterizes the response is a function of the ambient conductivity. This instrument has been tested in the Earth atmosphere during several balloon campaigns with a Huygens Probe mock-up provided by LPCE (Orléans, France). The results have validated the principle of the technique and the performance of the instrument (López-Moreno et al., 2001). However, contrary to the Earth lower atmosphere, where the balloon campaigns took place, the high atmosphere of Titan is expected to include free electrons in addition to positive and negative ions (Molina-Cuberos et al., 2001).

The potential of the source with respect to the vehicle structure is measured once, for reference, before the start of each relaxation sequence. The following 40 samples are taken at a rate of $50\,s^{-1}$; the last ones are all collected in pair every 2 s, each pair consisting of nearly redundant measurements taken 1 ms apart. The signal is sampled at different rates during the initial and final phases of the relaxation, in order to acquire both rapid and slow responses with acceptable time resolutions. The basic sequence of measurements consists of four relaxation cycles of 56 s, where the source potential is successively given the values: $+5$, 0, -5, and 0 V, and is repeated during the whole descent, until touchdown.

The source is disconnected at $t = 0$. We assume that the potential of the Huygens Probe body is in equilibrium with its environment and does not influence that of the electrode. Then the potential of the latter with respect to

Table 1
PWA operation mode as a function of time and altitude

PWA mode	HASI status	Time T	Altitude a	Measurements
Entry	Descent 1	T_0-10 min	$a \geqslant 160$ km	None
A	Descent 2	$T_0+2.5$ min	60 km $\leqslant a < 160$ km	AC, SH, MI, RP
C	Descent 3	T_0+32 min	7 km $\leqslant a < 60$ km	AC, SH, AU, MI, RAE, RP
D	Descent 4	–	1 km $\leqslant a < 7$ km	AC, SH, AU, MI, RAE, RP
D	Impact	–	0 m $\leqslant a < 1$ km	AC, SH, AU, MI, RAE, RP
G	Surface	–	$a = 0$	AC, SH, AU, MI

Information on altitude and time is delivered to each instrument by the Huygens command and data management unit.

the vehicle follows, in a first approximation, the exponential law:

$$V = (V_0 - \Delta V_f)e^{-t/\tau} + \Delta V_f, \quad (1)$$

where V_0 is the source potential and ΔV_f the floating potential of the electrode, both measured with respect to the Huygens body; τ is the time constant of the discharge.

When Eq. (1) applies, the quantity

$$\sigma = \frac{\varepsilon_0}{\tau}, \quad (2)$$

where ε_0 is the permittivity of vacuum, which is the conductivity of the medium. When $V_0 - \Delta V_f$ is negative, the electrode attracts positive charges and V increases; conversely, when $V_0 - \Delta V_f$ is positive, the electrode attracts negative charges and V decreases. In other words, σ gives the polar conductivity of the positive, or negative charge carriers, according as $dV/dt > 0$ or $dV/dt < 0$, respectively.

Information about the possible existence of a global atmospheric current can also be gleaned, if we make the assumption that the asymptotic potential ΔV_f is induced by a vertical quasi-static electric field E_z. Then

$$E_z = \frac{\Delta V_f}{L}, \quad (3)$$

where $L \sim 12$ cm is the vertical effective length of the antenna made by the RP and the Huygens Probe body (Cadène, 1995).

PWA carries two RP. One sensor, RP1, yields directly the time constant τ that appears in Eq. (1). The input of the amplifier which measures the potential of the other sensor, RP2, is shunted by a capacitor $\gamma = 352$ pF, so that the time constant of the discharge is artificially increased by the factor $(\gamma + C)/C = 142$. This feature was introduced to facilitate the observation of fast and slow relaxations with commensurate time resolutions.

3.2. Relaxation measurements

The first RP measurements were stored in the onboard memory at $T_0 + 212$ s, when Huygens was at an altitude of ~139 km. Data collection and transmission continued until touchdown. The RP1 and RP2 data were transmitted separately to Cassini on Channels A and B, respectively. Unfortunately the information carried by Channel A was not recorded on the Orbiter, and only the relaxations observed with RP2 are available.

The RP2 sensor was especially designed for highly conductive environments and shows no measurable relaxation when the conductivity is low, i.e. $V \sim V_0$ at the end of the cycle (Eq. (1)). We do not report here measurements from which no relaxation time constant can be derived.

The most significant relaxation curves collected with $V_0 = +5$ V, between 134 and 52 km, are plotted in Figs. 3 and 4 illustrates how an exponential law with a time constant of 45 s is fitted to the cycle recorded at around 84 km. The time constants derived from the 11 curves

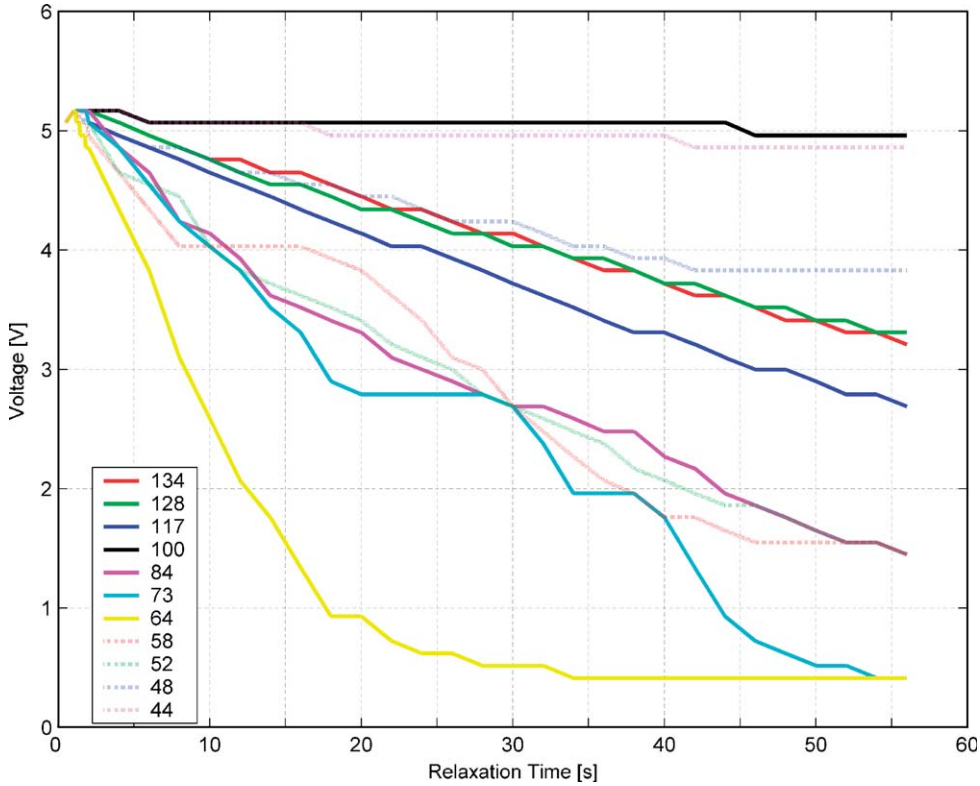

Fig. 3. Relaxation curves of RP2 due to the collections of negative charge carriers ($V_0 = +5$ V). The labels indicate the average altitude, in km, at which the measurements are taken.

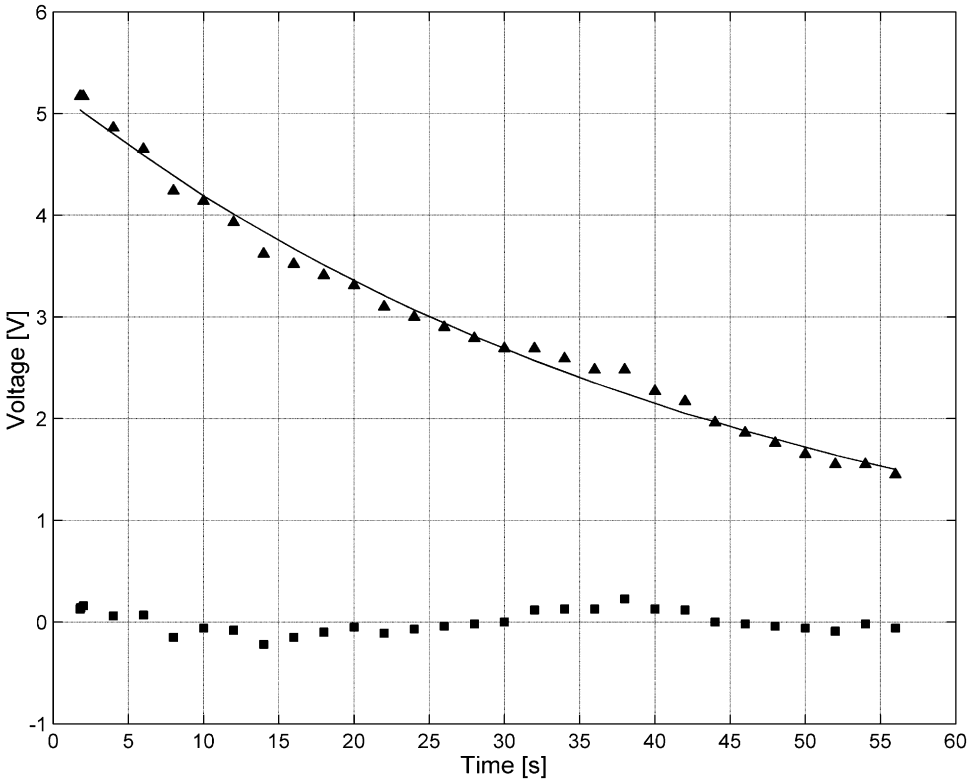

Fig. 4. Relaxation of the potential of RP2 recorded between 84.8 and 81.9 km (triangles), exponential fit to the measurements (solid line) and residuals (squares).

shown in Fig. 3 are listed in Table 2. Table 3 gives the 7 time constants obtained with $V_0 = -5$ V. The corresponding relaxation curves are not shown.

Neutrals and charge carriers are in thermal equilibrium and the energy supplied by the source is transferred from the charge carriers to the neutral particles by isotropic scattering. The random velocity of a particle is inversely proportional to its mass, whereas its drift velocity in a given electric field, and the conductivity of the related species, are inversely proportional to the square root of the particle mass. The measured time constants of the negative charge carriers ($V_0 = +5$ V) are significantly smaller (by an average factor of the order of 10) than those of the positive charge carriers ($V_0 = -5$ V), thus confirming the presence of free electrons in the atmosphere of Titan. The time constants are proportional to the mobilities and concentrations of the charge species in the medium. A detailed study of this topic is model dependent, and will be the subject of a dedicated analysis. The ratios of the two time constants measured with the RP clearly indicate that, in addition to free electrons, electrophilic species and/or charged aerosols may also be present.

The following additional conclusions can tentatively be drawn from Tables 2 and 3: (1) No negative and positive charge carriers above the threshold of the instrument are detected at altitude lower than 44 and 67 km, respectively. (2) The fastest decay for negative charge carriers is obtained at an altitude of 64 km, which sets the peak of

Table 2
Time constant of the negative charge carriers as a function of altitude

Altitude (km)	τ (s)
134.0±1.3	114.4±1.0
128.2±1.1	122.4±1.1
117.5±1.2	84.6±0.6
99.8±1.2	1900±200
84.2±1.5	45.1±0.6
72.1±1.0	22.2±1.0
63.5±0.8	11.5±0.7
57.6±0.6	39.7±1.1
52.4±0.6	43.9±0.4
47.9±0.5	176±5
43.9±0.4	930±50

Table 3
Time constant of the positive charge carriers as a function of altitude

Altitude (km)	τ (s)
140.3±1.6	2000±200
128.3±1.2	1960±195
118.0±1.1	1430±110
107.9±1.9	1280±85
90.6±1.7	1430±125
77.1±1.3	1235±75
67.1±0.95	1925±185

the ionized layer with free electrons at an altitude less than it had been anticipated (Capone et al., 1976; Borucki et al., 1987; Molina-Cuberos et al., 1999, 2001). (3) The shorter time constants are observed at different altitudes for both species, positive and negative, which implies a variable electron/negative ion concentration ratio or the presence of positive and negative heavy ions. Charged aerosols, i.e. heavy ions, do not contribute to the relaxation mechanism, due to their relatively large masses; they are responsible for an *apparent* absence of positive and negative charge carriers, or an *apparent* discrepancy between their densities.

The asymptotic potential ΔV_f is close to the sensitivity threshold of the measurements (Eq. (1)). It lies in the range 0.1–0.3 V throughout the descent, and is consistent with an upward electric field $E_z \sim 1\,\mathrm{Vm}^{-1}$ (Eq. (3)). This assertion must be somewhat moderated. Electrostatic charging of the system by ambient charged particles is controlled by the electron temperature (about 100 K), and should not exceed a few −10 mV, but the associated Debye length is so large in the lower atmosphere that the charging induced by any unidentified mechanism, such as an interaction with charged aerosols, cannot be shielded by the medium.

4. Atmospheric permittivity

4.1. Mutual impedance probe (MIP)

The mutual impedance probe measures the complex permittivity of the atmosphere during the descent. A sinusoidal current of constant amplitude, $I \sim 10^{-9}$ A, with a frequency $f = 45$ Hz, and an associated wavelength much larger than the size of the instrument, is injected between two transmitting electrodes, TX1 and TX2, and induces a voltage, V, between two receiving electrodes, RX1 and RX2. The complex ratio V/I is the mutual impedance of the array. If the amplitude and phase of the voltage are A_0 and φ_0 in a vacuum and A and φ in a given environment, the electron conductivity and relative permittivity of the medium are:

$$\sigma = \frac{A_0}{A}\omega\varepsilon_0 \sin(\varphi - \varphi_0), \tag{4}$$

$$\varepsilon_r = \frac{A_0}{A}\cos(\varphi - \varphi_0), \tag{5}$$

where ω is the angular frequency of the working signal (Grard, 1990a,b).

It can be shown (Grard, 1992) that ε_r, the relative dielectric constant of a very collisional environment, is nearly equal to unity, so that Eqs. (4) and (5) reduce to

$$\sigma = \omega\varepsilon_0 \tan(\varphi - \varphi_0). \tag{6}$$

The measurement is independent of the sizes and shapes of the electrodes and of the array configuration.

The PWA-MIP electrodes are mounted on a deployable boom system. The AC current source consists of a voltage generator with a pair of small capacitors, C_k, in series with TX1 and TX2. On the receiving side, the signals picked up by RX1 and RX2 are coupled to high impedance preamplifiers through coupling capacitors C_k. The differential signal is fed, via an ADC, into a processor that yields the amplitude and phase. The circuit diagram of MIP is illustrated in Fig. 5.

It was anticipated (Grard et al., 1995) that the relatively low conductivity of the atmosphere would produce small phase shifts (Eq. (4)) and a low working frequency, 45 Hz, was therefore selected for the descent. The mode of operation, the level of the stimulus (TX) and the gain of the receiver (RX), are changed automatically by the onboard software, according to predetermined sequences.

The instrument with deployed booms was calibrated on the ground, in dry air, for each mode of operation. The precise knowledge of every discrete and stray circuit component is essential to the evaluation of systematic amplitude and phase errors which cannot be calibrated on the ground, because they are due to the effect of the environment on the load of the current source and on the input impedance of the preamplifiers. Accuracies of a few percents in amplitude and better than one degree in phase are achieved with the highest stimulus level and gain combination.

4.2. Permittivity measurements

The failure of the Channel A recorder entails a partial, or even total, loss of the information collected by most PWA sensors, but does not affect MIP. The data produced by this instrument were fortunately processed onboard and reduced to one amplitude and one phase per measurement, which were transmitted on both telemetry channels.

Fig. 6 shows the phase, φ, and amplitude, A, of the 45 Hz signal measured with the TX1–TX2 antenna. At the end of the descent, the phase is very close to that measured during calibration, φ_0, which indicates that, the electron conductivity is very small at low altitudes (Eq. (6)). Significant phase shifts are measured in the early phase of the descent, reflecting the existence of an electron layer with peak conductivity at an altitude of about 60 km. These results corroborate those obtained with the RP. The discrepancies are partly due to the facts that the Debye length is commensurate with the sensor radii in the electron layer, and that the two techniques do not measure the same

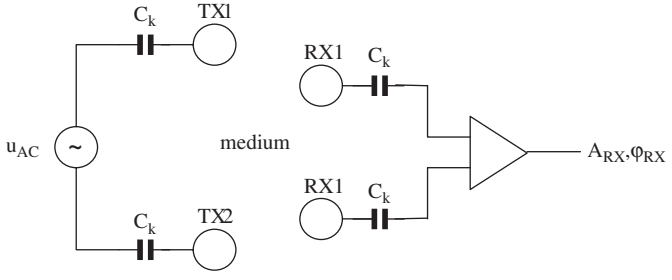

Fig. 5. Simplified mutual impedance probe circuit diagram.

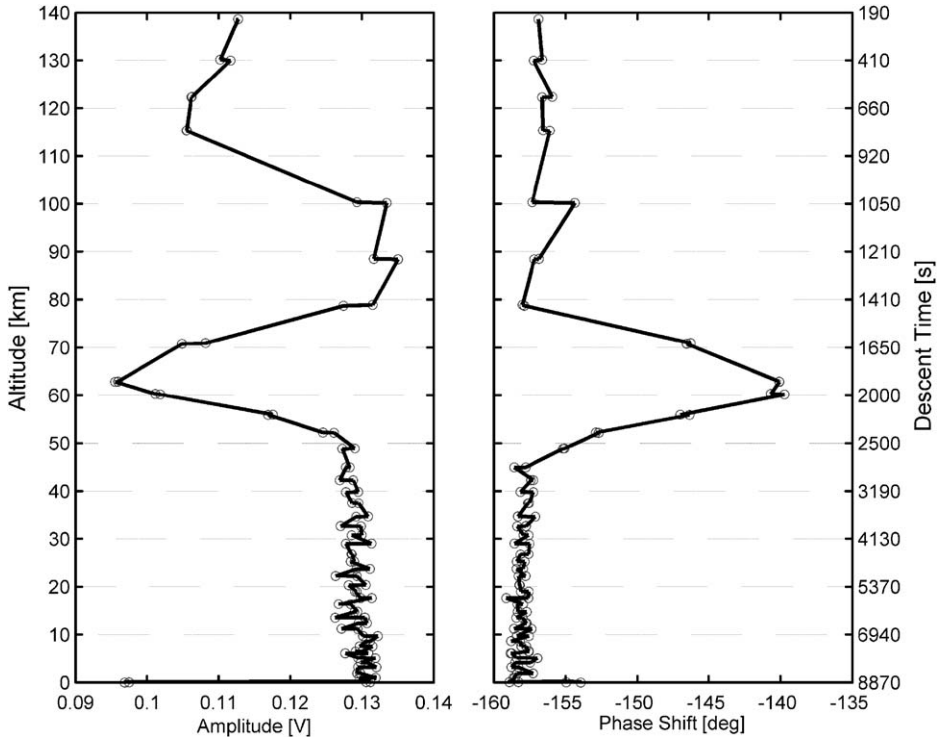

Fig. 6. MIP phase and amplitude measurements during the descent (raw data).

quantities: RP measures the electron and light ion conductivities, whereas MIP is sensitive to electrons only.

The signal magnitude shows a profile that deviates from the expected trend. A constant level, close to that observed during pre-flight calibration, was anticipated. Instead, the level is up to 26% above the nominal value, about 0.1 V, during most of the time ($T > 3000$ s). The amplitude signal also shows fluctuations when the parachute is deployed ($T = 903$ s) and during the crossing of the electron layer. A straightforward application of Eq. (5) to this data set would lead, in this altitude range, to a real part of the permittivity (ε_r) significantly different from unity, which is strictly impossible in very collisional plasma, such as a conductive atmosphere. This behaviour is not understood. Possible effects due to the descent velocity and the accretion of aerosols on the electrodes are presently under investigation. The calibration results of the flight instrument will also be checked against those of an identical mock-up.

5. Electromagnetic and acoustic waves

The electric component of electromagnetic and, possibly, electrostatic waves are measured with the dipole made by the electrodes RX1 and RX2, distant of about 2 m. Fig. 7 gives a synopsis of the wave measurements performed during the descent. The dynamic spectrum shown in Panel 7a covers the frequency range 0–9.22 kHz and is recorded when a current of amplitude $\sim 10^{-9}$ A and frequency 45 Hz is injected between TX1 and TX2 (active mode, see Section 4.1). Panel 7b shows a dynamic spectrum similar to the previous one, but without any stimulus (passive mode) in the frequency range 0–11.5 kHz. The discontinuity seen at around 2000 s and a slight variation of the noise level are caused by a modification of the frequency resolution due to a change in the mode of operation (see Section 2.2). Panel 7c is the same as Panel 7b, but in the bandwidth 0–100 Hz. Finally, Panel 7d is the dynamic spectrum of the signal recorded by the acoustic sensor below 61.5 km, in the bandwidth 0–6.7 kHz.

Comparison of spectra recorded in the active and passive modes shows that the second spectrogram not only displays the signals seen in the first spectrogram, but also includes a broad frequency noise in the altitude range 115–175 km. If this phenomenon is not a non-linearity effect of the instrument, it might result from an interaction between the electrons and the energy injected in the medium at 45 Hz, and deserves further investigation. Both spectrograms also show an enhancement of the signal in the lower frequency range at altitude lower than 22 km. The transition occurs at 22.5 ± 0.2 km and approximately coincides with a haze layer detected by DISR at 21.0 ± 0.5 km (Tomasko et al., 2005).

Several events display the spectral characteristics of lightning discharges and are under scrutiny. A narrow band wave emission at around 36 Hz, well visible in Panel 7c after 1000 s, is reminiscent of a resonance generated by lightning activity in the spherical wave guide formed by the surface of Titan and the inner boundary of the ionosphere (Polk, 1982). This signal lasts throughout the whole descent; it is less visible before 1000 s and after 2000 s, but its existence can always be revealed by summing-up a

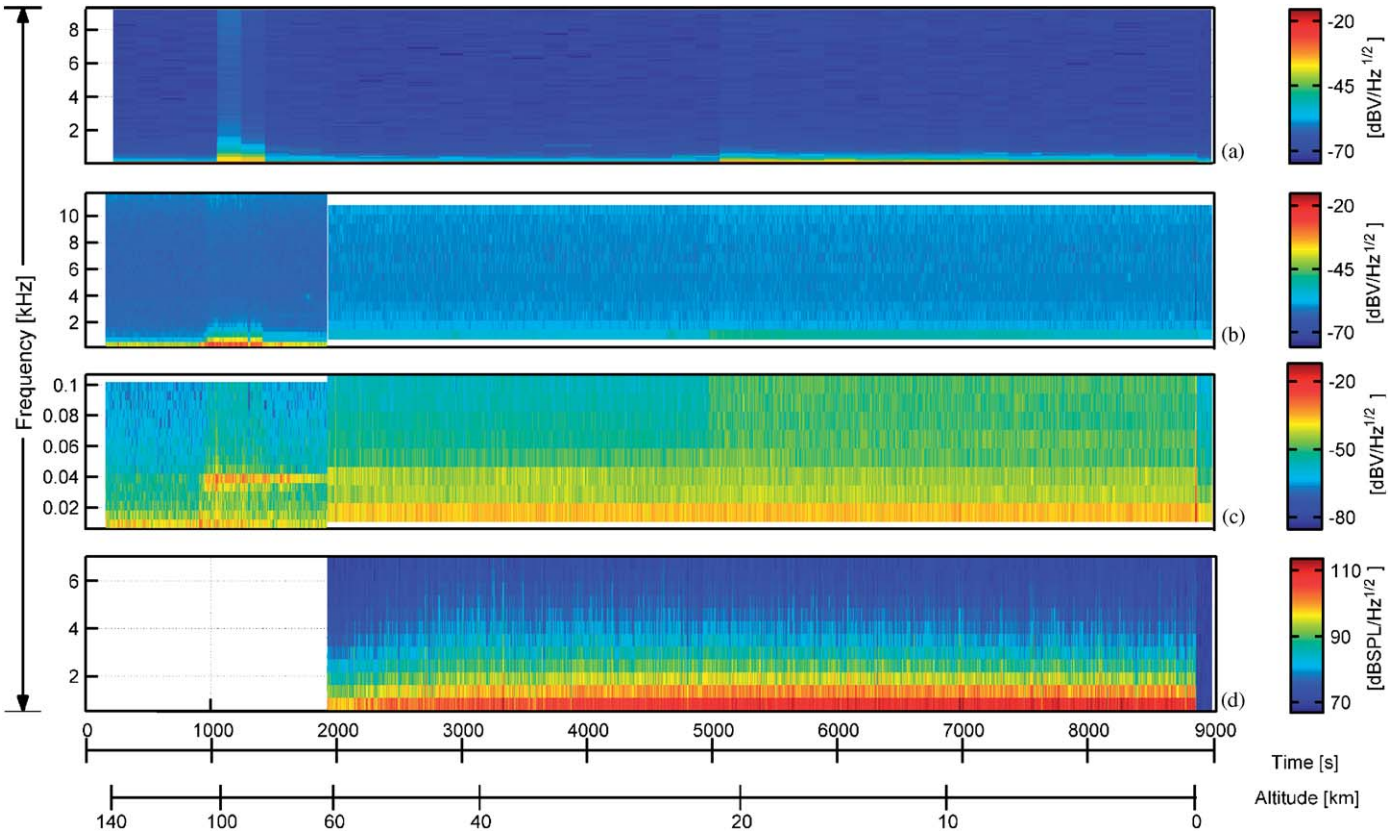

Fig. 7. Dynamic spectra of the receiver input voltage and of the acoustic pressure vs. time and altitude. The colour scales shown on the right-hand side give the spectral levels. From top to bottom: (a) Active mode in 0–9.22 kHz bandwidth; (b) passive mode in 0–11.5 kHz bandwidth; (c) passive mode in 0–100 Hz bandwidth; (d) acoustic pressure in 0–6.7 kHz bandwidth.

few successive spectra. No thunder clap has been identified so far with the acoustic sensor.

6. Radar return signal

Huygens carries two frequency modulation continuous wave (FMCW) radars (Lebreton and Matson, 2002; Trautner et al., 2005). Their primary function is to support the payload operation, which depends upon altitude. The scientific data obtained with one radar only are available, due to the loss of telemetry Channel A, but the altitude and automatic gain control (AGC) of the two radars can be found in the Huygens Probe housekeeping data, which was transmitted on both channels.

The frequency of the FMCW radar is modulated by a triangular waveform of peak to peak amplitude Δf, whose period T_R is automatically adjusted so that a constant intermediate frequency $f_0 = 200\,\text{kHz}$ is produced by mixing the transmitted and returned signals. This is achieved when the slopes of their modulation waveforms have the same sign and when, of course, the echo is strong enough. The RAE, a unit dedicated to analogue processing and conditioning, converts the frequency band from $200 \pm 7.5\,\text{kHz}$ down to the baseband $10 \pm 7.5\,\text{kHz}$, in the VLF range. The RAE delivers to PWA: (1) a VLF waveform which contains information about the atmosphere and the surface topography and (2) a flag, called blanking signal, which indicates the periods of validity of this baseband signal. PWA insures the acquisition, numerical processing and formatting of the data.

It can be easily calculated that the altitude is given by

$$a = k_a T_R, \tag{7}$$

where

$$k_a = c\frac{f_0}{4\Delta f} \tag{8}$$

is a constant equal to $\sim 10^6\,\text{m s}^{-1}$ and c is the speed of light.

When the echo is too weak, the altitude range 150–60 km is scanned by continuously modifying the period T_R. The radar locks to the return signal as soon as the latter is strong enough (Eq. (7)). The green dots in Fig. 8 correspond to atmospheric backscatter, observed while the radar is scanning. The associated altitude gives the distance from which the incident wave is backscattered. Combining the return signal amplitude and the AGC yields the strength of the echo, thus imposing constraints on aerosol concentration in clouds, which have not been evaluated yet. When the radar is locked, PWA records the Huygens Probe altitude profile represented by the red dots.

The VLF baseband signal, which contains information about the surface relief, is sampled with the ADC. A fast Fourier transform (FFT) is performed on each sample

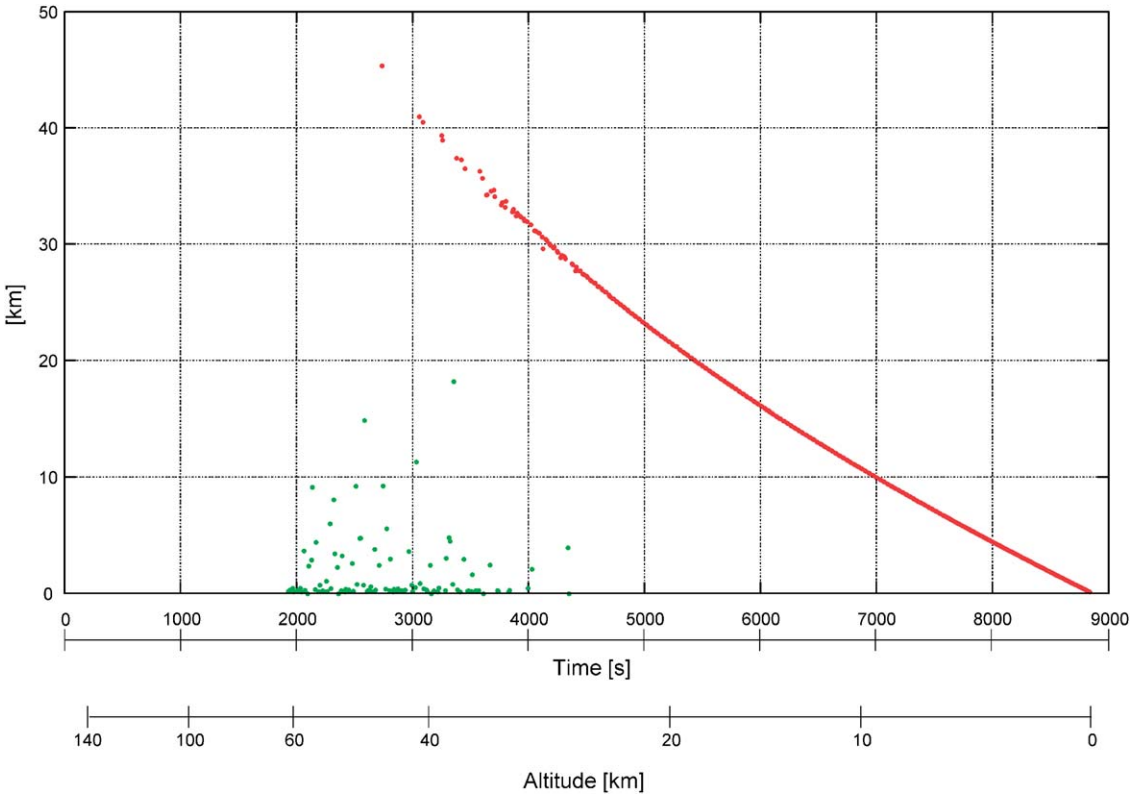

Fig. 8. Atmospheric backscatter distance (green) and Huygens Probe altitude (red) measured by PWA.

Table 4
PWA-Radar mode of operation as a function of altitude

Radar mode	Telemetry data	Averaging	FFT δf	Approx. altitude
52	2×52 point FFT	8-fold	360 Hz	Down to 3.4 km
26	4×26 point FFT	8-fold	720 Hz	3.4–1.7 km
13	8×13 point FFT	8-fold	1440 Hz	1.7–0.85 km
0	104 time samples	None	–	Below 0.85 km

series collected during valid intervals, as indicated by the blanking signal. Successive FFT's are then averaged and telemetered. Table 4 summarizes the main features of the operational modes in given altitude ranges. It is seen that, due to insufficient data acquisition, no onboard processing is performed for $a < 0.85$ km, and that the ADC output is directly forwarded, instead. The relief height resolution is written:

$$\delta h = a\frac{\delta f}{f_0}, \tag{9}$$

where δf is the frequency resolution of the FFT.

The surface roughness is characterized by spectra such as that illustrated by Fig. 9. The shape of the spectra is highly variable and depends upon the topology of the subjacent terrain. This study is under progress and its outcome will be compared with images recorded by the onboard camera.

7. Permittivity of the surface

The PWA mutual impedance probe is not only operated during the descent through the atmosphere, at $f = 45$ Hz, but also after touchdown at five frequencies: 45, 90, 360, 1440 and 5760 Hz. We make the hypothesis that the geometry of the array is not modified by impact, a reasonable working assumption since Huygens presumably landed on a relatively soft spot (Zarnecki et al., 2005). We consider also, in this first analysis, that the instrument calibration is not altered or, in other words, that the emitter current and receiver gain remain unchanged after landing.

The modulus and phase shift of the 45 Hz signal induced between the receiving electrodes are shown in Fig. 10.

The dielectric properties of the neutral atmosphere are very close to those of vacuum, $\sigma = 0$ and $\varepsilon_r = 1$, and the average modulus and phase measured before landing are taken as references. The apparent conductivity and relative dielectric constant of the ground are therefore derived from Eqs. (4) and (5), where $A_0 = 1$ and $\varphi_0 = 0$, which yields

$$\sigma_a = \frac{\varepsilon_0 \omega}{A} \sin\varphi \tag{10}$$

and

$$\varepsilon_{ra} = \frac{1}{A} \cos\varphi. \tag{11}$$

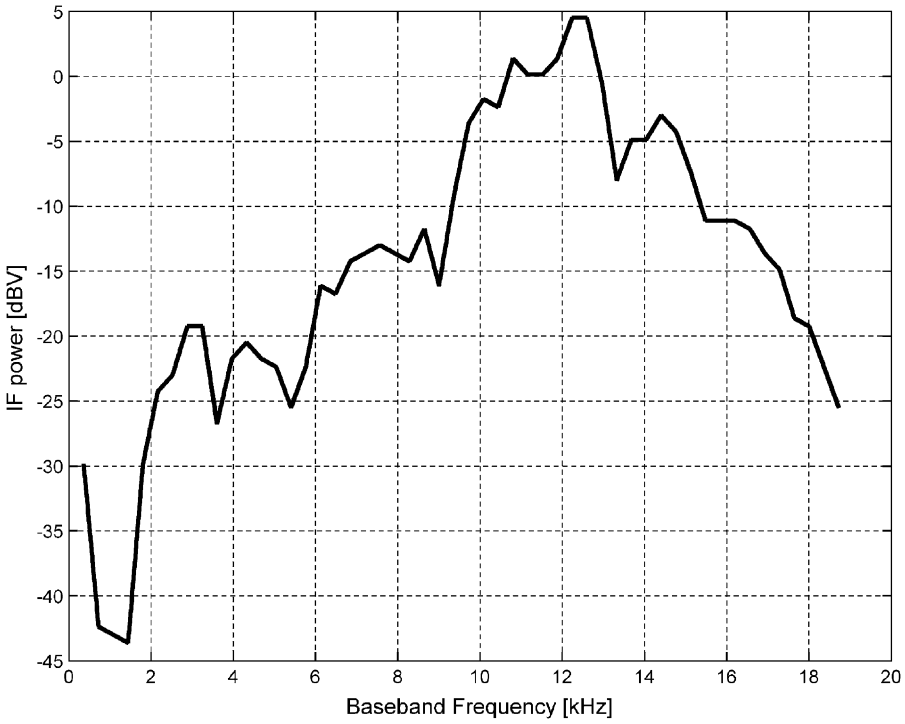

Fig. 9. Spectral representation of the surface roughness observed from an altitude of 23.9 km.

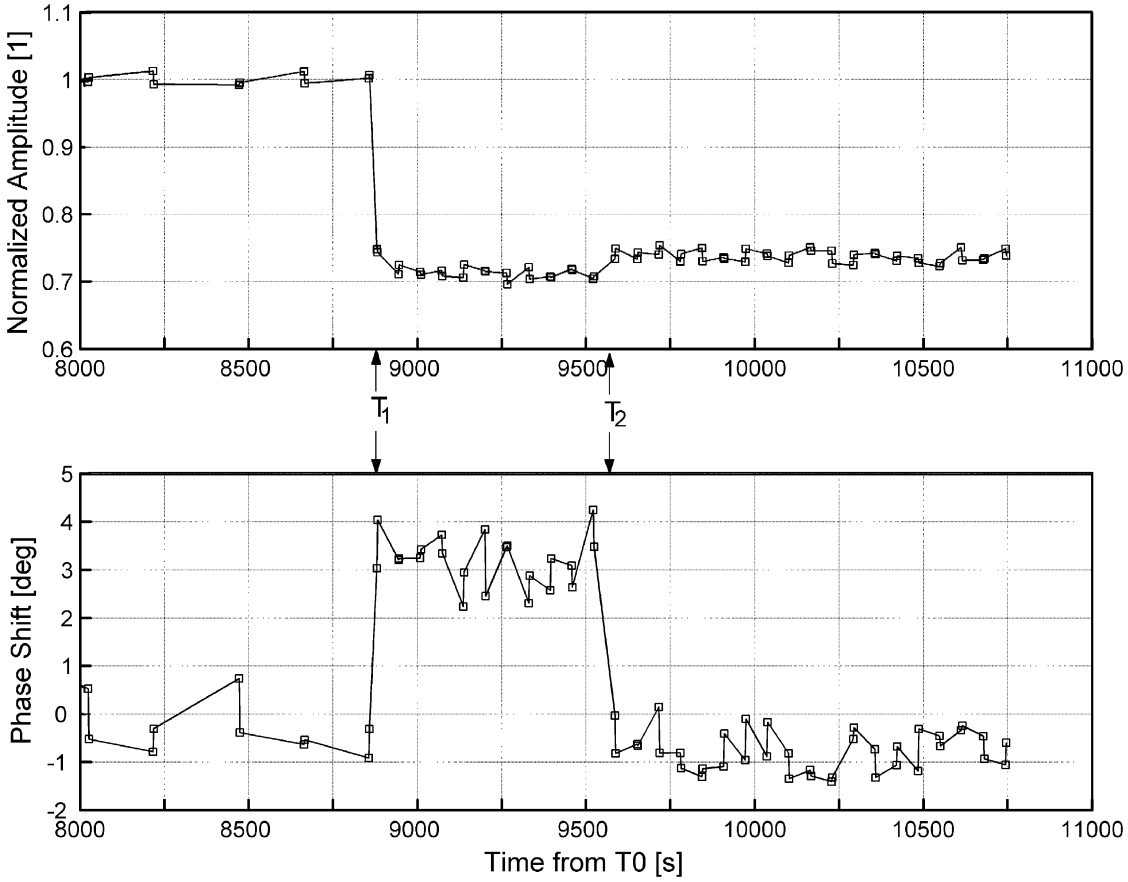

Fig. 10. Relative amplitude (top) and phase shift (bottom) of the 45 Hz signal measured with the receiving dipole. The nominal time of landing is close to $T_1 = 8880$ s. Significant discontinuities are observed approximately 12 min later, at time $T_2 \approx 9550$ s. The average amplitude and phase measured during the final phase of the descent, before T_1, serve as references and are arbitrarily set to 1 and 0, respectively.

We assume, in a preliminary approach, that the influence of the vehicle body is negligible and that the four electrodes, which form the array, are in contact with the surface, locally planar, of a homogeneous soil. Then the apparent conductivity and dielectric constant measured on the surface, σ_a and ε_{ra}, are simply the averages of the quantities relative to the ground, σ_g and ε_{rg}, and to the neutral atmosphere (Grard, 1990a,b),

$$\sigma_g = 2\sigma_a \tag{12}$$

and

$$\varepsilon_{rg} = 2\varepsilon_{ra} - 1. \tag{13}$$

Immediately after touch down, in the time interval $[T_1, T_2]$, the signal amplitude is reduced by 30% and the phase is shifted by 3°, in average. Eqs. (10)–(13) give an apparent dielectric constant $\varepsilon_{ra} = 1.4$ and an apparent conductivity $\sigma_a = 2 \times 10^{-10}\,\mathrm{S\,m^{-1}}$, which yields, in first approximation, a ground dielectric constant $\varepsilon_{rg} = 1.8$ and a ground conductivity $\sigma_g = 4 \times 10^{-10}\,\mathrm{S\,m^{-1}}$. The discontinuities observed at T_2 are consistent with a 3.5% decrease of the ground dielectric constant, and a reduction of the conductivity beyond the minimum measurable value.

The presence of the metallic vehicle body cannot be taken into account analytically; besides the array geometry and a possible tilt of the system prevent any 2D simplification. A 3D finite element model is therefore developed, and implemented with the Comsol Multyphysics software and a specific Matlab post-processing algorithm, to solve Poisson equation,

$$\nabla \cdot (\varepsilon_r(r)\nabla\Phi(r)) = -\rho(r)/\varepsilon_0, \tag{14}$$

where Φ is the potential, ε_r the relative permittivity, ρ the charge volume density and r the space variable. Dirichlet boundary conditions are imposed on the body of the Huygens Probe and on the quadrupolar array, as well as continuity conditions at the planar interface between the two media, atmosphere and ground (Fig. 11).

Eq. (14) is first solved under the assumption that $\sigma_g = 0$, in order to probe the influence of the body upon the determination of the ground dielectric constant. In fact, the algorithm computes, for a given charge distribution on the two transmitting electrodes and for a specific rest position of the Huygens Probe upon the surface, the ground dielectric constant that reduces the received voltage after landing to 70% of its level in vacuum.

The system rest attitude is not known with accuracy. The symmetry axis of the vehicle body makes an angle probably less than 10° with the normal to the surface and the body does not penetrate the soil by more than 15 cm, as it can be inferred from the measurements performed with several other instruments: Descent Imager-Spectral Radiometer—DISR (Tomasko et al., 2005), Surface Science Package—SSP (Zarnecki et al., 2005) and Huygens Atmospheric Structure Instrument—HASI (Fulchignoni et al., 2005). It is nevertheless important to test how sensitive is the determination of the dielectric constant to small penetration depths and tilt angles. The simulation outputs are summarized in Table 5 for several combinations of these two attitude parameters. We only consider tilts in the plane

Table 5
Ground dielectric constant derived from the finite element model, for various tilt angles and penetration depths

	Tilt (deg)		
Depth (cm)	0	5	10
0	2.53	2.62	3.13
5	1.95	2.41	3.19
10	1.91	2.15	–

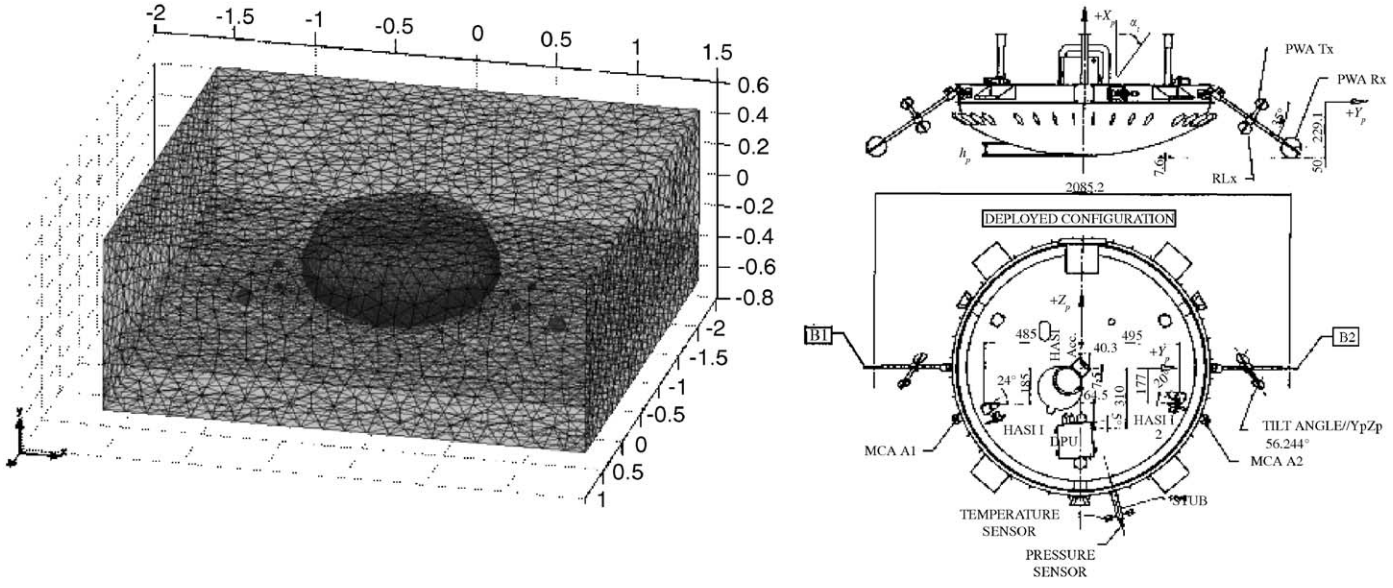

Fig. 11. Finite element mesh model representing the Huygens Probe and the quadrupolar array partially buried into the soil (left), and definitions of the penetration depth h_p and the tilt angle α_t, in the plane defined by the symmetry axis of the system, and the booms which carry the sensors (right).

defined by the PWA booms, because the results are not very sensitive to small rotations in the orthogonal planes. It is seen in Table 5 that the permittivity of the ground lies in the range 2–3, which can be compared to the earlier straightforward estimate from Eq. (13) ($\varepsilon_{rg} = 1.8$). A more accurate determination of the surface permittivity can be given, once precise information about the vehicle attitude becomes available. It can nevertheless be stated, as anticipated, that the error induced by the vehicle body upon the determination of the ground permittivity is not drastic. The same simplifying assumption does not necessarily apply to atmospheric measurements, since electrostatic charging of the Huygens Probe surface might interfere with quasi-static electric field measurements, as discussed briefly at the end of Section 3.2.

The mean relative dielectric constant of the ground at the landing site within the range of the PWA quadrupolar probe, i.e. approximately a volume with a radius of 1 m and a depth of 2 m, is of the order of 2, in fair agreement with the measurements performed, on a much larger scale, by the radar onboard Cassini (Elachi et al., 2005). The working frequencies of the Cassini radar and of PWA–MIP differ by more than 8 orders of magnitude, and this agreement is possibly fortuitous, but the permittivity of most materials, including water ice, is generally independent of frequency at extremely low temperatures.

The reduction of the complex permittivity 12 min after landing is not an artefact and cannot be easily explained in terms of vehicle settling motion, which is not detected by any onboard accelerometer or tilt-meter, or failure of the instrument, whose performance is nominal until the end of the data acquisition. This rapid variation of the ground electrical properties may reflect a phase-change due to a local warming of the ground by the Huygens Probe body. To set the ideas, the evaporation or sublimation of a few percents in volume of a mixture component, such as methane at a temperature close to 94 K, could explain this phenomenon. It is expected that the knowledge of the dielectric properties of the ground will impose constraints on models of its composition.

8. Conclusion

The analysis of the PWA measurements is still in progress and these concluding remarks are necessarily preliminary.

An ionized layer has undoubtedly been detected with two independent techniques in the altitude range 44–90 km. The RP shows that the time constants relative to the negative and positive charges are minimum at 64 and 77 km, respectively (Tables 2 and 3). The maximum phase deviation recorded by the mutual impedance probe, which is sensitive to electrons only, is observed at around 62 km (Fig. 6). It is not yet possible to derive with confidence the conductivities of the different charge species from the measured parameters (Eqs. (2) and (6)), due to errors which cannot be removed with pre-flight calibrations, but which will be reduced with simulation algorithms. For example: (1) the mutual impedance of the quadrupole is affected by the self impedance of its electrodes, so that Eq. (6) is not strictly valid; (2) the response of the relaxation probe is possibly affected by the fact that the potential of the Huygens Probe structure may not be stable, as it would be in the lower Earth atmosphere, due to the presence of free electrons in Titan's atmosphere. In spite of the fact that the accuracy of the RP measurement is severely affected by the loss of one telemetry channel, it is hoped that merging the RP and MIP results will yield a coherent picture of the charged particle distributions in Titan's atmosphere.

Several indices plead in favour of a lightning activity and are under investigation, in spite of the fact that no conclusive signature has been forwarded yet. (1) The steady 36 Hz signal analogous to a Schumann resonance is not an artefact. It is seen throughout the descent, but it is not understood why its level increases at the opening of the stabilizer parachute, $T = 900$ s. (2) The asymptotic potential of the relaxation probe is consistent with a fair weather upward electric field $E_z \sim 1\ \mathrm{V\,m^{-1}}$, but it is close to the measurement threshold and possibly influenced by surface charging. (3) A large number of faint impulsive events, not visible in the spectrograms, are observed in a more sensitive channel, but the acoustic measurements bear no evidence of thunder clap.

The knowledge of the ground complex permittivity constrains the ground composition and it is hoped that significant progress can be achieved along this line, in synergy with the measurements performed with the radars carried by both Huygens and Cassini.

Many questions must be answered before physical parameters can be safely derived from the measured quantities, and a definite conclusion can be drawn about the existence of a global circulation current similar to that observed on Earth. The presentation of these preliminary results will therefore be followed by reports on complementary studies, which are presently under way or will be initiated in the near future, on the following topics:

- effect of the vehicle descent velocity upon the relaxation and mutual impedance measurements;
- perturbation of the ambient electric field and atmospheric conductivity by various charging mechanisms;
- detailed investigation of the 36 Hz wave emission;
- statistical study of the faint impulsive electric events recorded during the descent;
- characterization of the aerosol concentration; and Titan's surface roughness from the radar data.

This wealth of information is unprecedented and will remain unique for a long time. This data set therefore deserves a very careful evaluation for many years to come, supported by analysis, modelling, and comparison with the measurements performed, or to be performed, in the laboratory and the Earth atmosphere with an identical mock-up instrument.

Acknowledgements

The authors thank the International Space Science Institute (Bern, Switzerland) for hosting and supporting team meetings. The first author is indebted to CETP/IPSL-CNRS (Saint Maur des Fossés, France) for invaluable support. JJLM, GJMC, RR, VGJB, JMJ and LML were funded under ESP-2003-00357.

References

Borucki, W.J., Levin, Z., Whitten, R.C., Keesee, R.G., Capone, L.A., Summers, A.L., Toon, O.B., Dubach, J., 1987. Predictions of the electrical conductivity and charging of the aerosols in Titan's atmosphere. Icarus 72, 604–622.

Bragin, Y.A., Kocheev, A.A., Bragin, O.A., 1973. Direct measurements of the electrical conductivity and relaxation time of ionized air in the stratosphere and mesosphere. Cosmic Res. 11, 110–114.

Cadène, F., 1995. Methodology for measuring planetary atmospheric conductivities. Thèse d'Université, Electronique, Université de Paris 6, Ph.D. Thesis (in French).

Capone, L.A., Whitten, R.C., Dubach, J., Prasad, S.S., Huntress Jr., W.T., 1976. The lower ionosphere of Titan. Icarus 28, 367–378.

Elachi, C., Wall, S., Allison, M., Anderson, R., Boehmer, Y., Callahan, P., Encrenaz, P., Flamini, E., Franceschetti, G., Gim, Y., Hamilton, G., Hensley, S., Janssen, M., Johnson, W., Kelleher, K., Kirk, R., Lopes, R., Lorenz, R., Lunine, J., Muhleman, D., Ostro, S., Paganelli, F., Picardi, G., Posa, F., Roth, L., Seu, R., Shaffer, S., Soderblom, L., Stiles, B., Stofan, E., Vetrella, S., West, R., Wood, C., Wye, L., Zebker, H., 2005. Cassini radar views the surface of Titan. Science 308, 970–974.

Falkner, P., 2004. Permittivity, waves and altimeter analyser for the ESA/NASA Cassini-Huygens Project. Technical University of Graz, Rechbauerstraße 12 A—8010 Graz, Austria. Ph.D. Thesis (in German).

Fulchignoni, M., Ferri, F., Angrilli, F., Bar-Nun, A., Barucci, M.A., Bianchini, G., Borucki, W., Coradini, M., Coustenis, A., Falkner, P., Flamini, E., Grard, R., Hamelin, M., Harri, A.M., Leppelmeier, G.W., Lopez-Moreno, J.J., McDonnell, J.A.M., McKay, C.P., Neubauer, F.H., Pedersen, A., Picardi, G., Pirronello, V., Rodrigo, R., Schwingenschuh, K., Seiff, A., Svedhem, H., Vanzani, V., Zarnecki, J., 2002. The characterization of Titan's atmosphere physical parameters by the Huygens atmospheric structure instrument (HASI). Space Sci. Rev. 104, 395–431.

Fulchignoni, M., Ferri, F., Angrilli, F., Ball, A.J., Bar-Nun, A., Barucci, M.A., Bettanini, C., Bianchini, G., Borucki, W., Colombatti, G., Coradini, M., Coustenis, A., Debei, S., Falkner, P., Fanti, G., Flamini, E., Gaborit, V., Grard, R., Hamelin, M., Harri, A.M., Hathi, B., Jernej, I., Leese, M.R., Lehto, A., Lion Stoppato, P.F., López-Moreno, J.J., Mäkinen, T., McDonnell, J.A.M., McKay, C.P., Molina-Cuberos, G., Neubauer, F.M., Pirronello, V., Rodrigo, R., Saggin, B., Schwingenschuh, K., Seiff, A., Simões, F., Svedhem, H., Tokano, T., Towner, M.C., Trautner, R., Withers, P., Zarnecki, J.C., 2005. In situ measurements of the physical characteristics of Titan's environment. Nature, doi:10.1038/nature04314.

Grard, R., 1990a. A quadrupolar array for measuring the complex permittivity of the ground—application to Earth prospection and planetary exploration. Meas. Sci. Technol. 1, 295–301.

Grard, R., 1990b. A quadrupolar system for measuring in situ the complex permittivity of materials—application to penetrators and landers for planetary exploration. Meas. Sci. Technol. 1, 801–806.

Grard, R., 1992. The significance of meteoric ionisation for the propagation of lightning spherics in the atmosphere of Titan. Proceedings of the Symposium on Titan, Toulouse, France, ESA SP-338, pp. 123–128.

Grard, R., Svedhem, H., Brown, V., Falkner, P., Hamelin, M., 1995. An experimental investigation of atmospheric electricity and lightning activity to be performed during the descent of the Huygens Probe on Titan. J. Atmos. Terrest. Phys. 57, 575–585.

Grard, R., Smit, A., Smit, L., Van Der Hoek, J., 1997. Development and qualification of a deployable boom system for the Huygens Probe. Proceedings of the Seventh European Space Mechanics and Tribology Symposium, ESTEC, Noordwijk, The Netherlands. ESA SP-410, pp. 181–183.

Lebreton, J.-P., Matson, D.L., 2002. The Huygens probe: science, payload and mission overview. Space Sci. Rev. 104, 59–100.

Lindal, G.F., Wood, G.E., Holtz, H.B., Sweetnam, D.N., Eshleman, V.R., Tyler, G.L., 1983. The atmosphere of Titan—an analysis of the Voyager 1 radio occultation measurements. Icarus 53, 348–363.

López-Moreno, J.J., Molina-Cuberos, G.J., Rodrigo, R., Hamelin, M., Schwingenschuh, K., 2001. Polar ionic conductivity profile in fair weather conditions Terrestrial test of the Huygens/HASI-PWA instrument aboard the Comas Sola balloon. J. Atmos. Solar-Terrest. Phys. 63, 1959–1966.

Molina-Cuberos, G.J., López Moreno, J.J., Lara, L.M., Rodrigo, R., O'Brien, K., 1999. Ionization by cosmic rays of the atmosphere of Titan. Planetary Space Sci. 47, 1347–1354.

Molina-Cuberos, G.J., López-Moreno, J.J., Rodrigo, R., Schwingenschuh, K., 2001. Electrical conductivity in Titan. Capability of PWA-HASI to measure conductivity. Adv. Space Res. 28, 1511–1516.

Ogawa, T., 1985. Fair-weather electricity. J. Geophys. Res. 90, 5951–5960.

Polk, C., 1982. Schumann resonances. In: Volland, H. (Ed.), Handbook of Atmospherics, Vol. 1. CRC Press, Boca Raton, FL, pp. 111–178.

Tomasko, M.G., Archinal, B., Becker, T., Bézard, B., Bushroe, M., Combes, M., Cook, D., Coustenis, A., de Bergh, C., Dafoe, L.E., Doose, L., Douté, S., Eibl, A., Engel, S., Gliem, F., Grieger, B., Holso, K., Howington-Kraus, E., Karkoschka, E., Keller, H.U., Kirk, R., Kramm, R., Küppers, M., Lanagan, P., Lellouch, E., Lemmon, M., Lunine, J., McFarlane, E., Moores, J., Prout, G.M., Rizk, B., Rosiek, M., Rueffer, P., Schröder, S.E., Schmitt, B., See, C., Smith, P., Soderblom, L., Thomas, N., West, R., 2005. Rain, winds and haze on Titan. Nature, doi:10.1038/nature04126.

Trautner, R., Svedhem, H., Lebreton, J.-P., Floury, N., Plettemeier, D., Couzin, P., Hughes, N., Edenhofer, P., 2005. FMCW Radars for Entry Probes and Landers: Lessons learned from the Huygens Radar Altimeter, ESA SP-607, in press.

Wahlund, J.-E., Boström, R., Gustafsson, G., Gurnett, D.A., Kurth, W.S., Pedersen, A., Averkamp, T.F., Hospodarsky, G.B., Persoon, A.M., Canu, P., Neubauer, F.M., Dougherty, M.K., Eriksson, A.I., Morooka, M.W., Gill, R., André, M., Eliasson, L., Mueller-Wodarg, I., 2005. Cassini measurements of cold plasma in the ionosphere of Titan. Science 308, 986–989.

Zarnecki, J.C., Leese, M.R., Hathi, B., Ball, A.J., Hagermann, A., Towner, M.C., Lorenz, R.D., McDonnell, J.A.M., Green, S.F., Patel, M.R., Ringrose, T.J., Rosenberg, P.D., Atkinson, K.R., Paton, M.D., Banaszkiewicz, M., Clark, B.C., Ferri, F., Fulchignoni, M., Ghafoor, N.A.L., Kargl, G., Svedhem, H., Delderfield, J., Grande, M., Parker, D.J., Challenor, P.G., Geake, J.E., 2005. A soft solid surface on Titan at the Huygens landing site as measured by the Surface Science Package (SSP). Nature 10 doi:10.1038/nature04211.

Paper 4

A new numerical model for the simulation of ELF wave propagation and the computation of eigenmodes in the atmosphere of Titan: did Huygens observe any Schumann resonance?

Simões, F., Grard, R., Hamelin, M., López-Moreno, J.J., Schwingenschuh, K., Béghin, C., Berthelier, J.-J., Besser, B., Brown, V.J.G., Chabassière, M., Falkner, P., Ferri, F., Fulchignoni, M., Hofe, R., Jernej, I., Jeronimo, J.M., Molina-Cuberos, G.J., Rodrigo, R., Svedhem, H., Tokano, T., Trautner, R.

Planetary and Space Science **55**, 1978-1989 (2007)

Available online at www.sciencedirect.com
ScienceDirect
Planetary and Space Science 55 (2007) 1978–1989
Planetary and Space Science
www.elsevier.com/locate/pss

A new numerical model for the simulation of ELF wave propagation and the computation of eigenmodes in the atmosphere of Titan: Did Huygens observe any Schumann resonance?

F. Simões[a,*], R. Grard[b], M. Hamelin[a], J.J. López-Moreno[c], K. Schwingenschuh[d], C. Béghin[e], J.-J. Berthelier[a], B. Besser[d], V.J.G. Brown[c], M. Chabassière[e], P. Falkner[b], F. Ferri[f], M. Fulchignoni[g], R. Hofe[d], I. Jernej[d], J.M. Jeronimo[c], G.J. Molina-Cuberos[h], R. Rodrigo[c], H. Svedhem[b], T. Tokano[i], R. Trautner[b]

[a]*CETP/IPSL-CNRS 4, Avenue de Neptune, 94107 Saint Maur, France*
[b]*RSSD, ESA-ESTEC, European Space Agency, Keplerlaan 1, 2200 AG Noordwijk, The Netherlands*
[c]*Instituto de Astrofísica de Andalucía IAA-CSIC, Camino Bajo de Huétor 50, 18008 Granada, Spain*
[d]*Space Research Institute, Austrian Academy of Sciences (IWF), Schmiedlstrasse 6, 8042 Graz, Austria*
[e]*LPCE-CNRS 3A, Avenue de la Recherche Scientifique, 45071 Orléans cedex 2, France*
[f]*CISAS "G. Colombo", Università di Padova, Via Venezia 15, 35131 Padova, Italy*
[g]*LESIA, Observatoire de Paris, 5 Place Janssen, 92195 Meudon, France*
[h]*Applied Electromagnetic Group, Department of Physics, University of Murcia, Murcia 30100, Spain*
[i]*Institut für Geophysik und Meteorologie, Universität zu Köln, Albertus-Magnus-Platz, 50923 Köln, Germany*

Accepted 13 April 2007
Available online 27 April 2007

Abstract

The propagation of extremely low frequency (ELF) electromagnetic waves in the Earth's ionospheric cavity and the associated resonance phenomena have been extensively studied, in relation with lightning activity. We perform a similar investigation for Titan, the largest moon of Saturn. There are important differences between Earth and Titan, as far as the cavity geometry, the atmospheric electron density profile, and the surface conductivity are concerned. We present an improved 3D finite element model that provides an estimate of the lowest eigenfrequencies, associated quality factors (Q-factors), and ELF electric field spectra. The data collected by the electric antenna of the Permittivity, Waves, and Altimetry (PWA) instrument reveals the existence of a narrow-band signal at about 36 Hz during the entire descent of Huygens upon Titan. We assess the significance of these measurements against the model predictions, with due consideration to the experimental uncertainties.

Keywords: Titan; Huygens probe; Atmospheric electricity; ELF electric field; Schumann resonance

1. Introduction

The propagation of low frequency electromagnetic waves within the cavity formed by two, highly conductive, concentric, spherical shells, such as those formed by the surface and the ionosphere of Earth, was first studied by Schumann (1952) and was subsequently observed by Balser and Wagner (1960). When a cavity is excited with broadband electromagnetic sources, a resonant state can develop provided the average equatorial circumference is approximately equal to an integral number of wavelengths of the electromagnetic waves. This phenomenon is known as the Schumann resonance; it provides information about thunderstorm and lightning activity at Earth and acts, for example, as a "global tropical thermometer" (Williams, 1992). We shall apply the same approach to Saturn's satellite.

Titan and Earth are both wrapped up in thick atmospheres and conductive ionospheres (Schwingenschuh

*Corresponding author. Tel.: +33 1 4511 4273; fax: +33 1 48 89 44 33.
E-mail address: Fernando.Simoes@cetp.ipsl.fr (F. Simões).

0032-0633/$ - see front matter © 2007 Elsevier Ltd. All rights reserved.
doi:10.1016/j.pss.2007.04.016

et al., 2001; Molina-Cuberos et al., 2004) but there are important differences between the two bodies, regarding: (i) the radii and relative separation between the shells (i.e. altitude of the ionospheres), and (ii) the losses in the medium and at the inner boundaries (atmospheric and surface conductivities differing by orders of magnitude). The frequency of the Schumann resonance on Titan was first estimated by Morente et al. (2003), prior to the arrival of the Huygens Probe. These authors used theoretical models for the atmospheric electrical conductivity profile and concluded that the fundamental frequency would lie between 11 and 15 Hz. However, Yang et al. (2006) have obtained a significant lower value, in the range 8–10 Hz, for the same theoretical profile. Nickolaenko et al. (2003) assumed different conductivity profiles and obtained a higher resonance frequency in the range 17.5–20 Hz.

The surface of Earth is generally assumed to be a perfect electric conductor (PEC) because its conductivity is of the order of 0.01 and $1\,\mathrm{S\,m^{-1}}$ (Lide et al., 2005) on land and sea, respectively, whereas that of Titan is closer to a good dielectric and has a conductivity in the order of $10^{-10}\,\mathrm{S\,m^{-1}}$ (Grard et al., 2006).

A low conductivity implies a weaker surface reflectivity and a much larger skin depth. A lossless model is therefore not appropriate to Titan and a simple Earth like approach has a limited validity. A more elaborated modelling may even provide information about the depth of a possible conductive boundary below the surface. Several authors have indeed predicted the presence of subsurface water on Titan (Lunine and Stevenson, 1987; Sohl et al., 1995; Tobie et al., 2005).

In situ observations were performed in the atmosphere of Titan during the entire descent of the Huygens Probe, from an altitude of approximately 140 km, down to the surface. The Permittivity, Waves and Altimetry (PWA) analyser (Grard et al., 1995), a subsystem of the Huygens Atmospheric Structure Instrument (Fulchignoni et al., 2002), measured the electric properties of the atmosphere and of the surface. Electric signals in the extremely low frequency (ELF, 0–100 Hz) and very low frequency (VLF, 0–10 kHz) ranges, which are trapped within the ionospheric cavity, were detected with a dipole made of two electrodes distant by about 2 m (real and effective length of ~2.1 and ~1.6 m, respectively). A narrow band signal at around 36 Hz was observed throughout the descent (Fulchignoni et al., 2005; Grard et al., 2006).

In this paper, we first recapitulate the theory of Schumann, which makes use of a single second order differential equation and of the transverse magnetic (TM) and electric fields approximation. We then describe the complete set of Maxwell equations that solves the problem of wave propagation in cavities with complex permittivity, introduce the finite element method and simulation algorithms used in this novel approach, define the input parameters, and validate the numerical code output against the analytical results that can be derived in a simple situation. We present thereafter the numerical predictions obtained for a few selected configurations and conductivity models of Titan's cavity. Finally, we tentatively investigate to which degree the observations performed during the descent of Huygens can be explained by the simulation results.

2. Analytical approach

2.1. Preliminary considerations

Neglecting sphericity and equating the circumference to an integer number of wavelengths, the resonant angular frequency of a thin void cavity is written as

$$\omega_n = n\frac{c}{R}, \tag{1}$$

where n is an integer which identifies the eigenmode, c the velocity of light in the medium and R the average radius of the cavity. Including a 3D spherical correction yields (Schumann, 1952)

$$\omega_n = \sqrt{n(n+1)}\frac{c}{R}. \tag{2}$$

On Earth and on Titan, the first few Schumann resonances, or longitudinal modes, have frequencies that fall within the ELF range.

In addition to the longitudinal modes that are functions of the cavity radius, there exist local transverse modes along the vertical direction. When the shells that form the cavity are PECs, the transverse mode requires that the electric field be zero at the boundaries. A resonance develops whenever the separation between the shells, generally the height of the ionosphere, h, is an integer number, p, of half-wavelengths,

$$\omega_p = p\frac{c\pi}{h}. \tag{3}$$

The value $p = 0$ is associated with a possible electrostatic field between the ionosphere and the surface. For a given order, the longitudinal and transverse eigenfrequencies differ by more than two orders of magnitude on Earth ($h_E/R_E \sim 0.01$) and by much less on Titan because, there, the cavity inner radius is smaller and the separation between the boundaries larger ($h_T/R_T \sim 0.2$).

Unlike Earth, Titan presents significant losses, not only in the atmosphere, but also on the surface. Furthermore, the larger ratio between ionosphere height and cavity radius makes analytical approximations more critical on Titan, because the coupling between transverse and longitudinal modes is stronger. However, these two characteristics play opposite roles in the quality factor (Q-factor) of the cavity, which can be written as

$$Q_m \equiv \frac{\mathrm{Re}(\omega_m)}{2\mathrm{Im}(\omega_m)} \approx \frac{\omega_m^{\mathrm{peak}}}{\Delta\omega_m}, \tag{4}$$

where Re and Im are the real and imaginary parts of the complex eigenfrequency, $\omega_m{}^{\mathrm{peak}}$ the peak power frequency of mode m, and $\Delta\omega_m$ the width of the line at half-power.

Although the cavity of Titan is more intricate than that of Earth, an expedient way of estimating the Q-factor consists in using the ratio between the resonator thickness and the skin depth of the electric field (Nickolaenko and Hayakawa, 2002). The latter is given by Balanis (1989) as

$$\delta_h = \sqrt{\frac{2}{\mu_o \varepsilon_o}} \frac{\left(\sqrt{1+(\sigma/\omega\varepsilon_o)^2}-1\right)^{-1/2}}{\omega}, \quad (5)$$

where ε_o and μ_o are the permittivity and magnetic permeability of vacuum, ω the angular frequency of the propagating wave, and σ the medium conductivity.

Thus $Q \propto h/\delta_h$, in first approximation. Increasing the ionosphere height augments the Q-factor, whereas losses are more important when the boundary is poorly conducting and the skin depth large.

Geometric optics is not a good approximation for the calculation of cavity losses and is not strictly applicable in the ELF–VLF range, but the ray tracing technique still provides qualitative information about the variation of the Q-factor with boundary separation. The minimum number of reflections required for circling a void cavity of inner and outer radii, R_{int} and R_{ext},

$$n_R = \frac{\pi}{\cos^{-1}(R_{int}/R_{ext})}, \quad (6)$$

is approximately 5 for Titan and 22 for Earth. Other things being equal, a lower number of reflections are required in a thicker cavity, which confirms that increasing the distance between the boundaries reduces the losses in the system. A more accurate model should include the losses due to the atmosphere, in addition to those due to the boundaries, which also lowers the theoretical value of the Schumann resonance on Titan (Morente et al., 2003; Molina-Cuberos et al., 2004).

2.2. Formulation of the resonant cavity

A full treatment of the Schumann resonance in the cavity of Titan requires the solution of Maxwell equations,

$$\nabla \times \boldsymbol{E} = -\frac{\partial \boldsymbol{B}}{\partial t}, \quad (7)$$

$$\nabla \times \boldsymbol{H} = \sigma \boldsymbol{E} + \frac{\partial \boldsymbol{D}}{\partial t}, \quad (8)$$

$$\boldsymbol{D} = \varepsilon\varepsilon_o \boldsymbol{E}, \quad B = \mu_o \boldsymbol{H}, \quad (9)$$

where $\boldsymbol{E}$ and $\boldsymbol{D}$ are the electric and displacement fields, $\boldsymbol{H}$ and $\boldsymbol{B}$ the magnetic field strength and flux density, and ε the relative permittivity.

Taking into account the cavity characteristics and decoupling the electric and magnetic fields, Eqs. (7)–(9) can be solved in spherical coordinates, using the harmonic propagation approximation. One mode is characterized by $H_r = 0$ and is called the TM wave, the other one by $E_r = 0$ and is known as the transverse electric (TE) wave. Neglecting the day–night asymmetry of the ionosphere, the standard method of separation of variables yields (Bliokh et al., 1980)

$$\left\{\frac{d^2}{dr^2} - \frac{n(n+1)}{r^2} + \frac{\omega^2}{c^2}\varepsilon(r) - \sqrt{\varepsilon(r)}\frac{d^2}{dr^2}\left(\frac{1}{\sqrt{\varepsilon(r)}}\right)\right\}(rR(r)) = 0, \quad (10)$$

where $R(r)$ is a radial function related to the electric and magnetic fields by the Debye potentials (Wait, 1962). This equation gives the eigenvalues of the longitudinal and transverse modes, assuming either $dR(r)/dr = 0$ or $R(r) = 0$ at both boundaries, respectively. For a thin void cavity the eigenvalues are those given by Eqs. (2) and (3). However, the previous approximation is no longer valid and Eq. (10) is not sufficiently accurate for thick cavities, such as that of Titan, because the coupling between longitudinal and transverse modes is strong. A numerical computation, based on a finite element model and including not only losses in the atmosphere but also on the surface, is therefore required.

3. The numerical approach

3.1. Model inputs

The numerical algorithms that solve the resonant cavity problem from Eqs. (7)–(9) are implemented with the finite element method (Zimmerman, 2006). The meshes are composed of 5×10^4 and 10^6 elements in the 2D and 3D approximations, respectively. Comparing the results obtained in 2D and 3D, when axial symmetry applies, assesses the accuracy. Continuity conditions are imposed at the surface of Titan unless the latter coincides with the inner boundary of the cavity (Fig. 1).

The numerical algorithms require the following model inputs:

(a) *Conductivity of the atmosphere and lower ionosphere* (σ_{atm}): Several atmospheric conductivity profiles are shown in Fig. 2. The conductivity CP1 is derived from theoretical predictions (Borucki et al., 1987; Molina-Cuberos et al., 2004). This profile can be adjusted in many ways to yield a number of hybrid profiles, CP2–CP5, which combine both theoretical and experimental inputs. Although the analysis of the PWA data is not finalized yet, preliminary conductivity profiles at altitudes less than 140 km have been obtained with the mutual impedance (Hamelin et al., 2007) and relaxation probes. The hybrid conductivity profiles are constrained by the measurements obtained with these two sensors. A peak in conductivity, at around 60 km, has been observed with PWA during the descent (Grard et al., 2006), which introduces a new feature in the profile; it also appears that the theoretical models tend to overestimate the electron conductivity by as much as two orders of magnitude at ~100 km. The CP5 profile

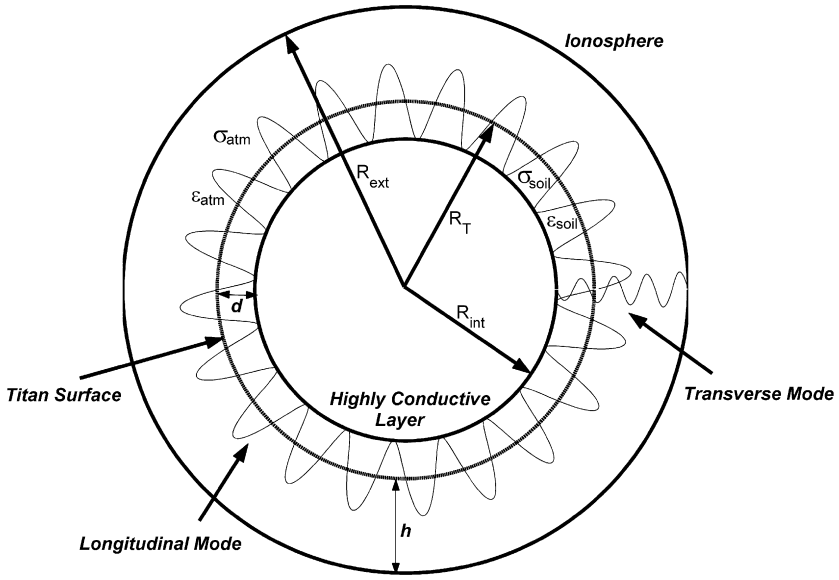

Fig. 1. Sketch of the model used for calculating the Schumann resonance on Titan. R_T: Titan radius; R_{int}: liquid layer radius; R_{ext}: ionosphere radius; h: altitude of the ionosphere; d: depth of the solid–liquid interface layer; ε_{soil}, ε_{atm}, σ_{soil}, σ_{atm}: permittivities and conductivities of the soil and atmosphere, respectively.

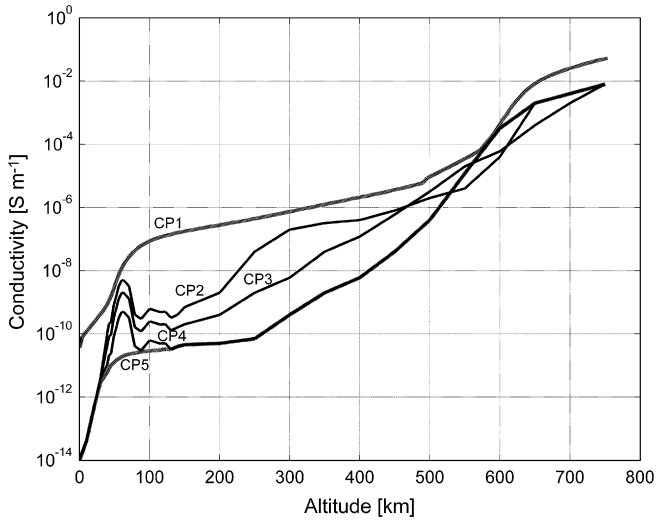

Fig. 2. Atmospheric conductivity profiles derived from theory, and obtained by combining theoretical predictions and PWA preliminary results at altitudes less than 150 km. CP1: theoretical model; CP2: conductivity constrained by mutual impedance probe measurements; CP3: intermediate profile; CP4: conductivity constrained by relaxation probe measurements; CP5: same as CP4 without low altitude feature.

provides a reference for studying the influence of the ~60 km conductivity peak. The cavity upper boundary is located between 140 and 750 km, where the conductivity is most uncertain. All hybrid profiles are fitted to Voyager and Cassini data at ~750 km. The differences between the various profiles (CP2–CP4) simulate variations that might result from extreme aerosol concentrations in that altitudes range (Borucki et al., 2006). The knowledge of the conductivity is not mandatory beyond 750 km, because the skin depth is less than 1 km.

(b) *Depth of the subsurface liquid layer* (d): A soil conductivity of $\sim 10^{-10}$ S m^{-1} implies that the penetration depth is >1000 km in the ELF range, and that the surface reflectivity is small. The skin depth of a pure liquid water layer is much smaller ($\delta_h \sim 50$ km) and it is anticipated that the penetration depth in a subsurface liquid layer is even lower due to the presence of salts and ammonia. Thus, the PEC approximation is applicable to such an inner boundary.

(c) *Permittivity and conductivity of the subsurface material* (ε_{soil}, σ_{soil}): The temperature of the soil varies between ~94 K on the surface and ~176 K in the solid–liquid interface, as suggested by theoretical models (Grasset and Sotin, 1996). In this temperature range the dielectric properties of water ice do not vary significantly, even at low frequencies. However, several models predict the presence of water–ammonia ice mixtures (Lunine and Stevenson, 1987; Tobie et al., 2006). The soil composition and porosity are unknown but a relative permittivity in the range 2–4 is tentatively assumed. The concentrations of ionic contaminants are not known and even small quantities can significantly increase the conductivity of the medium. The soil permittivity and conductivity are assumed to be uniform.

None of the models illustrated in Fig. 2 properly represent the conductivity of the atmosphere, but together they provide information about the sensitivity of the Schumann resonance frequency to the shape of the profile.

3.2. Description and validation of the simulation algorithms

The Comsol Multiphysics software (for details see Zimmerman, 2006) includes two algorithms that compute

Table 1
Comparison between the eigenfrequencies derived from the analytical and numerical models. Inner shell radii $R_T = 2575$ km and $R_E = 6370$ km

Cavity	Test	Spherical approximation (Eq. (10))		Finite element model	
		Longitudinal (Hz)	Transverse (Hz)	Longitudinal (Hz)	Transverse (Hz)
Earth	A	10.6	–	10.6	–
	B	10.5	1998	10.6	2008
	C	10.3	1670	8.86	1635
Titan	A	26.2	–	26.2	–
	B	22.9	201.2	23.1	201.2
	C	14.3	168.1	19.1	163.5

(A): $h \to 0$, $\sigma_{atm} = 0$, and $\varepsilon_{atm} = 1$; (B): Height of ionospheric boundaries $h_T = 750$ km and $h_E = 75$ km, $\sigma_{atm} = 0$, and $\varepsilon_{atm} = 1$; (C): Same as in (B), but the permittivity profile is represented by a sigmoid-type function, in the range 1–2. Perfect electric conductor boundaries are considered in all cases. The dimensions of Titan and Earth are identified by the subscripts T and E, respectively.

the eigenfrequencies and simulate the harmonic propagation modes. The first algorithm gives the complex frequencies of the eigenmodes, from which the Q-factors are derived. The eigenfrequency solver uses the ARPACK package based on a variant of the Arnoldi algorithm that is usually called the implicitly restarted Arnoldi method. For additional information see the links below.

The second algorithm solves stationary problems with the UMFPACK package. This harmonic propagation code computes the frequency spectra, identifies the propagating eigenmodes, calculates the electric field over a wide altitude range and evaluates the influence of the source distribution on the propagation modes. The solver employs the unsymmetrical-pattern multifrontal method and direct LU-factorization of the sparse matrix obtained by discretizing Eqs. (7)–(9). A detailed description about this implementation can be found in the links below.

The numerical algorithms have been validated by comparing the eigenfrequencies computed with the finite element model and those derived from Eq. (10). In the case of a thin lossless cavity, the same results are obtained from Eqs. (2) and (10), and from the finite element method (Table 1, Test A). The analytical and numerical results are similar, as long as the medium is lossless and homogeneous, and the PEC boundary conditions apply (Table 1, Test B). However, the two approaches give different results when the medium is heterogeneous (Table 1, Test C), which illustrates the limited validity of the analytical approximation.

The differences are more important, in the case of the longitudinal mode, for larger ratios of the ionosphere height over shell radius, especially when the medium filling the cavity is heterogeneous. Including the medium losses constrains further the application of Eq. (10). The numerical algorithms have also been validated against the set of parameters applicable to the Earth ionospheric cavity; the eigenfrequencies and Q-factors thus obtained

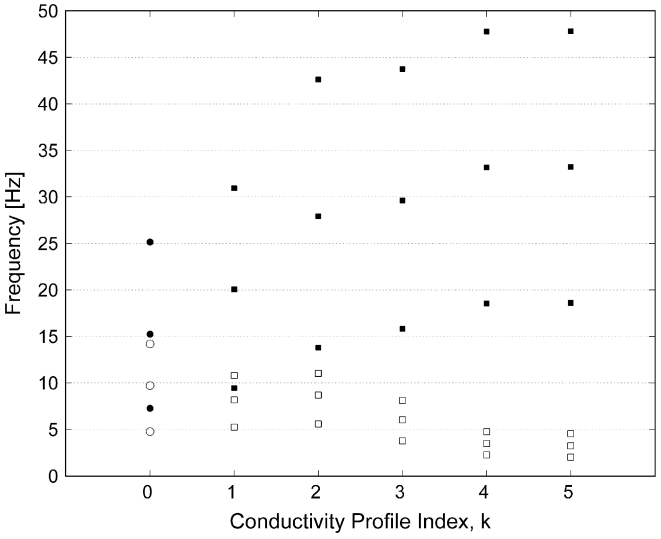

Fig. 3. The real and imaginary parts of the three lowest eigenfrequencies of the cavity are represented by the filled and empty symbols, respectively. *Squares* ($k = 1$–5): atmospheric conductivity profile CPk (see Fig. 2), with $d = 100$ km, $\varepsilon_{soil} = 3$, and $\sigma_{soil} = 10^{-9}$ S m^{-1}. *Circles* ($k = 0$): profile CP1 with perfectly reflecting surface ($d = 0$).

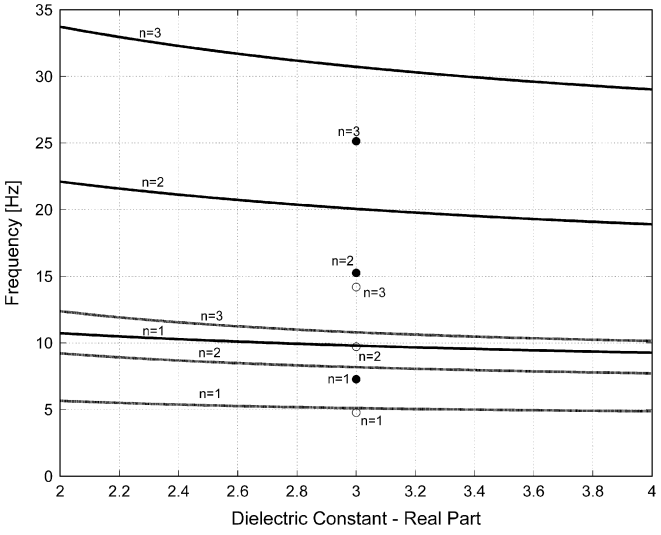

Fig. 4. The lowest three eigenfrequencies of the resonant cavity ($n = 1$–3), plotted against the real part of the soil dielectric constant, for $\sigma_{atm} = $ CP1, $d = 100$ km, and $\sigma_{soil} = 10^{-9}$ S m^{-1}. Solid and dashed lines represent the real and imaginary parts of the frequencies. The filled and empty dots represent, respectively the real and imaginary parts of the lowest eigenfrequencies, when the surface is a perfect reflector ($d = 0$).

are in fair agreement with expectations (Sentman, 1990; Nickolaenko and Hayakawa, 2002).

4. Numerical results

4.1. The eigenfrequency algorithm

This program calculates the eigenmodes for a set of parameters in the ranges: $d = 20$–200 km, $\varepsilon_{soil} = 2$–4, $\sigma_{soil} = 10^{-10}$–10^{-8} S m^{-1}, and an atmospheric conductivity

profile σ_{atm} represented by one of the CP1–CP5 models displayed in Fig. 2. Figs. 3–6 show the variations of the real and imaginary parts of the three lowest eigenfrequencies as functions of those parameters. The atmospheric conductivity, the presence of aerosols and the depth of the conductive boundary have a profound influence upon the eigenfrequencies. Therefore, the PWA data play an important role in constraining the cavity model and evaluating the Schumann resonance frequencies.

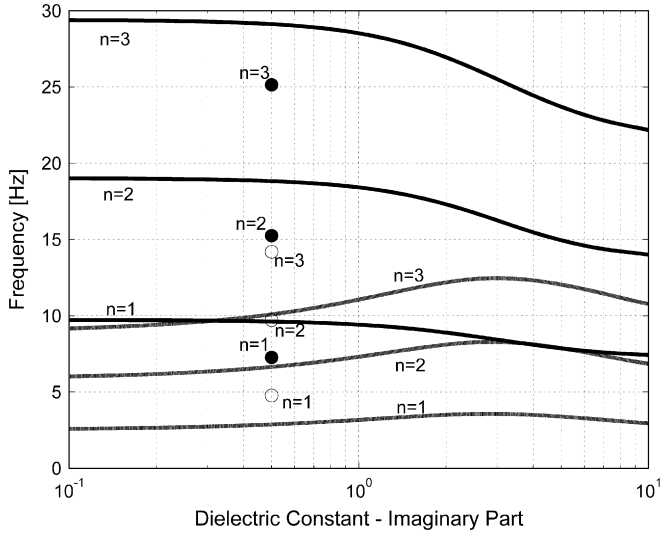

Fig. 5. Same caption as in Fig. 4, but $\varepsilon_{soil} = 3$, and the eigenfrequencies are plotted against the imaginary part of the soil dielectric constant.

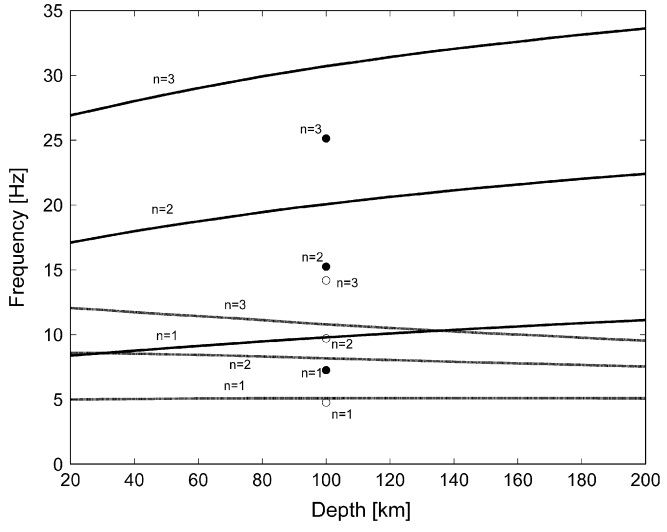

Fig. 6. The three lowest eigenfrequencies of the cavity as functions of the PEC depth, for $\sigma_{atm} = \text{CP1}$, $\varepsilon_{soil} = 3$, and $\sigma_{soil} = 10^{-9}\,\text{S m}^{-1}$ (lines and symbols as in Fig. 4).

Fig. 4 shows that an increase of permittivity reduces the eigenfrequencies of the cavity, because $\omega_n \propto \varepsilon^{-1/2}$ for a homogeneous medium. The same general behaviour is observed for the imaginary part of the frequency. The variations of the resonance frequencies as functions of the losses in the soil (Fig. 5) resemble the dielectric relaxation described by Debye's dipole polarization model. Increasing the depth of the PEC boundary has contrasting effects on the eigenfrequency, because the real part rises while the imaginary part decreases (Fig. 6). For comparison, the components of the complex eigenfrequencies are represented by circles in Figs. 3–6, when the surface is a PEC boundary (Table 2).

The knowledge of the real part of the eigenfrequency alone does not make it possible to distinguish between two cavity models. For example, this quantity equals 25 Hz for $n = 3$ in Fig. 5, not only when $d = 0$, but also when $d = 100\,\text{km}$ and the imaginary part of the dielectric constant is about 3.5. There is no ambiguity for the imaginary part of the frequency, since the latter is always larger when $d = 0$ than when $d = 100\,\text{km}$, whatever the imaginary part of the soil dielectric constant may be. Therefore, measuring the sole resonance frequencies is insufficient for a proper characterization of the cavity, and other parameters, such as the Q-factors, must be considered to constrain the results.

Contrary to all expectations a subsurface inner boundary does not necessarily entail an increase of the losses, especially if the soil bulk conductivity is small. For example, with reference to Eq. (4), Fig. 6 and the atmospheric profile CP1, it is seen that the Q-factor of the cavity is of the order of $\sim$1 when $d = 0$ and $\sim$1.5 when $d = 100\,\text{km}$. In fact, $Q \propto h/\delta_h$ in a first approximation, and an increase in shell separation can balance additional losses in the soil. The Q-factors of a cavity with the atmospheric profiles CP2–CP3 and CP4–CP5 are $\sim$2.5 and $\sim$5, respectively (Fig. 3). The results obtained with the atmospheric profile CP1 show that ELF waves are strongly attenuated, whereas for CP5 the propagation conditions are similar to the cavity of Earth.

4.2. The harmonic propagation algorithm

The harmonic propagation approach is especially suited to the analysis of global features and to the study of the

Table 2
Comparison between the lowest eigenfrequency modes (Hz) on Titan for different conductivity profiles (CP1–CP5) and a lossless atmosphere. The PEC boundaries are located at $R_{int} = R_T$ and $R_{ext} = R_T + h_T$

Profile mode	CP1	CP2	CP3	CP4	CP5	$\sigma = 0$
First	7.27 + 4.77i	13.43 + 6.25i	16.05 + 4.01i	19.15 + 2.27i	19.22 + 2.02i	23.06
Second	15.25 + 9.71i	28.13 + 10.57i	30.29 + 6.73i	34.32 + 3.71i	34.37 + 3.45i	39.93
Third	25.31 + 14.80i	43.93 + 13.64i	44.97 + 9.32i	49.48 + 5.22i	49.51 + 4.97i	56.44

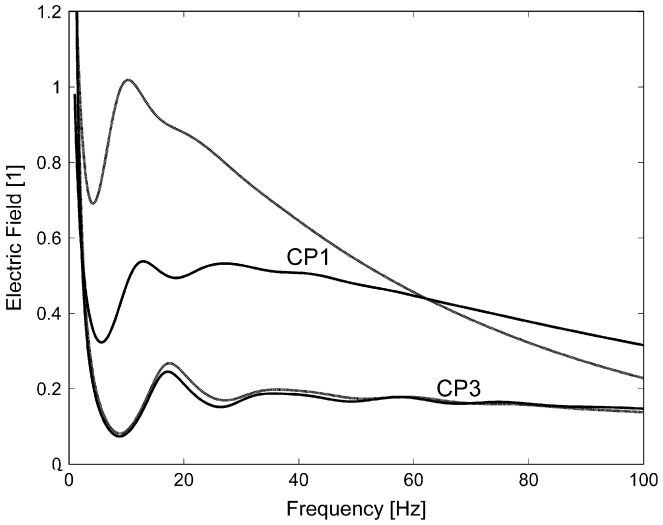

Fig. 7. Electric field frequency spectra for different conductivity profiles (CP1, CP3) and cavity configurations. The centre of the electromagnetic stimulus is located at an altitude of 35 km and the angular separation is 45° (see text for detail). Depth of the inner boundary: $d = 0$, dashed line; $d = 100$ km, solid line; $\varepsilon_{soil} = 3$; $\sigma_{soil} = 10^{-9}$ S m^{-1}.

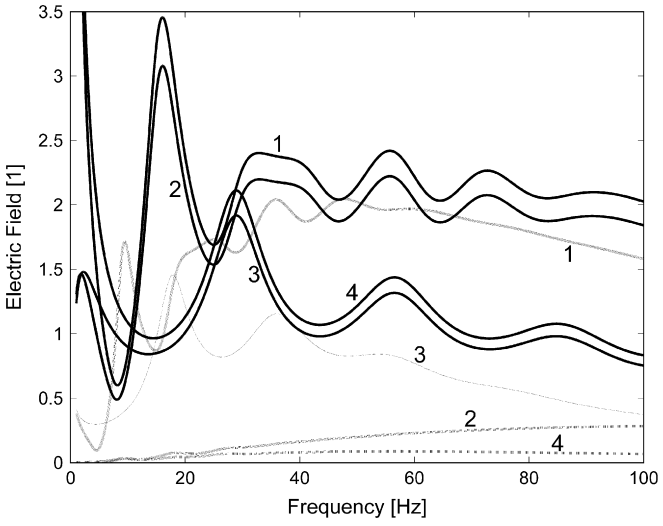

Fig. 8. Electric field frequency spectra for various angular separations, receiver altitudes and conductivity profiles. The subsurface boundary is located at $d = 100$ km ($\varepsilon_{soil} = 3$; $\sigma_{soil} = 10^{-9}$ S m^{-1}). Conductivity profile: CP3, solid line; CP1, dashed line. Angular separation and altitude: (1) 45° and 0 km; (2) 45° and 100 km; (3) 90° and 0 km; (4) 90° and 100 km.

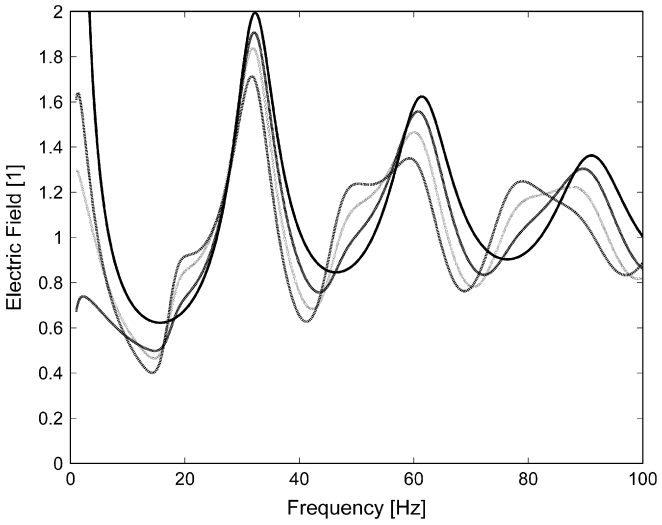

Fig. 9. Electric field frequency spectra for various receiver altitudes. The subsurface boundary is located at $d = 100$ km ($\varepsilon_{soil} = 3$; $\sigma_{soil} = 10^{-9}$ S m^{-1}); the atmospheric conductivity profile is CP4. The angular separation is 90°. Altitude: surface, solid line; 50 km, dashed line; 100 km, dotted line; 150 km, dashed–dotted line.

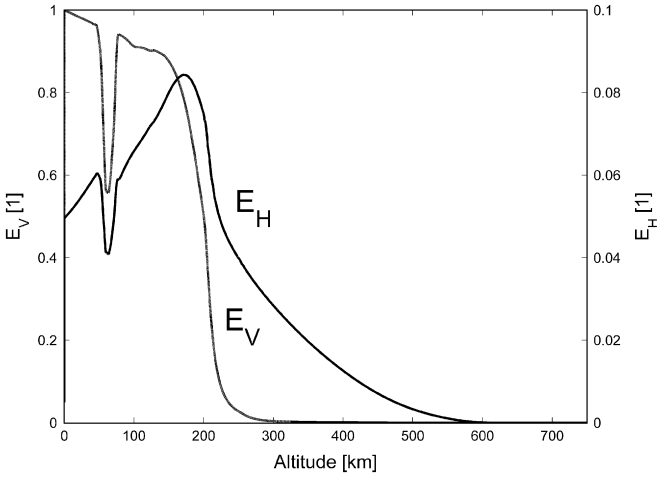

Fig. 10. Vertical (E_V, dashed line) and horizontal (E_H, solid line) electric field components as functions of altitude, at 36 Hz. The angular separation is 90° and the atmospheric model CP2. The subsurface boundary is located at $d = 100$ km ($\varepsilon_{soil} = 3$; $\sigma_{soil} = 10^{-9}$ S m^{-1}). Both components are normalized to the level of the vertical component on the surface.

electromagnetic field distribution generated by sparse sources. For the sake of simplicity, we shall assume a localized electromagnetic stimulus. The source is a pulsating monopole defined by an equipotential spherical surface of radius 15 km, whose centre is located at an altitude of 35 km. The monopole is considered to be infinitely small because its diameter is much smaller than the wavelength and cavity size. The algorithm calculates the frequency response of the cavity, in the range 1–100 Hz, and the electromagnetic field distribution as a function, for example, of the distance between the source and the receiver. The far field numerical results are very similar to those obtained for a vertical Hertzian dipole at an altitude of 50 km, approximated by two spheres, 15 km in radius and distance of 35 km.

Fig. 7 shows the frequency spectrum in the ELF range of the electric field generated by a source of arbitrary amplitude, for two conductivity profiles (CP1 and CP3), a PEC boundary on the surface and at a depth of 100 km, and an angular separation, that is the angle between the source centre and the receiver seen from Titan's centre, of 45°. The receiver rests on the surface. The stimulus signal is stationary and its spectrum is flat in the frequency band of interest.

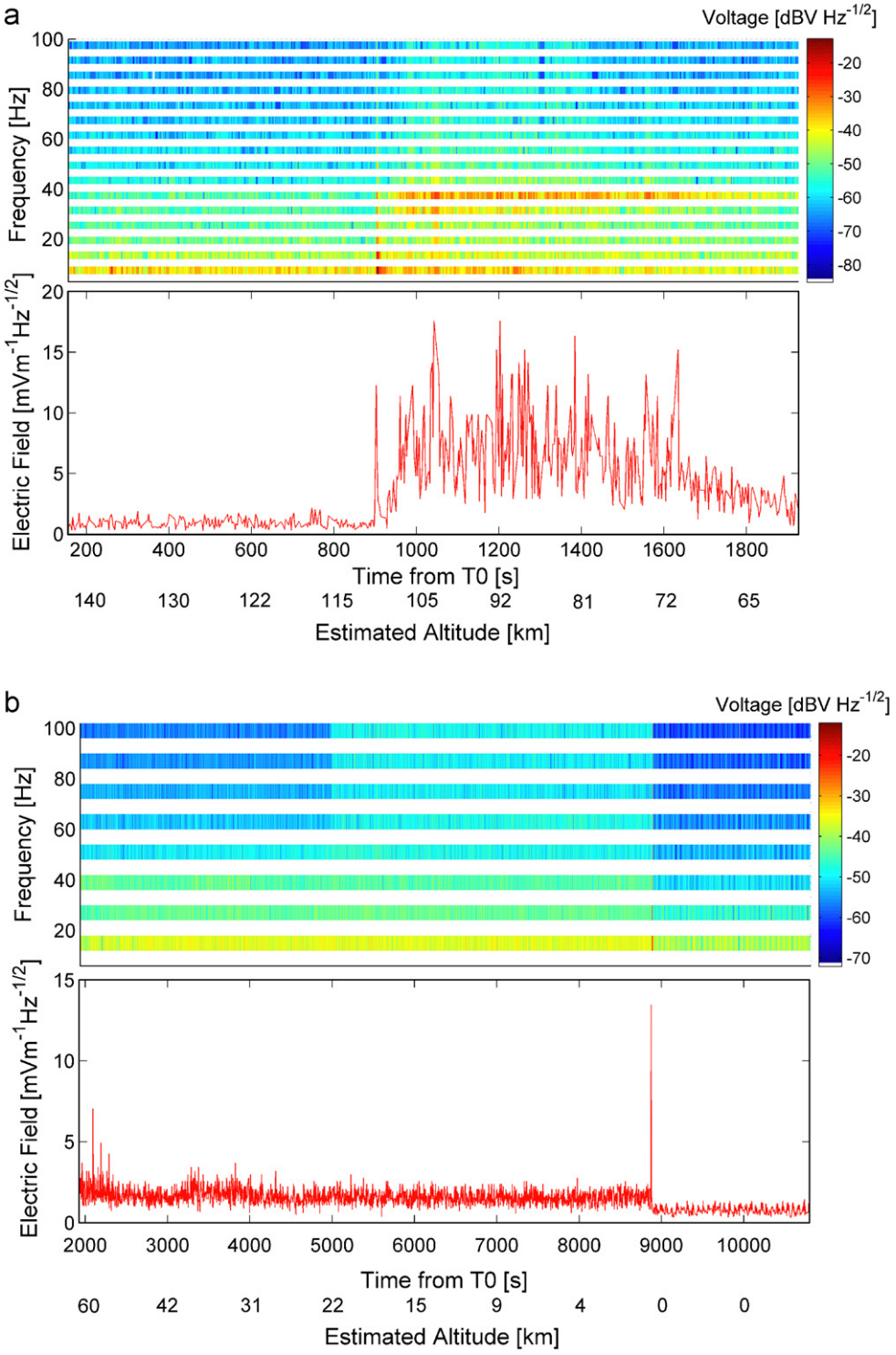

Fig. 11. Electric signal measured with the PWA receivers in the ELF range before (upper two panels: 1 and 2), and after (lower two panels: 3 and 4), the operation mode change. Panels 1 and 3: Dynamic spectra with frequency resolutions 3 and 6 Hz, respectively. Spectral levels are given by the color scales shown on the right-hand side. White stripes correspond to the data loss in channel A. Panels 2 and 4: Electric field of the spectral line around 36 Hz against time. The peaks at ~ 900 and ~8870 s are due to the deployment of the third parachute and touchdown, respectively.

The frequency spectrum of the received signal is plotted in Fig. 8, for several angular separations and cavity configurations. The first eigenmode, at around 16 Hz, is seen when the angular separation is 45°, but is not visible when this angle is 90°. Fig. 9 indicates that, for a given cavity configuration (see figure caption) and an angular separation of 90°, the frequency of the second harmonic, above 30 Hz, decreases by ~1 Hz when the altitude increases from 0 to 150 km. This frequency shift is also sensitive to small variations of the angular separation.

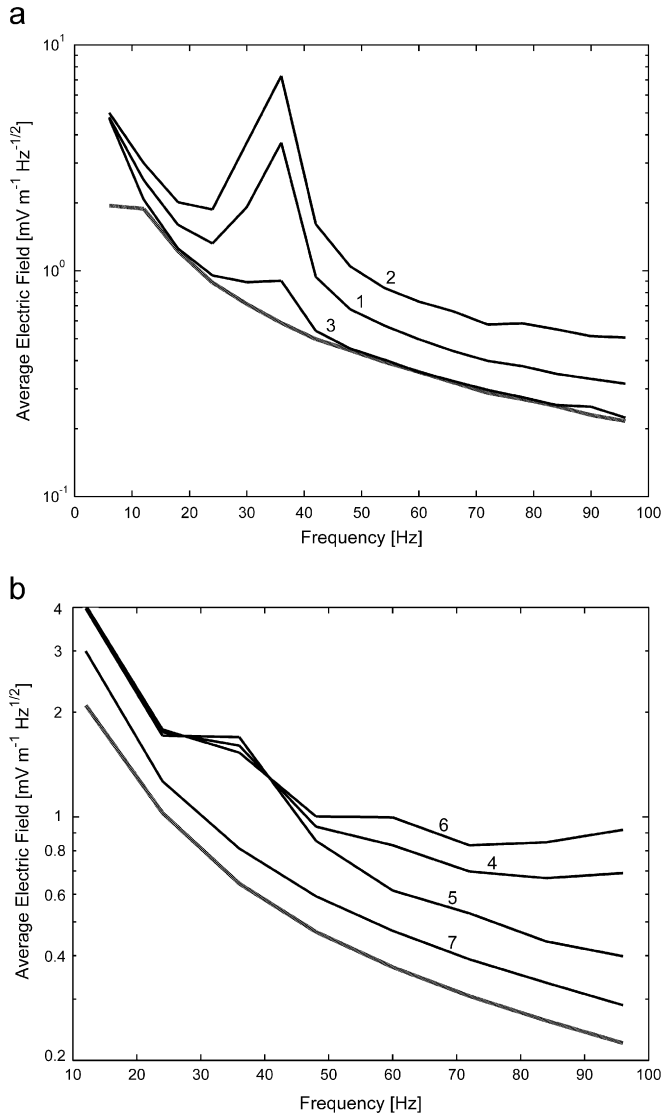

Fig. 12. Mean electric field measured by PWA in the ELF range before (left) and after (right) the mode change, in several altitude ranges: (1) 60–140 km; (2) 80–110 km; (3) 115–140 km; (4) 0–60 km; (5) 20–60 km; (6) 0–20 km; and (7) surface. The dashed lines represent the signal level during the cruise.

Fig. 10 shows how the vertical and horizontal components of the electric field vary with altitude for the atmospheric profile CP2, at 36 Hz.

5. The PWA measurements in the ELF range

We shall now present the ELF electric field observations performed in the atmosphere of Titan and, with reference to the numerical simulation results, investigate whether they display the spectral signature of a Schumann resonance.

The permittivity, waves and altimetry analyser on Huygens measures ELF electric fields from $t = T0 + 156$ s, corresponding to an altitude of approximately 140 km, until $t = T0 + 10798$ s, i.e. 32 min after touchdown, where $T0$ is the nominal starting time of the descent. The signal is

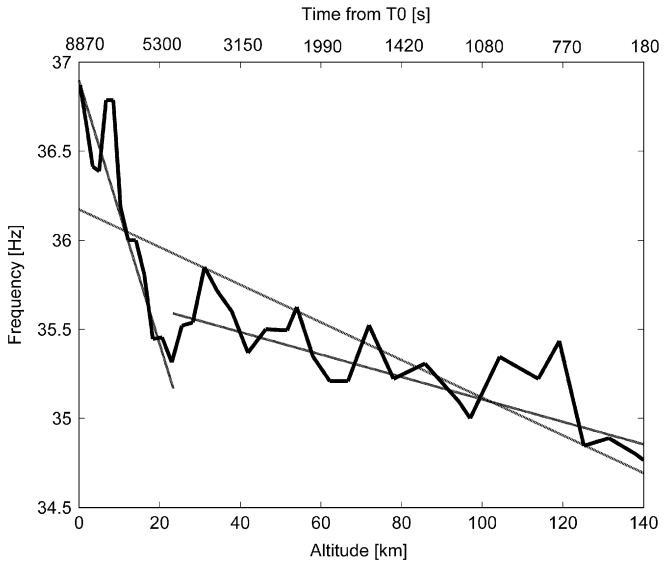

Fig. 13. Variation of the peak signal frequency during the descent (solid line), and linear fits to the data sets collected during the entire descent (dash–dot line) and at altitudes above and below 21 km (dashed line).

analysed in the range 3–99 Hz with a resolution of 3 Hz up to $t \sim T0 + 1930$ s (~61.5 km) and 6 Hz thereafter. Each spectrum is processed, split into odd and even lines, and sent on two telemetry channels (A and B). However, due to the loss of channel A, only even lines are available. PWA recorded 582 high- and 2588 low-resolution spectra.

The spectral bands covered before and after the operation mode change are partly overlapping and partly complementary. However, due to the data loss, about one quarter of the ELF range is not covered at all during the whole descent. This domain consists of 3 Hz stripes centred on the frequencies

$$f_{ab} = 3(4n_{ab} - 3), \tag{11}$$

where $n_{ab} = 1, 2, \ldots, 8$.

Fig. 11 shows the dynamic spectra of the ELF electric field and the strength of the lines at around 36 Hz. The signal is enhanced in the interval 950–1800 s and displays other features, such as spikes at 900 and 8870 s, which correspond to the deployment of the stabilizer parachute and to the touchdown. There is also an increase of the signal over the whole frequency range at ~5000 s (corresponding to an altitude of ~21 km), which seems to coincide with the time at which the Huygens camera detects a thin haze layer (Tomasko et al., 2005; Grard et al., 2006).

The signal enhancement at around 36 Hz is not always clearly visible in the dynamic spectra, but it nevertheless persists until touchdown. Fig. 12 shows the average spectra in several altitude ranges and, for comparison, the reference spectra recorded during the cruise. The line at 36 Hz can always be traced during the descent but not on the surface. A careful examination of the data set reveals that the "36 Hz" signal is visible in at least 50% of the

spectra in the terminal phase of the descent and during up to 95% of the times when its amplitude is enhanced.

The data sets recorded before and after the operation mode change are split in bins of 50 and 100 spectra, respectively, and the weighted arithmetic mean frequency of the emission, i.e. the average value of the 36 Hz and adjacent lines, is evaluated within each bin. The output of this crude analysis is reported in Fig. 13 and indicates that the peak frequency increases by about 1.5 Hz throughout the descent. The frequency is also sensitive to small variations of the angular separation.

6. Discussion and conclusion

Titan offers peculiarities different from those of Earth. The geometry of Titan's cavity is such that the eigenfrequencies of the longitudinal and transverse modes are coupled, which precludes the use of analytical approximations. The low conductivity ($\sim 10^{-10}$ S m^{-1}) and low reflectivity of the soil also call for a more elaborated approach, but make it possible to study the subsurface and to search for the ocean predicted by theoretical models, provided the electric properties of the soil vary little with depth (Figs. 1 and 3). The conductivity peak at 60 km splits the cavity in two sectors, influences the propagation of waves and enhances the electric field strength in the upper atmosphere (Fig. 10).

The novelty of this numerical approach is threefold:

(1) Maxwell equations are solved with the finite element method, whereas most previous efforts were based on semi-analytical approximations or TLM (transmission line model) and FDTD (finite difference time domain) numerical models.
(2) The conductivity profiles of the cavity are more realistic, since they are partly constrained by the measurements of the PWA–Huygens instrument, at low altitudes, and the Voyager and Cassini results, at high altitudes.
(3) The wave propagation simulation takes into account the effect of subsurface losses.

The simulation results provides an overview of the ELF wave distribution in the resonant cavity; the eigenfrequencies and Q-factors obtained with CP1 lie in the same range as those presented by Yang et al. (2006) with the FDTD approach. A significant aerosol concentration at high altitude increases the Q-factor (Eq. (4), Table 2), which can be higher than on Earth.

The ELF electric field measurements performed during the descent of the Huygens Probe through the atmosphere of Titan reveals the existence of a narrow-band emission at around 36 Hz (Fig. 11). The maximum and average amplitudes recorded during the descent are 17.5 and 2 mV m^{-1} Hz$^{-1/2}$, respectively; the mean frequency increases steadily during the descent, from 35 Hz at 140 km to 37 Hz before touchdown (Fig. 13). The transition at an altitude of about 21 km (Fig. 11) seems to match the occurrence of a thin haze layer imaged by the camera onboard the Probe. If one discards the frequency points measured at altitudes less than ~21 km, then the mean variation observed in Fig. 13 is close to 1 Hz.

For most cavity models, a spectral peak at 36 Hz can match the second eigenfrequency (Fig. 3). Furthermore, the lowest eigenmode is either matching an absent line or the corresponding amplitude is small. The latter phenomenon can be understood if the angular separation between the source and the receiver is close to 90°; the amplitude of the first eigenmode is negligible and only the second one is measurable (Fig. 8). Another possible, though less likely, reason for the absence of the fundamental mode is that its frequency coincides with the second missing spectral line ($n_{ab} = 2$ in Eq. (11)).

The peak spectral frequencies associated with a source at high latitude (angular separation ~90°) vary with the altitude of the receiver (Fig. 9). The frequency of the second eigenmode (~32 Hz) increases, for example, by approximately 1 Hz between an altitude of 150 km and the surface, in good agreement with the experimental results reported in Fig. 13; the variation can be larger if a small deviation of the angular separation is also taken into account (see the Huygens Probe descent trajectory; Lebreton et al., 2005).

The model polarization profile of the electric field is illustrated in Fig. 10. The horizontal component is roughly one order of magnitude smaller than the vertical one; it shows a trough that matches the conductivity peak, in accordance with Ampere law, and a peak close to 170 km. The PWA dipole is approximately horizontal and the variation of the "36 Hz" level with altitude (see Figs. 11 and 12) should be compared, in first approximation, with that of the model horizontal component (Fig. 10). The measurements indicate that the peak electric field is seen at ~90–100 km with a mean level of ~7 mV m^{-1} (Fig. 11). On Earth, the vertical component of the electric field related to the Schumann resonance is only ~0.1 mV m^{-1}. We conjecture that the amplitude of the measured signal is strongly affected by atmospheric turbulence and the variation of the angle made by the antenna and the field orientation. Therefore, the data will be revisited when accurate Huygens Probe attitude and atmospheric parameters are available.

Methane clouds have been observed at high latitudes (Brown et al., 2002; Griffith et al., 2005) but no related lightning activity has been reported. In fact, the narrow-band electric field recorded by Huygens is difficult to interpret in terms of an electromagnetic resonance associated with lightning activity. Its amplitude exceeds by one order of magnitude the level predicted by a simple scaling of the Earth model to Titan, which calls the source of the signal in question and leads us to wonder whether this observation can be explained by a natural phenomenon or an artefact.

An alternative source of energy is clearly required: corona discharges within clouds, an interaction between

the Huygens Probe and its ionised environment, a mechanism driven by the magnetosphere of Saturn, etc. Several options are scrutinized in a companion paper (Béghin et al., 2007). In short, if a global circuit exists on Titan, it might considerably differ from that of Earth.

No signal at 36 Hz has ever been detected during the interplanetary cruise checkouts, or during the ascending and descending phases of earlier balloon flights. The signal is not visible either after landing, possibly because the background noise level is significantly larger on Titan's surface than during the interplanetary cruise (Fig. 12); electrical interference generated by other instruments or subsystems can therefore be excluded.

The list of other possible artefacts includes micro phonic effects induced by vibrations of the parachutes, the platform that carries the instruments or the booms that hold the sensors. Effects of temperature and haze deposits have also been assessed, because the booms are exposed to the environment. Some of these artefacts have been thoroughly analysed (Béghin et al., 2007), others are still under active investigation, but none offers at present a more convincing and definite explanation than that developed in this paper.

Was the Schumann resonance really observed during the descent of the Huygens Probe upon Titan? Possibly, but the question is not entirely closed.

Acknowledgements

The Cassini–Huygens mission is a cooperative project of NASA, the European Space Agency (ESA) and the Italian Space Agency (ASI). The Huygens Atmospheric Structure Instrument (HASI) onboard the Huygens Probe is a multisensor package designed to measure the physical quantities characterizing Titan's atmosphere. The HASI Project Office is at CISAS "G. Colombo" of the University of Padova (UPD), Italy, and is coordinated by ASI's Observation of the Universe Directorate. The PWA subsystem has been designed, developed and tested by: the Research and Science Support Department (RSSD), ESTEC, ESA; the Institut für Weltraumforschung/ÖAW (IWF), Graz, Austria; the Laboratoire de Physique et Chimie de l'Environnement, (LPCE), CNRS—CNES, Orléans, France; the Instituto de Astrofísica de Andalucía (IAA -CSIC), Granada, Spain.

The authors thank the International Space Science Institute (Bern, Switzerland) for hosting and supporting their team meetings. The first author is indebted to Alain Péan for fruitful discussions about software and hardware optimisation.

References

Balanis, C.A., 1989. Advanced Engineering Electromagnetics. Wiley, New York.

Balser, M., Wagner, C.A., 1960. Observations of Earth-ionosphere cavity resonances. Nature 188, 638–641.

Béghin, C., Simões, F., Karnoselskhikh, V. Schwingenschuh, K., Berthelier, J.-J., Besser, B. Bettanini, C., Grard, R., Hamelin, M., Lopez-Moreno, J.J., Molina-Cuberos, G.J., Tokano, T., 2007. A Schumann-like resonance on Titan driven by Saturn's magnetosphere possibly revealed by the Huygens Probe. Icarus, http://dx.doi.org/10.1016/j.icarus.2007.04.005.

Bliokh, P.V., Nickolaenko, A.P., Filippov, Yu.F., 1980. Schumann resonances in the Earth-ionosphere cavity. In: Jones, D.L1. (Ed.). Peter Peregrinus, Oxford, England.

Borucki, W.J., Levin, Z., Whitten, R.C., Keesee, R.G., Capone, L.A., Summers, A.L., Toon, O.B., Dubach, J., 1987. Predictions of the electrical conductivity and charging of the aerosols in Titan's atmosphere. Icarus 72, 604–622.

Borucki, W.J., Whitten, R.C., Bakes, E.L.O., Barth, E., Tripathi, S., 2006. Predictions of the electrical conductivity and charging of the aerosols in Titan's atmosphere. Icarus 181, 527–544.

Brown, M.E., Bouchez, A.H., Griffith, C.A., 2002. Direct detection of variable tropospheric clouds near Titan's south pole. Nature 420, 795–797.

Fulchignoni, M., Ferri, F., Angrilli, F., Bar-Nun, A., Barucci, M.A., Bianchini, G., Borucki, W., Coradini, M., Coustenis, A., Falkner, P., Flamini, E., Grard, R., Hamelin, M., Harri, A.M., Leppelmeier, G.W., Lopez-Moreno, J.J., McDonnell, J.A.M., McKay, C.P., Neubauer, F.H., Pedersen, A., Picardi, G., Pirronello, V., Rodrigo, R., Schwingenschuh, K., Seiff, A., Svedhem, H., Vanzani, V., Zarnecki, J., 2002. The characterization of Titan's atmosphere physical parameters by the Huygens Atmospheric Structure Instrument (HASI). Space Sci. Rev. 104, 395–431.

Fulchignoni, M., Ferri, F., Angrilli, F., Ball, A.J., Bar-Nun, A., Barucci, M.A., Bettanini, C., Bianchini, G., Borucki, W., Colombatti, G., Coradini, M., Coustenis, A., Debei, S., Falkner, P., Fanti, G., Flamini, E., Gaborit, V., Grard, R., Hamelin, M., Harri, A.M., Hathi, B., Jernej, I., Leese, M.R., Lehto, A., Lion Stoppato, P.F., López-Moreno, J.J., Mäkinen, T., McDonnell, J.A.M., McKay, C.P., Molina-Cuberos, G., Neubauer, F.M., Pirronello, V., Rodrigo, R., Saggin, B., Schwingenschuh, K., Seiff, A., Simões, F., Svedhem, H., Tokano, T., Towner, M.C., Trautner, R., Withers, P., Zarnecki, J.C., 2005. *In situ* measurements of the physical characteristics of Titan's environment. Nature 438, 785–791.

Grard, R., Svedhem, H., Brown, V., Falkner, P., Hamelin, M., 1995. An experimental investigation of atmospheric electricity and lightning activity to be performed during the descent of the Huygens Probe on Titan. J. Atmos. Terr. Phys. 57, 575–585.

Grard, R., Hamelin, M., López-Moreno, J.J., Schwingenschuh, K., Jernej, I., Molina-Cuberos, G.J., Simões, F., Trautner, R., Falkner, P., Ferri, F., Fulchignoni, M., Rodrigo, R., Svedhem, H., Béghin, C., Berthelier, J.-J., Brown, V.J.G., Chabassière, M., Jeronimo, J.M., Lara, L.M., Tokano, T., 2006. Electric properties and related physical characteristics of the atmosphere and surface of Titan. Planet. Space Sci. 54, 1124–1136.

Grasset, O., Sotin, C., 1996. The cooling rate of a liquid shell in Titan's interior. Icarus 123, 101–112.

Griffith, C.A., Penteado, P., Baines, K., Drossart, P., Barnes, J., Bellucci, G., Bibring, J., Brown, R., Buratti, B., Capaccioni, F., Cerroni, P., Clark, R., Combes, M., Coradini, A., Cruikshank, D., Formisano, V., Jaumann, R., Langevin, Y., Matson, D., McCord, T., Mennella, V., Nelson, R., Nicholson, P., Sicardy, B., Sotin, C., Soderblom, L.A., Kursinski, R., 2005. The evolution of Titan's mid-latitude clouds. Science 310, 474–477.

Hamelin, M., Béghin, C., Grard, R., López-Moreno, J.J., Schwingenschuh, K., Simões, F., Trautner, R., Berthelier, J.J., Brown, V.J.G., Chabassière, M., Falkner, P., Ferri, F., Fulchignoni, M., Jernej, I., Jeronimo, J.M., Molina-Cuberos, G.J., Rodrigo, R., Tokano, T., 2007. Electron conductivity and density profiles derived from the Mutual Impedance Probe measurements performed during the descent of Huygens through the atmosphere of Titan. Planet. Space Sci., in press, doi:10.1016/j.pss.2007.04.008.

Lebreton, J.-P., Witasse, O., Sollazzo, C., Blancquaert, T., Couzin, P., Schipper, A.-M., Jones, J.B., Matson, D.L., Gurvits, L.I., Atkinson,

D.H., Kazeminejad, B., Perez-Ayucar, M., 2005. An overview of the descent and landing of the Huygens probe on Titan. Nature 438, 759–764.

Lide, D.R., et al., 2005. CRC Handbook of Chemistry and Physics, 86th ed. Taylor Francis, Boca Raton, FL.

Lunine, J.I., Stevenson, D.J., 1987. Clathrate and ammonia hydrates at high pressure-application to the origin of methane on Titan. Icarus 70, 61–77.

Molina-Cuberos, G.J., Porti, J., Besser, B.P., Morente, J.A., Margineda, J., Lichtenegger, H.I.M., Salinas, A., Schwingenschuh, K., Eichelberger, H.U., 2004. Schumann resonances and electromagnetic transparence in the atmosphere of Titan. Adv. Space Res. 33, 2309–2313.

Morente, J.A., Molina-Cuberos, G.J., Portí, J.A., Schwingenschuh, K., Besser, B.P., 2003. A study of the propagation of electromagnetic waves in Titan's atmosphere with the TLM numerical method. Icarus 162, 374–384.

Nickolaenko, A.P., Hayakawa, M., 2002. Resonances in the Earth-ionosphere Cavity. Kluwer Academic Publishers, Dordrecht, The Netherlands.

Nickolaenko, A.P., Besser, B.P., Schwingenschuh, K., 2003. Model computations of Schumann resonance on Titan. Planet. Space Sci. 51 (13), 853–862.

Schumann, W.O., 1952. On the free oscillations of a conducting sphere which is surrounded by an air layer and an ionosphere shell, Über die strahlungslosen Eigenschwingungen einer leitenden Kugel, die von einer Lutschicht und einer Ionosphärenhülle umgeben ist. Z. Naturforschung A 7, 149–154 (in German).

Schwingenschuh, K., Molina-Cuberos, G.J., Eichelberger, H.U., Torkar, K., Friedrich, M., Grard, R., Falkner, P., López-Moreno, J.J., Rodrigo, R., 2001. Propagation of electromagnetic waves in the lower ionosphere of Titan. Adv. Space Res. 28 (10), 1505–1510.

Sentman, D.D., 1990. Approximate Schumann resonance parameters for a two-scale height ionosphere. J. Atmos. Terr. Phys. 52, 35–46.

Sohl, F., Sears, W.D., Lorenz, R.D., 1995. Tidal dissipation on Titan. Icarus 115, 278–294.

Tobie, G., Grasset, O., Lunine, J.I., Mocquet, A., Sotin, C., 2005. Titan's internal structure inferred from a coupled thermal–orbital model. Icarus 175, 496–502.

Tobie, G., Lunine, J.I., Sotin, C., 2006. Episodic outgassing as the origin of atmospheric methane on Titan. Nature 440, 61–64.

Tomasko, M.G., Archinal, B., Becker, T., Bézard, B., Bushroe, M., Combes, M., Cook, D., Coustenis, A., de Bergh, C., Dafoe, L.E., Doose, L., Douté, S., Eibl, A., Engel, S., Gliem, F., Grieger, B., Holso, K., Howington-Kraus, E., Karkoschka, E., Keller, H.U., Kirk, R., Kramm, R., Küppers, M., Lanagan, P., Lellouch, E., Lemmon, M., Lunine, J., McFarlane, E., Moores, J., Prout, G.M., Rizk, B., Rosiek, M., Rueffer, P., Schröder, S.E., Schmitt, B., See, C., Smith, P., Soderblom, L., Thomas, N., West, R., 2005. Rain, winds and haze on Titan. Nature.

Wait, J., 1962. Electromagnetic Waves in Stratified Media. Pergamon Press, Oxford, New York, Paris.

Williams, E., 1992. The Schumann resonance: a global tropical thermometer. Science 256, 1184–1187.

Yang, H., Pasko, V.P., Yair, Y., 2006. Three-dimensional finite difference time domain modeling of the Schumann resonance parameters on Titan, Venus, and Mars. Radio Sci. 41, RS2S03.

Zimmerman, W.B.J., 2006. Multiphysics Modelling with Finite Element Methods. World Scientific, Abingdon, Oxon, UK.

Links

〈http://www.cise.ufl.edu/research/sparse/UMFPACK〉 (accessed January 2007).

〈http://www.caam.rice.edu/software/ARPACK〉 (accessed January 2007).

Paper 5

A Schumann-like resonance on Titan driven by Saturn's magnetosphere possibly revealed by the Huygens probe

Béghin, C., Simões, F., Karsnoselskhikh, V., Schwingenschuh, K., Berthelier, J.J., Besser, B.P., Bettanini, C., Grard, R., Hamelin, M., López-Moreno, J.J., Molina-Cuberos, G.J., Tokano, T.

Icarus **191**, 251-266 (2007)

Available online at www.sciencedirect.com
ScienceDirect
Icarus 191 (2007) 251–266
ICARUS
www.elsevier.com/locate/icarus

A Schumann-like resonance on Titan driven by Saturn's magnetosphere possibly revealed by the Huygens Probe

C. Béghin [a,*], F. Simões [b], V. Krasnoselskikh [a], K. Schwingenschuh [c], J.J. Berthelier [b], B.P. Besser [c], C. Bettanini [d], R. Grard [e], M. Hamelin [b], J.J. López-Moreno [f], G.J. Molina-Cuberos [g], T. Tokano [h]

[a] *LPCE-CNRS-Université d'Orléans, 3A, Avenue de la Recherche Scientifique, 45071 Orléans Cedex 2, France*
[b] *CETP, 4 Avenue de Neptune, 94107 Saint Maur, France*
[c] *Space Research Institute, Austrian Academy of Sciences (IWF), Schmiedlstrasse 6, 8042 Graz, Austria*
[d] *CISAS "G. Colombo," Università di Padova, Via Venezia 15, 35131 Padova, Italy*
[e] *RSSD, ESA-ESTEC, European Space Agency, Keplerlaan 1, 2200 AG Noordwijk, The Netherlands*
[f] *Instituto de Astrofisica de Andalucia IAA-CSIC, Camino Bajo de Huetor, 50, 18008 Granada, Spain*
[g] *Applied Electromagnetic Group, Department of Physics, University of Murcia, Murcia 30100, Spain*
[h] *Institut für Geophysik und Meteorologie, Universität zu Köln, Albertus-Magnus Platz, 50923 Köln, Germany*

Received 12 January 2007; revised 18 March 2007

Available online 21 April 2007

Abstract

The low-frequency data collected with the antenna of the Permittivity, Wave and Altimetry experiment on board the Huygens Probe that landed on Titan on 14 January 2005 have been thoroughly analyzed considering different possible natural and artificial effects. Although a definite conclusion is still subject to the outcome of complementary inquiries, it results from our analysis that the observations can be explained, for the most part, in term of natural phenomena rather than being artifacts. Extremely-low frequency waves generated in the ionosphere of Titan, driven by the corotating Saturn's frozen plasma flow, are assumed to be the most likely source for the observation of the second eigenmode of a Schumann-like resonance at around 36 Hz in the moon-ionosphere cavity. This particular mode is thought to be enhanced with respect to other harmonics because of the particular location of the landing site with respect to that of the supposed sources. The power budget of the observed wave amplitude seems to be consistent with a rough model of the global current of the wake-ionosphere circuit. Broadband low-frequency noise events which are observed sporadically during the descent are probably due to shot noise on the antenna when the Probe is crossing aerosol clouds, an interpretation supported by post-flight ground tests. Contrary to the situation encountered on Earth, atmospheric lightning does not appear to be the source of a conventional Schumann resonance on Titan.

Keywords: Satellites, atmospheres; Lightning; Saturn, magnetosphere; Titan

1. Introduction

The search for atmospheric lightning activity was one of the main objectives of the electric field measurements performed in the extremely-low and very-low frequency ranges (ELF-VLF) by the Permittivity, Waves and Altimetry (PWA) analyzer (Grard et al., 1995), as a sub-system of the Huygens Atmospheric Structure Instrument (HASI) (Fulchignoni et al., 2002) that landed on Titan on January 14, 2005. It was then hypothesized that different signatures of a significant lightning activity could be detected in the atmosphere by the instrument. Such a major scientific discovery would have strongly supported the importance of atmospheric electricity in the theoretical models that predict the sparking production of complex organic compounds and eventually of pre-biotic molecules (Raulin et al., 1998), as it is thought to have been the case in the primitive Earth's atmosphere.

One electric component of electromagnetic (EM) and, possibly electrostatic (ES) waves was measured with a dipole made of two electrodes Rx1 and Rx2, distant of about 2 m, with the

* Corresponding author.
E-mail address: cbeghin@cnrs-orleans.fr (C. Béghin).

0019-1035/$ – see front matter
doi:10.1016/j.icarus.2007.04.005

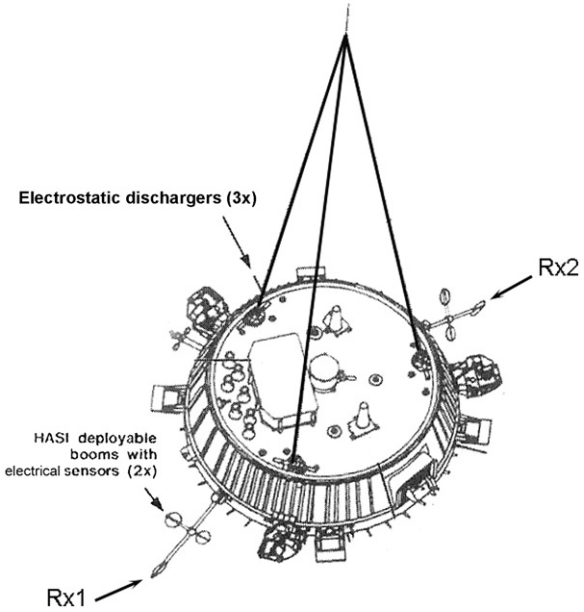

Fig. 1. General view of the Huygens payload and parachute bridles (after Lebreton and Matson, 2002).

Huygens Probe body in between (Fig. 1). Severe constraints imposed by the mission complexity leaded to design such short antenna with the consequence of reducing drastically the sensitivity. This is applicable as well to passive observations of natural waves, as to the active Mutual Impedance (MI) measurement, designed for deriving the local electron conductivity and density (Hamelin et al., 2007). However, in spite of those constraints and of the loss of one telemetry channel between the Probe and the orbiter (Grard et al., 2006), the optimized use of the resources allowed to perform both passive and active measurements throughout the descent from 140 km to landing for 2 h 25 min, and during 32 min at the surface until the end of the transmission session.

The onboard processing of the waveform received by the electric dipole was performed with the Fast Fourier Transform technique, within two frequency ranges, namely the so-called "Schumann" ELF band (3–96 Hz, with 3 Hz resolution) and a VLF band from 180 Hz to 11.5 kHz (for detail see Grard et al., 1995). In this paper, we will focus essentially our analysis on the ELF observations since the challenge of the passive measurements was the eventual detection of a Schumann resonance similar to that observed on Earth since the middle of the last century (Schumann, 1952; for a historical review see Besser, 2006). The existence of this phenomenon would be indeed an indirect evidence of a strong lightning activity.

2. Observations

In the ELF range, due to the loss of the second telemetry channel, one got only half of data, i.e., the even spectral lines by steps of 6 Hz, with 3 Hz resolution each, from 6 up to 96 Hz in the first part of the descent (Fig. 2). A pre-programmed mode change occurred at about 61 km, at 1930 s after ignition of the landing sequence, so that the available data until touch-down contain only the even spectral lines by steps of 12 Hz, with 6 Hz resolution (Fig. 3). A similar transition applies to the VLF range (not seen here), which also contains valuable data (Grard et al., 2006), put forward in Section 7 for the interpretation of the ELF noise. The spectrogram obtained during the first phase

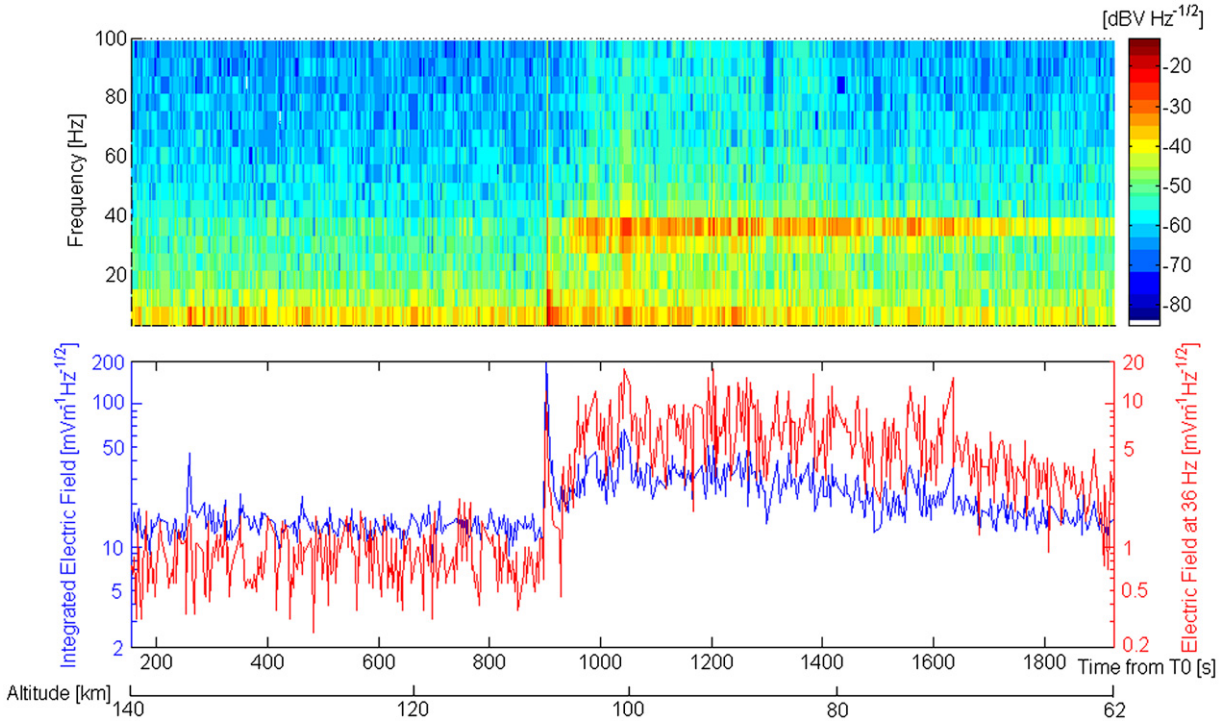

Fig. 2. Spectrogram of the ELF signal received with the electric dipole during the descent in Titan's atmosphere between 140 and 62 km. Top: spectrogram in the bandwidth 6–99 Hz; bottom: integrated field amplitude within the 99 Hz bandwidth (blue) and spectral level of the "36 Hz" line (red).

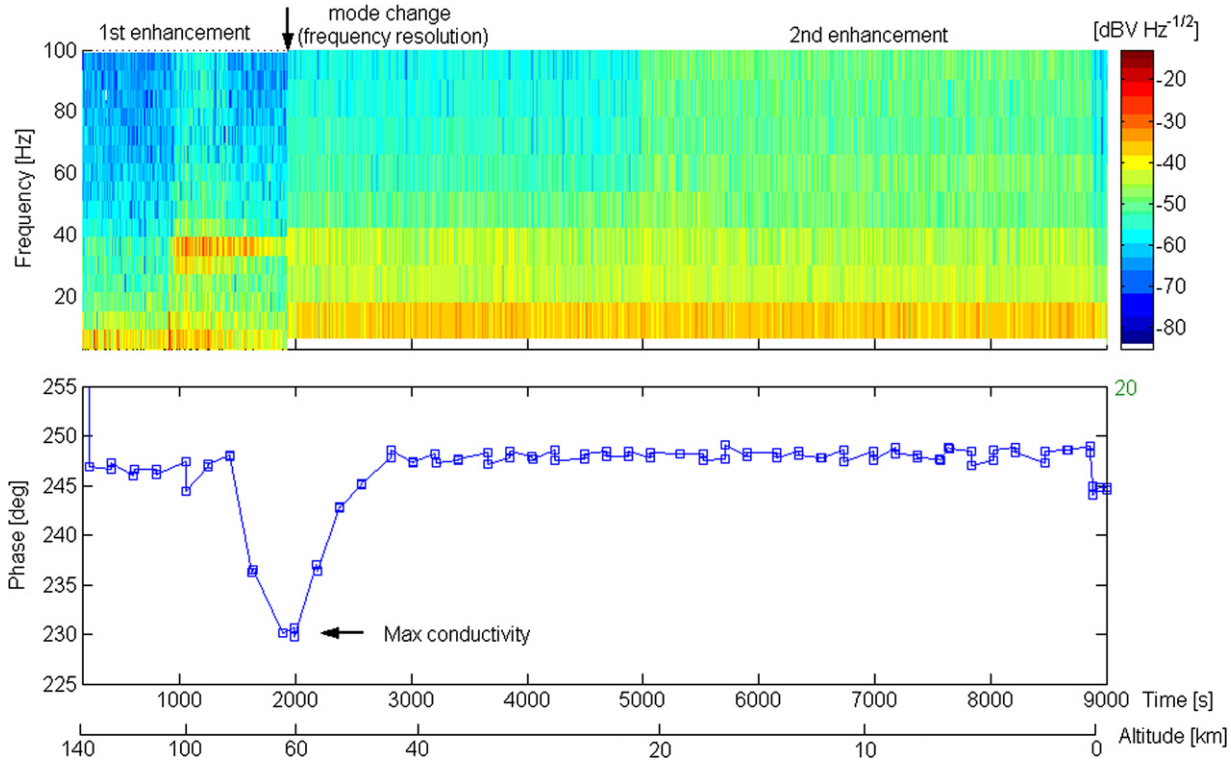

Fig. 3. ELF spectrogram (top) and phase variation of the mutual impedance (bottom) for the entire descent.

of the Huygens descent is enlarged in Fig. 2 because it displays the majority of the features that will be discussed in this paper. The main characteristics of the ELF signal are summarized hereunder:

(i) a quasi-monochromatic line, a few Hz wide, centered at around 36 Hz, is present almost continuously from the start of the PWA operation, at an altitude of 140 km, until touch-down (Fig. 3); most of the time its amplitude barely exceeds the noise threshold of the receiver, except between about 70 and 103 km, where the strength of the signal is strongly enhanced (Fig. 2);

(ii) a broadband noise almost simultaneous with the "36 Hz" line enhancement, extends from the lowest spectral line (6 Hz) to the uppermost one (96 Hz), and even stretches in the VLF range, up to about 1 kHz (not shown here); a second enhancement of the broadband noise only is observed from about 22 km down to the surface;

(iii) a small and steady increase of the central frequency of the "36 Hz" line, corresponding to an overall variation of about 1.5 Hz, is seen throughout the descent (Simões et al., 2007a);

(iv) the first broadband signal enhancement occurs at about 109 km, about 36 s (∼1.7 km) after the jettison of the main parachute and firing of the stabilizing drogue parachute, and vanishes off at about 80 km, just above the sudden rise of the conductivity layer (Fig. 3) discovered with the PWA instrument (Grard et al., 2006; Hamelin et al., 2007);

(v) the maximum amplitude of the "36 Hz" line occurs between 70 and 105 km; it reaches a surprisingly high input level at the dipole antenna (45 mV rms), which corresponds to a spectral density of some 16 mV m^{-1} Hz$^{-1/2}$ for an electric component aligned with the antenna whose effective length is about 1.6 m; the average level lies between 2 and 4 mV m^{-1} Hz$^{-1/2}$ throughout the rest of the descent;

(vi) the largest fluctuations of the "36 Hz" strength happen when the descent velocity and the tilt angle of the payload with respect to the vertical are the most variable;

(vii) no harmonic or sub-harmonic of the "36 Hz" line is clearly identified within the dynamic range of the instrument during the first period; however, a weak but visible second line appears progressively at around 60–66 Hz, more pronounced artificially when it is superimposed on the broadband noise, from about 22 km downwards (Fig. 3);

(viii) the second enhancement period of the broadband ELF-VLF noise at around 22 km exhibits a frequency spectrum similar to that of the first one, in shape and strength; the artificial increase at 61 km is due to the above-mentioned operation-mode change; contrary to the first event, the variation in broadband noise is not accompanied by any significant increase of the "36 Hz" amplitude.

The purpose of this paper is first to assess carefully all possible artifacts and interferences, taking into consideration the inherent limitation of the instrument capability in such an hostile environment. Then, we investigate in detail the physical mechanisms able to account for the observations. We finally rate the probability of each scenario in order to initiate further and deeper scientific interpretation of our finding.

3. Possible sources of ELF noise and "36 Hz" line

Several candidates have been identified as possible sources for the observed signals; they are briefly described hereafter:

(i) A hardware or software failure which could have developed during the descent can be ruled out. No similar narrow or broadband ELF noise has ever been observed during pre-flight and post-flight ground operations, as well as during cruise functional tests, nor during balloon flights using devices similar to that flown on Huygens.

(ii) The voltage at the input of the receiver is not necessarily induced by an ambient electric field, but can possibly result from an artifact. During post-flight calibration ground tests on the engineering model (Simões et al., 2007b), it was clearly proven that the PWA booms could generate strong electric noise at the amplifiers input, due to a microphone effect when the booms are vibrated at low frequency. However, an ambient DC electrostatic field could also induce an AC voltage at the boom vibration frequency and an aerodynamic stimulus on the Huygens structure or on the PWA booms (flutter) could produce similar effects.

(iii) A local source of electrostatic or corona discharges, associated with tribological effects on the parachute and the Huygens gondola, could have induced a broadband noise in the ELF-VLF range, with an intensity correlated with the variations of the dynamic pressure and/or the crossing of aerosols clouds.

(iv) It was anticipated by several authors (e.g., Tokano et al., 2001) that a strong thunderstorm activity in the Titan's atmosphere could generate lightning discharges, and the tremendous electric energy of such events would have been able to trigger the eigenmodes of the ground-ionosphere wave-guide, as it occurs permanently on Earth with the well known Schumann resonance (Schumann, 1952). Though the models for different profiles of Titan's ionosphere and for the surface properties predict that the first eigenmode mode of this resonance should lie rather at around 20 Hz, a significant enhancement of the second eigenmode of the standing waves could be observed nearly at around 32 Hz if the sources were located 90° away from the observer, instead of being uniformly distributed over the entire moon surface (Nickolaenko et al., 2003; Simões et al., 2007a).

(v) A wave signature of the interaction of Titan with the magnetosphere of Saturn was found for the first time during the Voyager 1 flyby on November 12, 1980 (Gurnett et al., 1982). The closest approach took place at a distance about 1.5 Titan radii from the surface in the wake formed by the corotational plasma flow, nearly in the equatorial plane of Saturn. An intense broadband electric field noise was observed in the ELF range, between ∼20 Hz and less than 1 kHz, while the spacecraft was crossing the neutral sheet from the northern to the southern tail lobe. This noise was interpreted as likely of the same nature as that observed in the ionosheath at Venus and the Earth's magnetosheath, but the Voyager 1 instrument did not enable the authors to conclude whether the wave was electromagnetic or electrostatic, nor to identify the source region. Nevertheless, the obvious similarity between the noise frequencies observed in Titan's wake by Voyager 1 and in the atmosphere by Huygens strongly suggests the possibility that both of them may have a common origin. Each of the above scenarios is analyzed in more detail in the following sections.

4. Aerodynamic driven vibrations

Since there is an apparent correlation between the exchange of parachutes and a sudden enhancement of the "36 Hz" line and ELF broadband noise, any artifact related to this event must be investigated seriously. The first possibility is a low frequency mechanical resonance induced on the Huygens gondola by the ropes of the two parachutes used sequentially during the HASI-PWA operations. In both cases, the Probe was attached to the parachute joints through three bridles of length $L \sim 3.91$ m each (Fig. 1). When a parachute is fully deployed, and if we consider that the atmospheric drag is just balanced by the payload weight, the three bridles are submitted to the same load, at least in a first approximation. For instance, after the stabilizing drogue chute inflation ($t > 905$ s), the load on each rope is

$$S = \frac{Mg}{3} = 90.45, \tag{1}$$

where M (201 kg) is the Probe mass after front shield jettison, g (1.35 m s^{-2}) is the average gravity in Titan's atmosphere and S is in Newton. Because of the relatively large descent velocity (20–80 m s^{-1}) and high atmospheric pressure, the wind might have easily sustained a nearly constant vibration of the ropes on the $\lambda/2$ mode, with a frequency

$$f = \frac{\sqrt{S}}{2L\sqrt{\mu}}, \tag{2}$$

where μ is the linear mass density of the bridle material.

Two points could support the above scenario. The first one is the fact that from 140 km downwards, the gravity increases by about 12%, which leads to an increase of the frequency by about 2 Hz which is of the same order of magnitude as the shift observed on the "36 Hz" line (Simões et al., 2007a). The second point is the correlation between the acceleration profile and the fading of the ELF noise versus altitude, just before the signal enhancement shown in Fig. 4. During the free-fall period, between $t = 905$ and 935 s, when the stress vanishes or decreases sharply, we observe a drastic reduction of the integrated noise down to the average level which prevailed before the parachute jettison.

However, with the above values for S and L, the value of μ for the bridle fabric of each parachute should have to be of about 1 g m^{-1} to vibrate at a frequency of 36 Hz. Such value is far too low compared to the actual one. According to the contractor's study report (Couzin, Alcatel Alenia Space, private communication, 2007), the mass of the three bridles for the main parachute is ∼836 g, leading to $\mu \sim 71$ g m^{-1}, while that of the stabilizer parachute is ∼91 g ($\mu \sim 7.8$ g m^{-1}). Considering a more sophisticated drag balance, including a payload

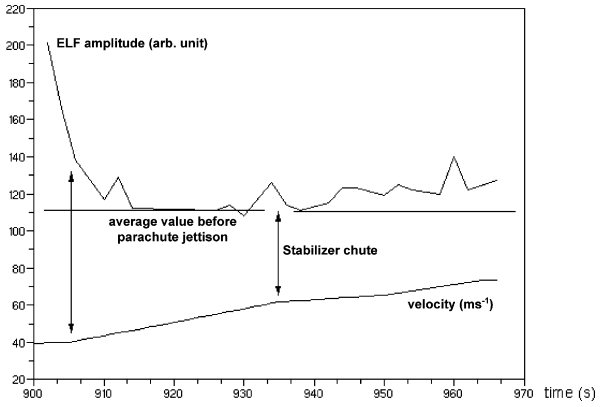

Fig. 4. Fading of the integrated ELF noise during the free fall of the payload (period between arrows), after the main parachute jettison.

pendulum motion, centrifugal forces and a high drag coefficient, the more optimistic value of μ able to produce a bridle resonance at 36 Hz does not exceed 4 g m^{-1} (Simões et al., 2007b), which is again too weak compared to the actual values. Moreover, since the same resonance frequency is seen with the two parachutes, the different values of bridle properties, added to the different lengths of rigging lines of the parachutes, allow us to rule out definitely the scenario of a 36 Hz vibration induced by the parachute ropes. However, it is not excluded that the bridles and/or other rigging lines may have induced broadband lower frequency vibrations on the Huygens structure.

A possible scenario is indeed the excitation of the boom antennas at their eigen-frequency, either triggered directly by the aerodynamic gas flow, or induced by low frequency and/or random vibrations of the Huygens gondola. Unfortunately, no prelaunch ground vibration test has ever been performed with the booms in a deployed position and with the experiment switched ON. Nevertheless, recent post-flight ground test and numerical simulation have been performed on different models of boom (mock-up, engineering and flight spare) at LPCE, University of Orléans (Simões et al., 2007b), and at CISAS, University of Padova (Bettanini, 2006), whose results are summarized hereafter.

During the tests, the boom terminal was fixed on a rigid interface, and the two perpendicular flexural modes were excited at the opposite tip, either manually or with an air blowing. A special test was performed (at CISAS) using a shaker, successively fed with sine-wave and random excitation profiles. In CISAS case, the boom was fastened through the deployment device similar to that of the flight model, while a firm encastred tubular interface was used during LPCE tests. During LPCE and some of CISAS tests, the boom antenna was operated, connected to the engineering model of PWA whenever the preamplifier could have the possibility to be not disturbed by the environment (e.g., shaker operation). In those conditions, the electric signal generated by microphone effect of the cabling stress within the boom could be recorded and analyzed during the vibrations by the PWA Digital Processing Unit (DPU). The resonance modes in the CISAS tests were measured using either a 3-axis accelerometer or a laser vibro-velocimeter. All tests exhibit well pronounced natural flexural and occasionally torsional modes, at frequencies which are summarized in Table 1.

During CISAS tests where the boom interface is really representative of the flight conditions, the dispersion of the first flexural modes lie between 15 and 18 Hz in the horizontal plane of Huygens's nominal attitude and between 20 and 25 Hz in the vertical plane. Notice that the hinge of the boom deployment mechanism presents a larger degree of freedom in the horizontal plane than in the vertical, leading to a significant dispersion of the average frequency between both modes. During preliminary tests on flight spare model, it appeared that the horizontal mode was not clearly observed on spare model #1 and that the torsional mode was prevailing on spare #2, at around 68 Hz. The fully integrated PWA spare model is installed in a clean room at CISAS, so that specific mechanical tests on booms must be agreed upon by ESA. Then, since these preliminary tests are not totally convincing, further tests will be performed as soon as they can fulfill a safety procedure. Nevertheless, according to Table 1, the overall average of the main flexural mode measured on CISAS booms to date is 22.5 ± 2.5 Hz.

This value is in fair agreement with that of the numerical simulation (21–23 Hz) performed with a finite element modeling (Bettanini, 2006), in which the academic assumption of an encastred beam is considered. The 30% larger boom resonance frequency of the LPCE boom is thought to be due to differences in the material used in the boom construction and in the foot interfaces. The resulting reduction of the boom free-length by about 12% explains the 25% frequency increase compared to the CISAS result. We will consider here that the mean frequency of the flexural modes measured at CISAS tests is the most realistic one.

The equivalent voltage induced on the electrode (20–30 mV peak amplitude), with a sustained oscillation amplitude of 15 mm peak-to-peak at the boom tip during the vibration tests, was deduced from the PWA-DPU data. Such voltage is comparable to the maximum value measured with the dipole (45 mV rms at 36 Hz) during the Huygens descent. The dynamic pressure of the air blow during the tests, leading to such

Table 1
Summary of the first eigenmode of different models of PWA booms, as seen in four directions: X is along the boom axis, Z is along the MI-TR and relaxation sensors; horizontal and vertical are for the nominal Huygens attitude; torsional is around X

Model	Eigenmode (Hz)					
	Flexural Z–X	Flexural Y–X	Flexural horizontal	Flexural vertical	Flexural average	Torsional
Mock-up (LPCE)	?	?	?	?	∼30	?
Engineering (CISAS)	20.8	23	15–18	21–23	∼20	∼60
Flight spare (CISAS)	?	?	?	∼25	25	∼68
Finite element modeling	24.2	25.2	NA	NA	24.7	75.3

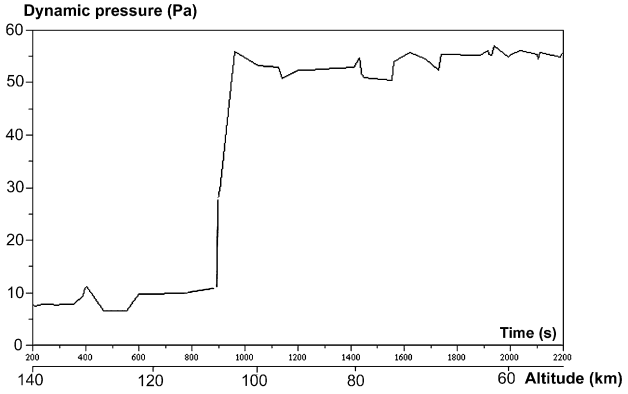

Fig. 5. Profile of the dynamic pressure during the first part of the descent.

amplitude, is estimated to be of the order of 1000–1500 Pa at the boom tip. The dynamic pressure during the Huygens descent is plotted in Fig. 5, as deduced from the altitude profiles of gas density and descent velocity, assuming a laminar velocity flow and using the standard equation

$$P_d = \frac{\rho V^2}{2}, \tag{3}$$

where the mass density ρ is derived from HASI's atmospheric data (Fulchignoni et al., 2005).

We notice an increase of the dynamic pressure at $t = 900$ s, i.e. at the time of the main parachute jettison, associated with the sudden rise of the broadband ELF noise, due obviously to a transient shock response lasting about 10 s (Fig. 4). No remarkable simultaneous enhancement is visible at 36 Hz in the spectrogram of Fig. 2, which is an argument against the self-resonance of the boom. Thereafter, the dynamic pressure increases during the free fall, for about 30 s, while the ELF noise is fading out; then P_d reaches a nearly constant value of about 55 Pa for another 30 s, the time required for the complete inflation of the stabilizer parachute, and remains almost constant until landing. As anticipated below, this sequence is consistent with an efficient parachute drag since the dynamic pressure on the canopy appears to be correctly balanced by the payload weight. Therefore, at the time when the strength of the "36 Hz" line is a maximum, i.e., between 1000 and 1600 s (Fig. 2), the dynamic pressure is about 20 times smaller than that of the air blowing during ground tests. Though it is debatable whether a linear relationship exists between the dynamic pressure and the amplitude of the first flexural mode, it looks most unlikely that a so weak pressure of 55 Pa uniformly distributed over the boom could produce a sustained oscillation comparable to that observed during the ground tests with 20 times more pressure.

As suggest above, one cannot rule out however the possibility for additional sources of random vibrations transmitted to the booms through the gondola after being initiated by aerodynamic excitation of parachute bridles or other ropes. According to the results of the shaker random vibrations at CISAS, an excitation level of 2 G rms, in the range 10–50 Hz, applied on the boom leads to bursts of transient oscillations of 5 to 6 mm peak-to-peak amplitude at the opposite tip, able to induce damped waveforms on the antenna with a maximum amplitude of about 7 to 10 mV. This corresponds roughly to the mean level of the "36 Hz" observed throughout the descent below 60 km. Another mechanism could contribute possibly to an additional electric signal, namely the voltage generated by the antenna vibration in a medium where a DC electrostatic field is present. A static field of 2.5 $\mathrm{V\,m^{-1}}$ would yield the observed signal, assuming the amplitude of oscillation of the order of 1 cm on each boom. Although no measurement of vibration level was made onboard during the descent, a valuable indication of the turbulence level affecting the gondola can be identified from the Surface Science Package data (Hofe, 2006). It appears that the strongest turbulent period stretches continuously from about 1000 to 5500 s (100–18 km), without any noticeable decrease within the conductive layer at around 63 km revealed by the PWA instrument (Grard et al., 2006; Hamelin et al., 2007). However, the "36 Hz" line reaches thereabouts a minimum amplitude, what makes more unlikely the excitation of a strong boom resonance by gondola vibrations.

Moreover, the major objection against this scenario is the frequency difference between the ground tests and the observed "36 Hz" on Huygens. According to the basic dynamic equation of an encastred flexible cylinder, the first flexural eigenmode is given in a first approximation by

$$f = \alpha \frac{d}{L^2}\sqrt{\frac{E}{\rho}}, \tag{4}$$

where α is a coefficient that depends on the cross-section, d is the diameter of the tube, L is the length, E is the flexure Young's modulus and ρ is the mass density of the material. The only two parameters which may vary significantly during the Huygens descent in Titan's environment compared to Earth conditions are the boom length and Young's modulus due to cryogenic effects. According to Eq. (4), at cryogenic temperatures (80–160 K), both parameters may increase the frequency since the boom is contracting and Young's modulus increases.

For epoxy embedded fibre-glass structures, the typical temperature shrinking coefficient from 300 K down to cryogenic range is about 2×10^{-3} (Mowers, 1968). Then we may ignore the effect concerning the length. As for Young's modulus, none data sheet is available about the fibre-reinforced epoxy material used in the construction of the PWA booms at ESTEC, but the cryogenic behavior of similar compounds is known to be extremely variable depending upon the materials and the authors (see, e.g., Ilichev et al., 1981; Mowers, 1968). It is generally admitted that in the cryogenic domain (around 77 K), Young's modulus of unreinforced bonding epoxies may increase by up to a factor 2 with respect to standard temperature, while for glass-reinforced laminate compounds this modulus may either increase or decrease as well. For instance, for epoxy-glass cloth laminates wound on cylinder, Young's modulus in a direction parallel to the fibres increases by 50–56% between 298 and 77 K (Mowers, 1968), while for aramide epoxy embedded fibres (type Kevlar K49) the same parameter decreases by more than 20% between room temperature and 4.2 K (Roy, CNRS/SPM/SERAS-Grenoble, private communication, 2006).

Therefore, although it looks quite unlikely, the above scenario cannot be definitely rejected until complementary mechanical and cryogenic tests have been implemented on the flight spare booms. However, even if the cryogenic effect could marginally account for 50% increase of the resonance frequency (∼225% increase for Young's modulus), the 15 mm peak-to-peak sustained amplitude of oscillations needed to account for the "36 Hz" amplitude during more than 10 min appears even more unlikely. We must also insist on the fact that no similar phenomenon has ever been observed during the parachute landing phase of balloon test campaigns. Moreover, the above argument in favor of an aerodynamic-driven vibration, involving the correlation between the ELF signal intensity and the parachute deployment sequences, is applicable as well to a natural electric field measured by the dipole antenna. A significant tilt angle of the payload with respect to the vertical must have produced a similar effect on the signal amplitude. Before exploring such a possibility, we will look first for a tribo-electrical ELF noise source associated with the parachute drag and/or with aerosol clouds crossings.

5. Tribo-electricity and aerosols impacts

Since the two ELF noise enhancement periods occur in particular conditions, such as a high dynamic pressure, a low electron conductivity (Hamelin et al., 2007), and the crossing of a haze layer (Grard et al., 2006), one might assume that tribo-electricity phenomena may play a role, e.g., static electrification of the gondola surface and parachute canopy, and/or glow around the needle dischargers. A preliminary report about recent laboratory tests on sparks and air-glow corona discharges (Jaffer and Schwingenschuh, 2006) indicates that most of the radiated electric energy nearby the source appears at high frequency up to 140 MHz. Consequently, no significant ELF contribution can be expected from isolated sporadic discharges. Nevertheless, a high rate of individual discharges could generate a broadband ELF noise. Though no direct observation of electrostatic discharges associated with tribo-electricity on balloon flights in the Earth's atmosphere has been reported to date, such an eventuality cannot be ruled out.

However, there is a more likely scenario involving an interaction with the Probe environment. During recent post-flight ground tests, it has been demonstrated that spraying aerosols on the antenna generates a broadband ELF noise with a similar signature to that seen in Huygens data (Simões et al., 2007b). Two kinds of aerosol spray were used, one consisting of fresh water, and the other of liquid difluoroethane. These tests must be considered qualitatively, but the ELF noise exhibits a spectrogram, shown in Fig. 6, similar to those observed during the two enhancement periods seen in Fig. 3. It is difficult to say precisely which physical mechanism may produce the observed effect, but it is unlikely that it could be associated with microphone or mechanical vibration of the boom, because none significant shaking or tremor was visible during spraying. Whatever the exact mechanism, likely associated with as shot noise on the sensor surface, the tests seem to account satisfactorily for the flight observations. In each region where the broadband ELF

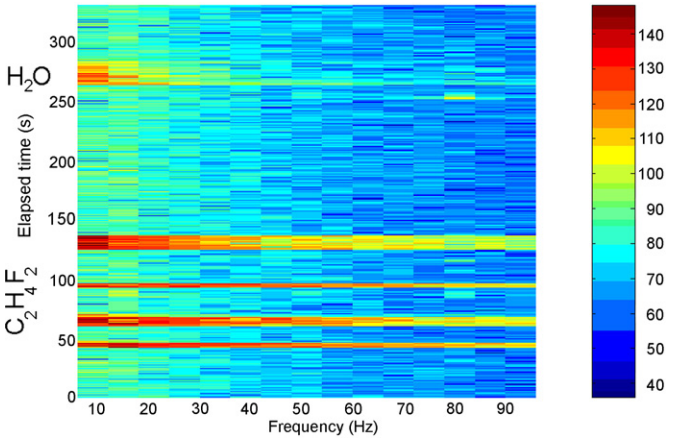

Fig. 6. Spectrograms (arbitrary units) obtained on the ground with sprays of fresh water and difluoroethane ($C_2H_4F_2$) haze on the antenna.

noise enhancement is seen, a modification of the environment is detected indeed by other instruments. In the first period, the abnormal behavior of the MI measurement (Hamelin et al., 2007) suggests that Huygens crosses a layer of solid ethane aerosols between 100 and 80 km, a region where these highly electrophylic particles are thought to be present. The post-flight tests have shown that not only a broadband ELF noise is generated, but that the MI phase response is perturbed when the sensors are sprayed with difluoroethane aerosols (Simões et al., 2007b). A high optical opacity was observed throughout the descent from about 30 km down to the surface by the Descent Imager/Spectral Radiometer (DISR) camera, and a thin haze layer was detected at 21.0 ± 0.5 km (Tomasko et al., 2005), in almost perfect coincidence with the beginning of the second ELF noise enhancement period. Such a layer is thought to reveal the presence of solid methane condensates (Tokano et al., 2006).

It seems therefore most likely that the occurrence of the two ELF broadband enhancements observed during the descent is correlated with the crossing of haze layers consisting of solid aerosols. The same explanation cannot be applied to the "36 Hz" because no narrow band signal was generated during the spraying tests (Fig. 6). Moreover, one can check in Fig. 3 that the "36 Hz" level does not increase below 22 km during the second enhancement period of the broadband noise. One concludes that the ELF broadband noise and the "36 Hz" line have probably different origins, although they exhibit a sudden enhancement almost simultaneously between 105 and 80 km (see discussion in Sections 8 and 9).

6. Lightning discharges

As a preliminary remark, it would be very surprising that the quasi-horizontal electric field component of the second eigenmode of the Schumann resonance triggered by lightning could reach a peak value of 16 $\mathrm{mV\,m^{-1}\,Hz^{-1/2}}$. This level is almost two orders of magnitude larger than the average amplitude of the vertical component of the first eigenmode observed on Earth, lying between 0.1 and 1 $\mathrm{mV\,m^{-1}\,Hz^{-1/2}}$, at about 7.8 Hz (see, e.g., Belyaev et al., 1999). Moreover, the first harmonic is never totally absent in Earth's records in spite of

the presence of several high order modes. This is because the thunderstorm sources stretch over large zones throughout almost the entire globe. On the contrary, the Huygens spectra display essentially a single line (Fig. 2), which is assumed to be nearly the second eigenmode. This fact is explained by theoretical models provided the sources are concentrated at about 90° away from the observer (see Nickolaenko et al., 2003; Simões et al., 2007a). According to a rough model of pure standing waves, in a spherical geometry system, this location corresponds to an antinode for the electric component of even submultiples of the fundamental wavelength fitting the longitudinal size of the cavity.

Although no lightning discharges had been observed during the Voyager 1 flyby of Titan, it was expected that several flybys of Cassini would offer a better opportunity with the Radio and Plasma Wave Science (RPWS) experiment (Gurnett et al., 2004) to detect the high frequency signatures of the electric spikes able to cross the ionosphere of Titan (Lammer et al., 2001). Unfortunately, up to date, there is no evidence of short bursts above a few hundred of kHz, around the closest approaches of Titan (Fischer and Kurth, University of Iowa, private communication, 2006). The selection criterion for such events is a drop-off in intensity with a $1/r^2$ law (where r is the distance to Titan), as it could be expected for lightning discharges in the moon's atmosphere. However, this lack of evidence does not imply that no discharge at all occurs in the atmosphere, but their radiated electric energy should not exceed 10 kJ, given the detection threshold of the RPWS instrument (Lammer et al., 2001). Notice that such flashes would be several orders of magnitude less powerful than typical return strokes on Earth. If they exist, they could probably be associated with precursors within low altitude methane clouds, similar to the leaders of return strokes between clouds and surface.

The HASI-PWA wave experiment was designed for the observation of "spherics" in the VLF frequency range up to 11.5 kHz. On Earth, these events are usually associated with nearby lightning and they appear like dispersed tones ("tweeks") after multiple radial reflections within the ionosphere-ground cavity, when they are produced by distant thunderstorms. However, the limited sensitivity of the PWA instrument and its time resolution in this range do not definitely allow us to conclude whether several events observed during the descent display the spectral characteristics of lightning discharges or whether they are due to interferences (Grard et al., 2006). We will nevertheless take an optimistic approach and assume that these events are real. We consider a rate of about 120 events during roughly 2 h of observation, i.e., an average of about 1 flash per minute in a limited region around the landing site. Given the poor sensitivity of the receiver, we assume that the maximum visibility area for detection of 10 kJ flashes around Huygens is limited to a distance of about 100 km. If the distribution of these active zones is assumed to be quasi-uniform over Titan's surface, the maximum global flash rate is estimated at about 45 s^{-1} by taking into account the relevant area ratio. In such conditions, the maximum available global electric power from 10 kJ discharges is about 4.5×10^5 W. Considering the spectral distribution proposed by Lammer et al. (2001), such as half of the energy (2.25×10^5 W) stretches approximately uniformly over the frequency range below 4 kHz, we obtain a spectral power density less than 60 W Hz^{-1} in the ELF range.

We assume that this energy is transferred without any loss into the second eigenmode of the Schumann resonance, and that most of the power of the standing wave is concentrated essentially between 65 and 105 km altitude, where the maximum signal is actually seen. Then, a global cross-section of about 6×10^{11} m^2 is filled with an energy flux of 10^{-10} W m^{-2} Hz^{-1}. If we retain the value of 16 mV m^{-1} $Hz^{-1/2}$ as a maximum amplitude for the observed signal, with a free-space impedance of 377 Ω, we get a necessary energy flux of about 7×10^{-7} W m^{-2} Hz^{-1}, which is nearly 40 dB larger than the above optimistic estimate. This rough calculation implies that the global available power of lightning should have to be at least 4×10^5 W Hz^{-1} in the ELF range instead of 60 W Hz^{-1} in order to comply with the PWA data. Therefore, we may rule out definitely the possibility that the observed 36 Hz line is a Schumann resonance obeying the above scenario, unless we consider a more speculative option.

Instead of a mean lightning energy of 10 kJ, which otherwise should have been detected easily by RPWS on the orbiter during the closest flybys, let us assume now that suitable physical conditions permit a strong concentration of quasi-simultaneous and numerous flashes within low altitude clouds. Each flash would have a mean energy of the order of one kJ only, i.e., nearly the energy of commercial high power electronic flash units and stroboscopes that are easily visible several km away on Earth. The electric signature of so weak discharges would be seen neither by RPWS, nor by PWA. Although standard electric discharges within clouds (or between clouds) are rather unlikely because of the global negative space charge of clouds (Tokano et al., 2001), we cannot rule out that some unexpected conditions could allow locally the occurrence of discharges with such intensity. We can hypothetically assume that such conditions could occur at polar latitudes. In order to comply with the condition that the observed "36 Hz" is the second eigenmode of the Schumann resonance, we saw above that the sources must be located nearly 90° away from the Huygens landing site. Therefore, since the latter is located at around 10° South latitude (see Section 8), this fact is in favor of the assumption that the active sources would be concentrated in polar region.

Let us evaluate the global rate of such discharges necessary to fit the level of the PWA signal. If we assume the source regions to lie 90° away, at this location, the antinode for electric field of the standing wave coincides with a node for the magnetic component. In these conditions, the energy is no more distributed equally between electric and magnetic components as for traveling waves in free space. Then, after Nickolaenko et al. (2003), the wave impedance Z should be at least 12 times larger than its free-space value of 377 Ω. Assuming a conservative Poynting energy-flux, the wave power density of the "36 Hz" would lie now closer to 6×10^{-8} W m^{-2} Hz^{-1} than to the previous estimate (7×10^{-7} W m^{-2} Hz^{-1}), so that the required global power spectral density would be reduced accordingly down to about 3×10^4 W Hz^{-1}. With the same assumption for the spectral distribution as above, a rate of $\sim 2.5 \times 10^5$ s^{-1} is

then necessary for 1 kJ flashes. The area of the active zone is also reduced with respect to the previous global uniform distribution, and becomes of the order of 3×10^7 km^2. In short, a rate of about 1 flash per second in average is required within active cells of 120 km^2, about 12 km in diameter. The brightness at UV, infrared or visible wavelengths of such discharges seen through the atmosphere is not known, but we may anticipate that dedicated observations from the orbiter could constrain whether they exist or not.

In addition to hypothetical optical detection, the massive production of complex organic compounds by such a large number of discharges in methane clouds could be assessed in the framework of an updated atmospheric chemistry modeling in order to check whether the above assumption is realistic or not. Nevertheless, after a few tens of flybys since the arrival of the mission at Saturn, no evidence of any lightning activity has been reported to date. Therefore, a Schumann resonance driven by lightning so far appears somewhat unlikely. However, this does not rule out the existence of scattered or diffuse lightning discharges such as those which have possibly been observed during the descent (Grard et al., 2006).

7. Interaction of Titan with Saturn's magnetosphere

The sketch of the subsonic interaction between Titan and the corotating Saturn's magnetosphere shown in Fig. 7, is based upon current models (see review by Blanc et al., 2002). In this system, different mechanisms can develop electromagnetic instabilities, particularly in the ELF range. Given the exceptionally high power flux of the "36 Hz" signal, up to 6×10^{-8} W m^{-2} Hz^{-1} as derived above, the first idea is to search for some coherent generation process such as ULF magnetic pulsations which are the only natural emissions inducing an even larger power flux on Earth (Al'pert and Fligel, 1970). The production mechanism of these magneto-hydrodynamic (MHD) waves involves energetic ions or electrons trapped between conjugate points, leading subsequently to a coherent resonance of the field line at a frequency below the ion gyrofrequency f_{ci}. The growth rate is maximum where f_{ci} is minimum, so that the source region is the equatorial portion of the field line. Similar kinds of MHD waves have even been proposed as a complementary source to lightning for the Earth's Schumann resonance (Abbas, 1968). In the case of Titan, a periodic process of trapped particles has been evoked by Hartle et al. (1982) as a probable mechanism for the atmospheric diffusion of electrons of energy larger than 400 eV along Saturn's tubes of force draped around Titan (Fig. 7). It matters little for our purpose whether or not this mechanism could trigger an MHD emission along the field line at a distance of about 20 Saturn's radii, since our frequency range of interest lies well above the proton gyrofrequency at this location ($f_{ci} < 0.1$ Hz), and we cannot reasonably invoke any Doppler shift to raise such a low frequency up to 36 Hz. A similar generation mechanism has been considered in a preliminary approach by Gurnett et al. (1982) as a possible source of the ELF "sheath noise" seen by Voyager 1, assuming that the ion-cyclotron instability could be triggered in Titan's wake by accelerated pick-up ion on the anti-Saturn direction (see Fig. 7). But these authors ruled out this mechanism because the Doppler shift effect is too weak to raise frequencies from a fraction of Hz up to ~1 kHz.

Moreover, due to the widely inhomogeneous medium sketched in Fig. 7, it is rather unlikely that a coherent narrow band ELF emission produced somewhere in this system could be Doppler-shifted before emerging in Titan's atmosphere exactly with a frequency of 36 Hz. It is more likely that a narrowband filter in the ionosphere–atmosphere cavity makes the suitable selection from incoming external broadband noise, as for the Schumann resonance excited by lightning. We shall restrict therefore our investigation to the mechanisms that can not only be sustained by the system, but can also generate waves that propagate downwards with a frequency of at least 36 Hz.

Table 2 recapitulates the main features of the plasma in Titan's environment, such as they have been measured in situ, or extrapolated from Voyager 1 and Cassini flyby data (e.g., Hartle et al., 1982; Nagy and Cravens, 1998; Wahlund et al., 2005; Backes et al., 2005). According to the Linden-Bell–Goldreich model (Goldreich and Linden-Bell, 1969), the electric field induced in the frame of reference of a conductive planet of diameter L moving with a velocity $\boldsymbol{V}$ across a steady magnetic field $\boldsymbol{B}_0$, obeys the conventional relationship $\boldsymbol{E}_0 = \boldsymbol{V} \wedge \boldsymbol{B}_0$ and develops a voltage $U = \boldsymbol{E}_0 * \boldsymbol{L}$ across the body, along the direction parallel to the field. This voltage is of the order of 400 kV for the moon Io.

We assume a simple corotation model for Titan through the Saturn's frozen plasma, with a velocity of the order of 150 to 200 km s^{-1}. With an undisturbed magnetic field at the moon orbit of about 5 to 7 nT (Backes et al., 2005), the induced electric field (~1 mV m^{-1}) may induce a potential drop through Titan of 3 to 6 kV, depending upon the cross-section of the involved ionospheric region. This field is more or less parallel to the horizontal plane in Fig. 7, pointing in the anti-Saturn direction. Fresh ions generated in Titan's upper atmosphere by charge exchange process with fast Saturn's protons are then picked-up and accelerated towards the lobe edges on the anti-Saturn side with the velocity of the plasma flow, while the ions generated on the Saturn-side are precipitation in Titan's atmosphere. More relevant for our purpose, is the fact that the induced potential drop is part of a field-aligned current system somewhat similar to the tail-in-wake model applied to planets devoid of intrinsic magnetic field. It is known that such a situation supports two lobes with current sheaths. In case of jovian system, the current is closed through the ionospheres of Io and Jupiter (e.g., Shawhan et al., 1973, 1975; Scarf, 1976), and leads to the possible formation of a beam-type electron distribution with a characteristic energy including a significant part of the above potential drop.

In case of Titan, the potential drop is smaller, but the same physics applies with however an important difference, i.e., the current system is closed on one side through Titan's ionosphere, and on the other side, in the wake through the lobe-sheaths (see review by Blanc et al., 2002). In addition, Titan's ionosphere may interact directly on the ram side with the frozen plasma and the particles trapped in Saturn's magnetic field. This situation is favorable to the development of two kinds of ELF instabili-

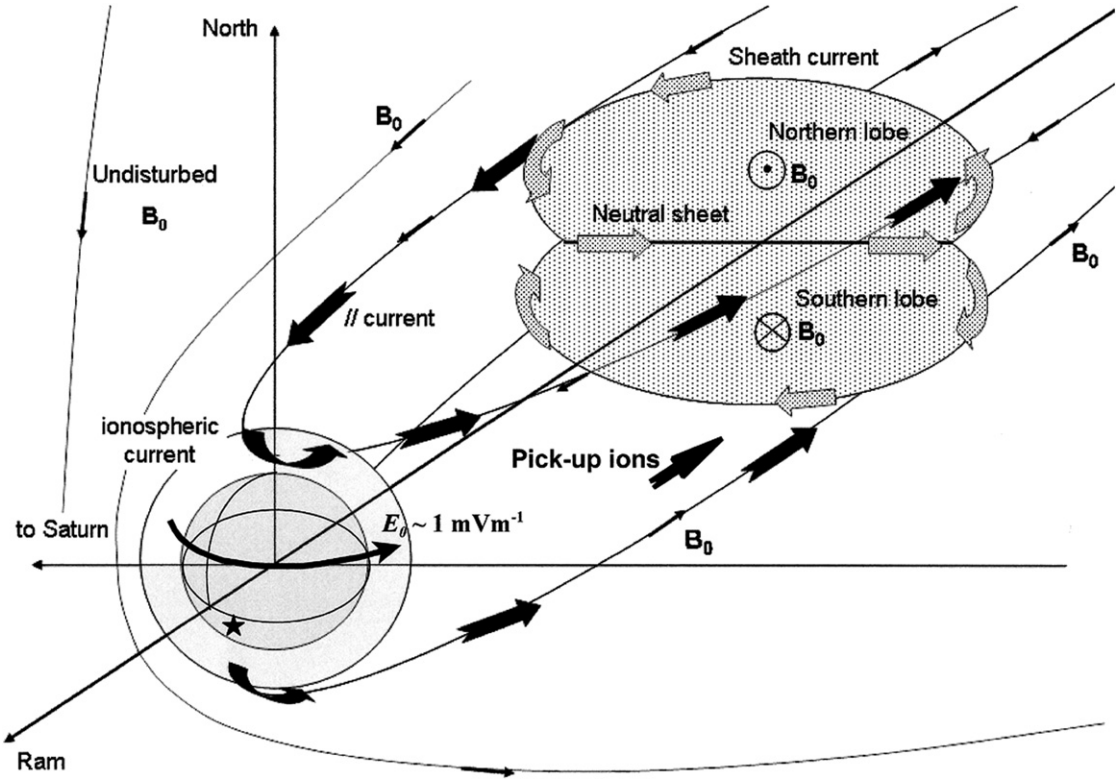

Fig. 7. Sketch of the wake interaction between Titan and Saturn's magnetosphere, and the induced driven current system (Huygens landing is site pointed out by a star).

ties, namely: (a) the electron–cyclotron instabilities, and (b) the current driven instabilities, which are further-considered here under.

The electron–cyclotron instabilities develop in non-Maxwellian magnetized plasmas, for different electron distributions, such as runaway electrons, bump-in-tail distribution, or anisotropies in the energetic population. Depending upon the ratio of the plasma frequency over the electron gyrofrequency (f_p/f_{ce}), the waves are generated in different modes, either in the upper oblique Z mode above f_p or f_{ce}, whichever the larger, or in the lower oblique mode below f_p or f_{ce}, whichever the lower (Stix, 1962). The emitted frequency depends upon the angle made by the wave vector $\boldsymbol{k}$ and $\boldsymbol{B}_0$. In Earth's polar and auroral ionosphere, where intense emissions of that kind are frequently observed within the source region (Béghin et al., 1989), the electron gyrofrequency is generally larger than the plasma frequency and the mode just below f_p, is the only one to be excited. According to these observations, the level of these waves usually reaches a fraction of $\mathrm{mV\,m^{-1}\,Hz^{-1/2}}$, with frequencies of a few hundreds kHz. In Titan's ionosphere, the conditions are totally different since the condition $f_p/f_{ce} \gg 1$ holds everywhere, so that both modes are possible theoretically (Stix, 1962). But since we are concerned by ELF emissions, we will only consider here the lower mode below f_{ce}, that is the usual whistler mode.

The whistler-mode instability occurs in presence of loss-cone and anisotropic distributions (Mikhailovskii, 1974). These emissions are frequently observed in the radiation belts of Earth's magnetosphere and their generation mechanism has been extensively studied for several decades (Kennel and Petschek, 1966). Their frequency range extends from f_{ce} down to the lower hybrid resonance (LHR), defined as $f_{lh} = f_{ce} M_i^{-1/2}$, where M_i is the mean ion mass in amu. At present, the only well identified LHR and ELF hiss emissions, have been observed in Saturn's inner magnetosphere and are indeed associated with field-aligned electron beams (Gurnett et al., 2005). This is consistent with the observation 3000 km above Titan's surface of a bite-out in the electron energy distribution above 400 eV, thought to be associated with bouncing electrons along Saturn's field lines draped around Titan's ionosphere (Hartle et al., 1982). The possibility that these emissions would be a direct source of the ELF waves observed in the atmosphere is discussed below.

Titan's upper ionosphere, from about 1200 km (closest approach of Cassini orbiter flybys) up to 2000–3000 km, is thought to contain a plasma made mostly of thermalized electrons with energies less than 1 eV (Wahlund et al., 2005), so that it appears unlikely that a direct emission in the whistler-mode could take place there, if we refer to Earth's ionosphere where similar conditions prevail (Béghin et al., 1989). We will rather consider an ionospheric mechanism of a different nature involving the current driven instabilities, and merely regard the other mechanism as able to occur more likely at higher altitude in the outer lobes.

The so-called current driven instabilities are caused by the differential velocity between electrons and ions. The most common mode, the ion-acoustic instability, has been studied by several authors, because it plays a crucial role in the phenom-

Table 2
Expected plasma parameters in Titan's ionosphere and in the wake of Saturn's corotating plasma

Region	Parameter							
	f_{ce} (Hz)	n_e (cm^{-3})	f_p (kHz)	$\langle M_i \rangle$ (amu)	f_{pi} (Hz)	T_e (eV)	λ_D (m)	v_{is} ($km\,s^{-1}$)
Titan's ionosphere	<50–250	$\leqslant 10$–10^3	30–300	20–30	125–1500	0.02–1	<0.1–2	0.5–5
Inner lobes and outer edges	100–300	10–100	30–90	5–10	200–1000	1–5	1–5	5–20

enon of anomalous resistivity (e.g., see review by Galeev and Sagdeev, 1984). The major condition for its generation is that the relative electron–ion velocity V_{ei} be larger than the ion-acoustic velocity v_{is} in the system, i.e.,

$$V_{ei} > v_{is} \quad \text{with } v_{is} = \sqrt{\frac{K(T_e + 3T_i)}{m_i}}, \tag{5}$$

where K is the Boltzmann's constant, m_i the ion mass (proton mass multiplied by M_i), T_e and T_i the electron and ion temperature, respectively. The instability threshold depends on the ratios T_e/T_i and V_{ei}/v_{is}, but if the electron and ion temperatures are of the same order of magnitude, the instability is obtained for $k\lambda_D < 1$, where λ_D is the Debye length. For the above conditions, the waves are ion-acoustic oscillations with the following dispersion equation given by Mikhailovskii (1974):

$$f \approx \frac{f_{pi}}{\sqrt{1 + 1/(k\lambda_D)^2}} \sqrt{1 + 3\frac{T_i}{T_e}} \quad \text{with } f_{pi} = \frac{f_p}{\sqrt{m_i}}, \tag{6}$$

where f_{pi} is the ion–plasma frequency (Table 2). If, besides, the condition $k\lambda_D \ll 1$ is fulfilled, the broadband emission is bounded by f_{pi}, and the dispersion equation reduces to

$$\omega_k \approx k v_{is}, \tag{7}$$

i.e., the waves propagate with the ion-acoustic velocity (they are not dispersive), and the growth rate is given by

$$\frac{\gamma}{\omega_k} \approx \sqrt{\frac{m_e}{m_i}}. \tag{8}$$

The best conditions for the generation of such oscillations are met when the relative electron–ion velocity is maximum and the ion-acoustic velocity is minimum, i.e., in the ionosphere (see Table 2). These oscillations are the source of usual electrostatic turbulences, observed in many plasma environments throughout the Solar System, and stand among the most powerful ELF emissions. They are believed to be the source of Earth's magnetosheath noise (Rodriguez, 1979). The features of the intense ELF "sheath noise" observed by Voyager 1 during Titan's flyby, including a wideband integrated level of 0.5 $mV\,m^{-1}$, agree quite well with the generation process of the ion-acoustic turbulence, as proposed indeed by Gurnett et al. (1982).

First, let us check in Table 2 whether the electron–ion velocity exceeds the required threshold of a few $km\,s^{-1}$ within some region of the upper ionosphere, say around the estimated altitude of the ionopause (∼1500 km). Ignoring the existence of any internal magnetic field on Titan, or if any, with a so weak strength than we can forget it, Saturn's magnetic field lines are thought to penetrate the ionopause down to the neutral atmosphere, where the field vanishes (Nagy and Cravens, 1998). The DC current responsible for this magnetic field drop should obey Ampere–Maxwell's equation curl $\boldsymbol{B}_0 = \mu_0 \boldsymbol{J}$. In the optimistic case, let us assume that the field amplitude decreases from about 15 nT at an altitude of about 1000 km down to almost zero below 500 km. Then, the current density associated with such a drop over a vertical distance D of 500 km is roughly given by $\Delta \boldsymbol{B}_0 (\mu_0 D)^{-1}$, i.e., $J \sim 2.5 \times 10^{-8}\,A\,m^{-2}$. The corresponding electron drift velocity is

$$V_{ei} = \frac{J}{n_e q_e}, \tag{9}$$

where n_e and q_e are the electron density and charge, respectively. In order to fulfill the instability condition, the electron density in the considered region would have to be lower than $10^8\ m^{-3}$. However, the density measured in this region during Cassini flyby is at least one order of magnitude larger (Wahlund et al., 2005). Since the above requirement is rather marginally fulfilled, we will therefore consider a more convenient model involving the quasi-horizontal current associated with the electric field induced by Saturn's corotating magnetic field. This current is the ionospheric contribution for closing the global wake circuit sketched in Fig. 7. This process is thought to involve the highly conductive region below the ionopause, because the electron diffusion through the neutral atmosphere is maximum in that region (Hartle et al., 1982). Moreover, the magnetic field decreases sharply below 1000 km and Hall and Pedersen conductivities are negligible compared to the scalar electron conductivity. Therefore, the current density simply obeys the generalized Ohm's law ($\boldsymbol{J} = \sigma \boldsymbol{E}$) and the drift velocity is given by

$$V_{ei} = \mu E = \frac{\sigma E}{n_e q_e}, \tag{10}$$

where μ is the electron mobility and σ the electron conductivity. With an induced electric field of the order of 1 $mV\,m^{-1}$, a mobility of $10^6\ m^2\,V^{-1}\,s^{-1}$ would be sufficient to trigger the instability, especially at lower altitudes where T_e and T_i are less than a fraction of eV. This yields an ion-acoustic velocity as low as a few hundred meters per second (see Table 2). Thus, in a large region below the ionopause the conditions for triggering the ion-acoustic instability are probably satisfied down to about 500–600 km, where the conductivity is expected to lie between 10^{-5} and $10^{-6}\ S\,m^{-1}$ (Simões et al., 2007a) and the electron density to be of the order of $10^8\ m^{-3}$ or less. The altitude range ∼500–1000 km, is therefore a likely region for the generation of a strong ion-acoustic turbulence.

Now, let us evaluate the maximum power flux available in such turbulent medium. Admitting that the current circuit induced by the dynamo effect in that region of Titan's ionosphere

is closed in the tail, we may derive the profile of the current density J_h deduced from Ohm's law in the range 500–1000 km. We neglect the anomalous resistivity in a first approach. Assuming a conductivity scale height H of the order of 30–40 km, with $\sigma \sim 1\ \mathrm{S\,m^{-1}}$ at 1000 km (Simões et al., 2007a) and an electric field of 1 $\mathrm{mV\,m^{-1}}$, J_h would decay exponentially from about 10^{-3} down to $10^{-9}\ \mathrm{A\,m^{-2}}$. Let us consider a crude model where two conjugate draped current sheaths, associated with the northern and southern lobes respectively, are extending over roughly 60° in latitude and facing the ram direction (Fig. 7). The total ionospheric current carried by each sheath is equivalent to that of a thin layer of thickness H, and is given by

$$I = \frac{\pi R}{3} J_{1000} \int_{500}^{1000} \exp\left(\frac{h-1000}{H}\right) \mathrm{d}h \approx \frac{\pi R H}{3} J_{1000}. \qquad (11)$$

With $J_{1000} = 10^{-3}\ \mathrm{A\,m^{-2}}$, $R \sim 3000$ km and $H = 36$ km, one get $I \sim 10^8$ A, which leads to a theoretical maximum available power of 5×10^{11} W, assuming a potential drop of about 5 kV. In reality, since this current is assumed to generate the ion-acoustic turbulence, the medium would react through the anomalous resistivity due to the saturation of the mechanism (Galeev and Sagdeev, 1984). Then, the above estimate based upon the linear Ohm law must be drastically revised. The actual current can be better evaluated from the knowledge of the magnetic field in the outer lobes. Assuming that the total sheath current I is distributed through a constant skin current density j_s, over an effective lobe length L_x, the magnetic field induction inside the lobe obeys the expression $|B_0|\mu_0^{-1} = j_s = I L_x^{-1}$. Then, with $L_x \sim 10$ Titan radii and $|B_0| \sim 10$ nT, the lobe current is about 2×10^5 A, i.e., 0.2% of the above absolute maximum. Such a difference may indeed be attributed to anomalous resistivity, so that the power reservoir available for wave emission in the ionosphere is accordingly reduced to about 10^9 W.

Using the estimated wave power density of $6 \times 10^{-8}\ \mathrm{W\,m^{-2}\,Hz^{-1}}$ for the "36 Hz" signal (see Section 6), and considering a uniform distribution within an equatorial cross-section of about $6 \times 10^{11}\ \mathrm{m^2}$, we obtain a source power of about $3.6 \times 10^4\ \mathrm{W\,Hz^{-1}}$. Assuming that the energy transfer is taking place essentially in a bandwidth of about 600 Hz (with reference to the Voyager 1 observation), we conclude that a source with a wave power of roughly 2×10^7 W is required. Thus, an efficiency of a few percents for transforming a fraction of the above available power (10^9 W) into the ELF turbulence, and subsequently into the EM mode, would be compatible with the power budget of the "36 Hz" signal. We must now evaluate the power flux actually available from the ion-acoustic turbulence in the source region.

The ion-acoustic instability is saturated due to the angular diffusion of the electron distribution function, and the maximum level of turbulence in a quasilinear regime has been evaluated by Galeev and Sagdeev (1984) as

$$\frac{W_k}{K n_e T_e} \approx \left[\frac{\omega_k \gamma_k}{2k^5 v_{Ti}^2}\right] \ln(1/k\lambda_D), \qquad (12)$$

where W_k is the spectral density of the wave energy per volume unit in k space. According to Poynting's theorem, the wave power flux through a surface unit is obtained by integrating the product $W_k v_{\mathrm{is}}$ within the entire k space, which reads

$$P = v_{\mathrm{is}} \iiint W_k\, \mathrm{d}k^3 = 2\pi v_{\mathrm{is}} K n_e T_e \int \frac{\omega_k \gamma_k}{k^3 v_{Ti}^2} \ln(1/k\lambda_D)\, \mathrm{d}k. \qquad (13)$$

Using the previous expressions and approximations, taking $k\lambda_D = 1$ as an upper limit and $(k\lambda_D)_{\min} = 7.5 \times 10^{-2}$ as a lower limit corresponding to $\lambda_D \sim 10$ cm, with $f_{\mathrm{pi}} = 125$ Hz and $v_{\mathrm{is}} = 10^3\ \mathrm{m\,s^{-1}}$, the above integral reduces to

$$P \approx 4\pi \left(\frac{m_e}{m_i}\right)^{1/2} \ln^2[k\lambda_D]_{\min} v_{\mathrm{is}} K T_e n_e \quad \text{with } T_i \sim T_e. \qquad (14)$$

Introducing $v_{\mathrm{is}} = 10^3\ \mathrm{m\,s^{-1}}$, $M_i = 30$, $n_e = 10^8\ \mathrm{m^{-3}}$ and $T_e = T_i = 200$ K in the above equation, we obtain a power flux of about $10^{-10}\ \mathrm{W\,m^{-2}}$. The corresponding turbulent electric field strength in the source region, integrated within the entire $\boldsymbol{k}$ space, must satisfy the relation $v_{\mathrm{is}} \varepsilon_0 E^2 = P$. Then, we found the electric field of the order of 100 $\mathrm{mV\,m^{-1}}$, a significant level indeed. Assuming a uniform spectral distribution within a bandwidth of 100 Hz, we obtain a spectral density of 10 $\mathrm{mV\,m^{-1}\,Hz^{-1/2}}$. If some direct coupling mechanism from ES oscillations into EM waves could exist with conservation of the energy flux, a wave packet, starting with the above power flux of $10^{-10}\ \mathrm{W\,m^{-2}}$ propagating upwards, would arrive at the altitude of Voyager 1 flyby with an ELF electric field strength of 0.2 $\mathrm{mV\,m^{-1}}$, comparable to 0.5 $\mathrm{mV\,m^{-1}}$ reported by Gurnett et al. (1982).

However, this broadband field strength leads to 20 $\mu\mathrm{V\,m^{-1}\,Hz^{-1/2}}$ at 36 Hz, which is again nearly three orders of magnitude too low. Although our estimate of the global power budget between the available power in the source region and the power flux density of the "36 Hz" signal is favorable, it is wrong to believe that the electrostatic turbulence may propagate downward through the ionosphere according to the above crude conversion ratio. We propose in the next section a rather more efficient conversion mechanism which yields EM wavelets emitted from a huge number of turbulence cells scattered within the source regions.

8. Coupling mechanism between ion-acoustic turbulence and EM waves

The existence of energy conversion processes between upward acoustic waves generated in the Earth's atmosphere and ionospheric turbulence and electromagnetic waves has been demonstrated by powerful explosions on the ground (Blanc and Rickel, 1989; see review by Pokhotelov et al., 1994). Such a phenomenon implies the existence of a steady magnetic field. This is applicable in Titan's case for upward propagation if the source is located in the upper ionosphere, where a significant magnetic field is present. However, an essential condition must be satisfied, that is the frequency of the ELF-EM wave must be lower than the local electron gyrofrequency. It is not credible that the magnetic field in Titan's wake be as large as 35 nT, thus the condition $f_{\mathrm{ce}} \ll 1$ kHz is true everywhere. Then, the "sheath noise" observed at frequencies of up to 1 kHz by Voyager 1, at rest with respect to the downstream plasma flow, must

have been Doppler shifted above the value of f_{ce} at the source location, as proposed by Gurnett et al. (1982). In that case, this process would validate our model of ion-acoustic turbulence generated in the ionosphere.

However, for downward propagation, the situation is more complex. According to the models, the magnetic field in the lobes is assumed to decrease sharply from about 15 nT ($f_{ce} \sim$ 420 Hz) at around 1500 km, down to nearly zero at the bottom of the ionosphere in the absence of intrinsic field (Nagy and Cravens, 1998). Measurements performed during the first Cassini–Titan flyby lead to about 10 nT ($f_{ce} \sim 280$ Hz) at around 5000 km within the outer southern lobe on Saturn side (Backes et al., 2005). Then, regardless of the altitude at which an EM wave is generated, it must propagate through negative vertical gradients for both electron density and magnetic field, what is a situation quite different from that encountered on Earth. It has been indeed anticipated for a long time that beam-induced electrostatic instabilities in Earth's ionosphere could generate electromagnetic noise detectable on the ground (e.g., Lepechinsky and Rolland, 1964).

Here, we need at first a process able to convert a quasi-steady ion-acoustic turbulence into an electromagnetic wave. Such a process exists and the relevant theory is applicable in different kinds of artificial and natural plasmas (e.g., Erokhin and Moiseev, 1979). The coupling between the electric field components of the ion-acoustic turbulence and electromagnetic wave in the ELF range is possible provided the divergence of the combined electric fields is not zero; a condition which requires the presence of a steady magnetic field. The EM mode below the electron gyrofrequency evoked in the previous section is the right-hand polarized whistler-mode, and the coupling conditions are

$$(k_{/\!/})_{EM} = k_{ES} \quad \text{and} \quad f \sim f_{ce} \cos\theta, \tag{15}$$

where θ is the angle between the magnetic field and the wave vector $\boldsymbol{k}$. In the cold plasma approximation, the dispersion equation of the whistler-mode is

$$k_{/\!/} = \frac{2\pi f}{c}\left[1 + \frac{f_p^2}{f(f_{ce}\cos\theta - f)}\right]^{1/2}. \tag{16}$$

Using Eq. (7) of the ion-acoustic wave, we obtain the following coupling condition:

$$\frac{c}{v_{is}} = \left[1 + \frac{f_p^2}{f(f_{ce}\cos\theta_c - f)}\right]^{1/2}, \tag{17}$$

the solution of which yields a frequency f very close to the oblique resonance defined by $f_{or} = f_{ce}\cos\theta_c$. Therefore, the "36 Hz" signal may be generated anywhere above the altitude where the magnetic field has decreased down to ~1.3 nT, and then the wave propagates downwards with an angle θ that tends asymptotically towards zero.

As mentioned in Section 7, we cannot rule out the possibility that a whistler-mode emission be produced directly somewhere in this region. However, following the discussion on the upward propagation at the Voyager 1 flyby altitude, whatever the generation mechanism, a wave with a frequency as large as 420 Hz

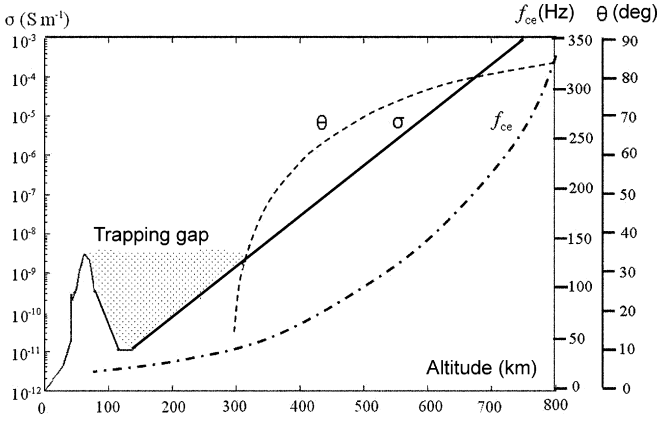

Fig. 8. Model of altitude profiles for conductivity, electron gyrofrequency and $\boldsymbol{k}$ vector direction with respect to the magnetic field, for a 36 Hz component of an ELF broadband whistler-mode emission generated above ~300 km.

($B_0 \sim 15$ nT) in the source region cannot propagate downwards in the atmosphere because of the cut-off frequency at f_{ce}. This remark is applicable even to lower frequencies than the value of f_{ce} in the source region, because of the upstream Doppler shift effect when the source extends outside the ionopause within the high velocity plasma flow. Consequently, the ELF broadband noise seen on Huygens during the two enhancement periods shown in Fig. 3, extending at least up to 1 kHz in the VLF channel (Grard et al., 2006), cannot by produced in Titan's ionosphere, what confirms the conclusion of Section 5. Let us now return to the "36 Hz" emission, and consider the following simple model.

Using the conductivity measurements obtained by the Mutual Impedance instrument from the surface up to 140 km (Hamelin et al., 2007) and assuming an exponential law from 150 up to 800 km with an estimated scale height of 30 km (Simões et al., 2007a), we obtain the profile plotted in Fig. 8. Due to the lack of data for a vertical profile of the magnetic field within the lobes, we assume that $|\boldsymbol{B_0}|$ decreases from 12 nT at 800 km down to about 1.3 nT at 300 km with a scale height of 250 km. This rough model allows one to include the possibility of a weak intrinsic magnetic field of the order of 1.3 nT ($f_{ce} \sim 36$ Hz) without any loss of generality, since in any case, the transition at around 300 km takes place at an altitude where the plasma is so collisional that the magnetic properties of the medium may be ignored. We have plotted in Fig. 8 the value of the angle θ that satisfies the coupling condition (17) for $f = 36$ Hz. According to this model, one can check that any EM component at that frequency can be generated anywhere down to the lower boundary of the ionosphere. Then, as it occurs for natural whistlers on Earth, in the highly collisional D region, the waves are scattered backward within a wide solid angle due to the sudden decrease of the refractive index. In Titan case, the new-born whistler-mode wavelets encounter, at around 90 km, the "Huygens" conductive layer where the maximum conductivity of about 3×10^{-9} S m^{-1} (Hamelin et al., 2007), offers a cut-off to the 36 Hz electric field component. Then, we anticipate that those waves are trapped in the gap between the two cut-off altitudes, i.e., between about 300 and 60 km in the model plotted in Fig. 8.

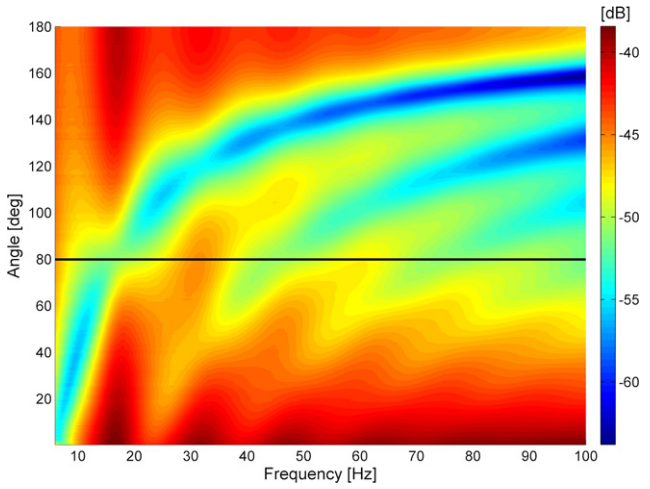

Fig. 9. Map of the electric field amplitude (arbitrary normalized units) received from an isotropic EM source located at 200 km altitude, versus frequency, as a function of angular distance, at the altitude of 100 km (see text).

In order to check the above scenario, we have run a simulation code which has been developed for atmospheric lightning sources (Simões et al., 2007a). A first algorithm is used for computing the complex eigenfrequencies from which the Q-factors are derived; and a second one for studying the harmonic propagation modes. The second algorithm solves the set of Maxwell equations using the finite element method, with proper boundary conditions, computes the frequency spectra, identifies the propagating eigenmodes, calculates the electric field over a wide range of altitude and distance, and finally evaluates the influence of the source distribution on the trapped modes. A perfectly conducting boundary is assumed at 100 km below the surface, and the soil is given a relative permittivity of 3 and a conductivity of 10^{-9} S m^{-1} (Simões et al., 2007a).

We have introduced in the code the conductivity profile plotted in Fig. 8, and an isotropic EM source is placed at 200 km altitude. The amplitude of the electric field versus the frequency at 100 km is shown in Fig. 9, under the form of a 2-dimensional color map as a function of angular distance from the source. One can check that for an angular distance of 80° from the source (horizontal solid line), the maximum amplitude of the electric field corresponds to the second and the fourth eigenmodes, at around 30 and 60 Hz, respectively, as anticipated by the rough model of pure standing waves. The whistler-mode wavelets are supposed to emerge from regions where the ionospheric currents close the northern and southern sheath currents, i.e., mainly in the polar caps through connection paths towards the neutral sheet in the North-Saturn plane (Fig. 7). Then, in order to fulfill the condition for observation of the second order eigenmode, the Huygens Probe should have been located at low latitude, on the ram side. The landing site in Titan's coordinates lies indeed at about 10° South and 168° East, which is 27° West from the asymptotic approach velocity vector (Lebreton et al., 2005). Since the Probe velocity pointed towards Titan's center and made an angle of about 130° with the moon orbital velocity (JPL report, 2004), the landing trajectory was nearly 10° South, about 20–25° eastward from the supposed ram direction (pointed out by a star in Fig. 7), i.e., in a right position, as shown in Fig. 9.

The above model of generation mechanism for a plasma driven Schumann-like resonance must be considered as a first approach, and several points must be investigated more deeply in the near future. A first necessary development will consist to solve the full-wave problem of an emerging right-hand polarized whistler-mode, trapped in the wave-guide between 60 and 300 km, what could explain satisfactorily the enhancement observed just above the "Huygens" layer. When the processed RPWS data obtained during many Cassini's Titan flybys will be available and interpreted, it will be possible to check the assumption of the source localization for the "36 Hz." It would be also worth to investigate whether our model is applicable to the Earth. The contribution of magnetospheric waves emerging from the ionosphere in the auroral zones has been proposed indeed by Abbas (1968) in order to explain the occurrence of Schumann resonance at noon local time under middle latitudes, though the author concluded that the power budget for ionospheric direct transmission coefficients was not theoretically compatible with the observations.

9. Discussion and conclusion

We summarize in Table 3 the main arguments pro and con each scenario, according to the conclusions drawn in the relevant Sections. We cannot firmly conclude yet that only one scenario can explain the ELF and "36 Hz" line seen in the PWA data, but we can reasonably constrain the degree of likelihood among all possibilities that we have investigated. Next to each entry in Table 3 one rates the consistency between the experimental data and the possible mechanisms.

The most probable scenario is that the PWA instrument observed the second and possibly the fourth eigenmode of a Schumann-like resonance, driven by the interaction of the corotating Saturn's magnetosphere with Titan's ionosphere, what is consistent with a global power budget. The proposed model involves the production of a high level of ELF ion-acoustic turbulence in the ionospheric regions that load the wake currents, and a subsequent coupling mechanism between the ES turbulence and whistler-mode wavelets able to emerge downwards in the atmospheric cavity. This model accounts for a strengthening of the electric component of even Schumann's eigenmodes, as observed at the particular location of the landing site with respect to that of the supposed source regions.

The scenario for the "36 Hz" line implies a different generation mechanism for the broadband ELF-VLF noise (up to 1 kHz), which is found probably unable to come from the ionosphere because of a maximum threshold for the magnetic field strength in this region. Although a first enhancement period occurs approximately at the same time for both signals, such a coincidence is perhaps not entirely fortuitous. Within the low conductivity cavity which is thought to be deepened by a high concentration of electrophylic aerosols, between the bottom of the regular ionosphere and the "Huygens" conductivity layer, the emerging 36 Hz wavelets are assumed to be reflected upwards. Then, the horizontal electric component of

Table 3
Summary of pro and con arguments for each scenario

Scenario	Consistency with				
	36 Hz line emission	Line frequency increase	Descent events & in situ parameters	Power budget	Updated Titan's knowledge
EMI from S/C	No never seen before	NA	No	Possible	NA
Bridles vibration	No	Yes	Yes	Unlikely	NA
Boom vibration	Most unlikely	Possible	Possible	Unlikely	NA
Tribo-electricity aerosols	No	No	Yes for broadband ELF	Possible	Yes
Schumann by lightning	Yes if polar source	Yes	Possible: tilted dipole axis	Doubtful (TBC)	No detection by Cassini
Schumann by plasma	Yes: as above	Yes	As above + conductive layer	Possible	Yes, with current models

those waves may be subsequently enlarged, as seen on the "36 Hz" between 105 and 70 km. Almost simultaneously, between 109 and 80 km, one observes a probable shot-noise broadband emission due to the same aerosols impacting the electrodes of the antenna, as simulated in the laboratory.

However, there is a clear correlation between a short ELF burst ($\sim$10 s duration) and the mechanical shock associated with the main parachute jettison. This fact suggests a possible additional contribution to the ELF-VLF noise due to aerodynamic vibrations. But the latter contribution is not applicable to the "36 Hz" line, neither to the broadband noise during the second enhancement period, when no particular source of vibration can be invoked, except for the crossing of a haze layer.

The Schumann resonance triggered by lightning is quite unlikely, because no signature of any electric discharges has been observed to date in Titan's atmosphere able to sustain the "36 Hz" line amplitude, in spite of many Titan flybys. However, this scenario would have to be revised if a high rate ($\sim 10^5$ s^{-1}) of weak discharges ($\sim$1 kJ) undetectable electrically by the RPWS instrument onboard the Cassini orbiter could be seen optically. The possible microphone effect due to PWA boom vibrations excited by aerodynamic appears unable to explain the "36 Hz" resonance for two main reasons: (i) the power budget is not compatible with the results of the laboratory tests, and (ii) the resonance flexural modes of all PWA model booms tested to date in laboratory (22.5 ± 2.5 Hz), are out of known limits for cryogenic properties of boom material necessary to explain an increase of the resonance frequency by more than 50% in the atmosphere of Titan. However, additional mechanical and cryogenic tests must be scheduled on the flight spare booms, in order to reach a firm conclusion.

Other kinds of artifact, such as electromagnetic interferences or hardware anomaly can be ruled out definitely since such phenomena were never observed during ground tests, neither during balloon test flights and cruise functional tests. Nevertheless, the general conclusion of this paper must be confirmed or invalidated by further investigation, such as complementary ground tests, additional theoretical works and simulations, and, if possible, dedicated operations during forthcoming Cassini flybys. However, it will be long before a new ground-truth validation of the plasma-driven Schumann-like resonance on Titan may be done.

Acknowledgments

The authors thank the International Space Science Institute, Bern, Switzerland for hosting and supporting the members of Team No. 84, "Titan's Ground-Ionosphere Cavity after Huygens, Atmospheric Electricity and Surface" during three fruitful meetings.

References

Abbas, M., 1968. Hydromagnetic wave propagation and excitation of Schumann resonances. Planet. Space Sci. 16, 831–844.

Al'pert, Ya.L., Fligel, D.S., 1970. Propagation of ELF and VLF Waves near the Earth, Wait, J.R. (Ed.). Consultants Bureau, New York/London/Boulder, pp. 1–171.

Backes, H., and 10 colleagues, 2005. Titan's magnetic field signature during the first Cassini encounter. Science 308, 992–995.

Béghin, C., Rauch, J.L., Bosqued, J.M., 1989. Electrostatic plasma waves and HF auroral hiss generated at low altitude. J. Geophys. Res. 94, 1359–1378.

Belyaev, G.G., Schekotov, A.Yu., Shvets, A.V., Nickolaenko, A.P., 1999. Schumann resonances observed using Poynting vector spectra. J. Atmos. Solar Terr. Phys. 61, 751–763.

Besser, B.P., 2006. Synopsis of the historical development of Schumann resonances. Radio Sci. 42, doi.10.1029/2006RS003495, RS2S02, in press.

Bettanini, C., 2006. Vibration test on PWA EM boom. Technical report PWA-BOOM-TN-001, CISAS G. Colombo, Padova University.

Blanc, E., Rickel, D., 1989. Nonlinear wave fronts and ionospheric irregularities observed by HF sounding over a powerful acoustic source. Radio Sci. 24, 279–288.

Blanc, M., and 29 colleagues, 2002. Magnetosphere and plasma science with Cassini–Huygens. Space Sci. Rev. 104, 253–346.

Erokhin, N.S., Moiseev, S.S., 1979. Wave processes in an inhomogeneous plasma. In: Leontovich, M.A. (Ed.), Reviews of Plasma Physics, vol. 7. Consultants Bureau, New York/London, pp. 181–255.

Fulchignoni, M., and 27 colleagues, 2002. The characterization of Titan's atmosphere physical parameters by the Huygens Atmospheric Structure Instrument (HASI). Space Sci. Rev. 104, 395–431.

Fulchignoni, M., and 42 colleagues, 2005. In situ measurements of the physical characteristics of Titan's environment. Nature 438 (8), 785–791, doi:10.1038/nature04314.

Galeev, A.A., Sagdeev, R.Z., 1984. Current instabilities and anomalous resistivity of plasma. In: Sudan, G. (Ed.), Handbook of Plasma Physics, vol. 2.

North-Holland Phys. Publishing, Amsterdam/Oxford/New York/Tokyo, pp. 271–303.
Goldreich, P., Linden-Bell, D., 1969. Io, a jovian unipolar conductor. Astrophys. J. 156, 59–78.
Grard, R., Svedhem, H., Brown, V., Falkner, P., Hamelin, M., 1995. An experimental investigation of atmospheric electricity and lightning activity to be performed during the descent of the Huygens Probe on Titan. J. Atmos. Terr. Phys. 57, 575–585.
Grard, R., and 19 colleagues, 2006. Electric properties and related physical characteristics of the atmosphere and surface of Titan. Planet. Space Sci. 54, 1124–1136.
Gurnett, D.A., Scarf, F.L., Kurth, W.S., 1982. The structure of Titan's wake from plasma wave observations. J. Geophys. Res. 87, 1395–1403.
Gurnett, D.A., and 26 colleagues, 2004. The Cassini radio and plasma wave investigation. Space Sci. Rev. 114, 395–463.
Gurnett, D.A., and 29 colleagues, 2005. Radio and plasma wave observations at Saturn from Cassini's approach and first orbit. Science 307, 1255–1262.
Hamelin, M., and 17 colleagues, 2007. Electron conductivity and density profiles derived from the Mutual Impedance Probe measurements performed during the descent of Huygens through the atmosphere of Titan. Planet. Space Sci., doi:10.1016/j.pss.2007.04.008, in press.
Hartle, R.E., Sittler Jr., E.C., Ogilvie, K.W., Scudder, J.D., Lazarus, A.J., Atreya, S.K., 1982. Titan's ion exosphere observed from Voyager 1. J. Geophys. Res. 87, 1383–1394.
Hofe, R., 2006. Signal analysis of the electric and acoustic field measurements by the Huygens instrument HASI/PWA. Diploma thesis, I.B.C., University of Technology, Graz, Austria.
Ilichev, V.Ya., Vladimirova, V.L., Telegon, A.I., Maslii, G.I., 1981. Mechanical properties of some glass-reinforced plastics at low temperature. J. Strength Mater. 12, 472–476.
Jaffer, G., Schwingenschuh, K., 2006. Lab experiments of corona discharges. Technical report, Space Research Institute, Austrian Academy of Science (IWF), Graz.
JPL report, 2004. Huygens Probe (Titan-C) Mission description. JPL D-5564, Rev 0, Jet Propulsion Laboratory, Cal. Inst. of Technology.
Kennel, C.F., Petschek, H.E., 1966. Limit on stably trapped particle fluxes. J. Geophys. Res. 71, 1–28.
Lammer, H., Tokano, T., Fischer, G., Stumptner, W., Molina-Cuberos, G.J., Schwingenschuh, K., Ruckeret, H.O., 2001. Lightning activity on Titan: Can Cassini detect it? Planet. Space Sci. 49, 561–574.
Lebreton, J.P., Matson, D.L., 2002. The Huygens Probe: Science, Payload and Mission overview. Space Sci. Rev. 104, 59–60.
Lebreton, J.P., and 11 colleagues, 2005. An overview of the descent and landing of the Huygens Probe on Titan, 2005. Nature 438 (8), 758–764, doi:10.1038/nature4347.
Lepechinsky, D., Rolland, P., 1964. On plasma instabilities and their probable role in ionospheric phenomena. J. Atmos. Terr. Phys. 26, 31–40.
Mikhailovskii, A.B., 1974. Theory of Plasma Instabilities, vol. 1. Consultant Bureau, New York/London.
Mowers, R., 1968. Properties of non-metallic materials at cryogenic temperatures. In: Proceedings of the 1968 Summer Study on Superconducting Devices and Accelerators, part 1, Brookhaven National Laboratory, available online at: http://www.bnl.gov/magnets/staff/gupta/Summer1968/, pp. 326–367.
Nagy, A.F., Cravens, T.E., 1998. Titan's ionosphere: A review. Planet. Space Sci. 46, 1149–1155.
Nickolaenko, A.P., Besser, B.P., Schwingenschuh, K., 2003. Model computations of Schumann resonance on Titan. Planet. Space Sci. 51, 853–862, doi:10.1016/S0032-0633(03)00119-3.
Pokhotelov, O.A., Pilipenko, V.A., Fedorov, E.N., Stenflo, L., Shukla, P.K., 1994. Induced electromagnetic turbulence in the ionosphere and the magnetosphere. Phys. Scr. 50, 600–605.
Raulin, F., Coscia, D., Gazeau, M.C., Sternberg, R., Bruston, P., Israel, G., Gautiert, D., 1998. An exobiological view of Titan and the Cassini–Huygens mission. Adv. Space Res. 22, 353–362.
Rodriguez, P., 1979. Magnetosheath electrostatic turbulence. J. Geophys. Res. 84, 917–930.
Scarf, F., 1976. Plasma physics and wave–particle interactions at Jupiter. In: Gehrels, T. (Ed.), Jupiter, Studies of Interior, Atmosphere, Magnetosphere and Satellites. Univ. of Arizona Press, Tucson, pp. 870–895.
Schumann, W.O., 1952. Über die strahlungslosen Eigenschwingungen einer leitenden Kugel, die von einer Luftschicht und einer Ionosphärenhülle umgeben ist (On the free oscillations of a conducting sphere which is surrounded by an air layer and an ionosphere shell). Z. Naturforschung 7a, 149–154.
Shawhan, S.D., Goertz, C.K., Hubbard, R.F., Joyce, J., Gurnett, D., 1973. Sheath acceleration of photoelectrons by Jupiter's moon Io. In: Grard, R. (Ed.), Photon and Particle Interactions with Surfaces in Space. Reidel, Dordrecht, pp. 405–413.
Shawhan, S.D., Goertz, C.K., Hubbard, R.F., Gurnett, D., Joyce, J., 1975. Io accelerated electrons and Ions. In: Formisano, V. (Ed.), Magnetospheres of Earth and Jupiter. Reidel, Dordrecht, pp. 375–389.
Simões, F., and 20 colleagues, 2007a. A new numerical model for the simulation of ELF wave propagation and the computation of eigenmodes in the atmosphere of Titan: Did Huygens observe any Schumann resonance? Planet. Space Sci., doi:10.1016/j.pss.2007.04.016, in press.
Simões, F., Béghin, C., Bettanini, C., Hamelin, M., Grard, R., 2007b. Internal notes on post-flight ground tests performed on Mock-up, EM and Spare Model of MI- PWA experiment. Technical report CETP/LPCE-Université d'Orléans.
Stix, T.H., 1962. The Theory of Plasma Waves. McGraw–Hill, New York/San Francisco/Toronto/London, pp. 1–283.
Tokano, T., Molina-Cuberos, G.J., Lammer, H., Stumptner, W., 2001. Modelling of thundercloud and lightning generation on Titan. Planet. Space Sci. 47, 493–520.
Tokano, T., McKay, C.P., Neubauer, F.M., Atreya, S.K., Ferri, F., Fulchignoni, M., Niemann, H.B., 2006. Methane drizzle on Titan. Nature 442, 432–435.
Tomasko, M.G., and 39 colleagues, 2005. Rain, winds and haze during the Huygens Probe's descent to Titan surface. Nature 438 (8), 765–778, doi:10.1038/nature04126.
Wahlund, J.-E., and 17 colleagues, 2005. Cassini measurements of cold plasma in the ionosphere of Titan. Science 308, 986–989.

Paper 6

Electron conductivity and density profiles derived from the mutual impedance probe measurements performed during the descent of Huygens through the atmosphere of Titan

Hamelin, M., Béghin, C., Grard, R., López-Moreno, J.J., Schwingenschuh, K., Simões, F., Trautner, R., Berthelier, J.J., Brown, V.J.G., Chabassière, M., Falkner, P., Ferri, F., Fulchignoni, M., Jernej, I., Jeronimo, J.M., Molina-Cuberos, G., Rodrigo, R., Tokano, T.

Planetary and Space Science **55**, 1964-1977 (2007)

Available online at www.sciencedirect.com
ScienceDirect
Planetary and Space Science 55 (2007) 1964–1977
Planetary and Space Science
www.elsevier.com/locate/pss

Electron conductivity and density profiles derived from the mutual impedance probe measurements performed during the descent of Huygens through the atmosphere of Titan

M. Hamelin[a,*], C. Béghin[b], R. Grard[c], J.J. López-Moreno[d], K. Schwingenschuh[e], F. Simões[a], R. Trautner[c], J.J. Berthelier[a], V.J.G. Brown[d], M. Chabassière[b], P. Falkner[c], F. Ferri[f], M. Fulchignoni[g], I. Jernej[e], J.M. Jeronimo[d], G.J. Molina-Cuberos[d,h], R. Rodrigo[d], T. Tokano[i]

[a]*CETP-IPSL, 4 Avenue de Neptune, 94107 Saint Maur, France*
[b]*LPCE-CNRS, 3A, Avenue de la Recherche Scientifique, 45071 Orléans cedex 2, France*
[c]*RSSD, ESA-ESTEC, European Space Agency, Keplerlaan 1, 2200 AG Noordwijk, The Netherlands*
[d]*Instituto de Astrofísica de Andalucía IAA-CSIC, Camino Bajo de Huétor, 50, 18008 Granada, Spain*
[e]*Space Research Institute, Austrian Academy of Sciences (IWF), Schmiedlstrasse 6, 8042 Graz, Austria*
[f]*CISAS "G. Colombo", Università di Padova, Via Venezia 15, 35131 Padova, Italy*
[g]*LESIA, Observatoire de Paris, 5 Place Janssen, 92195 Meudon, France*
[h]*Applied Electromagnetic Group, Department of Physics, University of Murcia, Murcia 30100, Spain*
[i]*Institut für Geophysik und Meteorologie, Universität zu Köln, Albertus-Magnus Platz, 50923 Köln, Germany*

Accepted 13 April 2007
Available online 22 April 2007

Abstract

During the descent of the Huygens probe through the atmosphere of Titan, on January 14th, 2005, the permittivity, waves and altimetry (PWA) subsystem, a component of the Huygens atmospheric structure instrument (HASI), detected an ionized layer at altitudes around 63 km with two different instruments, the relaxation probe (RP) and the mutual impedance probe (MIP). A very detailed analysis of both data sets is required, in order to correct for environmental effects and compare the two independent estimates of the electrical conductivity. The present work is dedicated to the MIP data analysis. New laboratory tests have been performed to validate or improve the available calibration results. Temperature effects have been included and numerical models of the MIP sensors and electric circuitry have been developed to take into account the proximity of the Huygens probe body. The effect of the vertical motion of the vessel in the ionized atmosphere is estimated in both analytical and numerical ways. The peculiar performance of the instrument in the altitude range 100–140 km is scrutinized. The existence of a prominent ionized layer, and of enhancements in the conductivity and electron density profiles at 63 km, are discussed in the light of previous theoretical predictions.

Keywords: Titan; Atmospheric electricity; Huygens probe; Electron density; Atmospheric conductivity

1. Introduction

The upper atmospheres of planets and satellites are ionized, partly due to interactions with solar photons and cosmic rays. The lower atmosphere of Earth is poorly conductive and is permeated by a current system that is driven by active thunderstorm clouds which act as generators, with return currents in fair weather regions. The highly conductive ground and ionosphere form the boundaries of this global electric circuit. Lightning has been observed on Jupiter and Saturn (Gurnett et al., 1979; Lanzerotti et al., 1996; Fischer et al., 2006), but the Voyager 1 spacecraft did not detect any such activity on Titan during its 4000 km low altitude flyby of this satellite of Saturn. The Cassini–Huygens mission combined remote sensing observations from the Cassini orbiter and *in situ* instruments performed on the Huygens lander to study

*Corresponding author. Tel.: +33 1 4511 4279; fax: +33 1 48 89 44 33.
E-mail address: Michel.Hamelin@cetp.ipsl.fr (M. Hamelin).

0032-0633/$ - see front matter © 2007 Elsevier Ltd. All rights reserved.
doi:10.1016/j.pss.2007.04.008

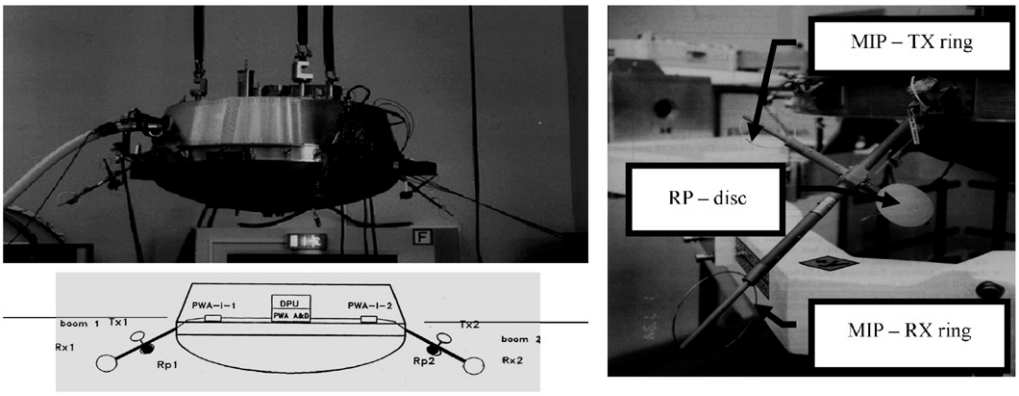

Fig. 1. The PWA electrode arrangement on Huygens. Top left: Huygens with PWA booms in deployed position during calibrations at the aerospace company DASA (Ottobrunn, Germany). Bottom left: sketch of the PWA sensors and electronics. The rings Tx1 and Tx2 are the transmitter electrodes; Rx1 and Rx2 are the receiver rings; the RP1 and RP2 discs are the RP electrodes. Right: close view of one boom with MIP and RP electrodes.

Titan's atmospheric electricity. The PWA (permittivity waves and altimetry) instrument (Grard et al., 1995), a subsystem of HASI (Huygens atmospheric structure instrument) was carried by the Huygens probe (Lebreton et al., 2005), and measured the conductivity of the atmosphere, and DC and AC electric fields, with two complementary sensors, a mutual impedance probe (MIP) and a relaxation probe (RP). Both RP and MIP instruments detected peaks in the electron concentration and conductivity at the altitude of 63 km (Fulchignoni et al., 2005; Grard et al., 2006), but it was clear that the information derived from a preliminary analysis of the two data sets was not fully consistent and could not yield reliable profiles for the conductivity and electron density. The present paper focuses on the analysis of the conductivity measured with MIP; the RP measurements will be treated in a forthcoming paper.

The operation of PWA started at 141 km, following the jettison of the Huygens thermal shield, the inflation of the parachute and the deployment of the HASI-PWA booms (Lebreton et al., 2005). The Huygens probe and the MIP electrodes setup are shown in Fig. 1. The booms length was limited by the space available under the heat shield and it is therefore necessary to take into account the influence of the probe body on the measurements.

The measurement technique and the data set acquired during the descent in the atmosphere of Titan are presented in Section 2. We then give some detail about the critical instrumental and scientific issues prerequisite to the validation of the electron density and conductivity profiles, and mention the main difficulties encountered during the analysis of the data. In Section 3, we report on the end-to-end calibration procedure, and demonstrate the importance of the probe velocity effects on the measurements. In Section 4, the experimental results are presented and compared to theoretical predictions published before the mission (Borucki et al., 1987; Molina-Cuberos et al., 1999a,b, 2002) and to more recent models (Borucki et al., 2006).

2. The MIP measurements

2.1. Measurement principle

2.1.1. The mutual impedance technique

The conductivity of a homogeneous and isotropic medium can be measured with a self-impedance probe. This simple instrument consists of two electrodes, fed by an AC current generator. The self impedance of the dipole, ratio of the difference between the electrode potentials over the injected current, reflects the conductivity of the medium, provided its homogeneity is perturbed neither by the injected current, nor by the dipole itself. This situation is generally never encountered in electrolytes and plasmas, due to the charged sheaths that form around the electrodes.

The MIP, or quadrupolar probe, has been introduced in geophysics at the beginning of the 20th century for measuring the earth conductivity, as an aid to oil prospecting (Wenner, 1915; Schlumberger, 1920). The mutual impedance is the ratio of the voltage measured by a receiving dipole to the current injected into the medium through a neighbouring transmitting dipole. The main advantage of the MIP over the simpler self-impedance technique is that the former is not sensitive to the perturbations induced around the electrodes. The injected current can be measured or estimated, irrespective of any sheath, and the voltage induced within the receiving dipole is measured outside the non-homogeneous regions that may form around the transmitting electrodes. The perturbations are smaller around the receiving electrodes than around the transmitting ones, but any differential effect is cancelled if the receiving electrodes are identical. For earth conductivity measurements both DC and AC current sources are used.

The quadrupolar probe technique was transposed to space plasmas by Storey et al. (1969) and applied in many ionospheric and magnetospheric experiments, such as CISASPE, PORCUPINE, VIKING, GEOS, and

ARCAD-3 (see e.g. Béghin and Debrie, 1972; Chasseriaux et al., 1972; Décréau et al., 1982, 1987; Pottelette et al., 1981; Béghin et al., 1982). The quadrupole technique is particularly appropriate in a plasma, because the electrodes are always surrounded by ion sheaths that contaminate the self-impedance measurement. In the most regions of the Earth ionosphere and magnetosphere, where the electron–neutral collision frequency is relatively low, the frequency response of the mutual impedance yields the electron density and temperature from the analysis of the plasma resonances. The resonances vanish in the low terrestrial ionosphere where the plasma is highly collisional, but the technique can still be used. Then the measurable parameter is the complex permittivity, which is directly associated with the electron–neutral collisions. Odero (1972) and Storey and Malingre (1976) pointed out the difficulties of such measurements. On Earth, very few experimental data have been collected in this altitude range (80–120 km), which can only be crossed by rockets at very high velocities. The terrestrial stratosphere is accessible to balloons but, due to the lack of free electrons, the electrical conductivity is driven by positive and negative ions. The quadrupolar approach is not suitable there, and the ionic polar conductivities are usually measured using the RP technique (López-Moreno et al., 2001) or Gerdien condenser techniques (Gerdien, 1905).

Titan's atmosphere is on the contrary a non-oxidizing medium with a free electron concentration which was modelled by Borucki et al. (1987, 2006), and Molina-Cuberos et al. (1999a,b, 2002). The free electron contribution to the conductivity has been measured with the mutual impedance technique that was implemented in the PWA–HASI experiment on the Huygens probe. The PWA–MIP electrodes consist of four rings mounted on two relatively short booms (Grard et al., 1997) as shown in Fig. 1 (the discs carried by the same booms are the RP sensors).

On rockets and satellites the geometry of the quadrupolar electrode array is such that (i) the separations between the electrodes are much larger than their size, (ii) the satellite or rocket body is sufficiently distant from the electrodes and does not significantly influence the mutual impedance. Under these conditions, the electrodes are considered to be punctual and the basic theory of the quadrupolar array applies (Storey et al., 1969). In the case of the MIP experiment on Huygens, condition (i) is roughly fulfilled but condition (ii) not at all. Then the conductive probe body becomes part of the measurement system and its influence has to be taken into account.

2.1.2. Basic principle: pin point electrodes

We consider a pin point electrode located at the origin O, through which a current $I = I_0 \exp(\mathrm{i}\omega t)$ is injected, where I_0 is the amplitude, ω is the angular frequency, t is time, and $\mathrm{i} = \sqrt{-1}$. The medium is infinite, homogeneous and isotropic.

It results from the spherical symmetry of the problem that the magnetic field is $\mathbf{H} = 0$. Then we can write the Maxwell harmonic equation:

$$\nabla \times \mathbf{H} = \mathbf{j}_0 + \sigma \mathbf{E} + \mathrm{i}\omega\varepsilon \mathbf{E} = 0, \tag{1}$$

where $\mathbf{E}$ is the electric field, ε the dielectric constant and σ the conductivity. The radial source current density $\mathbf{j}_0$ is inversely proportional to the square of the radial distance r, and has a singularity at O that fulfills the Poisson equation $[\Delta(1/r) = -4\pi\delta(\mathbf{r})]$, where δ is the Dirac distribution, such that:

$$\nabla \cdot \mathbf{j}_0 = -I_0 \delta(\mathbf{r}). \tag{2}$$

Using the dielectric description of the medium, Eq. (1) can be written as

$$\mathbf{j}_0 + \mathrm{i}\omega\varepsilon^* \mathbf{E} = 0, \tag{3}$$

where $\varepsilon^* = \varepsilon - \mathrm{i}\sigma/\omega$ is the complex permittivity.

Because of spherical symmetry, the model implies a source current density varying in the whole space like r^{-2}. In practice, a wire drives the current to the electrode, but we neglect the associated magnetic effect at low frequencies. Wires are often omitted from circuit diagrams, but we will show in Section 2.3.3 that their quasi-static influence can be modelled.

The electric potential V is defined by $\mathbf{E} = -\nabla V$. It vanishes at infinity, and is derived from (2) and (3):

$$V = \mathrm{i} I_0/(4\pi\omega\varepsilon^* r). \tag{4}$$

We note from the above equation that, due to the finite conductive current in the medium, the charge at point O is no longer equal to $I_0/\mathrm{i}\omega$ as in a vacuum (of permittivity ε_0), but that it must be multiplied by $\varepsilon_0/\varepsilon^*$. The charge density ρ is given by

$$\nabla \cdot (\varepsilon \mathbf{E}) = \rho, \tag{5}$$

and, using (2) and (3), can be written as

$$\rho = \mathrm{i}\frac{I_0}{\omega}\left(\frac{\varepsilon}{\varepsilon^*}\right)\delta(\mathbf{r}). \tag{6}$$

In this approach, motion of the charges is not taken into account for the calculation of the potential, i.e. the medium is assumed to be homogeneous and space charge effects are ignored.

Let us label the pinpoint electrodes as follows: 1 and 2 for the transmitter with positive current injected on 1; 3 and 4 for the receiver. Using (4), the mutual impedance defined by $Z = \Delta V/I_0$, where $\Delta V = V_3 - V_4$, is given by

$$Z = \frac{\mathrm{i}}{4\pi\omega\varepsilon^*}\left(\frac{1}{r_{13}} - \frac{1}{r_{14}} - \frac{1}{r_{23}} + \frac{1}{r_{24}}\right), \tag{7}$$

where r_{mn} is the distance between the points m and n.

2.1.3. Mutual impedance with finite size electrodes and in presence of other conductors

We consider that the medium is homogeneous and isotropic and make no assumption about the size of the electrodes. We also take into account the presence of other conductors, such as the Huygens probe body, especially if they are electrically connected to the electrodes through finite impedances. This is necessary because the separations

between the electrodes are not large with respect to the size of the body.

The potential given by Eq. (4) is that developed by a single charge $q = i(\varepsilon_0/\varepsilon^*)(I_0/\omega)$ in a vacuum. The quasi-static electric field and potential developed at one point by a given charge distribution in a dielectric and conductive medium are homothetic to their respective values in a vacuum. We can consequently deduce the impedance characteristics of a system of N conductors from their capacitive characteristics in a vacuum. If only perfect current generators and voltmeters connect the conductors, the relative complex permittivity of the medium is equal to *any* of the normalized admittances that characterize the system. Hence the geometry of the system is irrelevant, assuming perfect electronics, no noise and perfect calibrations in a vacuum. Under these conditions, the conductivity and the dielectric constant are

$$\sigma = \frac{A_0}{A}\omega\varepsilon_0 \sin(\varphi - \varphi_0) \quad \text{and} \quad \frac{\varepsilon}{\varepsilon_0} = \frac{A_0}{A}\cos(\varphi - \varphi_0), \qquad (8)$$

where A and A_0, and φ and φ_0 are the amplitudes and phases of the difference between the potentials of *any* pair of electrodes, in the medium and in a vacuum, respectively.

In practice, the transmitting and receiving circuits are not ideal. Stray capacitors and resistors cannot be ignored and the equivalent circuit must take into account both the medium and the electronic network. This purpose can be achieved in two ways: (i) by solving Laplace equation in the medium, using the Comsol Multyphysics™ software, with a fair geometrical model of the Huygens probe body, but a poor representation of the electrodes and no consideration for the wires; (ii) by using the finite element surface charge distribution (SCD) method (Béghin and Kolesnikova, 1998), with a precise description of the electrodes and connecting wires but a rough model of the Huygens probe body.

2.2. The MIP instrument setup

2.2.1. The MIP measurement circuit

The MIP electrodes configuration is shown in Fig. 1 and the electronic circuit is schematically drawn in Fig. 2. The receiving electrodes Rx are connected by tri-axial cables, through coupling capacitors, to high input impedance preamplifiers located in the small HASI-I boxes mounted on the Huygens instrument platform. The first shield is actively biased to about the same potential as that of the inner wire to minimize its capacitance with respect to the structure. The outer conductor is a shield connected to the Huygens potential reference. The preamplifier low impedance output signals are sent to a differential amplifier in the PWA-A analogue board. After low pass filtering, the signal is amplified with two possible gains, fed into a 16 bits A/D converter (in PWA-A) and processed in the data signal processor (DSP) of the PWA-D board. On the transmitter side, the DSP sends a sine table to the D/A converter of the PWA-D board. The resulting analogue signal is amplified with three possible gains, filtered and split into two signals with opposite phases which are sent to the transmitting electrodes Tx through coaxial cables and coupling capacitors. The transmitted current is not measured. The coupling capacitance that is much smaller than the electrode capacitance in a vacuum insures that the transmitting dipole acts approximately as a current source. The potential difference induced in the receiving dipole is measured with a high input impedance preamplifier that acts as a quasi-ideal voltmeter.

2.2.2. Working frequency

Eqs. (8) indicate that the phase is measured with a better accuracy by using a low frequency and stationary signal. On the other hand, the measurement theory assumes a steady environment. In consequence, the medium should

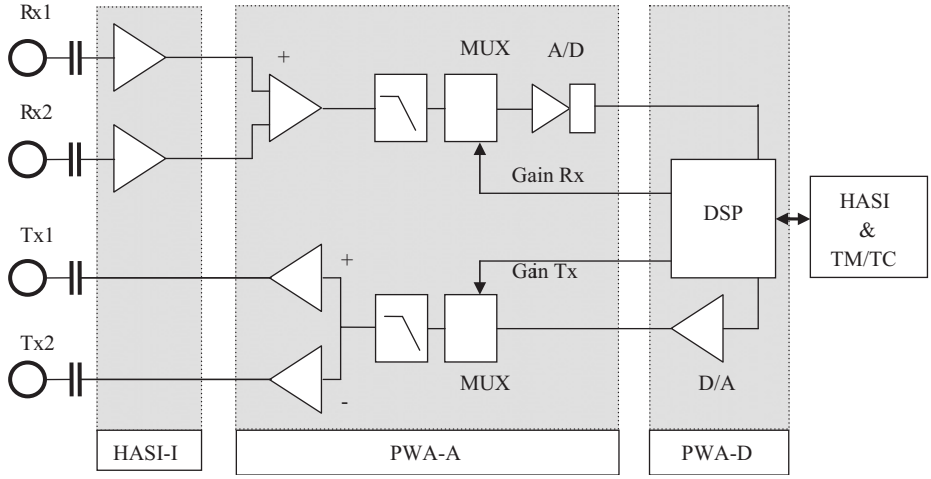

Fig. 2. The MIP simplified circuit layout. The right box represents the power and telecommand/telemetry (TM/TC) interfaces with HASI and Huygens. The transmitter signal is generated in the DSP of the PWA-D board and converted into an analogue signal sent to the PWA-A board. Then after gain selection by a multiplexer (MUX), the signal is duplicated in an inverter and both signals are sent to the Tx electrodes via coupling capacitors. The potentials on the receivers are measured by the two high impedance preamplifiers of the HASI-I boards, and then sent to the inputs of a differential amplifier in the PWA-A board. After gain selection in the receiver MUX, the signal is converted to digital and sent to the DSP for numerical analysis.

not change too much during the measuring sequence (the Huygens probe descends ~50–100 m in 1 s). The selected frequency, 45 Hz, is a trade off between these two constraints. However, a frequency so close to the standard frequencies of electric power distribution on Earth raises practical difficulties for the calibration of the instrument.

2.2.3. Digital processing

We shall complete this description with a short explanation of the signal generation and digital processing. The 45 Hz transmitted signal is generated continuously during the descent from a 1024 points sine table read at a frequency of 46 kHz. On the receiving side, the signal was sampled at the same frequency during successive — not contiguous — 22.22 ms intervals, but synchronized with respect to the transmitted signal. An FFT (fast Fourier transform) is calculated for each of the 25 consecutive intervals and each FFT component is averaged over the 25 intervals. Both the real and imaginary parts of the 45 Hz averaged component are forwarded; only the amplitudes of the other spectral lines are measured. A more detailed account can be found in Falkner (2004).

Each part of the analogue and digital boards introduces amplitude and phase modifications that must be calibrated or estimated in other ways.

2.3. Calibration matters and models

2.3.1. Calibrations

2.3.1.1. End to end MIP calibration. As shown by Eqs. (8), the determination of the conductivity relies on both *in situ* measurements and calibrations in a vacuum. A proper calibration of the flight model (FM) with booms deployed should have been performed in a vacuum, far from any obstacle and support equipment, at temperatures similar to those encountered during the descent, and in a quiet electromagnetic environment. Fig. 1 shows that most of these conditions could not be fulfilled in the laboratory. The Huygens FM was kept as far as possible from walls and ceiling, but was immersed in an environment perturbed by 50 Hz power supplies that could not be switched off (as the cooling device whose pipe is visible in Fig. 1). Moreover, room temperature lies well above the 77–157 K range encountered in the atmosphere of Titan. End to end measurements were performed by connecting the transmitting and receiving electrodes, to test the functionality of the instrument and eliminate the environmental effect. Most parts of the MIP circuit elements have been calibrated separately in standard laboratory conditions, except for the booms and coupling circuits that were also tested at 93 K.

2.3.1.2. Temperature effects. The outer skin of the Huygens probe, made of aluminium, is exposed to Titan's atmosphere, but all instruments are kept at approximately room temperature by means of an efficient insulation and to radioactive heaters. There is roughly a 200 °C difference between room and ambient temperatures during the descent in Titan's atmosphere. The external parts are submitted to a relatively important temperature stress, which causes a constriction of about 0.35–0.45% on most structural elements, corresponding to a reduction of ~5 mm of the diameter of Huygens. This implies small changes in all inter-electrode distances and changes in the size of the electrodes themselves. Although small, these constriction effects are corrected for but, for the sake of simplicity, a single dilatation coefficient of 3.6×10^{-3} for a 200 K temperature increment is assumed (the coefficients in deg^{-1} range from ~ 1.2–2.0×10^{-5} for fibreglass, to $\sim 1.8 \times 10^{-5}$ for copper alloys and $\sim 2.2 \times 10^{-5}$ for aluminium).

2.3.1.3. DSP and software. The DSP software performs a straightforward procedure that is nominal in the absence of any superimposed electric noise. In a conductive medium, a small error may result from the transient response that affects the first of the 25 consecutive sequences whose average yields a single MIP measurement. This error is negligible in practice. In other respects the phase shift introduced by the numerical procedure itself is well defined and equals 0.52° at 45 Hz.

2.3.1.4. Analogue circuit. The transfer functions have been measured in the laboratory at room temperature (i.e. in not a too different thermal environment from that prevailing inside the insulated Huygens probe body during the descent in the atmosphere of Titan). The gain of the analogue circuit, from the differential input amplifier to the ADC, including the −9.37 dB attenuator in the PWA-D circuit, is $G_a = G_{am} \exp(i\varphi_a)$, with $G_{am} = 36.52$ dB and $\varphi_a = 26.91°$, at 45 Hz.

2.3.1.5. Receiving preamplifiers and coupling circuits. The preamplifier, the tri-axial cable, the coupling circuit (guarded capacitor) and the receiver ring electrode form a single unit. The inner shield of the cable acts as a guard, and is biased at a potential equal to 99.9% that of the axial wire that carries the signal. The coupling capacitance (~0.4 pF), embedded in the guard termination is not easily measured with precision (Trautner and Falkner, 2000), but the transfer function of the whole electronic chain has been monitored and has remained remarkably stable over a period of 10 years. The performance of the instrument was stable during the cruise, as confirmed by the flight checkouts. A specific test was performed on the FM model with the booms at 93 K and the preamplifiers at room temperature (like during the descent in Titan's atmosphere), leading to small corrections of the gain and of the phase shift (Hamelin and Chabassière, 2006). At room temperature (25 °C), the gain from the receiver electrode Rx to the preamplifier output is $G_p = G_{pm} \exp(i\varphi_p)$, where $G_{pm} = -13.55$ dB and $\varphi_p = 4.45°$. At 93 K, the gain parameters are $G_{pm} = -13.26$ dB and $\varphi_p = 3.46°$ and the

equivalent input impedance consists of a 0.3 pF capacitor in parallel with a 0.7 TΩ resistor.

2.3.1.6. Transmitter circuit. The AC signal from the 10 V source is sent via a coaxial cable to a coupling capacitor, like on the receiving side, but a stray capacitance is present between the electrode side of the circuit and the grounded coaxial shield. Precise measurements on the Tx circuit integrated in the boom could not be performed, due to its very high input impedance and its extreme sensitivity to the environment. At this time we expected that the overall MIP calibration in a vacuum would provide the best reference. The coupling capacitance was estimated to be 0.43 pF ±20% from measurements performed on spare components (Trautner and Falkner, 2000). The temperature effect due to the capacitor constriction is only ~1%.

2.3.1.7. Electrodes. The Rx and Tx electrodes are rings of diameter 100 and 65 mm, respectively, and are made of 1.2 mm square section wires. The self-capacitances of the Rx and Tx rings, calculated with a Comsol Multyphysics™ finite element model (~10^5 elements), are 2.64 and 1.85 pF, respectively, for square wire sections. These values differ by only 0.02 pF from the theoretical values obtained for an equivalent circular section ($C_{\text{ring}} \approx 4\pi^2\varepsilon_0 a/\ln(16a/d)$, where a and d are the radius of the ring and the diameter of the wire, respectively). As for other external parts the constriction effect is estimated to be 0.36%. The mutual capacitance between Tx, or Rx, and the Huygens body is ~1.0% larger than the self-capacitance of the ring.

2.3.2. The seven-conductors model

A first numerical model was developed by Cadène (1995) to evaluate the influence of the Huygens body on the mutual impedance measurements and to estimate the potential induced at the Rx locations by the charges carried by the Tx electrodes. A new model taking into account all electrodes, including those of RP, and the Huygens body, seven conductors in total, has been recently developed with the Comsol Multyphysics™ software. The general electrostatic problem is that of N conductors in a vacuum (e.g. Durand, 1966). The charges are related to the potentials through the relation

$$\mathbf{Q} = [\mathbf{K}]\mathbf{V}, \tag{9}$$

with $\mathbf{Q} = \{q_1, q_2, \ldots, q_N\}$ and $\mathbf{V} = \{V_1, V_2, \ldots, V_N\}$; q_n and V_n are, respectively, the charges and potentials of the conductor n for $n = 1 \ldots N$. $[\mathbf{K}]$ is the capacitance–influence matrix (with $K_{mn} > 0$ and $K_{mn} < 0$ if $m \neq n$).

In harmonic conditions the current vector $\mathbf{I_e} = \{I_{e1}, I_{e2}, \ldots, I_{eN}\}$ injected in the conductors and the potential vector $\{V_1, V_2, \ldots, V_N\}$ are linked by the equation:

$$\mathbf{I_e} = \mathrm{i}\omega[\mathbf{K}]\mathbf{V}. \tag{10}$$

Let us now define a circuit according to the following procedure: each conductor m is linked to the conductor n through the admittance Y_{mn} and to a zero potential reference at infinity through the admittance Y_{mm}. The case of three conductors is illustrated in Fig. 3. The circuit equations, with (9) and (10) yield:

$$\begin{aligned} Y_{mm} &= \mathrm{i}\omega\Sigma K_{mn} \quad (\text{sum}: \ n = 1, \ldots, N), \\ Y_{mn} &= -\mathrm{i}\omega K_{mn} \quad (m \neq n). \end{aligned} \tag{11}$$

In a vacuum, Y_{mn} are the admittances of elements whose capacitances C can be computed from the configuration of the conductor set, solving Laplace equation with the general finite element software Comsol Multyphysics™. In a dielectric and conductive medium, each capacitance C is replaced by a capacitance $C_{\text{eq}} = (\varepsilon/\varepsilon_0)C$ in parallel with a resistance $R_{\text{eq}} = \varepsilon_0\omega/\sigma C$. All Y_{mn} are therefore proportional to ε^*. The discrete electronic components of the instrument are included in the equivalent circuit and the full system can then be solved, which yields ε^*. The Huygens probe is represented by a 3D realistic model but, due to mesh and computer memory limitations, the ring electrodes are replaced by spheres of equal capacitances (Fig. 4). This exercise is required even if a proper vacuum calibration can be performed. The model parameters and the resulting K_{mn} matrix coefficients are shown

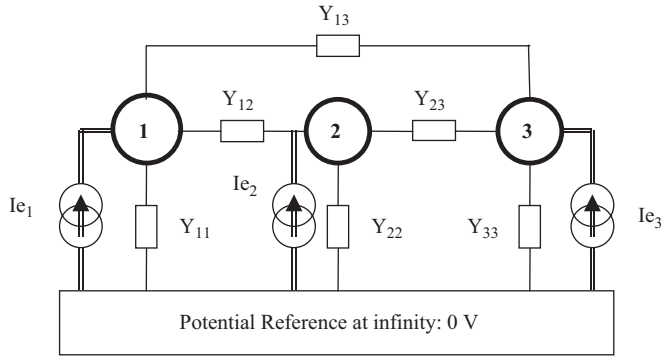

Fig. 3. Equivalent circuit of a system of three conductors in an uniform medium (the currents injected by the instrument in the medium, $I_{e1} \ldots I_{e3}$, are represented by double lines).

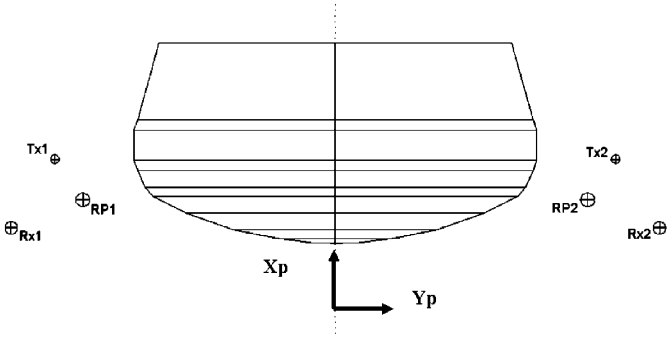

Fig. 4. Geometrical model of Huygens and MIP–RP electrodes used in Comsol Multyphysics™ software (Huygens revolution axis: Xp).

Table 1
Geometrical models of Huygens and of the electrodes

Name	Geometry	Dimensions	Capacitance (pF)	Equivalent sphere radius (mm)	Coordinates of sphere centers (m)		
					x	y	z
Probe	Axis symmetric model	$\phi = 1.3 \times 0.7$ m	62.83	–	–	–	–
Tx1	Ring 1.2 mm	$\phi = 65$ mm	1.85	16.6	0.27	−0.90	−0.07
Tx2	Ring 1.2 mm	$\phi = 65$ mm	1.85	16.6	0.27	0.90	−0.07
Rx1	Ring 1.2 mm	$\phi = 100$ mm	2.64	23.7	0.05	−1.04	0
Rx2	Ring 1.2 mm	$\phi = 100$ mm	2.64	23.7	0.05	1.04	0
RP1	Disc	$\phi = 70$ mm	2.50	22.8	0.14	−0.81	0.04
RP2	Disc	$\phi = 70$ mm	2.50	22.8	0.14	0.81	0.04

Table 2
Capacity–influence matrix [**K**] (pF)

	(1) Huygens	(2) Tx1	(3) Tx2	(4) Rx1	(5) Rx2	(6) RP1	(7) RP2
(1) Huygens	67.72	−1.07	−1.07	−1.25	−1.25	−1.69	−1.69
(2) Tx1	−1.07	1.88	-1.03×10^{-3}	−0.11	-2.22×10^{-3}	−0.15	-1.3×10^{-3}
(3) Tx2	−1.07	-1.03×10^{-3}	1.88	-2.22×10^{-3}	−0.11	-1.3×10^{-3}	−0.15
(4) Rx1	−1.25	−0.11	-2.22×10^{-3}	2.73	-4.92×10^{-3}	−0.17	-2.89×10^{-3}
(5) Rx2	−1.25	-2.22×10^{-3}	−0.11	-4.92×10^{-3}	2.73	-2.92×10^{-3}	−0.17
(6) RP1	−1.69	−0.15	-1.3×10^{-3}	−0.17	-2.92×10^{-3}	2.67	-1.74×10^{-3}
(7) RP2	−1.69	-1.3×10^{-3}	−0.15	-2.89×10^{-3}	−0.17	-1.74×10^{-3}	2.67

Conductors are: (1) Huygens body; (2) MIP–Tx1; (3) MIP–Tx2; (4) MIP–Rx1; (5) MIP–Rx2; (6) RP1; (7) RP2.

in Tables 1 and 2. After defining all components of the equivalent circuit, the problem is reduced to a linear system of seven equations (Hamelin and Simões, 2006).

For a 10 V (high gain) signal applied to the coupling circuit, the potential of Tx derived from the above circuit is 1.64 V; the potential difference between the receiving electrodes is 124 mV. This improved equivalent model takes into account all the electrodes and the impedances through which they are connected to the reference body. These results are, however, very sensitive to several parameters, the most critical ones being the coupling capacitors of the Tx electrodes and the stray capacitances between these electrodes and the Probe body.

2.3.3. The surface charge distribution (SCD) method

We consider again a set of N conductors in a vacuum, but the surface of the conductors is split into $M \gg N$ small elements where the surface charge density is assumed to be constant (the small elements will overlap not only the seven former main conductors but also their extensions as signal connections and triaxial shields). The potential of element m can be written as (from Durand, 1966)

$$V_m = \sum_{n=1}^{M} p_{mn} Q_n \quad \text{with } Q_n = S_n \rho_{S_n} \quad \text{and}$$
$$p_{mn} = \frac{1}{4\pi S_m S_n \varepsilon_0} \int_{S_m} \int_{S_n} \frac{1}{r_{mn}} \, \mathrm{d}s_m \, \mathrm{d}s_n, \tag{12}$$

where S_m, S_n and $\mathrm{d}s_m$, $\mathrm{d}s_n$, are, respectively, the surfaces and infinitesimal elements of surface m and n; r_{mn} is the distance between elements $\mathrm{d}s_m$ and $\mathrm{d}s_n$ and ρ_{S_n} is the surface charge density of element S_n. The charge of element is Q_n. The quantities p_{mn} are the inverses of distances that can be calculated from the model. The potential of element m is written as the sum of all the charge contributions Q_n ($n = 1 \ldots M$) at distances $1/p_{mn}$. The whole system of conductor elements is characterized by the $M \times M$ matrix $[\mathbf{P}]_{\mathbf{mn}} = p_{mn}$. Inverting the matrix we obtain the charges as functions of the potentials:

$$\mathbf{Q_M} = [\mathbf{P}]^{-1} \mathbf{V_M} \tag{13}$$

(the $N \times N$ matrix [**K**] of Eq. (9) can be easily deduced from $[\mathbf{P}]^{-1}$ by setting all V_M components corresponding to each of the N conductors to 1 V and the others to 0 V). Contrary to the former approach that is based on volume elements, this method involves surface elements and requires less computer memory for the same resolution, but the practical limitation comes from the difficulty encountered in inverting a very large matrix.

The method has been developed for satellites in space plasmas by Béghin and Kolesnikova (1998). All conductive parts of the system are split into as many finite elements as necessary to give a representative mesh structure of the full system, including the discrete electric connections between elements. The geometry of the model has to comply with the constraints of a general-purpose code that is designed

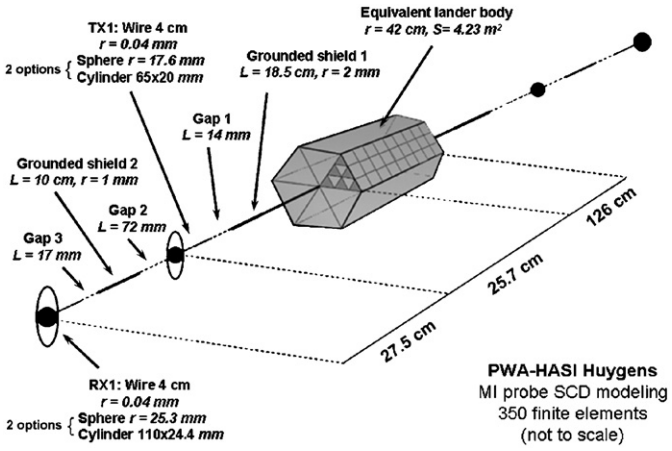

Fig. 5. SCD modelling in axial geometry (revolution axis parallel to Yp of Fig. 4).

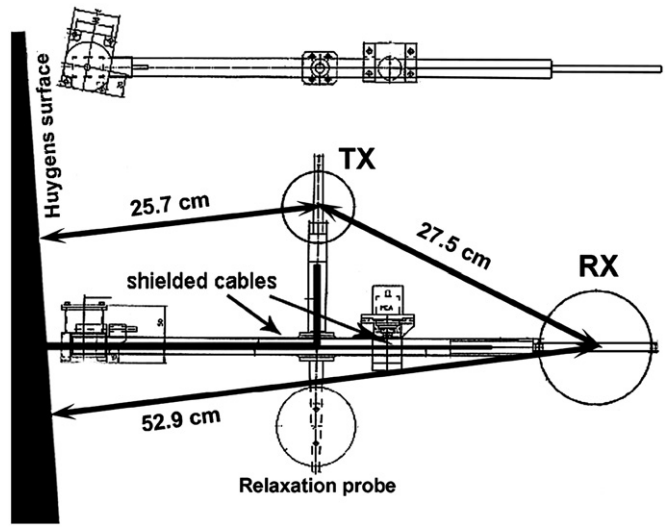

Fig. 6. Boom configuration and sensor lay-out, with the characteristic distances used in the SCD code.

for an axial symmetry (Fig. 5). Nevertheless, the actual distances between the antennas and the gondola structure are respected (Fig. 6). The parasitic electrostatic coupling between the sensors and the cabling inside the booms (shielded harness) is also included in the model.

In this simulation, the transmitting and receiving rings are replaced either by spheres or by cylinders with the same free-space capacitance, and are loaded with the actual output and input impedances, respectively (Fig. 7). In a vacuum, the SCD model gives voltages between the Rx electrodes with amplitudes of 113.2 and 120.6 mV, and phases of 0° and 0.4°, for spherical and cylindrical electrodes, respectively. These differences provide an estimate of the influence of geometrical simplifications.

2.4. Experimental results

The mutual impedance was measured in the atmosphere of Titan at 45 Hz from the altitude of 139 km (reference time $t = 200$ s) to the impact on the surface ($t = 8870$ s). Two consecutive measurements are performed within an interval of 2 s every 64 s, but only the high gain mode data collected every three 64 s cycle are reported. In order to facilitate the comprehension of the raw data, the digital telemetry output is converted into a potential difference between receiving electrodes, V_r.

The measured amplitudes and phases of V_r are represented by dots in Fig. 8; they are deduced from the telemetry data using the inverse transfer functions of the digital and analogue circuits, including preamplifiers. The voltage amplitude derived from the seven-conductor model in vacuum is shown on the left-hand side (dashed-dotted line), and is bracketed by the two levels that differ by $\pm 10\%$ from this value (dashed lines). Thin and thick solid lines indicate the amplitudes predicted by the SCD model with spherical and cylindrical electrodes, respectively, in vacuum. The modelling results are reasonably consistent. For example, the relative difference between the amplitudes given by the SCD model and the seven-conductor model with cylindrical sensors is only ~3%, which validates both approaches and provides an estimate of the accuracy that can be achieved with modelling. The predicted phase shift in vacuum is ~0° for all models. The large amplitude and phase deviations observed at $t < 3000$ s have already been interpreted as the signatures of an increase in electron conductivity due to the presence of an ionized layer at an altitude of around 63 km (Grard et al., 2006). The amplitude of the received voltage is significantly reduced at lower altitudes, and after a steep decrease at ~50 km the phase decreases slowly below 0° at lower altitudes, reaching a minimum value of ~−1.7° before touch down.

It must be emphasized that the best possible calibration of the MIP instrument is that performed in a vacuum or a neutral gas, and in a geometrical configuration and a thermal environment similar to those prevailing during the descent in Titan's atmosphere. The quasi-constant impedance observed in the terminal phase of the descent suggests that the conductivity of the medium lies below the measurement threshold, a fact that is supported by the modelling results and independently corroborated by the RP measurements (Grard et al., 2006). In consequence, it appears to be justified to use the phase and amplitude measured at low altitudes (−1.7° and 128 mV, respectively, instead of 0° and 124 mV given by the seven-electrode model) as the vacuum references A_0, and φ_0, defined in Eq. (8).

The normalization with respect to the average complex potential (amplitude and phase) measured at low altitudes is therefore used as a way of calibrations. The results are reported in Fig. 9 under the form of a polar representation of the complex normalized mutual impedance Z_N defined by its modulus A/A_0 and phase $\varphi - \varphi_0$. The solid line is the location of the theoretical points derived from the seven-electrodes model for increasing values of the normalized conductivity σ/ε_0. The measurements close to the instrument sensitivity level are clustered around $Z_N = 1$, the

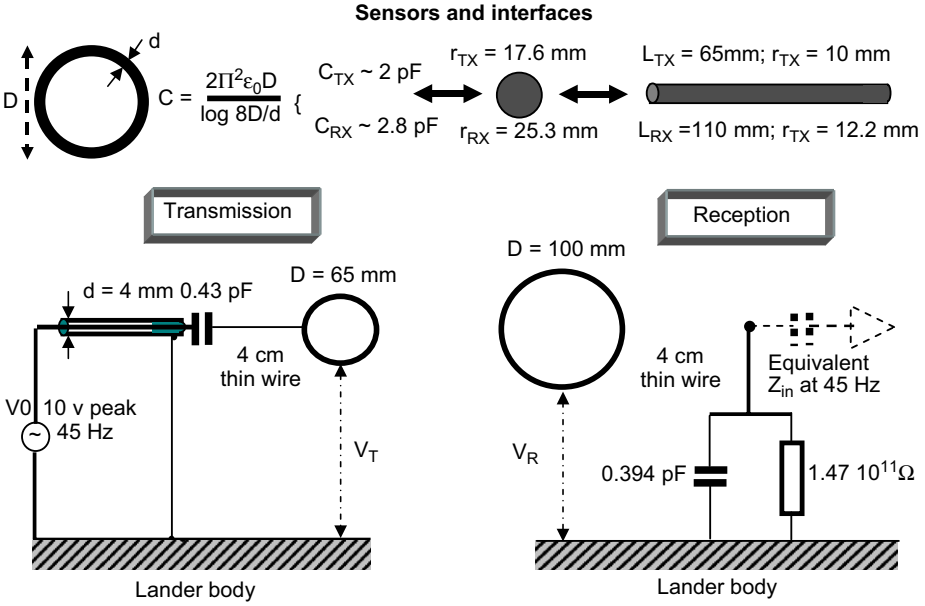

Fig. 7. Modelling of the rings and equivalent circuits of the transmission and reception units. Rings are represented by either spheres or cylinders of equivalent capacitance (see text).

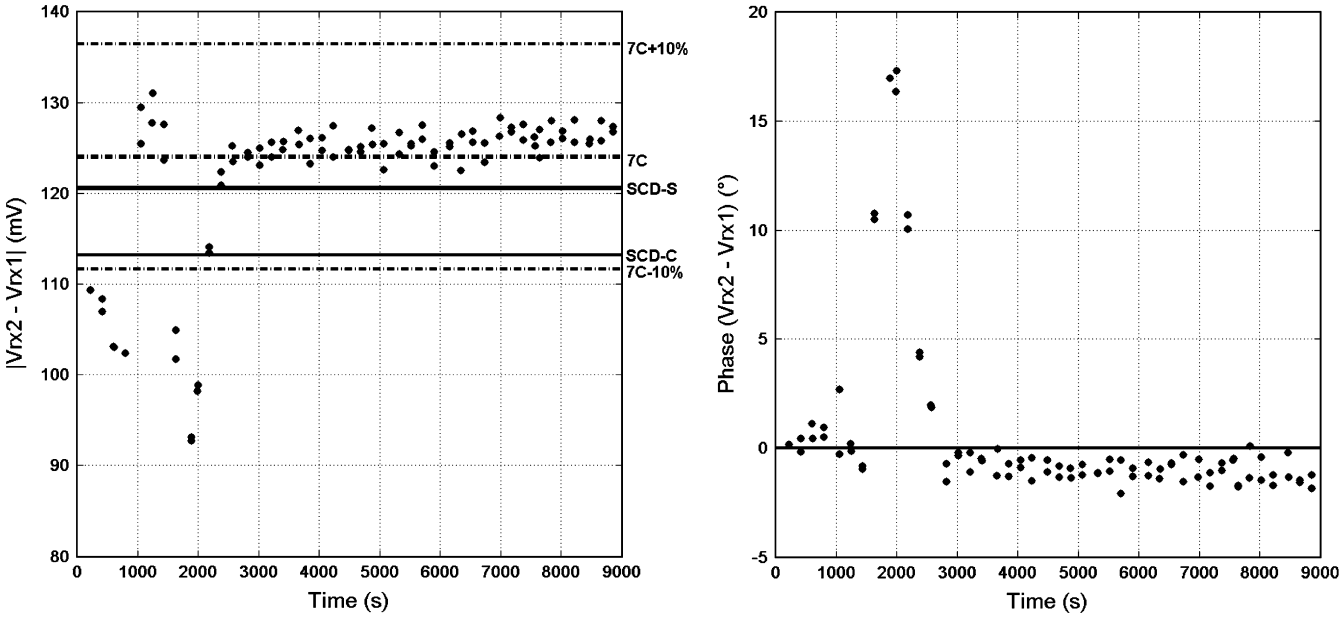

Fig. 8. MIP data: potential difference measured with the receiving dipole during the descent in the atmosphere of Titan (dots). Left: amplitude (the values in vacuum derived from the SCD model are represented by the thin and thick solid lines for spherical and cylindrical electrodes respectively; the value derived from the seven-conductors model is the dash-dot thick line and the two thin dash-dot lines show the $\pm 10\%$ level with respect to the computed value). Right: phase (at the end of the descent the measured phases lay between -2 and -1°.

impedance of vacuum. The dispersion of the measurements used to define the vacuum reference ($t > 7000$ s) is $\sim \pm 10^{-3}$ ($\sim \pm 0.06^\circ$ for the phase) and the mean difference between the couples of measurements taken within each 2 s interval is only $\sim \pm 1\%$ ($\sim \pm 0.5^\circ$ for the phase). Hence the fluctuations of the medium are very small at the end of the descent.

The measurements performed at higher altitudes significantly differ from theoretical predictions. The points collected at $t > 1400$ s (marked $+$) lie somewhat below the theoretical curve (we refer to these points as group A). For $t < 1400$ s, the two points (marked *) for which $Z > 1$, are not physically meaningful (group B). A third class of points is concentrated near the real axis, at $Z = 0.8$ (group C). A preliminary conclusion can be drawn at this point: a peak in conductivity is observed at an altitude of around 63 km, but it is not possible yet to plot its profile. A more detailed analysis is required, and the effect of velocity should be taken into account.

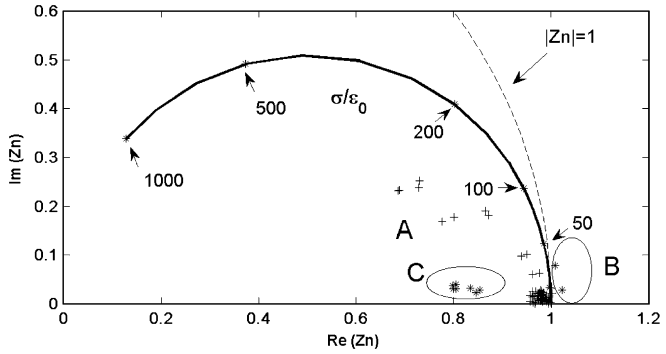

Fig. 9. MIP data: normalized mutual impedance in polar coordinates. The theoretical mutual impedance falls on the solid line, at the location indicated by the reduced conductivity σ/ε_0 marked along the line (arrows). A dashed line represents the unit circle. Points *: $t<1400$ s; points +: $t>1400$ s.

3. Descent velocity effects

3.1. Theoretical approach

The effects of velocity on mutual impedance measurements have been evaluated in the case of rockets or satellites in the cold plasma approximation (Béghin and Renard, 1970) and in thermal plasmas. The Huygens probe descent velocity is small compared to those of rockets and satellites, but we will use the same Laplace transform (LT) technique that leads to much simpler calculus than in the frequency domain.

An impulsive point charge at $t=0$ can be represented by the charge $q(t)=Q\delta(t)$. The definition of the LT is

$$Q(\mathrm{i}\omega)=\int_0^\infty q(t)\exp(-\mathrm{i}\omega t)\,\mathrm{d}t. \tag{14}$$

In the steady case (frequency domain) the potential at the distance r_0 is

$$V(\omega)=\frac{Q}{4\pi\varepsilon_0 r_0}\frac{\mathrm{i}\omega}{\mathrm{i}\omega+\sigma/\varepsilon_0}. \tag{15}$$

The inverse LT of (15) is given in Roberts and Kaufman (1966):

$$\begin{aligned}V(t)&=\frac{1}{2\mathrm{i}\pi}\int_{\mathrm{i}\omega=c-\mathrm{i}\infty}^{\mathrm{i}\omega=c+\mathrm{i}\infty}V(\mathrm{i}\omega)\exp(\mathrm{i}\omega t)\,\mathrm{d}(\mathrm{i}\omega)\\&=\frac{Q}{4\pi\varepsilon_0 r_0}\left[\delta(t)-\frac{\sigma}{\varepsilon_0}\exp\left(-\frac{\sigma t}{\varepsilon_0}\right)\right].\end{aligned} \tag{16}$$

If the receiving point is moving relative to the source with a velocity U and at an angle θ_r, as illustrated in Fig. 10, its distance from the source is written as

$$r=r_0\sqrt{1+(Ut/r_0)^2+2(Ut/r_0)\cos\theta_r}. \tag{17}$$

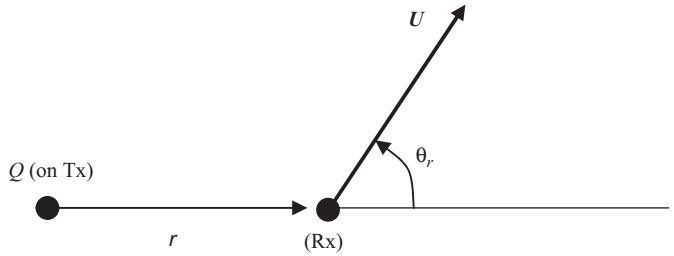

Fig. 10. Model geometry: source (Q on Tx), receiver (Rx) and velocity (U).

Then the potential at the moving receiving point is

$$\begin{aligned}V(\omega)=\frac{Q}{4\pi\varepsilon_0 r_0}\int_0^\infty&\frac{\delta(t)-(\sigma/\varepsilon_0)\exp(-(\sigma/\varepsilon_0)t)}{\sqrt{1+(Ut/r_0)^2+2(Ut/r_0)\cos\theta_r}}\\&\times\exp(-\mathrm{i}\omega t)\,\mathrm{d}t.\end{aligned} \tag{18}$$

This expression must be calculated numerically except if θ_r is equal to 0, $\pi/2$ or π. Although the orientation of the Tx–Rx direction with respect to the velocity vector differs from these particular values, it is informative to derive an analytic formula for $\theta_r=0$. The LT transform of $1/(t+b)$ is $-\exp(\mathrm{i}\omega b)\,E_i(-\mathrm{i}\omega b)$, where E_i is the exponential integral function (Roberts and Kaufman, 1966), which gives:

$$\begin{aligned}V(\omega)=\frac{Q}{4\pi\varepsilon_0 r_0}\Bigg[1-\frac{\sigma r_0}{\varepsilon_0 U}&\exp(r_0\omega/U\varepsilon_0+\mathrm{i}\omega r_0/U)\\&\times E_i(r_0\omega/U\varepsilon_0+\mathrm{i}\omega r_0/U)\Bigg].\end{aligned} \tag{19}$$

Eq. (18) is solved with a numerical code written in Matlab™ and has been tested with success against Eq. (19), for $\theta_r=0$. The code is not applicable in the strictly anti-parallel direction ($\theta_r=\pi$) due to a singularity. This case can be treated analytically or numerically with an improved code, but is irrelevant for a descending probe.

3.2. Estimation of the effect of the descent velocity on the mutual impedance

The effect of velocity on the mutual impedance is extremely complex, since the flow is controlled by aerodynamic and electrodynamic interactions around the Huygens body. We tentatively assume a uniform vertical velocity field around the electrodes. The current injected between the Tx electrodes is nearly constant, and we neglect any small variation due to velocity. We consider only the coupling between the two electrodes Tx and Rx which are located on the same boom, and apply (19) to take into account the effect of velocity upon the contribution of Tx to the potential of Rx (the minor contribution of the opposite boom cannot be really estimated due to the presence of the Huygens body). We compute the relative

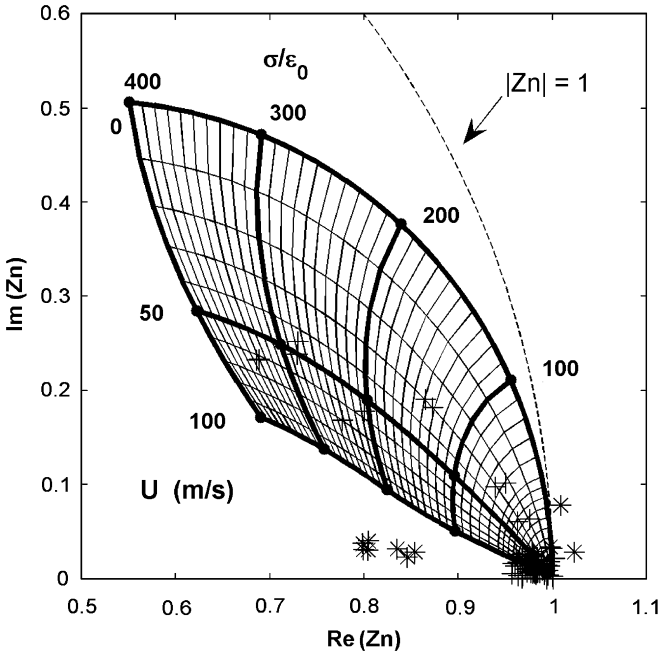

Fig. 11. Measured normalized mutual impedances and theoretical values vs velocity and conductivity (same symbols as in Fig. 9).

variation of the Rx potential with respect to the steady case for arbitrary conductivity and velocity, and apply this corrective factor to the theoretical value of the complex mutual impedance (Eq. (7)). The components of the Tx–Rx segment along, and perpendicularly to the velocity direction are 0.22 and 0.156 m, respectively. The results are given in Fig. 11 which shows the curves of constant σ/ε_0 and constant velocity. The velocity does not affect the theoretical prediction in a vacuum, but in a lossy medium an increase in velocity reduces the phase of the voltage induced by Tx at the location of Rx and moves the mutual impedance towards the real axis, closer to the experimental points of group A.

The measurements that form the group A have been collected below an altitude of 100 km, through the ionized layer. They are consistent with a descent velocity of 50 ($\pm$20) ms^{-1}, in reasonable agreement with the measured velocity, of the order of 40 ms^{-1}. This discrepancy can be explained in a simple way by considering in our model that the velocity is uniform is an approximation. Close to the Huygens body the flow is deflected and accelerated by up to ~20% with respect to the nominal descent velocity. We shall not attempt, at this stage, to improve further this first order model, and we tentatively conclude that the relative velocity effect is reasonably confirmed for the group A measurements. The conductivity is obtained with the abacus drawn in Fig. 11, and is read on the constant conductivity line passing through each experimental point.

The two points in group B, close to the origin but outside the unity circle, do not yield any meaningful value for the permittivity. These measurements are made at $t = 1050$ and 1242 s, whereas those made 2 s before, at $t = 1048$ and 1240 s, respectively, lie inside the unit circle. This period follows the second parachute opening, and the attitude of Huygens may not be stabilized yet. One might also argue that, within 2 s, the system travels over a vertical distance of ~100 m and that the medium might change noticeably. For lack of a better explanation, we reject the group B data, but we keep the presumably valid measurements performed at $t = 1048$ and 1240 s that give low conductivities, <0.15 nS m^{-1}.

The group C is clearly out of range: the amplitude and phase of the mutual impedance are apparently not compatible with any descent velocity. These measurements were collected under the first large parachute, between the times $t = 200$ and 800 s and we exclude them from the standard data analysis procedure. There are two possible explanations to this apparent inconsistency:

- Following the test performed in a Faraday cage at LPCE on the spare model of MIP, the abnormal response from the nominal start of the descent to about 1400 s could coincide with the crossing of a cloud of aerosols. There are several arguments in favour of this explanation. First, the altitude range (90–140 km) is thought to be a likely region for condensate haze. Second, a clear reduction of conductivity has already been inferred from a preliminary analysis (Grard et al., 2006) and predicted by theoretical models (Boruki et al., 1987). The last argument is provided by the tests performed at LPCE. A haze cloud has been simulated with an aerosol spray. We have generated a cloud of liquid difluoroethane aerosol around the booms and the sensors during a few seconds. A very thin, but visible deposit was sublimated 5–10 s later. We observed a net variation of the amplitude and phase shift associated with this deposit. This qualitative test supports the hypothesis that a similar deposit may have occurred between 140 and about 100 km above the surface of Titan. It is concluded that the small phase shift (0–4°) observed in this region (see Fig. 8) reflects the fact that, due to the attachment of the electrons to aerosol particles, the medium conductivity is extremely small $<10^{-10}$ S m^{-1}. However, the attachment of electrons should yield normalized impedance close to 1. Then the hypothesis compatible with the data consists of both attachment of electrons on aerosols and a deposit on the booms introducing additional paths for stray currents.
- A reduction of the received signal could result from the partial deployment of one boom. The booms are released by magnetic actuators (MCA) and deployed by springs. Titan's gravity (~1.4 ms^{-2}) and rotational acceleration help the deployment but the acting forces are very small: the group C measurements start at t~400 s when the rotation is inverted and end at t~800 s, when the rotation rate is ~4 rpm (Lebreton et al., 2005) and the rotational acceleration at the boom location is ~0.1 ms^{-2}. The reasons for a possible partial deployment are uncertain, either aging in vacuum during the cruise or aerosol deposits at the start of the descent.

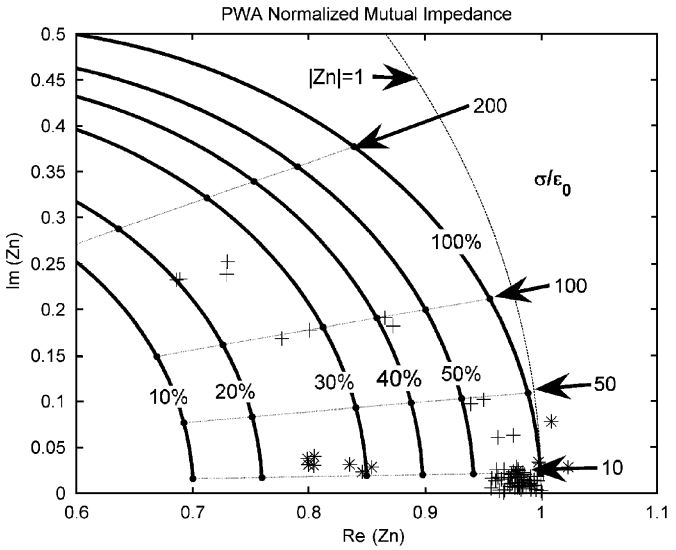

Fig. 12. Simulation of MIP measurement with one boom partially deployed (10–50% deployment, and 100%).

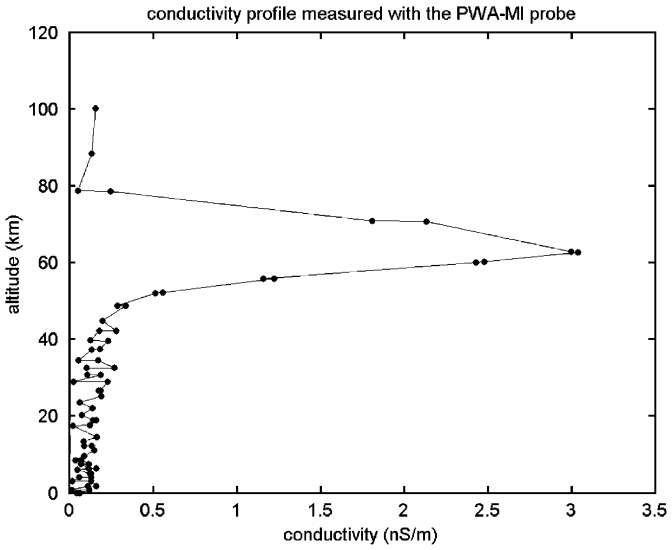

Fig. 13. Electron conductivity profile below 100 km.

Then the shock due to the opening of the stabilizing parachute ($t>900$ s) would have achieved the deployment. With a partial deployment the amplitude would be further reduced by the proximity of the Huygens body. We have simulated the consequences of such a scenario, using the seven-electrode model with one boom partly deployed (10–50° rotation, instead of 100°). The apparent mutual impedance, normalized to that of the fully deployed dipole in vacuum, is plotted in the complex plane of Fig. 12, together with the measurements, as a function of normalized conductivity. The experimental points are dispersed mostly along the real axis, which could be caused by the rotation of the unlocked boom (25–30% of the nominal rotation angle). Under this assumption, a conductivity less than $\sim 0.2\,\mathrm{nS\,m^{-1}}$ can be estimated from the measurements.

It is impossible to validate any of these two hypotheses, but both lead to conductivity less than $2\times10^{-10}\,\mathrm{S\,m^{-1}}$ in the altitude range 100–140 km.

4. Results and discussion

4.1. Conductivity and electron density profiles

The conductivity profile deduced from the chart of Fig. 11 is shown in Fig. 13 at altitudes less than 100 km, where the mutual impedance phase and amplitude are compatible with the velocity effect. The relative error on the conductivity depends strongly on its level, and varies from ~50% at $10^{-10}\,\mathrm{S\,m^{-1}}$ to ~20% at its peak, $3\times10^{-9}\,\mathrm{S\,m^{-1}}$. The uncertainty is mostly due to the insufficiently accurate modelling of the velocity effect.

The measurements taken at very small time interval (2 s) are generally very similar, and their relative difference is small, of the order of $\sim 0.01\,\mathrm{nS\,m^{-1}}$ (see Fig. 13).

The electron density is derived by combining the conductivity measured by PWA with the neutral density and temperature measured by HASI (Fulchignoni et al., 2005). These quantities are linked by the electron mobility formula (Banks and Kockarts, 1973):

$$\mu_e = q_e/(2.33\times10^{-17}\,N_n T m_e). \quad (20)$$

where q_e and m_e are the electron charge and mass, respectively. The N_n and T are the density and temperature of the neutrals.

The density profile (Fig. 14) is limited intentionally, downwards, to the altitude of 40 km because of the lack of accuracy when the conductivity decreases (a consequence of the calibration with respect to low altitude conductivity measurements). The ionized layer extends from ~50 to 80 km and the maximum electron density is $\sim 650\,\mathrm{cm^{-3}}$. This raises the question of the space charge that has been neglected in our models. If a sheath develops around Huygens its size would be of the order of the Debye length, ~5 cm in the ionized layer but larger outside, eventually embedding the MIP electrodes. No noticeable sheath is present as the DC difference of potential between RP and Huygens is less than ~100 mV. On the other hand, no space charge effects are expected around ring electrodes.

4.2. Comparison with models and discussion

The major feature of the conductivity and electron density profiles is the prominent peak that was not predicted by models. The electron density and the cosmic rays ionization rate (Molina-Cuberos et al., 1999a) reach their maximum at about the same altitude (~65 km).

The magnitude of the peak electron density suggests that the ionosphere consists mostly of cluster ions, although additional removal process is required for the electrons. The model of Molina-Cuberos et al. (1999b) assumes a dominant population of clusters ions and predicts a peak

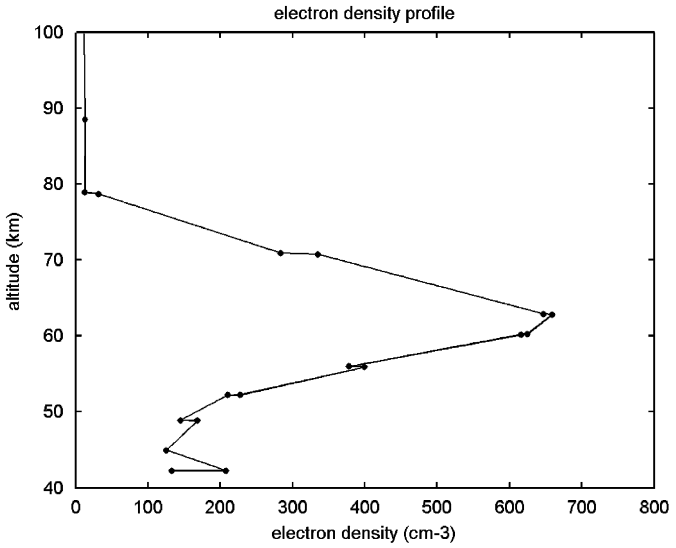

Fig. 14. Electron density profile between 40 and 100 km altitude.

electron density of 1300 cm^{-3}, around twice that measured (~650 cm^{-3}) at the same altitude. If covalently bound ions are the most abundant, a maximum density of ~4000 cm^{-3} is expected at 65 km. Borucki et al. (1987) and Molina-Cuberos et al. (1999a) predicted a much higher maximum in electron concentration, 1600 and 2100 cm^{-3}, respectively, at altitudes of 95 and 90 km.

Aerosols can decrease the concentration of electrons by charge capture process or increase it by photo ionization. In a recent paper, Borucki et al. (2006) consider both processes and conclude that during day-time, when the Huygens descent took place, the ionization by photoemission from aerosols irradiated by solar ultraviolet overwhelms the ionization produced by GCR. They obtained a profile with an electron density about one order of magnitude larger than that observed by MIP.

In fact, around the altitude of 63 km, all models differ from our measurements by a factor of only ~2–3, but the general shapes of the conductivity and electron density profiles are similar. Larger differences develop as the altitude rises above 63 km, from 80 up to 100 km and possibly 140 km, where the measured conductivity falls down to less than 0.3 $nS\,m^{-1}$. This emphasizes the major role played by aerosols, as illustrated by the differences between the models of Borucki et al. (1987) and Borucki et al. (2006). The upper edge of the ionized layer appears to be steeper than the lower edge. From the two conductivity measurements performed at around 70 km, the electron density scale height can be estimated to be ~400 m, a small quantity compared to the neutral density and temperature scale heights which lay in the range 20–40 km and too small to be explained in term of ionization processes. This altitude corresponds to a peak of the temperature gradient but there seems to be no meaningful correlation between these two features. On the lower edge, at around 55 km, the electron density scale height is ~800 m, for a neutral atmosphere scale heights in the range 200–230 km. Then the steepness of the ionized layer boundaries should be related to a corresponding steepness in the aerosol profile. It is anticipated that the presence of aerosols reduces mostly the conductivity even on the dayside.

5. Conclusion

A mutual impedance probe has been used with reasonable success to measure the electron conductivity in a dense planetary atmosphere. The instrument had to comply with the severe constraints imposed by a planetary mission and a detailed analysis has been performed to validate the measurements.

The main contribution of the PWA-MIP experiment is the discovery of an ionospheric layer between ~50 and 80 km, characterized by a maximum conductivity of 3 $nS\,m^{-1}$ and a peak electron density of ~650 cm^{-3} at an altitude of about 63 km, and by small conductivity and electron density from 80 up to at least 140 km. The ionized layer shows relatively steep boundaries (~400 and 800 m scale heights for the upper and lower boundaries, respectively), which is not in agreement with existing models. These features are probably caused by electron attachment in aerosol layers. The differences between our measurements and the model predictions have therefore to be explained in terms of aerosol physics and atmospheric chemistry. The MIP results will be compared with the relaxation probe measurements in a forthcoming paper.

Acknowledgements

The authors thank all the national and international institutions that made the success of this experiment possible and especially International Space Science Institute for hosting their working-team meetings.

References

Banks, P.M., Kockarts, G., 1973. Aeronomy. Academic Press, New York and London.

Béghin, C., Debrie, R., 1972. Characteristics of the electric field far from and close to a radiating antenna around the LHR in the ionospheric plasma. J. Plasma Phys. 8, 287–310.

Béghin, C., Renard, C., 1970. The effect of collisions and movement on the transfer impedance of a quadrupole probe near the lower hybrid resonance in the ionosphere. In: Thomas, J.O., Landmark, B.J. (Eds.), Plasma Waves in Space and in the Laboratory, vol. 2. Edinburgh University Press, Edinburgh, pp. 299–317.

Béghin, C., Kerczewski, J.F., Poirier, B., Debrie, R., Massevitch, N., 1982. The ARCAD-3 Isoprobe experiment for high time resolution thermal plasma measurements. Ann. Geophys. 38, 615–629.

Béghin, C., Kolesnikova, E., 1998. Surface-charge distribution approach for modelling of quasi-static electric antennas in isotropic thermal plasma. Radio Sci. 33, 503–516.

Borucki, W.J., Levin, Z., Whitten, R.C., Keesee, R.G., Capone, L.A., Summers, A.L., Toon, O.B., Dubach, J., 1987. Predictions of the electrical conductivity and charging of the aerosols in Titan's atmosphere. Icarus 72, 604–622.

Borucki, W.J., Whitten, R.C., Bakes, E.L.O., Barth, E., Tripathi, S., 2006. Predictions of the electrical conductivity and charging of the aerosols in Titan's atmosphere. Icarus 181, 527–544.

Cadène, F., 1995. Methodology for measuring planetary atmospheric conductivities. Thèse d'Université, Electronique. Ph.D. Thesis, Université de Paris 6 (in French).

Chasseriaux, J.M., Debrie, R., Renard, C., 1972. Electron density and temperature measurements in the lower ionosphere as deduced from the warm plasma theory of the quadrupole probe. J. Plasma Phys. 8, 231–253.

Décréau, P.ME., Béghin, C., Parrot, M., 1982. Global characteristics of the cold plasma in the equatorial plasmapause region as deduced from the GEOS 1 mutual impedance probe. J. Geophys. Res. 87, 695–712.

Décréau, P.M.E., Hamelin, M., Massif, R., Deferaudy, H., Pawela, E., Perrault, S., Pottelette, R., Bahnsen, P.A., 1987. Plasma probing with the Viking satellite. Ann. Geophys. Ser. A 5, 181–185.

Durand, E., 1966. Électrostatique, Problèmes généraux conducteurs, vol. 2, Masson Éditeurs, Paris, pp. 154–155 (in French).

Falkner, P., 2004. Permittivitäts Wellen und Altimeter Analysator für das ESA/NASA Projekt Cassini-Huygens. Ph.D. Thesis, Technical University, Graz, Austria (in German).

Fischer, G., Desch, M.D., Zarka, P., Kaiser, M.L., Gurnett, D.A., Kurth, W.S., Macher, W., Rucker, H.O., Lecacheux, A., Farrell, W.M., Cecconi, B., 2006. Saturn lightning recorded by Cassini/RPWS in 2004. Icarus 183, 135–152.

Fulchignoni, M., Ferri, F., Angrilli, F., Ball, A.J., Bar-Nun, A., Barucci, M.A., Bettanini, C., Bianchini, G., Borucki, W., Colombatti, G., Coradini, M., Coustenis, A., Debei, S., Falkner, P., Fanti, G., Flamini, E., Gaborit, V., Grard, R., Hamelin, M., Harri, A.M., Hathi, B., Jernej, I., Leese, M.R., Lehto, A., Lion Stoppato, P.F., López-Moreno, J.J., Mäkinen, T., McDonnell, J.A.M., McKay, C.P., Molina-Cuberos, G., Neubauer, F.M., Pirronello, V., Rodrigo, R., Saggin, B., Schwingenschuh, K., Seiff, A., Simões, F., Svedhem, H., Tokano, T., Towner, M.C., Trautner, R., Withers, P., Zarnecki, J.C., 2005. *In situ* measurements of the physical characteristics of Titan's environment. Nature 438, 785–791.

Gerdien, H., 1905. Demonstration eines Apparates zur absoluten Messung der elektrischen Leitfähigkeit der Luft. Phys. Z. 6, 800–801 (in German).

Grard, R., Svedhem, H., Brown, V., Falkner, P., Hamelin, M., 1995. An experimental investigation of atmospheric electricity and lightning activity to be performed during the descent of the Huygens probe on Titan. J. Atmos. Terr. Phys. 57, 575–585.

Grard, R., Smit, A., Smit, L., Van Der Hoek, J., 1997. Development and qualification of a deployable boom system for the Huygens probe. Proceedings of the Seventh European Space Mechanics and Tribology Symposium, ESTEC, Noordwijk, The Netherlands, ESA SP-410, pp. 181–183.

Grard, R., Hamelin, M., López-Moreno, J.J., Schwingenschuh, K., Jernej, I., Molina-Cuberos, G.J., Simões, F., Trautner, R., Falkner, P., Ferri, F., Fulchignoni, M., Rodrigo, R., Svedhem, H., Béghin, C., Berthelier, J.-J., Brown, V.J.G., Chabassière, M., Jeronimo, J.M., Lara, L.M., Tokano, T., 2006. Electric properties and related physical characteristics of the atmosphere and surface of Titan. Planet. Space Sci. 54, 1124–1136.

Gurnett, D.A., Shaw, R.R., Anderson, R.R., Kurth, W.S., 1979. Whistlers observed by voyager 1—detection of lightning on Jupiter. Geophys. Res. Lett. 6, 511–514.

Hamelin, M., Chabassière, M., 2006. Simple model for the MI receiver sensor and preamplifier of PWA. Internal Report, CETP, November 2006.

Hamelin, M., Simões, F., 2006. Calculation of electrodes capacitance influence on the HASI-PWA relaxation and mutual impedance probes. Internal Report, CETP, July 2006.

Lanzerotti, L.J., Rinnert, K., Dehmel, G., Gliem, F.O., Krider, E.P., Uman, M.A., Bach, J., 1996. Radio frequency signals in Jupiter's atmosphere. Science 272, 858–860.

Lebreton, J.-P., Witasse, O., Sollazzo, C., Blancquaert, T., Couzin, P., Schipper, A.-M., Jones, J.B., Matson, D.L., Gurvits, L.I., Atkinson, D.H., Kazeminejad, B., Perez-Ayucar, M., 2005. An overview of the descent and landing of the Huygens probe on Titan. Nature 438, 758–764.

López-Moreno, J.J., Molina-Cuberos, G.J., Rodrigo, R., Hamelin, M., Schwingenschuh, K., 2001. Polar ionic conductivity profile in fair weather conditions. Terrestrial test of the Huygens/HASI-PWA instrument aboard the Comas Sola balloon. J. Atmos. Solar-Terr. Phys. 63, 1959–1966.

Molina-Cuberos, G.J., López Moreno, J.J., Lara, L.M., Rodrigo, R., O'Brien, K., 1999a. Ionization by cosmic rays of the atmosphere of Titan. Planet. Space Sci. 47, 1347–1354.

Molina-Cuberos, G.J., López-Moreno, J.J., Rodrigo, R., Lara, L.M., 1999b. Chemistry of the galactic cosmic ray induced ionosphere of Titan. J. Geophys. Res. 104 (E9), 21,997–22,024.

Molina-Cuberos, G.J., Schwingenschuh, K., López-Moreno, J.J., Rodrigo, R., Lara, L.M., Anicich, V., 2002. Nitriles produced by ion chemistry in the lower ionosphere of Titan. J. Geophys. Res. 107 (E11), 5099–5110.

Odero, D., 1972. Possibilités d'utilisation d'une sonde quadrupolaire dans la gamme 0–1000 Hz pour mesurer les fréquences de collision des particules chargées dans l'ionosphère, Ann. Géophys 28, 541–574 (in French).

Pottelette, R., Hamelin, M., Illiano, J.M., Lembege, B., 1981. Interpretation of the fine structure of electrostatic waves excited in space. Phys. Fluids 24, 1517–1526.

Roberts, G.E., Kaufman, H., 1966. Table of Laplace Transforms. W.B. Saunders Co., Philadelphia, London.

Schlumberger, C., 1920. Etude de la prospection électrique du sous-sol. Gauthier-Villars, Paris (in French).

Storey, L.R.O., Malingre, M., 1976. A proposed method for the direct measurement of enhanced resistivity. Proceedings of the Symposium 'European Programmes on Sounding-rocket & Balloon Research in the Auroral Zone', Schloss Elmau, Germany, ESA SP-115, Noordwijk, The Netherlands, pp. 387–409.

Storey, L.R.O., Aubry, M.P., Meyer, P., 1969. A quadrupole probe for the study of ionospheric resonances. In: Thomas, J.O., Landmark, B.J. (Eds.), Plasma Waves in Space and in the Laboratory. Edinburgh University Press, pp. 303–332.

Trautner, R., Falkner, P., 2000. Equivalent circuit model, systematic error calculation and measurement range estimation for HASI-PWA mutual impedance (MI) probe. Internal Report, ESA/ESTEC, April 2000.

Wenner, F., 1915. A method of measuring the Earth resistivity. U.S. Bur. Stand. Bull. Sci. Pap. 25 (12), 469–478.

Paper 7

Huygens Probe in situ Measurements of Titan Surface Dielectric Properties

Simões, F., Hamelin, M., Grard, R., López-Moreno, J.J., Schwingenschuh, K., Béghin, C., Berthelier, J.-J., Brown, V.J.G., Chabassière, M., Falkner, P., Ferri, F., Fulchignoni, M., Jernej, I., Jeronimo, J.M., Molina-Cuberos, G.J., Rodrigo, R., Svedhem, H., Tokano, T., Trautner, R.

To be submitted – Draft version

Title:
Huygens Probe in situ Measurements of Titan Surface Dielectric Properties

Authors

Abstract

Introduction
Titan is wrapped in a thick gaseous envelope permeated with haze that impairs visible imaging quality of the surface. Infrared spectroscopy analysis is also intricate due to significant methane concentration in the atmosphere. Because of these constraints, instruments that use larger wavelengths play an important role regarding surface characterization. The Cassini Radar that studies surface properties at large scale and the in situ measurements made by the Huygens Probe contribute considerably to characterize the surface and the substrate material at shallow depths. The surface measurements performed by the Huygens Probe can be used as ground truth for the Cassini Orbiter and ground-based observations.
After some flybys, the Radar instrument identified, or at least provided strong evidences of, several surface features, including mountains, dome-like volcanic constructs, impact craters, lakes, dunes, intricate flows, channels and shore lines (Elachi et al., 2005; Lorenz et al., 2006; Stofan et al., 2007). Comparison with visible and infrared mapping instruments leads to better interpretation of various large scale features. The in situ measurements performed by the Huygens Probe are specially suited to characterize the vicinity of the landing site and contribute to constrain composition scenarios. Huygens landed on a wet dark unconsolidated material of low electrical conductivity and scattered with bright pebbles (Tomasko et al., 2005; Zarnecki et al., 2005; Grard et al., 2006). The observation of atmospheric methane mole fraction increasing and temperature variation after landing attests that surface properties were modified (Niemann et al., 2005; Fulchignoni et al., 2005).
The Permittivity, Waves and Altimetry (PWA) analyser (Grard et al., 1995), a subunit of the Huygens Atmospheric Structure Instrument (HASI) (Fulchignoni et al., 2002), is one element of the scientific payload carried by the Huygens Probe that landed on Titan. The PWA analyzer was mainly designed for the investigation of the electric properties and other related physical characteristics of the atmosphere of Titan, from an altitude about 140 km down to the surface. Preliminary results reported electron and ion density peaks in the lower atmosphere and low conductivity surface at the landing site (Fulchignoni et al., 2005; Grard et al., 2006). Further analysis has been improving our knowledge of PWA measurements and clarifying previous assumptions about Titan electric environment, namely the atmospheric electron and ion conductivity profiles (Hamelin et al., 2007; López-Moreno et al., 2007) and the intriguing low frequency electric signals recorded during the descent (Simões et al., 2007; Béghin et al., 2007).
The successful landing of Huygens extended PWA operations approximately 32 min until the experiment was turned-off. The major goal of the surface operation mode was the measurement of substrate dielectric properties at shallow depths. Evaluation of terrain dielectric properties introduces composition constraints that can be used by other instruments, laboratory experiments, and modelling to improve our understanding of Titan environment, namely of the surface. The characterization of the surface and substrate at shallow depths is relevant for modeling several aspects of the global environment, including: Titan formation, evolution and interior dynamics by studying mass ejects due to cryovolcanism and impacts; surface features, in particular weathering processes due to fluvial and Aeolian erosion; climate models, specifically the methane cycle; atmospheric and ionospheric chemistry, such as

aerosols and soots production, atmospheric electricity phenomena, and synthesis of hydrocarbon and nitril molecules that permeate the gaseous envelope and eventually deposit on the surface.
Huygens landed on an organic rich spot but composition description is far from being completed. Water ice, methane, and solid organic materials (tholins) have been identified though other constituents remain unknown (Tomasko et al., 2005; Niemann et al., 2005). Here we report the calibrated surface measurements performed with the PWA Mutual Impedance Probe (MIP), evaluate the dielectric properties in the low frequency range, discuss data peculiar events, and present a few composition scenarios significant to surface characterization.

Dielectric Properties

The PWA surface data

The mutual impedance principle was introduced in geophysics for measuring soil conductivity (Wenner, 1915) and suggested by Grard (1990) for studying the surface of planetary environments. The mutual impedance is the ratio of the voltage measured by a receiving dipole to the current injected in the medium through a neighbouring transmitting dipole.
The complete description of the PWA analyzer can be found elsewhere (Grard et al., 1995; Fulchignoni et al., 2002). Hamelin et al. (2007) already discussed the calibration procedure of the MIP for the atmospheric measurements. Therefore, we extend the calibration procedure for the other frequencies and include specific corrections, namely those related with Huygens geometry and attitude on the surface. The PWA-MIP electrodes consist of four rings mounted on two relatively short booms (Grard et al., 1997) and the instrument is operated after touchdown at five frequencies: 45, 90, 360, 1440, and 5760 Hz. The surface mode is a loop sweeping the 5 frequencies, starting at 45 Hz and making two consecutive measurements at each frequency every 62 s (Falkner, 2004). The lowest frequency was also used during the descent for measuring the atmospheric electron conductivity.
The touchdown occurred at about 8870 s after T0 (Lebreton et al., 2005), where T0 is defined as the start of the descent sequence, and triggered the surface operation mode. The first and last MIP measurements were registered at 8880 and 10778 s, respectively, and 60 data points were recorded at each frequency in the interval. The panels of Fig. 2 show the MIP amplitude and phase data recorded on the surface mode and, for the sake of comparison, also the last 4 points registered before the impact on the surface. Specific events are also considered, namely about the touchdown and approximately 11 min after landing. The MIP surface data is split in 3 groups: A – corresponding to the first two data points of each frequency after touchdown [8870, 8914] s; B – the first plateau [8944, 9532] s; C – the second plateau [9546, 10778] s.
In group-A data, whereas phase remains constant at all frequencies, there is a consistent amplitude variation for each pair of measurements. The amplitude reaches a stable value within the interval [8914, 8944] s, about one minute after touchdown. Furthermore, the amplitude of the second point is always smaller than the first one at each frequency.
The B-C transition takes place at about 9539 s and is more evident on phase at low frequency. Likely, the sudden transition occurs during the measurements at 360 Hz because the data points recorded at 9538 and 9540 s almost fit plateaus B and C, respectively, suggesting a fast transition that lasts no more than a few seconds. The phenomenon, which produces amplitude increase and lower phase shift, is obvious in the lower frequency range and stronger in phase measurements. However, the effect is not noticeable at the highest frequency and PWA functions nominally until the end of the experiment.
Preliminary data analysis of the surface mode is made by Grard et al. (2006), where rough estimations and initial interpretation are presented. In a first approximation, amplitude

variation and phase shift are related with permittivity and conductivity, respectively. Surface data is consistent with permittivity ~2 and very low surface conductivity though detailed analysis requires information about Huygens attitude on the ground, namely of the tilt and penetration in the substrate. Furthermore, the A-type data and the B-C transition deserve deeper investigation.

To calculate the dielectric properties of the medium with higher accuracy, we use a specific algorithm that solves Maxwell equations in the time-harmonic quasi-static approximation with a 3D finite element model. Detailed description of the employed method is presented below, including Huygens Probe attitude, the inversion problem strategy, and the parameters that play a major role in dielectric properties evaluation. The most uncertain parameters of the model are the tilt on the surface, the fore dome penetration depth, and surface roughness; we use several attitude parameters to cover different hypotheses.

Group-A data reveals consistent amplitude decreasing and no substantial phase variation for each pair of measurements at different frequencies. Unlike the relatively fast settling of the Huygens vessel, boom rest position seems to be reached only 1 min after touchdown. Pre-flight calibrations had shown that boom deployment implies major amplitude variation but negligible phase changes. Group-A data interpretation suggests that the impact did not break the booms, which were slowly settling; the accelerometers onboard the Huygens Probe were not sensitive enough to detect boom motion. If the boom tips did not hit any hard material the array rest configuration should be approximately the same as before touchdown, as attested by experiments made on Earth during balloon/parachute campaigns aiming to test landing on snow-like substrates. Therefore, the most likely scenario suggests that at least one boom is sliding on the terrain, for example on top of a pebble, or slightly penetrating the substrate. Though unlikely, because phase variation should have been also observed, an alternative scenario would involve medium properties modification during this period.

The 11-min event

The analysis of the event that occurred 11 min after landing must include a scenario that considers the following conditions: (C1) the transition lasts no more than a few seconds and occurs at about 9539 s; (C2) the variation is larger at the lower frequencies; (C3) the transition is more perceptible on phase than on amplitude; (C4) the phase of post-transition and pre-landing at 45 Hz is similar; (C5) the transition increases the amplitude and decreases the phase shift; (C6) the instrument seems to function nominally until the end of the experiment (Figure 2).

Several scenarios, including artefacts and natural phenomena, that can explain at least one of the observations are assessed: (S1) change of vessel attitude; (S2) partial electric failure of the boom embedded capacitors; (S3) methane condensation on booms; (S4) sudden modification of array configuration; (S5) loss of galvanic contact between receiving electrodes and the surface; (S6) modification of substrate material properties. The only scenario that explains all the conditions (C1-C6) is S6 though the phenomena taking place on the surface are not fully understood.

The scenario S1 is not conceivable because no sudden attitude variation was detected after the Huygens vessel settling. If a capacitor failure occurred then an electrical signature in the PWA passive mode would have been also detected (Simões et al., 2007); hence S2 is not valid. Methane condensation on the PWA booms, scenario S3, produces a thin film with higher conductivity than the reinforced fibreglass that holds the electrodes. Aerosol spraying on the PWA booms has been shown to produce amplitude and phase variations (Simões 2007; Béghin et al., 2007). However, conditions C2 and C5 are not fulfilled and there is no obvious explanation to obtaining similar phase shifts as those before touchdown (C4); consequently, S3 can be ruled out. According to qualification tests performed with the Huygens Probe,

change of boom configuration produces significant variations on MIP amplitude but negligible phase shift; therefore, at least conditions (C3-C4) do not match scenario S4. The loss of galvanic contact between the receiver and the substrate material, scenario S5, can be related with medium collapsing and evaporation close to the receiving electrodes, or changes of array configuration. Scenario S5 cannot be ruled out definitely though some conditions suggest that it is not a likely explanation. In fact, experiments suggest that loss of galvanic contact is effective in the entire frequency range and visible on amplitude and phase. Contrary to the previous scenarios, S6 matches all the observations under the hypothesis that occur sudden surface conductivity variation associated to percolation phenomena.

Percolation is a theory developed to study phenomena in disordered media and derives from the Latin 'percolare', which simply means the act of filtering a fluid through some type of porous matter (Stauffer and Aharony, 1994). In mathematics, percolation describes the behavior of connected clusters in a random graph and is associated to probabilistic descriptions; in chemistry and physics concerns, for example, the movement and filtering of fluids through porous media. It is often related to sudden phase transitions and used to study complex systems, namely critical phenomena and dynamical systems that involve fractal structures (Bunde and Havlin, 1996). In materials science, percolation theory is frequently used to study the dielectric properties of mixtures made of insulating and conductive phases. For example, several composites that include insulating and conducting phases show an electric conductivity transition larger than 10 orders of magnitude whilst composition suffers little changes (Lundberg and Sundquist, 1986). The aim of a percolation model is to compute the probability of cluster pathways formation that connect one boundary to the other and is used to determine physical parameters of the medium. The formation of such random spanning clusters generally allows the identification of critical points, known as percolation thresholds, which correspond to sudden transitions of medium properties. In the present case, percolation is associated to liquid flowing and evaporation processes that occurred on the surface after touchdown. Methane flowing and evaporation through substrate material interstices can possibly generate percolation effects; for example, similar phenomena are observed on Earth in soils with low moisture (Hunt, 2005).

The transition observed about 11 min after landing can be interpreted as a percolation effect. The gas chromatograph and mass spectrometer instrument detected methane concentration increasing after touchdown; this effect is an evidence of volatiles evaporation enhancement due to surface warming. The surface is continuously dried and, after a certain time, the fraction of liquid methane in the medium is not sufficient to drive a current between the MIP electrodes and a sudden conductivity transition is observed.

Laboratory experiments intended to confirm percolation phenomena used a PWA mock-up. The booms lay on a thin absorbing paper layer over a flat insulating surface, and the receiving electrodes are in galvanic contact with the paper. It is used a simple array configuration without the Huygens vessel and a shorter distance between the booms. The experiment only allows qualitative measurements because neither boom configuration nor medium properties are representative of Titan in situ measurements. The experiment lasts roughly 30 min and is started in a dry environment. After 5 min (Event 1 – Ev1), the absorbing paper layer is slightly sprayed with water and MIP amplitude and phase variations occur roughly 1 min later. A few minutes later (Ev2), the paper is dried with a heating flow and immediately observed a fast variation on amplitude and phase at the lower frequencies. After about 20 min (Ev3), the paper is sprayed with water until reaching saturation; a new transition is immediately visible. The MIP amplitude and phase at 5 frequencies recorded during the laboratory experiment are plotted in Figure 1.

The comparison between Figures 1 and 2 shows that most features of the laboratory experiments match the conditions C1-C6 existing on Titan MIP surface data, strengthening

scenario S6 further. In fact, it was anticipated that surface dielectric properties variation would comply with several features observed in PWA surface data though the sudden amplitude and phase transitions were not foreseen.
Surface properties evolution and the transition event can be confirmed by two other independent measurements. Figure 3 shows the atmospheric temperature measured by HASI after touchdown. Although the temperature variation is, on average, only 0.1-0.15 K, there is a perfect matching between temperature and phase data at about 9539 s. Figure 4 presents the velocity of sound and temperature spreading measured by the Acoustic Properties Instrument - Velocimeter (API-V) of the Surface Science Package (SSP) (Zarnecki et al., 2002, 2005; Rosenberg, 2007). The API-V data spreading starts about 20 s after the PWA data transition.
Despite a detailed description of the processes that occurred on the surface after landing cannot be established, different measurements suggest that substrate properties evolved after touchdown due to warming on Huygens vicinity, and a preliminary interpretation is already possible. At the landing site, the surface is permeated with liquid methane, which starts to evaporate after Huygens touchdown due to surface warming. The PWA booms reach a rest position during the first minute after landing, methane evaporation rate increases during two minutes until a stationary state is reached (GCMS data), and the atmospheric temperature increases about 0.2 K during four minutes (HASI data, Figure 3). Then, during six minutes, atmospheric temperature and surface dielectric properties are stable, methane evaporation is constant, but surface temperature slowly increases (SSP data, Figure 4). Eleven minutes after landing there is a sudden transition in atmospheric temperature and surface conductivity probably because a percolation threshold is reached; most likely, this effect is due to substrate material drying processes. The percolation phenomenon also influences the velocity of sound in the medium. Whereas the variation of MIP amplitude is very small suggesting that permittivity is not appreciably changed, the phase shift varies considerably and conductivity decreases below instrument sensitivity; after transition, surface conductivity is lower than 3×10^{-11} Sm^{-1}, at least two orders of magnitude lower than before the percolation effects took place. After the transition, no significant variation of the dielectric properties is observed until the PWA experiment is turned-off.

Conclusions

Methods

The 3D potential distribution function in the substrate material is computed by solving Maxwell equations in the time-harmonic quasi-static approximation, i.e. the generalized Poisson equation in a lossy medium. The model employs the finite element method (Zimmerman, 2006) and requires accurate information about Huygens geometry, boom configuration, electrodes size, MIP current density, tilt of the Huygens vessel with respect to the surface, and fore dome penetration in the soil. Additionally, knowledge of surface roughness is also requested. We use a numerical model to obtain the dielectric properties that fit PWA data because analytical approximations are inaccurate due to interface and geometry intricacy (Lebreton and Matson, 2002). The model includes the parameters: tilt, penetration depth, surface roughness, amplitude and phase measurements, frequency, and transmitters MIP current density; and the variables: medium permittivity and conductivity and spatial coordinates. The model follows the inverse problem approach (Tikhonov and Arsenin, 1977) to determine the dielectric properties that match the various parameters. It is used a dedicated algorithm that iteratively solves the generalized Poisson equation and verifies whether the computed amplitude and phase at the receiving electrodes position match PWA data. The algorithm follows the Euler-Lagrange minimization scheme to compute the updated values of the dielectric properties of a homogeneous substrate until predefined accuracy is obtained.

We make the following assumptions in the model: (a) considering a representative geometry of the Huygens probe without vanes, stub, and other details because their contribution to the electric model is negligible and meshing is simplified; (b) the array configuration does not change after landing, which seems reasonable because Huygens landed on a soft soil (Zarnecki et al., 2005), landing on snow-like material revealed safe on Earth, and group-A data suggests that boom settling lasts about 1 min; (c) MIP ring electrodes are approximated by spheres with the same capacitance for meshing simplification purposes; (d) Huygens tilt on the surface it is important for assessing soil dielectric properties (Grard et al., 2006), but rest attitude is not certain (Fulchignoni et al., 2005; Tomasko et al., 2005; Zarnecki et al., 2005) – tilt is in the range [0, 11°]; (e) Huygens penetration depth in the soil is not known, hence we consider the range [-1, 12] cm (Zarnecki et al., 2005; Karkoschka et al., 2007); (f) it is considered a flat surface but the presence of nearby dielectric blocks for simulating 'ice rocks' it is also assessed, which contributes to establish model sensitivity.

The most uncertain parameters of the model are indeed the tilt on the surface and the fore dome penetration depth. Tomasko et al. (2005), using the Descent Imager/Spectral Radiometer (DISR) instrument, suggest a tilt with 1.7° pitch and negligible roll; Zarnecki et al. (2005) and Fulchignoni et al. (2005) claim a tilt of 10.3° and 11° measured with tiltmeters. However, it is not clear whether imaging and tiltmeters are using the same reference axis, namely if the surface is not perpendicular to gravity vector. In fact, a local slope of the surface might explain the difference obtained with the two techniques.

The most suitable information about the MIP tilt angle is provided by DISR roll, which represents the angle of the Y_p axis of Huygens with respect to the surface (Fulchignoni et al., 2002; Tomasko et al., 2002). A pitch of 1.7° and negligible roll keep the MIP receivers position balanced with respect to the surface and, therefore, implies minor corrections in the model. Although there is some uncertainty about the significance of SSP Til-X and Til-Y data (Zarnecki et al., 2005; Lorenz et al., 2007), we use the data to derive the projection angle over the antenna direction (Y_p) and obtain ~2° at touchdown. The penetration depth of the fore dome in the soil is also important for assessing the dielectric properties. At the present time there are two contradicting scenarios: (a) Huygens touches the surface and the penetration depth is ~12 cm (Zarnecki et al. 2005); (b) the vessel does not hit the surface (Karkoschka et al., 2007). Hence, these parameters are used to test dielectric properties variability with attitude.

References

Béghin, C. Simões, F. Karsnoselskhikh, V. Schwingenschuh, K. Berthelier, J.J. Besser, B. Bettanini, C. Grard, R. Hamelin, M. López-Moreno, J.J. Molina-Cuberos, G.J., Tokano, T. 2007. A Schumann-like resonance on Titan driven by Saturn's magnetosphere possibly revealed by the Huygens probe. *Icarus* **191**, 251-266.

Bunde, A., Havlin, S., 1996. *Fractals and Disorderd Systems.* 2nd ed., Springer, Berlin, Germany.

Elachi, C., Wall, S., Allison, M., Anderson, Y., Boehmer, R., Callahan, P., Encrenaz, P., Flamini, E., Franceschetti, G., Gim, Y., Hamilton, G., Hensley, S., Janssen, M., Johnson, W., Kelleher, K., Kirk, R., Lopes, R., Lorenz, R., Lunine, J., Muhleman, D., Ostro, S., Paganelli, F., Picardi, G., Posa, F., Roth, L., Seu, R., Shaffer, S., Soderblom, L., Stiles, B., Stofan, E., Vetrella, S., West, R., Wood, C., Wye, L., Zebker, H., (2005). Cassini Radar Views the Surface of Titan. *Science* **308**, 970-974.

Fulchignoni, M., Ferri, F., Angrilli, F., Bar-Nun, A., Barucci, M.A., Bianchini, G., Borucki, W., Coradini, M., Coustenis, A., Falkner, P., Flamini, E., Grard, R., Hamelin, M., Harri, A.M., Leppelmeier, G.W., Lopez-Moreno, J.J., McDonnell, J.A.M., McKay, C.P., Neubauer, F.H., Pedersen, A., Picardi, G., Pirronello, V., Rodrigo, R., Schwingenschuh, K., Seiff, A., Svedhem, H., Vanzani, V., Zarnecki, J., 2002. The characterization of Titan's atmosphere physical parameters by the Huygens Atmospheric Structure Instrument (HASI). *Space Sci. Rev.* **104**, 395-431.

Fulchignoni, M., Ferri, F., Angrilli, F., Ball, A.J., Bar-Nun, A., Barucci, M.A., Bettanini, C., Bianchini, G., Borucki, W., Colombatti, G., Coradini, M., Coustenis, A., Debei, S., Falkner, P., Fanti, G., Flamini, E., Gaborit, V., Grard, R., Hamelin, M., Harri, A.M., Hathi, B., Jernej, I., Leese, M.R., Lehto, A., Lion Stoppato, P.F., López-Moreno, J.J., Mäkinen, T., McDonnell, J.A.M., McKay, C.P., Molina-Cuberos, G., Neubauer, F.M., Pirronello, V., Rodrigo, R., Saggin, B., Schwingenschuh, K., Seiff, A., Simões, F., Svedhem, H., Tokano, T., Towner, M.C., Trautner, R., Withers, P., Zarnecki, J.C., 2005. In situ measurements of the physical characteristics of Titan's environment. *Nature* **438**, 785-791.

Grard, R., 1990. A quadrupolar system for measuring in situ the complex permittivity of materials – Application to penetrators and landers for planetary exploration. *Measurement Science and Technology* 1, 801-806.

Grard, R., Svedhem, H., Brown, V., Falkner, P., Hamelin, M., 1995. An experimental investigation of atmospheric electricity and lightning activity to be performed during the descent of the Huygens Probe on Titan. *J. Atmos. Terr. Phys.* **57**, 575-585.

Grard, R., Smit, A., Smit, L., Van Der Hoek, J., 1997. Development and qualification of a deployable boom system for the Huygens Probe. *Proceedings 7th European Space Mechanics and Tribology Symposium*, ESTEC, Noordwijk, The Netherlands. **ESA SP-410,** 181-183.

Grard, R., Hamelin, M., López-Moreno, J.J., Schwingenschuh, K., Jernej, I., Molina-Cuberos, G.J., Simões, F., Trautner, R., Falkner, P., Ferri, F., Fulchignoni, M., Rodrigo, R., Svedhem, H., Béghin, C., Berthelier, J.-J., Brown, V.J.G., Chabassière, M., Jeronimo, J.M., Lara, L.M., Tokano, T., 2006. Electric properties and related physical characteristics of the atmosphere and surface of Titan. *Planet. Space Sci.* **54**, 1124–1136.

Falkner, P., 2004. *Permittivity, waves and altimeter analyser for the ESA/NASA Cassini-Huygens Project*. Technical University of Graz, Graz, Austria (PhD Thesis, in German).

Hamelin, M., Béghin, C., Grard, R., López-Moreno, J.J., Schwingenschuh, K., Simões, F., Trautner, R., Berthelier, J.J., Brown, V.J.G., Chabassière, M., Falkner, P., Ferri, F., Fulchignoni, M., Jernej, I., Jeronimo, J.M., Molina-Cuberos, G.J., Rodrigo, R., Tokano, T. 2007. Electron conductivity and density profiles derived from the mutual impedance probe measurements performed during the descent of Huygens through the atmosphere of Titan. *Planet. Space Sci.* **55**, 1964-1977.

Hunt, A., 2005. *Percolation theory for flow in porous media*. Springer, Heidelberg, Germany.

Karkoschka, E., Tomasko, M.G., Doose, L.R., See, C., McFarlane, E.A., Schröder, S.E., Rizk, B., 2007. DISR imaging and the geometry of the descent of the Huygens probe within Titan's atmosphere. *Planet. Space Sci.* **55**, 1896-1935.

Lebreton, J.-P., Matson, D.L., 2002. The Huygens Probe: science, payload and mission overview. *Space Sci. Rev.* **104**, 59-100.

Lebreton, J.-P., Witasse, O., Sollazzo, C., Blancquaert, T., Couzin, P., Schipper, A.-M., Jones, J.B., Matson, D.L., Gurvits, L.I., Atkinson, D.H., Kazeminejad, B., Perez-Ayucar, M., 2005. An overview of the descent and landing of the Huygens probe on Titan. *Nature* **438**, 759-764.

López-Moreno, J.J., Molina-Cuberos, G.J., Hamelin, M., Grard, R., Simões, F., Godard, R., Schwingenschuh, K., Béghin, C., Berthelier, J.-J., Brown, V.J.G., Falkner, P., Ferri, F., Fulchignoni, M., Jernej, I., Jerónimo, J.M., Rodrigo, R., Trautner, R., 2007. Characterization of the hidden ionosphere of Titan with a Relaxation Probe onboard Huygens. *Submitted to Science*.

Lorenz, R.D., Wall, S., Radebaugh, J., Boubin, G., Reffet, E., Janssen, M., Stofan, E., Lopes, R., Kirk, R., Elachi, C., Lunine, J., Mitchell, K., Paganelli, F., Soderblom, L., Wood, C., Wye, L., Zebker, H., Anderson, Y., Ostro, S., Allison, M., Boehmer, R., Callahan, P., Encrenaz, P., Ori, G.G., Francescetti, G., Gim, Y., Hamilton, G., Hensley, S., Johnson, W., Kelleher, K., Muhleman, D., Picardi, G., Posa, F., Roth, L., Seu, R., Shaffer, S., Stiles, B., Vetrella, S., Flamini, E., West, R., (2006). The sand seas of Titan: Cassini RADAR observations of longitudinal dunes. **Science 312**, 724-727.

Lorenz, R.D., Zarnecki, J.C., Towner, M.C., Leese, M.R., Ball, A.J., Hathi, B., Hagermann, A., Ghafoor, N.A.L., 2007. Descent motions of the Huygens probe as measured by the Surface Science Package (SSP): Turbulent evidence for a cloud layer. *Planet. Space Sci.* **55**, 1936-1948.

Lundberg, B., Sundquist, B., 1986. Resistivity of a composite conducting polymer as a function of temperature, pressure, and environment: application as a pressure and gas concentration transducer. *J. Appl. Phys.* **60**, 1074–1079.

Niemann, H.B., Atreya, S.K., Bauer, S.J., Carignan, G.R., Demick, J.E., Frost, R.L., Gautier, D., Haberman, J.A., Harpold, D.N., Hunten, D.M., Israel, G., Lunine, J.I., Kasprzak, W.T., Owen, T.C., Paulkovich, M., Raulin, F., Raaen, E., Way, S.H., 2005. The abundances of constituents of Titan's atmosphere from the GCMS instrument on the Huygens probe. *Nature* **438**, 779-784.

Rosenberg, P.D., 2007. *Huygens' Measurements of the Speed of Sound on Titan*. PhD Thesis, The Open University, Milton Keynes, UK.

Simões, F., 2007. *Resonances in ionospheric cavities of planets and their satellites: progresses and perspectives*. PhD thesis, Université Pierre et Marie Curie, Paris 6, France.

Simões, F., Grard, R., Hamelin, M., López-Moreno, J.J., Schwingenschuh, K., Béghin, C., Berthelier, J.-J., Besser, B., Brown, V.J.G., Chabassière, M., Falkner, P., Ferri, F., Fulchignoni, M., Hofe, R., Jernej, I., Jeronimo, J.M., Molina-Cuberos, G.J., Rodrigo, R., Svedhem, H., Tokano, T., Trautner, R., 2007. A new numerical model for the simulation of ELF wave propagation and the computation of eigenmodes in the atmosphere of Titan: did Huygens observe any Schumann resonance? *Planet. Space Sci.* **55**, 1978-1989.

Stauffer, D., Aharony, A., 1994. *Introduction to Percolation Theory*. Taylor and Francis, CRC Press, revised 2nd ed., London, UK.

Stofan, E. R., Elachi, C., Lunine, J. I., Lorenz, R.D., Stiles, B., Mitchell, K.L., Ostro, S., Soderblom, L., Wood, C., Zebker, H., Wall, S., Janssen, M., Kirk, R., Lopes, R., Paganelli, F., Radebaugh, J., Wye, L., Anderson, Y., Allison, M., Boehmer, R., Callahan, P., Encrenaz, P., Flamini, E., Francescetti, G., Gim, Y., Hamilton, G., Hensley, S., Johnson, W.T.K., Kelleher, K., Muhleman, D., Paillou, P., Picardi, G., Posa, F., Roth, L., Seu, R., Shaffer, S., Vetrella, S., West, R., (2007). The lakes of Titan. *Nature* **445**, 61-64.

Tikhonov, A.N., Arsenin, V.A., 1977. *Solution of Ill-posed Problems*. Winston & Sons, Washington, DC, US.

Tomasko, M.G., Buchhauser, D., Bushroe, M., Dafoe, L.E., Doose, L.R., Eibl, A., Fellows, C., Farlane, E.M., Prout, G.M., Pringle, M.J., Rizk, B., See, C., Smith, P.H., Tsetsenekos, K., 2002. The Descent Imager/Spectral Radiometer (DISR) experiment on the Huygens Entry Probe of Titan. *Space Sci. Rev.* **104**, 469-551.

Tomasko, M.G., Archinal, B., Becker, T., Bézard, B., Bushroe, M., Combes, M., Cook, D., Coustenis, A., de Bergh, C., Dafoe, L.E., Doose, L., Douté, S., Eibl, A., Engel, S., Gliem, F., Grieger, B., Holso, K., Howington-Kraus, E., Karkoschka, E., Keller, H.U., Kirk, R., Kramm, R., Küppers, M., Lanagan, P., Lellouch, E., Lemmon, M., Lunine, J., McFarlane, E., Moores, J., Prout, G.M., Rizk, B., Rosiek, M., Rueffer, P., Schröder, S.E., Schmitt, B., See, C., Smith, P., Soderblom, L., Thomas, N., West, R., 2005. Rain, winds and haze on Titan. *Nature* **438**, 765-778.

Wenner, F., 1915. A method of measuring the Earth resistivity. *U.S. Bur. Stand. Bull., Sci. Pap.* **25** 469-478.

Zarnecki, J.C.; Leese, M.R.; Garry, J.R.C.; Ghafoor, N.; Hathi, B., 2002. Huygens' Surface Science Package. *Space Sci. Rev.* **104**, 593-611.

Zarnecki, J.C., Leese, M.R., Hathi, B., Ball, A.J., Hagermann, A., Towner, M.C., Lorenz, R.D., McDonnell, J.A.M., Green, S.F., Patel, M.R., Ringrose, T.J., Rosenberg, P.D., Atkinson, K.R., Paton, M.D., Banaszkiewicz, M., Clark, B.C., Ferri, F., Fulchignoni, M., Ghafoor, N.A.L., Kargl, G., Svedhem, H., Delderfield, J., Grande, M., Parker, D.J., Challenor, P.G., Geake, J.E., 2005. A soft solid surface on Titan at the Huygens landing site as measured by the Surface Science Package (SSP). *Nature* **438**, 792–795.

Zimmerman, W.B.J., 2006. *Multiphysics Modelling with Finite Element Methods*. World Scientific, Oxon, UK.

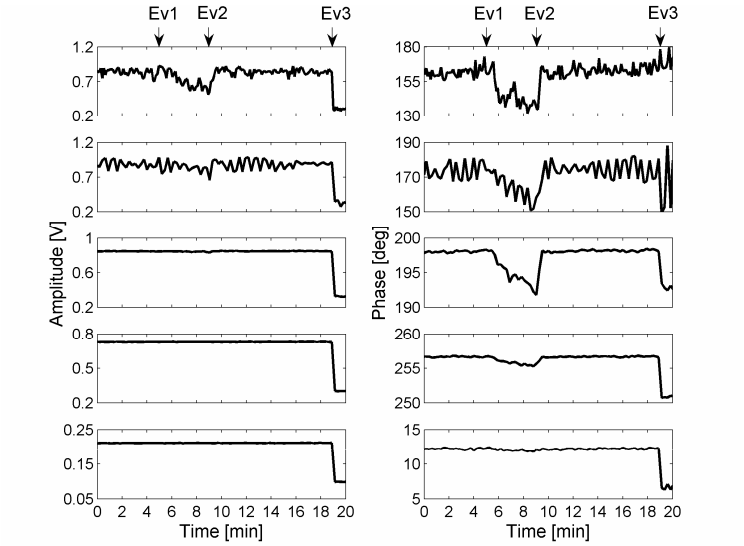

Figure 1: Laboratory measurements of MIP amplitude and phase recorded with the PWA mock-up. The most significant events are represented by arrows: Ev1) diffuse water spraying on the paper layer; Ev2) paper drying; Ev3) water spraying until paper is saturated.

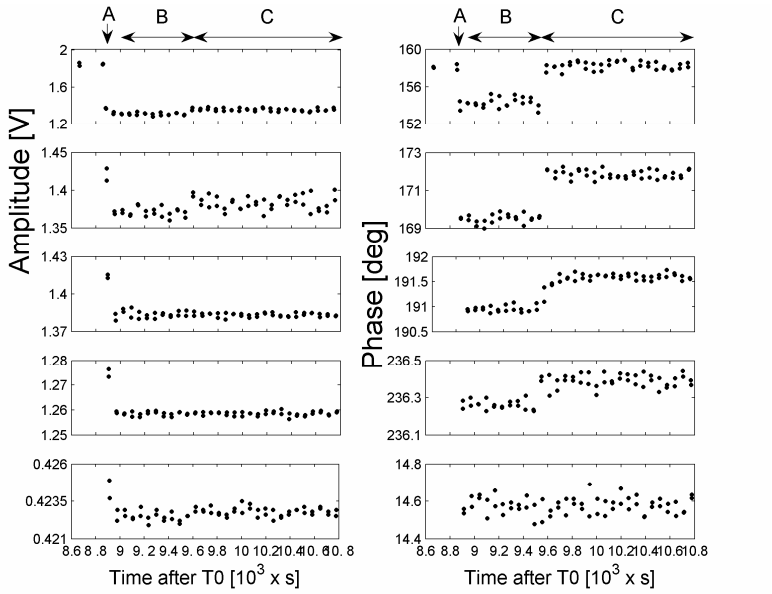

Figure 2: Titan data recorded with the MIP in the PWA surface mode. The panels represent the amplitude (left) and phase (right) and, from top to bottom, at 45, 90, 360, 1440, and 5760 Hz. A transition in surface data is observed about 9539 s and identified by arrows. The last four data points at 45 Hz before touchdown are also presented for comparison purposes.

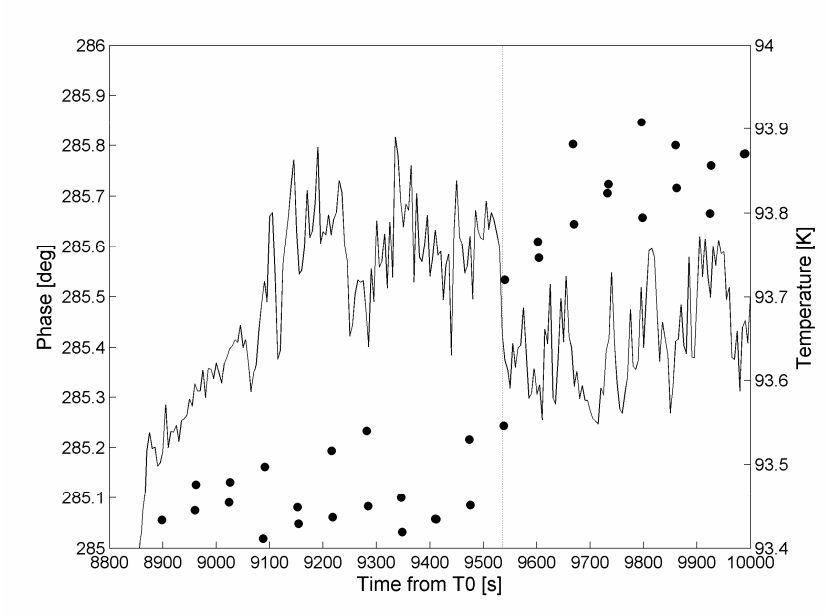

Figure 3: Temperature (solid line) and MIP phase at 360 Hz (filled circles) measured after touchdown. The vertical dashed line identifies the transition that occurred at 9539 s.

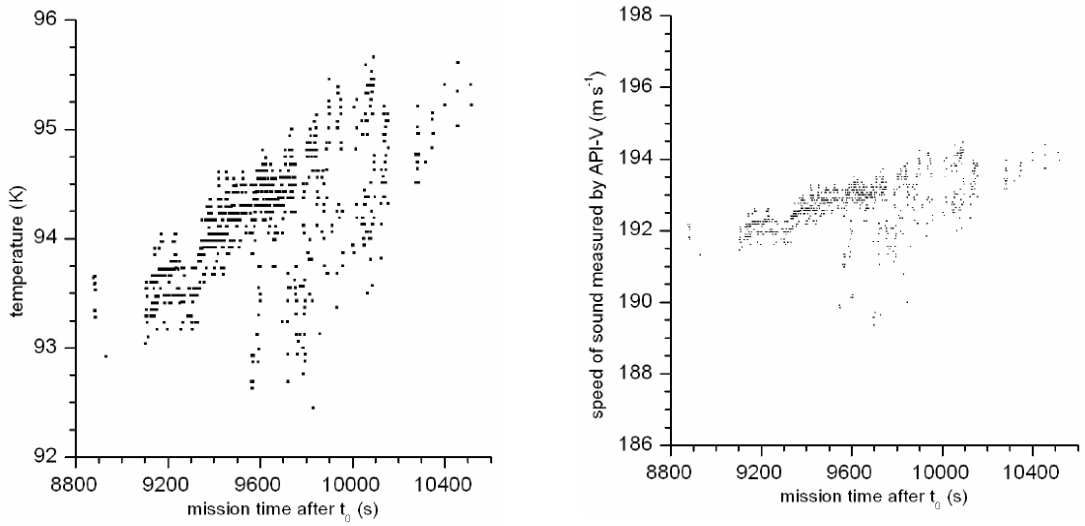

Figure 4: Temperature and acoustic velocity inferred from API-V data; spreading starts at 9565 s.

Paper 8

Low Frequency Electromagnetic Wave Propagation in Large Cavities: a Tool for Investigating Planetary Electric Environments. Study of the Cavity of Titan after the Cassini-Huygens Mission

Simões, F., Hamelin, M.

Proceedings of the Comsol Multiphysics Conference Paris-2006, 23-29 (2006)

Low Frequency Electromagnetic Wave Propagation in Large Cavities: a Tool for Investigating Planetary Electric Environments. Study of the Cavity of Titan after the Cassini-Huygens Mission.

F. Simões* and M. Hamelin

CETP/IPSL-CNRS 4, Avenue de Neptune, 94107 Saint Maur, France.
*Corresponding author: Fernando.Simoes@cetp.ipsl.fr.

Abstract: The propagation of low frequency electromagnetic waves in the cavity of the Earth has been extensively studied, namely for inferring thunderstorm and lightning activity. The same theory can be applied for studying other planetary bodies that hold an ionosphere, and the measurement of resonant states provides useful information for the analysis of the electric environment in the cavity. The model is applicable not only to the cavity of the Earth but also to other planetary environments, namely Venus, Mars, and Titan. We present a 3D finite element model of the cavity, compute the lowest eigenfrequencies and Q-factors, and illustrate the spectrum produced by localized electromagnetic sources.

Keywords: Wave propagation, electromagnetic fields, atmospheric electricity, surface properties.

1. Introduction

The Cassini-Huygens mission [1,2], a joint endeavour of NASA and ESA, is dedicated to study Saturn and its moons. The mother ship was inserted in orbit of Saturn in July 2004. In December, the Cassini spacecraft released the Huygens Probe that three weeks later descent through the atmosphere of Titan on January 14, 2005 and landed safely on the surface. During the descent, the Huygens Probe recorded valuable data for modelling the environment of Titan. Among other instruments, the Huygens Probe carried the Permittivity, Waves and Altimetry (PWA) analyser [3], a subunit of the Huygens Atmospheric Structure Instrument [4], for collecting data in the atmosphere and on the surface of Titan. The PWA analyser measured the conductivity profile during the descent and recorded electromagnetic spectra below 100 Hz. A noticeable resonance at 36 Hz was observed during the whole descent of the Huygens Probe [5,6]. A tentative interpretation is that the signal resembles to a Schumann resonance.

The propagation of low frequency electromagnetic waves within the cavity formed by two highly conductive spherical shells, such as those formed by the surface and the ionosphere of Earth, was first studied by Schumann [7] and subsequently observed by Balser and Wagner [8]. When a cavity is pumped with appropriate electromagnetic sources, resonant states can develop, where the average equatorial circumference of the cavity is approximately equal to integral numbers of the signal wavelengths. This effect is known as the Schumann resonance. On Earth, the phenomenon is widely known and investigated in many fields, including lightning activity, climate models, interaction between the ionosphere, the magnetosphere and the solar wind, etc.

There are, however, important differences between the characteristics of the cavities of Titan and the Earth, including: the radii of the cavities; the relative separations between the shells (i.e. altitudes of the ionospheres); the possible sources of electromagnetic energy; the losses in the atmospheres due to the presence of free electrons; the inner boundaries (the surface conductivities differ by several orders of magnitude). In fact, unlike for the Earth, it is not possible to consider the surface of Titan as a perfect electric conductor (PEC) and a more general approach is required. Therefore, we suggest a new approach that is suitable to investigate not only the low ionosphere and the atmosphere but also the interior of Titan, namely for assessing the subsurface ocean predicted by theoretical models [9].

In this paper, we describe a numerical model to study the electric environment of planetary cavities, in particular applied to Titan, using the Comsol Multyphysics tools, namely the harmonic propagation and eigenfrequency modes of the electromagnetic module, and present eigenfrequencies and Q-factors of the cavity. Other possible mechanisms that could generate the 36 Hz signal are also briefly discussed.

2. Wave Propagation in Large Cavities

2.1 The Schumann Mode

The Schumann eigenfrequencies are derived from the resonance condition of the cavity (see Figure 1). Considering a thin cavity and equating the circumference to an integer number of wavelengths, the resonant angular frequency is written

$$\omega_n = n\frac{c}{R}, \qquad (01)$$

where n is an integer that identifies the eigenmode, c is the velocity of light in the medium and R is the average radius of the cavity. Including a 3D spherical correction yields [7]

$$\omega_n = \sqrt{n(n+1)}\frac{c}{R}. \qquad (02)$$

On Earth and other planets, as well as on Titan, the first few Schumann resonances, or longitudinal modes, have frequencies that fall within the extreme low frequency (ELF) range.

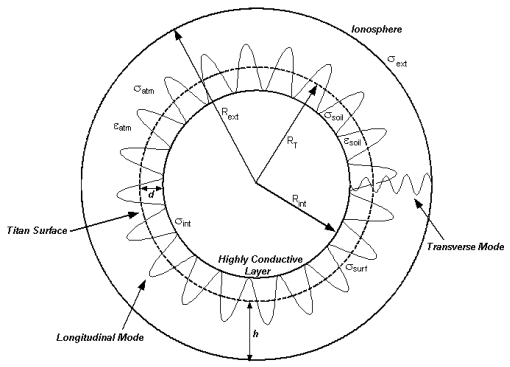

Figure 1. Sketch of the model used for calculating the Schumann resonance on Titan. R_T – Titan radius; R_{int} – liquid layer radius; R_{ext} – ionosphere radius; h – altitude of the ionosphere; d – depth of the solid-liquid interface layer; ε_{soil}, ε_{atm}, σ_{soil}, and σ_{atm} – permittivity and conductivity of soil and atmosphere, respectively; σ_{int}, σ_{ext}, and σ_{surf} – conductivity of inner and outer boundaries, and surface.

In addition to the longitudinal modes that are function of the cavity radius, there exist local transverse modes along the radial direction. When the shells that form the cavity are PECs, the transverse mode requires that the electric field be zero on the boundaries. A resonance develops whenever the distance between the shells, generally the height of the ionosphere, h, is an integer number, p, of half-wavelengths,

$$\omega_p = p\frac{c\pi}{h}. \qquad (03)$$

The value p=0 is associated with a possible electrostatic field between the ionosphere and the surface.

2.2 Theoretical Formulation

A full treatment of the Schumann resonance in the cavity of Titan requires the solution of Maxwell equations, which are written

$$\nabla\times\boldsymbol{E} = -\frac{\partial \boldsymbol{B}}{\partial t}, \qquad (04)$$

$$\nabla\times\boldsymbol{H} = \sigma\boldsymbol{E} + \frac{\partial \boldsymbol{D}}{\partial t}, \qquad (05)$$

with

$$\boldsymbol{D} = \varepsilon\varepsilon_o\boldsymbol{E}, \quad \boldsymbol{B} = \mu_o\boldsymbol{H}, \qquad (06)$$

where, ε_o and μ_o are the permittivity and magnetic permeability of vacuum, $\boldsymbol{E}$ and $\boldsymbol{D}$ are the electric and displacement fields, $\boldsymbol{H}$ and $\boldsymbol{B}$ are the magnetic field strength and flux density, and ε is the relative permittivity.

The system of Equations (04-06), together with the cavity constraints, can be solved analytically in spherical coordinates, using the harmonic propagation approximation and decoupling the electric and magnetic fields. One mode is characterized by H_r=0 and is termed transverse magnetic (TM) wave, the other one by E_r=0 and is known as transverse electric (TE) wave. Neglecting the day-night asymmetry of the ionosphere, the standard method of separation of variables yields [10]

$$\left\{\frac{d^2}{dr^2} - \frac{n(n+1)}{r^2} + \frac{\omega^2}{c^2}\varepsilon(r) - \sqrt{\varepsilon(r)}\frac{d^2}{dr^2}\left(\frac{1}{\sqrt{\varepsilon(r)}}\right)\right\}(rR(r)) = 0, \qquad (07)$$

where $R(r)$ is a radial function related to the electric and magnetic fields by the Debye potentials [11]. This equation gives the eigenvalues of the longitudinal and transverse

modes, assuming either dR(r)/dr=0 or R(r)=0 at both boundaries, respectively. For a thin void cavity the eigenvalues are those given by Equations (02) and (03). For example, Equation (07) is valid only when the height of the ionosphere is much lower than cavity radius, i.e. $h<<R$, which is not the case for the cavity of Titan. However, this equation is useful for validating the finite element model under specific conditions.

3. The Numerical Model

3.1 Parameters Description

The model uses the finite element method (FEM) and the tools provided by Comsol Multiphysics to solve Equations (04-06) and also utilizes continuity conditions on the surface, whenever applicable, and PEC boundary conditions. The model includes the following parameters (see sketch in Figure 1):

a) Conductivity profile of the atmosphere and lower ionosphere (σ_{atm}). The conductivity profile is split in three sectors: for h<150 km it is used PWA non calibrated data (a correction factor in the range 0.5-2 is expected for calibrated values); in the upper boundary it is used Cassini and Voyager data that shows a skin depth lower than 1 km; the conductivity profile is interpolated in the range 150-750 km. The theoretical model before the arrival of the Huygens Probe on Titan is also presented (Figure 2).

b) Depth of the subsurface liquid layer (*d*). A soil conductivity of ~10^{-10} Sm^{-1} as measured on the surface at the Huygens Probe landing site [6] implies that the penetration depth would be >1000 km in the ELF range, and that the surface reflectivity is small. However, the skin depth of pure liquid water is two orders of magnitude lower and it is expected that the penetration depth in a subsurface liquid layer be even smaller due to the presence of salts and ammonia. Thus, we apply the PEC condition to the inner boundary and use a depth of 100 km as a first approximation.

c) Permittivity and conductivity of the interior (ε_{soil}, σ_{soil}). In the temperature range expected on the surface and interior of Titan the dielectric properties of water ice, the major component of the soil, do not vary significantly, even at low frequencies. However, several models predict the presence of water-ammonia ice mixtures and the dielectric properties are more difficult to assess. The soil composition and porosity are unknown but a relative permittivity in the range 2-4 will tentatively be assumed. The concentrations of ionic contaminants are not known and even small quantities can significantly increase the conductivity of the medium. After these considerations, we assume that the conductivity is constant down to the applicable depth. The values used in the simulations are ε_{soil}=3 and σ_{soil}=10^{-9} Sm^{-1}.

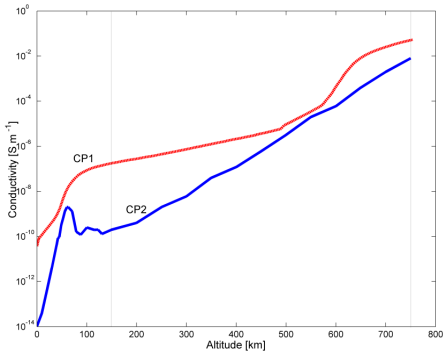

Figure 2. Theoretical and measured/modified conductivity profiles used in the numerical model. CP1 – theoretical model; CP2 – non calibrated profile using Huygens (h<150 km) and Cassini (h=750 km) data. The values in the range 150<h<750 km are interpolated.

The model also includes the following interface and boundary conditions:

d) Upper boundary describing the lower bond of the ionosphere (σ_{ext}). For an altitude of 750 km, the lowest altitude probed with propagation techniques, the skin depth is lower than 1 km at 36 Hz. Therefore, it is acceptable to assume a PEC at the upper boundary of the cavity.

e) Lower boundary describing the solid-liquid interface that is expected to describe the predicted subsurface ocean (σ_{int}). The skin depth for pure water at 36 Hz is lower than 50 km, and brines/ammonia mixed in the liquid increase the conductivity. Thus, a PEC boundary condition is suitable at the inner boundary of the cavity.

f) Surface interface (σ_{surf}). Whenever the surface does not coincide with the lower boundary, the continuity condition is applicable. It is used a sigmoid-type function for representing the

surface transition instead of a step function. This approximation produces smoother results, mainly in the electric field, which reveals incoherent surface results otherwise. Moreover, a smoother transition on the surface also allows to produce coarser meshes.

The conductivity profile of the model is function of the radius only. Therefore, there are neglected the day-night asymmetry of the electron density distribution and, consequently, perturbations of the spherical geometry.

The finite element model is solved in 3D for a general distribution of electromagnetic sources but it can be reduced to a 2D-axisymmetric problem in the following conditions:

a) eigenfrequency mode for calculating the eigenfrequencies and the Q-factors;

b) harmonic propagation mode with a single source located at a pole;

c) harmonic propagation mode with a ring source located at the equator.

3.2 Model Validation

Two algorithms are used for solving the resonant cavity problem: eigenfrequency and harmonic propagation modes that are included in the electromagnetic module. The first algorithm gives the complex frequencies of the different eigenmodes, from which we derive the Q-factor of the cavity. The second algorithm computes the frequency spectra as function of the excitation source, and identifies the propagation eigenmodes, calculates the electric field over a wide altitude range, and evaluates the influence of sources distribution on the propagation modes.

The numerical model is validated by comparing the eigenfrequencies computed with the finite element model and Equation (07). In the case of a lossless thin cavity in a vacuum the same results are obtained from Equations (02) and (07), and the finite element model (Table 1, Test A). Furthermore, the results obtained with equation (07) and FEM are similar when we use a lossless medium and PEC boundary conditions (Table 1, Test B). Whereas the results shown in Table 1 confirm the validity of the two models for lossless homogeneous conditions, the eigenfrequency values are appreciably different if the medium is heterogeneous (Table 1, Test C), which shows validity limits of Equation (07) and of the analytical approximations. The differences are more significant in the case of the longitudinal mode and large *h/R*, especially when the medium filling the cavity is heterogeneous. Inclusion of losses in the medium constrains Equation (07) validity even further. The model is also checked with Earth parameters and the expected eigenfrequencies and approximate Q-factors are obtained.

		(Equation 07)		FEM	
Cavity	Test	L [Hz]	T [Hz]	L [Hz]	T [Hz]
Earth	A	10.6	-	10.6	-
	B	10.5	1998	10.6	2008
	C	10.3	1670	8.86	1635
Titan	A	26.2	-	26.2	-
	B	22.9	201.2	23.1	201.2
	C	14.3	168.1	19.1	163.5

Table 1. Comparison of the eigenfrequency modes (L-longitudinal; T- transverse) for different analytical and numerical models (FEM). Validation checkout: R_T=2575 km and R_E= 6370 km for the inner shell radius; h_T=750 km, h_E=75 km for ionospheric height. (Test A): $h\rightarrow 0$, $\sigma_{atm}=0$, and $\varepsilon_{atm}=1$; (Test B): $h=h_T$ or $h=h_E$, $\sigma_{atm}=0$, and $\varepsilon_{atm}=1$; (Test C): $h=h_T$ or $h=h_E$, $\sigma_{atm}=0$, and sigmoid-type function for permittivity. A perfect electric conductor boundary is considered in all cases.

4. Results

The models compute the eigenmodes for each set of parameters in the ranges: d=20-675 km; ε_{soil} =2-4; $\sigma_{soil}=10^{-10}$-10^{-8} Sm^{-1}, where the σ_{atm} profile is represented either by CP1 or CP2 (typical example in Figure 3).

We infer that the eigenfrequencies vary with the atmospheric conductivity profile, especially at low and mid altitudes. Moreover, considering the PEC approximation on the surface introduces a significant error in the cavity model when the conductivity is low. An increase of the medium permittivity reduces the eigenfrequencies in the cavity because $\omega_n \propto \varepsilon^{-1/2}$ for an homogeneous medium. The same general behaviour is observed for the imaginary part of the frequency. Finally, increasing the depth of the PEC boundary has contrasting effects on the eigenfrequency, because the real part rises while the imaginary part decreases. Results are reported in greater detail elsewhere [9].

On Earth, knowledge of the atmospheric conductivity provides a good estimation of Schumann resonance. Therefore, variations of

the ELF spectrum allow to survey the atmosphere and the lower bound of the ionosphere. However, the conductivity profile of the atmosphere of Titan is known with less detail and other relevant parameters are mostly unknown, which reduce model accuracy.

Profile / Mode	CP1	CP2	$\sigma_{atm}=0$
First	7.27+4.77i	16.05+4.01i	23.06
Second	15.25+9.71i	30.29+6.73i	39.93
Third	25.31+14.80i	44.97+9.32i	56.44

Table 2. Comparison between the lowest eigenfrequency modes (in Hz) for different conductivity profiles, with loss (CP1-CP2) and lossless (σ=0) atmospheres. The PEC boundary conditions are considered at $R_{int}=R_T$ and $R_{ext}=R_T+h_T$, where h_T, the ionospheric height boundary, is 750 km.

Profile / Mode	CP1	CP2	$\sigma_{atm}=0$ $\sigma_{soil}=0$
First	9.62+2.87i	16.88+3.03i	22.30
Second	18.84+6.65i	30.03+5.67i	38.61
Third	29.11+10.11i	43.34+8.45i	54.59

Table 3. The same caption as in Table 2 but with $R_{int}=R_T$ – 100 km and $\varepsilon_{soil}=3$ $\sigma_{soil}=10^{-9}$ Sm^{-1}. In the case of the lossless test (right column), the conductivity of the soil is neglected.

From Tables 2 and 3 it is possible to derive the quality factor of the cavity. The Q-factor (defined by the ratio between the real part and twice the imaginary part of the eigenfrequency) of the cavity with CP1 is of the order of ~0.8 when the PEC inner boundary coincides with the surface, and ~1.5 when this boundary lies under the surface. Contrary to all expectations a subsurface inner boundary does not necessarily entail an increase of the losses, especially if the soil bulk conductivity is small. In fact, in a first approximation, an increase in shell separation can balance the additional losses in the soil. The quality factor of a cavity with CP2 is ~2 and ~3 when the inner boundary lays on the surface or at a depth of 100 km, respectively.

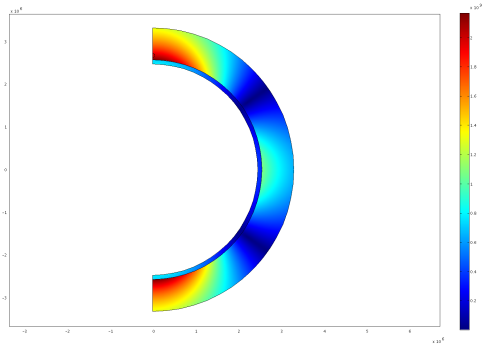

Figure 3. Electric field amplitude of the second eigenmode computed with the 2D model with axial symmetry. The transition between the soil and the atmosphere is clearly visible.

The harmonic propagation approach is especially suited to the analysis of global features and to the study of the electromagnetic field distribution generated by sparse sources. The algorithm calculates the frequency response of the cavity, in the range 1-100 Hz, and the electromagnetic field distribution as a function, for example, of the distance between the sources and the receiver.

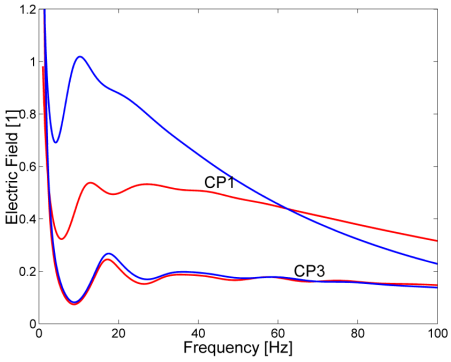

Figure 4. Electric field as a function of frequency for the two conductivity profiles and cavity configurations ($R_{int}=R_T$-100km – red, $R_{int}=R_T$ – blue). The soil properties, whenever applicable, use default values. The electromagnetic source is a small pulsating sphere located at an altitude of 35 km and the angular separation (the angle between the source and the receiver as seen by an observer at the centre of the planet) is 45°.

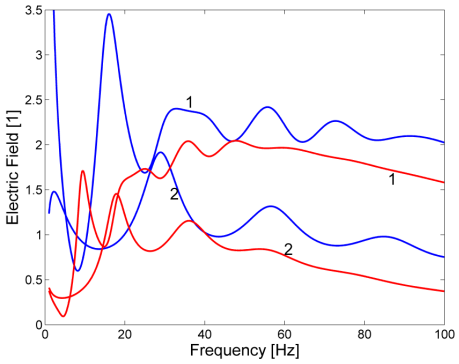

Figure 5. Electric field plotted as a function of frequency. The subsurface layer is located at 100 km, the conductivity profile is either CP2 (blue) or CP1 (red), for two angular separations: 1- 45°; 2- 90°.

Figure 4 shows the spectrum of the electric field generated in the ELF range by a source of arbitrary amplitude for the two conductivity profiles with PEC boundaries on the surface and at a depth of 100 km. The transmitted signal is stationary and its spectrum is flat in the frequency band of interest. The spectrum varies with the conductivity profile and cavity geometry, mainly for the profile with higher losses (CP1).

Figure 5 illustrates the electric field as function of frequency and cavity configuration, with different conductivity profiles and angular separations. The most important result is that the lowest eigenmode is absent at 90°.

Comparing results between CP1 and CP2 it is possible to see that wave dumping is much stronger for the theoretical profile. The second case enhances wave propagation in the cavity, and it is likely that an improved conductivity profile rises the Q-factor of cavity even further due to the presence of high concentration of aerosols in the upper atmosphere of Titan.

5. Discussion and Conclusions

The descent of the Huygens Probe through the atmosphere of Titan revealed a conspicuous signal at 36 Hz in the ELF spectra of PWA. In fact, the signal is present during the whole descent but not on the surface. None of the explanations presented so far is able to explain the origin of this signal. The data analysis of the ELF spectra has revealed:

A1) There is a conspicuous resonance at 36 Hz that is present during the descent but not on the surface;
A2) The loss of Channel A has decreased frequency resolution and, therefore, some spectral lines are absent;
A3) The amplitude of the signal is stronger in the altitude range 80-110 km;
A4) Data calibration is not finished but the amplitude is likely higher than 10 mV m^{-1} $Hz^{-1/2}$.

Several hypotheses have been raised and are under investigation. The possible explanations of the intriguing signal include artifacts and the interaction with the environment of Titan. The possible artifacts are:
B1) Instrument malfunction - Does not seem to be a probable explanation because the PWA analyzer worked nominally in laboratory, in balloon campaigns, and during the descent on Titan.
B2) Interference from the other instruments – nothing was reported during balloon campaigns and electromagnetic compatibility did not reveal any interference with other instruments.
B3) Microphonic effect resonance induced by parachute string vibration – data acquisition during the descent is performed under two parachutes at different stages. The parachutes are dissimilar, parachute strings and bridle vibration may only produce resonances at lower frequencies.
B4) Mechanical resonance induced by the Huygens Probe, PWA booms, and instruments platform – this effect is not ruled out but PWA booms alone do not show any resonance in the meaningful range. Furthermore, because of launch requirements, a careful assessment of the vibration response was performed. However, some complementary tests and modeling are foreseen.

The natural phenomena that might generate the resonance include:
C1) Schumann resonance in the cavity – if there are enough sources inside or when external electromagnetic fields are able to penetrate the ionosphere and pump the cavity;
C2) Local discharges produced by the haze – Titan atmosphere is appreciably permeated with charged aerosols.

The artifact option is not completely ruled out but the 36 Hz signal seems to be a natural phenomenon. However, the Schumann resonance model is not able to explain the last result (A4).

The instrument did not measure any resonance below 36 Hz and this value cannot be the lower eigenvalue of the cavity. However, the model predicts that an angular separation of 90° would not allow the instrument to measure the first harmonic (see Figure 5). Although less likely, the lowest mode could match an absent line in the spectrum. The amplitude of the signal is stronger around 100 km and that could be explained by the presence of the peak conductivity at 60 km, which enhances the electric field above the conductivity local maximum. Finally, the signal stops after landing and PWA recorded only noise, but the receiving antenna was likely touching the ground and the conductivity of the soil would reduce the signal below a measurable value. However, the intensity of the signal is not supported by the standard models of lightning activity and other atmospheric phenomena that plays a role on Earth.

Although the cavity model of Titan is a promising approach for explaining the PWA data it does not provide a clear explanation for all the questions. The refinement of the model requires a more accurate conductivity profile, which will be provided by other instruments flown onboard the Huygens Probe and the Cassini orbiter. Nevertheless, the cavity model offers other promising tools for studying the subsurface of Titan and, if enough and reliable data is available, may contribute to identify the subsurface ocean predicted by theoretical models.

The nature of the 36 Hz signal observed during the descent of the Huygens Probe on Titan is not fully understood yet. None of the explanations has been able to clarify the origin of the 36 Hz signal and, therefore, the source of this intriguing spectra remains unknown.

6. References

1. Matson, D.L. et al, The Cassini/Huygens mission to the Saturnian system, *Space Science Review*, **104**, 1-58 (2002).
2. Lebreton, J.-P. and Matson, D.L., The Huygens probe: Science, payload and mission overview, *Space Science Review*, **104**, 59-100 (2002).
3. Grard, R. et al, An experimental investigation of atmospheric electricity and lightning activity to be performed during the descent of the Huygens Probe on Titan, *J. Atmos. Terr. Physics*, **57**, 575-585 (1995).
4. Fulchignoni, M. et al, The characterization of Titan's atmosphere physical parameters by the Huygens Atmospheric Structure Instrument (HASI), *Space Science Review*, **104**, 395-431 (2002).
5. Fulchignoni, M. et al, In situ measurements of the physical characteristics of Titan's environment, *Nature*, **438**, 785-791 (2005).
6. Grard, R. et al, Electric properties and related physical characteristics of the atmosphere and surface of Titan, *Planetary and Space Science*, in press (2006).
7. Schumann, W.O., On the free oscillations of a conducting sphere which is surrounded by an air layer and an ionosphere shell, *Z. Naturforschaftung A*, **7**, 149– 154 (in German) (1952).
8. Balser, M. and Wagner, C.A., Observations of Earth-ionosphere cavity resonances, *Nature*, **188**, 638–641 (1960).
9. Simões, F. et al, Was the Schumann resonance observed during the descent of the Huygens Probe upon Titan?, *Planetary and Space Science* (submitted).
10. Bliokh, P.V. et al, Schumann resonances in the Earth-ionosphere cavity, D. L1. Jones-ed, Peter Peregrinus, Oxford, England (1980).
11. Wait, J., Electromagnetic waves in stratified media. Pergamon Press, Oxford (1962).

7. Acknowledgements

The authors are indebted to Alain Péan for fruitful discussions about software and hardware optimisation (memory swap management). This work has been supported by CNRS and IPSL.

Paper 9

The Schumann resonance: a tool for exploring the atmospheric environment and the subsurface of the planets and their satellites

Simões, F., Grard, R., Hamelin, M., López-Moreno, J.J., Schwingenschuh, K., Béghin, C., Berthelier, J.-J., Lebreton, J.-P., Molina-Cuberos, G.J., Tokano, T.

Icarus **10.1016/j.icarus.2007.09.020** (2007)

Available online at www.sciencedirect.com
ScienceDirect
Icarus ••• (••••) •••–•••
ICARUS
www.elsevier.com/locate/icarus

The Schumann resonance: A tool for exploring the atmospheric environment and the subsurface of the planets and their satellites

F. Simões [a,*], R. Grard [b], M. Hamelin [a], J.J. López-Moreno [c], K. Schwingenschuh [d], C. Béghin [e], J.-J. Berthelier [a], J.-P. Lebreton [b], G.J. Molina-Cuberos [f], T. Tokano [g]

[a] *CETP/IPSL-CNRS, 4, Avenue de Neptune, 94107 Saint Maur, France*
[b] *Research and Scientific Support Department, ESA-ESTEC, Keplerlaan 1, 2200 AG Noordwijk, The Netherlands*
[c] *Instituto de Astrofisica de Andalucia IAA-CSIC, Camino Bajo de Huetor, 50, 18008 Granada, Spain*
[d] *Space Research Institute, Austrian Academy of Sciences, Schmiedlstrasse 6, 8042 Graz, Austria*
[e] *LPCE-CNRS, 3A, Avenue de la Recherche Scientifique, 45071 Orléans cedex 2, France*
[f] *Applied Electromagnetic Group, Department of Physics, University of Murcia, Murcia 30100, Spain*
[g] *Institut für Geophysik und Meteorologie, Universität zu Köln, Albertus-Magnus-Platz, 50923 Köln, Germany*

Received 2 February 2007; revised 19 September 2007

Abstract

The propagation of extremely low frequency (ELF) electromagnetic waves and resonance phenomena in the Earth atmosphere has been extensively studied, in relation with ionospheric dynamics, and thunderstorm and lightning activities. A similar investigation can be performed for any other planet and satellite environment, provided this body is wrapped into an ionosphere. There are, however, important differences between Earth and other bodies, regarding the surface conductivity, the atmospheric electron density, the ionospheric cavity geometry, and the sources of electromagnetic energy. In a first approximation, the size of the cavity defines the range of the resonance frequency; the electron density profile, up to the upper atmospheric boundary, controls the wave attenuation; the nature of the electromagnetic sources influences the field distribution in the cavity; and the body surface conductivity, which gives the reflection and transmission coefficients, indicates to what extent the subsurface can be explored. The knowledge of the frequencies and attenuation rates of the principal eigenmodes provides unique information about the electric properties of the cavity. Instruments capable of monitoring the electromagnetic environment in the ELF range are, therefore, valuable payload elements on balloons, descent probes and landers. We develop models for selected inner planets, gaseous giants and their satellites, and review the propagation process of ELF electromagnetic waves in their atmospheric cavities, with a particular emphasis on the application of the Schumann resonance observation to subsurface studies. The instrumentation suitable for monitoring the electromagnetic environment in geophysical cavities is briefly addressed.

Keywords: Planets; Interiors; Atmospheres, structure; Ionospheres; Lightning

1. Introduction

The propagation of low frequency electromagnetic waves within the cavity formed by two highly conductive spherical shells, such as the surface and the ionosphere of Earth, was first studied by Schumann (1952) and subsequently observed by Balser and Wagner (1960). When a cavity is excited with an electromagnetic source, resonant states develop, where the average equatorial circumference of the cavity is approximately equal to integral numbers of the signal wavelengths. This phenomenon, known as the Schumann resonance, is the signature of thunderstorm and lightning activities, and is sometimes coined "the global tropical thermometer" (Williams, 1992). This subject is not only related to lightning activity, but also to climatology, to coupling mechanisms between ionosphere, magnetosphere and solar wind, and, to a lesser extent, to investigations of the subsurface at shallow depths, using the

* Corresponding author. Fax: +33 (0) 1 48 89 44 33.
E-mail address: fernando.simoes@cetp.ipsl.fr (F. Simões).

0019-1035/$ – see front matter
doi:10.1016/j.icarus.2007.09.020

transverse resonant mode (Guglielmi and Pokhotelov, 1996; Nickolaenko and Hayakawa, 2002).

The same formalism has been used for the cavities of other celestial bodies, such as Mars (e.g. Molina-Cuberos et al., 2006) and Titan (e.g. Simões et al., 2007). Simpler approaches have sometimes been applied to other bodies, Venus, Jupiter, and Io (Nickolaenko and Rabinovich, 1982; Sentman, 1990). There are important differences between the characteristics of these cavities, namely the reflectivity of the surface, the radius of the inner shell (R_{int}), the altitude of the ionosphere (h), the atmospheric electron density profile, the nature and distribution of the electromagnetic sources. In a first approximation, the inner radius of the cavity defines the frequencies of the Schumann resonances, which lies in the extremely low frequency (ELF) range; taking into account the other features of the cavities brings in first- and second-order corrections that tend to decrease the frequencies. Atmospheric conductivity induces losses that attenuate the propagating waves; if the conductivity is large enough, the waves are evanescent and no resonant state develops.

On Earth, lightning activity pumps energy into the cavity but other phenomena do also contribute. Charge generation and separation produce lightning-like electrical sparks, hundreds of meters long, during volcanic eruptions (Rakov and Uman, 2003). Triboelectric charging within a turbulent particle flow produces discharges (Farrell and Desch, 2001). Hydromagnetic waves may also contribute to the excitation of the Schumann modes (Abbas, 1968). The same mechanisms will generate electromagnetic radiation in the cavities of other planets and satellites. In dry atmospheres, like that of Mars, dust devils and dust storms may induce electrical discharges (Aplin, 2006). A similar assumption can be made about the cavity of Titan, where haze and charged aerosols, and a significant conductivity, could also play a role.

The boundaries of the cavity are located where the skin depth of the propagating waves is much smaller than the separation between the shells. On Earth, the inner (R_{int}) and outer (R_{ext}) boundaries coincide with the planet's surface and the lower limit of the ionosphere. The conductivity of the surface is the order of 0.01 and 1 S m^{-1} on land and sea, respectively (Lide et al., 2006), and the perfect electric conductor (PEC) approximation applies. The skin depth in the Chapman layer is several orders of magnitude smaller than that in the atmosphere and the lower boundary of the ionosphere acts as a perfect reflector for ELF waves. The definition of the boundaries, especially the inner boundary, is less straightforward in other environments and has to be analyzed case-by-case. On Venus, for example, the surface can be considered as the inner shell of the cavity only if the soil conductivity is larger than 10^{-4} S m^{-1}, but this assumption is not valid on Titan, where the surface conductivity is extremely low. The cavities of the giant planets are even more mysterious because they have no well-defined surface, and modeling their characteristics is a significant challenge. The cavity generally consists of the atmosphere, up to the ionosphere, and of the solid outer layer of the body, when the conductivity of the subsurface material is small enough. On Earth, the skin depth at the surface for ELF is less than 1 km, but the situation is quite different on Titan and possibly on the giant planets.

The cavity of Titan is particularly interesting. The electron density profile is known to some extent in the lower atmosphere (Hamelin et al., 2007); the soil at the Huygens Probe landing site is similar to a good dielectric (Grard et al., 2006), at least at shallow depths, and the skin depth is large. Several models predict the presence of a subsurface ocean, possibly a water–ammonia mixture (Lunine and Stevenson, 1987; Sohl et al., 1995; Tobie et al., 2005), and the study of wave propagation in the cavity might provide some indications about the depth of the solid–liquid interface (Simões et al., 2007).

In this paper, we review the propagation process of ELF waves in planetary cavities, and estimate eigenfrequencies and Q-factors with a finite element model especially developed for Titan. This approach is novel and brings in several improvements: (a) the technique is applicable not only to Earth but also to other planets; (b) the conductivity profile within the cavity is arbitrary; (c) the subsurface can be explored when the surface of the body is not the inner boundary of the cavity; (d) the conductivity profile is sensitive to water content and information about the atmospheric composition of the giant planets can be derived. We present results obtained for recent models of the giant planets and assess the role played by the dielectric properties of their subsurface. Finally, we review the scientific significance of the Schumann resonance and briefly describe the technical requirements associated with its observation.

2. Wave propagation in the cavity

The Schumann eigenfrequencies are derived from the resonance condition of a cavity. The resonant angular frequency of a thin spherical cavity is written (Schumann, 1952)

$$\omega_n = \sqrt{n(n+1)}\frac{c}{R}, \tag{1}$$

where n is an integer that identifies the eigenmode, c the velocity of light in the medium and R the average radius of the cavity. In addition to the longitudinal modes that are functions of the cavity radius, there exist local transverse modes along the radial direction. When the spherical shells that form the cavity are PEC's, the transverse mode requires that the electric field be zero on the boundaries. A resonance develops whenever the distance between the shells, generally the height of the ionosphere, h, is an integer number, p, of half-wavelengths,

$$\omega_p = p\frac{c\pi}{h}. \tag{2}$$

The analytical approximations are usually solved by decoupling the longitudinal and transverse modes, which is a fair approximation when the height of the ionosphere is much smaller than cavity radius, i.e. $h/R \ll 1$. This condition is applicable, for example, to Earth and Venus but not to Titan.

The full treatment of the Schumann resonance in the cavity requires the solution of Maxwell equations

$$\nabla \times \boldsymbol{E} = -\frac{\partial \boldsymbol{B}}{\partial t}, \tag{3}$$

Please cite this article in press as: F. Simões et al., The Schumann resonance: A tool for exploring the atmospheric environment and the subsurface of the planets and their satellites, Icarus (2007), doi:10.1016/j.icarus.2007.09.020

$$\nabla \times \boldsymbol{H} = \sigma \boldsymbol{E} + \frac{\partial \boldsymbol{D}}{\partial t}, \tag{4}$$

with

$$\boldsymbol{D} = \varepsilon \varepsilon_o \boldsymbol{E}, \qquad \boldsymbol{B} = \mu_o \boldsymbol{H}, \tag{5}$$

where $\boldsymbol{E}$ and $\boldsymbol{D}$ are the electric and displacement fields, $\boldsymbol{H}$ and $\boldsymbol{B}$ are the magnetic field strength and flux density, ε_o and μ_o are the permittivity and magnetic permeability of vacuum, and σ and ε are the conductivity and the relative permittivity of the medium.

The system of Eqs. (3)–(5), together with the cavity constraints, can be solved analytically in spherical coordinates, using the harmonic propagation approximation and decoupling the electric and magnetic fields. One mode is characterized by $H_r = 0$ and is called transverse magnetic (TM) wave, the other one by $E_r = 0$ and is known as the transverse electric (TE) wave. However, many approximations used for the Earth cavity, where the condition $h/R \ll 1$ is valid, are not applicable to other environments (Simões et al., 2007).

Unlike that of Earth, the surfaces of several other bodies offer larger losses due to their lower reflectivity. The most typical example is Titan, whose surface conductivity is extremely low, $\sigma_{\text{surf}} \sim 10^{-10}\,\text{S}\,\text{m}^{-1}$, as measured by the Huygens Probe (Grard et al., 2006). An intermediate situation should be encountered on Venus and Mars. Propagation below the surface and wave attenuation are related to the skin depth, δ, by (Balanis, 1989)

$$\delta = \sqrt{\frac{2}{\mu_o \varepsilon_o}} \frac{\left(\sqrt{1 + (\frac{\sigma}{\omega \varepsilon_o})^2} - 1\right)^{-1/2}}{\omega}, \tag{6}$$

where ω is the angular frequency. These considerations are of course not relevant when the surface satisfies the PEC condition.

The quality factor is another useful parameter since it partly controls the wave attenuation in the cavity. This quantity is defined by the ratio between the real and the imaginary parts of the eigenfrequencies

$$Q_m \equiv \frac{\text{Re}(\omega_m)}{2\,\text{Im}(\omega_m)} \approx \frac{\omega_m^{\text{peak}}}{\Delta \omega_m}, \tag{7}$$

where Re and Im are the real and imaginary parts of the complex eigenfrequency, and $\Delta\omega_m$ is the width at half-power level of the line with peak frequency ω_m^{peak} and mode m. The Q-factor measures the ratio of the accumulated field power to the power lost during one oscillation period; $Q \propto \omega/\alpha$ is inversely proportional to the absorption coefficient, α, and characterizes the propagation conditions in the cavity. The absorption coefficient quantifies the rate at which power decreases with distance. An expedient way of estimating the quality factor consists, in a first approximation, in using instead the ratio between the resonator height and the skin depth of the electric field, $Q \propto h/\delta$ (Nickolaenko and Hayakawa, 2002). It is seen that increasing the ionosphere height augments the quality factor, whereas the larger skin depth of a poorly conducting boundary amplifies the losses in the cavity.

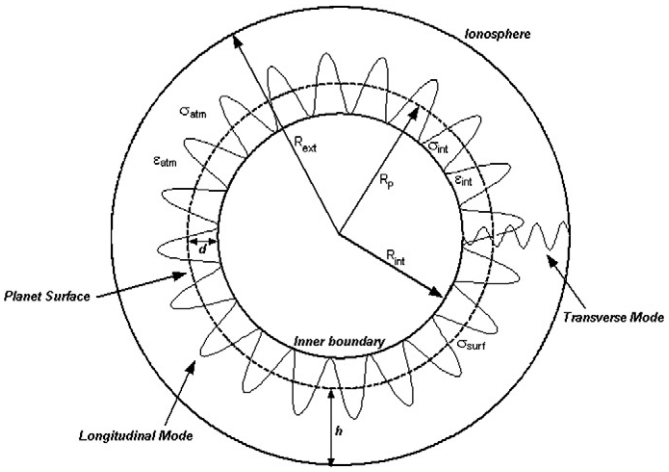

Fig. 1. Sketch of the model used for calculating the Schumann resonance. R_P: planet radius; R_{int}: lower boundary radius; R_{ext}: ionosphere radius; h: altitude of the ionosphere; d: depth of the lower boundary; σ_{surf}: surface conductivity; ε_{int}, ε_{atm}, σ_{int}, σ_{atm}: permittivities and conductivities of the interior and atmosphere, respectively.

3. The numerical approach

The numerical model uses the finite element method (Zimmerman, 2006) for solving Eqs. (3)–(5) with specific boundary conditions and medium properties. The algorithm calculates the eigenfrequency, Q-factor, and electromagnetic field distribution in the cavity. The numerical model is validated by comparing the eigenfrequencies given by the finite element model with theoretical approximations for the Earth cavity. The validation procedure and the model sketched in Fig. 1 are further discussed by Simões et al. (2007) in the case of Titan. For the sake of clarity, we define the interior of the gaseous giants as the region where the pressure is larger than 1 bar and this reference level determine the radius of the planet. The parameters that play a major role are listed below:

(a) *Conductivity profile of the atmosphere and lower ionosphere* (σ_{atm}). The conductivity is derived from the electron density and collision frequency profiles, obtained from pressure, temperature and atmospheric composition data.

(b) *Permittivity profile of the atmosphere and lower ionosphere* (ε_{atm}). The permittivity is a weak function of atmospheric gas density and does not significantly deviate from that of vacuum, even for Venus.

(c) *Depth of the inner boundary* (d). This parameter gives the depth of the inner PEC boundary; $d = 0$ at Earth, because the surface is a good reflector.

(d) *Conductivity profile of the interior* (σ_{int}). The subsurface conductivity of Earth is not relevant, but this is not necessarily true for other rocky bodies, whose soil properties play an important role. However, the variation of conductivity with depth is difficult to assess. Theoretical models predict that the conductivity of the gaseous giants should increase with depth, in different ways for Jupiter and Saturn, and for Uranus and Neptune.

(e) *Permittivity profile of the interior* (ε_{int}). The relative permittivity of the interior of the rocky planets is considered con-

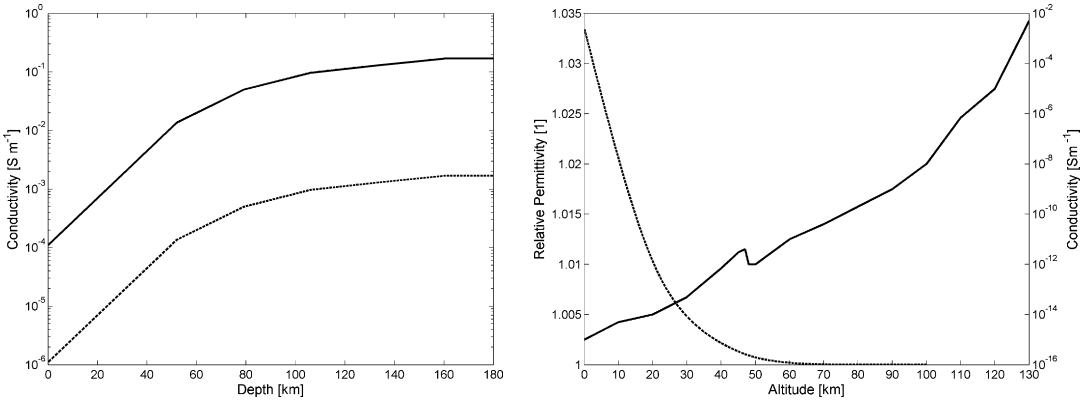

(a) (b)

Fig. 2. Dielectric parameters of the venusian cavity. Left: Conductivities as functions of depth for high (solid) and low (dashed) surface conductivities; right: conductivity (solid) and permittivity (dashed) of the atmosphere.

stant with depth and of the order of 3 and 5–10 for icy and rocky soils, respectively. The permittivity of the interior of the giant planets should increase with depth and density. The relative permittivity of liquid hydrogen is ∼1.25 (Lide et al., 2006). Therefore, the relative permittivity of the gaseous envelope is assumed to increase with depth in the range 1–1.25, reaching its maximum at the solid (Uranus and Neptune) or liquid (Jupiter and Saturn) interface.

4. Cavity parameterization

The various cavity environments encountered in the Solar System can be grouped in two major classes: (1) partly rocky/icy and (2) entirely gaseous cavities. By definition, the radius of the gaseous planets is determined by the 1-bar reference surface that is of little interest for our purpose. We shall now describe the models and compute the eigenfrequencies and Q-factors for Venus; Earth; Mars; Jupiter and Saturn; Titan, Europa and Io; Uranus and Neptune.

4.1. Venus

Our knowledge of Venus has been gained from ground-based observations, and orbiter flyby, balloon and lander space missions. The properties of the upper ionosphere are measured with propagation techniques during radio occultation, but the electron density in the lower ionosphere and atmosphere is not known. Data from several missions, such as Voyager and Pioneer Venus (Brace et al., 1997) are available, but the conductivity of the atmosphere (Fig. 2b) is inferred from theoretical models (Borucki et al., 1982). The carbon dioxide mole fraction of the atmosphere of Venus is ∼0.965 and the minimum altitude of the sulphuric acid clouds is ∼57 km. Lightning activity continues to be a controversial issue. The atmospheric pressure increases the breakdown voltage and prevents cloud-to-ground discharges but phenomena analogue to terrestrial sprites are possible (Strangeway, 2004).

The temperature and pressure profiles of the atmosphere were provided by the Pioneer Venus probes and properties of the surface by the Venera landers and Magellan. A surface temperature and a pressure of the order of 750 K and 92 bar, respectively, yield an atmospheric density about 54 times that on Earth. The relative permittivity is ∼1.034 at the surface level and does not significantly affect the eigenfrequencies. The permittivity profile of the atmosphere, that is a function of density, is plotted in Fig. 2b.

Volcanic processes, and many constructs and plains covered with extensive lava flows, dominate the surface of Venus. The radar altimeter onboard Pioneer Venus (Pettengill et al., 1988) has shown that the radar-bright spots could be explained either by roughness with a scale commensurate with the wavelength of the mapping signal, or by a larger dielectric constant of the surface material due to the presence of moderately conductive minerals such as iron sulfides and oxides. The radar imager onboard Pioneer Venus measured the surface relative permittivity; the average over the rolling plains and the lowlands is 5.0 ± 0.9, and suggests that the surface is overlaid with a few cm of soil or dust. There is no evidence of significant water vapor concentration in the atmosphere and on the surface. The soil should possess the dielectric properties of a dry igneous medium, such as basalt, at ∼750 K. The relative permittivity considered in the model is of the order of 4–10; the conductivity is assumed to lie in the range 10^{-6}–10^{-4} S m^{-1}, based on the values observed on Earth for the same composition and temperature range (Shanov et al., 2000; Lide et al., 2006). The conductivity profile (Fig. 2a) is a function of the interior temperature (Arkani-Hamed, 1994) in the depth range 0–150 km. The dielectric parameters are not dramatically different if high silica content is considered, and the soil permittivity does not play a role because the conductivity is sufficiently large.

4.2. Earth

Schumann has studied the propagation of ELF electromagnetic waves in the cavity of Earth and estimated its resonant frequencies. Subsequent research on the topic has identified lightning activity as the major source of energy, and revealed the role of many factors: day–night asymmetry of the ionosphere, climate variability, influence of the solar wind on the upper boundary, etc. The correlation between the distribution of thun-

Please cite this article in press as: F. Simões et al., The Schumann resonance: A tool for exploring the atmospheric environment and the subsurface of the planets and their satellites, Icarus (2007), doi:10.1016/j.icarus.2007.09.020

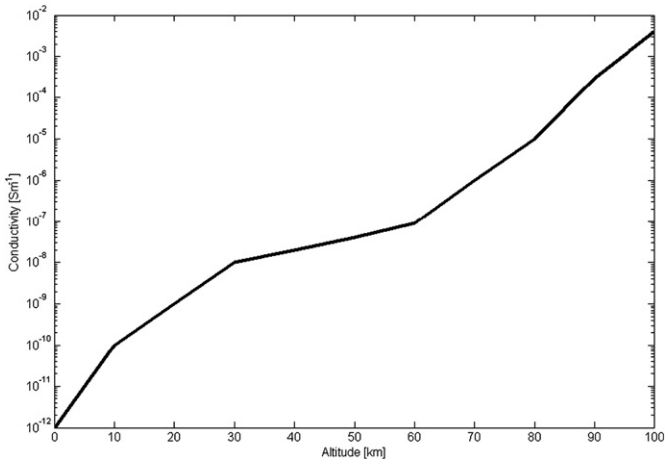

Fig. 3. Conductivity profile of the martian atmosphere.

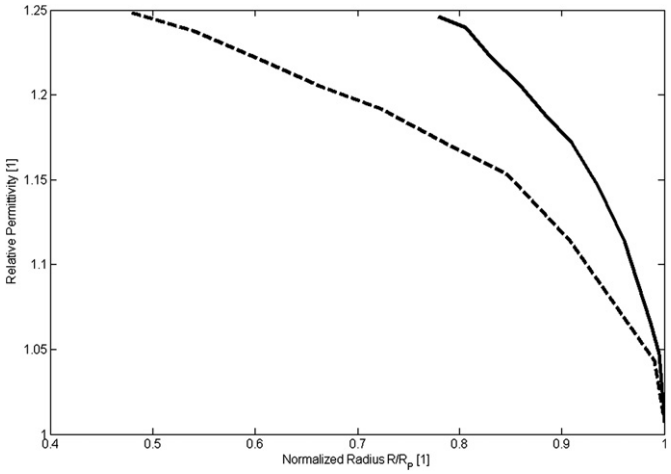

Fig. 4. Permittivity profiles of Jupiter (solid) and Saturn (dashed) interiors.

derstorms and the occurrence of the Schumann resonance in the cavity provides information about atmospheric activity. The work of Nickolaenko and Hayakawa (2002), and hundreds of references therein, testify the importance of this topic. With the exception of the phenomenon recorded during the descent of the Huygens Probe through the atmosphere of Titan (Simões et al., 2007), which is still under investigation, the Schumann resonance has never been identified so far on any celestial body but Earth.

Earth is used for the validation of the finite element model because the relevant parameters, permittivity, conductivity, and boundary conditions, are known with a fair accuracy, and the Schumann resonance has been extensively studied experimentally (e.g. Sentman, 1995). The average Schumann frequencies and Q-factors are 7.9, 14, and 20 Hz and 4, 4.5 and 5, respectively, for the three lowest eigenmodes.

4.3. Mars

Although many missions have been flown to Mars, electron density measurements are available for the ionosphere only (e.g. Fjeldbo et al., 1977; Pätzold et al., 2005). Theoretical models are therefore used to extend the conductivity profile down to the surface (Cummer and Farrell, 1999; Pechony and Price, 2004; Molina-Cuberos et al., 2006). Different profiles are found in the literature and, in some instances, ELF wave propagation is questionable due to strong cavity losses. We shall use the conductivity profile shown in Fig. 3. The atmosphere consists mostly of CO_2, with a mole fraction of ∼0.953; the atmospheric density is about 70 times less than on Earth and the permittivity is very close to that of vacuum.

The martian environment has been studied using Earth-based, remote sensing, and in situ observations, but the electrical properties of the surface are still poorly known. Theoretical models yield conflicting results for surface conductivity and permittivity. According to Christensen and Moore (1992), the relative permittivity of the regolith lies in the range 2.4–12.5, but no figure is given for that of the subsurface. The conductivity of the surface is also poorly defined and estimates vary between 10^{-12} and 10^{-7} S m^{-1} in the literature. Berthelier et al. (2000) tentatively restrict the range down to 10^{-12}–10^{-10} S m^{-1}. Contrasting compositions are seen at low and high latitudes, due to the presence of ice deposits in the polar regions. The subsurface dielectric properties of the regolith should vary with depth and composition, especially if water/ice/brines are embedded in the medium. We shall assume that the dielectric constant and conductivity of the soil are homogeneous with depth and lie in the ranges 4–10 and 10^{-12}–10^{-7} S m^{-1}, respectively.

There is no evidence of lightning activity on Mars but it is generally accepted that, due to triboelectric effects, massive dust storms might enhance atmospheric electrification, in particular in dust devils, as simulated on Earth (Krauss et al., 2003; Farrell and Desch, 2001). The spectral features of these emissions should however considerably differ from those observed in the Earth cavity.

4.4. Jupiter and Saturn

The atmospheres of the jovian planets are mainly composed of hydrogen and helium (the mean concentrations are H_2: 0.82 and 0.94, and He: 0.18 and 0.06, for Jupiter and Saturn, respectively) with much lower mole fractions for other components, such as methane, ammonia and water vapor. The pressure and temperature profiles are given by Justus et al. (2005). The atmospheric density increases drastically with depth and the vacuum approximation is no longer valid for the permittivity. Deep in the molecular hydrogen envelope, the density increases beyond the gaseous phase threshold and a liquid environment is expected. The permittivity therefore increases with depth until it reaches the value of liquid hydrogen, which is ∼1.25. The permittivity profiles shown in Fig. 4 are derived from the interior density models of the jovian planets (e.g. Lewis, 1995). The normalized radii of the solid–liquid interfaces are ∼0.76 and ∼0.48 for Jupiter and Saturn, respectively.

The conductivity profile of the interior (Fig. 5) is adopted from a theoretical model developed by Liu (2006). The conductivity of the atmosphere is derived from the electron density, pressure, temperature, and composition data collected by several spacecraft. The conductivity of the lower atmosphere is

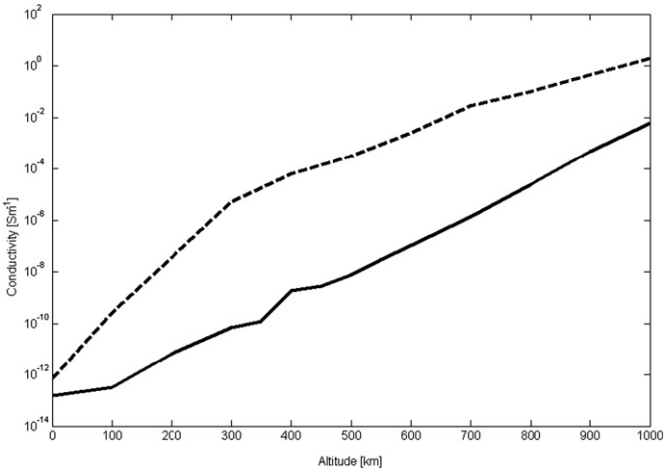

Fig. 5. Conductivity profiles of Jupiter (solid) and Saturn (dashed) atmospheres.

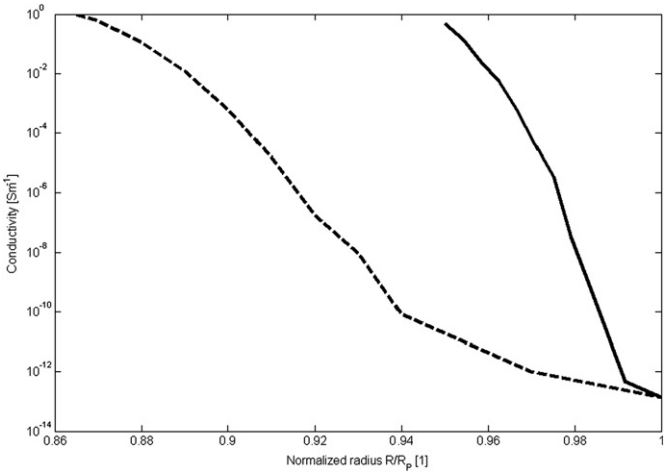

Fig. 6. Conductivity profiles of Jupiter (solid) and Saturn (dashed) interiors.

interpolated between that of the lower ionosphere and that of the upper interior (Figs. 5 and 6). Majeed et al. (2004) present an overview of the ionosphere–thermosphere of the giant planets, which is a useful reference for comparison.

Lightning activity is present on Jupiter and Saturn; it has been observed with Voyager 1, Galileo and Cassini (Gurnett et al., 1979; Lanzerotti et al., 1996; Fischer et al., 2006) and is probably the major source of energy.

4.5. Titan, Europa and Io

This work deals not only with planets but also with a few moons. Titan, Europa, and Io environments are all different and unique. Therefore, studying the propagation of ELF waves and the resonance that can develop in their cavities is an interesting exercise.

The conductivity profile of the atmosphere of Titan was directly measured with mutual impedance and relaxation probes during the descent of the Huygens Probe from an altitude ∼140 km down to the surface (Hamelin et al., 2007). The conductivity is unknown at higher altitude, up to ∼750 km where Voyager and Cassini spacecraft have measured the electron

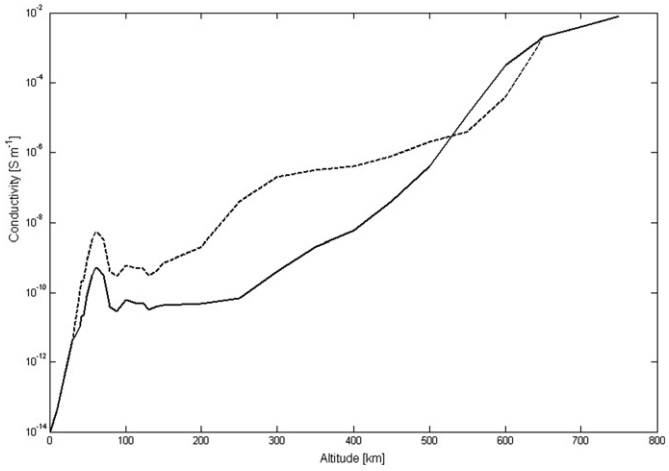

Fig. 7. Atmospheric conductivity profiles based on the Huygens preliminary results at altitudes less than 150 km, for high (H, solid) and low (L, dashed) aerosol concentrations. The profiles match the electron conductivity derived from the measurements of Cassini and Voyager at ∼750 km.

density (e.g. Wahlund et al., 2005). The conductivity profile (Fig. 7) is therefore interpolated between 140 and 750 km, in an altitude range where aerosols play a significant role. The atmospheric density on the surface is ∼4.5 times that on Earth, thus the vacuum approximation is valid for the permittivity. As already mentioned, the relative permittivity and conductivity at shallow depths are ∼2 and $\sim 10^{-10}$ S m^{-1} at the Huygens Probe landing site (Grard et al., 2006). The variation of the dielectric parameters with depth is not known but some general assumptions can be made. The temperature of the soil varies between ∼94 K on the surface and ∼176 K at the solid–liquid interface, as suggested by theoretical models (Grasset and Sotin, 1996). In this temperature range the dielectric properties of water ice do not vary significantly, even in the ELF frequency range. Several models predict the presence of water–ammonia ice mixtures (Lunine and Stevenson, 1987; Tobie et al., 2006) and the dielectric properties are more difficult to assess. The composition and porosity of the soil are unknown but a relative permittivity in the range 2–4 is tentatively assumed, which fits that of water ice in the considered temperature and frequency ranges. The concentrations of ionic contaminants are not known and even small quantities can significantly increase the conductivity of the medium.

The existence of an ionospheric layer and, therefore, of a cavity does not necessarily imply that Schumann resonances develop. The jovian moons, Io and Europa, possess an ionosphere (Kliore et al., 1974, 1997) and, alike for Titan, models also predict the existence of a subsurface ocean on Europa, the moon that displays the smoothest surface in the Solar System. However, the electron density in the thin atmosphere of Europa is such that it prevents the development of resonant states, and the subsurface cannot be explored with ELF waves. In fact, the conductivity is high and ELF waves are damped. The subsurface of this Galilean satellite can however be accessed in another way. The electrical conductivity of the ionosphere and interior prevents the penetration of the time varying fraction of the external magnetic field, a phenom-

Please cite this article in press as: F. Simões et al., The Schumann resonance: A tool for exploring the atmospheric environment and the subsurface of the planets and their satellites, Icarus (2007), doi:10.1016/j.icarus.2007.09.020

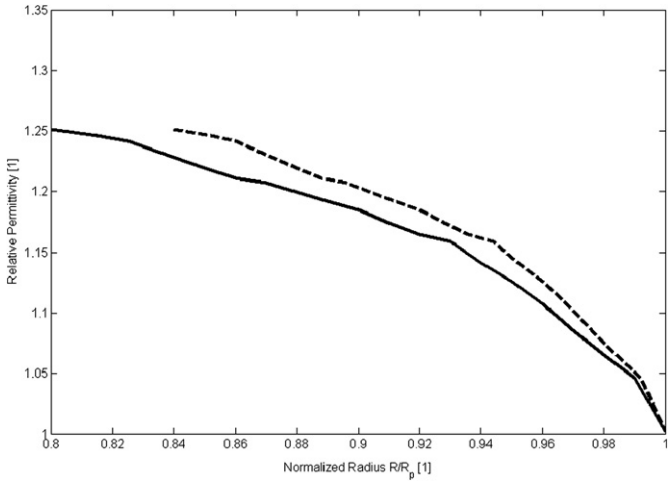

Fig. 8. Permittivity profiles of Uranus (solid) and Neptune (dashed) interiors.

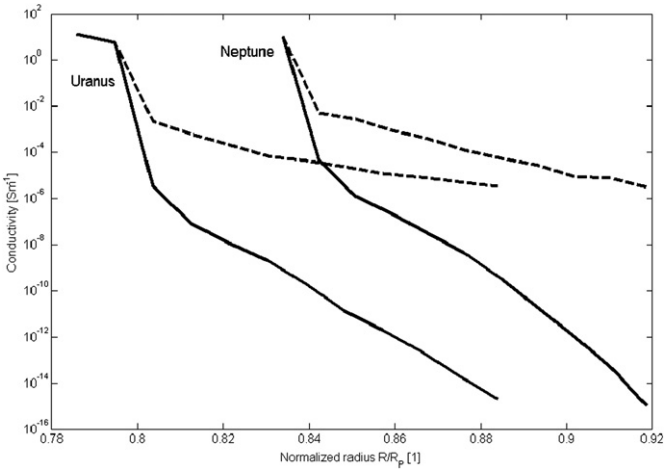

Fig. 9. Conductivity profiles of Uranus and Neptune interiors for gravimetric water contents of 0 (solid) and 15% (dashed).

enon that should in principle reflect the presence of an ocean beneath the surface (Russell, 2000). On Io, volcanic activity is a likely source of energy, but as for Europa, only evanescent waves can be produced because of the high conductivity of its thin atmosphere.

4.6. Uranus and Neptune

The cavities of the uranian planets are quite different from those of Jupiter and Saturn. Their atmospheres are essentially composed of hydrogen and helium (H_2: 0.74 and 0.68, He: 0.26 and 0.32 for Uranus and Neptune, respectively) and the molar fractions are closer to solar abundances than those of the other gaseous giants. Voyager 2 measured the electron density (Lindal et al., 1987; Lindal, 1992) with some discrepancy between ingress and egress, especially in the case of Uranus. Two conductivity profiles are derived for Uranus from the Voyager data sets, based on analogy with Earth and on modeling; in the case of Neptune a single profile is used (Capone et al., 1977; Chandler and Waite, 1986). The eigenfrequencies are not much affected by uncertainties about the atmospheric conductivity because the subsurface contribution is dominant.

The interior of Uranus and Neptune significantly differs from that of the jovian planets. A solid mantle of ices is substituted for the liquid hydrogen metallic mantle of Jupiter and Saturn. Discontinuities in the permittivity profile and in the derivative of the conductivity profile are expected at the solid–gaseous interface (Liu, 2006). The profiles (Figs. 8–10) are evaluated in the same way as for the jovian planets. The water content of the uranian planets is unknown and a concentration of only a few percent could increase the conductivity by orders of magnitude.

As for the jovian planets, though in a less degree of confidence, the Voyager 2 measurements indicate that lightning activity is the major source of electromagnetic energy in the cavities of Uranus and Neptune (Zarka and Pedersen, 1986; Gurnett et al., 1990).

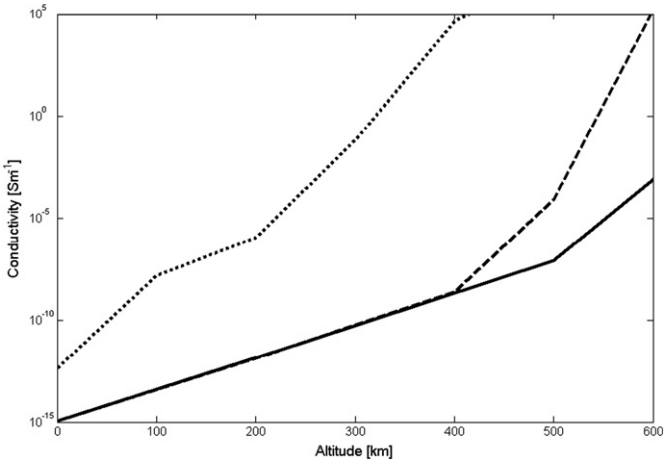

Fig. 10. Atmospheric conductivity profiles of Uranus (solid—ingress; dashed—egress) and Neptune (dotted).

5. Numerical results

Table 1 recapitulates the main geometrical features of the cavities and the corresponding fundamental eigenfrequencies calculated with Eq. (1), where most radii are estimated from osculating orbital data (Woan, 1999). All eigenfrequencies lie about the ELF range; the result given for Titan is less accurate because the relative thickness of its cavity is significantly larger than for the planets. The most probable sources of electromagnetic energy in each cavity are listed in Table 2.

Table 3 shows the numerical results obtained for the different bodies using the finite element method with, in some cases, several cavity configurations. The values obtained by other authors with analytic, semi-analytic and numerical approaches, are also listed for the sake of comparison. Though comparison between our model and other approaches is sometimes difficult or inappropriate, we present a global analysis of the different models. The first conclusion is that analytic and semi-analytic approximations produce less accurate results. However, other interpretation can be made:

Table 1
Configuration and lowest resonance frequency of selected geophysical cavities

Body	R_p [km]	h for $\sigma \sim 10^{-3}$ S m^{-1} [km]	d [km]	h/R_p	Frequency [Hz] [Eq. (1)]
Venus	6052	130	40	0.022	11.2
Earth	6378	100	0	0.016	10.6
Mars	3397	100	10	0.030	19.9
Jupiter	71,493	900	2000	0.013	0.9
Saturn	60,268	600	5500	0.010	1.1
Titan	2575	750	100	0.291	26.2
Uranus	25,559	600 (?)	5000	0.024	2.6
Neptune	24,764	400 (?)	4000	0.016	2.7

Table 2
Major energy sources in various cavities

Body	Electromagnetic source	Reference
Venus	Possibly lightning	Russell (1991); Strangeway (2004)
Earth	Lightning	e.g. Nickolaenko and Hayakawa (2002)
Mars	Possibly dust devils/dust storms	Farrell and Desch (2001); Aplin (2006)
Jupiter	Lightning	Gurnett et al. (1979); Lanzerotti et al. (1996)
Saturn	Lightning	Fischer et al. (2006)
Titan	Possibly lightning/haze	Fischer et al. (2004); Béghin et al. (2007)
Uranus	Likely lightning	Zarka and Pedersen (1986)
Neptune	Likely lightning	Gurnett et al. (1990)

Table 3
The complex frequency of the three lowest Schumann resonances calculated with the finite element model. For the sake of comparison, other results are also given, but all have been obtained with different approaches

Planetary body	Parameters				Computed resonance frequency			Former results	
	Atmosphere	ε_{int} [1]	σ_{int} [S m^{-1}]	d [km]	$n=1$	$n=2$	$n=3$	$n=1$	Reference
Venus	Fig. 2	–	–	0	$9.01+0.56i$	$15.81+0.97i$	$22.74+1.42i$	11.2	Guglielmi and Pokhotelov (1996)
		[5, 10]	Fig. 2—H	150	$8.80+0.91i$	$15.77+1.38i$	$22.67+1.76i$	9	Nickolaenko and Hayakawa (2002)
		[5, 10]	Fig. 2—L	150	$7.95+0.74i$	$14.17+1.20i$	$20.37+1.60i$	10	Pechony and Price (2004)
Earth	Measured values				$7.85+0.79i$	$13.95+1.33i$	$20.05+1.79i$		Nickolaenko and Hayakawa (2002)
Mars	Fig. 3	–	–	0	$8.31+2.19i$	$15.64+4.27i$	$23.51+6.59i$	13	Sukhorukov (1991)
		[5, 10]	10^{-7}	5	$8.28+2.10i$	$15.49+3.66i$	$22.82+5.53i$	8.6	Pechony and Price (2004)
		5	10^{-10}	5	$8.55+2.07i$	$15.93+3.62i$	$23.44+5.49i$	11–12	Molina-Cuberos et al. (2006)
		10	10^{-10}	5	$8.41+2.08i$	$15.72+3.63i$	$23.13+5.49i$		
		[5, 10]	10^{-7}	10	$7.93+2.06i$	$14.93+3.94i$	$22.41+6.04i$		
		5	10^{-10}	10	$8.47+2.03i$	$15.85+3.89i$	$23.68+5.97i$		
		10	10^{-10}	10	$8.20+2.03i$	$15.40+3.89i$	$23.05+5.96i$		
Jupiter	Fig. 5		Figs. 4 and 6		$0.68+0.04i$	$1.21+0.07i$	$1.74+0.10i$	0.76	Sentman (1990)
								0.95	Guglielmi and Pokhotelov (1996)
								1	Nickolaenko and Hayakawa (2002)
Io	Negligible		–			Evanescent wave		–	Nickolaenko and Rabinovich (1982)
Europa	Negligible		–			Evanescent wave		–	–
Saturn	Fig. 5		Figs. 4 and 6		$0.93+0.06i$	$1.63+0.12i$	$2.34+0.18i$	–	–
Titan	Fig. 7—high	3	10^{-9}	100	$13.43+6.25i$	$28.13+10.57i$	$43.93+13.64i$	11–15	Morente et al. (2003)
	Fig. 7—low	3	10^{-9}	100	$19.15+2.27i$	$34.32+3.71i$	$49.48+5.22i$	17–20	Nickolaenko et al. (2003)
								8–10	Yang et al. (2006)
Uranus	Figs. 8–10		Ingress—low water content		$2.44+0.06i$	$4.24+0.11i$	$6.00+0.15i$	–	–
	Figs. 8–10		Ingress—high water content		$1.02+0.25i$	$1.99+0.49i$	$3.03+0.67i$		
	Figs. 8–10		Egress—low water content		$2.47+0.06i$	$4.27+0.11i$	$6.04+0.16i$		
	Figs. 8–10		Egress—high water content		$1.12+0.33i$	$2.17+0.58i$	$3.26+0.8i$		
Neptune	Figs. 8–10		High water content		$1.10+0.54i$	$2.03+0.96i$	$2.96+1.69i$	–	–
	Figs. 8–10		Low water content		$2.33+0.12i$	$4.12+0.22i$	$5.90+0.31i$		

(a) Venus—a vacuum approximation for the cavity only provides a rough estimation of the eigenfrequencies (Guglielmi and Pokhotelov, 1996); the model mentioned by Nickolaenko and Hayakawa (2002) produces more accurate results with par-

Please cite this article in press as: F. Simões et al., The Schumann resonance: A tool for exploring the atmospheric environment and the subsurface of the planets and their satellites, Icarus (2007), doi:10.1016/j.icarus.2007.09.020

ticular surface conditions; Alike the present model, Pechony and Price (2004) have used Borucki et al. (1982) atmospheric conductivity profile (Fig. 2b) and obtained larger eigenfrequencies, indicating that surface losses play an important role in wave propagation.

(b) Earth—the numerical model is validated (Simões et al., 2007) with an experimental conductivity profile and reproduces the measured eigenfrequencies (Nickolaenko and Hayakawa, 2002); however, the computed Q-factors are slightly higher than the experimental values.

(c) Mars—the models of Sukhorukov (1991) and Molina-Cuberos et al. (2006) give higher frequencies than the results of Pechony and Price (2004); the present model uses the same conductivity profile as Pechony and Price (2004) and the results are similar because the PEC boundary depth is small.

(d) Jupiter—rough estimations using Eq. (1) have been calculated by Guglielmi and Pokhotelov (1996) and Nickolaenko and Hayakawa (2002); however, the model developed by Sentman (1990) that places the lower boundary deeper in the planet provides closer results to those of the present model.

(e) Titan—the model of Nickolaenko et al. (2003) predicts a large value for the Schumann resonance, based on a particular conductivity profile. Morente et al. (2003) and Yang et al. (2006) employ different numerical models, transmission line modeling and finite difference time domain respectively, but the same conductivity profile (Molina-Cuberos et al., 2004). According to Yang et al. (2006), the difference between the results is due to the various altitudes adopted for the upper boundary. This hypothesis has been confirmed by Simões et al. (2007) using the present finite element model; improved results taking into account a more realistic conductivity profile based on results from the Cassini–Huygens mission are also reported.

(f) Saturn, Uranus and Neptune—no reference has been found regarding the Schumann resonance in these environments.

All cavities are unique; and must be explored in different ways. Comparing their properties within each group, i.e. rocky/icy bodies and giant planets, is nevertheless quite instructive. For example, the Q-factors and absorption coefficients are derived from the real and imaginary parts of the eigenfrequencies given in Table 3; they provide an insight into the wave propagation conditions in each group of cavities.

On Venus, the nature of the surface drives the quality factor of the cavity ($Q > 5$), which is larger than on Earth for several cavity configurations. When the soil conductivity decreases, the losses are larger and the eigenfrequency and Q-factor are reduced, but this effect is small if the conductivity is larger than 10^{-4} S m^{-1}. The atmospheric conductivity profile at low altitude is unknown but the high neutral density of the atmosphere prevents cavity losses from playing a significant role in ELF wave propagation. In fact, wave attenuation at altitudes below ~40 km can be neglected, like in the Earth cavity.

Contrary to the surface of Venus, whose dielectric properties are assumed to be uniform, the martian regolith appears complex and asymmetric. The ice caps are mostly composed of water ice (Bibring et al., 2004); hence, the surface conductivity is larger at the poles than in the equatorial regions. The models also predict that the regolith is highly depleted in water ice at low latitudes, and that liquid water should be found at a depth increasing from 2 to 10 km, between the equator and the poles (Squyres et al., 1992); the conductivity should therefore vary with depth and latitude. The presence of water and brines should introduce major changes on the reflectivity coefficient. Estimates of the surface conductivity lie in the range 10^{-12}–10^{-7} S m^{-1}. Uncertainties about the subsurface stratigraphy and water content limit our understanding of wave propagation. Several options are therefore considered: PEC on the surface (unlikely); subsurface reflector at 5 and 10 km; subsurface conductivity of 10^{-7} and 10^{-10} S m^{-1}; permittivity in the range 5–10. It is anticipated that the dielectric properties vary with depth and temperature, but it is difficult to quantify this effect. Temperature should nevertheless have a second order effect, compared to surface conductivity.

The eigenfrequencies of a martian cavity with high atmospheric conductivity significantly differ from those calculated with lossless approximation. Wave attenuation is stronger than on Earth and the absorption coefficient is, at least, twice as large. Contrary to expectations, the absence of a perfect reflector on the surface does not necessarily imply higher losses in the cavity. In fact, several parameters have contrasting effects; a larger conductivity increases the losses and a larger permittivity shifts the eigenmodes towards lower frequencies, but a lower cavity radius increases the eigenfrequencies.

Titan has a peculiar environment. A peak in electron density at ~60 km splits the cavity in two concentric shells, and the presence of aerosols influences the propagation of the waves in the cavity (Table 3). The surface low conductivity may lead to the identification of the subsurface liquid ocean predicted by theoretical models. The high concentration of aerosols in the atmosphere increases the extinction coefficient in the infrared and visible domains though it has contrasting effects at low frequencies. In fact, electron attachment to aerosols reduces the atmospheric conductivity and, consequently, also the absorption coefficient. However, the conductivity profile becomes more intricate due to aerosol stratification. Depending upon aerosol concentration, the absorption coefficients and the Q-factors resemble either those of Earth or those of Mars.

The cavities of the gaseous giants are characterized by a smooth transition between the atmosphere and the interior, and the effective inner boundary is located where the skin depth is much smaller than the cavity thickness. In the case of the jovian planets the effective inner boundary is significantly larger than the gas–liquid interface radius. The quality factors for Jupiter and Saturn, $Q \sim 8$, are larger than for Earth. The situation differs for the uranian planets, where several theoretical models are compatible with high or low water content. The absence of water implies large quality factors, of the order of 20 and 10 for Uranus and Neptune, respectively, and increases the Schumann resonance frequencies by a factor of two compared to cavities with high water content. When the water content in the gaseous envelope is ~15%, the Q-factor is reduced by one order of magnitude, the absorption factor increases and wave propagation is hindered.

In the present study, we have neglected several factors that can play an important role, such as the day–night asymmetry and the presence of an intrinsic magnetic field. These contributions are discussed in a forthcoming paper essentially dedicated to Venus.

6. Instrumentation

Instruments that measure electric and magnetic fields in the ELF range provide the measurements from which the eigenfrequencies and Q-factors of the cavity are calculated. These data yield information about the cavity environment: electromagnetic sources, conductivity profile and, in some circumstances, atmospheric composition and subsurface properties.

Like on Earth, the main field components are the vertical (radial) electric and horizontal (azimuthal) magnetic fields. The electric field component can be measured with a vertical dipole antenna. The horizontal component of the magnetic field can be detected with loop antennas. Magnetic antennas usually possess a core, but it is possible to use large loop antennas with multiple turns (Polk, 1969; Burrows, 1978). The output voltage of the magnetic antenna is proportional to the magnetic induction and loop effective area. It is important to avoid mechanical vibrations or ensure, at least, that their frequencies do not fall within the ELF range. An external electrostatic field can easily induce an electric signal in a vibrating antenna and mask the Schumann resonance signal (Béghin et al., 2007). Vehicle vibrations induced by air flow are also observed during balloon campaigns devoted to atmospheric electricity. It is easier to measure Schumann resonances in a steady state than during ascent or descent. Electrostatic and ELF electromagnetic noise decrease instrument sensitivity and limit the measurement threshold to about a fraction of 1 mV. Static modules on the surface or atmospheric vehicles floating at a constant altitude minimize turbulence and antenna vibrations.

The architecture of the antenna is necessarily constrained by the type of mission, namely lander, balloon or descent probe. In the case of surface probes, such as static structures or rovers, a mast is probably most convenient (e.g. Berthelier et al., 2000). For buoyant probes such as balloons and airships, other configurations may be preferred, e.g. flexible magnetic loops attached to—or embedded in—the structure of the vessel, or booms attached to a gondola, as on the Huygens Probe (Grard et al., 1995). Recording the waveform facilitates the data analysis but an onboard spectral processing is generally more convenient due to memory constraints. On Earth, during strong lightning activity and in controlled experimental conditions, up to 13 peaks associated with the Schumann resonance have been identified (Füllekrug, 2005). During stratospheric balloon campaigns, we have observed 7 peaks in a quiet environment at a constant altitude, but only 2 during ascent, which confirms that the vessel trajectory and dynamics impose significant constraints on the measurement.

7. Conclusion

The propagation of ELF electromagnetic waves has been extensively studied in the cavity of Earth, where lightning activity is the major energy source. The same approach can be used for other planetary environments. At present, lightning activity has undoubtedly been detected on Earth, Jupiter and Saturn; it is likely on Uranus and Neptune, and possible on Venus and Titan.

The Schumann resonance has been identified only on Earth. The Titan in situ measurements performed by the Huygens Probe are still under investigation and should confirm whether ELF resonances have been observed or not (Simões et al., 2007). This work recapitulates the models and predictions that have been published for Venus, Mars, Jupiter, Io, and Titan, and extends them to other planets, namely Saturn, Uranus, and Neptune.

Unlike most previous techniques that are based on analytical and semi-analytical approximations, we use a 3D finite element model that includes losses not only in the atmosphere and ionosphere, but also below the surface. Several authors have already proposed the utilization of the Schumann resonance as a tool for investigating the inner boundary of the ionosphere. This work also discusses the suitability of the Schumann resonance for sounding the subsurface of planets and satellites to an appreciable depth when the soil conductivity is lower than $\sim 10^{-6}$ S m^{-1}.

Whenever resonant states develop in planetary cavities, the measurement of Schumann resonance provides useful information about wave propagation conditions. In the case of the rocky planets, Venus and Mars, the contribution of the subsurface brings a minor correction to the eigenfrequencies (Table 3) and, therefore, accurate measurements are required in order to extract any information about the soil properties. A different scenario might occur in the cavities of the giant planets, mainly Uranus and Neptune.

According to theoretical models, the conductivity of the gaseous envelope of the uranian planets is strongly dependent on the water/ice content. Besides, the conductivity of water-depleted and water-rich (∼10–15%) atmospheres may differ by as much as 10 orders of magnitude, which significantly changes wave propagation conditions. In fact, the presence of water in the atmosphere can easily divide the eigenfrequencies by a factor of two (Table 3); the Schumann resonance could therefore be a valuable tool for probing the conductivity profile and, indirectly, estimating the water mixing ratio of the gaseous envelope.

Acknowledgment

The first author is indebted to Alain Péan for fruitful discussions about software and hardware optimization.

References

Abbas, M., 1968. Hydromagnetic wave propagation and excitation of Schumann resonances. Planet. Space Sci. 16, 831–844.

Aplin, K.L., 2006. Atmospheric electrification in the Solar System. Surv. Geophys. 27, 63–108.

Arkani-Hamed, J., 1994. On the thermal evolution of Venus. J. Geophys. Res. 99, 2019–2033.

Balanis, C.A., 1989. Advanced Engineering Electromagnetics. Wiley, New York.

Please cite this article in press as: F. Simões et al., The Schumann resonance: A tool for exploring the atmospheric environment and the subsurface of the planets and their satellites, Icarus (2007), doi:10.1016/j.icarus.2007.09.020

Balser, M., Wagner, C.A., 1960. Observations of Earth-ionosphere cavity resonances. Nature 188, 638–641.

Béghin, C., Simões, F., Karsnoselskhikh, V., Schwingenschuh, K., Berthelier, J.J., Besser, B., Bettanini, C., Grard, R., Hamelin, M., López-Moreno, J.J., Molina-Cuberos, G.J., Tokano, T., 2007. A Schumann-like resonance on Titan driven by Saturn's magnetosphere possibly revealed by the Huygens probe. Icarus 191, 251–266.

Berthelier, J.-J., Grard, R., Laakso, H., Parrot, M., 2000. ARES, atmospheric relaxation and electric field sensor, the electric field experiment on NETLANDER. Planet. Space Sci. 48, 1193–1200.

Bibring, J.-P., Langevin, Y., Poulet, F., Gendrin, A., Gondet, B., Berthé, M., Soufflot, A., Drossart, P., Combes, M., Bellucci, G., Moroz, V., Mangold, N., Schmitt, B., and OMEGA team, 2004. Perennial water ice identified in the south polar cap of Mars. Nature 428, 627–630.

Borucki, W.J., Levin, Z., Whitten, R.C., Keesee, R.G., Capone, L.A., Toon, O.B., Dubach, J., 1982. Predicted electrical conductivity between 0 and 80 km in the venusian atmosphere. Icarus 51, 302–321.

Brace, L.H., Grebowsky, J.M., Kliore, A.J., 1997. Pioneer Venus orbiter contributions to a revised Venus reference ionosphere. Adv. Space Res. 19, 1203–1212.

Burrows, M.L., 1978. ELF Communications Antennas. Peter Peregrinus, London, UK.

Capone, L.A., Whitten, R.C., Prasad, S.S., Dubach, J., 1977. The ionospheres of Saturn, Uranus, and Neptune. Astrophys. J. 215, 977–983.

Chandler, M.O., Waite, J.H., 1986. The ionosphere of Uranus—A myriad of possibilities. Geophys. Res. Lett. 13, 6–9.

Christensen, P.R., Moore, H.J., 1992. The martian surface layer. In: Kieffer, H.H., Jakosky, B.M., Snyder, C.W., Matthews, M.S. (Eds.), Mars. Univ. of Arizona Press, Tucson, AZ, pp. 686–729.

Cummer, S.A., Farrell, W.M., 1999. Radio atmospheric propagation on Mars and potential remote sensing applications. J. Geophys. Res. 104 (E6), 14149–14158.

Farrell, W.M., Desch, M.D., 2001. Is there a martian atmospheric electric circuit? J. Geophys. Res. 106, 7591–7595.

Fjeldbo, G., Sweetnam, D., Brenkle, J., Christensen, E., Farless, D., Mehta, J., Seidel, B., Michael Jr., W., Wallio, A., Grossi, M., 1977. Viking radio occultation measurements of the martian atmosphere and topography—Primary mission coverage. J. Geophys. Res. 82, 4317–4324.

Fischer, G., Tokano, T., Macher, W., Lammer, H., Rucker, H.O., 2004. Energy dissipation of possible Titan lightning strokes. Planet. Space Sci. 52, 447–458.

Fischer, G., Desch, M.D., Zarka, P., Kaiser, M.L., Gurnett, D.A., Kurth, W.S., Macher, W., Rucker, H.O., Lecacheux, A., Farrell, W.M., Cecconi, B., 2006. Saturn lightning recorded by Cassini/RPWS in 2004. Icarus 183, 135–152.

Füllekrug, M., 2005. Detection of thirteen resonances of radio waves from particularly intense lightning discharges. Geophys. Res. Lett. 32, doi:10.1029/2005GL023028. L13809.

Grard, R., Svedhem, H., Brown, V., Falkner, P., Hamelin, M., 1995. An experimental investigation of atmospheric electricity and lightning activity to be performed during the descent of the Huygens Probe on Titan. J. Atmos. Terr. Phys. 57, 575–585.

Grard, R., Hamelin, M., López-Moreno, J.J., Schwingenschuh, K., Jernej, I., Molina-Cuberos, G.J., Simões, F., Trautner, R., Falkner, P., Ferri, F., Fulchignoni, M., Rodrigo, R., Svedhem, H., Béghin, C., Berthelier, J.-J., Brown, V.J.G., Chabassière, M., Jeronimo, J.M., Lara, L.M., Tokano, T., 2006. Electric properties and related physical characteristics of the atmosphere and surface of Titan. Planet. Space Sci. 54, 1124–1136.

Grasset, O., Sotin, C., 1996. The cooling rate of a liquid shell in Titan's interior. Icarus 123, 101–112.

Guglielmi, A.V., Pokhotelov, O.A., 1996. Geoelectromagnetic Waves. Institute of Physics Publishing, London, UK.

Gurnett, D.A., Shaw, R.R., Anderson, R.R., Kurth, W.S., 1979. Whistlers observed by Voyager 1—Detection of lightning on Jupiter. Geophys. Res. Lett. 6, 511–514.

Gurnett, D.A., Kurth, W.S., Cairns, I.H., Granroth, L.J., 1990. Whistlers in Neptune's magnetosphere—Evidence of atmospheric lightning. J. Geophys. Res. 95, 20967–20976.

Hamelin, M., Béghin, C., Grard, R., López-Moreno, J.J., Schwingenschuh, K., Simões, F., Trautner, R., Berthelier, J.J., Brown, V.J.G., Chabassière, M., Falkner, P., Ferri, F., Fulchignoni, M., Jernej, I., Jeronimo, J.M., Molina-Cuberos, G.J., Rodrigo, R., Tokano, T., 2007. Electron conductivity and density profiles derived from the mutual impedance probe measurements performed during the descent of Huygens through the atmosphere of Titan. Planet. Space Sci. 55, 1964–1977.

Justus, C.G., Duvall, A., Keller, V.W., Spilker, T.R., Lockwood, M.K., 2005. Connecting atmospheric science and atmospheric models for aerocapture at Titan and the outer planets. Planet. Space Sci. 53, 601–605.

Kliore, A., Cain, D.L., Fjeldbo, G., Seidel, B.L., Rasool, S.I., 1974. Preliminary results on the atmospheres of Io and Jupiter from the Pioneer 10 S-band occultation experiment. Science 183, 323–324.

Kliore, A.J., Hinson, D.P., Flasar, F.M., Nagy, A.F., Cravens, T.E., 1997. The ionosphere of Europa from Galileo radio occultations. Science 277, 355–358.

Krauss, C.E., Horányi, M., Robertson, S., 2003. Experimental evidence for electrostatic discharging of dust near the surface of Mars. New J. Phys. 5, 70.1–70.9.

Lanzerotti, L.J., Rinnert, K., Dehmel, G., Gliem, F.O., Krider, E.P., Uman, M.A., Bach, J., 1996. Radio frequency signals in Jupiter's atmosphere. Science 272, 858–860.

Lewis, J.S., 1995. Physics and Chemistry of the Solar System. Academic Press, San Diego, CA.

Lide, D.R., et al., 2006. CRC Handbook of Chemistry and Physics, 87th ed. Taylor and Francis, Boca Raton, FL.

Lindal, G.F., 1992. The atmosphere of Neptune—An analysis of radio occultation data acquired with Voyager 2. Astron. J. 103, 967–982.

Lindal, G.F., Lyons, J.R., Sweetnam, D.N., Eshleman, V.R., Hinson, D.P., 1987. The atmosphere of Uranus—Results of radio occultation measurements with Voyager 2. J. Geophys. Res. 92, 14987–15001.

Liu, J., 2006. Interaction of magnetic field and flow in the outer shells of giant planets. Ph.D. thesis, Caltech, California.

Lunine, J.I., Stevenson, D.J., 1987. Clathrate and ammonia hydrates at high pressure-application to the origin of methane on Titan. Icarus 70, 61–77.

Majeed, T., Waite, J.H., Bougher, S.W., Yelle, R.V., Gladstone, G.R., McConnell, J.C., Bhardwaj, A., 2004. The ionospheres–thermospheres of the giant planets. Adv. Space Res. 33, 197–211.

Molina-Cuberos, G.J., Porti, J., Besser, B.P., Morente, J.A., Margineda, J., Lichtenegger, H.I.M., Salinas, A., Schwingenschuh, K.U., Eichelberger, H., 2004. Schumann resonances and electromagnetic transparence in the atmosphere of Titan. Adv. Space Res. 33, 2309–2313.

Molina-Cuberos, G.J., Morente, J.A., Besser, B.P., Portí, J., Lichtenegger, H., Schwingenschuh, K., Salinas, A., Margineda, J., 2006. Schumann resonances as a tool to study the lower ionospheric structure of Mars. Radio Sci. 41. RS1003.

Morente, J.A., Molina-Cuberos, G.J., Portí, J.A., Schwingenschuh, K., Besser, B.P., 2003. A study of the propagation of electromagnetic waves in Titan's atmosphere with the TLM numerical method. Icarus 162, 374–384.

Nickolaenko, A.P., Hayakawa, M., 2002. Resonances in the Earth–Ionosphere Cavity. Kluwer Academic Publishers, Dordrecht.

Nickolaenko, A.P., Rabinovich, L.M., 1982. The possibility of existence of global electromagnetic resonances on Solar-System planets. Kosm. Issled. 20, 82–88 (in Russian).

Nickolaenko, A.P., Besser, B.P., Schwingenschuh, K., 2003. Model computations of Schumann resonance on Titan. Planet. Space Sci. 51, 853–862.

Pätzold, M., Tellmann, S., Häusler, B., Hinson, D., Schaa, R., Tyler, G.L., 2005. A sporadic third layer in the ionosphere of Mars. Science 310, 837–839.

Pechony, O., Price, C., 2004. Schumann resonance parameters calculated with a partially uniform knee model on Earth, Venus, Mars, and Titan. Radio Sci. 39. RS5007.

Pettengill, G.H., Ford, P.G., Chapman, B.D., 1988. Venus—Surface electromagnetic properties. J. Geophys. Res. 93, 14881–14892.

Polk, C., 1969. Relation of ELF noise and Schumann resonances to thunderstorm activity. In: Coronoti, S.C., Hughes, J. (Eds.), Planetary Electrodynamics, vol. 2. Gordon and Breach, New York, pp. 55–83.

Rakov, V., Uman, M., 2003. Lightning. Cambridge Univ. Press, Cambridge, UK.

Russell, C.T., 1991. Venus lightning. Space Sci. Rev. 55, 317–356.

Russell, C.T., 2000. Some simple guidelines to the interpretation of the magnetic signatures seen at the Galilean moons. Adv. Space Res. 26, 1653–1664.

Schumann, W.O., 1952. On the free oscillations of a conducting sphere which is surrounded by an air layer and an ionosphere shell. Z. Naturforsch. A 7, 149–154 (in German).

Sentman, D.D., 1990. Electrical conductivity of Jupiter's shallow interior and the formation of a resonant of a resonant planetary-ionospheric cavity. Icarus 88, 73–86.

Sentman, D.D., 1995. Schumann resonances. In: Volland, H. (Ed.), Handbook of Atmospheric Electrodynamics. CRC Press, Boca Raton, FL.

Shanov, S., Yanev, Y., Lastovickova, M., 2000. Temperature dependence of the electrical conductivity of granite and quartz-monzonite from south Bulgaria: Geodynamic inferences. J. Balkan Geophys. Soc. 3, 13–19.

Simões, F., Grard, R., Hamelin, M., López-Moreno, J.J., Schwingenschuh, K., Béghin, C., Berthelier, J.-J., Besser, B., Brown, V.J.G., Chabassière, M., Falkner, P., Ferri, F., Fulchignoni, M., Hofe, R., Jernej, I., Jeronimo, J.M., Molina-Cuberos, G.J., Rodrigo, R., Svedhem, H., Tokano, T., Trautner, R., 2007. A new numerical model for the simulation of ELF wave propagation and the computation of eigenmodes in the atmosphere of Titan: Did Huygens observe any Schumann resonance? Planet. Space Sci. 55, 1978–1989.

Sohl, F., Sears, W.D., Lorenz, R.D., 1995. Tidal dissipation on Titan. Icarus 115, 278–294.

Squyres, S.W., Clifford, S.M., Kuzmin, R.O., Zimbelman, J.R., Costard, F.M., 1992 . Ice in the martian regolith. In: Kieffer, H.H., Jakosky, B.M., Snyder, C.W., Matthews, M.S. (Eds.), Mars. Univ. of Arizona Press, Tucson, AZ, pp. 523–554.

Strangeway, R.J., 2004. Plasma waves and electromagnetic radiation at Venus and Mars. Adv. Space Res. 33, 1956–1967.

Sukhorukov, A.I., 1991. On the Schumann resonances on Mars. Planet. Space Sci. 39, 1673–1676.

Tobie, G., Grasset, O., Lunine, J.I., Mocquet, A., Sotin, C., 2005. Titan's internal structure inferred from a coupled thermal-orbital model. Icarus 175, 496–502.

Tobie, G., Lunine, J.I., Sotin, C., 2006. Episodic outgassing as the origin of atmospheric methane on Titan. Nature 440, 61–64.

Wahlund, J.-E., Boström, R., Gustafsson, G., Gurnett, D.A., Kurth, W.S., Pedersen, A., Averkamp, T.F., Hospodarsky, G.B., Persoon, A.M., Canu, P., Neubauer, F.M., Dougherty, M.K., Eriksson, A.I., Morooka, M.W., Gill, R., André, M., Eliasson, L., Müller-Wodarg, I., 2005. Cassini measurements of cold plasma in the ionosphere of Titan. Science 308, 986–989.

Williams, E., 1992. The Schumann resonance: A global tropical thermometer. Science 256, 1184–1187.

Woan, G., 1999. The Cambridge Handbook of Physics Formulas. Cambridge Univ. Press, Cambridge, UK.

Yang, H., Pasko, V.P., Yair, Y., 2006. Three-dimensional finite difference time domain modeling of the Schumann resonance parameters on Titan, Venus, and Mars. Radio Sci. 41, doi:10.1029/2005RS003431. RS2S03.

Zarka, P., Pedersen, B.M., 1986. Radio detection of uranian lightning by Voyager 2. Nature 323, 605–608.

Zimmerman, W.B.J., 2006. Multiphysics Modelling with Finite Element Methods. World Scientific, Oxon, UK.

Please cite this article in press as: F. Simões et al., The Schumann resonance: A tool for exploring the atmospheric environment and the subsurface of the planets and their satellites, Icarus (2007), doi:10.1016/j.icarus.2007.09.020

Paper 10

Electromagnetic wave propagation in the surface-ionosphere cavity of Venus

Simões, F., Hamelin, M., Grard, R., Aplin, K.L., Béghin, C., Berthelier, J.-J., Besser, B., Falkner, P., Lebreton, J.-P., López-Moreno, J.J., Molina-Cuberos, G.J., Schwingenschuh, K., Sittler, E.C., Svedhem, H., Tokano, T.

Submitted to Journal of Geophysical Research

Title: Electromagnetic Wave Propagation in the Surface-Ionosphere Cavity of Venus

Authors:

F. Simões[1,*], M. Hamelin[1], R. Grard[2], K.L. Aplin[3], C. Béghin[4], J.-J. Berthelier[1], B.P. Besser[5], P. Falkner[2], J.-P. Lebreton[2], J.J. López-Moreno[6], G.J. Molina-Cuberos[7], K. Schwingenschuh[5], H. Svedhem[2], T. Tokano[8]

Affiliations:

1) CETP/IPSL-CNRS 4, Avenue de Neptune, 94107 Saint Maur, France.
2) Research and Scientific Support Department, ESA-ESTEC, Keplerlaan 1, 2200 AG Noordwijk, The Netherlands.
3) Space Science and Technology Department, Rutherford Appleton Laboratory, Chilton, Oxon, OX11 0QX, United Kingdom.
4) LPCE-CNRS, 3A, Avenue de la Recherche Scientifique, 45071 Orléans cedex 2, France.
5) Space Research Institute, Austrian Academy of Sciences, Schmiedlstrasse 6, 8042 Graz, Austria.
6) Instituto de Astrofisica de Andalucia IAA-CSIC, Camino Bajo de Huetor, 50, 18008 Granada, Spain.
7) Applied Electromagnetic Group, Department of Physics, University of Murcia. Murcia 30100, Spain.
8) Institut für Geophysik und Meteorologie, Universität zu Köln, Albertus-Magnus-Platz, 50923 Köln, Germany.

[*]Corresponding author:

Fernando Simões
Address: 4, Avenue de Neptune, 94107 Saint Maur, France.
Phone: +33 (0)1 45 11 42 73; Fax: +33 (0)1 48 89 44 33.
e-mail: Fernando.Simoes@cetp.ipsl.fr.

Abstract

The propagation of extremely low frequency (ELF) waves in the Earth ionospheric cavity and the properties of the related Schumann resonances have been extensively studied in order to explain their relation with the electric mechanisms at work in the atmosphere. A similar approach can be used to understand the electric environment of Venus and search, in particular, for the evidence of a possible atmospheric lightning activity, which remains a controversial issue. We revisit the available models for ELF propagation in the cavity of Venus, recapitulate the similarities and differences with other planets, and present a full wave propagation finite element model with improved parameterization. The new model introduces corrections for refraction phenomena in the atmosphere; it takes into account the day-night asymmetry of the cavity and calculates the resulting eigenfrequency line splitting. The analytical and numerical approaches are validated against the very low frequency electric field data collected by Venera 11 and 12 during their descents through the atmosphere of Venus. Instrumentation suitable to the measurement of ELF waves in planetary atmospheres is briefly addressed

1. Introduction

The propagation of extremely low frequency (ELF) electromagnetic waves in the cavity bounded by two, highly conductive, concentric, spherical shells, like that approximated by the surface and the ionosphere of Earth, was first studied by Schumann (1952); this phenomenon was first observed by Balser and Wagner (1960). These early works have been reviewed by Besser (2007). When an electromagnetic source pumps energy in a spherical cavity, a resonant state develops whenever the average cavity perimeter approaches an integral multiple of the signal wavelength. This phenomenon is usually known as the Schumann resonance; it provides information about lightning activity and acts as a "global tropical thermometer" (Williams, 1992).

In spite of similarities, the electric environment of Venus is largely different from that of Earth; still, the same approach can be applied to the study of ELF wave propagation (Nickolaenko and Rabinovich, 1982; Pechony and Price, 2004; Simões et al., 2007b). However, the characterization of the Schumann resonance in the cavity of Venus is not straightforward because the low altitude electron density profile and the surface dielectric properties are not known. Compared to Earth, the surface conductivity is expected to be lower; days last longer; the planet lacks a significant intrinsic magnetic field; the atmospheric pressure on the surface is much larger; clouds stretch at higher altitudes. For example, whereas the surface of Earth is generally assumed to be a perfect electric conductor (PEC) because of its high conductivity, the soil of Venus is dry, which entails important subsurface losses. Unlike in Earth cavity, where vacuum permittivity is applicable, the atmosphere of Venus is so dense that refraction phenomena affect wave propagation.

The Schumann resonance has only been positively identified on Earth. In-situ measurements performed on Titan during the descent of the Huygens Probe are still under active investigation, which should confirm whether an ELF resonance has been observed or not (Simões et al., 2007a; Béghin et al., 2007). The Schumann resonance could help confirming the possible existence of lightning in the cavity of Venus, which continues to be a controversial issue (Strangeway, 2004). Radio waves observations that had been interpreted as due to lightning (Ksanfomaliti, 1979; Russell 1991, 1993) have not been widely confirmed by measurements in the visible spectrum, though two optical observations are claimed – one performed onboard Venera 9 (Krasnopol'sky, 1980) and another with a terrestrial telescope (Hansell et al., 1995). Similar radio waves detected by Galileo and Cassini were given different interpretations (Gurnett at al., 1991, 2001). Therefore, the study of ELF wave propagation in the cavity of Venus can provide an independent strategy for the detection and characterization of lightning activity.

The novelty of this cavity model includes: i) eigenfrequency corrections due to surface losses; ii) prediction of significant eigenfrequencies line splitting caused by cavity asymmetry; iii) analysis of the role of atmospheric refractivity upon the electric field profiles; iv) comparison with the VLF electric field profiles measured by the Venera landers.

In this work, we use an algorithm similar to that developed for the cavity of Titan (Simões et al., 2007a) and other planetary environments (Simões et al., 2007b) where resonances can develop. We first recapitulate the theory of Schumann, and describe the numerical method for solving the surface-ionosphere cavity problem. We extend the 3D model to take into account corrections due to a non negligible atmospheric density. After discussing the major input parameters proper to Venus, we estimate,

both theoretical and numerically, the effect of atmospheric refractivity upon ELF wave propagation and compute the eigenfrequencies, Q-factor, and electric and magnetic field profiles of the cavity. Then, we evaluate the expected line splitting introduced by the day-night asymmetry of the cavity. We finally review the implications of the numerical results for wave propagation, validate the simulation technique against the data returned by the Venera landers, in the VLF range, and briefly present possible instruments and operation strategies for probing the electromagnetic environment of Venus cavity.

2. Electromagnetic Wave Propagation in a Spherical Cavity

An ionospheric cavity can be approximated by two conductive concentric spherical shells. A resonance develops whenever the average perimeter of the cavity is, in first approximation, equal to an integral multiple of the wavelength. Hence, the angular resonant frequency is written

$$\omega_m = m\frac{c}{R}, \qquad (01)$$

where R is the radius of the cavity, m=1, 2,… is the eigenmode order and c is the velocity of light in the medium. Including a 3D spherical correction gives (Schumann, 1952)

$$\omega_m = \sqrt{m(m+1)}\,\frac{c}{R}. \qquad (02)$$

In addition to the Schumann or longitudinal resonance modes that, in the case of Venus, lie mostly in the ELF range, there are also, at higher frequencies, local transverse modes along the radial direction. In general, the formalism applicable to ELF wave propagation on Earth is also valid for Venus because the major characteristics of the two cavities are similar.

The development of a general model for calculating Schumann resonances in the cavity of Venus requires the solution of Maxwell equations, which are written

$$\nabla\times\boldsymbol{E} = -\frac{\partial \boldsymbol{B}}{\partial t}, \qquad (03)$$

$$\nabla\times\boldsymbol{H} = \sigma\,\boldsymbol{E} + \frac{\partial \boldsymbol{D}}{\partial t}, \qquad (04)$$

with

$$\boldsymbol{D} = \varepsilon\varepsilon_o\,\boldsymbol{E}, \qquad \boldsymbol{B} = \mu_o\,\boldsymbol{H}, \qquad (05)$$

where $\boldsymbol{E}$ and $\boldsymbol{D}$ are the electric and displacement fields, $\boldsymbol{H}$ and $\boldsymbol{B}$ are the magnetic field strength and flux density, ε_o and μ_o are the permittivity and magnetic permeability of vacuum, and ε and σ are the relative permittivity and conductivity of the medium, respectively.

The system of Eqs. (03-05) can be solved analytically in spherical coordinates for simple cavities, by considering the harmonic propagation approximation and decoupling the electric and magnetic fields (e.g., Nickolaenko and Hayakawa, 2002). Assuming spherical symmetry for the cavity geometry and medium properties, namely neglecting the day-night asymmetry of the ionosphere, and the time dependence of the electromagnetic field, Eqs. (03-04) can be decoupled in the

standard method of separation of variables, which yields (Bliokh *et al.*, 1980)

$$\left\{\frac{d^2}{dr^2}-\frac{m(m+1)}{r^2}+\frac{\omega^2}{c^2}\varepsilon(r)-\sqrt{\varepsilon(r)}\,\frac{d^2}{dr^2}\left(\frac{1}{\sqrt{\varepsilon(r)}}\right)\right\}(rR(r))=0\,, \quad (06)$$

where r is the radial distance, ω is the angular frequency of the propagating wave and $R(r)$ is a function related with the electric and magnetic fields by the Debye potentials (Wait, 1962). Equation (06) gives directly the eigenvalues of the longitudinal and transverse modes, which satisfy either condition, dR(r)/dr=0 or R(r)=0, at both boundaries, respectively. In the limit of a thin void cavity, the eigenvalues of the longitudinal modes converge towards those calculated with Eq. (02).

We shall now define three characteristic parameters of the cavity, namely the cavity quality factor, the atmospheric refractivity and skin depth in the medium.

(1) The quality factor, or Q-factor, measures the wave attenuation in the cavity and is defined by

$$Q_m \equiv \frac{\mathrm{Re}(\omega_m)}{2\,\mathrm{Im}(\omega_m)} \approx \frac{\omega_m^{peak}}{\Delta\omega_m}\,, \quad (07)$$

where *Re* and *Im* are the real and imaginary parts of the complex eigenfrequency, ω_m^{peak} is the peak power frequency of mode m, and $\Delta\omega_m$ is the line width at half-power. The Q-factor measures the ratio of the accumulated field power to the power lost during one oscillation period.

(2) The skin depth (Balanis, 1989),

$$\delta=\sqrt{\frac{2}{\mu_o\varepsilon_o}}\,\frac{1}{\omega\left(\sqrt{1+\left(\frac{\sigma}{\omega\varepsilon_o}\right)^2}-1\right)^{1/2}}\approx\sqrt{\frac{2}{\mu_o\sigma\omega}}\quad,\quad \text{for}\quad \sigma>>\mu_o\omega \quad (08)$$

measures the distance over which the amplitude of the field is divided by *e=2.718*.

(3) Finally, the refractivity, N, is related to the index of refraction, n, according to the definition

$$N\equiv(n-1)\times10^6 \quad (09)$$

and is, in a first approximation, proportional to the gas density.

An atmosphere is a weak dispersive medium, in particular for large wavelengths. The dispersion in a neutral gas is a function of composition and density, i.e. molecular structure, temperature, and pressure (e.g. Bean and Dutton, 1968). We deal first with Earth and then turn towards Venus. Air refractivity is a function of pressure, temperature, and water vapour and is written

$$N_{air}=\frac{273.15}{101325}\,\frac{N_{g,ph}}{T}\,p-\frac{11.27\,p_w}{T}\,, \quad (10)$$

where T [K] is the temperature, and p and p_w [Pa] are the air and partial water vapour pressures. The dispersive term, $N_{g,ph}$, where the indices g and ph refer to group and phase velocities, is given by the empirical relation:

$$N_{g,ph} = K + \frac{K_1}{\lambda^2} + \frac{K_2}{\lambda^4}, \qquad (11)$$

where K=287.6155 is the large wavelength limit, K_1=4.88600 or 1.62887 and K_2=0.06800 or 0.01360, for group and phase refractivity, respectively, and λ is the wavelength in μm (e.g., Ciddor, 1996; Ciddor and Hill, 1999). These values are valid for standard dry air, i.e. 0°C, 101325 Pa, and 0.0375% of CO_2. The following simplifications are possible for ELF waves in the cavity of Venus: (i) The medium is not dispersive, hence K_1= K_2=0; (ii) the weighted mean composition is assumed in the evaluation of the medium refractivity; (iii) the refractivity is proportional to gas density and Equation (10) is strictly valid; (iii) the water partial pressure is negligible and no additional term is due to the presence of SO_2 clouds. Table 1 shows the refractivities of selected gases at radio frequencies.

3. Numerical Model

3.1. Model Description

Earlier cavity models were based upon a simplified parameterization, assumed spherical symmetry and did not take into account subsurface losses, soil properties, and atmospheric refractivity (Nickolaenko and Rabinovich, 1982; Pechony and Price, 2004; Yang et al., 2006). In this work, we solve Eqs. (03-05) and evaluate the resonance modes with a finite element method (Zimmerman, 2006). A preliminary version of this new model has already been applied to several planets, including Venus; this first approach included the properties of the subsurface material, but not the effects of cavity asymmetry and atmospheric refractivity (Simões et al., 2007b). Surface losses can be neglected on Earth, but not on planets like Venus. The continuity conditions must therefore be imposed on the surface whenever the latter does not constitute the inner boundary of the cavity.

The model sketched on Fig. 1 includes the following parameters:

a) *Permittivity profile of the atmosphere* (ε_{atm}). In general, the permittivity of vacuum is assumed for the atmosphere but that is a crude approximation for Venus, because the pressure is high. Thus, a permittivity function that includes air refractivity variation with altitude is introduced.

b) *Conductivity profile of the atmosphere and lower ionosphere* (σ_{atm}). The electron density has only been measured above ~120 km but the conductivity at lower altitude plays an important role in cavity losses. The conductivity profile includes Pioneer Venus and Magellan radio occultation data for altitude higher than 120 km and a theoretical model below 80 km. Values in the range 80-130 km are obtained by interpolation.

c) *Subsurface permittivity* (e_{soil}). Pioneer Venus radar imaging yields an average surface permittvity of 5.0±0.9 for the rolling plains and lowlands, and suggests that the surface is overlaid by at most only a few cm of soil or dust (Pettengill et al., 1988). Campbell (1994) has inferred a permittivity of ~4.15 using Magellan data. We use a constant permittivity value with depth in the range 4-10 to cover different soil compositions.

d) *Subsurface conductivity* (σ_{soil}). The composition of the surface includes many oxides, mainly silicon oxide, and the high temperature of the surface suggests that liquid phase materials are absent. Therefore, we consider surface conductivities in the range 10^{-6}-10^{-4} Sm^{-1} that match many oxide mixtures at ~750 K. The temperature variation with depth is also considered, which leads to specific conductivity profiles.

e) *Height of the ionosphere* (*h*) *and cavity upper boundary* (R_{ext}). The upper boundary of the cavity is located where the skin depth of propagating waves is much smaller than the separation between the shells. Therefore, the upper boundary is placed at *h*~130 km at the subsolar point, where the skin depth is ~1 km for ELF waves. However, the slow rotation of the planet and the absence of a significant intrinsic magnetic field entail a highly asymmetric conductivity profile. In a first attempt and for lack of data, we tentatively adjust the conductivity profile to a height of 2*h* at subsolar point antipodes, which requires a conductivity variation with not only the altitude but also the angle. This conductivity profile is somewhat arbitrary but, at least, it provides a hint about the role of asymmetry on wave propagation. The effect is minor for Earth and corresponds to a small modification of the eigenmodes, but is more marked on Venus and may lead to eigenfrequency splitting.

f) *Depth of the subsurface interface* (*d*) *and cavity lower boundary* (R_{int}). The conductivity of the surface of Venus is expected to lie in the range 10^{-6}-10^{-4} Sm^{-1}, which implies a skin depth at shallow depths larger than 10 km. Therefore, the surface is not suitable as a PEC boundary and the lower shell must be placed lower down where the skin depth is less than, say, 1 km. In general, we shall assume *d*=100 km in the current model.

The model is solved not only in a 2D axisymmetric configuration, but also in 3D. The meshes are composed of ~10^4 and ~10^6 elements in the 2D and 3D, respectively. Comparing the results obtained in 2D and 3D, whenever axial symmetry applies, assesses the algorithm accuracy. The numerical model includes two dedicated algorithms. (i) The eigeinfrequency algorithm gives the complex frequencies of the eigenmodes, from which the Q-factors are derived. This solver uses the ARPACK numerical package based on a variant of the Arnoldi algorithm that is usually called the implicitly restarted Arnoldi method. (ii) The harmonic propagation algorithm solves stationary problems with the UMFPACK numerical package, which computes frequency spectra, identifies propagating eigenmodes, calculates electric and magnetic fields over a wide altitude range and evaluates the influence of source distribution on the propagation modes. The harmonic propagation solver employs the unsymmetrical-pattern multifrontal method and direct LU-factorization of the sparse matrix obtained by discretizing Eqs. (03-05). The numerical algorithms have already been used and validated against the set of parameters applicable to the Earth cavity (Simões et al., 2007a, 2007b). The finite element method and solvers are described by Zimmerman (2006).

3.2. Parameters Description

Our knowledge of Venus has been gathered from ground-based observations and orbiter, flyby, balloon, and lander space missions. The properties of the upper ionosphere are measured with propagation techniques during radio occultation, but the electron density in the lower ionosphere and atmosphere is not known. Atmospheric data has been provided by several missions, including Voyager, Pioneer Venus, and Magellan, but the conductivity of the lower atmosphere is inferred from theoretical models.

The atmospheric density profile is derived using pressure and temperature data obtained above ~34 km with propagation techniques and surface in situ measurements performed by the Venera landers; the profile is then fitted to match the gap at low altitude (e.g. Hinson and Jenkins, 1995; Jenkins, 1995). Considering a carbon dioxide mole fraction of ~0.965, pressure and temperature of ~92 bar and ~736 K on the

surface, the estimated atmospheric density is ~65 kgm^{-3}, which is about 55 times that on Earth. The relative permittivity, shown in Fig. 2, is then obtained by using Eq. (09-11) and the refractivity reference values presented in Table 1. Though refractivity varies with wavelength in the visible and infrared it can be considered constant at lower frequencies. The relative permittivity, the squared value of the refraction index, is ~1.034 on the surface of Venus.

The electron density and, consequently, the conductivity were measured with propagation techniques above ~120 km (e.g., Brace et al., 1997). Therefore, the profiles are only available for the upper part of the cavity and it is used a theoretical model to estimate the conductivity from 80 km down to the surface (Borucki et al., 1982). The conductivity data gap (80-120 km) is fitted between the measured and computed values at high and low altitudes, respectively.

Volcanic processes, and many constructs and plains covered with extensive lava flows, dominate the surface of Venus. The radar altimeter onboard Pioneer Venus has shown that the radar-bright spots could be explained either by a roughness with a scale commensurate with the wavelength of the mapping signal, or by a larger dielectric constant of the surface material due to the presence of moderately conductive minerals such as iron sulphides and oxides. As written above, we use a relative permittivity in the range 4-10, whose values fit Venus analogue materials. There is no evidence of significant water vapor concentration in the atmosphere or on the surface. Therefore, the soil might possess the conductivity of a desiccated igneous medium, such as basalt, at ~750 K. The surface conductivity is supposed to vary between 10^{-6} and 10^{-4} Sm^{-1}, supported by values measured on Earth for similar composition and temperature range (Shanov et al., 2000; Lide et al., 2005). The conductivity profile (Fig. 2) is a function of the interior temperature (Arkani-Hamed, 1994) in the depth range 0-180 km. The dielectric parameters are not dramatically different if high silica content is considered, and soil permittivity does not play a significant role because the soil conductivity is high enough.

To simulate the day-night asymmetry, we consider in a first instance the transformation of conductivity $\sigma(r) \rightarrow \sigma(R_V+(r-R_V)(1-0.5\times|sin(\theta/2)|))$, i.e. the conductivity profile at the subsolar point is stretched until it doubles the scale height at the subsolar point antipodes. The angle θ is measured with respect to the subsolar direction and axial symmetry is nevertheless preserved; R_V is the Venus radius.

4. Wave Propagation in the Atmosphere

4.1 Ray Tracing Approximations

The propagation of a wave in a cavity can be studied with the ray tracing technique, as long as the wavelength is less than the smallest dimension of the cavity and the relative variation of the refractive index is small over a commensurate distance. When either condition is not fulfilled, this approximation is no longer valid and a full wave approach is prerequisite.

The permittivity of the Earth atmosphere is close to that of vacuum and, in first approximation, does not play any significant role in the ELF range. However, the atmospheric conductivity profile and the associated wave attenuation must be taken into account when an extreme accuracy is required in the determination of the Schumann frequencies. The situation is quite different on Venus, due to high atmospheric densities and pressure gradients.

On Earth, tropospheric heterogeneities affect propagation of waves within the broadcasting frequency ranges, which are sometimes detected outside their intended

service area and interfere with other transmitter stations. In particular, the detection of radio waves much beyond the geometric horizon is an evidence of inhomogeneous atmospheric conditions. This phenomenon is related to tropospheric ducting rather than reflection in the ionosphere. A duct acts as a waveguide; it consists of a layer with a relatively larger refraction index, and often develops during periods of stable weather. In a standard environment the density and the refraction index decrease with altitude in the troposphere. When a temperature inversion takes place, i.e. the temperature increases locally with height, a layer with a higher refraction index might result. Radio waves are then partially trapped in the duct and can propagate beyond the horizon (Fig. 3).
At low frequencies, ray tracing provides a crude representation of wave paths in the cavity, and a qualitative understanding of refractivity phenomena. Using simple geometrical optics in spherical symmetry, one defines the refractive invariant along the ray path

$$n\, r \sin(z) = k\,, \tag{12}$$

where r is the radial distance, z the zenith angle and k a constant. A simple, though accurate, geometric derivation of the long time known refractive invariant, which can also be derived from Fermat principle, is presented by Young (2002). Differentiating Eq. (12) for z=90° (horizontal elevation) yields

$$\frac{dn}{dr} = -\frac{n}{r} \Rightarrow \frac{dn}{dr} \approx -\frac{1}{r}\ . \tag{13}$$

Maximum deviations of ~0.5° on Earth, and ~1° on Titan, can be computed from Eqs. (12-13) with a ray tracing algorithm, for light rays with horizontal elevation. The situation is drastically different on Venus because of the strong atmospheric refractivity. In fact, it is possible to find an altitude where light rays with z=90° circle the planet, provided attenuation is negligible.
Figure 4 shows the refractivity gradient in the atmosphere of Venus as a function of altitude, derived from the permittivity profile presented in Fig. 2. It is possible to derive from Eq. (13) the altitude at which a ray with horizontal elevation circles the planet. From $|dn(\rho)/d\rho|=1/(R_v+\rho)$, where we use the transformation $\rho=r-R_V$, we obtain $\rho\approx31.9$ km, which is represented by the horizontal dashed line, in close agreement with the altitude (33 km) derived by Steffes et al. (1994). Rays with horizontal elevation below this threshold altitude are trapped in the atmosphere. The vertical dashed line at 34 km indicates the lowest altitude at which orbiter data are available. Rays departing from the surface with zenith angles larger than ~80° are trapped within the atmosphere. These phenomena have important implications in the ELF electric field profile.

4.2 The ELF Wave Propagation Approximation

The effects of atmospheric refractivity in wave propagation conditions on the ELF range can be assessed solving Eqs. (03-05) in spherical coordinates. Though aiming a different purpose, we use a similar approach developed by Greifinger and Greifinger (1978) and Sentman (1990) to calculate approximate Schumann resonance parameters for a two-scale-height conductivity profile of the Earth ionosphere. Unlike these models that are concerned with exponential conductivity profiles of the cavity, we neglect conductivity and consider an exponential permittivity profile instead. The

relative permittivity profile of the atmosphere of Venus is rather similar to an exponential (Fig. 2). Making the usual separation of variables and considering the Lorentz gauge, the electric and magnetic fields of Eqs. (03-05) can be transformed in the scalar, ψ, and vector, $\boldsymbol{A}$, potentials. Since the vector potential has only a radial component, $\boldsymbol{A}=A_r$, the relation between the scalar and vector potentials can be written

$$\frac{\partial}{\partial r}\psi - i\omega\left(1 - m(m+1)\frac{c^2}{\omega^2 r^2 \varepsilon(r)}\right)A_r(r) = 0\,. \qquad (14)$$

We shall assume an exponential permittivity profile of the form

$$\varepsilon(r) = 1 + \varepsilon_s e^{-(r-R_V)/h_a} \qquad (15)$$

in the range $R_V \le r \le R_V+h$, ε_s=0.034 corresponds to permittivity correction close to the surface, and $h_a \approx$ 15.8 km is the atmospheric permittivity scale height that best fits the data (Fig. 2). Considering, in a first approximation, that the vector potential variation is negligible and differentiating Eq. (14) we find that the electric field has a maximum at an altitude of

$$h_E = h_a \ln\left(\frac{R_V \varepsilon_s}{2h_a}\right). \qquad (16)$$

The electric field maximum is reached, according to Eq. (16), at 29.6 km, whose altitude is similar to the value calculated with ray tracing approximations. The maximum of Eq. (14) is independent of frequency as long as the potential vector can be considered constant; hence, the same maximum is obtained in the ELF and VLF ranges. The correction introduced due to the permittivity profile deviation from an exponential law is calculated numerically.

5. Results and discussion

In this section we compare the results obtained among analytical approximations, full wave propagation numerical models, and ray tracing techniques; we also assess the effects of surface losses and asymmetric cavity configuration upon wave propagation.

The Tables 3 and 4 show the eigenfrequencies for several cavity configurations with lossless and lossy media, respectively. The corrections associated to the atmospheric permittivity profile are small compared to those due to the cavity losses associated with the conductivity profile. Cavity asymmetry partially removes eigenmodes degeneracy, in particular for the lowest engeinfrequency, where splitting can be higher than 1 Hz for a lossy medium. The degeneracy of the eigenmodes is not completely removed because axial symmetry remains; hence partially degenerated lines exist for each eigenfrequency. In fact, each eigenstate m is (2m+1)-fold degenerated for a symmetric cavity but day-night asymmetry partially removes degeneracy and produces m+1 lines, which means all lines but one are doubly degenerated.

On Earth, the upper boundary of the cavity does not have a spherical shape because several processes contribute to ionospheric layer distortion and, therefore, eigenfrequency degeneracy is removed. The most significant contributions are due to day-night asymmetry, polar heterogeneity, and intrinsic magnetic field. According to

numerical calculations made by Galejs (1972), frequency splitting due to day-night asymmetry is small. Consequently, the corrections introduced by the polar heterogeneity and geomagnetic field are dominant. However, despite many attempts to measure Schumann resonance line splitting, the topic is still controversial and no definite answer exists (Nickolaenko and Hayakawa, 2002). On the contrary, the major contribution for line splitting on Venus comes from day-night asymmetry because the ionosphere is highly deformed and other contributions can be neglected in a first order approximation. According to the present model, eigenfrequency splitting of Venus cavity is higher than of Earth due to not only larger cavity asymmetry but also higher Q-factor. Thus, Venus cavity spectrum has distinctive peaks because distance between adjacent splitting lines is larger and higher Q-factors produce better resolved peaks. Therefore, if Schumann resonance is excited in the cavity, frequency splitting due to day-night asymmetry should be unambiguously detected on Venus.

Although the ELF wave propagation and ray tracing models cannot be strictly compared, it is interesting to note that they predict similar altitudes for the maximum of the electric field (29.6 and 31.5 km for analytical and numerical approximations, respectively) and the ray that circles the planet at constant altitude (31.9 km). In fact, as shown in Fig. 5, the presence of a heterogeneous atmosphere refracts waves, which are preferentially focused at a particular altitude. Furthermore, introducing temperature lapse rate inversion, i.e. increasing density with altitude, allows the formation of local electric field maxima in a straightforward manner. The higher difference obtained with the analytical model is due to considering an exponential permittivity profile, which is only valid in a first approximation.

Alike on Earth, the thickness of the cavity is little with respect to the radius and, therefore, the electric field horizontal polarization (E_H) is almost two orders of magnitude smaller than the vertical polarization (E_V) (Fig. 6). A different scenario is expected on Titan where $E_H/E_V \sim 0.1$ because of smaller cavity radius and larger surface-ionosphere distance (Simões et al., 2007a).

Figure 7 shows the electric field amplitude at several frequencies in the range 1 Hz – 10 kHz. The electric field profiles are similar and show a peak roughly at the same altitude. The model was also run at higher frequencies but did not provide accurate results. In fact, higher frequencies require a finer mesh, which implies additional memory. This numerical limitation also indicates to what extent atmospheric heterogeneities distort the electric field profile and is useful to assess the extension of atmospheric turbulence.

Figure 8 illustrates the maps of the electric and magnetic fields amplitude distribution as functions of the source-receiver distance. The cavity parameterization is: $R_{int}=R_v$ and $R_{ext}=R_v+h$, where h=130 km, PEC boundary conditions, and the permittivity and conductivity profiles of Fig. 2. The electromagnetic source is a vertical Hertz dipole at an altitude of 50 km, approximated by two spheres, 5 km in radius and distant of 20 km. The dipole is stationary with uniform spectral radiance and arbitrary amplitude in the ELF range. On the maps shown on Fig. 8, frequency is measured along the abscissa and distance between source and receiver along the ordinate; amplitude is given by a color logarithmic scale in arbitrary units, for better visualization. As the source-receiver distance increases, the spectral peak rapidly decays, and the resonance frequency is shifted with distance; the nodes of the electric field correspond to the antinodes of the magnetic field, and vice-versa. Finally, the amplitude of the electric field increases when one approaches the source location or its antipodes; no eigenmodes are observed in various sectors where the field amplitude is small. Comparison with similar maps computed for the cavity of Earth shows that the

general features are similar but that the eigenmodes are more clearly identified on Venus. In fact, Venus spectra are sharper and less shifted due to lower losses in the cavity.

The properties of the Venus soil lie between those of the highly conductive regolith of Earth and those of the almost dielectric-like surface of Titan. The surface of Earth can be considered as a PEC boundary, which means the subsurface contribution to the cavity is negligible and soil permittivity can be ignored. On the contrary, the surface conductivity of Titan is extremely low and the surface is no longer the inner boundary, because the skin depth for ELF waves is significant. There, the soil complex dielectric properties must be taken into account, which includes not only the conductivity, but also the permittivity, variations with depth. On Venus, the range of the expected surface dielectric properties is such that the soil conductivity must be taken into account, but not the permittivity. Table 4 shows the three lowest complex eigenfrequencies calculated with several cavity configurations and subsurface contributions. The Q-factor can be calculated using Eq. (7), which yields values in the order of 8, 6.5, and 5 for configurations A, B, and C, respectively. These values are larger than for Earth, suggesting that ELF waves are less attenuated on Venus. It is interesting to compare the results obtained for the configurations B and C; in this case, lower soil conductivity implies higher losses but that is not universal because competing mechanisms can balance each other. The dielectric losses of the medium tend to decrease the Q-factor, whereas the lower inner radius increases the eigenfrequencies, as previously reported by Simões et al. (2007a) for the cavity of Titan.

The Venera Landers 11 and 12 carried a low frequency spectrum analyzer consisting of four channels with central frequencies at 10, 18, 36, and 80 kHz and bandwidths of 1.6, 2.6, 4.6, and 14.6 kHz, respectively. The experimental results (see Figs. 9-10) exhibit the following features: (i) the power spectra on both landers decrease with frequency; (ii) the spectral power increases below 40 km on Venera 11, and between 50 and 30 km on Venera 12; (iii) the noise decreases sharply below 10 km on Venera 11 data; (iv) the noise on both landers significantly decreases close to the surface; (v) the noise shows local maxima in the various channels of both landers in the altitude range 3-8 km for (Ksanfomaliti et al., 1979).

A comparison between the present model predictions and the Venera landers data show that the electric field profiles are generally consistent. The model shows effectively amplitude that is maximum at about 40 km and significantly smaller close to the surface. The maxima at about 5 km in the Venera data could be due to local temperature inversion.

The vertical electric and horizontal magnetic fields can be measured on Venus, like on Earth, with vertical dipole and loop antennas. The architecture of the antennas is often imposed by the mission, and is illustrated by the configurations proposed by Berthelier et al. (2000) for the surface of Mars and that used onboard the Huygens Probe in the atmosphere of Titan (Grard et al., 1995; Falkner, 2004) reveal promising solutions. Waveform recording facilitates data analysis but onboard spectral processing is generally more convenient due to memory constraints. However, the most important parameter is frequency resolution, which should be of the order of 0.1 Hz in order to resolve any line splitting of the eigenfrequency.

Because of vehicle vibrations induced by air flow, it is easier to measure Schumann resonances in a steady state than during ascent or descent. Electrostatic and ELF electromagnetic noise decrease instrument sensitivity and limit the measurement threshold to about a fraction of 1 mV. Static modules on the surface or atmospheric

vehicles floating at a constant altitude minimize turbulence and antenna vibrations. For example, the number of Schumann resonances identified during stratospheric balloon campaigns is lower than in a quiet environment, which confirms that the vessel trajectory and dynamics impose significant constraints on the measurement.

6. Conclusions

The distinctive properties of Venus atmosphere strongly influence the propagation of electromagnetic waves in the cavity. The atmospheric permittivity does not significantly modify the eigenfrequencies because the relative permittivity does not exceed ~1.034 close to the surface, but the density gradient produces a peak on the ELF electric field profile (Fig. 5). Wave attenuation is most likely less than on Earth (Table 4); the surface of Venus is not a PEC boundary, and subsurface losses contribute further to the intricacy of the cavity.

The high refractivity of Venus atmosphere facilitates ducting phenomena and propagation beyond the geometric horizon. In certain conditions, electromagnetic waves can travel at a constant altitude (~31.9 km) because planetary curvature can be balanced by atmospheric refraction (see sketch in Fig. 3). This phenomenon preferentially focus electromagnetic waves at mid altitudes: i) according to our theoretical approximation considering an exponential atmospheric permittivity profile, the electric field maximum is at 29.6 km; ii) the numerical model that uses a more accurate profile predicts 31.5 km. The overall model is roughly consistent with the experimental profile recorded by the Venera Probes (Fig. 9), in particular with the electric field decrease below 10 km (Fig. 10).

The predicted eigenfrequencies are roughly 1 Hz higher on Venus than on Earth and the Q-factors are of the order of 6, which implies a lower attenuation. Despite several attempts to measure line splitting of the Schumann resonance on Earth, there is no clear evidence yet of this phenomenon (see Nickolaenko and Hayakawa, 2002, and references therein). The three major reasons for Schumann resonance splitting at Earth are day-night asymmetry, polar non-uniformity and, most important, the existence of an intrinsic geomagnetic field. On Venus, on the contrary, the day-night asymmetry is clearly the dominant contribution and can remove eigenfrequency degeneracy and split the lines by as much as 1 Hz, depending upon the shape of the cavity (Tables 3 and 4). Besides, the higher Q-factors of Venus cavity provide better resolved peaks that make the detection of line-splitting easier than on Earth.

The addition of electric and magnetic antennas to the payloads of buoyant probes (balloons, airships, and descent crafts) and landers, to measure the vertical and horizontal polarization profiles of ELF electromagnetic fields in the altitude range 0-100 km (Fig. 6), provides a tool for studying wave propagation and atmospheric dynamics in the cavity of Venus. Such investigations would contribute to ascertain the presence of electromagnetic sources in the cavity, solve the issue of lightning on Venus.

Acknowledgements:
TO BE WRITTEN.

References:

Arkani-Hamed, J. 1994. On the thermal evolution of Venus. J. Geophys. Res. 99, 2019-2033.

Balanis, C.A., 1989. Advanced Engineering Electromagnetics. Wiley, New York.

Balser, M., Wagner, C.A., 1960. Observations of Earth-ionosphere cavity resonances. Nature 188, 638–641.

Bean, B.R., Dutton, E.J., 1968. *Radio Meteorology*. Dover Publications, New York, N.Y., US.

Béghin, C., Simões, F., Karnoselskhikh, V. Schwingenschuh, K., Berthelier, J.-J., Besser, B. Bettanini, C., Grard, R., Hamelin, M., Lopez-Moreno, J.J., Molina-Cuberos, G.J., Tokano, T., 2007. A Schumann-like resonance on Titan driven by Saturn's magnetosphere possibly revealed by the Huygens Probe. *Icarus*, 191, 251-266.

Besser, B.P., 2007. Synopsis of the historical development of Schumann resonances, *Radio Sci.* 42, RS2S02, doi:10.1029/2006RS003495.

Bliokh, P.V., Nickolaenko, A.P., and Filippov, Yu.F., 1980. Schumann resonances in the Earth-ionosphere cavity. D. L1. Jones-ed, Peter Peregrinus, Oxford, England.

Borucki, W.J., Levin, Z., Whitten, R.C., Keesee, R.G., Capone, L.A., Toon, O.B., Dubach, J., 1982. Predicted electrical conductivity between 0 and 80 km in the Venusian atmosphere. Icarus 51, 302-321.

Brace, L.H., Grebowsky, J.M., Kliore, A.J., 1997. Pioneer Venus orbiter contributions to a revised Venus reference ionosphere. Adv. Space Res. 19, 8, 1203-1212.

Campbell, B.A., 1994. Merging Magellan emissivity and SAR data for analysis of Venus surface dielectric properties. Icarus 112, 187-203.

Ciddor, P.E., 1996. Refractive index of air: new equations for the visible and near infrared. Applied Optics, 35, 1566-1573.

Ciddor, P.E., Hill, R.J., 1999. Refractive Index of Air. 2. Group Index. Applied Optics, 38, 1663-1667.

Falkner, P., 2004. Permittivity, waves and altimeter analyser for the ESA/NASA Cassini-Huygens Project. Technical University of Graz, Rechbauerstraße 12 A - 8010 Graz, Austria. (PhD Thesis, in German).

Galejs, J., 1972. Terrestrial propagation of long electromagnetic waves, Pergamon Press, New York.

Grard, R., Svedhem, H., Brown, V., Falkner, P., Hamelin, M., 1995. An experimental investigation of atmospheric electricity and lightning activity to be performed during

the descent of the Huygens Probe on Titan, J. Atmos. Terr. Phys. 57, 575-585.

Gurnett, D.A., Kurth, W.S., Roux A., Gendrin, R., Kennel, C.F., Bolton, S.J., 1991. Lightning and plasma wave observations from the Galileo flyby of Venus, Science 253, 1522–1525.

Gurnett, D.A., Zarka, P., Manning, R., Kurth, W.S., Hospodarsky, G.B., Averkamp, T.F., Kaiser, M.L., Farrell, W.M., 2001. Non-detection at Venus of high-frequency radio signals characteristic of terrestrial lightning, Nature 409, 313–315.

Hansell, S.A., Wells, W.K., Hunten, D.M., 1995. Optical detection of lightning on Venus, Icarus 117, 345–351.

Hinson, D.P., Jenkins, J.M., 1995. Magellan radio occultation measurements of atmospheric waves on Venus, Icarus 114, 310-327.

Jenkins, J.M., 1995. Reduction and analysis of seasons 15 and 16 (1991 - 1992) Pioneer Venus radio occulation data and correlative studies with observations of the near infrared emission of Venus, Technical Report. NASA/ARC, Moffett Field, CA.

Krasnopol'sky, V.A., 1980. Lightning on Venus according to information obtained by the satellites Venera 9 and 10, Kosmich. Issled. 18, 429–434.

Ksanfomaliti, L.V., 1979. Lightning in the cloud layer of Venus, Kosmich. Issled. 17, 747–762.

Ksanfomaliti, L.V., Vasil'chikov, N.M., Ganpantserova, O.F., Petrova, E.V., Suvorov, A.P., Filipov, G.F., Yablonskaya, O.V., Yabrova, L.V., 1979. Electrical discharges in the atmosphere of Venus, Sov. Astron. Lett., 5(3), 122-126.

Lide, D.R. et al., 2005. CRC Handbook of Chemistry and Physics, 86th Edition, Taylor and Francis, Boca Raton, Florida.

Nickolaenko, A.P., Rabinovich, L.M., 1982. The possibility of existence of global electromagnetic resonances on solar-system planets, Kosmich. Issled. 20, 82-88.

Nickolaenko, A. P., Hayakawa, M., 2002. Resonances in the Earth-ionosphere cavity. Kluwer Academic Publishers, Dordrecht, The Netherlands.

Pechony, O., Price, C., 2004. Schumann resonance parameters calculated with a partially uniform knee model on Earth, Venus, Mars, and Titan. Radio Sci. 39, doi:10.1029/2004RS003056.

Pettengill, G.H., Ford, P.G., Chapman, B.D., 1988. Venus - Surface electromagnetic properties. J. Geophys. Res. 93, 14881-14892.

Russell, C.T., 1991. Venus lightning, Space Sci. Rev. 55, 317–356.

Russell, C.T., 1993. Planetary lightning, Annu. Rev. Earth Planet. Sci. 21, 43–87.

Schumann, W. O., 1952. On the free oscillations of a conducting sphere which is surrounded by an air layer and an ionosphere shell, Über die strahlungslosen Eigenschwingungen einer leitenden Kugel, die von einer Lutschicht und einer Ionosphärenhülle umgeben ist, Z. Naturforschung A, 7, 149– 154 (in German).

Shanov, S., Yanev, Y., Lastovickova, M., 2000. Temperature dependence of the electrical conductivity of granite and quartz-monzonite from south Bulgaria: geodynamic inferences. J. Balkan Geophys. Soc. 3, 13-19.

Simões, F., Grard, R., Hamelin, M., López-Moreno, J.J., Schwingenschuh, K., Béghin, C., Berthelier, J.-J., Besser, B., Brown, V.J.G., Chabassière, M., Falkner, P., Ferri, F., Fulchignoni, M., Hofe, R., Jernej, I., Jeronimo, J.M., Molina-Cuberos, G.J., Rodrigo, R., Svedhem, H., Tokano, T., Trautner, R., 2007a. A new numerical model for the simulation of ELF wave propagation and the computation of eigenmodes in the atmosphere of Titan: did Huygens observe any Schumann resonance? Planet. Space Sci. 55, 1978-1989.

Simões, F., Grard, R., Hamelin, M., López-Moreno, J.J., Schwingenschuh, K., Béghin, C., Berthelier, J.-J., Lebreton, J.-P., Molina-Cuberos, G.J., Tokano, T., 2007b. The Schumann resonance: a tool for exploring the atmospheric environment and the subsurface of the planets and their satellites. Icarus, 10.1016/j.icarus.2007.09.020.

Steffes, P.G., Jenkins, J.M., Austin, R.S., Asmar, S.W., Lyons, D.T., Seale, E.H., Tyler, G.L., 1994. Radio occultation studies of the Venus atmosphere with the Magellan spacecraft. 1: Experimental description and performance. Icarus 110, 71-78.

Strangeway, R.J., 2004. Plasma waves and electromagnetic radiation at Venus and Mars. Adv. Space Res. 33, 1956–1967.

Wait, J., 1962. Electromagnetic waves in stratified media. Pergamon Press, Oxford, New York, Paris.

Williams, E. 1992. The Schumann resonance: A global tropical thermometer. Science 256, 1184-1187.

Yang, H., Pasko, V.P., Yair, Y., 2006. Three-dimensional finite difference time domain modeling of the Schumann resonance parameters on Titan, Venus, and Mars. Radio Sci. 41, RS2S03, doi:10.1029/2005RS003431.

Young, A.T., 2002. The refractive invariant. http://mintaka.sdsu.edu/GF/explain/atmos_refr/invariant.html, last access in October 2007.

Zimmerman, W.B.J., 2006. Multiphysics modelling with finite element methods, World Scientific, Abingdon, Oxon, UK.

Figures:

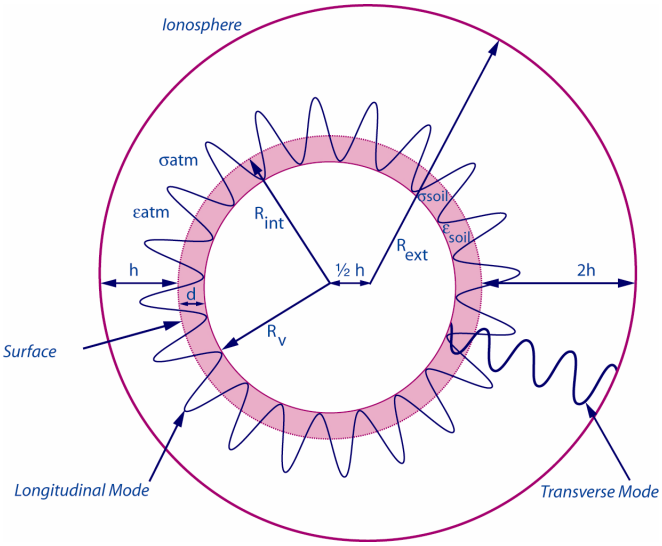

Figure 1: Sketch of the cavity model of Venus.

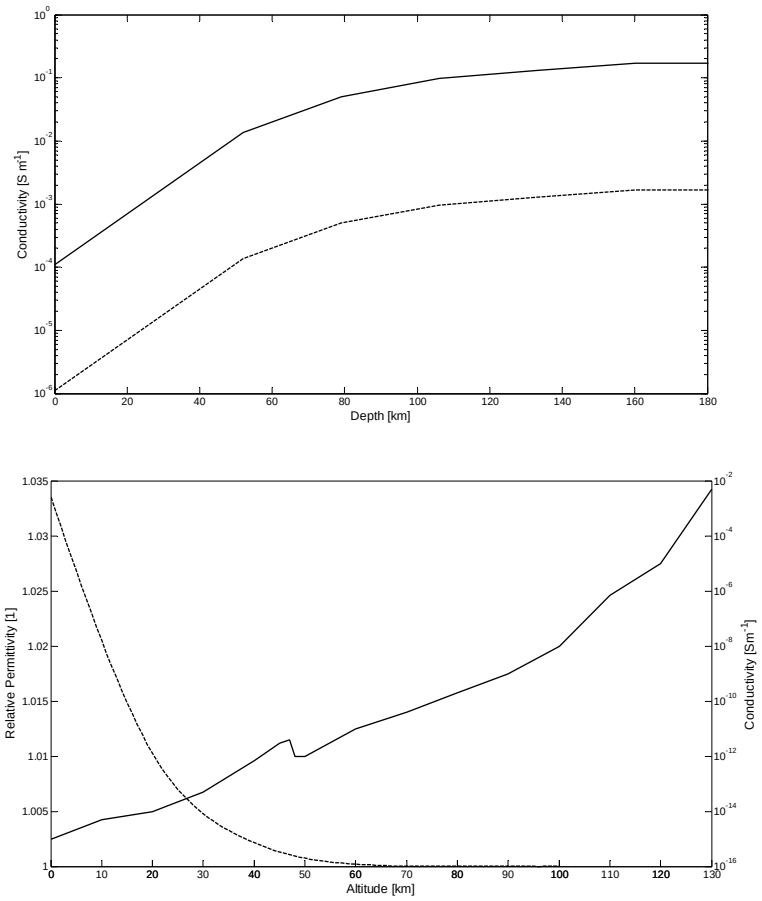

Figure 2: Permittivity and conductivity profiles in Venus's cavity. Top: Subsurface conductivity as a function of depth for high (solid) and low (dashed) soil conductivities; Bottom: conductivity (solid) and relative permittivity (dashed) of the atmosphere.

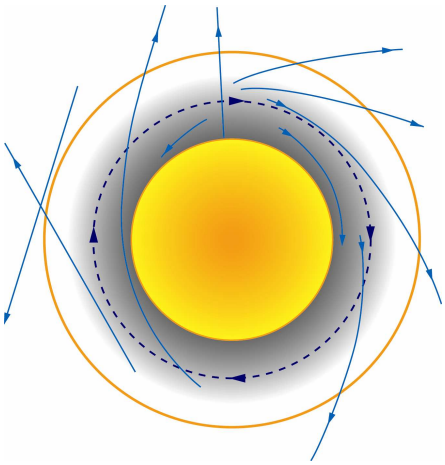

Figure 3: Schematic representation of atmospheric refraction. The yellow line represents the locus where refraction is balanced by curvature, which allows a wave to circle the planet.

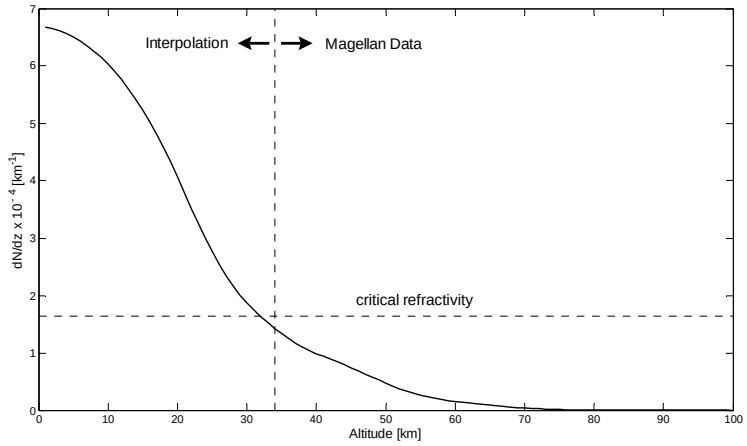

Figure 4: Refractivity gradient in the atmosphere of Venus as a function of altitude; the vertical dashed line marks the separation between the altitudes at which data have been collected from an orbiter (h>34 km) and those at which the information results from an interpolation (h<34 km); the horizontal dashed line identifies the refractivity gradient that balances curvature (curve intersection at 31.9 km).

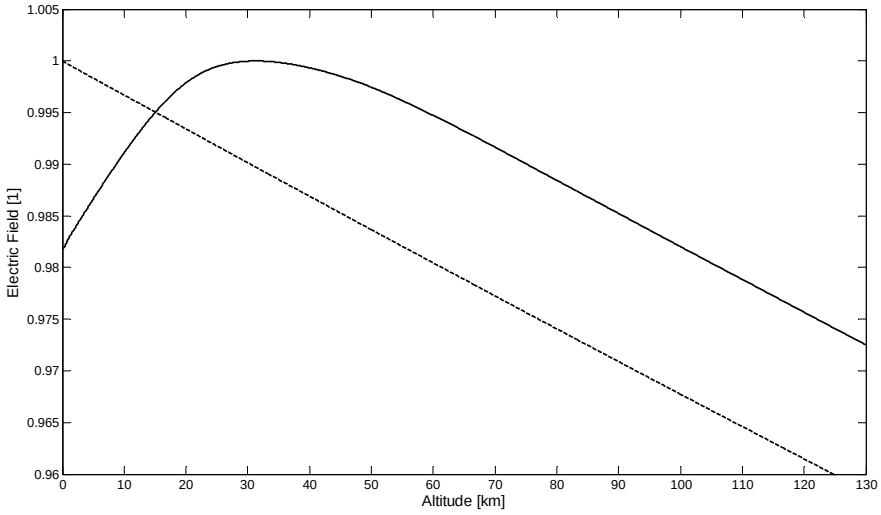

Figure 5: Electric field amplitude as a function of altitude in a lossless cavity with PEC boundaries, where $R_{int}=R_v$, $R_{ext}=R_v+h$, and h=130 km. The permittivity is given by the profile of Fig. 2 (solid line) or is assumed to be that of vacuum (dashed line). The electric field maximum is reached at 31.5 km.

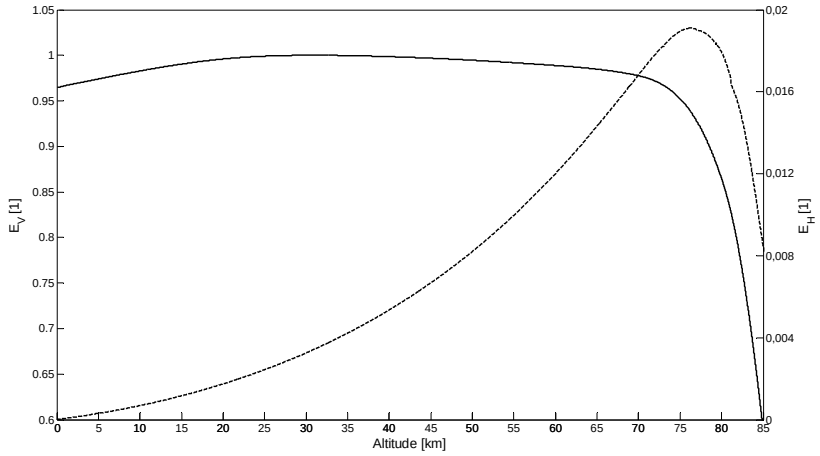

Figure 6: Vertical (E_V, solid line) and horizontal (E_H, dashed line) electric field components as functions of altitude in a cavity where $R_{int}=R_v$, $R_{ext}=R_v+h$, and h=130 km, PEC boundary conditions, and permittivity and conductivity profiles of Fig. 2. The values are normalized with respect to the electric field at 31.5 km.

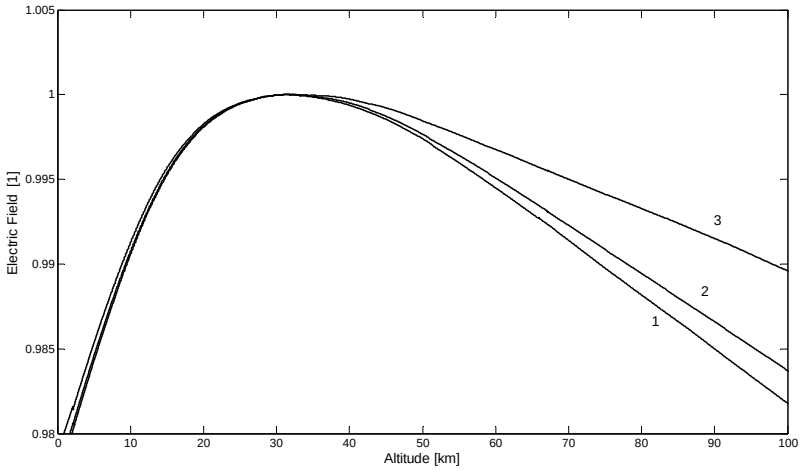

Figure 7: Electric field, in arbitrary units, as a function of altitude for various frequencies: (1) 1-100 Hz; (2) 1 kHz; (3) 10 kHz. The electric field maximum is located at approximately 31.5 km for all frequencies. The cavity configuration is the same as in Fig. 5.

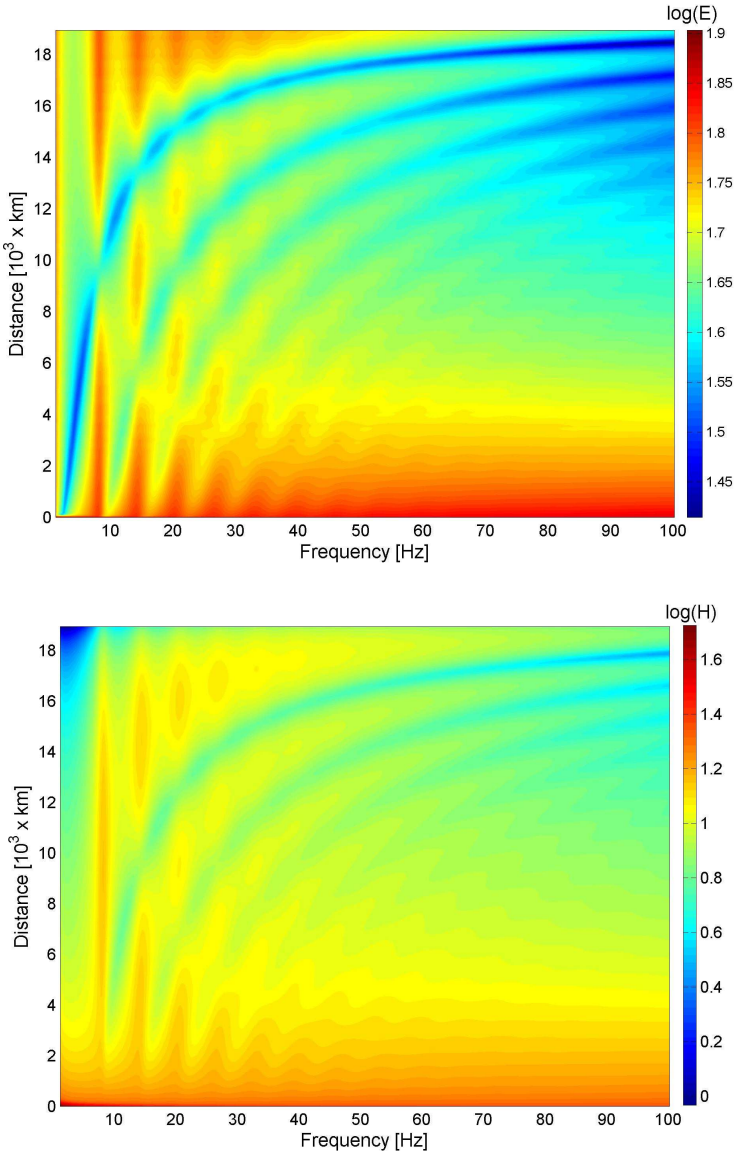

Figure 8: Maps of electric top) and magnetic (bottom) fields in the ELF range as functions of frequency and source distance with the cavity configuration of Fig. 6. Field amplitudes are in arbitrary units.

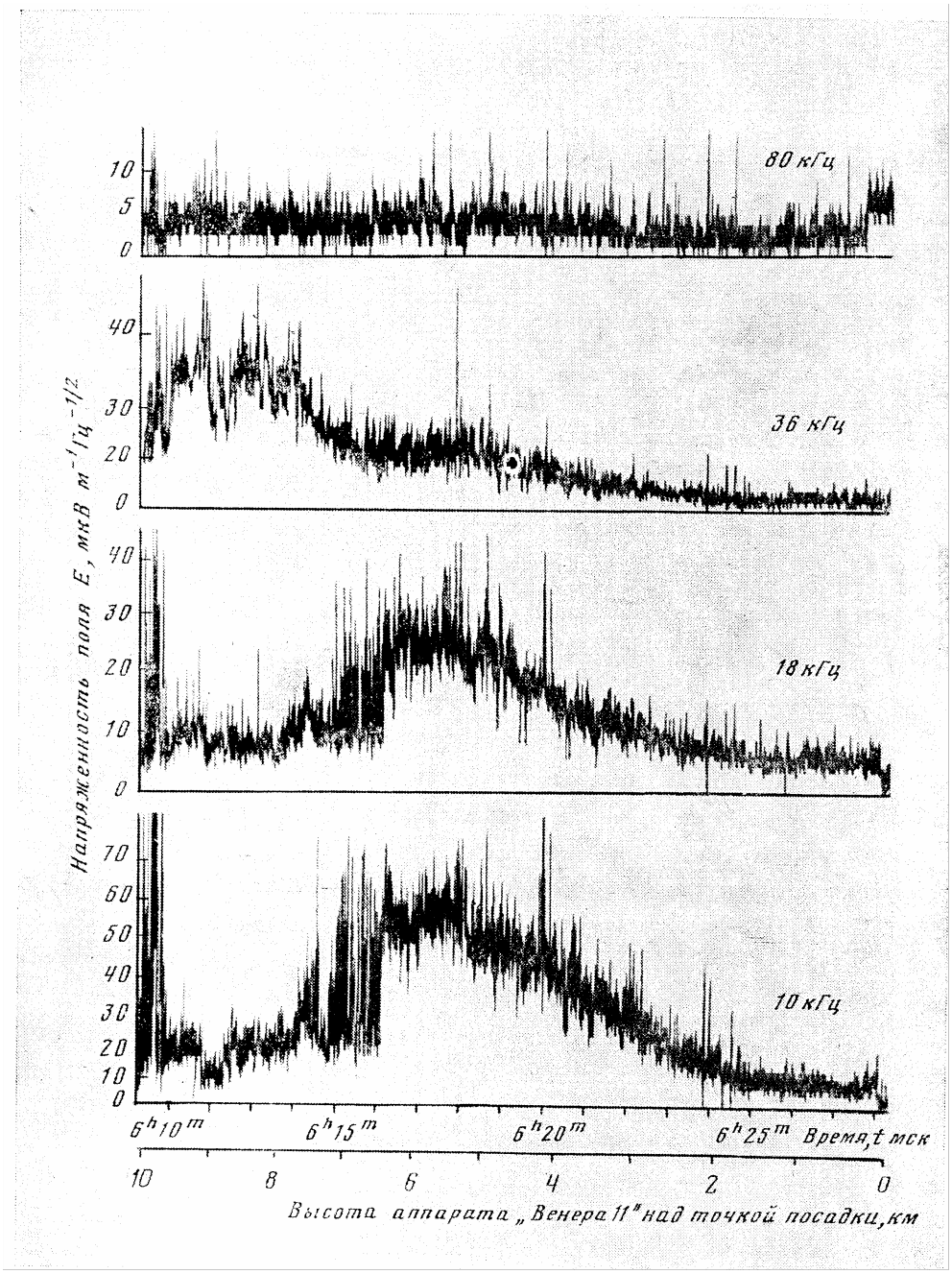

Figure 9: Electric field measurements performed by Venera 11 in the altitude range 0-10 km (after Ksanfomaliti et al., 1979).

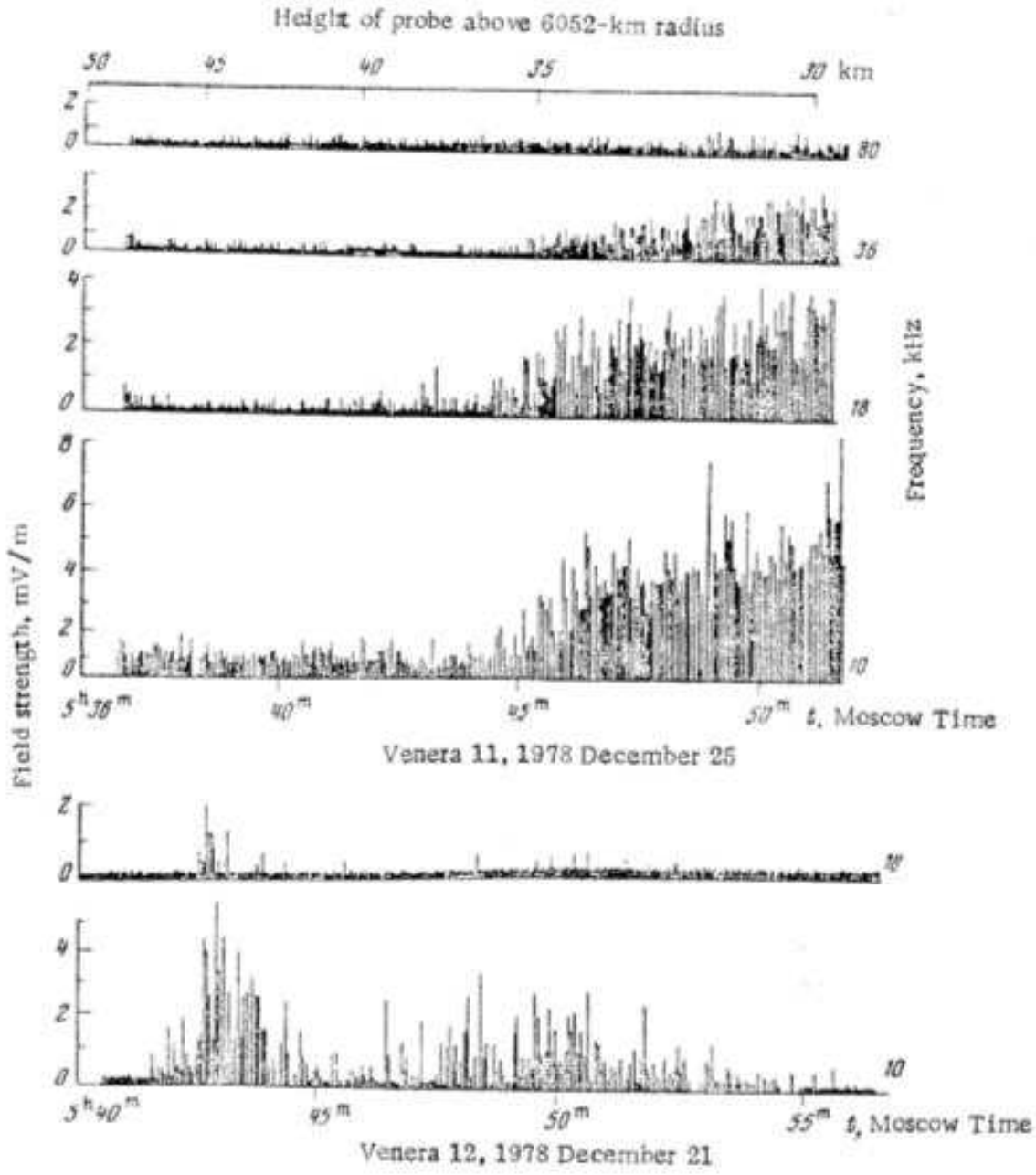

Figure 10: Electric field measurements performed by Venera 11 (top) and 12 (bottom) in the altitude range 30-50 km (after Ksanfomaliti et al., 1979).

Tables:

Gas	ELF Refractivity
N_2	294
O_2	266
CO_2	494
H_2O vapor	61 [1)]
SO_2	686 [2)]
Earth dry air 78% N_2 + 21% O_2	288
Venus atmosphere (96.5% CO_2 + 3.5% N_2)	487

Table 1: Refractivities measured and/or evaluated for radio waves at 0°C and 1 atm, except for **1)** 20°C, 1.333 kPa and **2)** 589.3 nm. Values inferred from Lide et al. (2005).

Altitude [km]	Environment	ELF Refractivity
0	736 K, 92 bar	16600
32 (critical refraction)	465 K, 7 bar	2070
49.5	340 K, 1 bar	370

Table 2: Refractivity of the atmosphere of Venus at various altitudes for 736 K and 92 atm on the surface, which correspond to a density of about 65 kg m^{-3}.

Configuration	1st eigenfrequency [Hz]	2nd eigenfrequency [Hz]	3rd eigenfrequency [Hz]
A	11.15	19.31	27.31
B	11.03	19.11	27.02
C	11.01	19.07	26.97
D	10.89 (2×) 11.07	18.95 (2×) 18.99 (2×) 19.07	26.82 (2×) 26.85 (2×) 26.88 (2×) 26.92

Table 3: Eigenfrequencies for several lossless cavity configurations, with $R_{int}=R_v$ and $R_{ext}=R_v+h$, where h=130 km, and PEC boundary conditions. (A) using Eq. (02); (B) void cavity; (C) atmospheric permittivity profile given by Fig. 2; (D) asymmetric cavity with the atmospheric permittivity profile of (C).

Configuration	1st eigenfrequency [Hz]	2nd eigenfrequency [Hz]	3rd eigenfrequency [Hz]
A	9.13+0.62*i*	16.22+1.01*i*	23.22+1.32*i*
B	8.85+0.75*i*	15.79+1.21*i*	22.70+1.62*i*
C	8.11+0.94*i*	14.61+1.51*i*	21.11+2.04*i*
D	(2×) 9.28+0.34*i* 10.61+0.19*i*	(2×) 15.53+0.62*i* 17.28+0.23*i* (2×) 17.93+0.52*i*	(2×) 21.48+0.95*i* (2×) 24.71+0.64*i* (2×) 24.93+0.87*i* 25.07+0.61*i*

Table 4: Eigenfrequencies for several cavity configurations as functions of subsurface properties and medium losses; with $R_{int}=R_v-d$ and $R_{ext}=R_v+h$, and h=130 km. Atmospheric permittivity and conductivity profiles are those of Fig. 2. (A) Symmetric cavity and d=0 (PEC surface); (B) d=100 km and high conductivity subsurface profile; (C) same as (B) but with low conductivity subsurface profile; (D) asymmetric cavity with d=0 and conductivity profile function of radius and angle (see text for details).

Paper 11

Detection and characterization of ice and water deposits on Mars by means of mutual impedance probes on surface and subsurface vehicles

Trautner, R., Simões, F.

Proceedings of the Second European Workshop on Exo-Astrobiology
ESA SP-518, 319-322

DETECTION AND CHARACTERIZATION OF ICE AND WATER DEPOSITS ON MARS BY MEANS OF MUTUAL IMPEDANCE PROBES ON SURFACE AND SUBSURFACE VEHICLES

R. Trautner[(1)], F. Simões[(1)]

[(1)] Space Science Department, ESA/ESTEC, 2200 AG Noordwijk, The Netherlands
E-mail: Roland.Trautner@esa.int, Fernando.Simoes@esa.int

ABSTRACT

In the field of Astrobiology, water is generally seen as one of the most important ingredients that allow the development of life. This is also valid for Mars, where recent research suggests the presence of considerable amounts of water in the Martian subsurface. The expected electrical characteristics of Martian material / ice mixtures are recapitulated. We introduce the design features of Mutual Impedance (MI) probes. Assumptions and methods used for model calculations are explained, and simulation results are presented. MI probe architectures for surface mapping and subsurface characterization are suggested, and strategies for identifying promising sampling locations are discussed.

1. INTRODUCTION

Mutual Impedance (MI) probes allow to measure the complex permittivity (conductivity and dielectric constant) of materials [1, 2]. An alternating current is injected into the material of interest using a set of transmitter electrodes, and the signal magnitude and phase shift is measured by means of receiver electrodes and associated electronics. The measurement result allows - in conjunction with the results from measurements in air or vacuum - to derive the complex permittivity of the material. MI probes can be designed for a large frequency range (few Hz to MHz). The geometry of the electrode array is not important, however it must remain constant in order to allow precise measurements. The measurement principle and its performance have been demonstrated successfully in laboratory and field tests [3], and flight instruments for atmospheric and surface investigation have been developed for the Huygens [4] and Rosetta Lander missions.

In the field of Astrobiology, water is generally seen as one of the most important ingredients that allow the development of life [5]. Mutual Impedance probes allow the detection of water in solid or liquid form by identifying it from its electrical signature. This is also valid for Mars, where recent research suggests the presence of considerable amounts of water in the Martian subsurface [6].

2. WATER ON MARS

The presence of liquid water in pure form is not likely on Mars due to the low surface and subsurface temperatures. Highly concentrated brines can have exceptionally low freezing points, and brines with freezing points lower than Mars average surface temperatures (-65 °C) are found on Earth [7]. Brines would have a very high conductivity and should therefore be easily detectable with electromagnetic methods. The electrical conductivity of Martian surface materials is expected to be very low. Oelhoeft et al. [8] estimate dry regolith conductivities of 10^{-9} to 10^{-10} Sm^{-1} for frequencies around 1 kHz based on measurements of lunar materials. For similar materials consisting of grains carrying a few monomolecular layers of water, a conductivity of 10^{-8} to 10^{-9} Sm^{-1} is estimated for the same frequency range. At ELF, where the signature of water is more pronounced, the conductivities are expected to be 1-2 orders of magnitude lower. When the water concentration exceeds 1-2% by mass (corresponding to a few monomolecular layers) a frequency and temperature dependence can be measured. Measurements performed by the Mars Odyssey spacecraft have revealed the presence of large amounts of hydrogen in the Martian soil especially north and south of 50-60 deg latitude [9, 10]. The hydrogen observed by the instruments is generally interpreted as the signature of large subsurface ice deposits. Models developed by Boynton et al. [6] suggest layered structures, consisting of an ice-bearing lower layer containing 35±15% of H_2O, and a surface layer containing 1-2% of H_2O. The thickness of this surface layer decreases towards higher latitudes. These water mass concentrations imply a subsurface material that is 60% ice by volume (ranging from 40 to 73%) for an assumed non-ice component of 2.5 gcm^{-3}. The conductivity of pure ice at –60° C is in the order of 10^{-7} Sm^{-1} [11]. Ice can be identified due to its particular complex conductivity signature not only in pure form but also in much lower concentrations [12].

3. LINEAR ARRAY MI PROBE

MI probes measure the complex permittivity of materials in a volume that is determined by the dimensions of the electrode array. If the electrode array is placed on a surface, the instrument will measure the properties of shallow subsurface materials when the array is small. A larger array will be sensitive to larger depths, and will allow the detection of buried layers consisting of materials that have different electrical properties. If both geometries are integrated into the same electrode array using multiple transmitter or receiver electrodes, it is possible to estimate the depth of an interface layer in the subsurface (as long as it is sensed with one of the array configurations) and estimate its electrical properties. For the simulations described in the next section, we assume a linear electrode array that is placed on a surface. Such an array could be ejected by a stationary lander, or trailed behind a mobile platform such as a rover.

4. SIMULATION MODELS

In order to assess the sensitivity of a MI instrument employing a surface array, a 2D simulation is presented, which allows the identification of the most favourable configuration for the assembly of the transmitters and the receivers. We have implemented a fully analytical model that cannot represent complex permittivity distributions, but allows a qualitative assessment of the MI probe sensitivity to subsurface interfaces. The model is based on the image method in the quasi-static approximation [13] and includes three lossless medium layers with different permittivity values (vacuum, dry soil, and soil/ice mixture).
A parallel circuit consisting of a resistor and a capacity can represent the medium between two equipotential surfaces generated by the transmitter current. The current carried by the resistor can be described by

$$|i_r| = u * \frac{s * A}{l} \qquad (1)$$

where u represents the potential difference between the surfaces, A and l represent the dimensions of a representative plate capacitor, and s is the electrical conductivity. The capacitor current can be described by

$$|i_c| = u * w * \frac{e_0 * e_r * A}{l} \qquad (2)$$

where $?$ is the angular frequency, and e_r and e_0 are the relative permittivity and the permittivity of vacuum, respectively. In order to allow the application of the image method for the qualitative assessment of the depth sensitivity, the condition

$$|i_c| > |i_r| \qquad (3)$$

should be fulfilled. Using the conductivity data from [7], this assumption is valid.
All the charge distributions considered in the model are linear and uniform. Inhomogeneous charge distributions have also been considered, but the results have shown significant differences only at positions very close to the charges.
By using the image method for point charges and adding the individual potential contributions, we obtain the 2D potential function. By comparing the single and double interface layer results, it is possible to determine the potential perturbation due to the water mixture layer.
The relative permittivity values used in the model are 1, 3, and 20, for vacuum, dry Martian regolith, and mixtures of regolith and ice, respectively. The following figures show the potential distribution due to the vacuum/soil and water/ice interfaces.

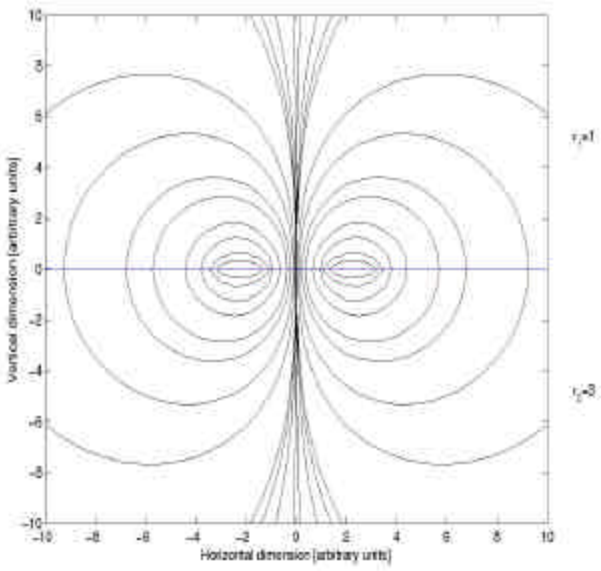

Fig. 1 – Equipotential lines for two linear charge distributions with one interface layer (vacuum/soil).

Figure 1 illustrates the equipotential lines generated by two uniform linear charge distributions in the soil/surface interface.

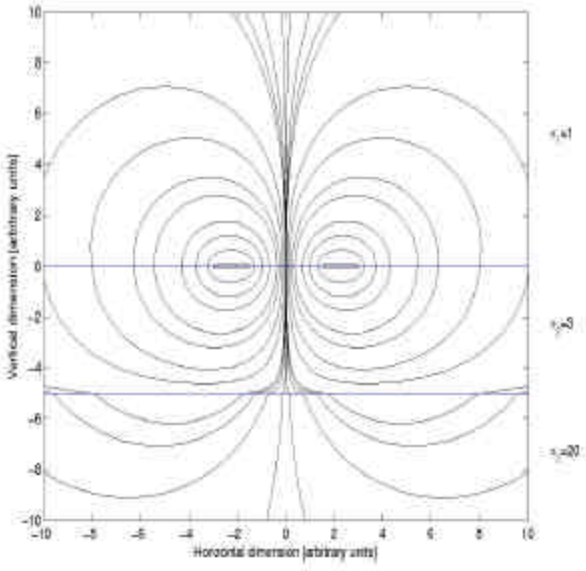

Fig. 2 – Equipotentials representing two linear charge distributions with two interface layers (vacuum/soil and soil/ice mixture).

In Fig. 2 a double interface model is presented, considering a low permittivity interface (vacuum/soil) and a high permittivity interface (soil/icy soil mixture). The equipotential lines are strongly distorted due to the high permittivity layer. Comparing both figures it is possible to see potential distortion due to the icy soil layer. Fig. 3 shows the ratio between disturbed and undisturbed equipotentials. Although the disturbance is stronger in the soil subsurface, there is also a measurable effect on the surface.

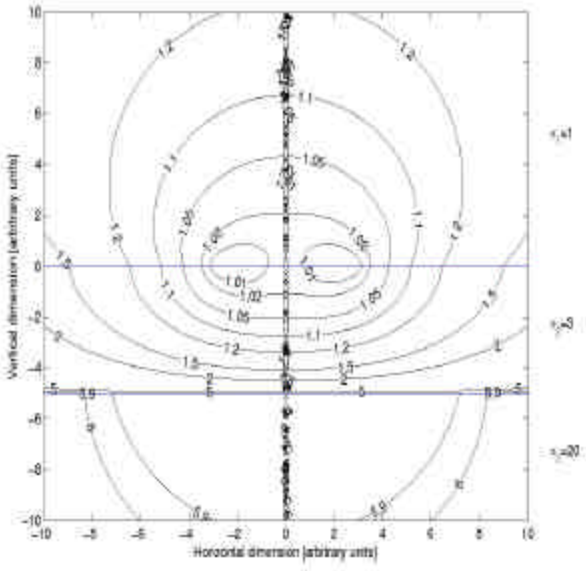

Fig. 3 – Lines show the ratio between the potentials with and without the high permittivity layer.

Using the theoretical image method applied to linear distribution of charges, it is possible to optimize the receiver positions in order to improve the instrument sensitivity with respect to subsurface interfaces.
For a system with losses, a more complex geometry, or a non-uniform layer distribution, the approximation is no longer valid and a numerical model must be used.

5. SIMULATION RESULTS

The simulations confirm that a MI probe can detect interfaces down to a depth that is commensurate with the size of the electrode array. The intensity distribution of the potential perturbation is related to the dielectric constant of the subsurface material and the lower interface depth. Thus, a fit of multiple receiver measurements with the calculated potential distribution will allow to determine the presence of ice in the subsurface and its interface depth in the regolith. The interface depth detection and its accuracy are related to the probe dimensions.
The perturbation effect caused by the subsurface interface is more pronounced in the subsurface, as shown in Fig. 3. If a subsurface tool is deployed in addition to the surface array, it could be equipped with an additional receiver electrode, which would allow the detection of interfaces at greater depth due to the larger potential distortions in the subsurface. If the subsurface tool is equipped with a complete set of transmitter and receiver electrodes, it can be used to determine the detailed structure of the subsurface interfaces. When applied in the context of Astrobiology research, a surface vehicle carrying a MI probe can map the shallow subsurface of a target area by moving along an optimized scan track. The subsurface tool can then be deployed at a promising location, and sampling mechanisms on the tool could retrieve materials for analysis.

6. CONCLUSIONS

Mutual Impedance probes can be used to identify water and ice due to its electrical properties, which are very different to the ones for dry Martian surface materials. The presence of water or ice in Martian regolith increases the conductivity by several orders of magnitude. Water also possesses a comparatively high and frequency dependent dielectric constant, which can be used to identify its presence down to –60º C. Mutual impedance probes operating on the surface are sensitive down to a depth which is commensurate with the dimensions of the electrode array. Using a combination of electrode arrays of different sizes, an instrument can probe the subsurface down to different depths, and allow determining the electrical properties

of various layers. It could therefore characterize layered surface structures similar to those anticipated on Mars based on Mars Odyssey data [10]. One possibility for the implementation of such an array would be in the form of a trailed cable, which carries a number of integrated transmitter and receiver electrodes. A MI probe operated on a vehicle could be used to create maps of subsurface ice abundance, which would be a valuable tool for the selection of sampling locations for the search of evidence for life.

7. REFERENCES

1. Grard, R., A quadrupolar array for measuring the complex permittivity of the ground: application to Earth prospection and planetary exploration, Meas. Sci. Technol., 1, 295-301, 1990.

2. Grard, R., A quadrupole system for measuring in situ the complex permittivity of materials: application to penetrators and landers for planetary missions, Meas. Sci. Technol., 1, 801-806, 1990.

3. Tabbagh A., A. Hesse, and R. Grard, Determination of electrical properties of the ground at shallow depth with an electrostatic quadrupole; field trials on archaeological sites, Geophysical Prospecting, 41, 579-597, 1993.

4. Grard, R., H. Svedhem, P. Brown, P. Falkner, and M. Hamelin, An experimental investigation of atmospheric electricity and lightning activity to be performed during the descent of the Huygens Probe onto Titan, J. Atmos. Terr. Phys., 57, 575-585, 1995.

5. Exobiology in the Solar System & The Search For Life on Mars, Report from the ESA Exobiology Team Study 1997-1998, ESA SP-1231, 1999.

6. Boynton, W.V., et al, Distribution of Hydrogen in the Near Surface of Mars: Evidence for Subsurface Ice Deposits, Science, Vol. 297, 81, 2002

7. Knauth, L.P., et al, Highly conductive eutectic brines rather than water expected in the Martian subsurface, Conference on the Geophysical Detection of Subsurface Water on Mars, Abs. No. 7043, 2001

8. Oelhoft, G.R., et al, Electrical Properties of the surface layers of Mars, Geophysical Research Letters, Vol. 1, No. 3, 1974

9. Feldman, W. C., et al., Global Distribution of Neutrons from mars: Results from Mars Odyssey, Science, Vol 297, 75, 2002

10. Mitrofanov, I., et al, Maps of Subsurface Hydrogen from the High Energy Neutron Detector, Mars Odyssey, Science, Vol. 297, 78, 2002

11. Carmichael, R.S., Practical Handbook of Properties of Rocks and Minerals, CRC Press, Inc., Boca Raton, Florida, 1989.

12. Hamelin, M., R. Trautner, and R. Grard, Detection of near-surface ice on Mars with Electromagnetic Techniques on board future surface vehicles, J. Geophys. Res., accepted, 2002.

13. Wait J. R., *Electromagnetic wave theory*, Harper & Row, New York, 10-17, 1985.

Paper 12

Conductivity and dielectric characteristics of planetary surfaces deduced by Mutual Impedance Probes: from Huygens and Rosetta Lander to Netlanders and future missions to solid planetary bodies

Hamelin, M., Grard, R., Laakso, H., Ney, R., Schmidt, W., Simões, F., Trautner, R.

Proceedings of the 37th ESLAB Symposium **ESA SP-543**, 169-174 (2004)

CONDUCTIVITY AND DIELECTRIC CHARACTERISTICS OF PLANETARY SURFACES MEASURED WITH MUTUAL IMPEDANCE PROBES. FROM HUYGENS AND ROSETTA LANDER TO NETLANDERS AND FUTURE MISSIONS

M. Hamelin[(1)], R. Grard[(2)], H. Laakso[(2)], R. Ney[(1)],W. Schmidt[(3)], F. Simoes[(2)], R. Trautner[(2)]

[(1)] CETP-IPSL, 4 av. de Neptune, 94107, Saint Maur, France
[(2)] ESA/RSSD, ESTEC, Postbus 299, NL-2200 AG Noordwijk ZH, The Netherlands
[(3)] FMI, P.O. Box 503, SF-00101 Helsinki, Finland
Email : Michel.Hamelin@cetp.ipsl.fr
Tel. 0033 (0) 1 4511 4279 Fax 0033 (0) 1 4889 4433

ABSTRACT

Both conductivity and dielectric constant measurements can contribute to the identification of sub-surface materials. They are of great interest in the case of water and ice possibly embedded in other materials due to the high variability with frequency of the dielectric constant of water ice, the high contrast between rocks and liquid water and also the high conductivity generally observed in wet terrains. A first instrument, Permittivity, Waves and Altimetry (PWA-HASI), on the HUYGENS probe should measure the complex permittivity of Titan after landing in January 2005. It consists of a particular mode of the Mutual Impedance (MI) probe designed mainly for atmospheric conductivity measurements. The success of the measurement depends strongly on the configuration of the probe after an uncontrolled landing and in any case the data analysis will be complex as the electrodes are very close to the probe body. A second instrument, the Permittivity Probe (PP-SESAME), on the Rosetta Lander is ready to be launched towards the Guerassimo-Churyumov comet in February 2004. In this case safe landing is a major requirement of the mission. The electrode array, using the lander feet and two other hosting deployable parts, is less influenced by the lander body than in the HUYGENS case. However the perturbing influence of neighbouring sensors has to be suppressed by active methods and such a system is better but again complex. In the Netlander project to the surface of Mars, actually in pause after its phase B study, the opportunity to use long GPR electric antennas deployed on the ground as permittivity sensors has been studied and will be implemented in the design with minor modifications. Our goal is to design the future generation of permittivity probes not considered as 'add on's but fully optimised for their task, making simpler the analysis and providing also the possibility to calibrate the former space pioneer instruments on selected earth targets. In addition, these future probes should be able to detect also the vertical inhomogeneity of the medium (match with a two layer model).
After presenting the actual instruments and projects (on HUYGENS, ROSETTA Lander and NETLANDER), we show the particular interest to use a flat system of electrodes laying on the surface at some distance from the spacecraft body that is particularly well suited for the case of a rover. We will show the design of a prototype actually prepared in CETP to be used in common calibrations with the other instruments in selected well-known terrains.

1. PRINCIPLE AND HERITAGE

The measurement of the planetary surface complex permittivity (electrical conductivity and dielectric constant) vs. frequency has a twofold interest: i) to contribute with other parameters to the identification of the close sub-surface materials without penetrating the surface; ii) to characterize the electrical properties of the planetary surface which control the boundary conditions for electromagnetic waves and fields, including possible DC atmospheric electric currents.
The mutual impedance (MI) probes of today's planetary missions are the heritage of the quadrupolar probes developed in the first half of the XXth century for oil prospecting [1]. The principle is to inject an AC current I in the planar homogeneous ground of relative permittivity ϵ_g through a first dipole and to measure the induced potential by this dipole or by a second dipole to

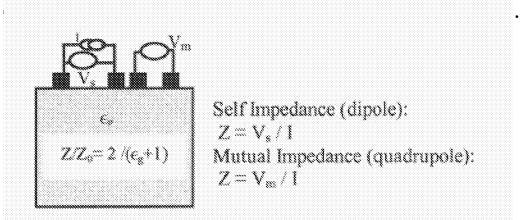

Figure 1. Principle of ground complex permittivity measurement with self and mutual impedance probes.

Proc. 37th ESLAB Symposium 'Tools and Technologies for Future Planetary Exploration', Noordwijk, The Netherlands, 2-4 December 2003 (ESA SP-543, February 2004)

It results from the image theory that the potential on the interface is the same than if the system was immersed in an infinite medium of permittivity equal to the mean permittivity (ϵ_g+1) / 2 of upper and lower materials. As the dipoles are located on the plane interface, if Z_0 is the impedance of the same system in vacuum, the permittivity is:

$$\varepsilon_g = -1 + 2 Z_0 / Z \qquad (1)$$

We point out here that it is unnecessary to make any assumption about the electrode size while they are flat on the interface.

It is worthwhile to use mutual impedance measurements rather than self impedance measurements as they are less sensitive to electrode contact problems and as a perfect contact between the electrodes and the ground is not mandatory [2,3]. We review now the various instruments.

2. HUYGENS (Titan)

The Huygens permittivity probe is part of the Huygens Atmospheric Structure Instrument (HASI). Its primary function is to measure the atmospheric conductivity profile during the descent under parachute in the atmosphere of Titan in January 2005 [4]. After landing on the surface (solid or liquid), it will operate in a special mode to measure the electrical properties of Titan. The operating frequencies are 45 Hz, 90 Hz, 360 Hz, 1440 Hz and 5670 Hz.

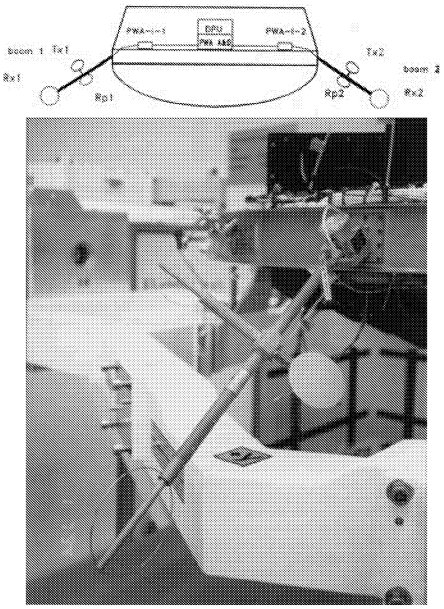

Figure 2. Location of the ring electrodes of the mutual impedance probe on HUYGENS.

In Fig. 2, TX1 and TX2 are the transmitting electrodes; RX1 and RX2 are the receiving electrodes. The electrodes, designed for atmospheric measurements, are rings as seen in the lower panel. It is obvious that they cannot lie all together in the ground plane after landing. A special study has been done to foresee the various cases of landing, in a liquid and on a soft or hard ground [5]. The MI probe will provide measurements complementary to those of the Surface Science Package if the surface is liquid and in any case will contribute to the in situ characterisation of the surface material.

3. ROSETTA LANDER (comet Churyumov-Gerassimenko)

The Permittivity Probe (PP) of SESAME is specially designed for comet surface measurements. The electrode array allows variable geometrical configurations with 3 transmitting electrodes (instead of 2), and because the lander body can rotate relatively to the landing gear. Some information about the inhomogeneity of the landing site can be acquired.
The electrodes are accommodated on other deployable instruments (APX and MUPUS), and on the feet of the lander. So, all electrodes will be in contact with the ground. Active guards have been installed around grounded parts too close to the electrodes to avoid current bypass. The instrument has delicate interfaces and accurate calibrations are required.

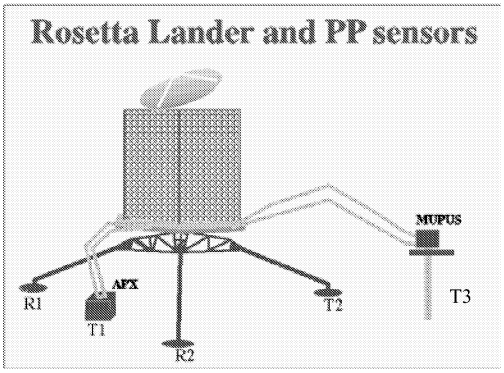

Figure 3. Geometry of the Rosetta Lander PP electrode array.

In the ideal case of a flat ground all electrodes will be in the plane interface. However the lander body which is the electrical reference of the instrument cannot be ignored as it acts as a sixth electrode which does not lie in the interface plane and which has also an electric image in the ground. This is tractable by numerical modelling.

4. GPR-PER FOR NETLANDER (Mars project)

GPR is a ground penetrating radar using 35m long antennas deployed radially from the lander body. The nominal radar frequency is 2 Mhz. An additional mode of operation at 200-800 kHz allows the measurement of the self and mutual impedances of the system of antennas laying on the ground (Fig.4).

The system cannot be described by the usual model of pinpoint charges. However the measurement of the impedances leads to the sub-surface permittivity if the impedance of the system in vacuum is known, either by calibration or numerical modelling (in the Netlander case it has been estimated by numerical modelling, due to the size of the system). The depth range of the measurement is commensurate with the size of the antennas. A small electrode, which can be considered as a pinpoint electrode, will be mounted on the MAG instrument at a short distance from the lander. Owing to the short distance from the lander it will provide a measurement relative to the upper layer of the material.

The whole system would allow differentiating an upper layer of dry regolith from on an underlying ice mixture, which is a representative model of the Martian surface at medium and high latitudes. The permittivity of both media and the thickness of the upper layer could be estimated.

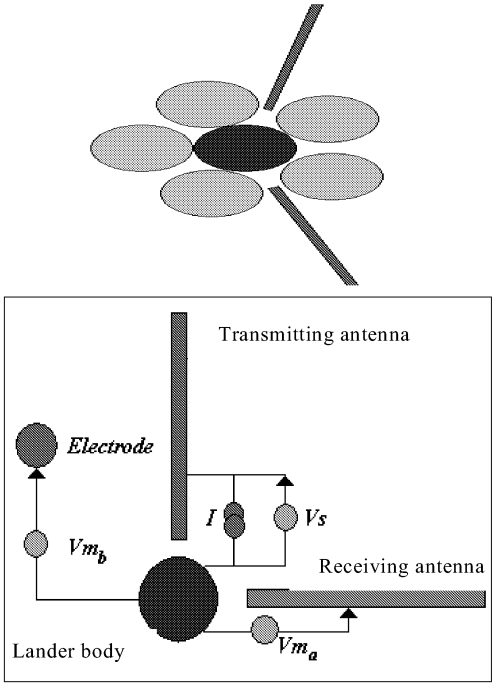

Figure 4. Top: geometrical set-up of GPR antennas (not to scale). Bottom: electric scheme of self and mutual impedance measurements.

5. BEPICOLOMBO MSE (Mercury)

A permittivity instrument on a Mercury lander could consist of a combination of surface and sub-surface electrodes including a mole, an instrument that measures the permittivity in situ [6]. The surface measurements would be perturbed in sunlight by photoelectrons. However, a mobile electrode would help to separate the conductivities of the photoelectron layer and of the surface material.

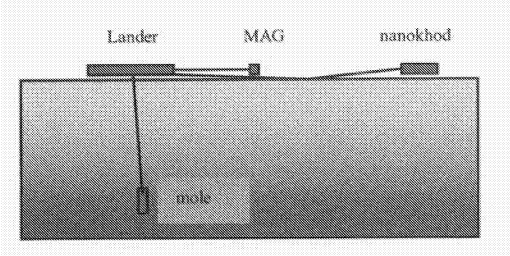

Figure 5. Tentative set-up of a permittivity instrument on BepiColombo.

6. MARS LONG DISTANCE ROVER AND FUTURE MISSIONS

The experience of the previous projects shows some ways to improve the future MI instruments. i) large flat electrodes of any shape can be used if the system can be modelled and reference calibrations in vacuum be performed. This allows a simple derivation of the permittivity and a better performance at low frequencies. If possible the electrode array should be apart from the carrier. ii) active guards shall be used to avoid current losses to grounded parts of close neighbouring instruments. iii) multi-electrode arrays allow investigating several depth ranges to detect possible vertical inhomogeneity. Then, for a rover, mobility along the track gives access to horizontal inhomogeneity.

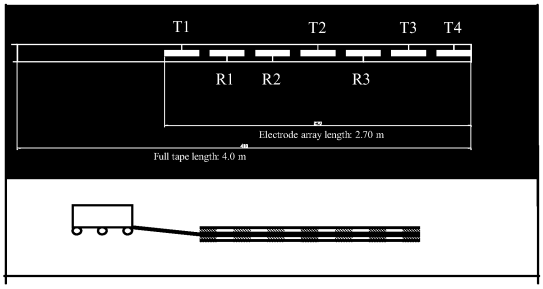

Figure 6. Multi-electrode MI probe PP7

A prototype of such a multi-electrode flat array has been built: it has 7 electrodes (4 transmitting (T1 to T4) and 3 receiving (R1 to R3)), which can be connected to the electronic transmitter and receiver (Fig.6). There are 18 different quadrupole

combinations including two classical Wenner arrays (T1T2 – R1R2) and (T1T4 – R2R3). The electronic system consists of a PC with DAC and ADC cards and two emission and reception analogical interface circuits that drive the guards and control the commutations to the different electrodes. The system is in late phase of achievement.

PP7 has been built in the scope of future long-range Mars rover missions. It is one of the options for permittivity measurements proposed in WISDOM for the PASTEUR program. The challenge is the detection of ice in the sub-surface of Mars. Ice should be present at medium latitudes under an upper layer of dry regolith (Fig.7). In the range of temperatures of Mars water ice can be identified through the variation of apparent permittivity with frequency as shown in Fig. 8. With the two entangled Wenner arrays of PP7 it will be possible to estimate the upper dry soil permittivity, the depth of the ice rich layer and its ice content [7].

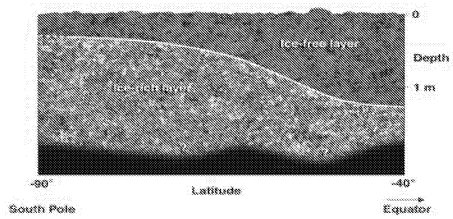

Credit: NASA/JPL/University of Arizona/Los Alamos National Laboratories

Figure 7. Model of the sub-surface of Mars

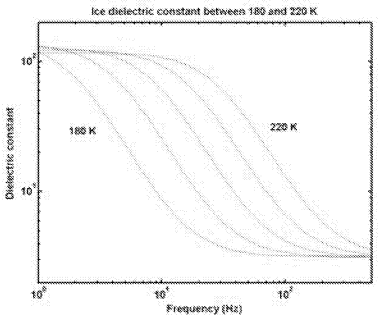

Figure 8. Ice dielectric constant as a function of frequency for Martian temperatures.

The case of Mars raises the problem of the inhomogeneity of the sub-surface. The entangled Wenner arrays configuration of PP7 solves in principle the problem with a two layers model but the reality is probably more complex. The WISDOM electromagnetic instruments are a Permittivity Probe and Ground Penetrating Radars (GPR). A high frequency GPR will sound the same volume of sub-surface than the MI probe. Then there is a synergy between these instruments as the GPR detects the interfaces and allows building precise sub-surface models. On the other hand the Permittivity Probe allows identifying water ice through the dry regolith.

7. CONCLUSION

The design of surface permittivity probes should be improved in future missions by the use of multiple electrode arrays to resolve vertical inhomogeneity and large (but light) flat electrodes to extend the operational range to low frequencies.
The Permittivity Probe is a particularly promising technique to identify water ice under a superficial layer of dry regolith in the case of Mars. As ice would be found at possible drilling depths, a mole holding a small MI probe and other instruments could be sent for in situ detection. The combination of MI and GPR measurements as proposed in WISDOM should be highly favourable in future rover missions on Mars. This should be proved by terrestrial tests on various terrains including permafrost.

8. REFERENCES

1. Wenner, F., A method of measuring the Earth resistivity, U.S. Bur. Stand. Bull., Sci. Pap., *25* (12), 469, 1915

2. Grard, R., A quadrupolar probe for measuring the complex permittivity of grounds: Application to Earth prospection and planetary exploration, *Meas. Sci. Tech.*, *1*, 295-301, 1990

3. Tabbagh, A., A. Hesse, and R. Grard, Determination of electrical properties of the ground at shallow depth with an electrostatic quadrupole: field trials on archaeologic sites, *Geophysical Prospecting*, *41*, 579-597, 1993

4. Fulchignoni, M. et al., The Huygens Atmospheric Structure Instrument (HASI), *ESA SP-1177*, 163-176 (1997).

5. Hamelin, M. et al., Surface and sub-surface electrical measurement of Titan with the PWA-HASI experiment on HUYGENS, *Adv. Space Res.*, **26**, pp. 1697-1704, 2000.

6. Trautner, R., F. Simoes, R. Grard and M. Hamelin, A new instrument for measuring the low frequency electrical properties of planetary subsurface materials, *ESA SP,* This issue, 2004.

7. Hamelin, M., R. Trautner and R. Grard, Detection of near-surface ice on Mars with electromagnetic techniques on board future surface vehicles, J. Geophys. Res., 108(E4), 8045, doi:10.1029/2002JE001893, 2003.

Paper 13

A new instrument for measuring the low-frequency electrical properties of planetary subsurface materials

Trautner, R., Simões, F., Grard, R., Hamelin, M.

Proceedings of 37th ESLAB Symposium **ESA SP-543**, 193-196 (2004)

A NEW INSTRUMENT FOR MEASURING THE LOW FREQUENCY ELECTRICAL PROPERTIES OF PLANETARY SUBSURFACE MATERIALS

R. Trautner[(1)], F. Simões[(1)], R. Grard[(1)], M. Hamelin[(2)]

[(1)] ESA/RSSD, ESTEC, Postbus 299, NL-2200 AG Noordwijk ZH, The Netherlands
[(2)] CETP-IPSL, 4 av. de Neptune, 94107, Saint Maur, France
Email: Roland.Trautner@esa.int
Tel. 0031 (0) 71 565 3955 Fax 0031 (0) 71 565 4697

ABSTRACT

Measuring the electrical properties of materials can provide important constraints on the characteristics of planetary environments. Quadrupolar probes are particularly suitable for this measurement due to their flexibility and immunity to interface effects [1]. Flight instruments have been built for atmospheric and surface investigations (Huygens, Rosetta Lander). Atmospheric investigations are comparatively straightforward due to the homogeneity of the medium, but the measurements of surface and shallow subsurface material properties are more difficult due to the variability of composition, stratigraphy, and topography. In general, only the bulk characteristics of surface and subsurface materials can be measured. A limited assessment of the electrical characteristics of individual layers is possible by employing multiple arrays [2]. However, the dimensions of the electrode arrays always limit the spatial resolution of such measurements. The Beagle2 lander onboard the European Mars Express Mission [3] will carry a so-called 'Mole' for the acquisition of subsurface samples [4]. Apart from a temperature sensor, it will not carry any other instrumentation. Future versions of this type of vehicle can provide an attractive platform for the investigation of subsurface material properties. In this paper, we present a quadrupolar probe prototype for accommodation on a Mole-type instrument platform. The measurement principle and the basic architecture of the prototype instrument are explained. Laboratory test results are presented. The accuracy and spatial resolution of the prototype measurements are discussed, and the capabilities of this type of instrument for subsurface investigations are pointed out.

1. MI PRINCIPLE

A mutual impedance probe consists essentially of a sensor array, a current generator and a voltmeter. An alternating (sinusoidal) current I, of frequency ω, is injected between two transmitting electrodes, TX1 and TX2, and induces a voltage A between two receiving electrodes, RX1 and RX2. The frequency is chosen such that the wavelength is much larger than the size of the electrode array. The complex ratio A/I is the mutual impedance of the circuit. If the amplitude and phase of the measured voltage are

A_0, ϕ_0 in a vacuum, and

A, ϕ in a given environment,

the apparent conductivity σ and relative permittivity ε_r of the medium are given by

$$\sigma = \frac{A_0}{A} * \omega * \varepsilon_0 * \sin(\varphi - \varphi_0)$$

and

$$\varepsilon_r = \frac{A_0}{A} * \cos(\varphi - \varphi_0), \qquad (1)$$

where ε_0 is the relative permittivity of vacuum. The mutual impedance reflects the bulk properties of the medium. Analytical solutions exist also for configurations where the electrode array is placed on the surface of a liquid or on a locally planar ground.

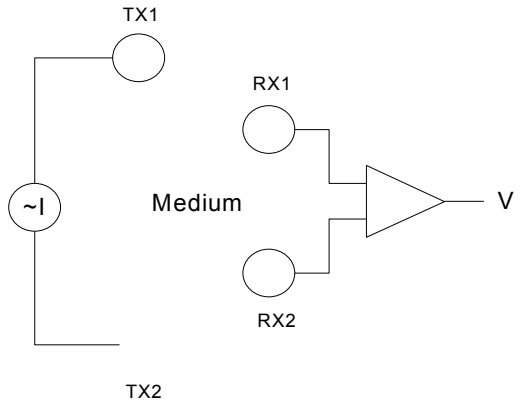

Fig. 1. Principle of Mutual Impedance measurement

2. PROTOTYPE ARCHITECTURE

The subsurface Mutual Impedance Probe prototype consists of the following components:

- The data acquisition system, which comprises a laptop computer and a standard data acquisition card (20 kS/sec, 16-bit, 16 analogue inputs)
- The signal generator, which is an external unit controlled by software (frequency, amplitude, waveform) via a serial interface
- The analogue electronics, which consists of transmitter current measurement circuitry, high impedance amplifiers, differential amplifiers, and temperature sensing electronics
- An electrode carrier, which is a mole shaped aluminium tube with electrode, isolation and guarding layers on its surface. Electrodes are connected to the electronics via coax cables
- Data acquisition and processing software based on MATLAB, which controls the data acquisition hardware and the signal generator

Both the electrode size and distance are in the order of few cm, which determines the spatial resolution of the system. The electrodes of the prototype are radially segmented, which allows testing the instrument's capability for spatially resolved measurements. Table 1 shows the basic characteristics of the prototype. The electrode carrier and the analogue electronics are shown in Figure 2.

parameter	Value
length	400 mm
diameter	38 mm
TX electrode areas	3 cm^2 and 12 cm^2
RX electrode areas	3 cm^2 and 12 cm^2
Frequency range *	16 Hz – 4096 Hz
Electronics mass **	ca. 27g
Electrodes + insulator mass	ca. 10g + 20g
Accuracy ***	~ 20%
Temperature Range	- 60 to +125 ºC
ADC resolution	16 bit
Maximum power consumption	80 mW

* limited by DAQ card, ~ 5 Hz to >100 kHz range is possible for analogue electronics

** analogue electronics

*** with current calibration models, for σ in the order of 10^{-8} S/m

Table 1. MI mole prototype characteristics

The selected prototype architecture allows modifying various hardware characteristics such as electrode size, shape and number, as well as the geometry of the guarding configuration. The electronics allows fast modifications of parameters like input stage amplification, amplifier bandwidth, differential amplifier gain, and transmitter current measurement range. A temperature sensor is integrated on the printed circuit board, and a second sensor can be connected for measuring the temperature of the medium.

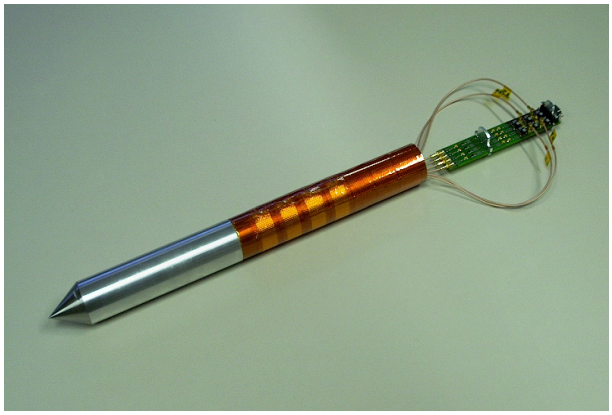

Fig. 2. Subsurface Mutual Impedance Probe prototype

3. CALIBRATION

While in theory the calculation of conductivity and permittivity according to (1) is straightforward, all real implementations of quadrupolar probes suffer from a number of parasitic effects, which have an important impact on the accuracy of the measurement. Optimized guarding systems and careful design of the instrument electronics can reduce the parasitic effects, but they cannot be eliminated completely. Therefore, the impact of these effects needs to be modeled and taken into account for the calibration of measurement data. The introduction of correction factors for amplitude and phase in (1) yields

$$\sigma = \frac{A_0 * k_{A0}}{A * k_A} * \omega * \varepsilon_0 * \sin(\varphi - k_\varphi - \varphi_0 + k_{\varphi 0})$$

and

$$\varepsilon_r = \frac{A_0 * k_{A0}}{A * k_A} * \cos(\varphi - k_\varphi - \varphi_0 + k_{\varphi 0}) \qquad (2)$$

The amplitude and phase correction factors k_{A0}, k_A, k_φ and $k_{\varphi 0}$ depend on the medium conductivity and permittivity. Since these parameters are the ones to be measured using the technique employed here, the data calibration involves an iterative process, which yields the calibrated measurement result if convergence is

achieved. This is only possible if the circuit models used for calculating the correction factors are sufficiently representative. For instrument architectures that involve close proximity of transmitter electrodes, receiver electrodes, and grounded structures, accurate circuit modelling is essential for achieving acceptable measurement results. Figure 3 shows a typical convergence process for a single measured data point.

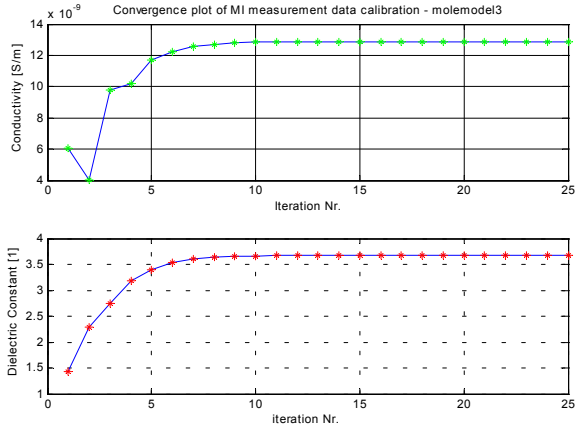

Fig. 3. Iterative calibration process convergence

4. TEST RESULTS

A number of initial tests of the mole prototype have been carried out in order to verify its proper function, and to assess its initial performance and its individual characteristics. Calibration measurements have been performed in air (as a substitute for vacuum), and in a fully guarded configuration in order to characterize the transmitter electrodes and electronics. Additional tests have been carried out in a low conductivity medium with direct (DC) contact of transmitter electrodes and medium in order to assess the electrical field configuration along the electrode array surface. Based on the data obtained during these measurements, representative circuit models have been developed and implemented in MATLAB. These models are employed by the calibration software in order to compensate parasitic effects. The MI mole prototype was tested using materials such as polyethylene, quartz glass beads, and JSC-1 Mars soil simulant [5,6]. Measurement data was acquired at 16, 32, 64, 128, 256, 1024, 2048, and 4096 Hz. At each frequency, the results from a number of measurements were averaged in order to reduce the effect of noise and interference from external sources. Correction factors for signal amplitude and phases were calculated and applied, and the measurement results for conductivity and dielectric constant were calculated according to (2). Figure 4 and Figure 5 show the calibrated measurement results for a test where the instrument was embedded in a container filled with quartz glass beads. The squares show the prototype measurement results after calibration. The triangles show the results of a reference measurement using the plate capacitor technique [5]. The measurement error with respect to the reference measurement is ~ 20 % on average. The main error sources that have been identified so far are the current measurement circuitry, the phase measurement accuracy, the accuracy of the representative circuit models, and various parasitic capacitances affecting the receiver electrodes.

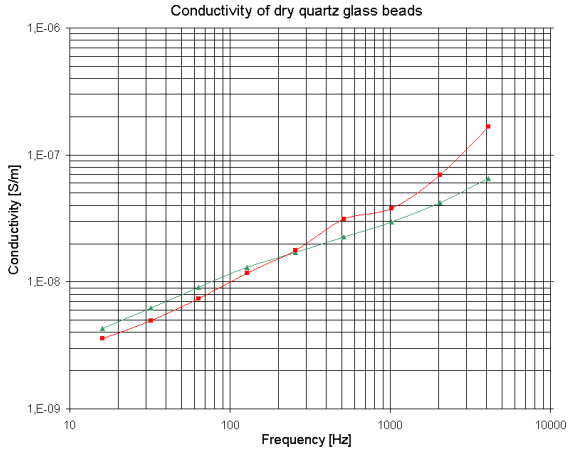

Fig. 4. Conductivity measurement results for quartz glass beads (calibrated)

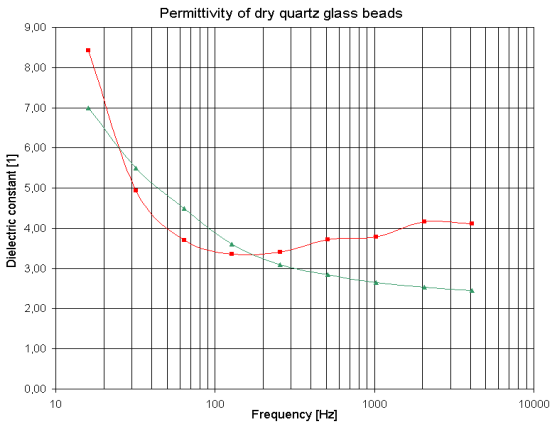

Fig. 5. Permittivity measurement results for quartz glass beads (calibrated)

5. INSTRUMENT CAPABILITIES

The accommodation of the quadrupolar electrode array on the mole surface allows performing measurements along the penetration path of the mole. The depth resolution is determined by the size of the electrode

array along the mole axis, which is in the order of 5 cm. Further miniaturization of the electrode array is possible but increases the impact of the parasitic effects, which decrease the measurement accuracy.
The electrodes areas on the prototype are radially divided into one 90 degree segment and a second 270 degree segment, which allow measurements in individual sectors perpendicular to the mole axis. The measurement data presented here was acquired using the smaller electrode segment.
If an electrode array of equally sized sectors is employed, the resulting measurement data can be represented as a two-dimensional electrical property map. This technique called 'electrical imaging' is used in geophysics applications for mapping the subsurface material conductivity along boreholes [7]. The resulting map represents the electrical properties of the surface and subsurface material along the mole path, and can provide important information not only on the profiles of electrical properties versus depth, but also on the spatial homogeneity of the subsurface, and the approximate size and distribution of buried objects. These measurements can be performed in a wide frequency range, which allows a further discrimination with respect to the composition of subsurface materials, for example the distinction of water bearing materials from dry ones.
The conductivity measurement range of the instrument is determined by the current measurement electronics and comprises several orders of magnitude. The frequency range is limited by the capabilities of the data acquisition card, which allows sampling frequencies up to 10 kHz for the number of data channels used in the prototype. The analogue electronics can be used for frequencies of few Hz to more than 100 kHz. For future flight instruments, the measurement range can be optimized easily for the expected range of surface material properties.

6. CONCLUSIONS

Quadrupolar probes can measure the electrical properties of a medium without being sensitive to interface effects. Flight instruments have been built for atmospheric and surface investigations (Huygens, Rosetta Lander). Future planetary missions are expected to provide instrument platforms for measurements under the surface, such as instrumented Moles and penetrating devices. A subsurface Mutual Impedance Probe prototype has been developed at ESA/ESTEC using standard data acquisition hardware and analogue electronics based on the Rosetta Lander permittivity probe. Data acquisition and calibration software has been implemented based on MATLAB. Various parasitic effects, which affect the measurement accuracy, need to be assessed and implemented in representative models in order to compensate their effects. Initial testing of the prototype, the representative circuit models and the corresponding software has been performed successfully, and the results have been verified by independent measurements based on the plate capacitor technique. The initial accuracy achieved is in the order of 20%. This result confirms that Mutual Impedance probes with surface mounted electrode arrays can be used for the measurement of the electrical properties of subsurface materials. An array of segmented electrodes on the outer surface of a mole will allow measuring the electrical properties of subsurface materials along the penetration path of the mole, and providing information on the spatial homogeneity of the subsurface with a resolution similar to the size of the electrode array. A number of areas for possible improvements have been identified, and the prototype development is continued towards future flight instruments.

7. REFERENCES

1. R. Trautner, R. Grard, and M. Hamelin, *Detection of subsurface ice and water deposits on Mars with a mutual impedance probe*, JGR Planets 108,8045, 2003.

2. R. Trautner, F. Simões, *Detection and Characterization of Ice and Water on Mars by means of Mutual Impedance Probes on Surface and Subsurface Vehicles*, ESA SP-518, 2002.

3. A. Chicarro, P. Martin, R. Trautner, *Mars Express – Unravelling the scientific mysteries of the red Planet*, ESA Bulletin Nr. 115, p18-25, 2003.

4. M.R. Sims et al., *Instrumentation on Beagle 2: The Astro-Biology Lander on ESA's 2003 Mars Express Mission*, SPIE Proceedings, 4137, p36-47, 2000.

5. C. C. Allen, R. V. Morris, D. J. Lindstrom, and J. P. Lockwook, *JSC Mars-1 - Martian regolith simulant*, Conf. paper, Houston, Texas, 16-20 March, 1997.

6. C. C. Allen, R. V. Morris, K. M. Jager, D. C. Golden, D. J. Lindstrom, M. M. Lindstrom, and J. P. Lockwook, *Martian regolith simulant JSC Mars-1,* 29th Annual Lunar and Planetary Science Conference, Houston, Texas, USA, Abstract #160, 1998.

7. F. Simões, R. Trautner, R. Grard, and H. Hamelin, *Laboratory measurements on Martian soil simulant JSC Mars-1 supporting the calibration of instruments for planetary missions*, this issue, 2004.

8. S. M. Luthi, *Geological Well Logs. Their Use in Reservoir Modelling,* Springer Verlag, Berlin-Heidelberg, 2001.

Paper 14

Laboratory measurements on Martian soil simulant JSC Mars-1: supporting the calibration of instruments for planetary missions

Simões, F., Trautner, R., Grard, R., Hamelin, M.

Proceedings of the 37th ESLAB Symposium **ESA SP-543**, 205-209 (2004)

LABORATORY MEASUREMENTS ON MARTIAN SOIL SIMULANT *JSC MARS-1* SUPPORTING THE CALIBRATION OF INSTRUMENTS FOR PLANETARY MISSIONS

F. Simões[1], R. Trautner[1], R. Grard[1], and M. Hamelin[2]

[(1)] ESA/RSSD, ESTEC, Postbus 299, NL-2200 AG Noordwijk ZH, The Netherlands
[(2)] CETP – Observatoire de Saint Maur, 94107, Saint Maur des Fossés cedex, France
(Fernando.Simoes@esa.int / Fax: +31 71 565 4697)

ABSTRACT

The concentration of water in the Martian regolith is an important parameter in many scientific domains. The abundance and distribution of water in the atmosphere and under the surface of Mars have fundamental significance for the geological, hydrological and climatic history of the planet. Furthermore, water is a fundamental ingredient of life and represents an important potential resource for future manned missions. Water possesses an electrical signature that allows the identification of its presence among other materials, even at very low concentrations. Not only the permittivity, but also the conductivity of permafrost and water-bearing rocks depends upon the presence of water. A laboratory facility has been set up to measure the complex permittivity of soil mixtures as a function of porosity, humidity, and temperature in the frequency range 10 Hz – 10 kHz. The experimental technique is presented and the results obtained with the *JSC Mars-1* soil simulant are discussed. A measurable gravimetric water content threshold is evaluated. The measurement of the dielectric properties of soil analogues allows estimating conductivity and permittivity of the Martian regolith, and supports the design of instruments for the detection of water and ice.

1. MEASUREMENT PRINCIPLE

The dielectric properties of materials can be measured in many ways, depending upon the frequency range. At frequencies below ~100 Hz, ultra low frequency bridges or DC transient systems are preferred. In the range 10 Hz – 10 MHz, auto balancing or Schering bridges are indicated. At higher frequencies, resonant circuits, coaxial lines, re-entrant cavities, cavity resonators and waveguides are more appropriate. In this work we apply the parallel plate capacitor technique between 10 Hz and 10 kHz, and use a circuit with an RC configuration [1]. The minimum experimental setup consists, in principle, of a wave generator, an oscilloscope, a parallel plate capacitor, and an RC circuit. The amplitude and phase shift of the signal in the resistor yields the dielectric constant of the material that fills the space between the capacitor plates. In practice, a HP4195A spectrum analyser is more suitable, especially at the lower end of the frequency range, where the phase shift is more susceptible to noise. In order to minimize the spurious capacitance of the circuitry, namely the cables and connectors, two measurements are performed. The capacitor is first short-circuited, and the modulus, or gain (G_o), and phase (φ_o) of the voltage across the resistor R, normalized to that applied between the terminals, are measured. The capacitor is then filled with the material and the new gain and phase, G and φ, are measured. Fig. 1 shows the equivalent circuit of the capacitor filled with the material (M), the spurious capacitive and resistive components (S), and the resistor R, across which the spectrum analyser measures a normalized voltage and phase shift. The spectrum analyser provides a calibration mode, which allows the compensation of gain and phase shift perturbations induced by cables and connectors. Better results are achieved if an external calibration is performed. The R_s and C_s values represent the calibration values. The R_M and C_M values are the resistance and capacitance of the medium, respectively. Although a high measurement resistance R reduces the noise, the measurement error increases due to the parasitic resistor capacitance. Thus, a resistor value of 10 kΩ has been selected in order to keep the resulting errors at a negligible level. The two sets of measurements yield the complex permittivity of the material.

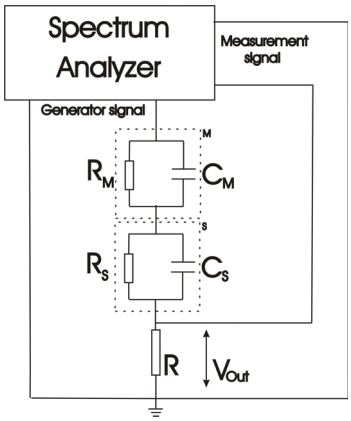

Fig. 1. Setup for calculating the dielectric properties of soils using the plate capacitor technique.

The conductivity and relative permittivity are calculated using

$$\sigma = \frac{\varepsilon_o}{C_o R_M}, \qquad (1)$$

and

$$\varepsilon_r = \frac{C_M}{C_o}, \qquad (2)$$

where ε_o and C_o are the permittivity and the capacitance in vacuum. The resistance and capacitance of the medium that fills the parallel plate capacitor are, respectively, written as

$$R_M = R\alpha\left(1+\beta^2\right), \qquad (3)$$

and

$$C_M = \frac{1}{\omega R}\frac{\beta}{\alpha\left(1+\beta^2\right)}, \qquad (4)$$

where

$$\alpha = \frac{\sin(\varphi_o-\varphi)/G_o - \cos(\varphi_o-\varphi)\sin\varphi_o}{\sin\varphi - \beta\cos\varphi}, \qquad (5)$$

and

$$\beta = \frac{\sin\varphi/G - \sin\varphi_o/G_o + \sin\varphi_o\cos\varphi_o}{\cos\varphi/G - \cos\varphi_o/G_o - \sin^2\varphi_o}. \qquad (6)$$

The plate capacitor has cylindrical geometry with radius of 85 mm and distance between the plates of 10 mm.

The ratio between the imaginary and real parts of the dielectric constant is the loss tangent, or dissipation factor, and is calculated by

$$\tan\delta = \frac{1}{\omega R_M C_M} = \frac{1}{\beta}. \qquad (7)$$

Peaks in the frequency response of the loss tangent reflect internal loss mechanisms at particular frequencies.

2. CALIBRATION

In order to provide an accurate calibration for the experimental setup, several standard tests for conductivity and permittivity have been performed. The conductivity measurement is calibrated with three different media, namely dielectric oil, pure water, and a standard KCl 0.01 mol dm^{-3} solution, which validate conductivity values within several orders of magnitude (from ~10^{-12} Sm^{-1} for oil to ~10^{-1} Sm^{-1} for the KCl solution) in the frequency range 10 Hz – 10 kHz. The measured values fit the theoretical results within an error of 0.5% both for oil and the KCl solution. The discrepancy for pure water is the order of 12%, which might be due to dissolved carbon dioxide, because the conductivity is much higher for CO_2 saturated water (~10^{-4} Sm^{-1}) than for pure water (5.5 × 10^{-6} Sm^{-1}, at 25°C) [2].

The permittivity calibration is made with the dielectric oil used in the conductivity calibration, pure acetone, and pure water. The error is 0.5% and 0.8% for oil and acetone, respectively. In acetone, permittivity was measured at 10 kHz only. The permittivity of pure water increases at extremely low frequencies (below 10 kHz) and does not match the theoretical prediction. However, the calibration measurements at 1 kHz have been confirmed with a RLC meter, with accuracy better than 0.25%. The whole experiment was conducted in a steady nitrogen flow, in a thermal chamber, at a temperature that was varied in steps of 15°C between -55°C and 20°C.

3. PROPERTIES OF *JSC MARS-1* SIMULANT

Estimates of the structure and composition of the Martian surface and interior have been derived from various sources. Figures for the mean density have been obtained from the gravity field by *Reasenberg* [3]. *In situ* measurements have been reported by *Moore* and *Jakosky* [4], who estimated the mechanical properties, grain size, and remote sensing signatures of the surface materials at the Viking landing sites. SNC (Shergottites-Nahklites-Chassigny) meteorites have been analyzed by *Morgan* and *Ander*s [5].

Spectroscopic observations of the surface have yielded the most common minerals, and the chemical composition of the surface, consisting mostly of oxides, has been reported [6].

Some knowledge about the mineralogical and chemical composition of the Martian regolith is a prerequisite for the development of earth-made soil analogues, or simulants. Palagonitic tephra from the *Pu'u Nene* cinder cone, located in the saddle between *Mauna Loa* and *Mauna Kea* volcanoes, in Hawaii, has been often cited as a close spectral analogue to the bright regions of Mars. It is commonly known as the *JSC Mars-1* simulant [7]. Another earth material claimed to be a

good Mars analogue, mainly for exobiological experiments, is found in the desert of Atacama, Chile.
We have selected the *JSC Mars-1* simulant for this experimental investigation. This analogue has already been studied by other experimenters [8]. *Allen et al*. [7] described the properties of the *JSC Mars-1* used in these experiments, namely mineralogy, chemical composition, magnetic properties, and other physical parameters. The water content of *JSC Mars-1* has been modified for the purpose of this work, but the chemical composition of this simulant has not been altered otherwise. The *JSC Mars-1* is highly hygroscopic, and the gravimetric water content (ratio between water content and dry soil in a sample) at the saturation point is about 0.6 for a porosity (ratio between bulk and particle densities) of 0.54. Thermal gravimetry was utilized to measure the water content of samples used in the experiments. Since the Mars soil simulant includes other volatiles, the precise measurement of the water content is difficult. Despite the fact that hydroxides are fully removed above 700°C, free water is eliminated below 200°C [9]. The sample has been heated at 180°C and some bond water may remain, but interlayer water is fully removed. In order to prevent the absorption of atmospheric humidity, the dried soil container remains sealed during the experiments.

4. RESULTS

The measurements are performed using *JSC Mars-1* simulants with different porosity and gravimetric water contents. Soil samples are dried at 180°C for several hours. The water content is modified by spraying distilled water over the desiccated simulant and subsequent mixing. The different porosity values are obtained by vibration compaction of the soil.
Fig. 2 to 5 show how the dielectric properties of the *JSC Mars-1* simulant (conductivity, relative permittivity and loss tangent) vary in the frequency range from 10 Hz up to 10 kHz, for different combinations of temperature (T), porosity (ϕ), and gravimetric water content (θ). The gravimetric water content refers to free water content, because traces of bond water may have remained in the soil. For the sake of clarity, data points severely contaminated by the mains, at 50Hz and harmonics, or by ambient noise, at low frequencies, have been eliminated.
An increase in the relative error of the measurements is observed, if frequency, temperature, or water content is decreased. Although less pronounced, a similar effect is observed when porosity decreases. One explanation for this behavior is that, for high impedance of the material under test, the circuit is more susceptible to interference from external sources.
The electric properties of the dry simulant are illustrated in Fig. 2 for different porosities. At a given frequency, both conductivity and permittivity show a quasi-linear increase with density. At 10 Hz the conductivity is in the order of $(5\pm1)\times10^{-10}$ Sm^{-1}, a value close to that expected for dry rocks without metallic components. For the sake of comparison, the conductivity in a *JSC Mars-1* saturated solution at 10Hz and at room temperature is ~ 5×10^{-4} Sm^{-1}.

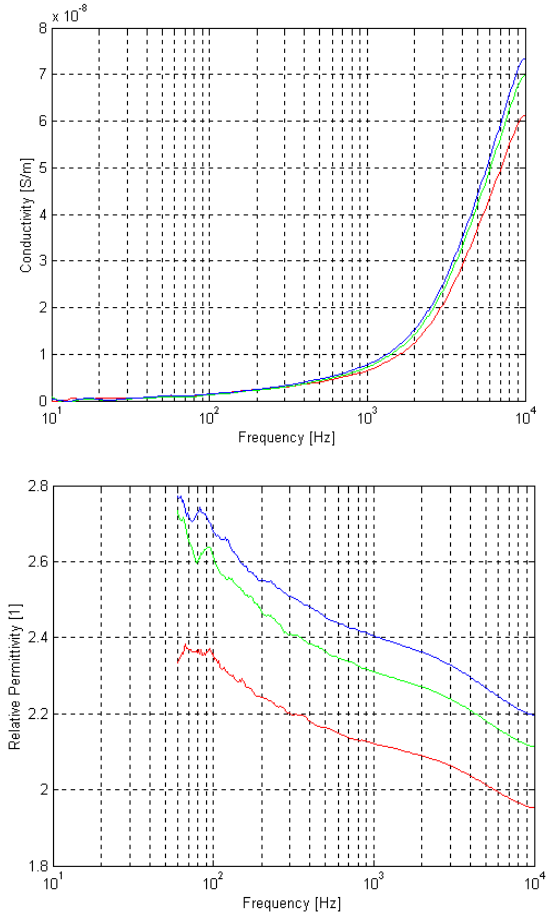

Fig. 2. Conductivity (top) and relative dielectric constant (bottom) of the dry *JSC Mars-1* simulant (θ<0.005), at T=+20ºC, for different porosities: ϕ=0.58 (red), ϕ=0.54 (green), and ϕ=0.52 (blue).

The temperature has been raised from -55°C to 20°C in steps of 15°C, with different gravimetric water contents. The results obtained at -55ºC and -25ºC are reported in Fig. 3 and 4. The results are seen from another perspective in Fig. 5, where the dielectric constant is plotted against frequency, with temperature as a parameter, for two selected values of the gravimetric water content. Quantitative results are illustrated in Tables 1 and 2.
Water content and temperature both increase the conductivity and permittivity of the soil simulant. This effect is mostly conspicuous when the gravimetric water content is larger than 0.05; below this threshold,

the electric properties of *JSC Mars-1* are not very sensitive to moisture and temperature.

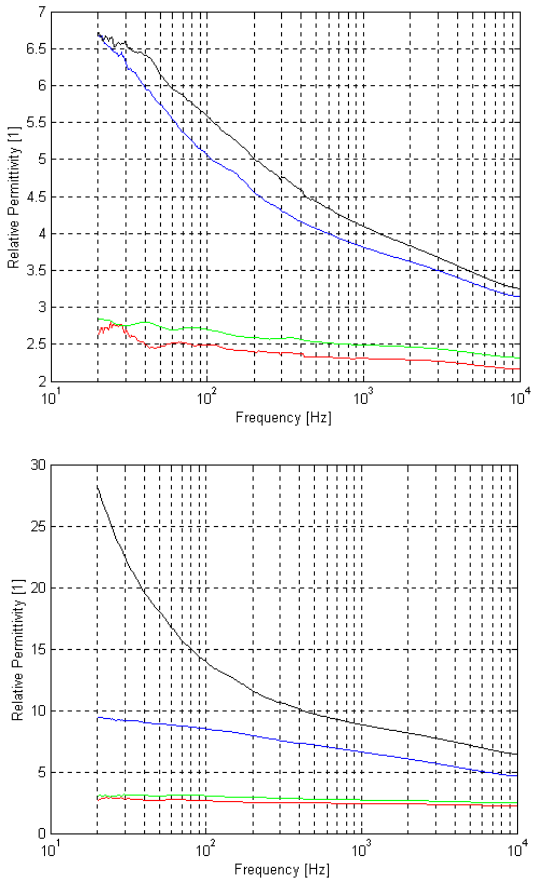

Fig. 3. Relative dielectric constant of the *JSC Mars-1* simulant as function of frequency, at ϕ=0.54, with different gravimetric water contents: θ<0.005 (red), θ=0.01 (green), θ=0.05 (blue), and θ=0.1 (black). T=-55°C (top) and T=-25°C (bottom).

Gravimetric water content	Frequency		
	20Hz	300Hz	10kHz
<0.005	5×10^{-10}	2.1×10^{-9}	1.8×10^{-8}
0.1	2.2×10^{-9}	8.3×10^{-8}	2.9×10^{-7}

Tab. 1. *JSC Mars-1* conductivity [Sm^{-1}] at –55°C for a porosity of 0.54.

Gravimetric water content	Frequency		
	20Hz	300Hz	10kHz
<0.005	2.7	2.4	2.2
0.1	6.7	4.7	3.3

Tab. 2. *JSC Mars-1* relative permittivity at –55°C for a porosity of 0.54.

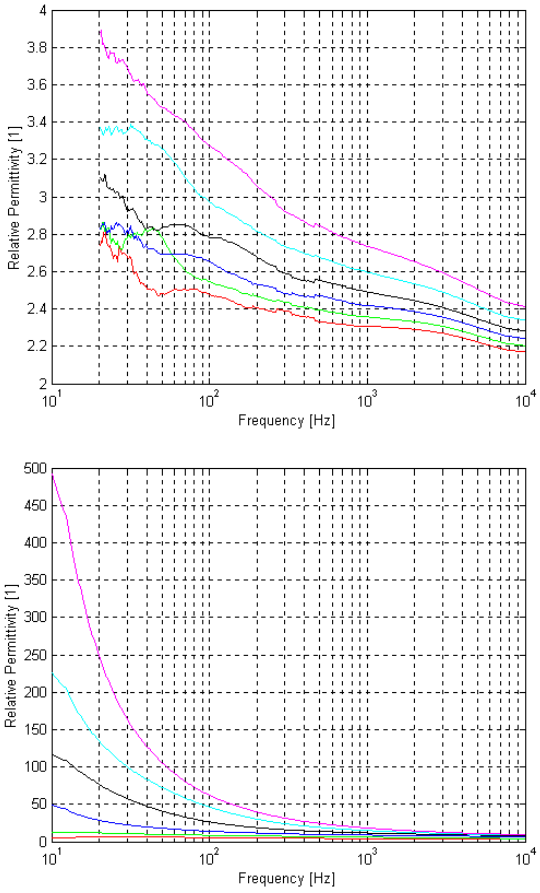

Fig. 4. Relative dielectric constant of the *JSC Mars-1* simulant with gravimetric water contents θ<0.005 (top) and θ=0.1 (bottom), as functions of frequency, for ϕ=0.54 and temperatures: T=-55°C (red), -40°C (green), -25°C (blue), -10°C (black), +5°C (cyan), and +20°C (magenta).

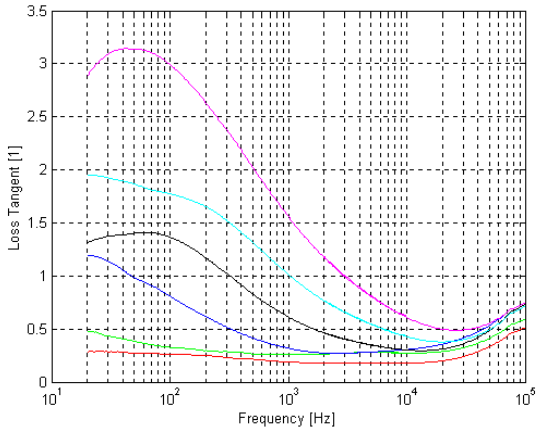

Fig. 5. Loss tangent of the *JSC Mars-1* simulant, for θ=0.1, ϕ=0.54 and temperature: T=-55°C (red), -40°C (green), -25°C (blue), -10°C (black), +5°C (cyan), and +20°C (magenta).

Plotting the loss tangent reveals new signatures whose complexities deserve further analysis. Two features, at least, are readily visible. The loss tangent increases

with the water content and temperature. Note, however, that the general ordering of the curves is different for θ=0.05 [1]. The study of these features may help to clarify which processes are at work in this frequency range.

5. CONCLUSIONS

The electrical properties of *JSC Mars-1* have been measured using the plate capacitor technique for different combinations of porosity, temperature, and gravimetric water content, in the extreme low frequency range 10 Hz – 10 kHz.

The expected behavior is observed, namely an increase of dielectric constant and conductivity when porosity decreases. The plots of *tan* δ for the different porosities show two loss peaks, at 150Hz and 6.5kHz, reflecting the possibility of two different polarization mechanisms are involved.

The permittivity of the *JSC Mars-1* mixtures increases with temperature at low frequencies, a behavior that is not in line with the predictions of standard models for gases and liquids, namely *Debye* and *Kirkwook* equations. The observed behavior of *JSC Mars-1* does not match pure water ice predictions [1, 10].

Mantovani and *Calle* [11] performed a similar experiment to measure the dielectric properties of the *JSC Mars-1* simulant at room temperature and at low pressure. They reported values for the bulk permittivity (~ 2.61 at 10 Hz, ~ 2.33 at 100 Hz, ~ 2.15 at 1 kHz, and ~ 1.89 at 10 kHz), which are in qualitative agreement with our results, but the lack of information about the porosity of the simulant used by these authors prevents any quantitative comparison.

The analysis of the *JSC Mars-1* loss tangent with varying temperature and water content shows an intricate behavior, proving that several concurrent polarization and conduction mechanisms are at work (peaks at ~100 Hz and above 100 kHz). A general increase of the loss tangent with water content is observed.

As expected from the theoretical results, this experiment confirms that both permittivity and conductivity increase when the water content increases and the porosity is reduced.

There are no pronounced changes in conductivity or permittivity as long as the gravimetric water content remains below 0.01, but gravimetric water content of 0.05 gives rise to unmistakable effects. This finding quantifies the lowest possible water concentration that can significantly modify the electrical properties of a planetary surface and be possibly detected *in situ* by instruments carried by landers and rovers [12]. It can be anticipated that the large diurnal variation of the Martian surface temperature will induce changes, possibly minute, that will reveal water contents at a level of a few percent.

6. REFERENCES

1. F. Simões , R. Trautner, R. Grard, and M. Hamelin, *The Low Frequency Electrical Properties of the Martian Soil Simulant JSC Mars-1 as Functions of Temperature, Porosity, and Water Content,* J. Geophys. Res., submitted, 2003.

2. D. R. Lide, *Handbook of Chemistry and Physics*, 83rd Edition, CRC Press, 2002.

3. R. D. Reasenberg, *The moment of inertia and isostasy of Mars*, J. Geophys. Res., 82, 369-375, 1977.

4. H. J. Moore, and B. M. Jakosky, *Viking landing sites, remote-sensing observations, and physical properties of Martian surface materials*, Icarus, 81, 164-184, 1989.

5. J. W. Morgan, and E. Anders, *Chemical composition of Mars*, Geochim. Cosmochim. Acta, 43, 1601-1610, 1979.

6. J. F. Bell, T. B. McCord, and P. D. Owensby, *Observational evidence of crystalline iron oxides on Mars*, J. Geophys. Res., 95, 14447-14461, 1990.

7. C. C. Allen, R. V. Morris, K. M. Jager, D. C. Golden, D. J. Lindstrom, M. M. Lindstrom, and J. P. Lockwook, *Martian regolith simulant JSC Mars-1,* 29th Annual Lunar and Planetary Science Conference, Houston, Texas, USA, Abstract #160, 1998.

8. C. D. Cooper, and J. F. Mustard, *Spectroscopy of loose and cemented sulfate-bearing soils: Implications for duricrust on Mars*, Icarus, 158, 42-55, 2002.

9. A. Yen, B. Murray, and G. Rossman, *Water content of the Martian soil: Laboratory simulations of reflectance spectra*, J. Geophys. Res., 103, 11125-11133, 1998.

10. V. F. Petrenko, and R. W. Whitworth, *Physics of Ice*, Oxford Univ. Press, Oxford, 1999.

11. J. G. Mantovani, and C. I. Calle, *Measurement of the Dielectric Properties of Granular Materials*, Proceedings of the ESA-IEEE Joint Meeting on Electrostatics 2003, Laplacian Press, Morgan Hill, CA, 688-693 (2003).

12. R. Trautner, F. Simões, R. Grard, and H. Hamelin, *A new instrument for measuring the low frequency electrical properties of planetary subsurface materials*, this issue, 2004.

Paper 15

The dielectric properties of Martian soil simulant JSC Mars-1 in the frequency range from 20 Hz to 10 kHz

Simões, F., Trautner, R., Grard, R., Hamelin, M.

Lunar and Planetary Science Conference **35** (2004)

THE DIELECTRIC PROPERTIES OF MARTIAN SOIL SIMULANT *JSC MARS-1* IN THE FREQUENCY RANGE FROM 20Hz TO 10kHz.

F. Simões[1], R. Trautner[1], R. Grard[1] and M. Hamelin[2]

[1]Research and Scientific Support Department, ESA/ESTEC, Keplerlaan 1, 2201 AZ Noordwijk, The Netherlands
[2]CETP, Observatoire de Saint Maur, 94107, Saint Maur des Fossés cedex, France (Fernando.Simoes@esa.int).

Introduction: The concentration of water in the Martian regolith is an important parameter in many scientific domains. Water possesses an electrical signature that allows the identification of its presence among other materials, even in low quantities. A laboratory facility has been setup to measure the complex permittivity of soil mixtures as a function of porosity, humidity, and temperature in the frequency range 20 Hz – 10 kHz. The influence of porosity and temperature are discussed, and a measurable gravimetric water content threshold is evaluated.

Measurement Setup: The dielectric properties of materials can be measured in many ways, depending upon the frequency range. In this work we apply the parallel plate capacitor technique between 20 Hz and 10 kHz, and use a circuit with an RC configuration [1]. A spectrum analyzer is used to measure the amplitude and phase shift of the signal injected in the material that fills the space between the capacitor plates. In order to minimize the impact of spurious capacitances of the circuitry associated to cables and connectors, two measurements are required. First, a calibration measurement is performed involving only the equipment in order to allow the elimination of errors caused by parasitic effects. A second measurement performed on a sample of the material under investigation provides data for the calculation of its conductivity and permittivity. In order to provide an accurate calibration for the experimental setup, several standard tests for conductivity and permittivity have been performed, namely with dielectric oil, pure water, acetone, and a KCl solution (0.01 mol dm^{-3}). The whole experiment was conducted under a steady nitrogen flow in a thermal chamber. The temperature was varied in steps of 15°C from -55°C to 20°C.

Properties of JSC Mars-1 simulant: Estimates of the structure and composition of the Martian surface and interior have been derived from various sources, and have allowed the development of soil analogues. One of the most common Mars soil simulants is known as *JSC Mars-1* [2], and was used in the experiments described here. The water content of *JSC Mars-1* has been modified for the purpose of this work, but the chemical composition of this simulant has not been altered otherwise. *JSC Mars-1* is highly hygroscopic, and the gravimetric water content at the saturation point is about 0.6 for a porosity of ϕ=0.54. Thermal gravimetry was utilized to measure the water content of the samples. Despite the fact that hydroxides are fully removed only above 700°C, free water can be eliminated below 200°C [3]. The sample has been heated to 180°C, thus interlayer water is fully removed. In order to prevent the absorption of atmospheric humidity, the dried soil container remained sealed during the experiments.

Results and Discussion: The measurements were performed using *JSC Mars-1* simulants with different porosity and gravimetric water contents. Figure 1 and Figure 2 show how the permittivity of the *JSC Mars-1* simulant varies in the frequency range from 20 Hz up to 10 kHz, with a porosity of ϕ=0.54, for different combinations of temperature (T) and gravimetric water content (θ).

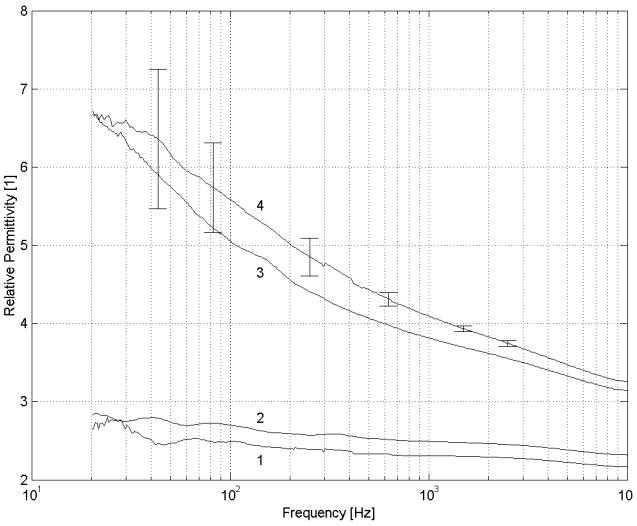

Figure 1. Relative dielectric constant of the *JSC Mars-1* simulant as function of frequency, at ϕ=0.54, with diferent gravimetric water contents: θ<0.005 (1), θ=0.01 (2), θ=0.05 (3), and θ=0.1 (4) for T=-55°C.

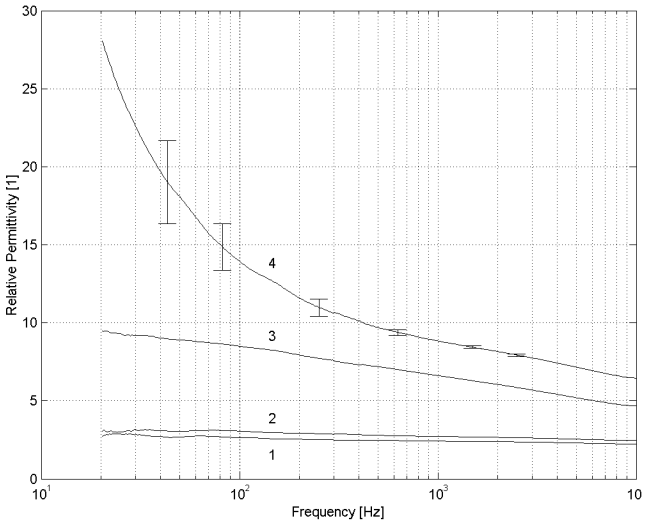

Figure 2. Relative dielectric constant of the *JSC Mars-1* simulant as function of frequency, at ϕ=0.54, with diferent gravimetric water contents: θ<0.005 (1), θ=0.01 (2), θ=0.05 (3), and θ=0.1 (4) for T=-25°C.

Additional results can be found elsewhere [1, 4]. At 20 Hz the conductivity of *JSC Mars-1* is the order of 5×10^{-10} Sm^{-1}, a value close to that expected for dry rocks without metallic components. For the sake of comparison, the conductivity in a *JSC Mars-1* saturated solution at 20 Hz and at room temperature is ~ 5×10^{-4} Sm^{-1}. An increase of dielectric constant and conductivity is observed when porosity decreases. The plots of loss tangent for the different porosities show two loss peaks, at 15 Hz and 6.5 kHz, reflecting the possibility that two different polarization mechanisms are involved [1]. The analysis of the *JSC Mars-1* loss tangent with varying temperature and water content shows an intricate behavior, proving that several concurrent polarization and conduction mechanisms are at work (peaks at ~100 Hz and above 100 kHz). A general increase of the loss tangent with water content is observed.

Conclusions: Water content and temperature both increase the conductivity and permittivity of the soil simulant. This effect is mostly conspicuous when the gravimetric water content is larger than 0.05; below this threshold, the dielectric properties of *JSC Mars-1* are not very sensitive to changes in moisture and temperature. A similar experiment has been performed to measure the dielectric properties of the *JSC Mars-1* simulant at room temperature and at low pressure [5], and those values are in qualitative agreement with our results at room temperature, but the lack of information about the porosity of the simulant used by those authors prevents any quantitative comparison. As expected from the theoretical results, this experiment confirms that both permittivity and conductivity increase when the water content increases and when the porosity is reduced.

There are no pronounced changes in conductivity or permittivity as long as the gravimetric water content remains below 0.01, but gravimetric water content of 0.05 gives rise to unmistakable effects. This finding quantifies the lowest possible water concentration that can significantly modify the electrical properties of a planetary surface and be possibly detected *in situ* by instruments carried by landers and rovers [6]. It can be anticipated that the large diurnal variation of the Martian surface temperature will induce changes, possibly minute, that will reveal water contents at a level of a few percent.

Although data analysis is very difficult at extreme low frequencies due to complex conductivity mechanisms and strong temperature dependence, these qualitative results indicate that water and ice can be detected among other materials, even at low contents, namely in the Martian regolith.

References: [1] Simões, F. et al. (2003) submitted to *JGR*. [2] Allen, C. C. et al. (1998), *LPS* XXIX, 160. [3] Yen, A. et al. (1998) *JGR* 103, 11125-11133. [4] Simões, F. et al. (2003) to be published in *ESLAB37*, ESA-SP. [5] Mantovani, J. G. and C. I. Calle (2003), Proc. *ESA-IEEE* Joint Meeting on Electrostatics, 688. [6] Trautner, R. et al. (2003) to be published in *ESLAB37*, ESA-SP.

Paper 16

Subsurface permittivity probe to detect water/ice in planetary environments

Simões, F.

ESA-ESTEC, Internal Report, December 2004, revised version (2004)

Subsurface Permittivity Probe to Detect Water/Ice in Planetary Environments

F. Simões

(Planetary Missions Division, RSSD, ESA-ESTEC)
(Revised version – December 2004)

Abstract

The concentration of water in the Martian regolith is an important parameter in many scientific domains, namely geophysics, atmospheric dynamics, and exobiology. Therefore, development of appropriate space instrumentation to measure the water/ice content of the regolith is a major objective for understanding Mars history. Additionally, water is an essential resource regarding human exploration of the red planet. In this work, there are presented the scientific rationale and technical requirements of a mutual impedance probe developed for in situ measurements of soil dielectric properties at shallow depths. The project also includes the study, development, assembly, and calibration of a subsurface permittivity probe that is suitable not only to evaluate the gravimetric water content of the regolith but to perform stratigraphic investigations.

Water possesses an electrical signature that allows the identification of its presence among other materials, even in low quantities. Initially, there are presented the scientific objectives regarding water ice detection at shallow depths and the latest developments about this research topic. Subsequently, there are described physical and chemical properties of the water molecule, such as polarization mechanisms, that play a role in dielectric properties measurements; the contributions of frequency, temperature, and soil composition effects are discussed. Then, there are presented the most significant components of the prototype, including electrodes architecture, analogue electronics, data acquisition card, control system, signal processing algorithms, and data analysis. Finally, there are presented laboratory experiments that employ Martian soil analogues, mainly the JSC Mars-1 soil stimulant, and discussed the calibration procedures taking into account several parameters, particularly gravimetric water content, medium porosity, grain size, composition, frequency, and temperature. The prototype records 2D electric mapping of assembled stratified media, which are used in stratigraphic capabilities optimization.

The subsurface permittivity probe prototype shows that an instrument with specific characteristics is able to measure gravimetric water contents down to a few percent and, simultaneously, perform stratigraphic studies, including interfaces, thin layers, and dielectric heterogeneities detection.